Methodology investigations for the synthesis of biologically important Nitrogen-containing heterocycles

Thesis presented by

Farhaan Dobah

Towards a *Doctor of Philosophy*

At the University of Cape Town,
Faculty of Science
Department of Chemistry

Supervisor: **Dr Wade F. Petersen**

Plagiarism declaration

1. I know that plagiarism is a serious form of academic dishonesty.
2. I have read the document about avoiding plagiarism, am familiar with its contents and have avoided all forms of plagiarism mentioned there.
3. Where I have used the words of others, I have indicated this by the use of quotation marks.
4. I have referenced all quotations and properly acknowledged other ideas borrowed from others.
5. I have not and shall not allow others to plagiarise my work.
6. I declare that this is my own work.
7. I am attaching the summary of the Turnitin match overview (when required to do so).

Signature _____

Declaration

I, ..., hereby declare that the work on which this thesis is based is my original work (except where acknowledgements indicate otherwise) and that neither the whole work nor any part of it has been, is being, or is to be submitted for another degree in this or any other university. I authorise the University to reproduce for the purpose of research either the whole or any portion of the contents in any manner whatsoever.

Signature: _____ Date: _____

Acknowledgements

The list of incredibly talented and brilliant people who have helped me along this journey is long enough to warrant a thesis of its own. Given the word limit, I must however highlight those whose influence has fundamentally shaped both this thesis and the person it has made me.

To this end I cannot start anywhere but with Kirti B Daya, whose orbit has wholly and completely drawn me in. The best of me has only been drawn out because of you.

My supervisor, Dr Wade Petersen, for his unwavering patience, guidance, support and enthusiasm, even in times they were undeserved. I cannot begin to repay the debt, thank you for taking a chance on me. My mentors who have always given me their valuable time: Daniel Kusza, Myles Smith, James Rossi Ashton, Dr Will Unsworth and James Donald.

My lab mates who have brought joy in the little moments everyday, Munashe Mazodze, Jonathan Da Luz, Megan Oddy, Josef Spath.

My friends, both those who have been there since the day one and anywhere along the way for making Cape Town a true home: Saif Khan, Wayne de Jager, Luke Garrod, Kaelan Lang, Chad EJ Peele, Phillip Ruhesi.

My parents who supported me despite their own reservations.

Thank you.

Abstract

Methodological investigations for the efficient synthesis of two nitrogen-containing heterocyclic molecules are described; these molecules represent a significant portion of the natural and pharmaceutical world with functions implied in almost all biological processes, hence the necessity for their effective synthesis is of importance.

Following an overview of the field in chapters one and two, the third chapter describes the development of a novel, $Mn(OAc)_3$-mediated radical cyclisation-dimerisation cascade sequence for the synthesis of sterically challenging 3,3'-bisoxindoles using two complementary simple, acyclic starting materials; β-oxoanilines and β-oxoacids. This method proved amenable to a variety of modifications to the core molecule, with yields of up to 96% across over twenty substrates bearing a variety of functional groups. Mechanistic insights, based on an exhaustive optimisation study, showcasing an oxidation, de-carboxylation and biradical coupling cascade, forging three C-C bonds in a single step, are also presented.

The second half of chapter three expands on the first, further developing the methodology towards an open-air, dual catalytic Manganese-Cobalt/Copper system. Substrate variation has been demonstrated with the synthesis of five analogues in yields of up to 70% as well biological evaluation of these molecules *in vitro*.

The fourth chapter describes a unique, directed $C(sp^3)$-H functionalisation under mild photoredox conditions, using catalytic amounts of a base, a photocatalyst and 450 nm light to forge the biologically relevant indolyisoxazoline motif. Applicability of this functionalisation has been demonstrated via the synthesis of twenty substrates bearing various functional handles. To conclude, a mechanistic proposal has been presented based on optimisation and substrate data.

Overall, this thesis provides an insight into the utility of both transition metal and photocatalysed radical chemistry and serves to deepen the understanding of the underlying mechanistic pathways for both.

List of abbreviations/symbols

α - alpha

β - beta

δ - delta

π - pi

% - percentage

μL – microlitre

μM – micromolar

℃ - degrees Celsius

4-CzIPN - 2,4,5,6-Tetra(9H-carbazol-9-yl)isophthalonitrile

^{t}OBu – *tert*-butoxide

^{13}C NMR - carbon nuclear magnetic spectroscopy

^{1}H - NMR - proton nuclear magnetic resonance spectroscopy

AcOH - acetic acid

Ar - argon

ACN – acetonitrile

br s - broad singlet

$BrCCl_3$ - bromotrichloromethane

Bu - butyl

Bn – benzyl

Bz - Benzoyl

C–Ar - carbon to aromatic group

C–C - carbon to carbon

C3 - carbon number three

CCl_4 – carbon tetrachloride

CDC - cross dehydrogenative coupling

CH_2Cl_2 – dichloromethane

CH_3Cl – chloroform

COSY – homonuclear correlation spectroscopy

2-CTX - 2-chlorothioxanthone

$Cu(OAc)_2$ – copper (II) acetate

$Cu(OTf)_2$ – copper (II) triflate

d - doublet

dd - doublet of doublets

dt – doublet of triplets

dq – doublet of quartets

dr - diastereomeric ratio

DCE - dichloroethane

DCM - dichloromethane

DIPEA - N, N-Diisopropylethylamine

DMSO - dimethyl sulphoxide

DMF - dimethyl formamide

ee - enantiomeric excess

Et – ethyl

Et_3N - triethyl amine

Et_2O - diethyl ether

Equiv./Eq. – equivalents

EtOAc – ethyl acetate

EtOH – ethanol

eV - electronvolts

g – grams

HAT – hydrogen atom transfer

HCl - hydrochloric acid

HOMO - highest occupied molecular orbital

HPI - hexahydropyrrolo[2,3-b]indole

hr(s)/h(s) - hour(s)

HRMS – high resolution mass spectrometry

HSQC - heteronuclear single quantum coherence or heteronuclear single quantum correlation experiment

hv – energy from a photon

Hz - hertz

Ir - Iridium

IR - infrared

ISC - intersystem crossing

J - coupling constant in *joules*

KHMDS - potassium hexamethyldisilazide

KOH – potassium hydroxide

LED – light emitting diode

$LiAlH_4$ - lithium aluminium hydride

LiHMDS - lithium hexamethyldisilazide

LUMO - lowest occupied molecular orbital

M - molar

m – multiplet

mM - millimolar

Me – methyl

Mes-Acr - mesitylene acridinium

MeO – methoxy

MeOH - methanol

min(s) - minutes(s)

mL - millilitre

MS - mass spectroscopy

MS-PCET - multi-step proton-coupled electron transfer

NaOH - sodium hydroxide

nm – nanometre

nM - nanomolar

NMR - nuclear magnetic resonance

NPhth N-phthalimido

O – ortho

Ox/[Ox] – oxidation

p - para

PC – photocatalyst

PC* - excited state photocatalyst

PET - photo induced electron transfer

PCET – proton-coupled electron transfer

Photoredox - photo reduction and oxidation

ppm - parts per million

PT - proton transfer

q - quartet

RT/rt - room temperature

redox - oxidation and reduction

Ru – ruthenium

s - singlet

SET - single electron transfer

SM - starting material

SN_2 – bimolecular nucleophilic substitution

SOMO - singularly occupied molecular orbital

t – triplet

td – triplet of doublets

tBuOK - potassium tert-butoxide

tBuOOH - tert-butyl hydroperoxide

THF - tetrahydrofuran

TLC - thin layer chromatography

TEMPO - (2,2,6,6-tetramethylpiperidin-1-yl)oxyl/(2,2,6,6-tetramethylpiperidin-1-yl)oxidanyl

Table of Contents

Chapter 1: Introduction

Introduction - Photoredox catalysis

Definition

In its most general description, photoredox catalysis refers to the chemical transformation of a substrate molecule using a catalytic photosensitizer, in the presence of visible light and a terminal redox reagent, required to turn over the catalytic cycle. A general scheme of this process can be seen in **Figure 1.1**; here an electron in the photosensitizer molecule (PC) is promoted to the excited state (PC*) after the absorption of a photon from a visible light source. This excited state species enables the activation of the substrate molecule, via a chemical process (Sub to Sub-A), to undergo unique and novel reactions (Sub-A with a redox reagent (Red)) to give a "product" that would be otherwise extremely challenging under thermal control conditions. The terminal redox reagent produced from the reaction (Red-X) then regenerates the active photosensitizer and the active redox reagent, turning over the cycle and enabling it to begin anew.[1–5]

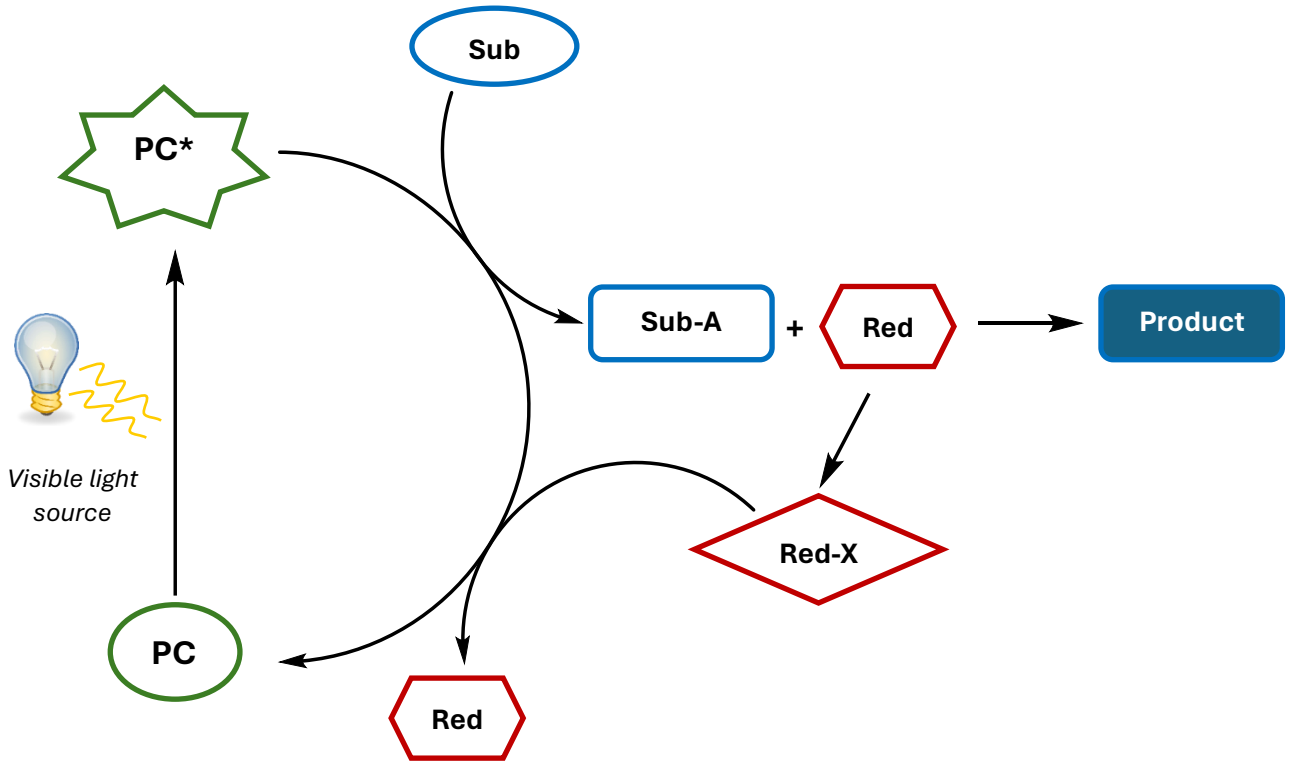

Figure 1.1. General scheme illustrating the concept of photoredox catalysis

History

An Ode to Nature

The concept of photoredox catalysis is not new; nature has long been chemistry's greatest pioneer and in the context of the development of photoredox catalysis, this statement still holds true. At the Earth's surface, the amount of solar energy received in one hour alone, eclipses the total energy consumed from other all sources in one year.[6] Of this irradiated energy, over 40% exists in the form of visible light photons;[7] nature was the first to exploit this abundant energy source through the evolution of Photosynthesis, a process developed over 3 billion years ago,[8] the cornerstone of almost all ecological systems known, which is a prime example of a photoredox catalysis process as seen in **Figure 1.2**.[9]

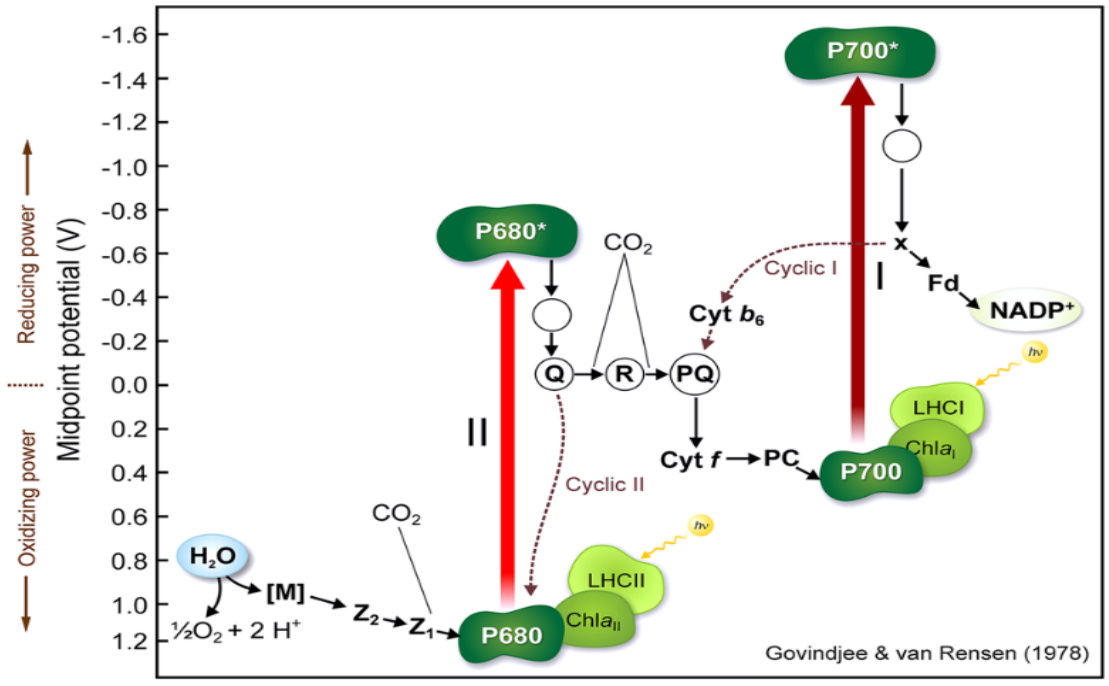

Figure 1.2. A simplified version of the Z-scheme, a light-dependent process, that occurs on the thylakoid membrane in chloroplast of photosynthetic organisms.

Here the general scheme in **Figure 1.2**, can be applied to a specific case. Absorption of visible light by the two photosensitizers (PCs), *P680* and *P700* complexes, promotes an electron to excited states, *P680** and *P700** (PC*), respectively. These excited electrons are transferred along an electron transport chain via a series of mediator molecules

(labelled *Q, R, PQ, Fd, PC* and *Cyt f* and b_6) which ultimately reduces a molecule of $NADP^+$ (the substrate). The cycle is completed via the lysis of H_2O (the terminal redox reagent), regenerating the active photosensitizers.[9] Through this process, photosynthetic organisms are able to harness solar energy, which is the driving force for almost all life on earth.

A Brief History Applied to Organic Synthesis

The turn of this century has been marked by a massive push to utilise renewable energy sources (wind, solar, tidal etc.), over fossil fuels to combat the looming threat of human-driven climate change. To that end, solar energy stands out a consistent, and as previously noted, abundant energy source which nature has provided with a working template for its harnessing. This natural system has been an inspiration to research groups around the world in developing synthetic photoredox systems capable of performing a variety of functions, such as splitting water and storage of energy.[10]

In the context of organic synthesis, it was revolutionary work by Giacomo Ciamician in the 1900s, which was one of the first showcases for the potential power of light-mediated processes. Specifically, he demonstrated the utility of visible light in the hydrolysis of various terpenes and camphors in solution, to high-value products such as isocitronella (**Figure 1.3**).[11]

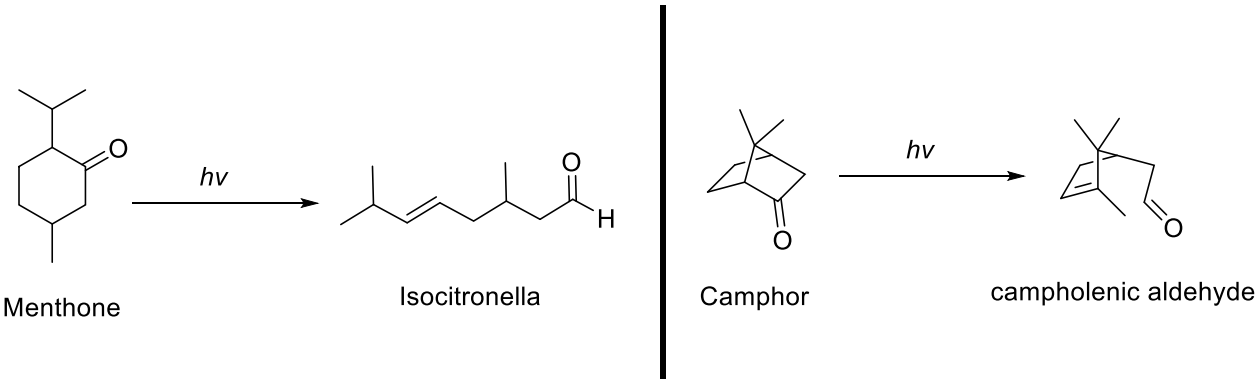

Figure 1.3. An early and influential example of the utility of photo-driven reactions by Ciamican and Silber.[12]

Despite this pioneering work, the development of light-mediated reactions failed to keep pace and there would not be another report on the topic for another 60 years. One of the largest bottlenecks in the development of photoreactions, was the methodology utilised

by scientists of this era, namely the direct irradiation of substrate organic molecules. As most who attempted this came to observe, the inability of many organic molecules employed in synthesis to absorb visible light, was a significantly barrier. Indeed, generation of the required excited states of such molecules required the use of short wavelength, high-energy UV light which were both energy inefficient and expensive.[4,10] Even for those few who were able to circumvent the associated costs, the high energy of the UV photons is a cause for uncontrolled decomposition and fragmentation in organic molecules.[13–15] The combination of these factors stunted the growth of the field up until the 1970s and 80s when photoredox catalysis, in its current form, was realised. The resurgence was driven by the realisation that the molecule, $Ru[(bpy)_3]Cl_2$, could act as a photosensitizer, absorbing visible light and subsequently activating the substrate rather than the direct substrate activation by the light. This was exemplified in work by Kellogg in 1978, on the reduction of sulfonium ions to alkanes and thioethers,[16] as well as by Deronizer and Cano-Yelo in 1984 who reported on the $Ru[(bpy)_3]Cl_2$ catalysed Pschorr reaction in the presence of light (**Figure 1.4**).[17]

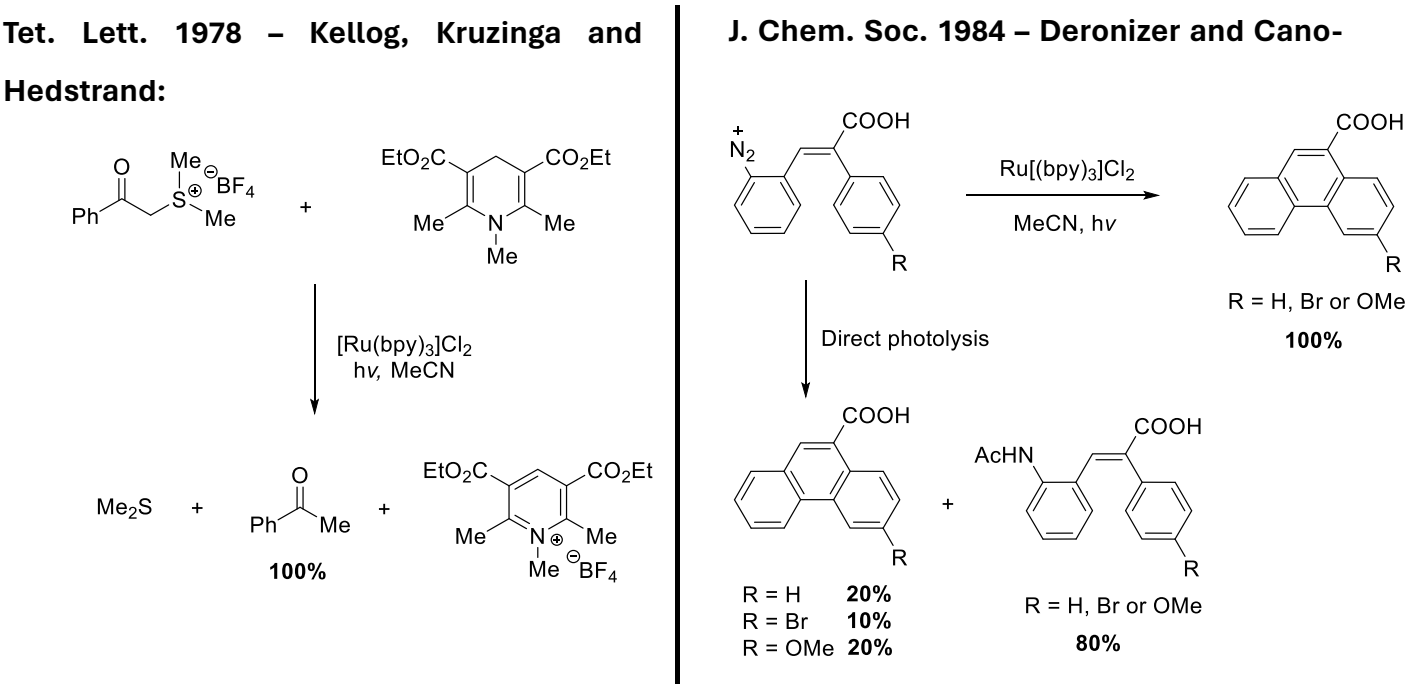

Figure 1.4. $Ru[(bpy)_3]Cl_2$ catalysed Pschorr reaction by Deronizer and Cano-Yelo, showing the superior yield of the phenanthrene relative to direct photolysis in 1984.[10]

Still, publications in the field remained low despite these reports laying a foundation and showcasing the synthetic utility of photoredox catalysis as seen in **Figure 1.5**[18]

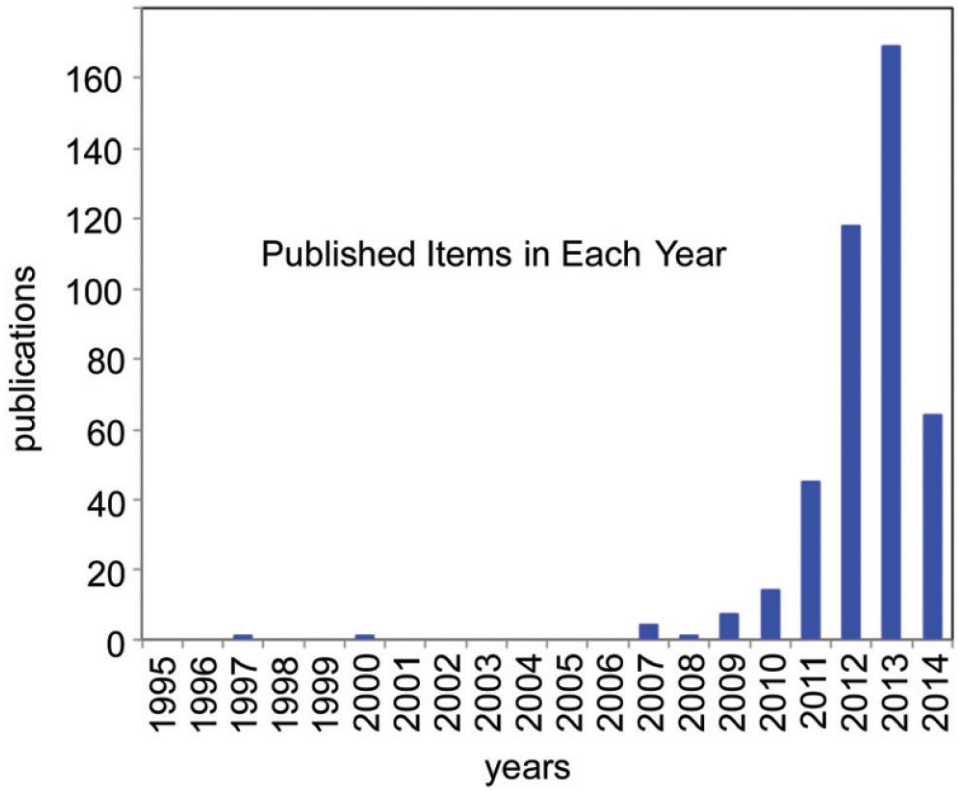

Figure 1.5. Graph showing the number of publications from the years 1995–2014 regarding the study of "Photoredox catalysis".[18]

Finally, in 2008 nearly a century since Ciamician's report, interest in the field exploded and continues to surge to this day. The sharp rise in publications from 2008 can attributed to three seminal reports published by MacMillan,[19] Yoon[20] and Stephenson[21] whose works highlighted the power and potential of photoredox catalysis (**Figure 1.6**).[4]

Science 2008 – MacMillan *et al.*[19]

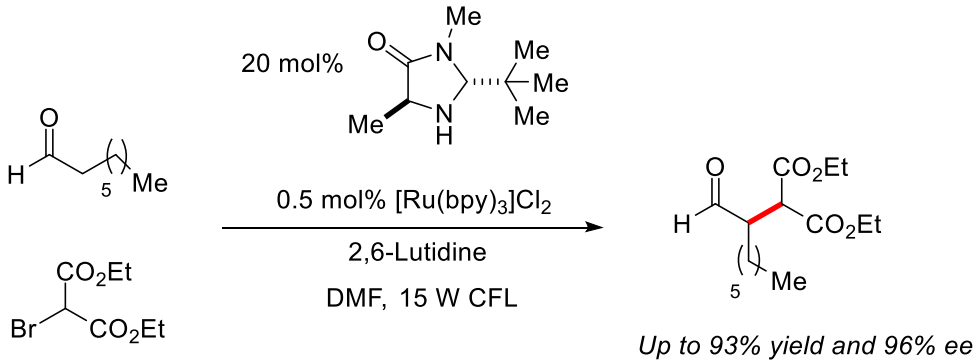

JACS 2008 – Yoon *et al.*[20]

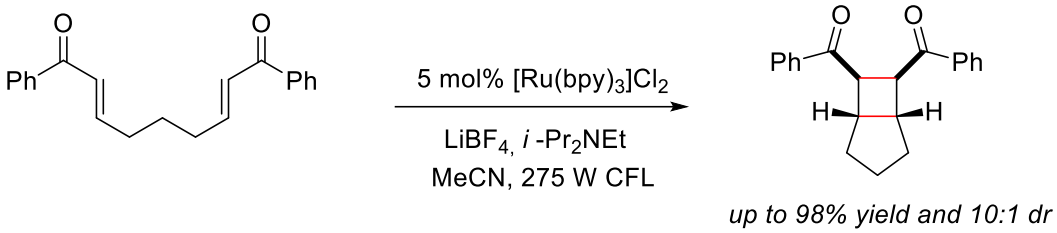

up to 98% yield and 10:1 dr

JACS 2009 – Stephenson *et al.*[21]

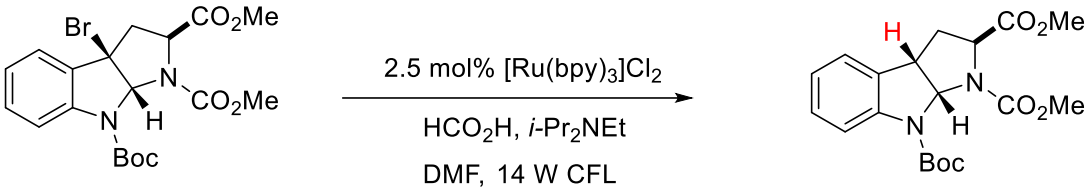

Up to 99% yield

Figure 1.6. The three publications by Yoon ([2+2] enone cycloadditions), MacMillan (direct, asymmetric alkylation of aldehydes) and Stephenson (Tin-free reductive dehalogenation of alkyl halides) that transformed the field of Photoredox catalysis.

Additionally, around the same time as these publications, the world had experienced a boom in awareness towards environmental issues which called for the development of greener, more sustainable chemistry. In line with this, photoredox catalysis stood out as a more environmentally benign alternative to traditional methodologies; the utilisation of light (and potentially sunlight) to achieve activation was a huge draw as it circumvented the need for reagent-based activation, which generates potentially toxic pollutants and avoids additional purification steps from the desired product. Moreover, in contrast to traditional catalysis which often employs high temperatures/pressures, photoredox reactions usually proceed under extremely mild conditions, at or near room temperature.[14]

The combination of these two factors, in addition to the advancement in LED technologies that allowed for narrow and specific wavelengths to be used, enabled the rapid development of a variety of photoredox methodologies over the past ~15 years, where photoredox catalysis has cemented itself as a powerful member of the organic chemist's toolbox.

Photocatalysts

The molecule $[Ru(bpy_3)]Cl_2$ was one of the first, and has been arguably the most influential photocatalyst in the development of photoredox catalysis, as seen in **Figure 1.5** and **1.6**. While it stills sees widespread usage today, advancements in the field has greatly expanded the repertoire of photocatalysts, which now include organic, inorganic as well as other transition metal complexes. Some examples of popular photocatalysts can be seen below in **Figure 1.7.**

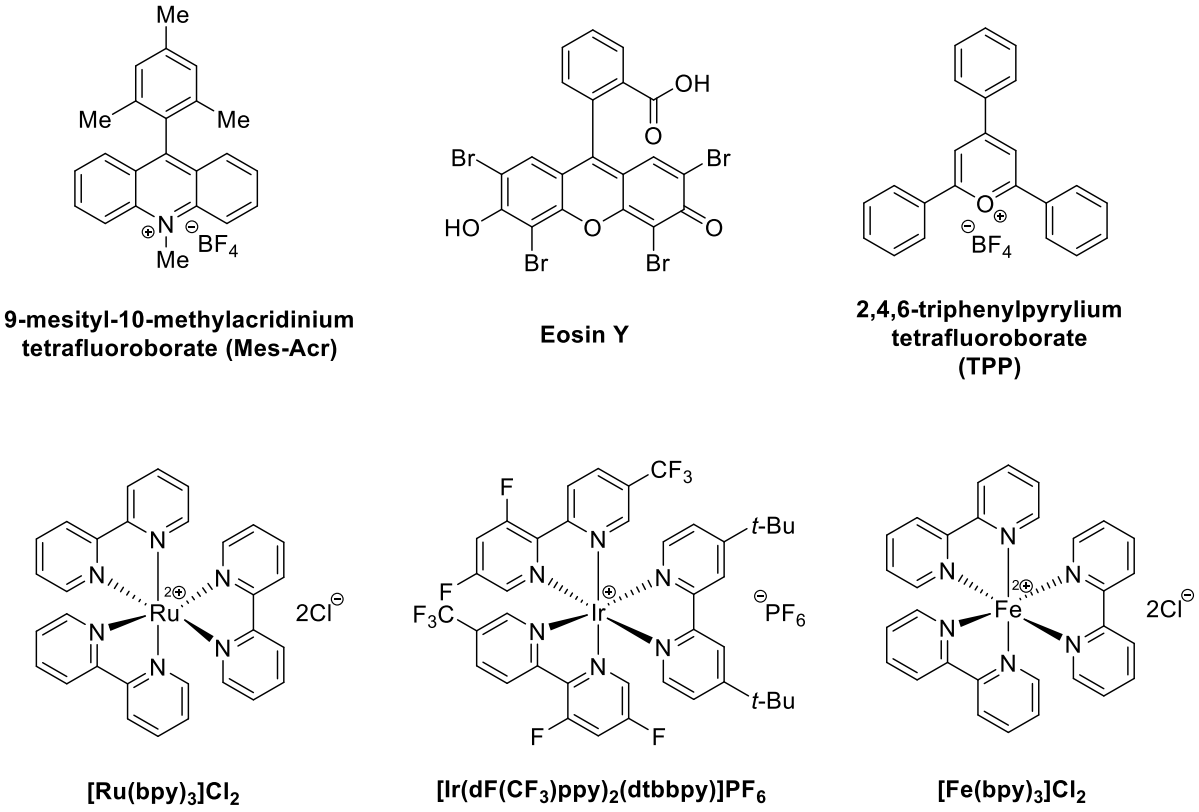

Figure 1.7. Some examples of commonly used photocatalysts.

Suitable photocatalysts (PCs) must possess a structural motif which allows for the sufficient absorption of visible light and, upon absorption, the photocatalyst must be able to produce an excited triplet state with a sufficiently long half-life (usually >~100 ns) to enable chemical transformations to occur.[18,22] Typically, as seen above, these are highly conjugated molecules with an exceptionally high functional group tolerance and can exist as either neutral or charged species.

This list above is far from exhaustive; it represents a mere drop of the diversity of structures available for photoredox catalysis. The desire for novel photocatalytic reactions continuously drives the development of newer photocatalysts and, as a result the library continues to expand year after year.

Generation of the excited triplet state

Formation of the excited triplet state of a photocatalyst is an important step towards substrate activation in every photoredox reaction.[2] As seen in **Figure 1.8A**, upon irradiation by visible light, an electron in a PC's HOMO (highest occupied molecular orbital) is promoted to the LUMO (lowest unoccupied molecular orbital), to form the excited state, PC*. At this stage, the frontier orbitals become SOMO's (singly occupied molecular orbitals), forming what can be referred to as an electron-hole pair. It is this that enables an excited state photocatalyst to act as both a strong (relative to the ground state PC) oxidant and reductant.[1,5,22,23]

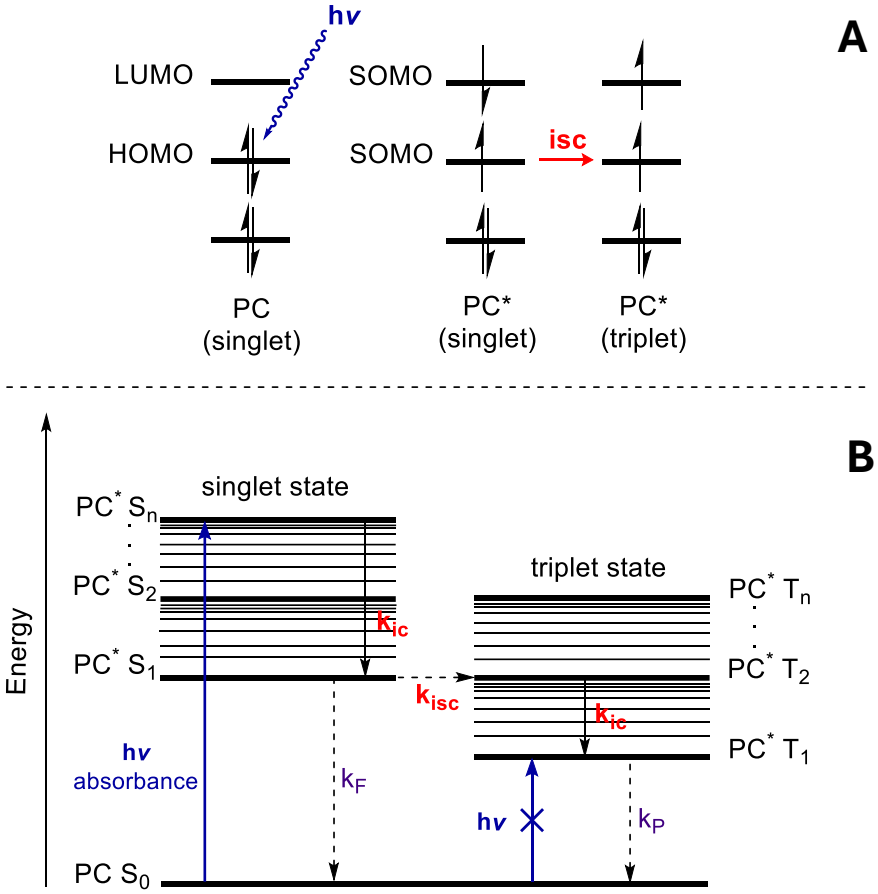

Figure 1.8. A) Orbital level diagram and **B)** Jablonski diagram showing the pathways of excitation and decay. S_n refers to the singlet states whereas T_n refers to triplet states. K_x refer to rate constant for internal conversion (ic), intersystem crossing (isc), fluorescence (F) and phosphorescence (P).

The pathway from ground singlet state to excited triplet state can be seen in more detail in the Jablonski diagram in **Figure 1.8B**. Excitation from ground singlet state (PC S_0), directly to a triplet state (PC* T_n) is a forbidden transition since the electron spin in this excited state is parallel to the ground state spin.[24] Consequently, accessing the excited triplet state first proceeds via the excitation to the excited singlet state PC S_n (Franck-Condon region) followed by vibrational relaxation (internal conversion) to the lowest-energy excited singlet state, PC* S_1. Intersystem crossing then populates the excited triplet state; importantly, since the corresponding triplet state is usually lower in energy, further relaxation to the lowest-energy triplet state is required to give the long-lived excited state triplet, PC* T_1.[25]

Modes of activation of photocatalyst

Once the lowest-energy triplet state has been achieved, substrate activation can proceed. Depending on the exact catalyst, the PC* can act as either an oxidant or reductant of much higher strength relative to the ground state species. Once formed, it can be intercepted by a substrate molecule, R, where three distinct activation modes exist as seen in **Figure 1.9.**

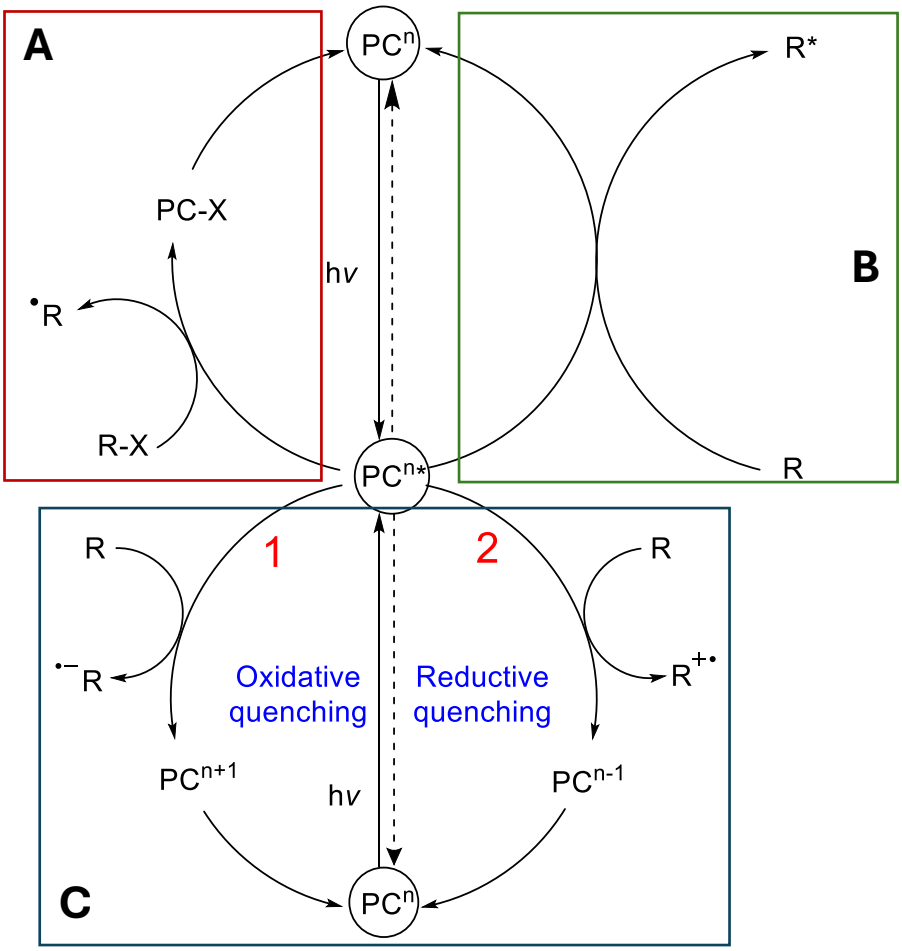

Figure 1.9. Diagram illustrating the three modes of substrate activation: photoinduced atom transfer (A), photoinduced energy transfer (B) and photoinduced electron transfer (C). PC^n (n = positive or negative integer value).

i) **Mode A – Photoinduced atom transfer:** In this mode there is a concerted transfer of an atom *from* the substrate (R-X), *to* the excited state photocatalyst (PC^{n}*), forming an intermediate photocatalyst adduct (PC-X) and generating the substrate radical ($^{\bullet}$R). When designing reactions of this type, the most important thermodynamic factor to consider is the R-X bond strength. While there have been many novel reactions which utilise this mode, the most popular of these is Hydrogen Atom Transfer (HAT) where X = H.[5,13,15]

ii) **Mode B – Photoinduced energy transfer:** In contrast to Mode A and Mode C (discussed next), this activation mode stands out as it proceeds without a change in the redox state of the substrate and catalyst. Instead, there is concerted electron transfer to and from both the excited state catalyst, PC^{n}*

and substrate, R.[1] **Figure 1.10**, shows a visualisation of this process at the orbital level:

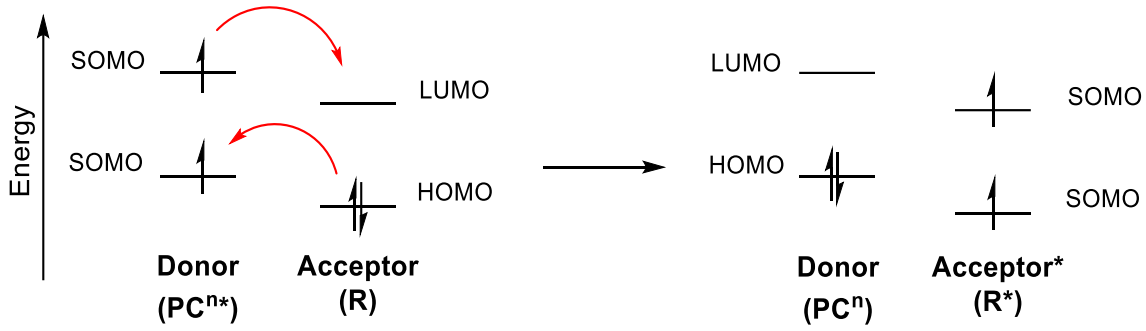

Figure 1.10. Photoinduced energy transfer at the orbital level between the PC* and substrate, R.

When an electron moves from the SOMO of the PC^{n}* to the LUMO of the substrate, it is accompanied by the simultaneous movement from the HOMO of the substrate, to the SOMO of the PC^{n}*. Thus excited triplet state is 'transferred' to the substrate and the PC^{n}* is brought back to ground state.[14] Consequently, reductive potentials cannot be used to guide reaction design, instead the energies of the excited triplet states of the PC^{n} and substrate are far more relevant.

iii) **Mode C – Photoinduced electron transfer (PET):** In PET there is a one-electron transfer between the excited photocatalyst, PC* and the substrate, R. There are two routes through which this process can occur (**Figure 1.9C**). In the first route, 1, the electron is transferred from the excited state PC^{n}*, to the substrate forming the radical anion, $^{\bullet-}$R. In doing so, the PC^{n}* is *oxidised* forming the ground-state PC^{n+1} species, thus this route is referred to as an *oxidative quenching* cycle with respect to the photocatalyst. In the second route, 2, the electron is transferred to excited state PC^{n}*, from the substrate forming the radical cation, $^{\bullet+}$R. Consequently, this *reduces* the photocatalyst forming the PC^{n-1} species, thus the route is referred to as a *reductive quenching* cycle.[1–3,22]

In the context of this thesis, PET processes will be the focus of this review.

Photoinduced Electron Transfer (PET)

Whether a PET cycle will follow either an oxidative or reductive quenching cycle depends on the relative energies of the HOMO and LUMO, between the photocatalyst and the substrate. The orbital energy diagram in **Figure 1.11**, shows which quenching cycles is followed depending on the energy differences:

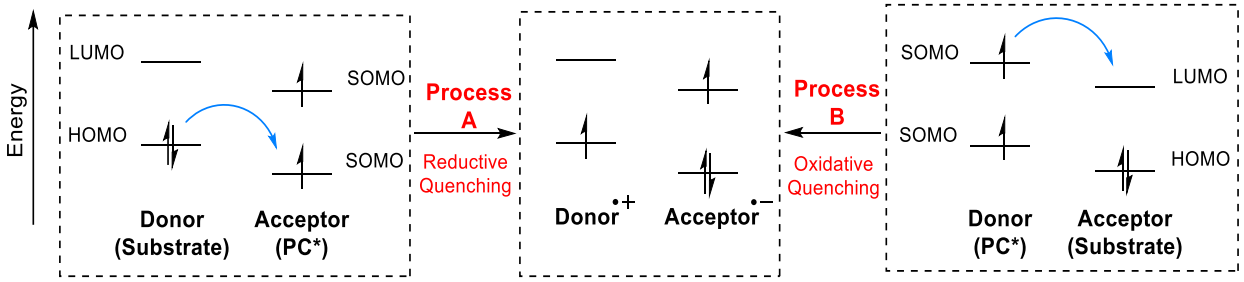

Figure 1.11. Orbital diagram showing oxidation/reduction of a substrate by a photocatalyst PC via orbital interactions and their energy levels.[1]

Following process A, if the HOMO of the substrate is higher in energy than a SOMO of the PC*, then the substrate molecule is oxidised (reductive quenching cycle). Conversely, in process B, when the SOMO of the PC* is higher in energy than the LUMO of the substrate, the substrate gets reduced (oxidative quenching cycle).[1,5,22,23]

The ability of the photosensitizer to act as both an oxidant or reductant within a single reaction mixture, is a sharp contrast to traditional redox chemistry in which the prevailing condition can be only net oxidative or net reductive. This unique feature allows for novel functionalisation to take place.[13,15]

As the process is designed to be catalytic, following the transformation of PC^{n}* to $PC^{n\pm x}$, it is necessary to regenerate the active photocatalyst, PC^{n}, for the catalytic cycle to turnover. Usually this is done by addition of a balancing redox equivalent, RE as shown in **Figure 1.12A**. In this example the PC^{n} follows a reductive quenching cycle with substrate (R) to form PC^{n-1} which the RE oxidises to back the PC^{n}, being reduced to RE^{-} in the process. However, a variation of this can exist whereby instead of the substrate interacting directly with the excited state catalyst, the RE first intercepts the excited PC^{n}* and forms the variant oxidation ground state PC^{n-1}. Thereafter, this can interact with the

substrate as seen in **Figure 1.12B**, where the it reduces the PC^{n-1} back to PC^{n}, in the process generating a radical anion which can be manipulated in the reaction.[15]

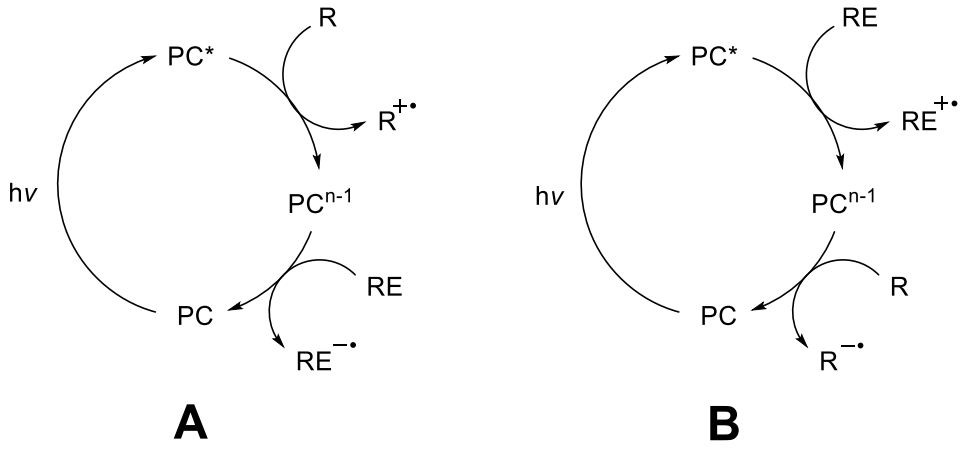

Figure 1.12. Illustration showing the differences between substrate quenching (A) and secondary reactant quenching (B).[15]

Kinetic and Thermodynamic Parameters

Several factors determine whether a PET process between a photocatalyst and substrate is feasible. Of thermodynamics, the most important consideration when predicting the feasibility of electron transfer (ET), is the reduction potentials of both excited state photocatalyst and substrate. This determines whether electron transfer will be exergonic or endergonic.[2,3,18]

For kinetics, the field relies on Marcus theory for the rate of electron transfer. Specifically, there are two outer-sphere ET processes to consider: i) ET between the excited state PC* and substrate (PC^{n}* and R, **Figure 1.12A**) and ii) ET between the $PC^{n\pm1}$ and the terminal redox reagent ($PC^{n\pm1}$ and RE, **Figure 1.12A**). While outer-sphere ET transfer does not involve bond formation and bond breaking, the photocatalyst and substrate must form a solvated precursor complex for efficient ET. Formation of this complex demands nuclear rearrangement and overcoming an activation energy barrier,[2,26,27] thus even when the thermodynamics are favourable the lifetime of an excited triplet state must be long enough to accommodate this process. In cases where the substrate-photocatalyst pairs are too endergonic, the reaction may not be feasible.[3] Finally back electron transfer (BET) can significantly hamper the process if the separation of the solvated precursor complex is slower than ET.[21]

Dual catalytic strategies

Thus far, photocatalytic systems with only one catalytic component have been the primary focus of this review; while they encompass the majority of photocatalytic reports to date, dual photocatalytic systems, which contain a secondary co-catalyst occupy a significant portion of the space and continue to grow in popularity.[5,15,18] One of the most enticing aspects to incorporating a second catalyst in the system is the ability to bridge together unfeasible substrate-photocatalyst pairs, when either the thermodynamics or kinetics are disfavoured. However, this is far from the limit of what is achievable with a combinatory catalytic approach. Given the large number of non-photoredox catalysts available, there has been a tremendous amount of experimentation using various combinations of photocatalyst. Of these, three strategies make up the majority of the space thus far:

1) Redox meditation

In redox mediation, rather than the substrate interacting with the photocatalytic cycle a secondary compound, the redox mediator (RM), bridges the two. This results in an extended electron transfer chain which proceeds via an intermediate rather than direct electron transfer via the substrate (the photosystem shown in **Figure 1.2** is a prime example of this). This is beneficial when the ET is too slow for the lifetime of the triplet state. As a redox mediator is in the ground state, the radical ion that arises has a much longer lifetime and ET between the RM and substrate is more efficient.[4,5,15]

Another example of this in action can be seen in **Figure 1.13.**

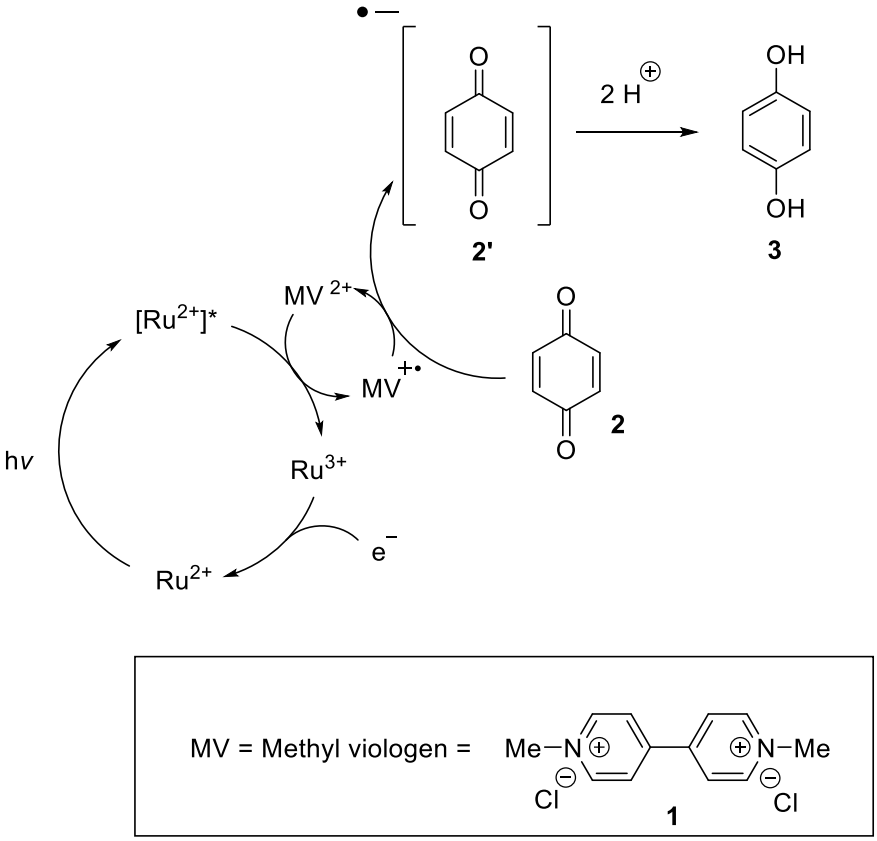

Figure 1.13. Reduction of benzoquinone to hydroquinone as mediated by methyl viologen.

Following the generation of $[Ru^{2+}]^*$ a molecule of methyl viologen (**1**), the redox mediator), oxidatively quenches the excited state catalyst, generating a radical cation. This is then intercepted by a molecule of benzoquinone (**2**) to form the radical anion, **2'**, which ultimately gets protonated to form hydroquinone, **3**.[28]

2) Organocatalysis

Pioneered by MacMillan for the functionalisation of aldehydes using chiral secondary amines, this involves the use of an organocatalytic cycle in tandem with the photoredox cycle.[15] Unlike redox mediation this strategy does not bridge unfeasible substrate-photocatalytic pairs, rather the combination of these two catalytic systems enables unique one-pot functionalisations to occur. Typically, one catalytic cycle activates a substrate, which enters the second cycle, reacting with another substrate. An additional benefit is that the two catalytic cycles typically turn each other over, eliminating the need for a terminal redox reagent. Finally, this has the secondary advantage of imparting a

measure of stereocontrol over the reaction as well. An example of this can be seen in the α-functionalisation of aldehydes by alkyl bromides below in **Figure 1.14.**[19]

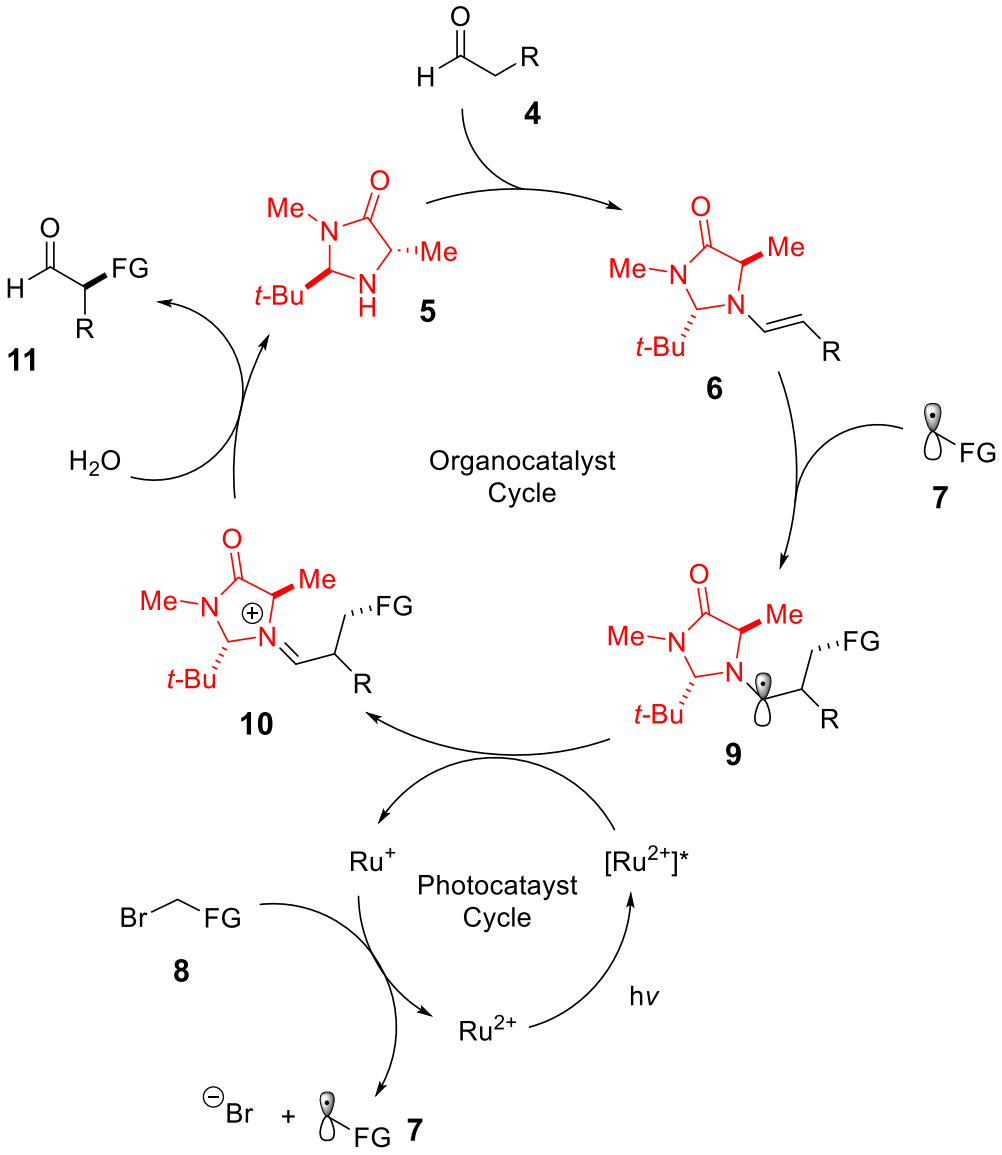

Figure 1.14. Dual organo and photoredox catalysis to generate α-functionalised aldehydes in an enantioselective manner.

Condensation of the aldehyde, **4**, with the cyclic secondary amine, **5**, forms the enamine, **6**. A small amount of enamine **6** is used to kick-start the photocatalytic cycle by oxidatively quenching the excited $[Ru^{2+}]^*$ to Ru^{+}. This kick-start generates a functionalised (FG) electrophilic radical, **7**, from the parent bromo species (**8**) which regenerates the active photocatalyst. Reaction of **6** with **7** forms the radical species **9**, which now quenches the excited photocatalyst in subsequent cycles. This forms the iminium ion **10**

in the process, which upon hydrolysis relieves the functionalised aldehyde, **11** and liberates the organocatalyst.

3) Transition metal catalysis

Like the organocatalytic cycle in **Figure 1.14**, a photoredox cycle can be combined with traditional transition metal catalysis for similar purposes (typically without stereocontrol). The photocatalytic cycle can be used to turn over the transition metal catalytic cycle or vice versa. An example of this was done in 2012 by Sanford *et al.* for the formation of trifluoromethylated aryl compounds from their corresponding boronic acids as shown in **Figure 1.15**.[29]

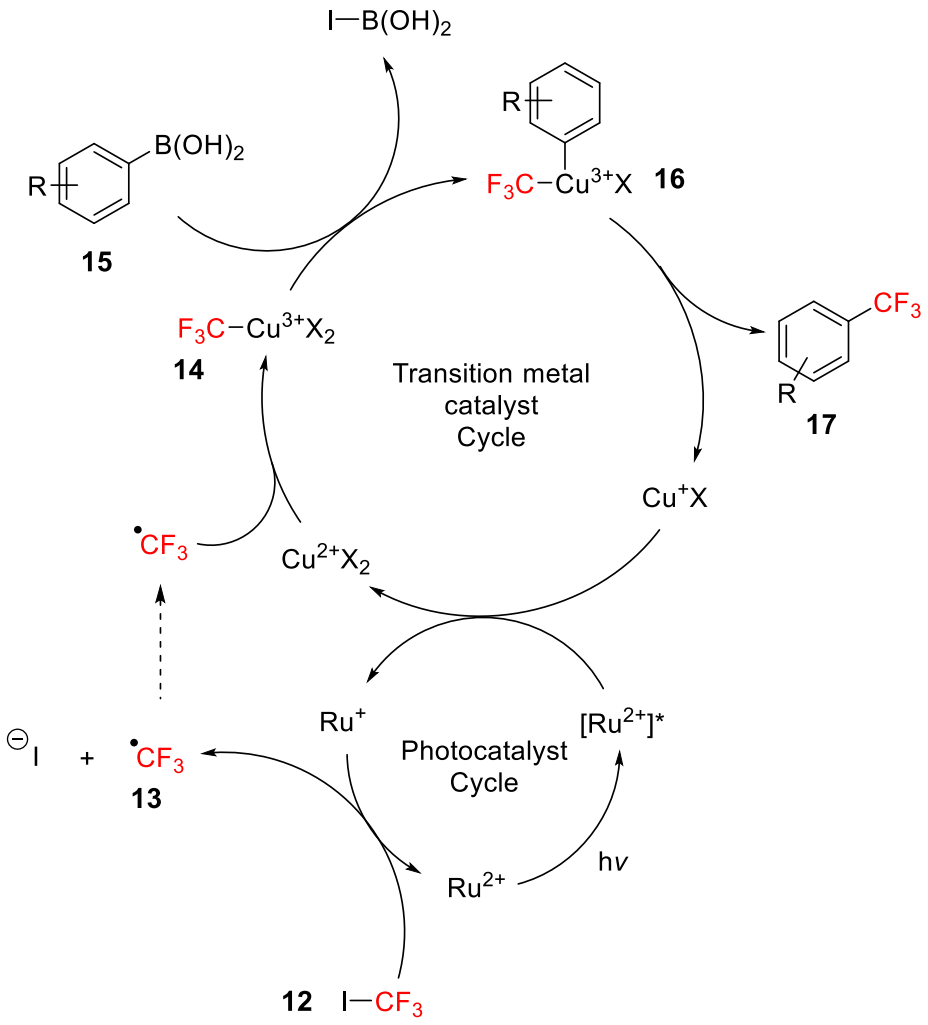

Figure 1.15. The dual Cu-photoredox catalysis cycle for the synthesis of trifluoromethylated aryls from boronic acids.[5]

The excited state photocatalyst is reductively quenched by CuX catalyst producing Ru^{+} and Cu^{2+} species. The Ru^{+} species cleaves CF_3I, **12**, generating a CF_3 radical, **13**, which complexes with the Cu^{2+} species to form complex **14**. Transmetalation of **15** forms **16** which can reductively eliminate to give the desired product, **17**.

These three strategies are prime examples of the power and potential that dual catalytic photoredox strategies have to offer. As both photoredox and other catalytic methods expand so too does the potential to merge the fields to develop novel, more efficient and more sustainable reactions.

Chapter 2: Aim

The Dimeric Hexahydropyrroloindole scaffold

The indole moiety, shown in red (**Figure 2.1**), is a ubiquitous structure in nature, found in every phylum of life from plants to animals and even simple prokaryotic organisms.[30–32] Thus, the indole scaffold represents a privileged motif with indole-containing molecules implicated in a wide variety of biological functions,[32] such as the amino acid tryptophan, a building block for many proteins and critical for correct protein folding, as well as active site catalysis, cell signalling molecules such as serotonin and melatonin, communication molecules such as pheromones and so many more.[33,34] Consequently indoles, which occupy a significant chunk of the chemical space in nature, have become attractive targets for pharmaceutical development,[35] with many successful drugs developed such as Velban,[36] Tadalafil,[37] and Lotronex.[38] Thus, they are an important pool from which to draw upon, for inspiration and guidance in the chemical arms race against pathogens.

Dimeric Hexahydropyrroloindoles (**Figure 2.1**, **18**) comprise a subset of the indole pool; they are C3-C3' oligomeric alkaloids, derived from the molecule tryptamine (**Figure 2.1**, **19**) compromising of two hexahydropyrroloindole scaffolds and are a relatively newly discovered group of indoles, with the first member, Calycanthine, only being discovered in 1888 and its structure only elucidated in 1952.[39]

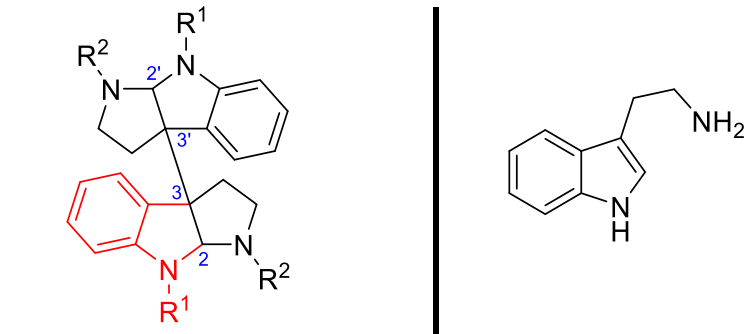

Hexahydropyrroloindole - **18** | Tryptamine - **19**

Figure 2.1. The dimeric hexahydropyrroloindole scaffold shown alongside tryptamine.

Since then, however, their ranks have been bolstered by the discovery of many new compounds, **Figure 2.2**. To date, these compounds have only been isolated from two families of plants, those belonging to *Calycanthaceae* and *Rubiaceae*.[40–42] Thus, while they have displayed interesting biological properties,[43–45] low recovery from natural

product extraction has been a barrier for further testing. Additionally, despite interest within the synthetic chemistry community; the presence of vicinal, sterically strained, quaternary centres has proven to be a significant challenge, with many syntheses being lengthy and low yielding.[46–48]

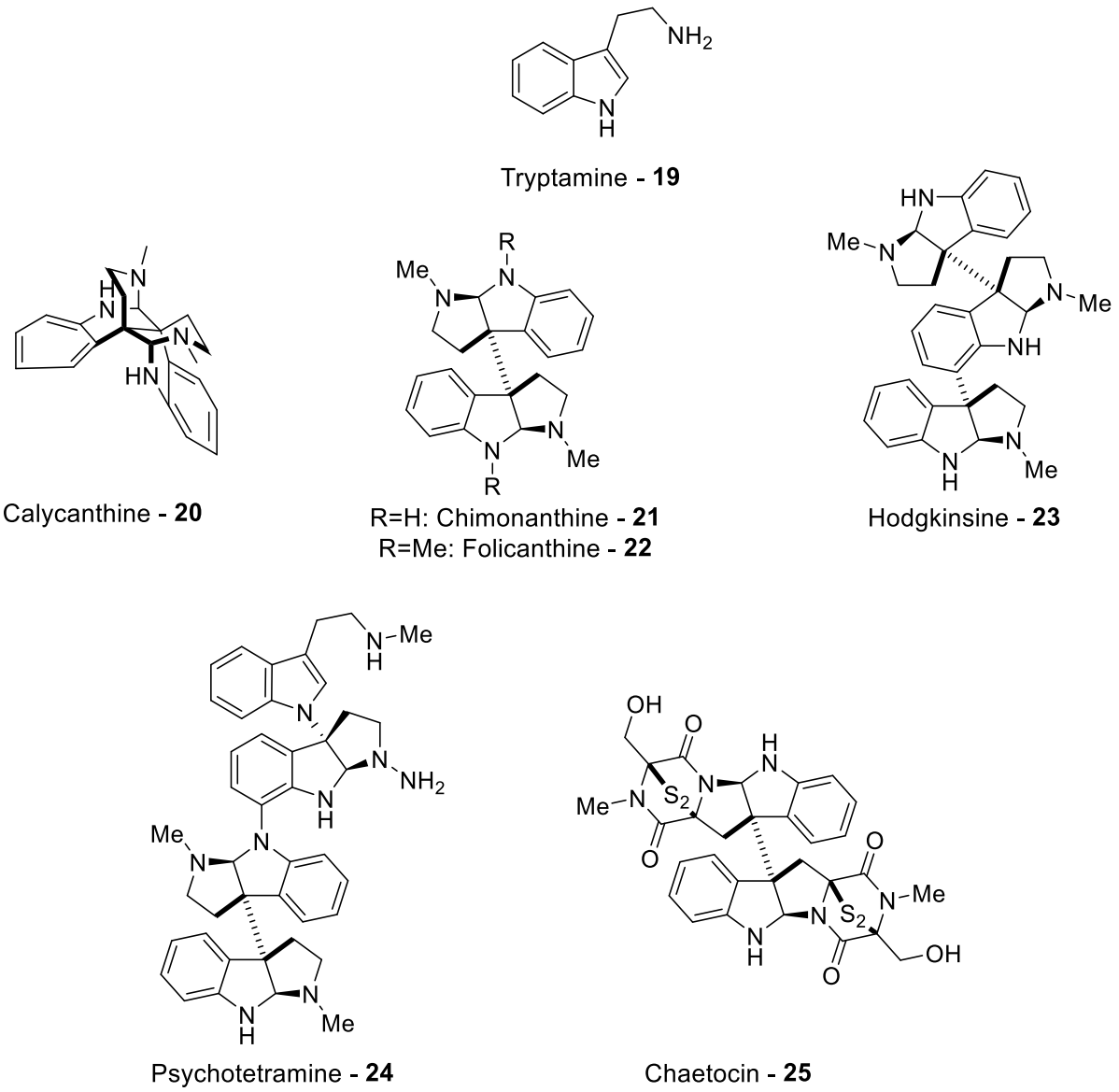

Figure 2.2. Some C3-C3' oligomeric indole natural product that have been isolated from plants of *Calycanthaceae* and *Rubiaceae* as well as the molecule tryptamine and the dimeric hexahydropyrroloindole scaffold.

The hexahydropyrroloindole core is the central backbone of these molecules and the common structural element that links them all together. As such, the vast majority of

total syntheses focused on these molecules (**20** – **25**),[40,47–52] revolves around efficient construction of this core as the penultimate step before final functionalisation. Thus, structure **18** represents an advanced intermediate towards the synthesis of these molecules.

Bisoxindoles: A key intermediate

Bisoxindoles are dimeric molecules consisting of two indolic subunits. While many variants of bisoxindoles exist, those linked at the 3-position of the indole are some of the most common[53] and the only ones that will be discussed in this thesis. Broadly speaking there are three bisoxindoles of this type, which can be characterised according to the nature of the link at the 3-position, both of which can be seen in **Figure 2.3** below:

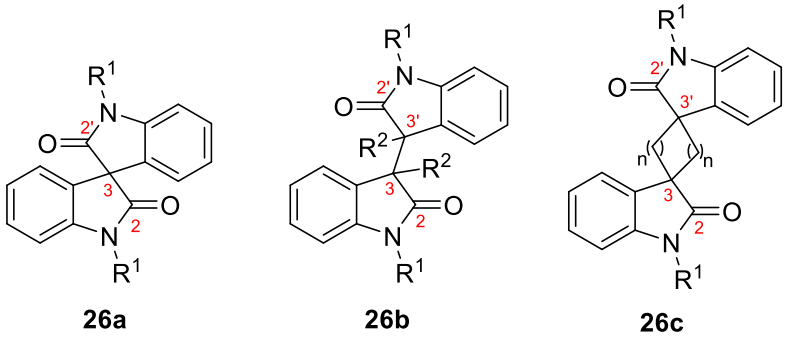

Figure 2.3. The three types of 3-bisoxindoles.

In the first type, **26a**, the two subunits share a common quaternary carbon that links them at the 3-position.[54,55] By contrast, in the second type, **26b**, a bond bridges the two subunits at each of their respective 3-positions.[52,56–59] The third, like the second, bridges the two quaternary carbons, via a link or spacer ring, typically containing a hetroatom.[60–62] While bisoxindoles themselves have shown some interesting biological properties that warrant their synthesis,[56,61,63] the second type **26b**, have been of particular interest to chemists as key intermediates in the synthesis of some dimeric hexahydropyrroloindole molecules. In 1963, Hino and Yamada[64] were able to successfully synthesise the alkaloid (±)-Folicanthine (**22**), in 15% yield from the bisoxindole **27**, using $LiAlH_4$ (**Figure 2.4**), thus bisoxindoles can be seen as gateway to the dimeric hexahydropyrroloindole scaffold.

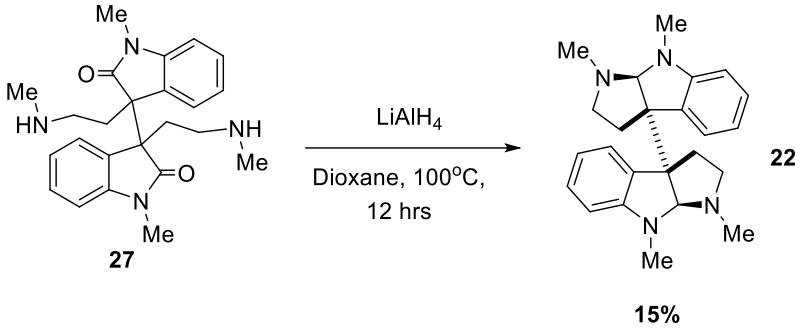

Figure 2.4. One of the earliest syntheses of dimeric hexahydropyrroloindoles from a bisoxindole precursor by Hino and Yamada.

Following to this work, interest in the synthesis of bisoxindoles of this type, piqued, and methodologies for their development began in earnest. Fast forward to today, three main strategies are currently employed their synthesis. Those are:

1) Modification of unfunctionalized bisoxindole – This strategy revolves around modification of the Boc-protected bisoxindole **28** (**Figure 2.5**). Kanai and Matsunaga[52] were the first to utilise this approach in 2012, using Mn(II) in the presence of a Schiff base to form the enolate of **28** which forms **29** via a double Michael addition of nitroethylene, which was later used in the synthesis of (+)-Chimonanthine. Later in 2018, Chen *et al*.[65] expanded on this strategy by demonstrating the homo and heterodialkylation of **28** to form bisoxindoles (**30**), using SPA-triazolium cations (**31**) which coordinates with **28** forming the enolate that then reacts with the electrophile (R-Br). This was used in the first synthesis of (–)-Chimonanthidine.

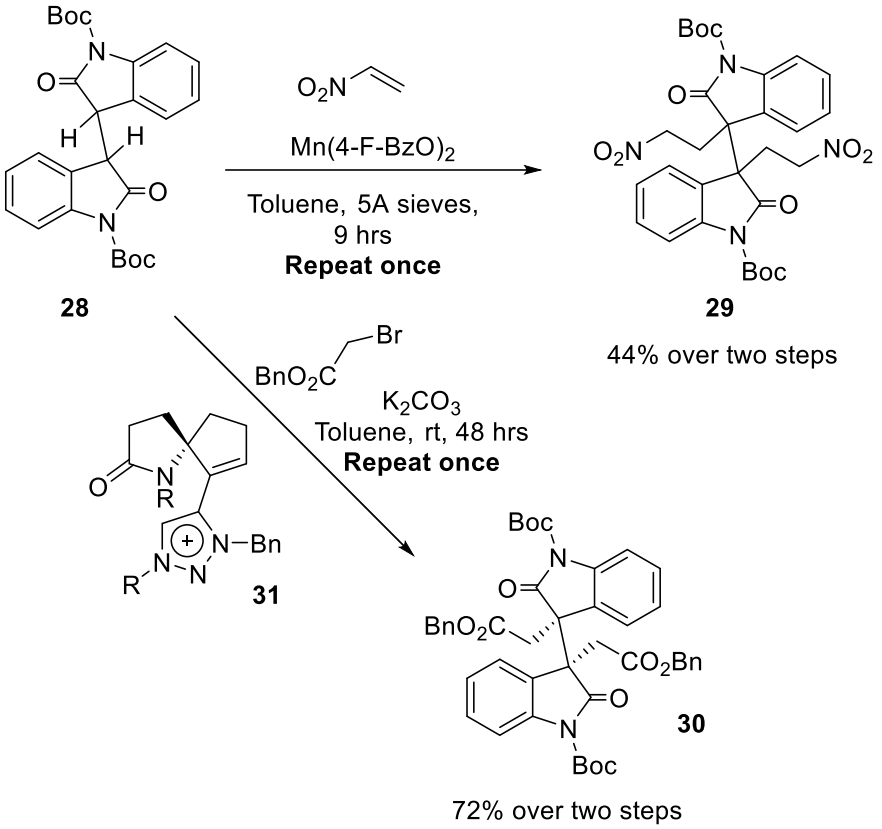

Figure 2.5. Methodologies of Kanai (**28** → **29**) and Chen (**28** → **30**) with conditions and reactants.

2) Addition to isatins and its derivatives – Strategies in this category focus on dimerization rather than modification, via the addition of an oxindole component to the molecule isatin or its derivatives. Mechanistically, these reactions are like the previous strategy, whereby formation of the enolate of the oxindole component is critical. Here however, this occurs on the oxindole component which can then add to isatin or its derivatives to form the bisoxindole. Examples of this can be seen in **Figure 2.6**; Zheng and Zhu[66] were the first to demonstrate this in 2014, using an isatin-based imine **32** and a protected 3-methyl-2-oxindole (**33**) as a model, to form bisoxindole **34** using a Lewis acid catalyst, which was adaptable to a variety of substrates. Later, in 2018, Wolf and co-workers[56] synthesised the first 3-fluoro-3'-hydroxy bisoxindoles (**35**) by the addition of *N*-Phenyl-3-fluorooxindole (**36**) to isatin (**37**) under catalytic amounts of triethylamine.

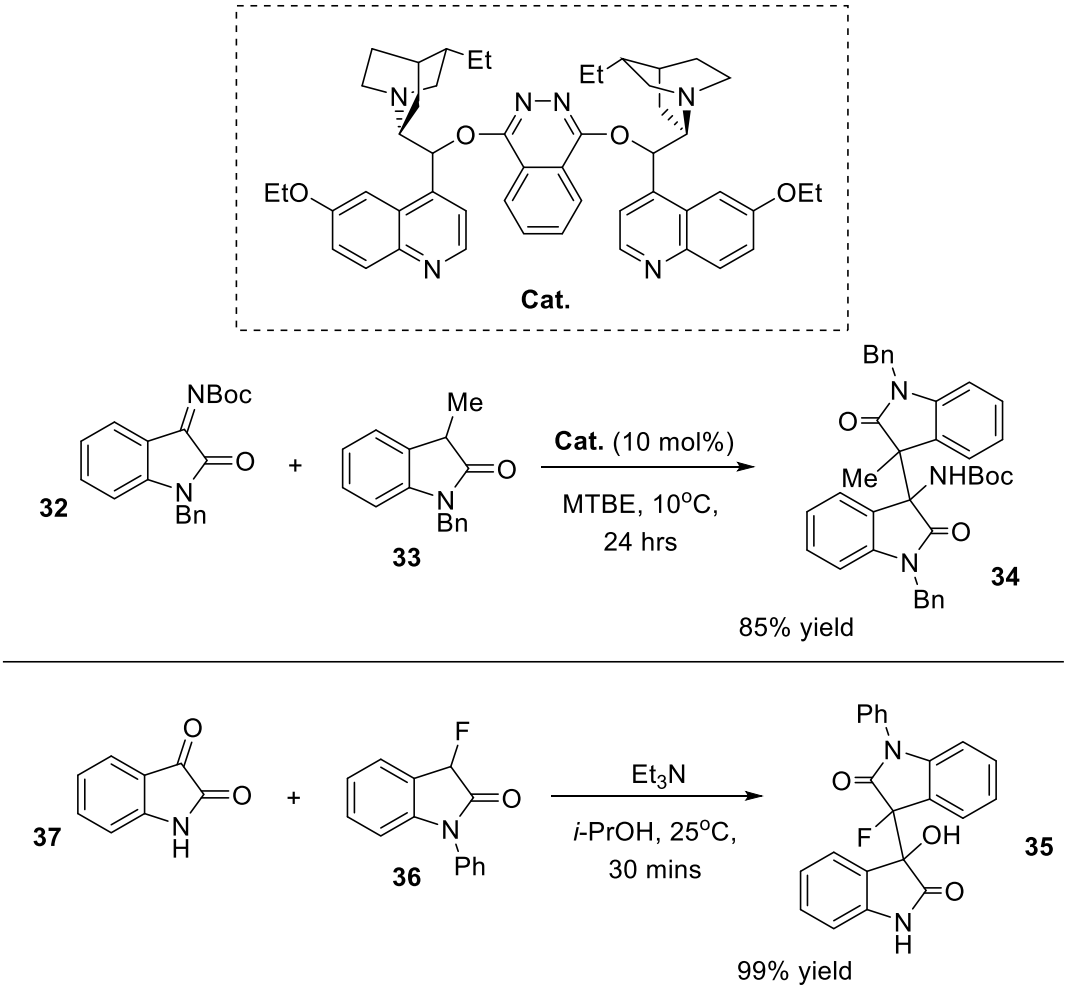

Figure 2.6 Current methodologies for the synthesis of bisoxindoles from Isatins.

3) Radical Dimerization – Methodologies in this category encompass the majority of publications on the synthesis of bisoxindoles and will be the main focus of this review. The common feature linking these methods together, is the use of two indole monomers to generate an intermediate radical species, that can homocouple to form the desired bisoxindole. The way in which they differ, is the method used to generate the radical species.

The first paper to demonstrate this method was published in 1994 by Rodrigo and co-workers,[40] who were able to furnish bisoxindole **38** in 53% yield, from oxindole **39** using carbon tetrachloride as an oxidant, in conjunction with sodium hydride in THF at -65 °C (**Figure 2.7**).

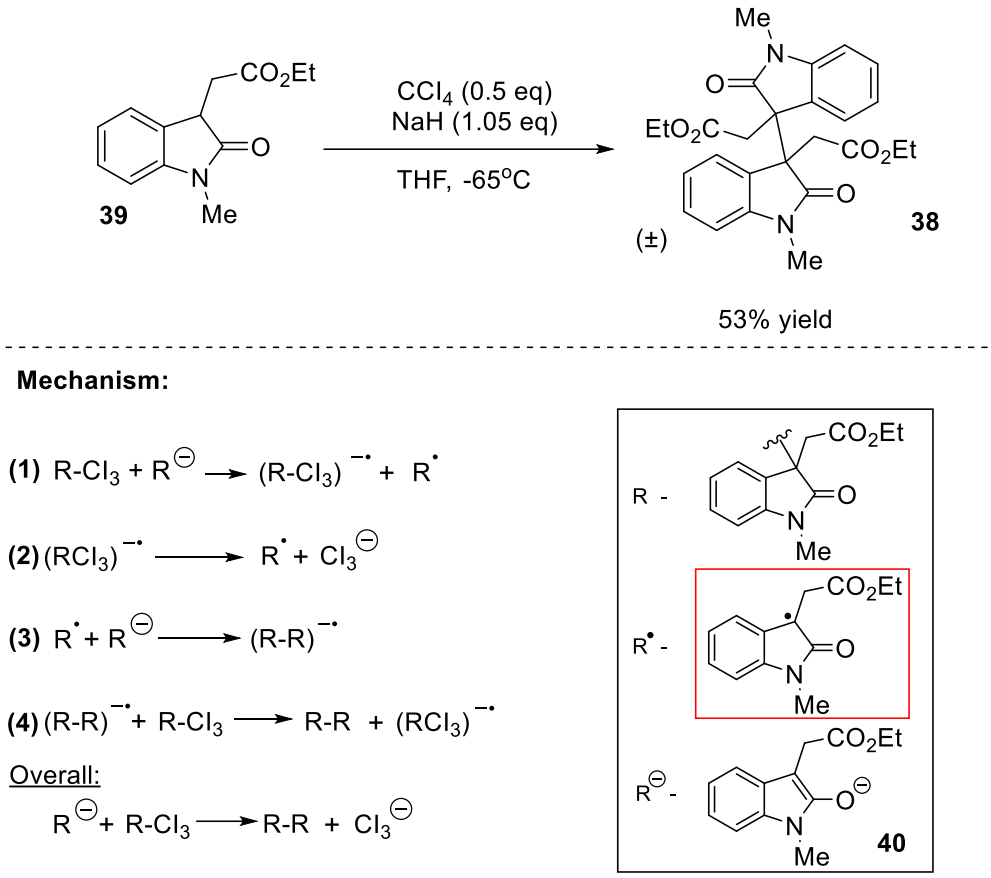

Figure 2.7. Scheme and mechanism of Rodrigo *et al.* method.

Mechanistically, the authors proposed a radical anion chain process for this method, starting from the 3-(triiodomethyl)oxindole (R-CI_3) which reacts with enolate **40** forming the radical anion of R-CI_3 and $R^{\bullet}$ (equation 1). The radical anion of R-CI_3 can fragment to give another equivalent of $R^{\bullet}$ (equation 2); once generated either from equation 1 or 2, this radical key species can then react to form the bioxindole anion radical $(R\text{-}R)^{-\bullet}$ (equation 3) which finally reacts with (R-CI_3), forming the bisoxindole product.

Following this, it was almost twenty years later in 2013, when the next method in this category was published. Kim *et al.*[67] demonstrated that bisoxindoles could be synthesised from their monomeric oxindole components by oxidative dimerization using either $Mn(OAc)_3$ or $Cu(OAc)_2$/AgOAc as oxidants. With oxindole **41** as a model, bisoxindole **42** was synthesised in 90% yield using both oxidants, separately, in benzene under N_2 and heat (**Figure 2.8**).

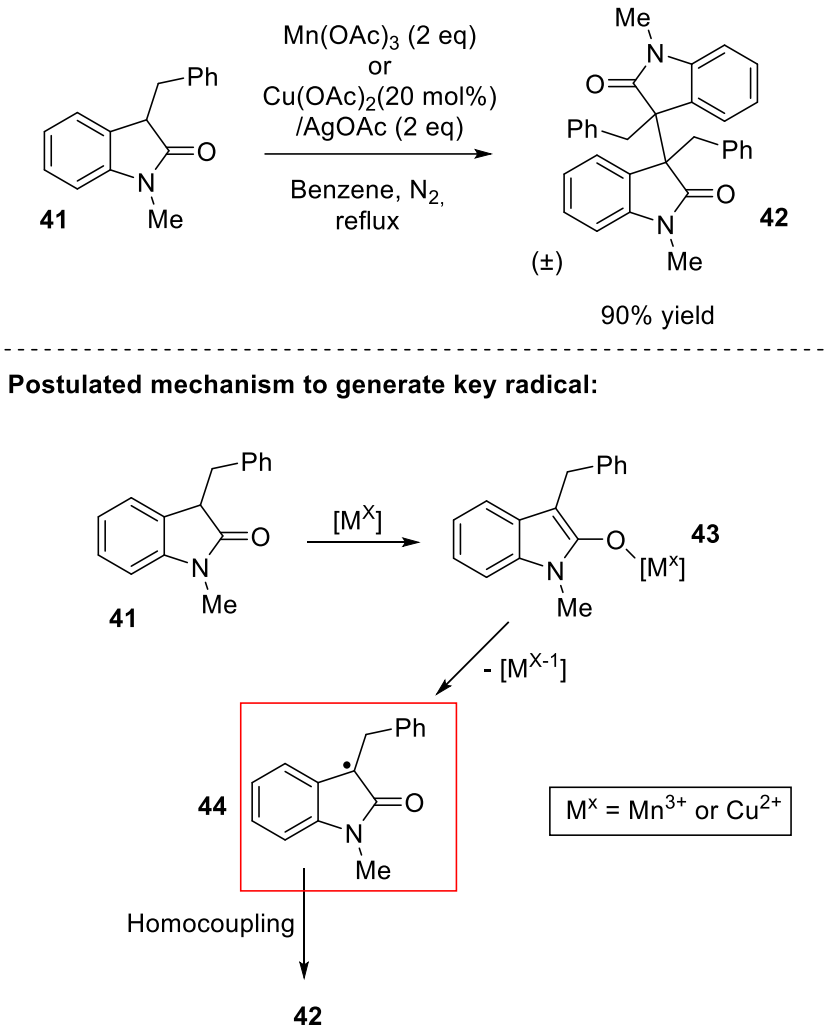

Figure 2.8. Kim *et al.* methodology for the synthesis of bisoxindoles using $Mn(OAc)_3$/$Cu(OAc)_2$ and likely mechanism.

The exact mechanism by which **42** is formed was not well established by the authors, however, by extrapolating from previous radical reactions involving Mn(III)[68] and Cu(II)[69] they postulated that **41** could proceed via a metal-enolate **43** to form the key radical species **44,** which can finally homocouple, giving bisoxindole **42**. This method proved adaptable to a wide range of substrates with various aliphatic, aromatic and ester constituents at the 3,3'-position.

Not long after, Bisai *et al.*[50] in 2015, developed a methodology using indole **45** as the substrate which contains an ester group at the 3-postion. They initially intended to exploit earlier work by Shi *et al.*[70] using Palladium (Pd) catalysed cross-coupling, however it was discovered that the reaction proceeds in the absence of Pd, using molecular iodine as an

oxidant and potassium *tert*-butoxide (K^{t}OBu) as a base, bisoxindole **46** was produced in 84% yield. They postulated that the reaction proceeds via deprotonation by the base, followed by SET from the *in situ* generated I-^{t}OBu, to give radical **47**, whose resonance form (**47'**) can then homocouple, giving the bisoxindole. (**Figure 2.9**). This methodology proved tolerable to changes to the protecting group, aromatic ring as well as utilising different ester groups. However, it showed less amenable to changing the ester group at the 3-postion to other functional groups.

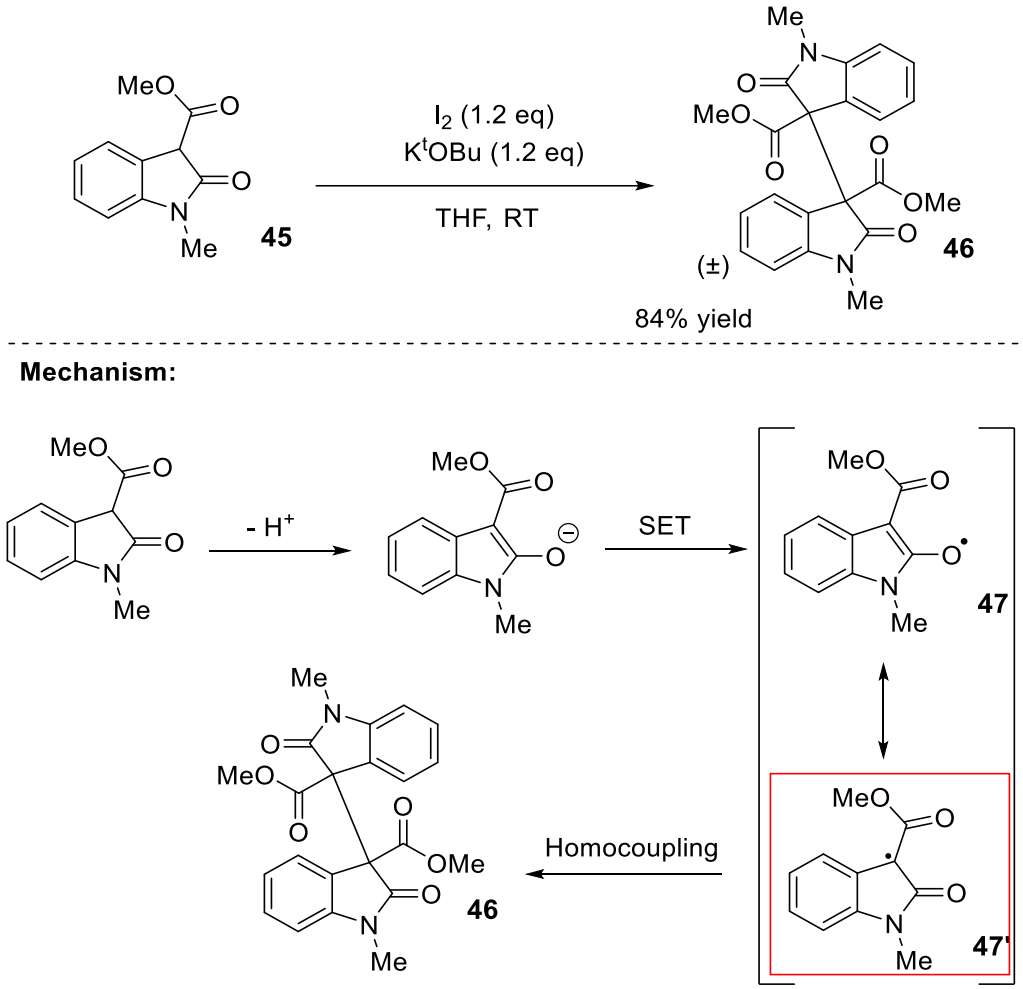

Figure 2.9. Methodology developed by Bisai *et al*. for bisoxindole synthesis.

A year later, in 2016, Wu and Liu[58] showcased that 3-chlorooxindoles **48** could homocouple in the presence of an iridium photocatalyst, *fac*-Ir(ppy)$_3$, 1,8-diazabicyclo[5.4.0]undec-7-ene (DBU) as a base and visible light to give bisoxindole **49** in 82% yield (**Figure 2.10**). This method proved more flexible to changes in the substrate than previous reported procedures; with a variety of functional groups tolerated,

including changes to the functional group identity at the 3-postion as well as the aromatic ring system. Mechanistically, they suggest an oxidative quenching cycle, whereby photoexcited $[Ir^{3+}]^*$ can be quenched by the substrate to give radical **50**, which can homocouple to a second molecule of itself thus generating the bisoxindole. SET from DBU then regenerates the active Ir^{3+} species thus turning over the cycle.

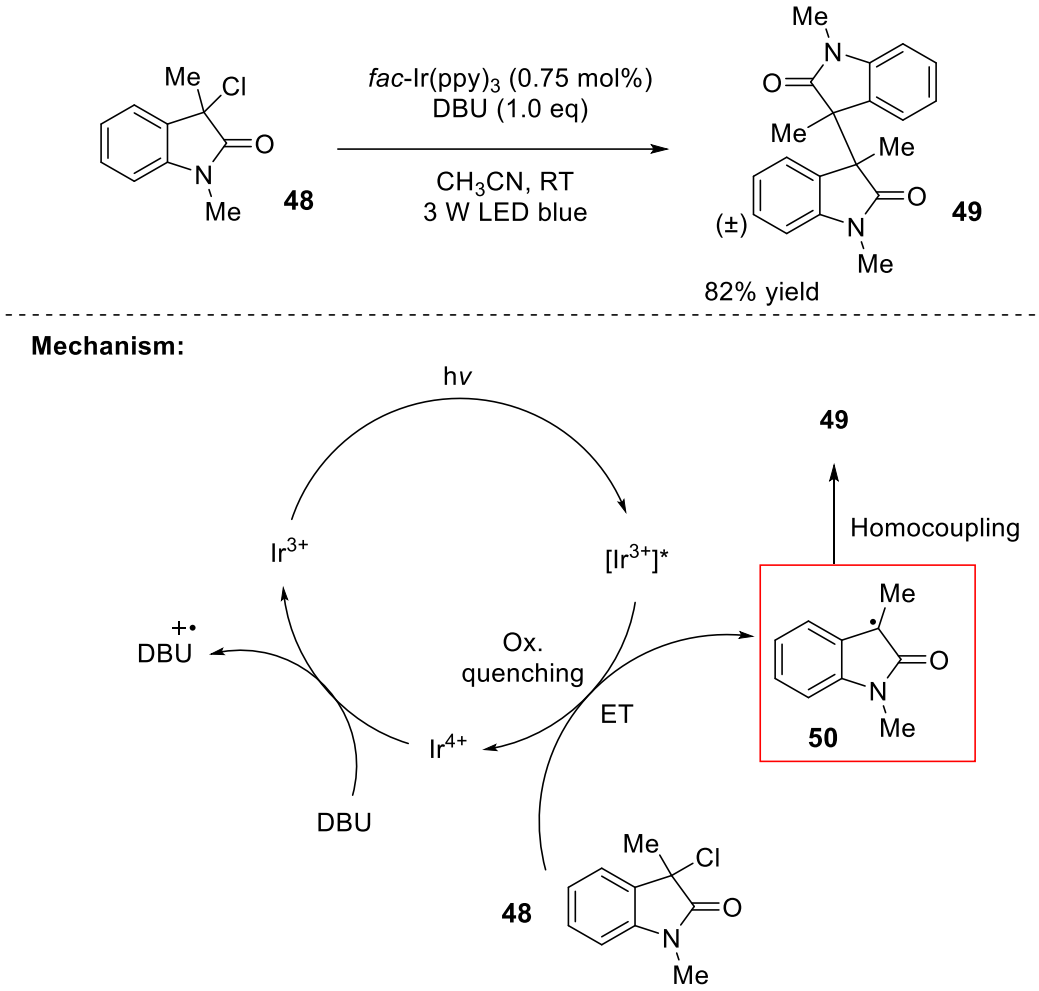

Figure 2.10. Methodology developed by Wu *et al*. for bisoxindole synthesis.

Following in the footsteps on Wu and Liu, Xiang and Yang[71] also published photoredox methodology, employing $[Ru(bpy)_3]^{2+}$ as the photocatalyst to access the bisoxindole via a radical intermediate. It should be noted that here, unlike other publications in this category, isatins are used as starting materials rather than monomeric oxindoles. (**Figure 2.11**).

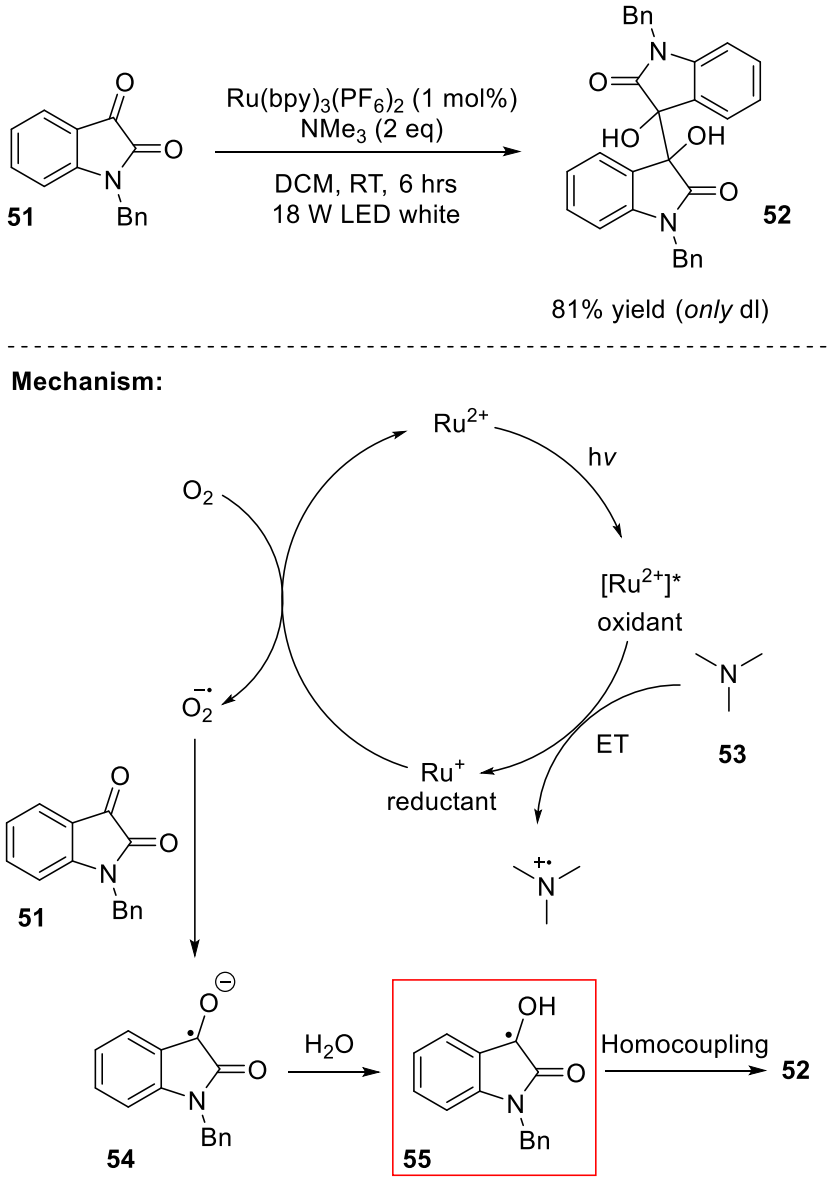

Figure 2.11. Xiang and Yang's methodology for the $Ru(bpy)_3$-facilitated synthesis of bisoxindoles from isatins.

Under the optimal set of conditions (RT, 18 W white light, trimethylamine), $Ru(bpy)_3(PF_6)_2$ was able to catalyse the dimerization of **51** to bisoxindole **52** in 81% yield. Interesting, unlike previous reports, this reaction was diastereoselective, largely favouring the *dl* isomer. More interestingly, when a sterically bulkier isatin derivative (**32**, **Figure 2.6**) was used, the diastereoselectivity of the reaction flipped, giving the *meso* product as the major isomer.

In contrast to Wu and Liu's method as well as other reports in this category, the authors suggest a reductive dimerization. Here, following photoexcitation of Ru^{2+}, trimethylamine

(**53**) oxidatively quenches the excited-state, $[Ru^{2+}]^*$, rather than the substrate, forming the Ru^{+} species. The reduced Ru^{2+} is regenerated via ET from molecular oxygen, producing the $O_2^{-\cdot}$ radical in the process. It is this radical that can react with isatin substrate, **51**, forming a radical anion (**54**) which, after reacting with water to form radical **55**, can homocouple, giving **52**. The authors note the origin of the diastereoselectivity likely stems from the homocoupling step; in the case of isatin, the key radical intermediate **55** could have secondary orbital interaction between the π-orbitals of the two carbonyls during homocoupling, which would direct a side-by-side interaction, favouring the formation of the *dl* isomer. In contrast the radical of **32** possessing the Boc group would likely force a face-to-face interaction to orient the two Boc groups away from each other to alleviate repulsion, thus favouring the *meso* isomer.

The final and most recent publication prior to the development of our work was by Wei *et al.*[57] in 2018. Here they sought to achieve dimerization without the addition of a stoichiometric amount of base, in contrast to the previous methods. The results were achieved by using 3-methylindole **56** as a substrate, in the presence of Copper (II) acetate and di-*tert*-butyl peroxide (DTBP) at 120 °C. which produced the desired bisoxindole product, **57**, in 81% yield. Like the previous methods, modifications at the N1, C3 and aromatic ring were all well tolerated. The authors suggest the homolytic fragmentation of DTBP by Cu catalyst initiates the reaction, producing ^{t}OBu radical which deprotonates **56** and forms radical **58**. Thereafter they suggest that **56** must undergo tautomerization to enol **56'**, which is deprotonated by the Cu catalyst, before it can react with **58** to form complex **59**. An O to C migration to form **60** then gives the bisoxindole after reductive elimination (**Figure 2.12**).

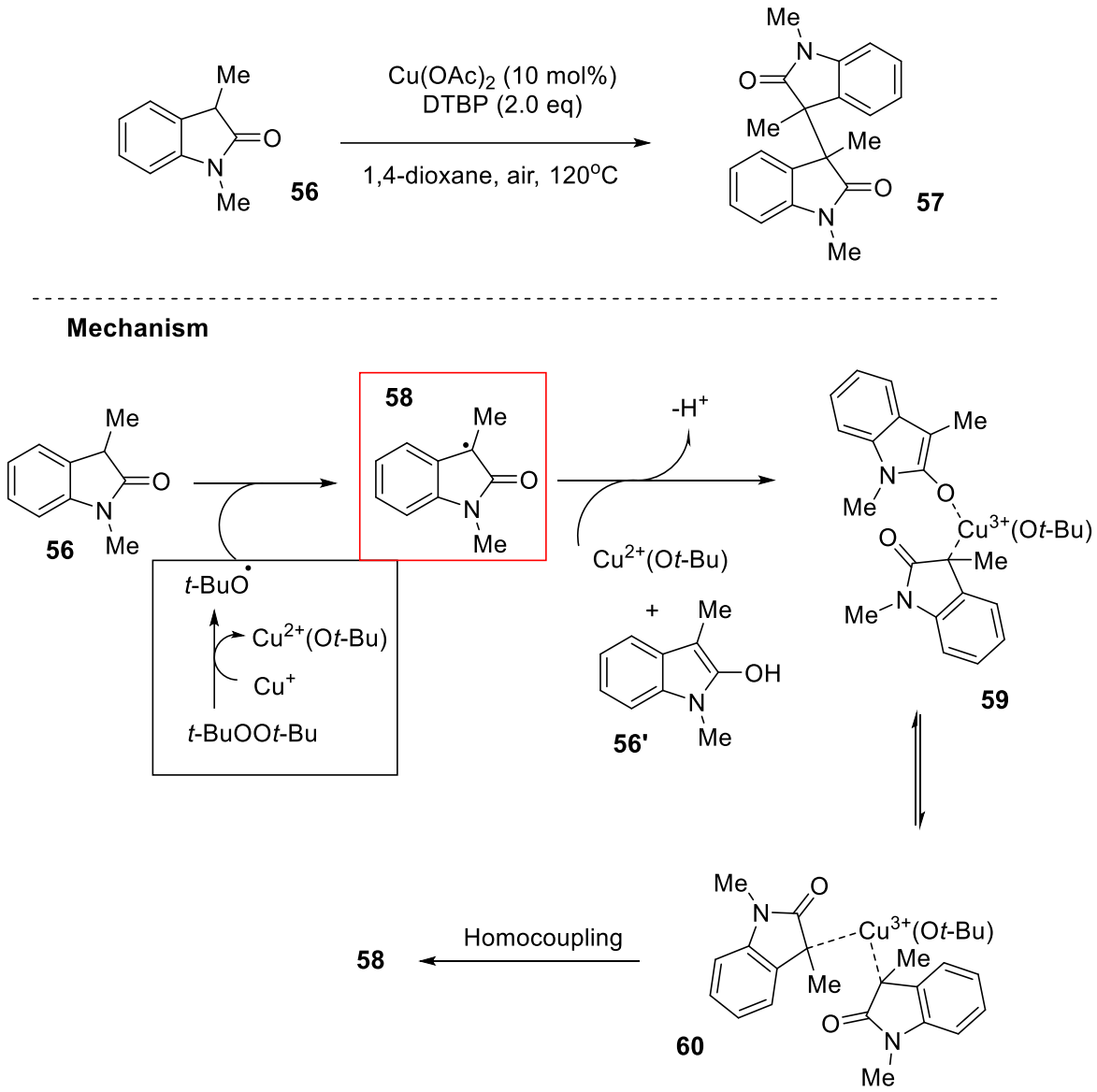

Figure 2.12. Methodology developed by Wei *et al*. for bisoxindole synthesis.

Considering the importance of bisoxindoles in accessing the dimeric hexahydropyrroloindole scaffold, our aim was to expand upon the repertoire of available methods towards their synthesis. Primarily, we noticed a gap in methodologies focused on using simple, acyclic starting materials, which we hoped would allow for the synthesis of novel analogues. With that goal in mind, we looked towards radical dimerization, which stood out as an extremely powerful, effective, and versatile method in the synthesis of bisoxindoles; our vision, and hope, was to elaborate on this already solid technique. We were inspired by the works of Gong,[54] as well as Du and Zhao[55] who developed methodologies to synthesise bisoxindoles (**63**/**64**) of the type **26a** from linear, acyclic bisanilines (**61**/**62**) under oxidative conditions (**Figure 2.13**).

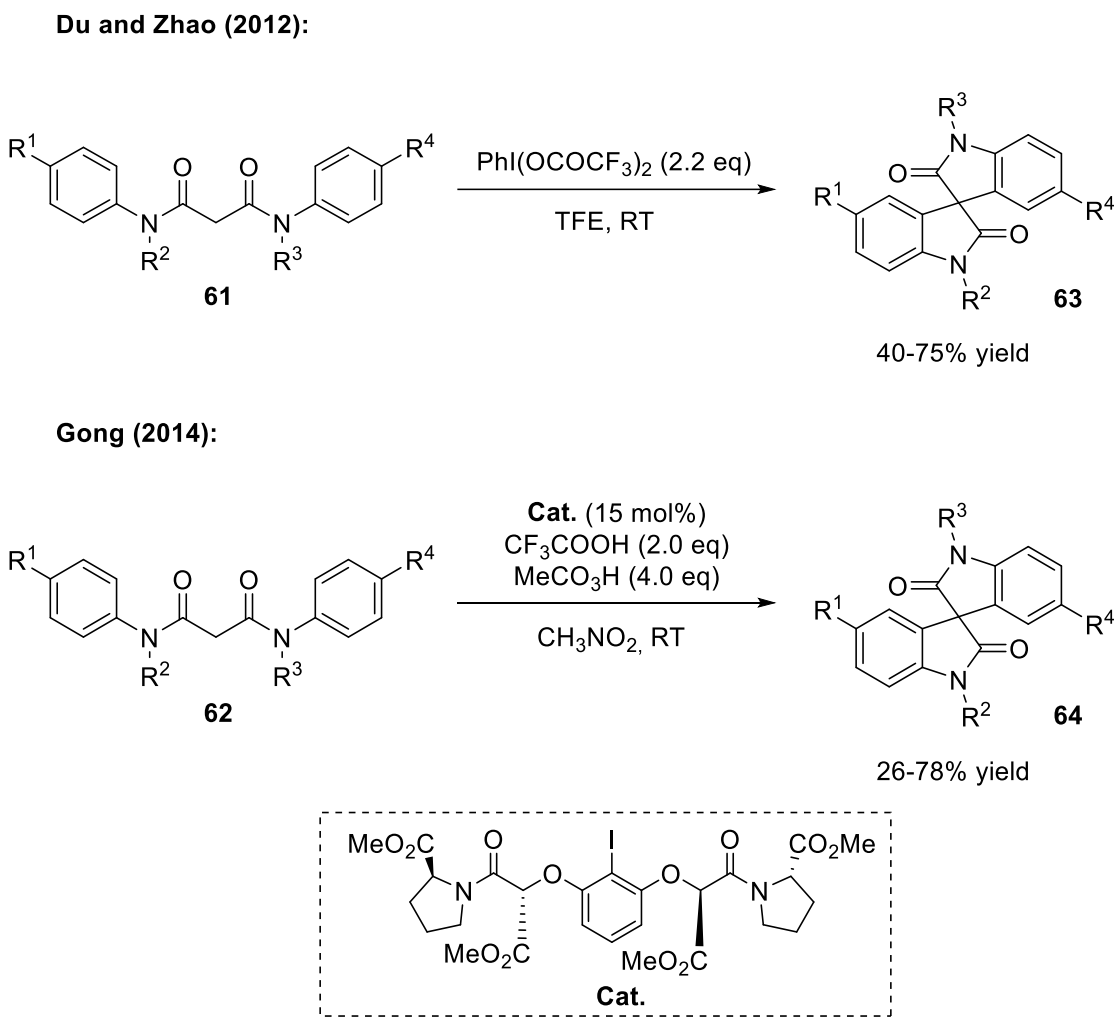

Figure 2.13. Methodologies of Gong/Du and Zhao for the conversion of linear bisanilines to bisoxindoles.

A notable trend in the previously mentioned radical dimerization is the use of already constructed indoles prior to dimerization, thus, encouraged by the above work we wondered whether a similar approach could be employed to synthesise bisoxindoles of type **26b** from linear, acyclic molecules. In addition to providing a more versatile route to access bisoxindoles, such an approach could allow for the synthesis of novel or difficult to access bisoxindoles unencumbered by the availability of the required 3-indole.

Design aim

The acyclic precursor

Our initial approach focuses on the use of photoredox catalysis, which, as shown in chapter 1, is powerful and versatile technique for the generation of radicals under benign conditions and has already been used to synthesise bisoxindoles (**Figure 2.10/2.11**). These relatively mild conditions, in tandem with our vision of environmental consciousness and sustainability within our synthesis and methodology, made a photoredox approach the natural choice.

Method in hand, the next, and perhaps most crucial step, was to determine the identity of the acyclic precursor molecule. We imagined a suitable, unactivated, acyclic molecule that, in the presence of a photocatalyst and visible light, could undergo cyclisation, to form the oxindole scaffold, then subsequently fragment to generate the key radical intermediate (**65**), that can finally dimerize. We hoped such a molecule could undergo this cyclisation-fragmentation-dimerization to produce the bisoxindole in a one pot cascade sequence.

Retrosynthetic analysis (**Figure 2.14**) gave insight into what such a molecule might look like:

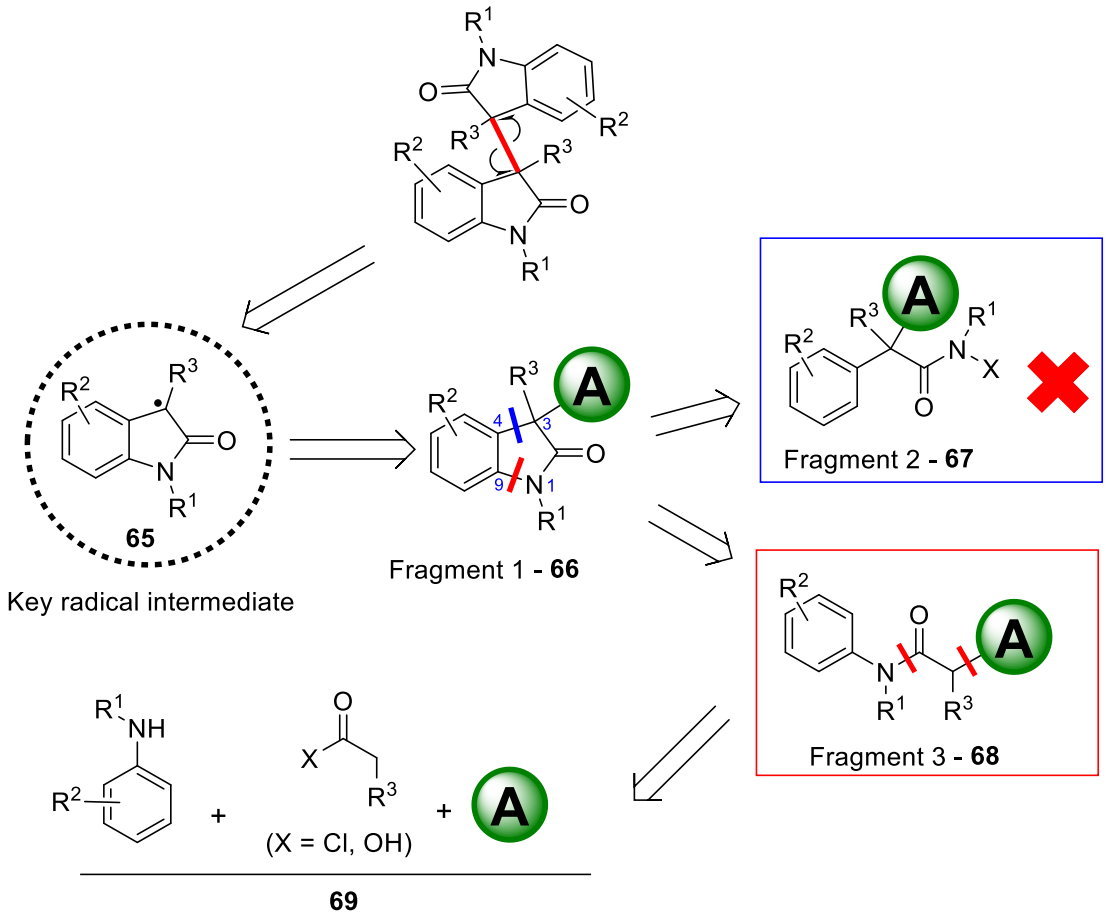

Figure 2.14 Retrosynthetic analysis from key radical intermediate **65**.

Beginning with the key radical intermediate (**65**), we visualised a fragmentation process from an indole, fragment 1 - **66**, possessing some labile group **A**. Thereafter two possibilities exist: either the C1-C9 bond can be split to give fragment 2 (**67**) or the C3-C4 bond can split giving fragment 3 (**68**). At this junction we opted to proceed via **68** over **67**; the rationale being that **67** would need to proceed via the generation of an amidyl radical to form **65**, which we anticipated would be quite challenging as the precursors for the formation of **67** are significantly more costly to synthesise both in terms of efficiency; they would add an extra step from anilines, as well as price; the required precursors would mandate the purchase of more expensive and rare starting materials, in addition to their high reactivity (e.g. *N*-halogens and *N*-nitrosoamides).[72] Consequently, this, in conjunction with the relative harshness of the reaction conditions necessary to form amidyl radicals, places constraints on the identity of the R_2 group, as many functional groups would be intolerant to the conditions.[73] Finally, the umpolung of the Nitrogen

means that H-abstraction often competes with the C-N bond formation, which has been shown to not only slow down the rate of cyclisation but, also inactivate the substrate.[74]

In comparison, we anticipated that generating the C3-centred radical from **68** to be notably less challenging; C3 sits adjacent to an enolisable carbonyl, thus we expected α-Hydrogen abstraction to form C3-centred radical of **68** to proceed under milder conditions.[75] Adding to this, the reaction rates of C-centred radicals, particularly in forming five-membered rings are faster relative to amidyl radical cyclisations.[73] Furthermore, the reaction conditions are usually more benign compared to those involving amidyl radicals, thus functional group tolerance of the R_2 was postulated to be less of a concern. Finally, H-abstraction by the C-radical would not be detrimental as in the case of the N-radicals. Following this, a final disconnection could be done on **68** to generate the three base components (**69**).

The leaving group

With a good baseline of what the fragment needed to form the key radical intermediate should look like (**68**), the last remaining piece of the puzzle was to determine a suitable leaving group. Given the nature of the reaction, it was critical that the lability of **A** be such that it would promote cyclisation before fragmentation i.e. stable enough not fragment straight away, but labile enough to fragment post-cyclisation. While not acyclic, we were inspired by Liu and Wu's approach (**Figure 2.10**); using a halooxindole which fragments to give the key radical intermediate. Halogenation is one of the most popular methods to generate C-centred radicals[76] however, based on the typical bond dissociating energies (BDE) for homolytic fragmentation, we anticipated that the C-X bond is presumably too weak relative to the α-C-H bond and thus would likely fragment before cyclisation (**Figure 2.15**). [77–79]

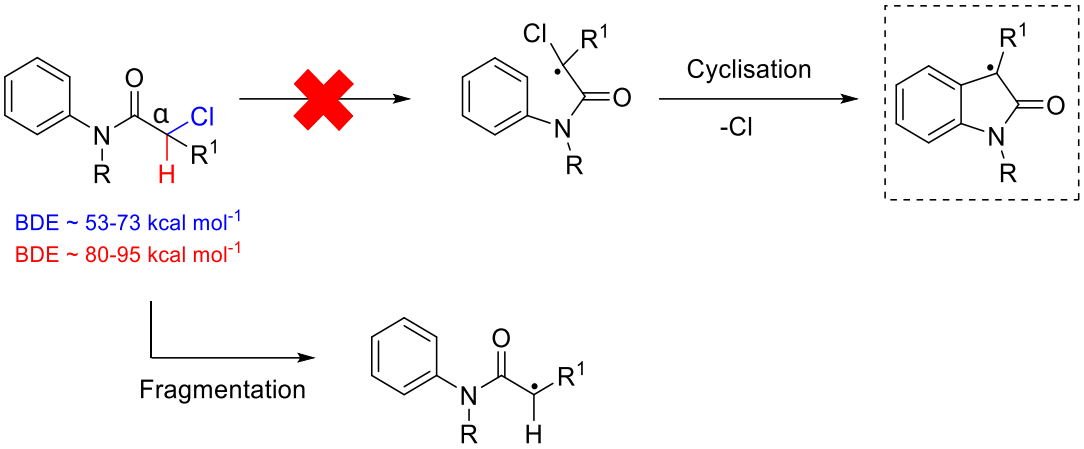

Figure 2.15. Predicted outcome of using a haloanilide acyclic precursor.

In searching for a suitable leaving group, acyl functional groups stood out as promising candidates (**Figure 2.16**, **70**). Previous work demonstrated the stability of various acyl groups during α-hydrogen abstraction to produce C-centred radicals,[80] which seemed promising for the envision mechanism. Narrowing it down further, we discounted ester groups (**71**) based on previous results by Rodrigo (**Figure 2.7**), Bisai (**Figure 2.9**) and Taylor[81] which demonstrated their stability to fragmentation when paired with an indole scaffold. Ketones (**72**) were also eliminated based on the results from Kim *et al.*, again on indoles, which showed similar stability to fragmentation.[67] From the remaining functional groups, the aldehyde and acid moieties (**73** and **74** respectively) were particularly interesting; despite the fact that an *N*-anilide with an either functional group (oxoanilides and oxoacid respectively) had not previously been synthesised, based on previous works,[82,83] it was noted that BDE for acyl groups is largely independent on the R group,[83] thus we could say with some confidence that the BDE for **73** and **74** would be much closer to the predicted BDE for the α-C-H (80-93 kcal mol^{-1}), at ~89 kcal mol^{-1}.

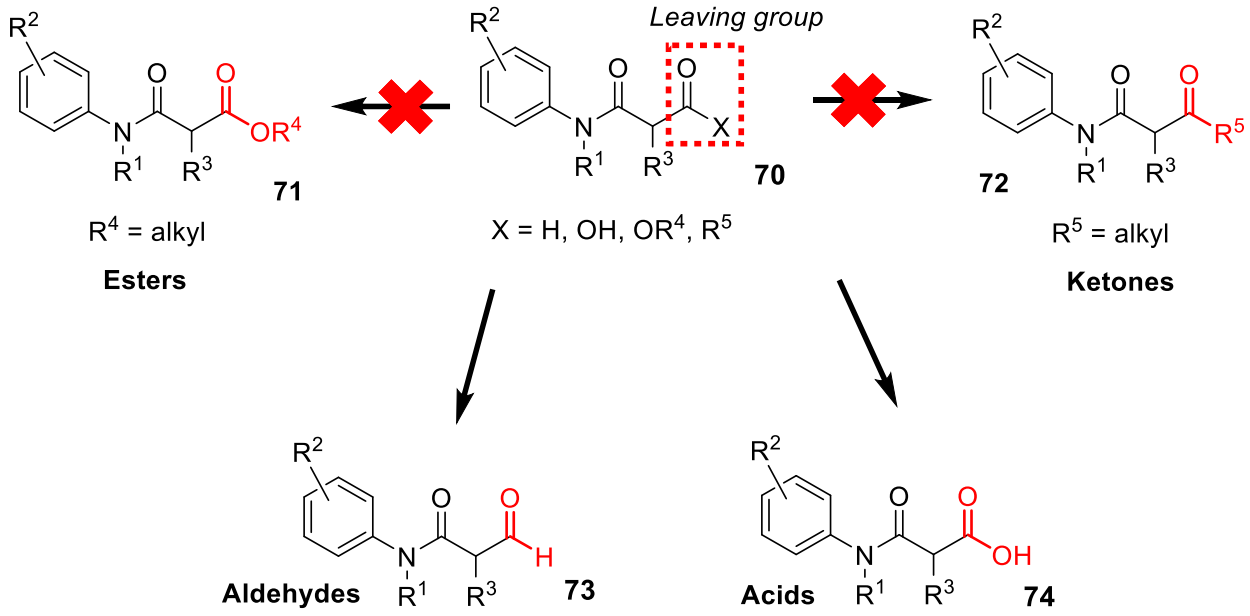

Figure 2.16. Proposed key acyclic molecule for the generation of fragment **65**, highlighting the leaving group, with suitable and unsuitable acyl groups shown.

While this was on the upper limit of our predictions, the presence of either aldehyde or acid would mean two enolisable groups between the α-C-H, which we hypothesised to have a BDE-lowering effect on the α-hydrogen, especially for a tertiary hydrogen, based on the trends seen in other dicarbonyl molecules.[78] Furthermore, there is strong evidence in the literature for the autooxidation of aldehydes by single electron oxidants such as Mn(III), which can lead to decarbonylation, via a concerted electron transfer from the aldehyde to metal species, M^{n+1}, reducing it and forming the C-centred radical in the process[83] (**Figure 2.17**).

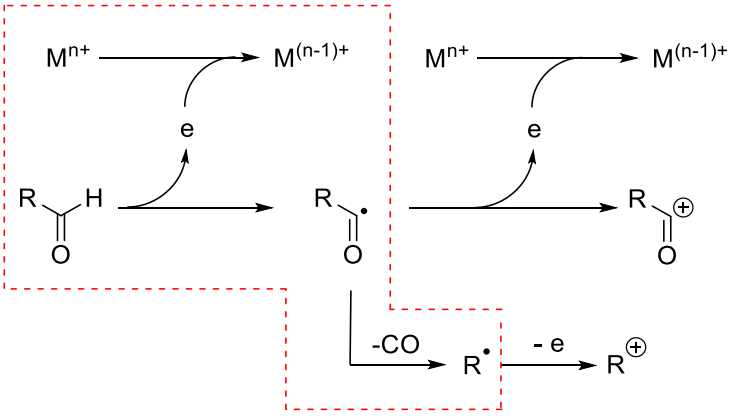

Figure 2.17. Mechanistic overview of the autooxidation and fragmentation of aldehydes to form C-centred radicals via a single electron oxidant.

Some specific examples of this process can be seen in **Figure 2.18**. The first, a β-(acyloxyl)alkyl radical rearrangement (Tanner and Law, 1969), is postulated to proceed *via* a radical decarbonylation of the 2-methyl-4-oxobutan-2-yl acetate (**75**), to form the *iso*-butyl acetate (**76**).[84] Another example is the tributyltin hydride mediated reaction of aryl bromides (**77**) by Grissom which proceeds *via* a key radical decarbonylation of a carbonyl radical, generated by a 1,5-hydride shift of the intermediate aryl radical (**77'**).[85] The combination of these factors gave us confidence in the aldehyde functionality as a suitable leaving group and hence, motivated us to pursue the synthesis of **73** as one of the key molecule for our methodology studies in the synthesis of bisoxindoles.

Tanner and Law (1969):

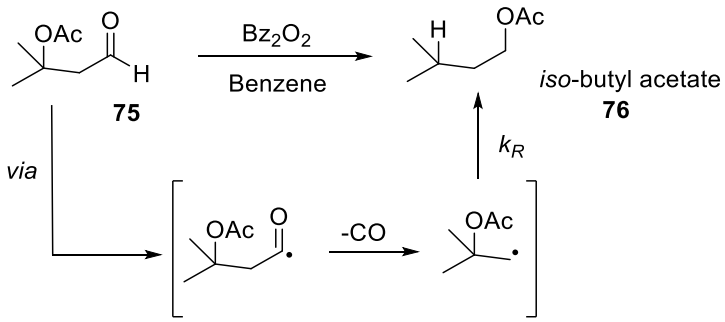

Grissom (1994):

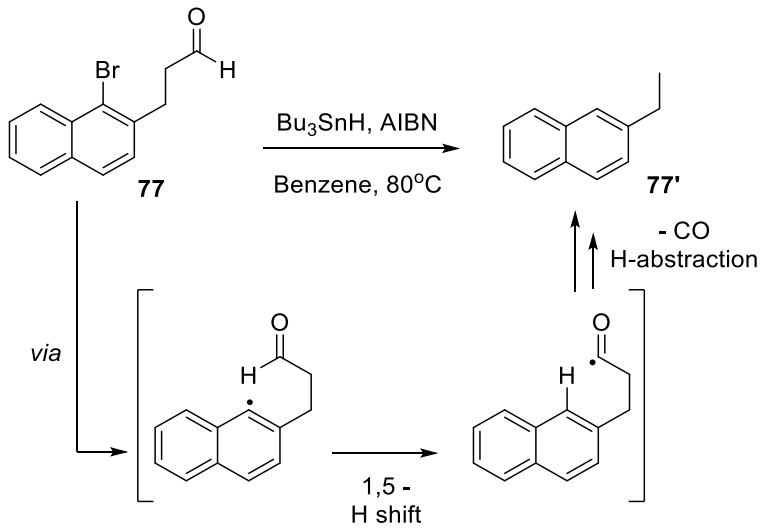

Figure 2.18. Postulated molecule with the aldehyde leaving group in the synthesis of bisoxindoles, with mechanism and examples of aldehyde autooxidation.

Similarly, radical decarboxylation is a widely studied mechanism that has been extensively utilised to generate C-centred radicals. While these methods initially relied on high temperatures (>250 °C) and stoichiometric or super stoichiometric amounts,[86] the methodology has since been significantly expanded to allow for decarboxylation under much more benign conditions including, but far from limited to, transition metal catalysis such as Palladium,[87,88] photoredox catalysis,[89–91] and even under metal-free conditions.[92]

Mechanistically, most follow a pathway of deprotonation, followed by extrusion of CO_2, typically via homolytic radical fragmentation. A quintessential example of this methodology can be seen in the work of Ventre, Petronijevic and MacMillan in 2015, whereby they achieved selective fluorination of aliphatic carboxylic acids via a decarboxylative photoredox strategy. The mechanism for this process can been seen in **Figure 2.19**.[93] To initiate the photocatalytic cycle the Ir^{3+} photocatalyst, ($Ir[dF(CF_3)ppy]_2(dtbbpy)PF_6$), is irradiated with blue light to form the excited state photocatalyst, $[Ir^{3+}]^*$. Thereafter, oxidative quenching and SET from this excited state species to the radical cation of Selectfluor® (**78**), generates the Ir^{4+} species. Note that while the mechanism shows **78** is only produced *after* photocatalytic cycle turnover, the authors postulated that a sacrificial quantity of Selectfluor (**78'**) can undergo homolytic fragmentation, as demonstrated by Sammie *et al.*,[94] which is sufficient to initiate the cycle. The generated Ir^{4+} species is strongly oxidising and generates a transient carboxyl radical from the substrate (**79**), which fragments via de-protonation and extrusion of CO_2 to provide key C-centred radical species (**79'**). Concurrently, this reduces the Ir^{4+} species and re-generates the active Ir^{3+} photocatalyst, thus turning over the photoredox cycle. Lastly, interception of the C-centre radical by **78'** allows for the direct transfer of fluorine to form the desired fluoroalkane (**80**).

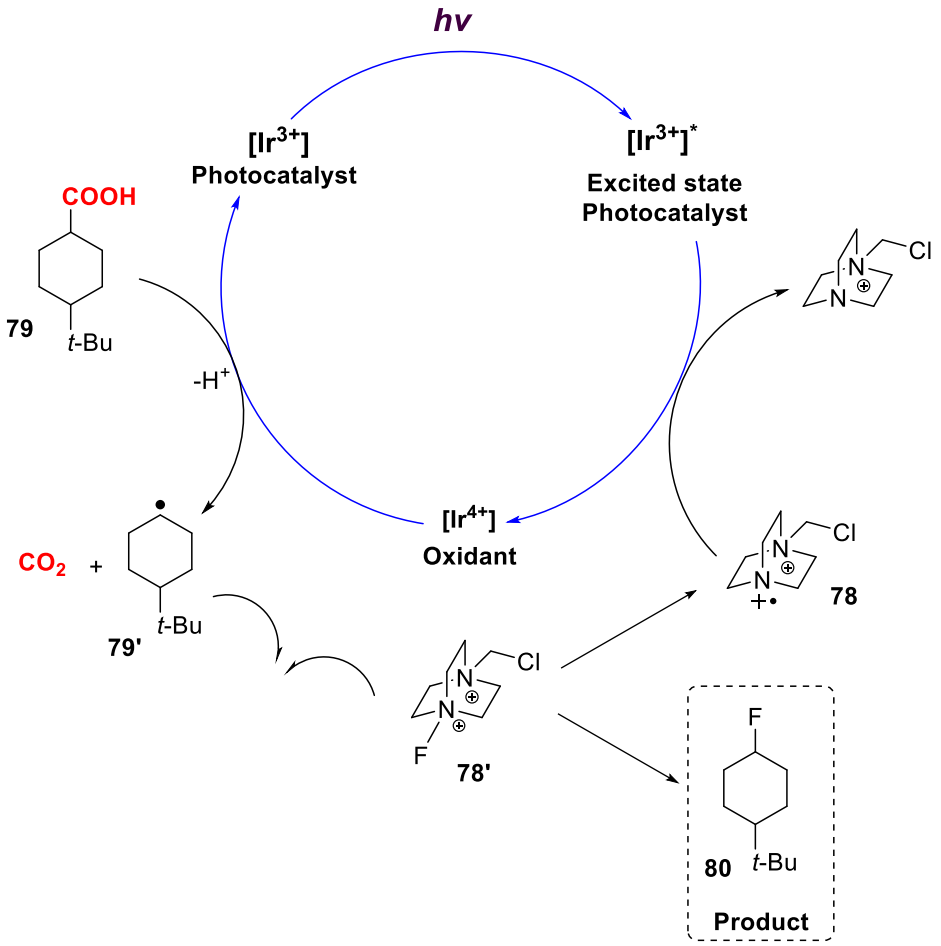

Figure 2.19. Photoredox-mediated fluorination of primarily aliphatic acids via radical decarboxylation.

Encouragingly, the diversity of functional groups bearing a -COOH, that have demonstrated tolerance to radical decarboxylation, is quite broad. In particular, methodologies have been especially effective when the acid in question is highly activated such as our postulated β-oxoacids.[95] This versatility, in conjunction with the volume of methodologies inspired confidence in **74** as the second key molecule for our desired transformation.

Mechanism

Given the structure of the key acyclic precursors **73** and **74**, as well as the retrosynthetic analysis performed in **Figure 2.14**, we hypothesised a pathway to generate to the key radical intermediate, **65**. More specifically, we envisioned a process to generate **65** directly via cascading three-oxidative step mechanism.

This idea can be seen visually in **Figure 2.20.** Starting from either **73** or **74**, enolization and subsequent oxidation would form the respective tertiary radicals, **73a**/**74a**. Thereafter, intramolecular cyclisation of this generated radical can form the resultant radical intermediate, **73b**/**74b**, which, could undergo a second oxidation step to form the cationic intermediate **73c**/**74c**. From here, we suggest that deprotonation of this intermediate would restore aromaticity and furnish the oxindole scaffold, **73d**/**74d**. At this point, the generation **65** could be achieved by a third oxidation, which, would generate the carbonyl and carboxylate radicals (**73e** and **74e** respectively), which could fragment homolytically, as per **Figure 33 & 111**, giving us the desired key radical intermeduate, **65**. In either case, once formed, we hoped **65** would immediately proceed to the desired bisoxindoles scaffold via a straightforward homolytic dimerization as seen in **Figures 2.7 – 2.11**.

Given the necessity for three oxidation steps, the ideal scenario would be a catalytic cycle that could oxidise **73**/**74**, be regenerated by a sacrificial oxidant, then repeat the process twice more with **73b**/**74b** and **73d**/**74d**. Based on this need, we proposed a series of three catalytic cycles (**Figure 2.21**).

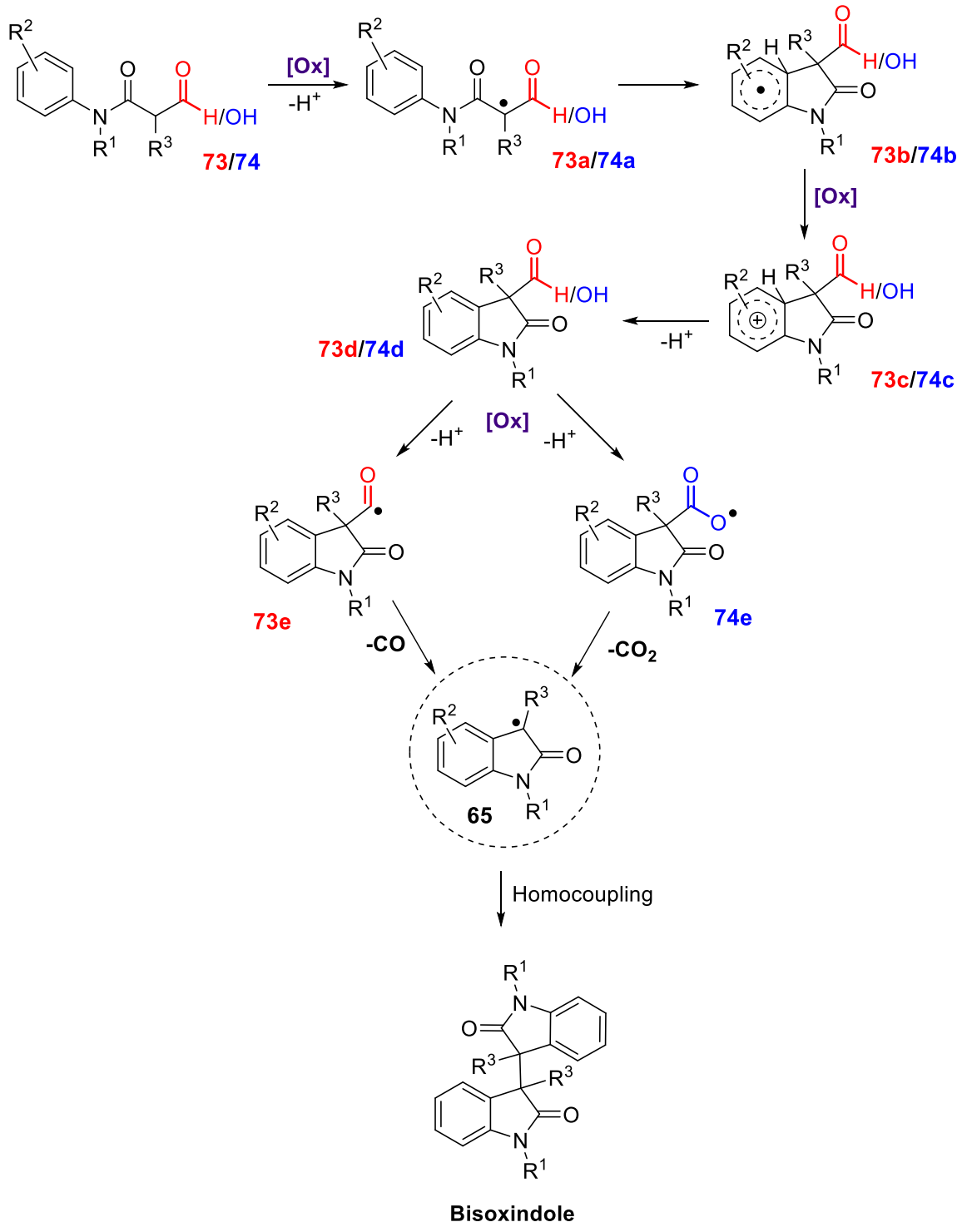

Figure 2.20. Mechanistic pathway to bisoxindoles scaffold from acyclic pre-cursors **73** and **74** via a triple-oxidation cascade cyclisation-dimerisation sequence.

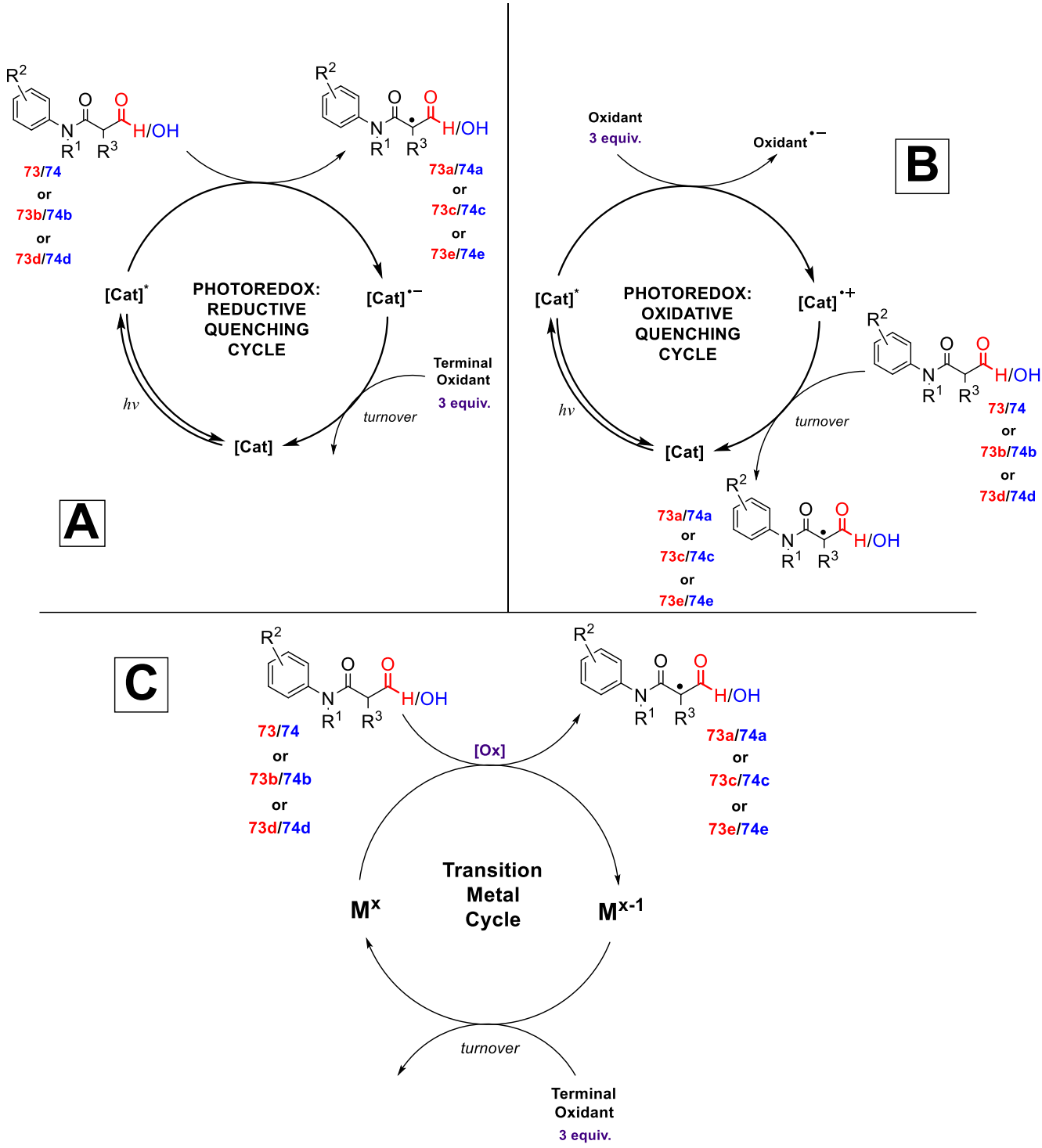

Figure 2.21. Our proposed catalytic cycles using A) Photoredox catalysis under a reductive quenching cycle. B) Photoredox catalysis under an oxidative quenching cycle. C) Transition metal catalysis.

The first two cycles **A** and **B** both utilise photoredox catalysis but differ in their modes of quenching as per **Figure 1.9**.

In the case of **A**, following the excitation of the photocatalyst **[Cat]** to the excited state, **[Cat]***, we suggest reductive quenching of this excited state directly by the substrates, yielding the resulting radicals and the reduced photocatalyst, $\mathbf{[Cat]}^{-}$. Regeneration of the active catalyst can then be achieved by oxidation by a terminal oxidant.

In contrast for **B**, we suggest quenching of the excited state by a sacrificial oxidant, rather than the substrate, which would follow an oxidative quenching cycle, to produce the oxidised photocatalyst $\mathbf{[Cat]}^{+}$. Interception of this oxidised catalyst by the substrates could then generate their respective radicals and turnover the catalytic cycle.

While a photoredox method was to be our preferred route, we thought to complement this approach with transition metal catalysis, **C**. Here, the same mechanism seen in **Figure 2.21C** would follow, with the oxidation of the respective substrates being done catalytically by a transition metal ion, $\mathbf{M}^{x}$, reducing the ion to the respective $\mathbf{M}^{x-1}$ species. As with **A**, regeneration of the active catalytic ion via oxidation could be achieved by a terminal oxidant.

In all three cases, the underlying mechanism, **Figure 2.20**, calls for three sequential oxidation steps *per substrate of **73**/**74***, which would necessitate a minimum of 3 equivalents of a sacrificial oxidant to generate three equivalents of oxidant.

Chapter 3:

Methodology studies on the synthesis of the bisoxindole scaffold via transition metal catalysis

We began our study by first focusing on the conceptualisation and synthesis of a model substrate for the aldehyde, **81**. The key requirements for the substrate were simplicity while conserving of the structural skeleton, (Chapter 1, **73**). The rationale of this choice was to streamline the synthesis and minimise the possibility of unwanted side reactions. Moreover, a structural simple and small molecule should further minimise potential side-reactions or inhibit reactivity due to sterics or other size-dependent factors and allow for relatively facile analysis during optimisation studies.

Retrosynthetically, we envisioned its formation via the formylation of an anilide intermediate, **82**. Synthesis of such anilides is well-documented and relatively facile from their respective anilines and a corresponding acids or acid chlorides (**Figure 3.1**).

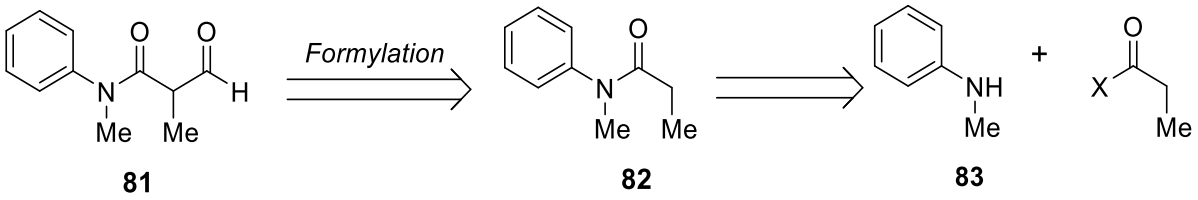

Figure 3.1. Retrosynthetic scheme for the synthesis of aldehyde **81**.

The first approach involved a peptide coupling strategy, which has been well established on similar systems in the presence of an *N*-methyl group,[81,96] utilising *N*-methylaniline **83**, which was accessed via two separate routes. The first used and propionic acid **84**, in the presence of a base and 2-Chloro-1-methylpyridinium iodide **85** as the coupling reagent (**Figure 3.2**).

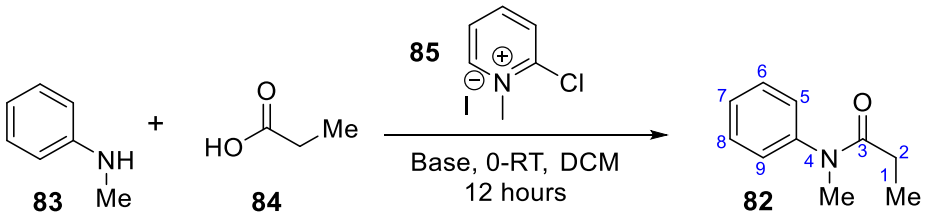

Figure 3.2 Route one in the synthesis of aniline, **82**.

The propionic acid, **84**, with **85** which generates a reactive pyridinium propionate ester that is susceptible to nucleophilic attack by aniline **83**. Choice of base seemed important here as the first run utilised triethylamine (NEt_3) as the base, which delivered the desired anilide **82**, as confirmed by matching spectra from previous reported syntheses,[96] in 56%

yield and returning the remainder as starting material. Switching to *N,N*-diisopropyethylamine (DIPEA) however, significantly improved the reaction, producing **82** in 72% yield and the remainder returned as starting material.

In the second approach, **83** was reacted with an excess of oxalyl chloride $(COCl)_2$ and the resulting acid chloride **86**, distilled under argon. Reaction of **86** with **83** and triethylamine in DCM at room temperature proved much more efficient, delivering the anilide in 98% yield (**Figure 3.3**). A series of acid and base washes could then be used to relieve the product, which was pure enough to be used without chromatographic separation. While this result gave a significantly better yield, the two methods were complimentary for constructing a library of compounds later, particularly in cases where the acid chloride was unavailable or unstable.

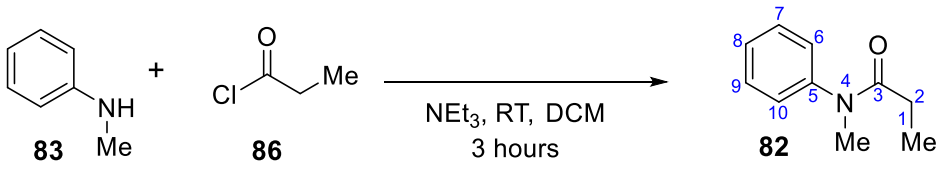

Figure 3.3. Route two in the synthesis of **82**.

With a facile route to **82** in hand we were able to begin investigation into the formylation for the synthesis of **81**. A search of the literature revealed that while many counterparts to **81** containing other carbonyl moieties are known, these specific compounds (i.e. formyl oxoanilides) were unreported. While brainstorming methods, we first turned to popular formylation reactions such as Vilsmeier-Haack, Reimer-Tiemann and Gattermann.[97] These however, are largely limited in scope to aromatics, while those on aliphatic chains such as Bouveault or Bodroux-Chichibabin reaction[98] utilise substitution of a halide or require the starting material to be a Grignard reagent, neither of which were applicable to **82**. In the context of our design aims and wanting to avoid modification of **82** and adding extra steps to the synthesis, we sought out other methods which could achieve formylation in one step from **82** without prior modification.

Our pursuits led us to the discovery of a one-step formylation procedure used by Tius *et al.* in their preparation of (((trimethylsilyl)ethoxy)methoxy) esters (**Figure 3.4**).[99] En route to these esters, they described the formylation of an inactivated ester substrate **87**, to

afford the 1,2-dicarbonyl product, **88**, using ethyl formate as the formylating reagent in the presence of titanium tetrachloride ($TiCl_4$) and NEt_3 (**Route A**) or via standard enolate chemistry (**Route B**). Given the structural similarity of these substrates to our amide system, we were encouraged that this protocol would be broadly transferable to the formylation of **82**.

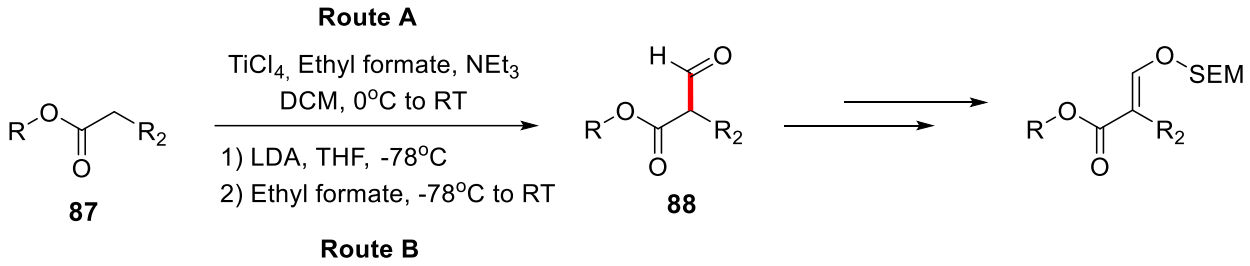

Figure 3.4. One step formylation developed by Tius *et al.* for the formylation of esters.

A summation of optimisation attempts for this reaction can be seen in **Table 3.1:** Optimisation of the formylation of **82**. [a]Anhydrous DCM used. [b] Tius's method modified to increase wait time between addition of $TiCl_4$ and DCM to ~1 hour.

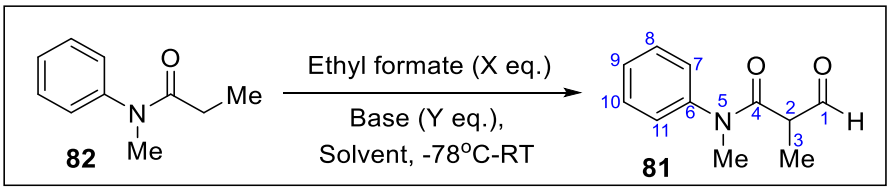

Entry	Base (eq.)	Formate (eq.)	$TiCl_4$ (eq.)	Solvent	Yield (%)
1	NEt_3 (1.2)	Ethyl (4.0)	-	THF	0
2	KHMDS (1.2)	Ethyl (1.2)	-	THF	15
3	KHMDS (1.2)	Ethyl (1.2)	-	DCM	9
4	KHMDS (2.0)	Ethyl (4.0)	-	THF	22
5	KHMDS (6.0)	Ethyl (10)	-	THF	23
6	LiHMDS (2.0)	Ethyl (4.0)	-	THF	0
7	LDA (1.1)	Ethyl (4.0)	-	THF	0

8	NEt_3 (2.4)	Ethyl (3.0)	2.0	DCM	17
9	NEt_3 (2.4)	Ethyl (3.0)	2.0	THF	27
10	NEt_3 (2.4)	Ethyl (3.0)	2.0	ACN	6
11	NEt_3 (2.4)	Ethyl (3.0)	2.0	DMF	19
12	NEt_3 (3.5)	Ethyl (3.0)	2.0	THF	34
13	NEt_3 (3.5)	Ethyl (6.0)	2.0	THF	45
14	NEt_3 (3.5)	Ethyl (6.0)	3.0	THF	53
15[a]	NEt_3 (3.5)	Ethyl (6.0)	3.0	DCM	60
16[a]	NEt_3 (3.5)	Methyl (6.0)	3.0	DCM	70
17[a,b]	NEt_3 (3.5)	Methyl (6.0)	3.0	DCM	82

We began our study by investigating the standard enolate chemistry procedures (**Route B, Figure 3.4**) using a variety of bases. The first run (entry 1) with **82**, triethylamine and ethyl formate failed to deliver aldehyde **81** with total recovery of starting material. Thus, we sought out stronger bases, settling on LDA, LiHMDS and KHMDS. In the first of these, KHMDS (entry 2), 15% of the starting material was consumed. By TLC, this product was characterised by a long streak which was more polar than the starting material in a mixture of ethyl acetate (EtOAc) and hexanes. NMR analysis of the isolated product vs starting material is shown in **Figures 3.5–3.6.** The ^{1}H-NMR of the product integrates for a total of thirteen protons, the same as that of the starting material. The distinction in the NMR of the product, (**Figure 3.5B/C.**) vs the starting material (**Figure 3.5A.**) is most pronounced in the differences between the signals 1 and 2 (which correspond to the C1-CH_3 and C2-CH_2 respectively of **82**). In the case of signal no. 1, the difference in multiplicity from triplet at 1.28 ppm in the **82** to a doublet of product is in line with what was expected if formylation occurred at the C2 position as there would be one less proton to couple to. In the case of signal no. 2, there was a downfield shift from 2.09 ppm in the starting material to 3.27 ppm in the product, where it overlaps with the *N*-methyl singlet; being α to a carbonyl carbon, this proton should be relatively deshielded, thus this shift

is in line with what was expected. Accompanying this shift was a difference in integrations of this signal against that of **82** from two protons to one proton, agreeing with the case made above for C2 modification. Finally, the product spectrum shows doublet at 9.57 ppm, signal no. 3, which was highly suggestive of formylation as the chemical shift of this signal was in the range where aldehyde proton signals are typical reported (9+ ppm). Moreover, the multiplicity of the signal was expected to appear as a doublet *via* vicinal coupling between the aldehyde and C2 proton of **81**.

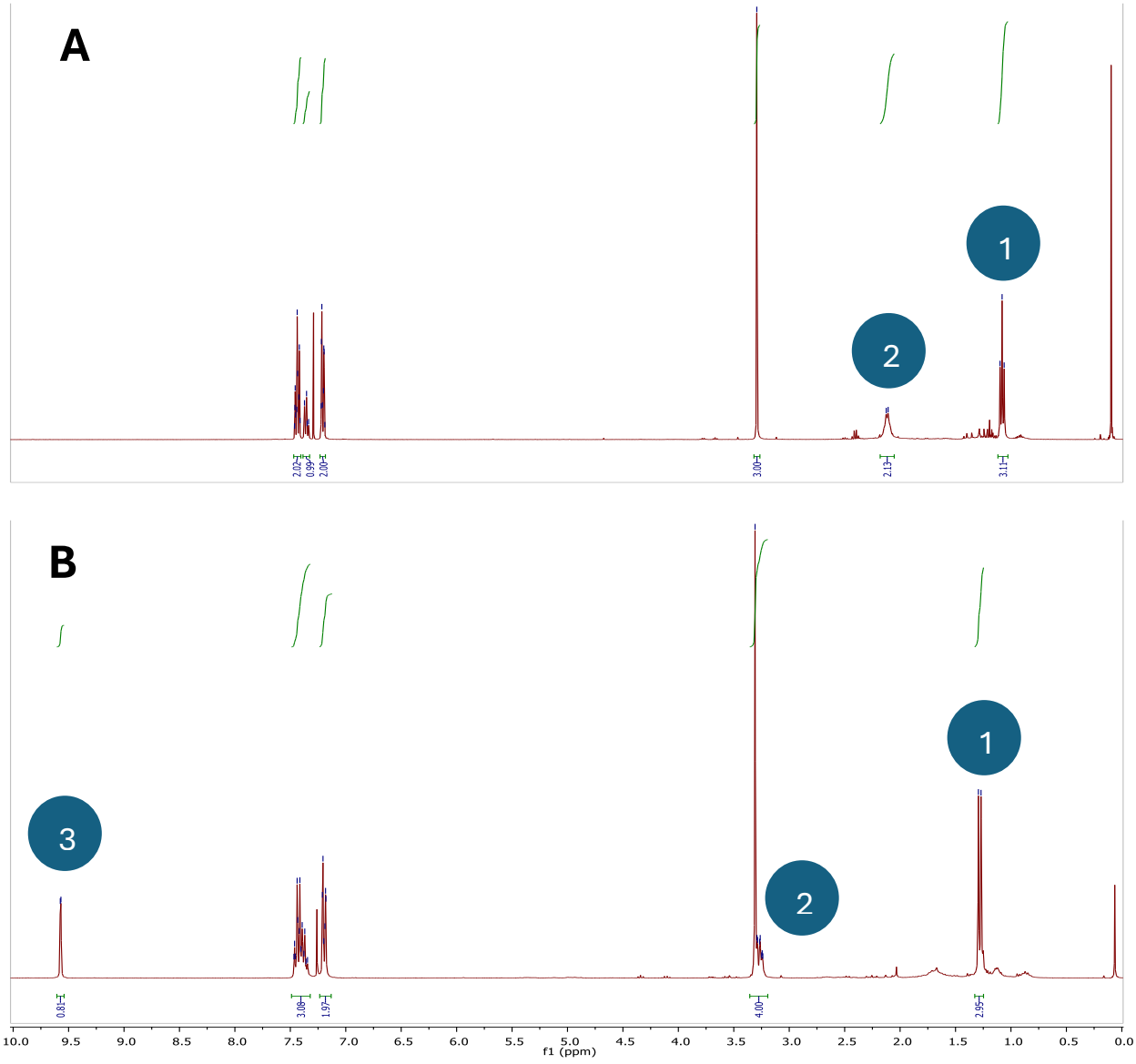

C

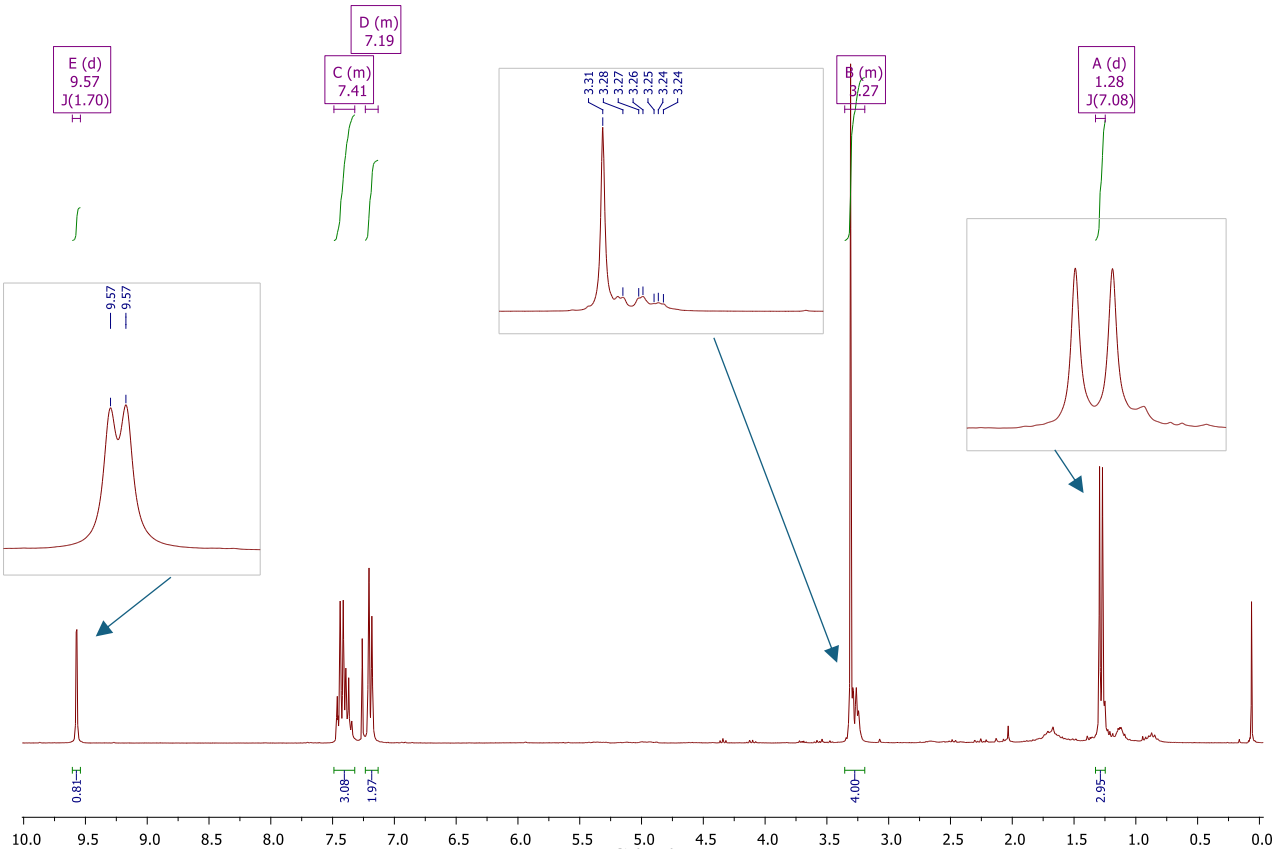

Figure 3.5. ^{1}H-NMR of product **81** (B) vs reactant **82** (A) under Tius's second conditions (**Table 3.1**, entry 2). Close up of ^{1}H-NMR spectrum of **81** (C).

When weighing in the ^{13}C-NMR and HSQC data, **Figure 3.6**, our confidence in formylation grew; more specifically the signal at 199 ppm (highlighted in **Figure 3.6B**) in the product (distinct from the amide signal at 170 ppm) is highly emblematic of carbonyl compounds (180 – 220 ppm). This signal forms a cross-peak with the doublet at 9.57 ppm in the HSQC which further made structure **81** more likely and finally, the doublet at 9.57 ppm is distinct from that of unreacted ethyl formate (8.04 ppm) and shows a cross-peak with signal no. 2 in **Figure 3.5B**, in the COSY which allowed us to rule out contamination of the product with residual ethyl formate.

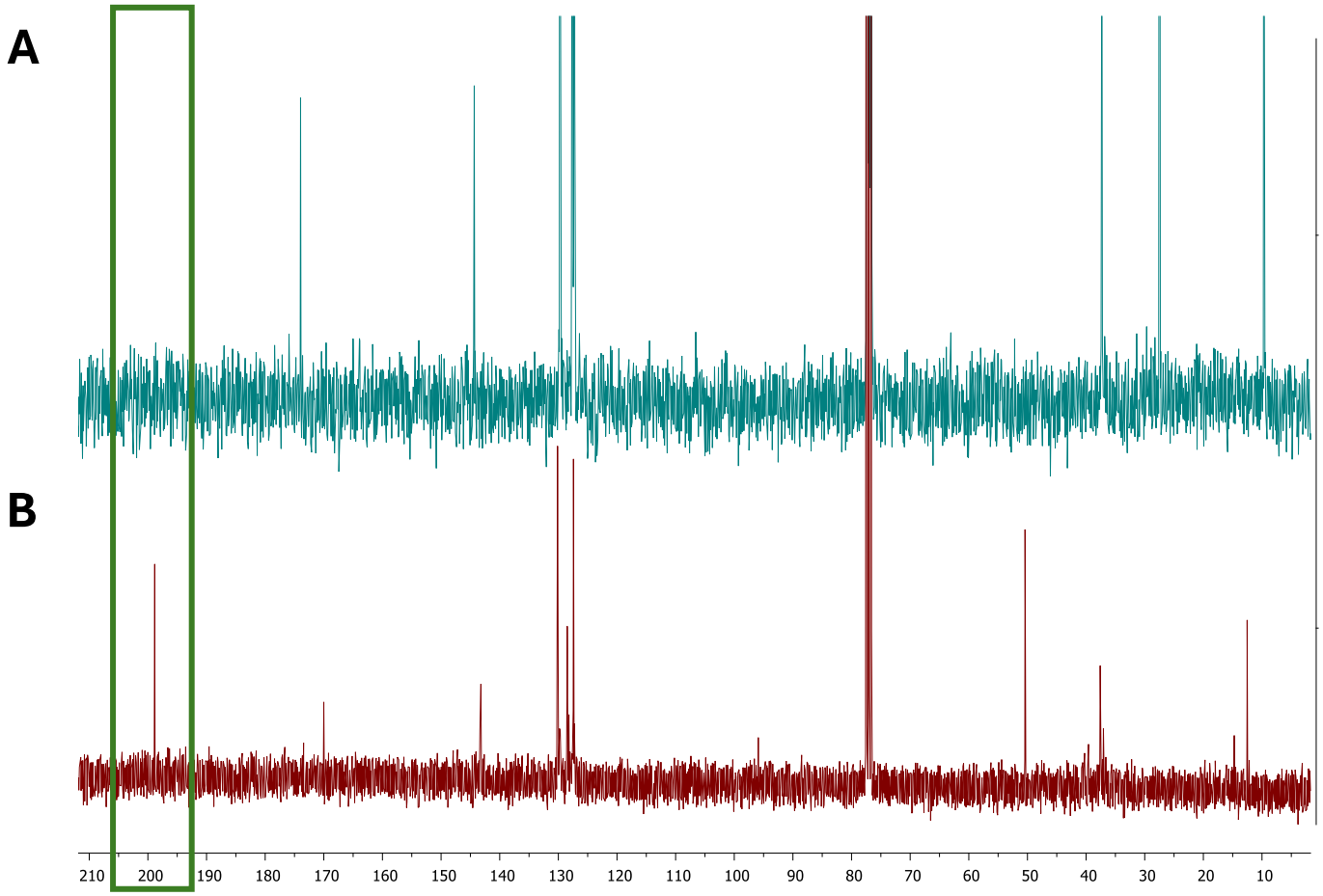

Figure 3.6. ^{13}C-NMR of **82** (A) vs product from the reaction of **81** under Tius's second conditions.

With the desired product in hand, we next attempted to optimise the reaction to bring the yield up. Switching the solvent from THF to DCM led to a decrease in yield to 9% and (entry 3), prompting us to increase the equivalents of KHMDS and ethyl formate. Using super-stoichiometric amounts of both (2.0 and 1.2 eq. respectively) successfully increased the yield to 22% (entry 4), however a further increase (6.0 and 10 eq. respectively) had diminishing returns (entry 5). Following this we attempted the reaction with LDA and LiHMDS (entries 6 and 7) we similarly observed no reaction, and the starting material was recovered. Next, we switched over to Tius's first set of conditions to gauge whether the aldehyde could form in better yield. In entries 8–11, Tius's 1st method was repeated with the same equivalents using DCM, THF, ACN and DMF. Under these conditions, which yielded **81** in 17%, 27%, 6% and 19% yield, respectively. With the best yield coming from THF, we took for further optimisations. Slow increase of reagent equivalents was met in

turn, by increasing yield as entries 12–14 illustrate. First an increase in NEt_3 equivalents bumped the yield up to 111% (entry 12). Following this increase in ethyl formate pushed the yield up to 45% (entry 13) and finally, further additions of $TiCl_4$ gave **81** (entry 14) in 53%.

At this point in the screen, we opted for use of anhydrous DCM (entry 15) which had a drastic increase on the yield, giving the desired aldehyde in 60% yield. Swapping the formylation agent from ethyl to methyl formate further increased this to 70% (entry 16). Finally, we noted that the time for enolate formation of **82** was of particular importance in the reaction. Previously, after addition of **82**, formylating agent and $TiCl_4$ at 0°C, a twenty-minute wait period was observed before addition of triethylamine. We observed that increasing the length of the period between addition of $TiCl_4$ and triethylamine, to at least one-hour, the reaction proceeds to completion with 82% of **81** recovered (entry 17).

Synthesis and optimisation of Bisoxindole

Preliminary CDC screen

At the time of writing there had been no reports of intramolecular cross-dehydrogenative coupling (CDC) to oxindoles using *N*-phenylalkylamides such as **81**, containing an aldehyde functional group, thus we turned to reported methods using similar systems (**Figure 3.7**) which led us to the works of Kündig (**3.7A**)[96] and Taylor (**3.7B/C**)[81] and Petersen (**3.7C**)[100] who had achieved cyclisation using copper-catalysis and molecular iodine, respectively, with an ester group in place of aldehyde. Similarly, MacMillan (**3.7D**)[101] had shown α-arylation of aldehydes was possible using cerium ammonium nitrate (CAN), a similar report had been described by Bisai (**3.7E**)[102] with 2,3-Dichloro-5,6-dicyano-1,4-benzoquinone (DDQ).

A - Kündig (2013)

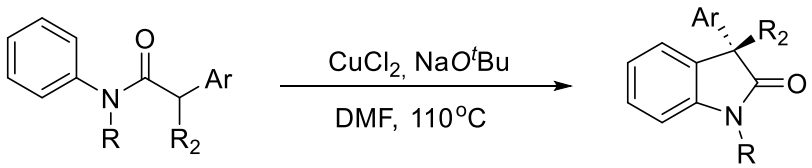

B - Taylor (2014)

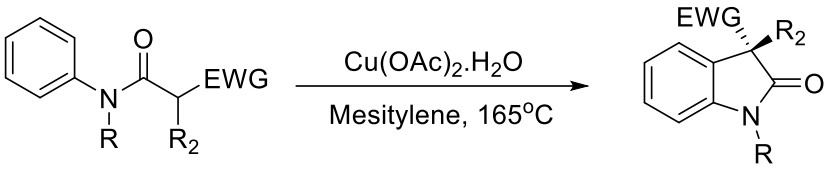

C - Petersen and Taylor (2017)

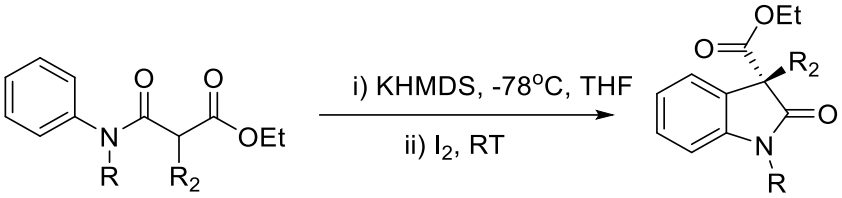

D - MacMillan (2009)

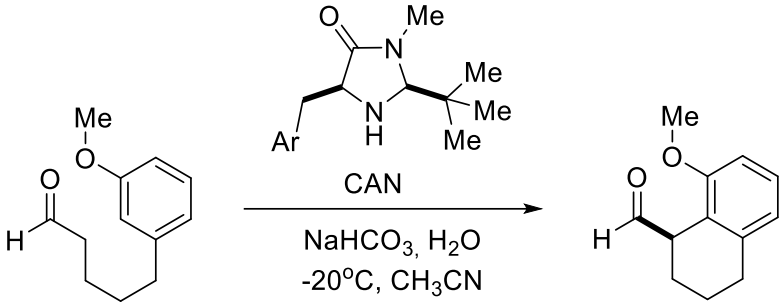

E - Bisai (2013)

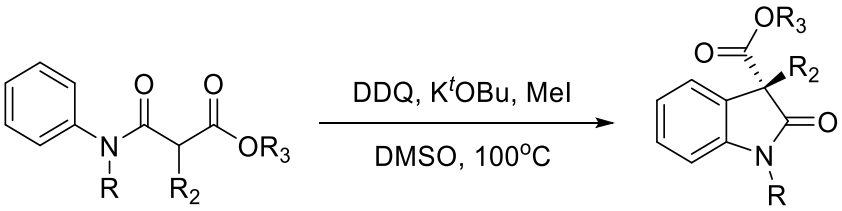

Figure 3.7. Reported intramolecular CDC reactions on similar scaffolds to **81**.

Importantly, these reactions were postulated by the authors to proceed the same key methine radical (**65**) which we require for our envisaged cascade, which encouraged us that these methods would be applicable to our system.

For our initial approach, the optimal conditions for the reactions in **Figure 3.2**, were trialled as at starting point then optimised further. In all cases trialled, only one set of conditions gave rise to the desired bisoxindole product, **89**.

A summary of our results using these methods are shown in **Table 3.2:** Preliminary screen of the viability of a CDC approach to bisoxindoles. *Entries 1–7 were performed under Ar, while entries 8–13 were open to air.*

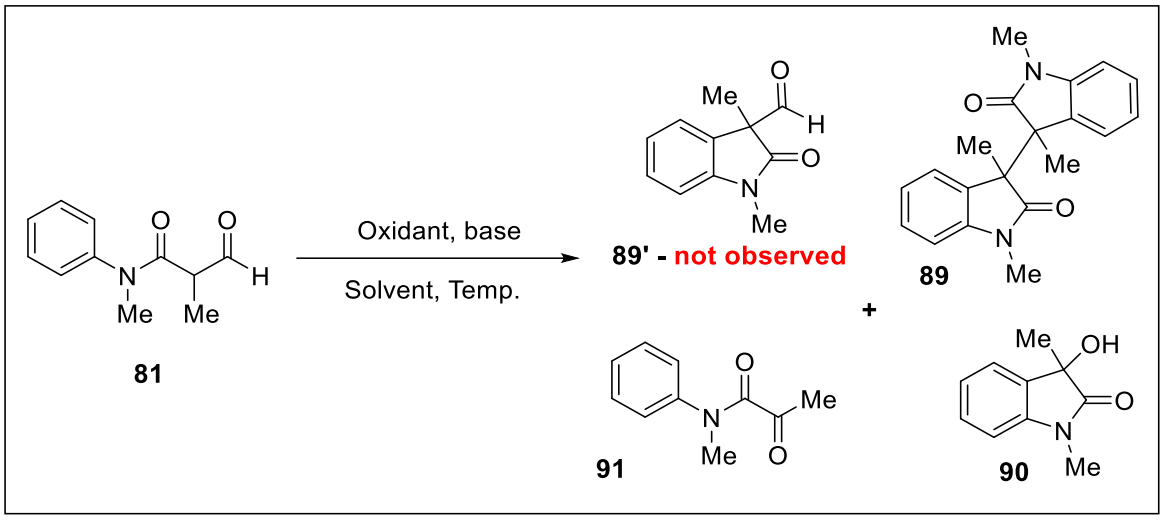

Entry	Oxidant (eq.)	Base (eq.)	Temperature (°C)	Solvent	Yield (%)		
					89	90	91
1	I_2 (1.2)	KHMDS (1.2)	-78→RT	THF	Trace	Trace	-
2	I_2 (1.2)	N/A	-78→RT	DMF	Trace	Trace	=
3	I_2 (1.2)	N/A	-78→RT	THF	Trace	Trace	=
4	DDQ (1.1)	KO^{t}Bu (1.2)	100	DMF	-	-	=
5	DDQ (1.1)	NaO^{t}Bu (1.2)	100	DMF	-	-	=
6	DDQ (2.5)	$NaHCO_3$	RT	Acetone	-	-	=
7	$CuCl_2$ (2.2)	KO^{t}Bu (5.0)	110	DMF	-	5	=
8	$Cu(OAc)_2.H_2O$ (5 mol%)	-	165	Mesitylene	19	32	29
9	CAN (2.5)	NEt_3 (3.0)	-78→RT	ACN	-	12	-
10	CAN (2.5)	$NaHCO_3$ (5.0)	-20→RT	ACN	-	22	-
11	CAN (2.5)	$NaHCO_3$ (5.0)	-20→RT	Acetone	-	34	-

12	CAN (1.0)	$NaHCO_3$ (5.0)	-20→RT	Acetone	-	17	-
13	CAN (2.5)	$NaHCO_3$ (5.0)	RT	Acetone	-	21	-

The first set of conditions for our CDC approach involved the use of low-temperature and iodine both with and without base (entries 1–3), at -78°C. While we were cognisant of the need for 3 equivalents of oxidant as per **Figure 2.20 – 2.21** to form the bisoxindoles, we were interested in isolating the monomeric oxindole pre-fragmentation and cyclisation (**89'**), according to Petersen and Taylor, as this would provide more control compared to methods using transition metals at high temperatures. We were however, unable to observe or isolate this product.

Monitoring the reaction by TLC, the disappearance of the SM with the concomitant formation of a single spot is observed. This was in line with what was reported by the authors, presumably the formation of C-iodinated intermediate. However, this could not be isolated as it immediately fragmented upon warming up to RT, with the major product being anilide **82** (87%) as well as *N*-methyl-*N*-phenylformamide (9%) (**Figure 3.8**).

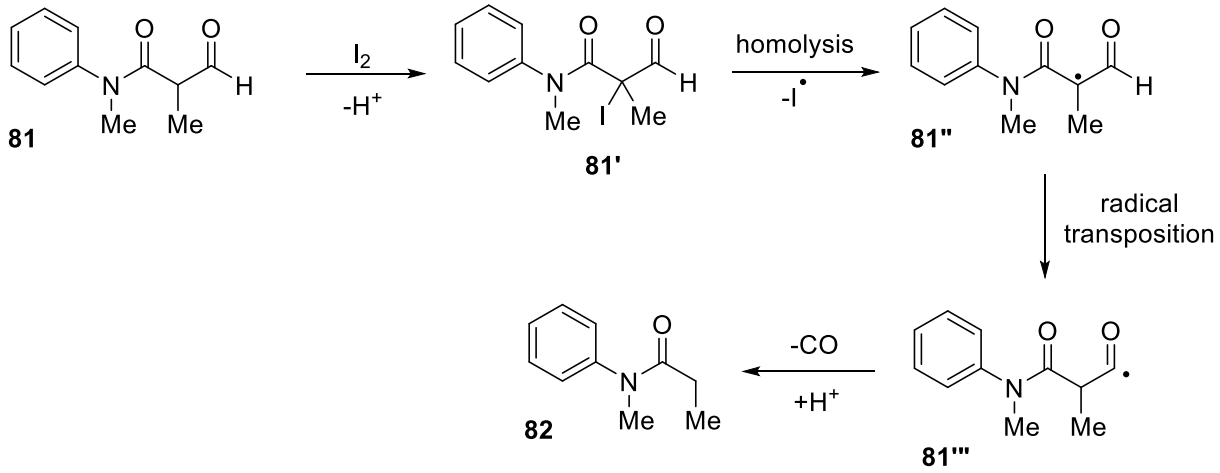

Figure 3.8. Postulated mechanism of the transformation of **81** to **82** via the iodinated intermediate.

After formation of the iodinated intermediated (**81'**), homolysis occurs forming radical **81"**, which transposes to radical **81'"** rather than cyclising which can then decarbonylate to return **82**. In addition to this, NMR analysis of the crude sample revealed weak peaks (3.07, 2.95, 1.74 and 1.66, all singlets) corresponding to the reported bisoxindole, **89**, as

reported by Wu and Liu. However, due to the small amount calculated (<1%), isolation proved challenging.

The reactions in DDQ (entries 4–5) proved equally unfruitful, with no observed peaks in the NMR, suggestive of the bisoxindole **89** nor the monomeric oxindole **89'**. Instead, degradation of **81** was much more pronounced with over 70% of **82** isolated as well as *N*-methylaniline, **83** (~15%) and N-methyl-N-phenylformamide (>10%). Presumably, this degradation of the oxoanilides occurs in a similar fashion to **Figure 3.8**, via radical transposition but without formation of the iodinated intermediate. Thinking the high temperatures might be detrimental, we switched to less harsh conditions; those reported by MacMillan for the CAN-mediated cyclisation (**Figure 3.7, D**), but with DDQ as the oxidant. Still however, no reaction occurred (entry 6).

A breakthrough was finally achieved using copper catalysis (entries 7–8). Here, to circumvent the possibility of aldehyde **81** instability, we increased the loading to pursue the envisioned cascade to form bisoxindole **89**. Under the conditions reported by Taylor (**Figure 3.7, B**) with copper(II) acetate as the oxidant, bisoxindoles **89** was formed in a combined 29% yield with a dr ratio of ~1:1.1 dl:meso, as well as returning anilide **82** in 38% yield. Most surprisingly however, we also noted the formation of the hydroxyoxindole **90**, confirmed by matching spectra of the NMR to that previously reported.

This was further observed when cerium ammonium nitrate (CAN) was used as the oxidant, under those conditions reported by MacMillan (**Figure 3.7, D**), entries 9–13, which failed to produce any bisoxindole **89**. Notably, we also observed the formation of α-ketoamide, **91** (**Figure 3.9**).

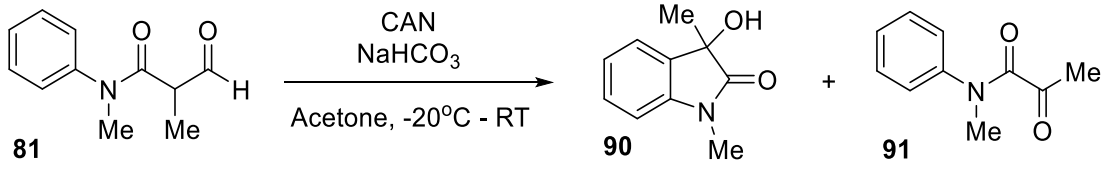

Figure 3.9. Products obtained from CAN-mediated oxidation of oxoanilide **81**.

We postulated that these products were being formed in a similar fashion to those described by Yu (2013),[103] Zhu (2011),[104] and Klumpp (2008),[105] who used a similar substrate to **81**, containing a ketone functionality in place of the aldehyde (**92**). Yu

described the formation of α-ketoamides **94**, using copper catalysis, molecular oxygen and $BF_3.OEt_2$ as a Lewis acid (**Figure 3.10**). A side product of this reaction, they observed was formation of the hydroxyoxindole, **93**, as a by-product. Previously Zhu and Klumpp had shown that conversion of α-ketoamides to the corresponding 3-hydroxyoxindoles was possible with Lewis acids.

$BF_3.OEt_2$ co-ordination to **92** gives intermediate enolate **92'** which can be oxidised to the corresponding radical **92"** by catalytic Cu^{2+} via a SET. Subsequent trapping of this radical by molecular oxygen can yield intermediate radical **95** which can either capture a proton to form **96a** or be oxidised by Cu^{+} to form **96b**. Thereafter intramolecular S_N2 of the carbonyl carbon by the peroxide oxygen can produce the 1,2-dioxetane **97**. Successive cleavage of the four-membered ring generates the desired α-ketoamide, **94** and acid **98**. **94** can then undergo Friedel-Crafts reaction to form **93**, via protonation and co-ordination by BF_3 at the two carbonyl oxygens to form **99** which, can undergo intramolecular cyclisation to form **100**, after which, proton transfer gives **93**.

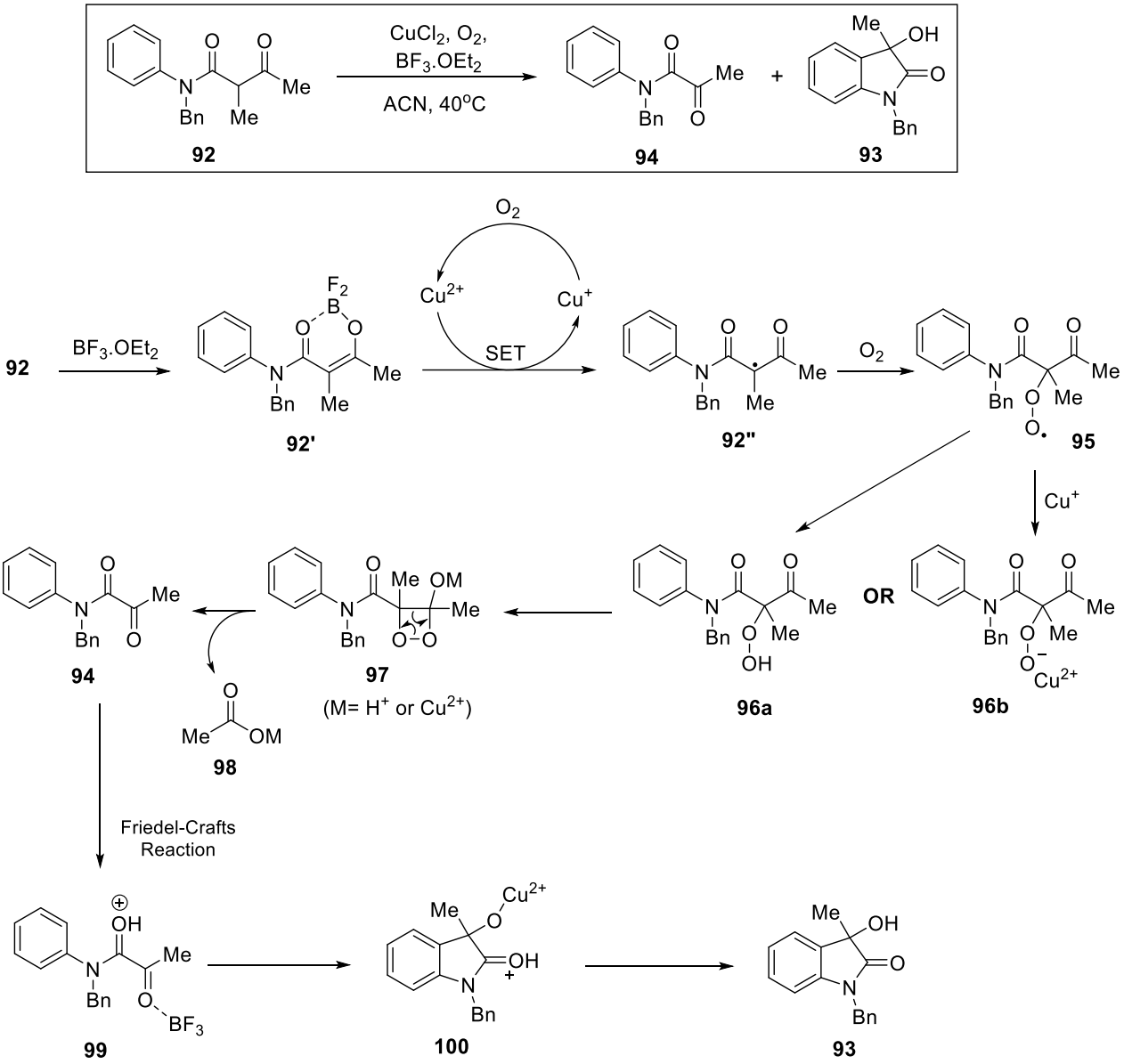

Figure 3.10. Mechanistic overview of Yu's methodology to convert **92** to α-ketoamides, **94** with side formation of **93**.

Presumably, it was this same process occurring with CAN (**Table 3.2**, entries 9–13); molecular oxygen competes with the dimerization reaction by trapping the α-carbonyl radical (**101**) to form the ketoamide and **91**. Then, in the presence of large excess of base and cerium ion acting as the Lewis acid, **91** could react to form **90** (**Figure 3.11**).

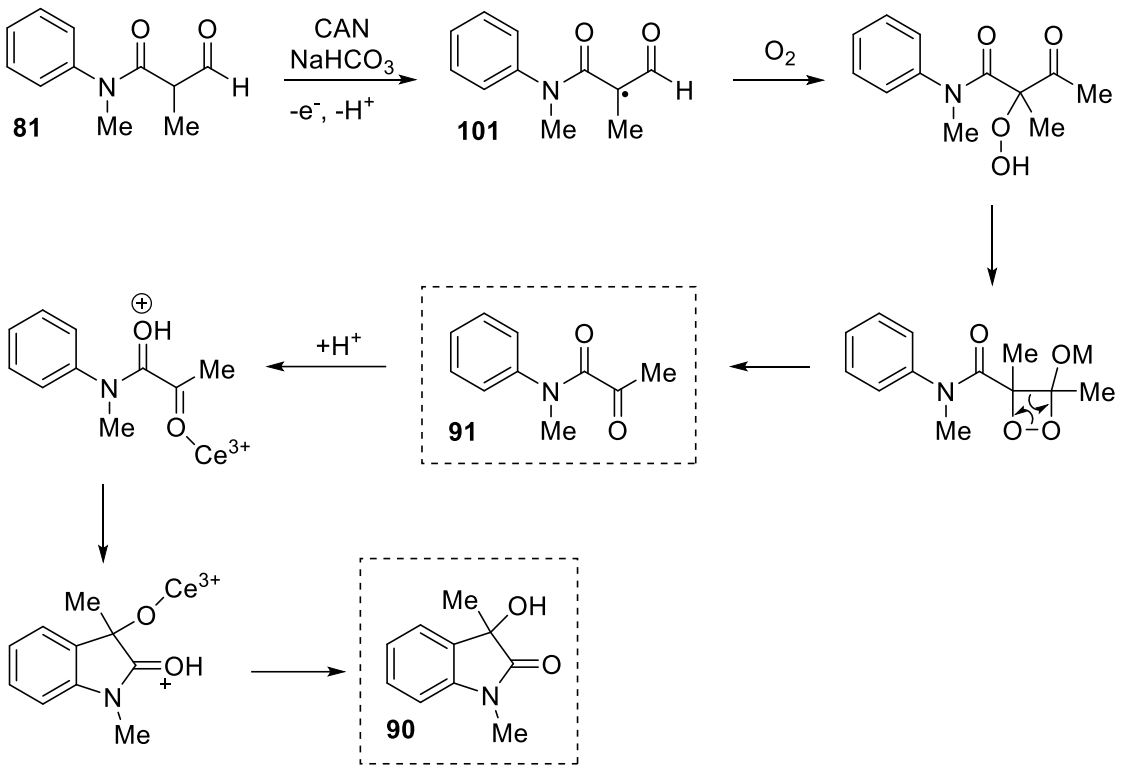

Figure 3.11. Proposed mechanism for the CAN-mediated formation of **90** and **91** from oxoanilide **81**.

The mechanism of $Cu(OAc)_2$-catalysed reaction (entries 7–8), was less straightforward. Oxygen was included under these conditions, as Taylor and Li described its presence to be critical in regenerating active Cu^{2+} species from the reduced Cu^{+}, hence the formation of **90**. However, unlike the CAN-mediated reaction no ketoamide was isolated. Indeed, even when the reaction stopped prematurely, before total consumption of starting material had occurred, ketoamide was notably absent as one of the products, even though **90** was usually present. This suggests that **90** was being generated via an alternate pathway (**Figure 3.12**). As Li noted, in reports which intramolecular CDC was sought via an α-carbonyl radical, in the absence of a Lewis acid, cyclisation is usually much faster than the competing trapping by oxygen. From this, we suggest that rather than **90** forming via ketoamide formation, it was plausible that after formation of radical **101**, cyclisation to **102** and deformylation could produce radical **103**. Homocoupling of this would produce bisoxindole **89**, however, in air **103** could be trapped by molecular oxygen to form the peroxide species, **104** which could subsequently hydrolyse to yield **90**.

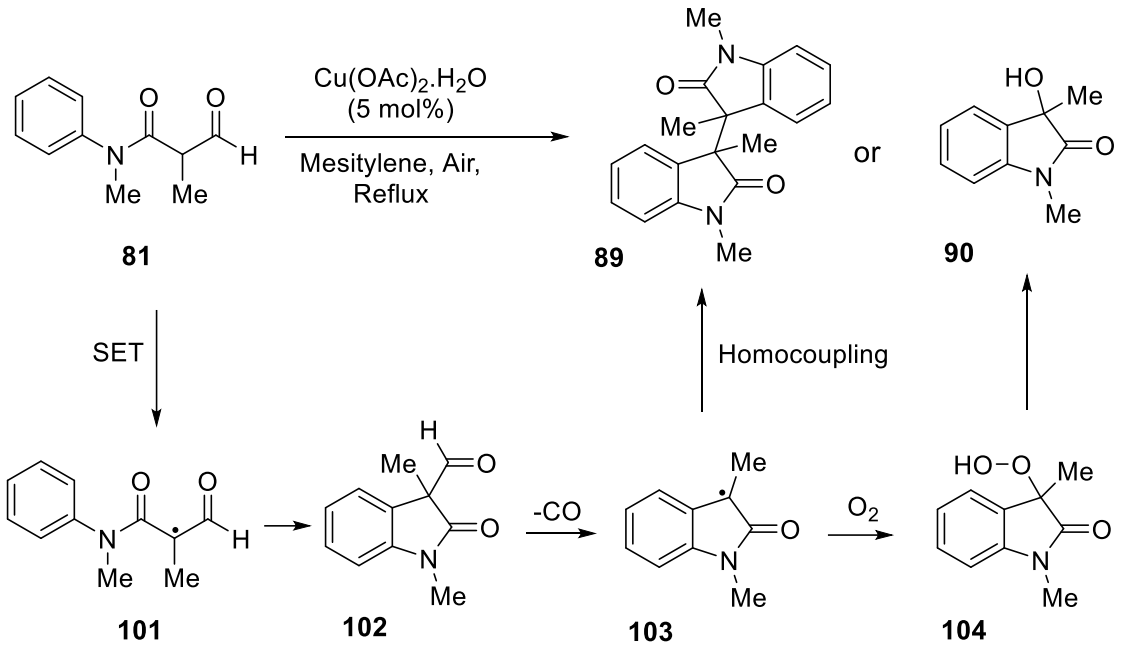

Figure 3.12. Proposed alternate route to **90** hydroxyoxindole from oxoanilide **81** under high temperature, air and $Cu(OAc)_2$.

In summary, of the trialled conditions only those involving copper catalysis were able to furnish bisoxindoles **89** from oxoanilide **81** in meaningful yields. Furthermore, an important note going forward was the competitive effect of molecular oxygen on the reaction, which competes with the with the direct CDC-coupling to form undesired 3-hydroxyoxindole and α-ketoamide.

Another important outcome from this screen was the separation and diagnostic challenges involving with using **81**. Quick diagnostics of the crudes by ^{1}H-NMR yield was our preferred method for rapid elucidation of the yields of **89**, **90** and **91**; however, as the *N*-methyl and tertiary methyl peaks of all three were in close proximity this became unfeasible. Moreover, isolation and separation of these products by column chromatography was equally challenging owing to the close R_f values of these products, particularly the *meso*-**89** and **90** which were nearly inseparable in almost all solvent mixtures trialled. Consequently, for future optimisations we opted to use oxoanilide **105**. The diastereotopic protons (H_x and H_y) (**Figure 3.13**), had proved to be more diagnostic in being able to quickly distinguish the desired bisoxindole from undesired ketoamides and hydroxyoxindoles. Furthermore, the above products with this substrate showed much more pronounced R_f differences which made separation substantially simpler.

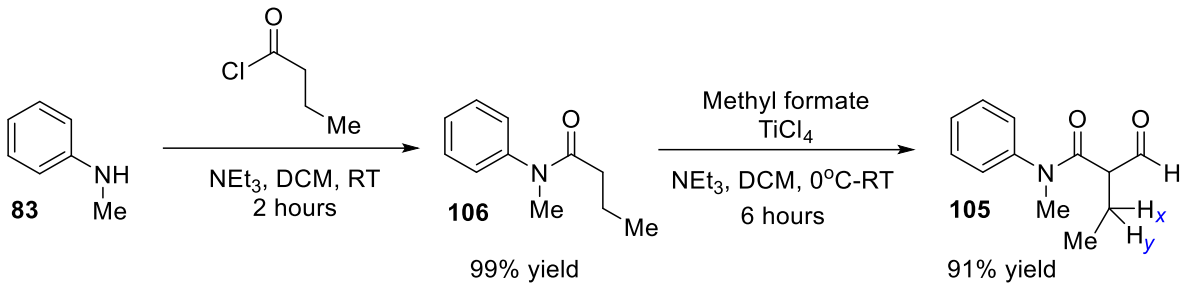

Figure 3.13. Synthesis of the oxoanilide **105** from **83**.

Repeating the peptide coupling with **83** and formylation under the previous ideal conditions, gave the products, **106** and **105** in 99% and 91% yield, respectively.

NMR analysis supported the structure assigned to the product; the presence of two multiplets at 1.94 and 1.78 ppm each integrating for a proton in **105** is distinct from the sextet in **106**, which integrates for two protons, suggestive of C2 modification. Furthermore, the presence of the doublet at 9.57 ppm in the ^{1}H NMR spectrum, as well as a signal at 200 ppm in the ^{13}C NMR spectrum which show a cross-peak to one another in the HSQC, supports the idea of formylation at the C2 postion. (**Figure 3.14**).

106

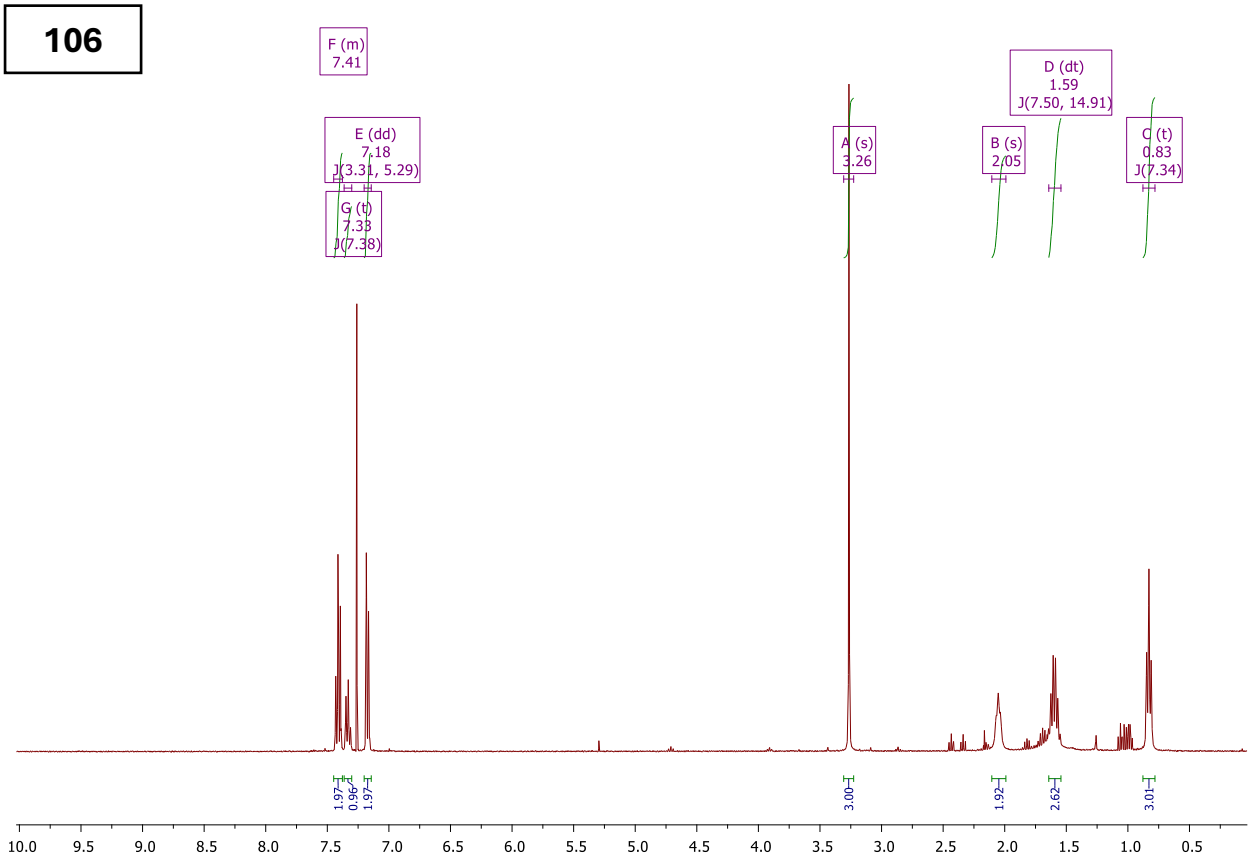

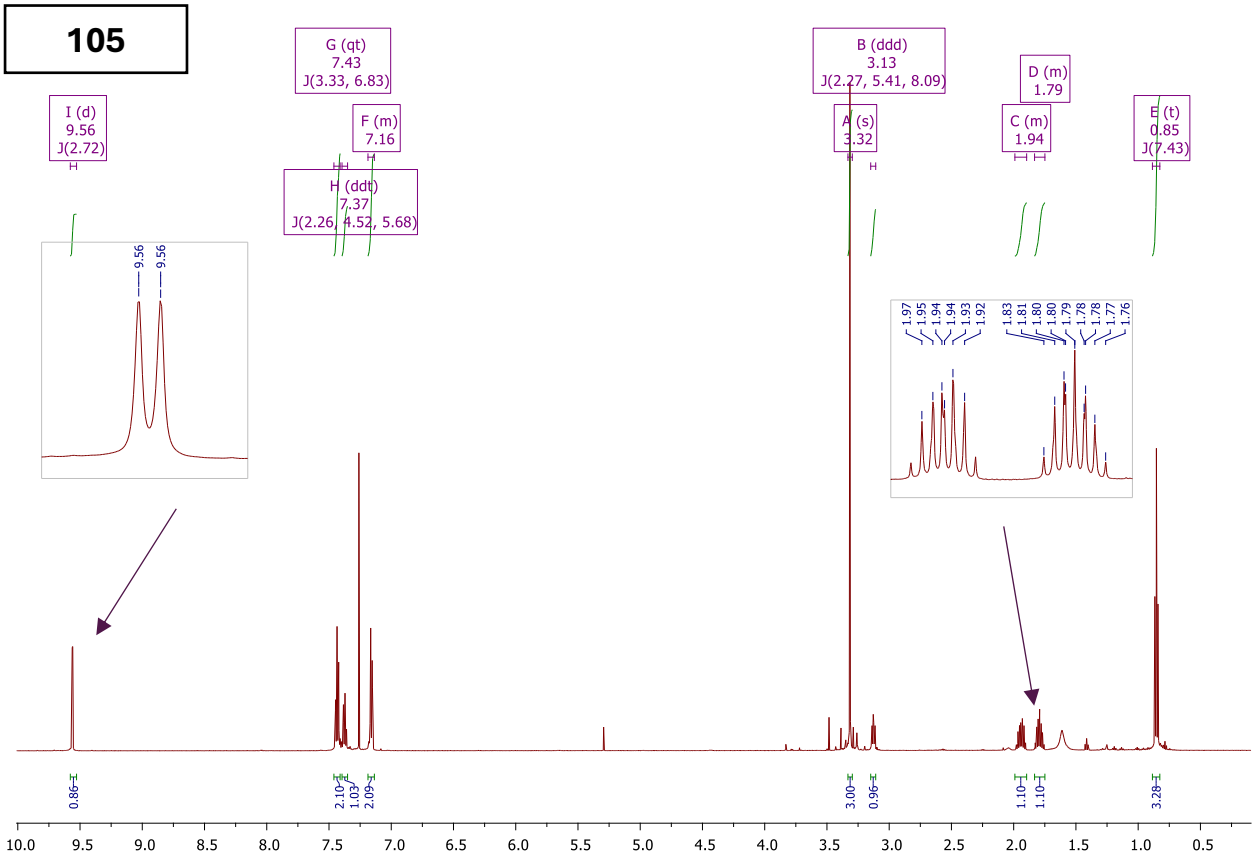

Figure 3.14. Comparison of ^{1}H-NMR of **105** vs **106**.

Synthesis of the oxoacid substrate

Before proceeding with further optimisations, we sought to synthesise the second of the two desired substrates, the oxoacid (Chapter 1**, 74**). We envision that oxoacid, **107**, could be synthesised from a relatively straightforward hydrolysis of literature-ubiquitous β-oxoesters (**108**), which itself could be obtained via amide coupling of malonic half-esters **109**. These half-esters are commercially available and can also be obtained by incomplete hydrolysis of malonic esters **110** (**Figure 3.15**).

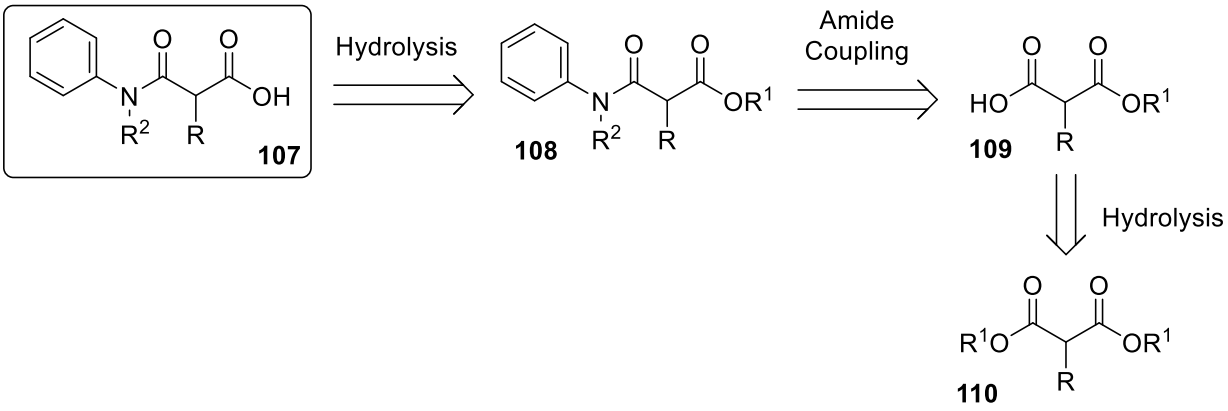

Figure 3.15. Proposed sequence for the synthesis of oxoacids from β-oxoesters.

For our first attempt we chose the substrate with R = Et and R^2 = Me (**111**), mirroring that of the oxoanilide (**105**) (**Figure 3.16**).

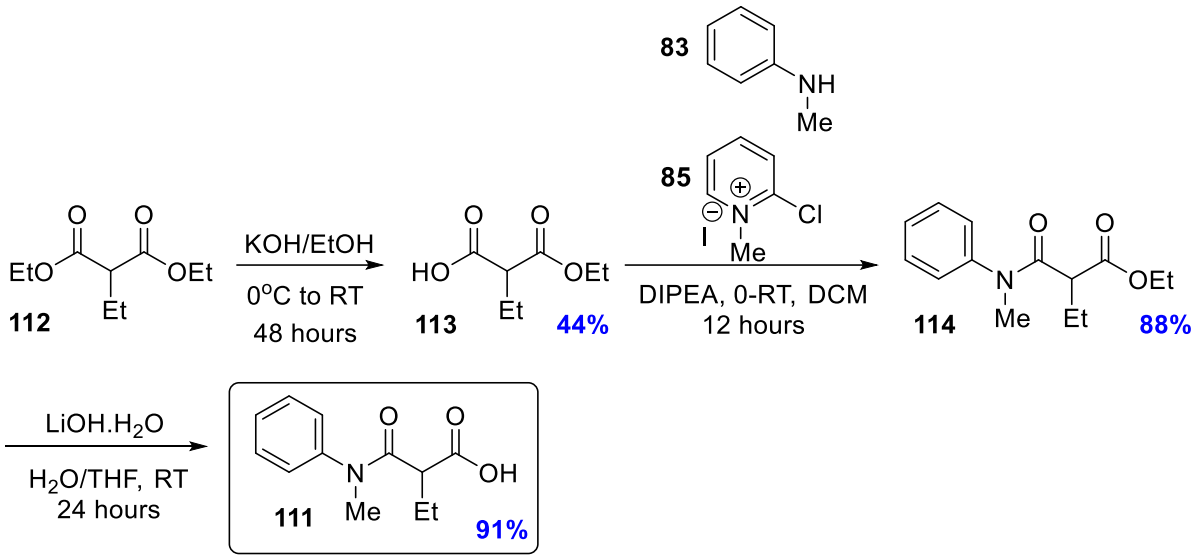

Figure 3.16. Conditions and reactions for the synthesis of **111** from **112**.

Diethyl ethyl malonate (**112**) was first hydrolysed with KOH in EtOH at 0 °C, which was warmed up to RT and left to stir for a period of 48 hours. After an aqueous/organic partition, the crude aqueous layer was separated and acidified to pH 3–4, after which a second aqueous/organic partition, isolation of the organic layer and removal of solvent gave the ethyl malonic half-acid (**113**) in 44% yield that was sufficiently pure to use in the following step.

Utilising the amide coupling procedure used in the synthesis of the anilines (**Figure 3.2**) on **113** yielded the β-oxoester (**114**) in excellent yield, the NMR of which can be seen in **Figure 3.17**.

The ^{1}H NMR spectrum integrates for a total of 19 protons, which matches the proton count of the proposed structure. The distribution of the signals also matches what was expected with two signals in the aromatic region (~7–8 ppm) integrating for a total of 5H. Additionally seen, are two triplets each integrating for 3H between 0.5–1.5 ppm, the expected range for shielded -CH_3 groups adjacent to a methylene group. Finally, we see a multiplet between 3.25–3.18 ppm integrating for 1H which is consistent with a tertiary malonate proton (green) and a downfield multiplet at 4.09 ppm integrating for 2H, for the methylene of the ester.

The ^{13}C NMR spectrum further supports the structure, with 17 peaks corresponding to 19 total carbons (the signals at a 129.9 and 127.8 ppm each showing a cross-peak to two aromatic protons in the HSQC), including two signals at 169.2 and 170.1 ppm for the two carbonyl groups.

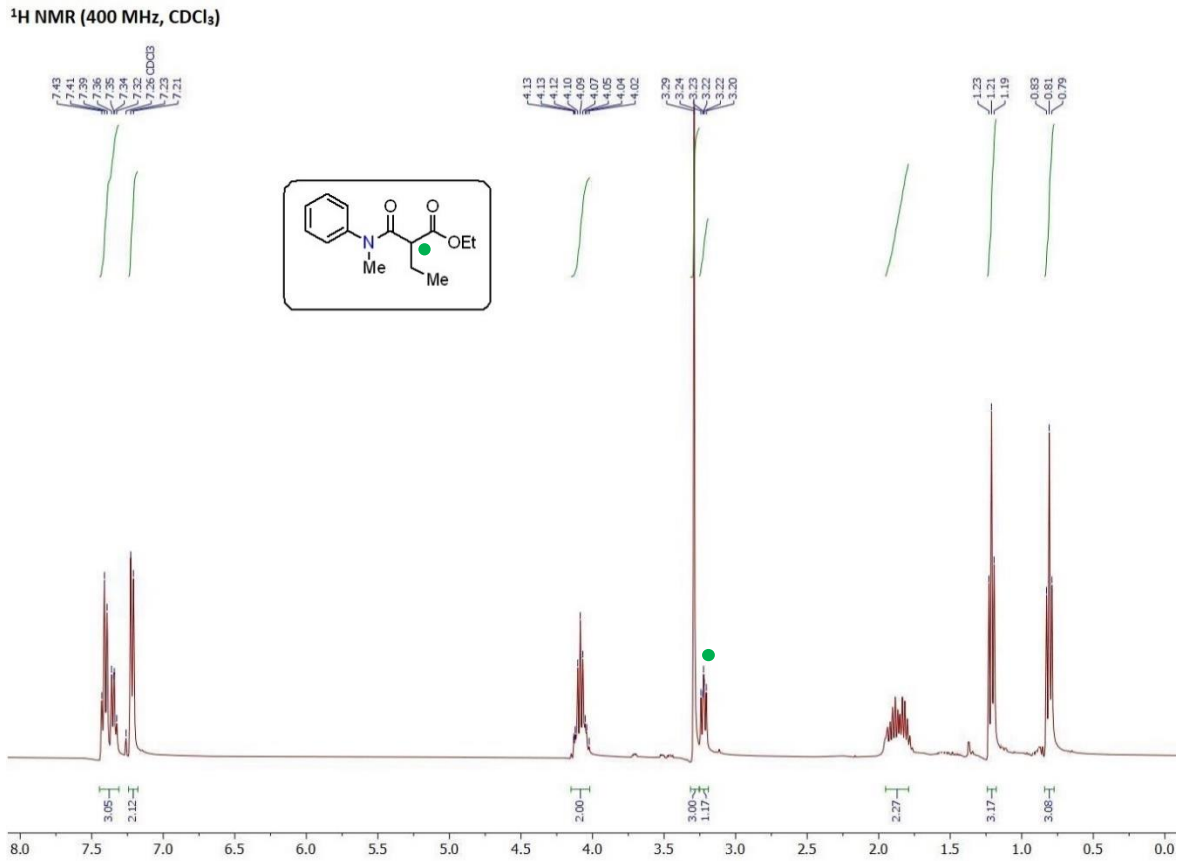

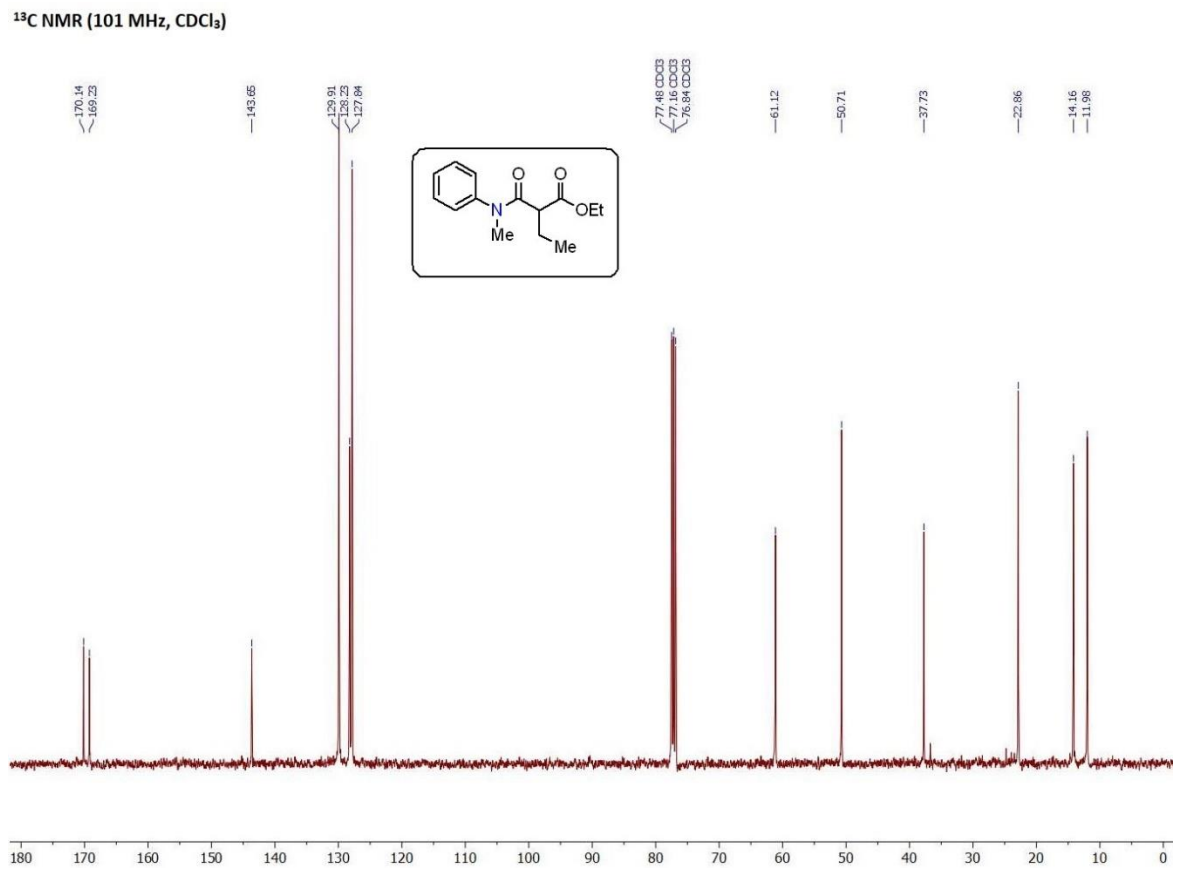

Figure 3.17. ^{1}H and ^{13}C-NMR for **114**.

Finally, hydrolysis with $LiOH.H_2O$ in a water/THF mixture furnished the desired oxoacid (**111**) in 91% yield after 24 hours. The ^{1}H and ^{13}C NMR spectra of which can be seen in **Figure 3.18**.

While the -OH signal is not present on this spectrum, compared to the ^{1}H NMR spectrum of **114**, **111** has only one triplet at 0.87 ppm; it also lacks the multiplet at 4.09 ppm which is consistent with what would be expected of ester hydrolysis. Furthermore, the presence of the triplet at 3.27 ppm suggests that the carbonyl group is still attached. This can be reinforced when looking at the ^{13}C NMR spectrum which has two less signals in the aliphatic region 10-60 ppm, expected of loss of $-CH_2CH_3$ and, more importantly shows a signal downfield from the amide carbonyl at 172.8 ppm. While this chemical shift is lower than that typical of carboxylic acids usually seen at <180 ppm, the IR spectrum shows a wide, broad band at 3300 cm^{-1} and finally we note the HRMS returned a mass of 221.1132, lying close to the calculated mass for this compound, 221.1125.

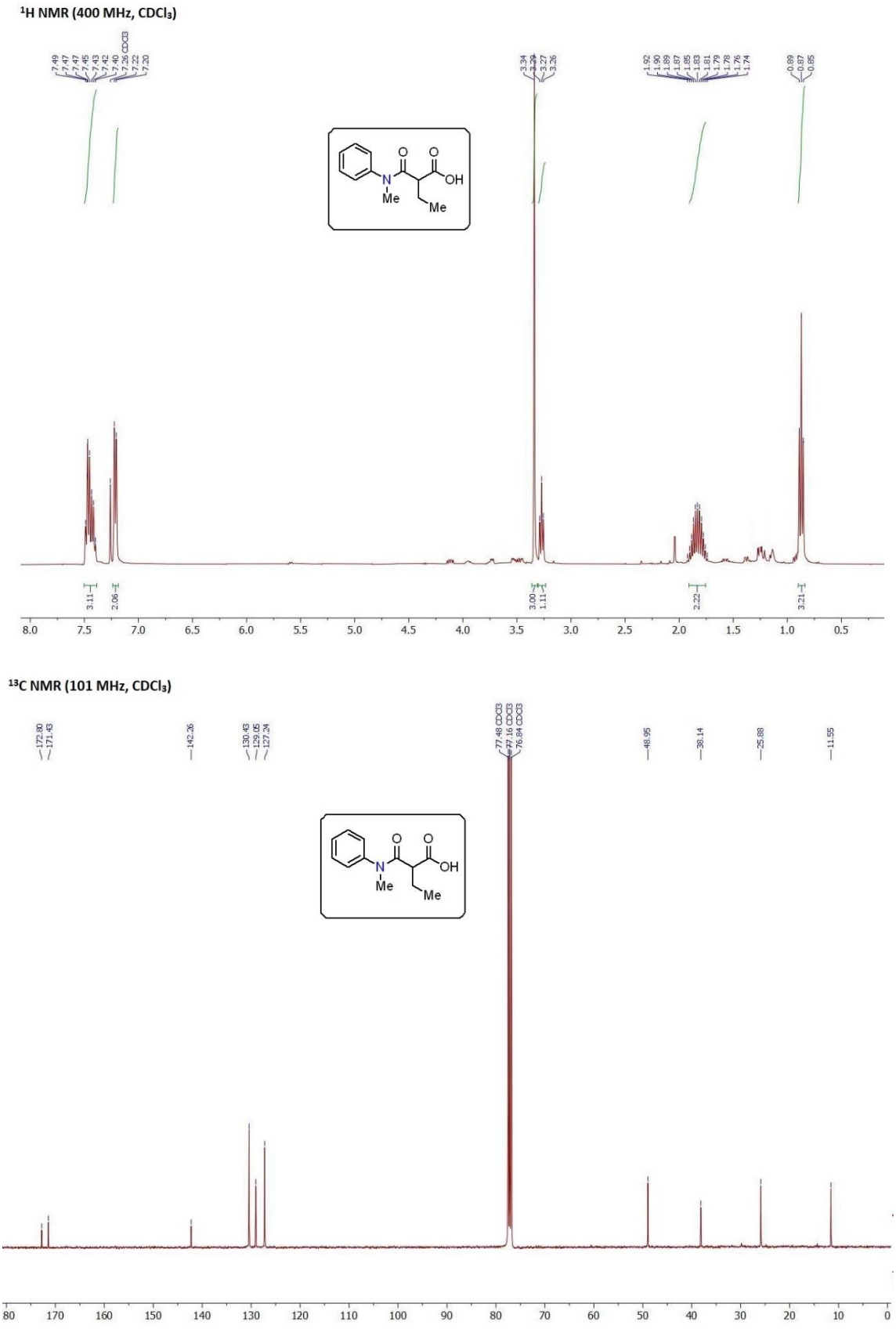

Figure 3.18. ^{1}H and ^{13}C-NMR for **111**.

Optimised CDC screen

With both substrates in hand, we began our CDC optimisations, subjecting aldehyde **105** and acid **111** in parallel. Note that this work was done in conjunction with another member of our research group, Dr Munashe Mazodze, as such, for efficiency the optimisation workload was split. Consequently, full discussion on every result is beyond the scope of this thesis. However, as this work was published all relevant results will be shown which will also aid in the discussion on the mechanism.

Works by Kim (**Figure 2.8**)**,** Wei (**Figures 2.12**) and Taylor (**Figure 3.7B**) have previously shown success in the dimerization of 3-alkyl and aryl indoles to their corresponding bisoxindoles using $Cu(OAc)_2$ and $Mn(OAc)_3$. This, in tandem with the previous results (**Table 3.2**) using copper catalysis, led us to begin optimisation with $Cu(OAc)_2$, which was one of the only trialled oxidants that had any success in converting oxoanilides to bisoxindoles (**Table 3.3**).

Table 3.3: Optimisation table for conversion of **105**/**111** to **115a**/**116**. In all cases, **115a** was isolated as ~1:1 mixture of *dl* and *meso* diastereomers. [a]Open to air. [b]Under reflux. [c]With NaO^{t}Bu (5 equiv.) at 110 ˚C.

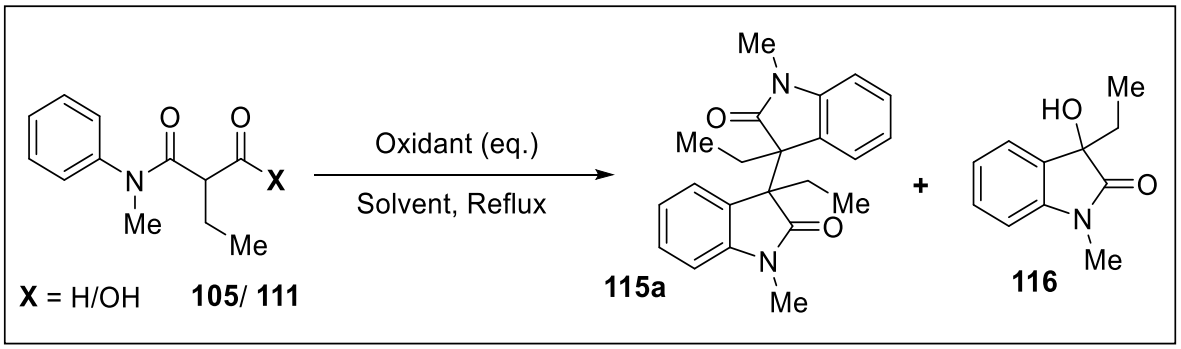

Entry	Substrate (105/111)	Oxidant (eq.)	Solvent	Yield (%)	
				115a	116
1[a]	105	$Cu(OAc)_2.H_2O$ (**5 mol%**)	Mesitylene	28	31
2[a]	111	$Cu(OAc)_2.H_2O$ (**5 mol%**)	Mesitylene	Trace	20
3[a]	105	$Cu(OAc)_2.H_2O$ (**10 mol%**)	Toluene	-	30
4[a]	111	$Cu(OAc)_2.H_2O$ (**10 mol%**)	Toluene	-	Trace

5[a]	105	$Mn(OAc)_3.2H_2O$ (**10 mol%**)	Toluene	-	-
6[a]	111	$Mn(OAc)_3.2H_2O$ (**10 mol%**)	Toluene	31	26
7[a]	105	$Cu(OAc)_2.H_2O$ (**50 mol%**)	Toluene	17	34
8[a]	111	$Cu(OAc)_2.H_2O$ (**50 mol%**)	Toluene	8	15
9[a]	105	$Mn(OAc)_3.2H_2O$ (**50 mol%**)	Toluene	53	32
10[a]	111	$Mn(OAc)_3.2H_2O$ (**50 mol%**)	Toluene	37	11
11[b]	105	$Cu(OAc)_2.H_2O$ (**3.0**)	Toluene	74	-
12[b]	111	$Cu(OAc)_2.H_2O$ (**3.0**)	Toluene	10	29
13[b]	105	$Mn(OAc)_3.2H_2O$ (**3.0**)	Toluene	76	-
14[b]	111	$Mn(OAc)_3.2H_2O$ (**3.0**)	Toluene	56	-
15[b,c]	105	$CuCl_2$ (**3.2**)	DMF	54	-
16[b]	105	$FeCl_3$ (**3.0**)	Toluene	-	-

Repeating the conditions reported by Taylor on aldehyde **105**, which had previously shown success (entry 1), we were able to isolate the desired bisoxindole **115a** was obtained in 28% yield, accompanied by 31% yield of the hydroxyoxindole **116**, a similar result to that obtained with oxoaniline **81** (**Table 3.2**). Applying this procedure to acid **111** (entry 2) only produced trace amounts of **115a**, and much lower yield of **116** (20%), overall, a significantly lower % conversion of starting material to either products.

An important distinction between substrates **105** and **111** for this transformation is the identity of the material not converted to **115a** and **116** (entry 1 vs 2); in the case of **105**, aniline **106** made up the bulk of isolated material post-separation (~33%), whereas in the case of **111**, the material returned was entirely unreacted starting material (~70%). This suggests lower stability for aldehyde **105** to oxidative conditions, compared to acid **111**, a trend that was seen in all subsequent reactions (entries 3 – 14).

While this result was encouraging, we were less than satisfied with a) the extreme temperature required (165 °C) b) Mesitylene as the solvent, which made isolation and purification of products challenging, owing to its high boiling point.

In response to these issues, the reaction was repeated with toluene as the solvent, under reflux (110 °C). Previously, Taylor postulated that high temperatures (165 °C) under Mesitylene was required for efficient catalytic turnover of $Cu^{+} \rightarrow Cu^{2+}$; thus, to compensate for the lower reaction temperature, a higher catalytic loading was used (entries 3 – 4). We hoped that the chemically similar nature of toluene to mesitylene, would furnish **115a** in a similar yield to entry 1, while the lower boiling point (110 °C vs 165 °C for mesitylene) would optimise the work-up and purification protocol. Unfortunately, no trace of **115a** was detected with either **105** or **111** as substrate, though in the case of **105**, **116** was returned in similar yield (30%) (entry 3).

Repeating these conditions with catalytic $Mn(OAc)_3$ as oxidant (entries 5 – 6) proved similarly unfruitful with **105**, returning mostly aniline **106** (entry 5). However, with acid **111**, we were gratified to observe decent conversion of starting material (56%) that was split between the desired bisoxindole **115a** (31%) and hydroxindole **116** (26%).

Encouraged by this result we further increased the catalytic loading of the oxidant to 50 mol% (entries 7 – 10). In doing so, we were finally able to observe formation of **115a** with copper catalysis, however in the case of both **105** and **111**, lower yields of the desired **115a** (17% and 8%, respectively) were compounded with a heavy favouritism for the formation of **116** at nearly a 2:1 ratio of **116**:**115a** (entries 7 – 8). Fortunately, this result was reversed with manganese (III) acetate as the oxidant (entries 9 – 10), with moderate yields using both substrates **105** and **111** (53% and 37% respectively) as well as a near 2:1 ratio in favour of the desired bisoxindole **115a** vs **116**.

At this stage we began to reassess the open-air catalytic system we initially proposed (**Figure 3.19**, **A**). While we hoped that molecular oxygen would efficiently function as the terminal oxidant to turnover the catalytic cycles after oxidation of **105/111a** and **b** to their respective radical/cations (**25**/**111c**, **d** and **e**), it was clear that interception of key radical **117** by molecular oxygen to form **116**, was a strong competitor of the intended homocoupling to form **115a** (**Figure 3.19**, **B**).

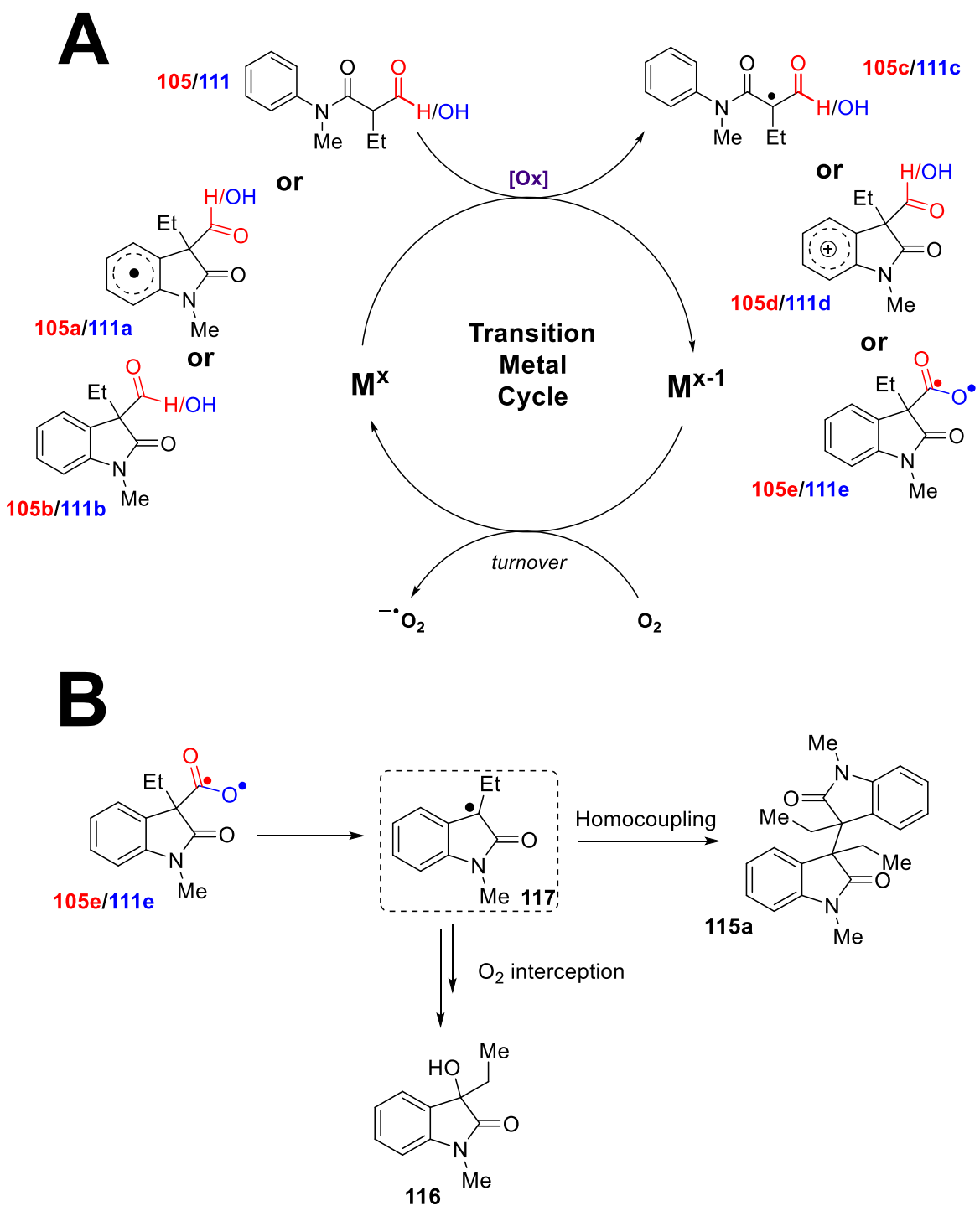

Figure 3.19. A) Postulated catalytic cycle with molecular oxygen for substrate **105** and **111**. B) Competing pathways in the formation of **115a** and **116**.

As such, we though to exclude air from the reaction entirely in hopes that the conversion of starting material that was going towards formation of the hydroxyoxindole, **116**, would go towards formation of the desired bisoxindole **115a** instead.

The results of this can be seen in entries 11 – 16; as we noted in the mechanism shown in Chapter 1, **Figure 2.20**, there are three separate oxidation steps for this transformation, as such, we switched to an inert system under argon with a stoichiometric amount (3 equivalents) of the metal salt. In doing so, we were immediately rewarded with a 74% yield of **115a** with **105** as the substrate, our highest yield thus far (entry 11), although bizarrely this was not mirrored with **111** as the substrate (entry 12), it is consistent with poor yields under copper catalysis when the substrate was acid **111** (entries 3, 8 and 11) which could be a consequence of mismatched standard reductive potential of the Copper ion with the BDE of the -COOH group.

Using 3 equivalents of manganese (III) acetate as the oxidant had similarly fruitful results, with a 76% yield of the desired bisoxindole **115a** for substrate **105** (entry 13) and 56% yield of **115a** with **111** as the substrate (entry 14), further suggesting that manganese is more suited for this transformation compared to copper for **111**.

In both cases with either copper or manganese, we were delighted to see no little to no formation of hydroxy oxindole **116**, and medium to high conversion of the starting materials. This result further reinforced the idea that the presence of molecular oxygen was detrimental to the dimerization reaction when a single oxidant is present.

With this, $Mn(OAc)_3$ cemented itself as the most effective oxidant to form **115a** (entries 13 and 14). $CuCl_2$ with Na^tOBu (entry 15; Kündig's conditions, **Figure 3.7A**) gave a moderate, albeit lower yield of **115a** at 54%, while $FeCl_3$ (entry 16) produced neither **115a** nor **116**.

As a result, we sought to further optimise the conditions that produced the highest yield, entries 13 and 14 (**Table 3.3**) by screening various solvents (**Table 3.4**).

Solvent screen

Table 3.4: Solvent screen for conversion of **105/111** using 3.0 equivalents of $Mn(OAc)_3.2H_2O$ under argon at respective reflux temperatures. [a]Yield obtained when refluxed vigorously (110 °C).

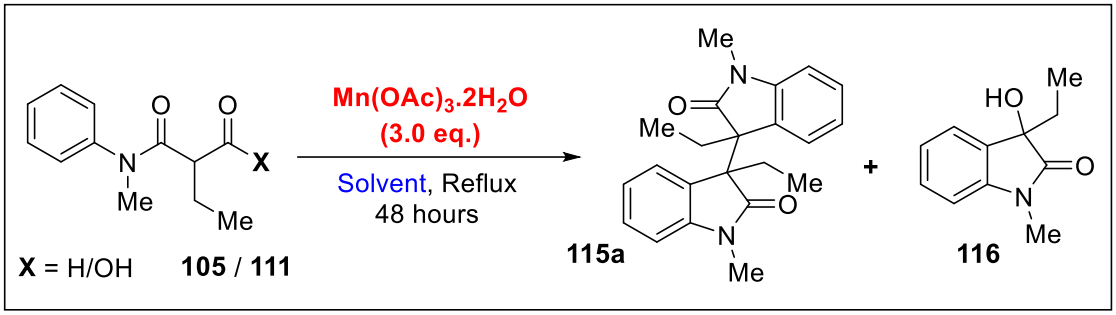

Entry	Substrate (105/111)	Solvent	Yield (%)	
			115a	116
1	105	Toluene	76	-
2	111	Toluene	56	-
3	105	DMF	35	24
4	111	DMF	24	30
5	105	Mesitylene	33	31
6	111	Mesitylene	Trace	36
7	105	DCM	18	-
8	111	DCM	Trace	-
9	105	ACN	92	-
10	111	ACN	64	36
11	105	THF	86	-
12	111	THF	72 (81)[a]	-

At 110 °C in toluene we were able to furnish solely the bisoxindole from both **105** and **111** at moderate to high yield, 76% and 56% respectively (entries 1 & 2). With this as our baseline, we first examined DMF as the solvent under reflux (153 °C) (entries 3 – 4). Interestingly at this higher temperature the total amount of starting material converted was only marginally higher than that observed in entries 1 & 2; the yield of **115a** was

unimpressive at 35% and 24% for **105** and **111**, respectively. Moreover, there was concomitant formation of **116** competing with the formation of the desired bisoxindole, possibly due to the presence of H_2O that could generate hydroxy radicals ($OH^{\bullet}$), that could compete with radical homocoupling via trapping in a similar manner to molecular oxygen.

Following this, mesitylene was screened under the new conditions (entries 5 & 6). While we had previously shied away from utilising it due to high temperature of reflux (165 °C) and associated separation issues, we were curious as to whether the elevated temperature would lead to full conversion of **105**/**111** to **115a**. In the case of both, a similar result to that obtained in **Table 3.3** (entries 1 & 2) was observed; **105** yielded a mixture of **115a** and **116** in an almost 1:1 ratio with only marginally higher conversion of starting material, whilst **111** produced only trace amounts of **115a** albeit almost double the yield of **116**. As with entries 3 & 4, the presence of **116** was surprising, given the lack of molecular oxygen or water, it was however, possible that the higher temperature was sufficient to cleave the C3-C3' bond of the bisoxindole post-homocoupling, which upon work-up in air could form the hydroxyindole, though this had not previously been reported for these types of molecules. (**Figure 3.20**).

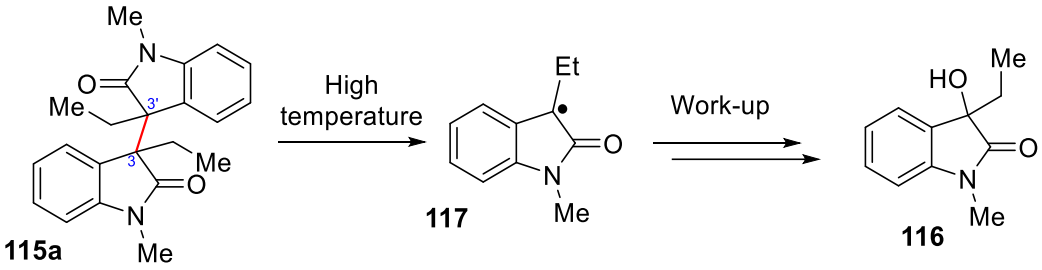

Figure 3.20. Postulated mechanism for formation of **116** from **115a** under high temperature and aqueous work-up.

This could also explain the formation of **116** in DMF under similarly high temperature.

From this, we switched to a solvent with significantly lower reflux temperature DCM (40 °C) (entries 7 & 8). Under these conditions conversion of starting material for both **105** and **111** was greatly diminished, with both returning primarily unreacted starting material and 18% of **115a** in the former and only trace amounts of the latter. Consequently, this

suggests that elevated are necessary for this transformation, possibly to aid in in deprotonation and formation of the first radical species **105a**/**111a** (**Figure 3.19**, **A**).

With this in mind, we looked to solvents with intermediate boiling points between 40 – 110 ℃. This led us to acetonitirile (ACN) (b.p = 82 ℃) and tetrahydrofuran (THF) (b.p = 66 ℃), entries 9 – 12.

Under acetonitrile, we were delighted to observe formation of **115a** with almost full conversion, 92% yield, with no trace of **116** when aldehyde **105** was used (entry 9). While acid **111** was far less straightforward (entry 10), it did proceed with full conversion of starting material and the highest observed formation of **115a** from **111** (64%), which was albeit marked by side-formation of **116**.

This, however, was rectified when we switched the solvent to THF (entries 11 &12); here we observe 72% yield of **115a** when utilising acid **111** with no competitive formation of **116**, which was increased to 81% when the reaction was subject to vigorous reflux at 110 ℃ (entry 12). Similarly, **105** in THF gave us an excellent yield of 86% of **115a** (entry 11), though this fell short when compared to entry 9.

With these results, we concluded our solvent screen and further optimisation for the time being, satisfied with the high yields for each **105** and **111**. The combination of **Table 3.3** & **3.4**, gave two complementary approaches for the efficient synthesis of **115a** without side formation of **116** for each substrate under 3 equivalents of manganese (III) acetate, under inert gas with ACN in the former case and THF in the latter case. Thus, we shifted focus to determining the flexibility of this procedure through exploration of the substrate scope.

Substrate scope

Oxoanilide

A variety of oxoanilides were synthesised with variations to the aromatic structure, protecting group and C3 position, the full list of bisoxindoles can be seen in **Figure 3.21**, including unsuccessful substrates. Products were all obtained as a separable mixture of diastereomers in 1:1.2 – 1:1 ratio of dl:meso dimers.

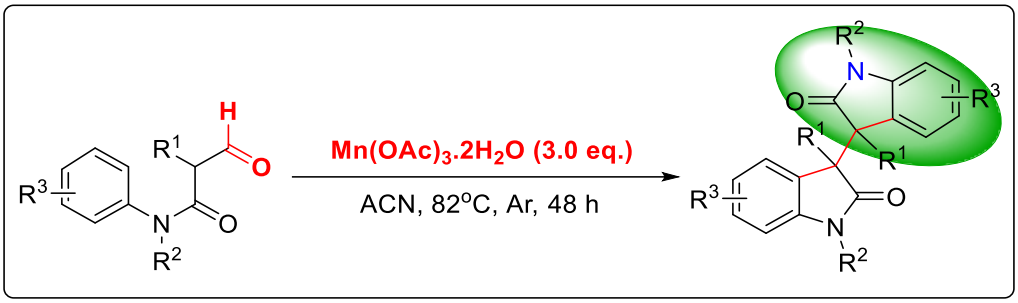

C3 variants

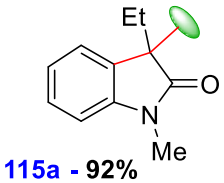
115a - 92%

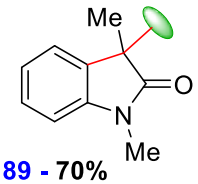
89 - 70%

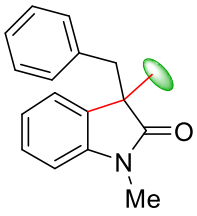
115b - 81%

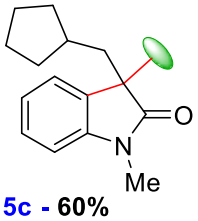
115c - 60%

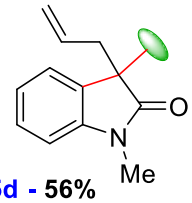
115d - 56%

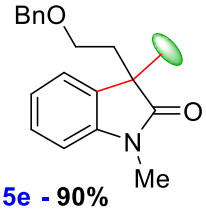
115e - 90%

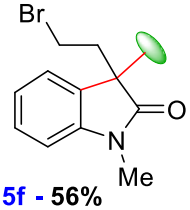
115f - 56%

Aromatic variants

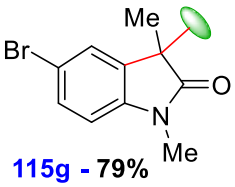
115g - 79%

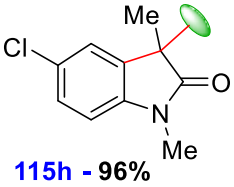
115h - 96%

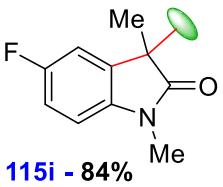
115i - 84%

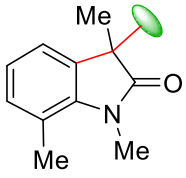
115j - 80%

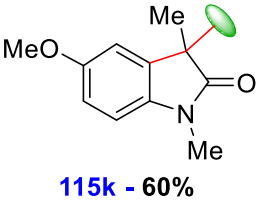
115k - 60%

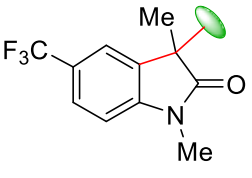
115l - 71%

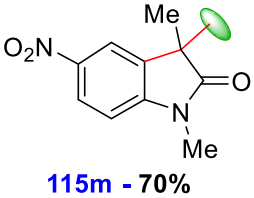
115m - 70%

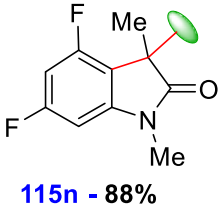
115n - 88%

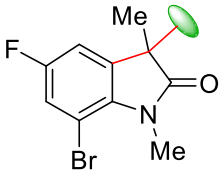
115o - 78%

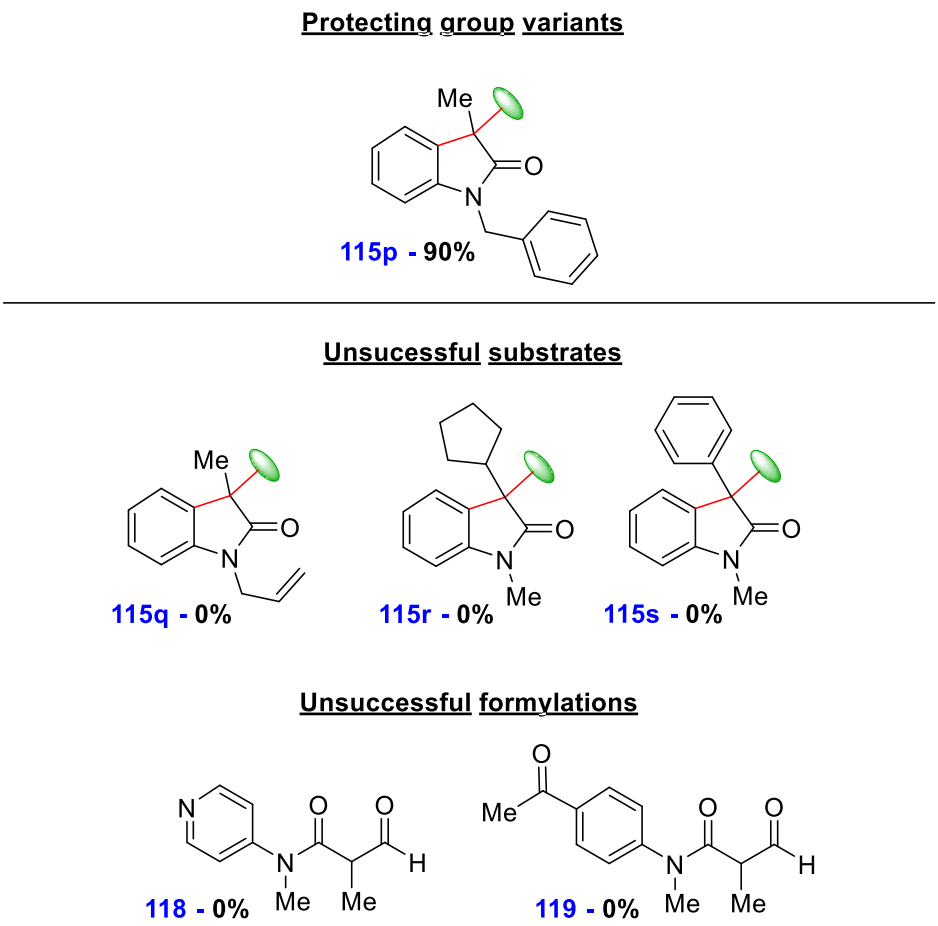

Figure 3.21. Substrate scope and unsuccessful substrates.

We were delighted to discover that the $Mn(OAc)_3$-mediated oxidation in ACN was amenable to large variety of substrates, with diverse array of different functional groups. Of the twenty-three substrates attempted, seventeen bisoxindoles were produced in moderate to excellent yields, with 59% being the lowest observed. These include seven C3 modifications including methyl (**89**) (70%), bulky ring systems such as phenyl (**115b**) and cyclopentyl (**115c**) with 81% and 60% yield, respectively. As well as longer chain alkyl bearing different functional handles: allyl (**115d**) and ethyl-*O*-benzyl (**115e**) and ethyl-bromide (**115f**) at 56%, 90% and 56% respectively.

Changes to the aromatic system was also well tolerated. These included: mildly withdrawing halogens (**115g**, **115h** and **115i**) which were formed in excellent yields; 79%, 96% and 84% respectively, donating groups such as -Me and-OMe (**115j** and **115k** in 80% and 60% yield respectively) and even strongly withdrawing groups such as $-CF_3$ and $-NO_2$ (**115l** and **115m**) in good yields, 71% and 70%. In addition, disubstituted halogenated

aromatics proved equally possible in excellent yield (**115n** and **115o**; 88% and 78% respectively).

Of note, we were gratified by the success in the synthesis of a protecting group variant, the *N*-benzyl (**115p**) in 90% yield which demonstrates the utility of this method; deprotection of this functional group to the free amine opens pathways for the synthesis of more novel HPIs.

A typical trend in bisoxindoles, seen in the papers of Wu/Wei/Bisai/Kim, is the polarity difference between the *meso* and *dl* isomers where the *dl* is usually less polar than the *meso*. Based on this pattern, we were able to estimate relative stereochemistry, however, full confirmation can only be obtained via crystal structure analysis.

Unsuitable substrates

Of the trialled oxoanilides, only five did not form the desired bisoxindoles under our conditions; one protecting group variant, containing an *N*-allyl (**115q**), and three C3 variants, with a cyclopentyl group (**115r**) and a phenyl group (**115s**).

In the case of **115q**, we instead observed the formation of the pyrrolidinone **115q'**, as the major product in 47% yield, indicating preference for radical trapping by the *N*-allyl group over intramolecular CDC. Mechanistically, this can occur via two possible routes either A) SET of the oxoanilide form radical **115q"**, which after radical transposition, forms radical **115q'"** that can deformylate and cyclise to form **115q'** or B) SET to form **115q'"** directly which proceeds via the same route. While Baldwin's rules suggest both intramolecular CDC onto the aromatic ring and *N*-allyl trapping are favoured (5-*exo*-trig and 6-*exo*-tet respectively), only product **115q'** is observed, suggesting that pathway B could be favoured (**Figure 3.22**).

Interestingly the same phenomenon is not observed with **115d**, as this would form a strained four-membered ring which would be less stable than the five-membered ring in the case of **115q'**.

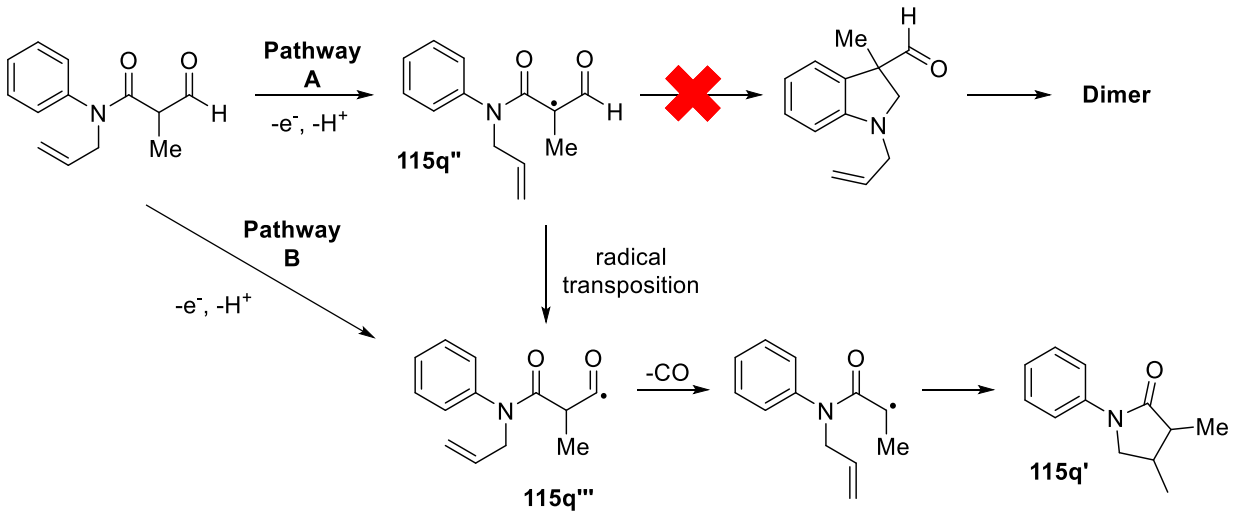

Figure 3.22. Proposed mechanism for the formation of pyrrolidinone **115q** from oxoanilide of **115q**.

For **115r**, possessing a cyclopentane at the C3 position, we observed sole formation of the undimerised oxindole **115r'**, in 62% yield (**Figure 3.23**). Presumably, the steric bulk of this group makes biradical coupling difficult and hence H-abstraction is preferable. We believe a similar problem would prevent the formation of **115s** however, in this case we were also unable to isolate the undimerised oxindole; presumably, due to the persistent radical effect, which prevents cyclisation to form the indole as well.

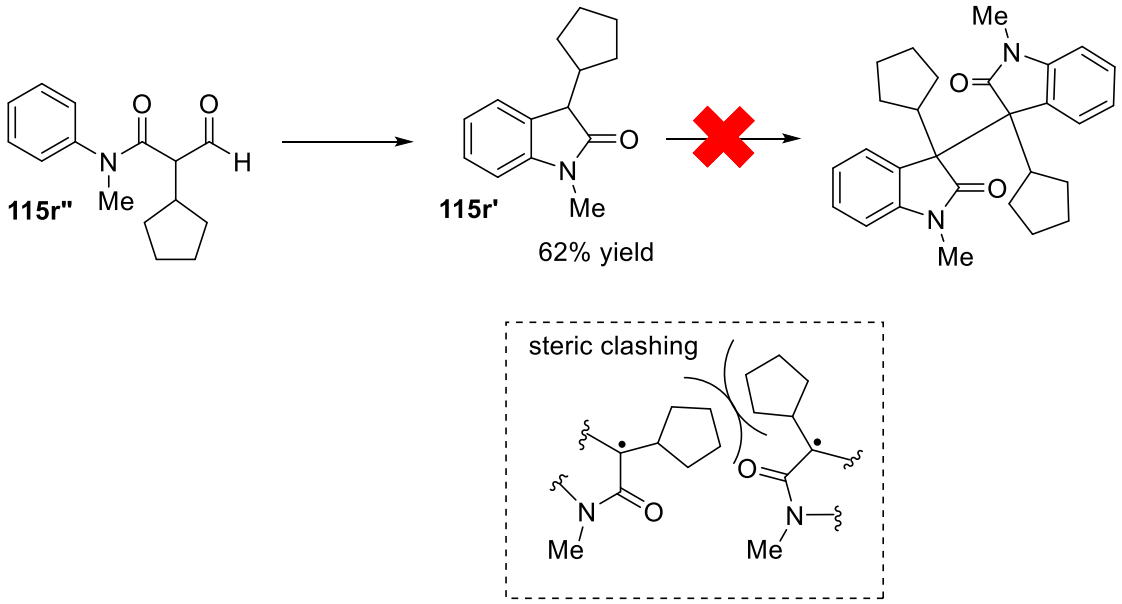

Figure 3.23. Product of the $Mn(OAc)_3$-mediated oxidation of oxoanilide **115r"**.

Oxoacid

Having established a route to access the oxoacid and an optimised dimerization protocol for from **111**, we created a library of different oxoacids with variations to the alkyl chain and aromatic group and protecting group (**Figure 3.24**).

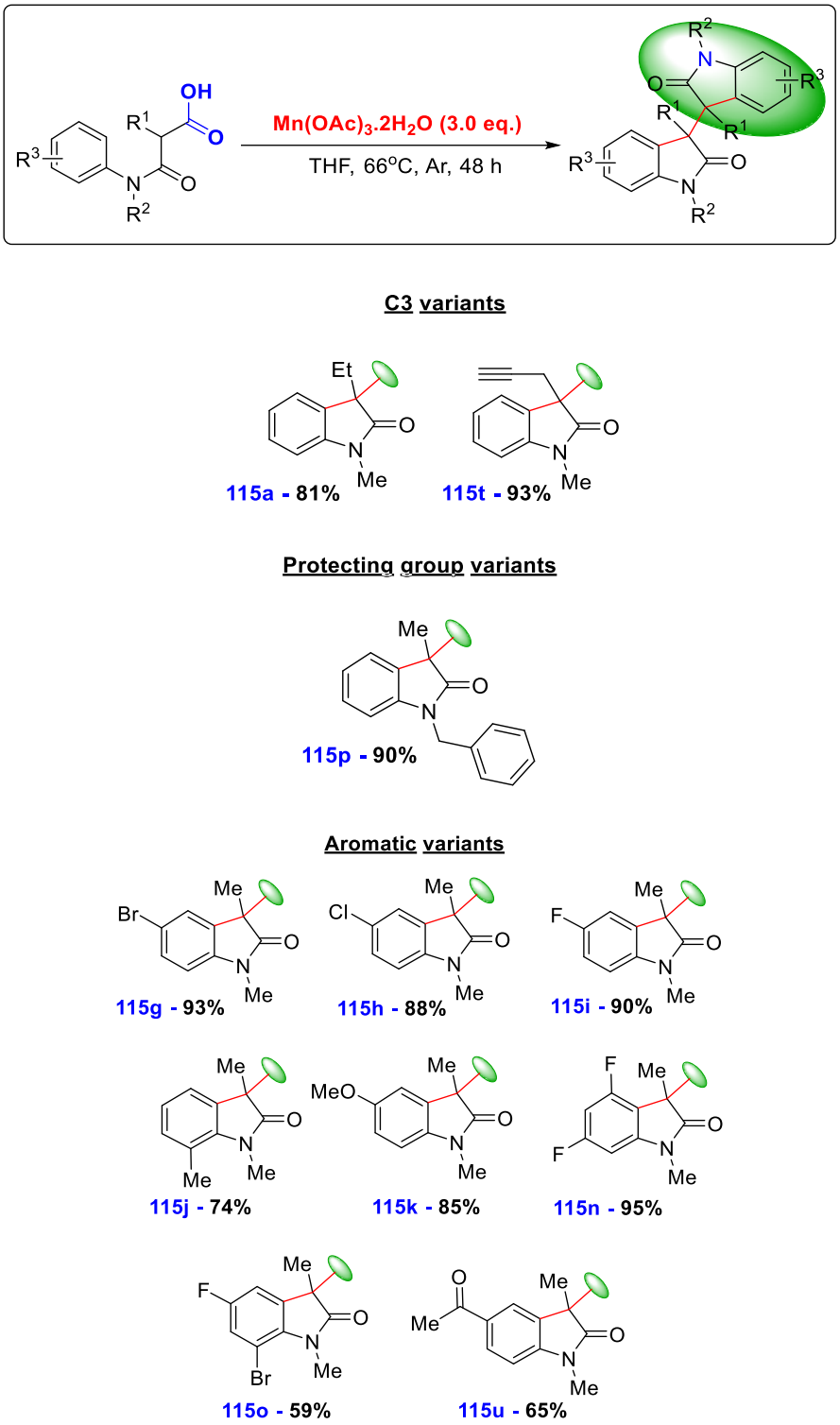

Figure 3.24. Substrate scope with the oxoacid.

The use of oxoacid as a substrate for dimerization was complementarily with the oxoanilide, allowing the formation of some bisoxindoles that were previously inaccessible. Of the C3 variants we note the synthesis of **115t**, bearing a propyne group, which was formed in excellent yield, 93%.

We were additionally gratified that the *N*-benzyl variant was amenable, formed in 90% yield (**115p**). For the aromatic variants, many previously synthesised via the oxoanilide were viable via the oxoacid **115g** – **115k** of the monosubstituted variants and **115n** and **115o** of the disubstituted; in some cases, improved yields were observed (**115g**, **115i** and **115n** in 93%, 90% and 95%, respectively vs 73%, 84% and 88% with the respective oxoanilide). Of these, we were most gratified that formation of the oxoacid with the acetyl substrate (**115u**) and subsequent dimerization was able a viable strategy giving the resultant bisoxindole in 65% yield.

Mechanistic insights

TEMPO ((2,2,6,6-Tetramethylpiperidin-1-yl)oxyl) (**Figure 3.25**, **120**) is a stable radical species that can trap and scavenge other radical species when they present. As a consequence, it has cemented itself as litmus in organic synthesis to determine whether reactions proceed via radical pathway.[106] Not only can TEMPO be used to examine if reactions proceed via radical pathways, the addition of TEMPO also effectively shut down these pathways, owing to its ability to act as a radical scavenger, thus, analysis of the resultant TEMPO-adducts or products is a powerful procedure to determine the identity of radicals within a specific pathway.[106–108]

Thus, to determine whether our proposed mechanism (**Figure 3.19**) did indeed proceed via radical intermediates, TEMPO experiments were performed. Here TEMPO (**64**) was added stoichiometrically with either **105** or **111** under the optimised conditions. (**Figure 3.25**).

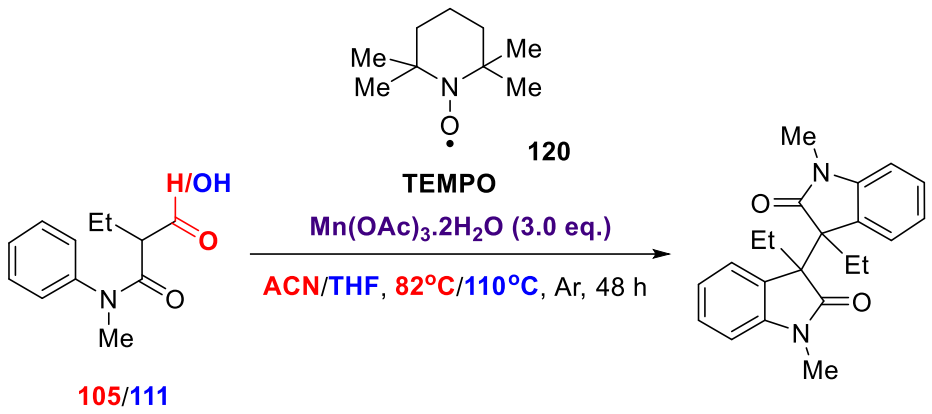

Figure 3.25. Conditions for TEMPO trapping experiment with **105** and **111**.

Under these conditions, bisoxindole **115a** was not produced when either **105** and **111** were used as substrates (**Figures 3.26** & **3.27**).

While neither substrate was able to furnish **115a** in the presence of TEMPO, we noted the formation of ketoamide **121** in both cases (33% and 45% for **105** and **111** respectively), as well as a 19% yield of **116** in the case of **105**.

These results were generally supportive of our proposed mechanism; the absence of dimer **115a** is highly suggestive of a radical pathway due to TEMPO inactivation. Furthermore, we can feasibly obtain ketoamide **121** from either **105** or **111** via trapping of the respective radical **105'** or **111'** to form the resulting TEMPO-adduct that fragment via either a one or two electron process, which has been noted in the works of Li and Yu.[103]

Similarly, in the case of **105**, trapping of the key radical **117** by TEMPO to form the resulting adduct, can fragment to furnish the hydroxindole **116** post-work up.[104] Formation of these radical species would thus be necessary to obtain **121** and **116**.

In addition, we revised our first hypothesis for the fragmentation of **105** (**Figure 3.26**). Previously, we postulated a mechanism that proceeds via CO extrusion, however, based on the literature precedent for Manganese (III)-mediated oxidations, it seemed more likely that formation of a metal-bound carboxylate species is first necessary; prior oxidations would produce **MnOH** as a byproduct, which can insert into the aldehyde functionality by an S_N2-like reaction, followed by oxidation of this carboxylate to the Mn(III) species (**105"**). Thereafter, radical fragmentation similar to **111** and extrusion of -HCO_2H would give rise to the key radical intermediate **117**.

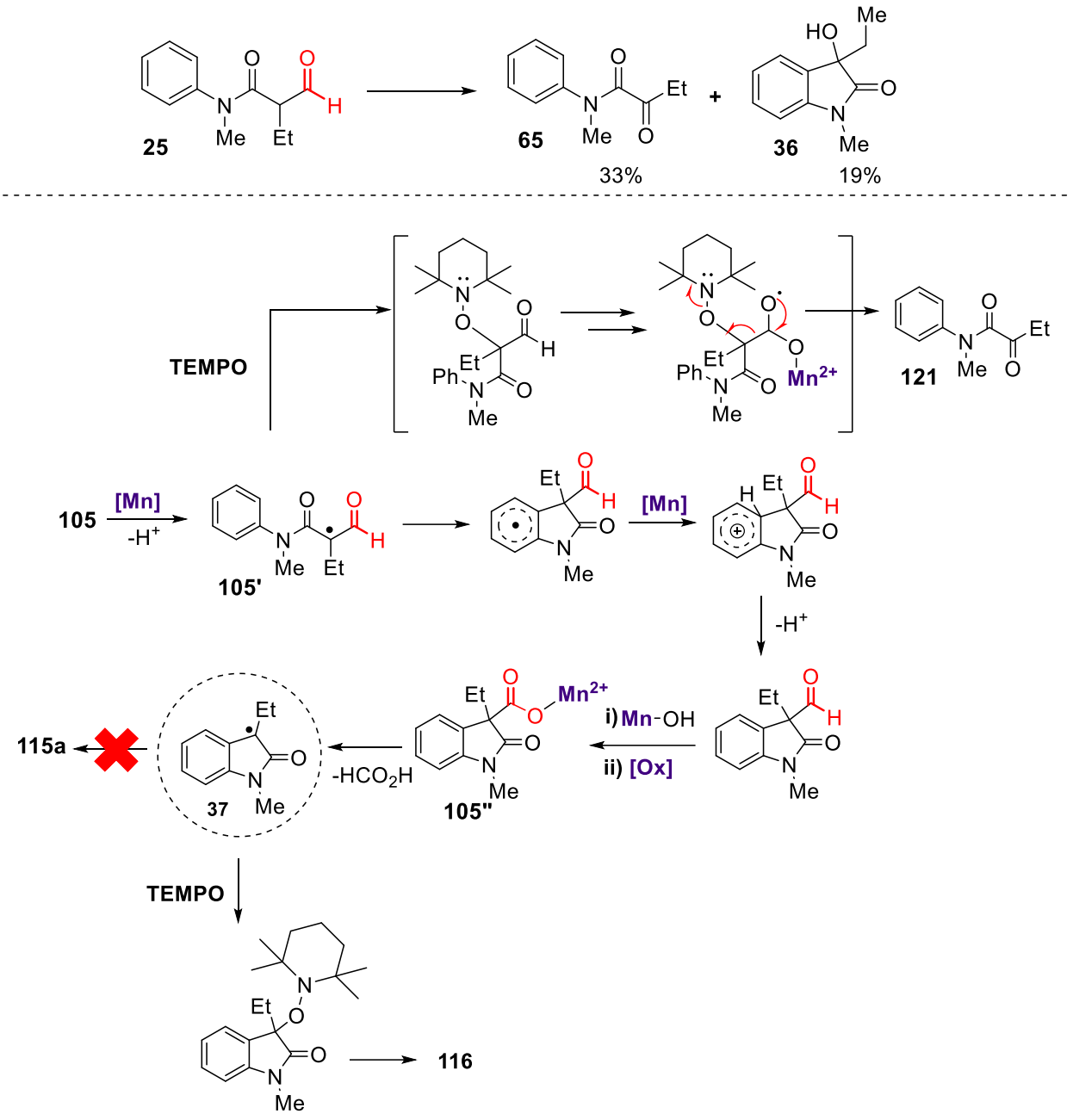

Figure 3.26. Products and proposed pathway to generate them of the TEMPO trapping experiment with aldehyde **105**, with updated mechanism.

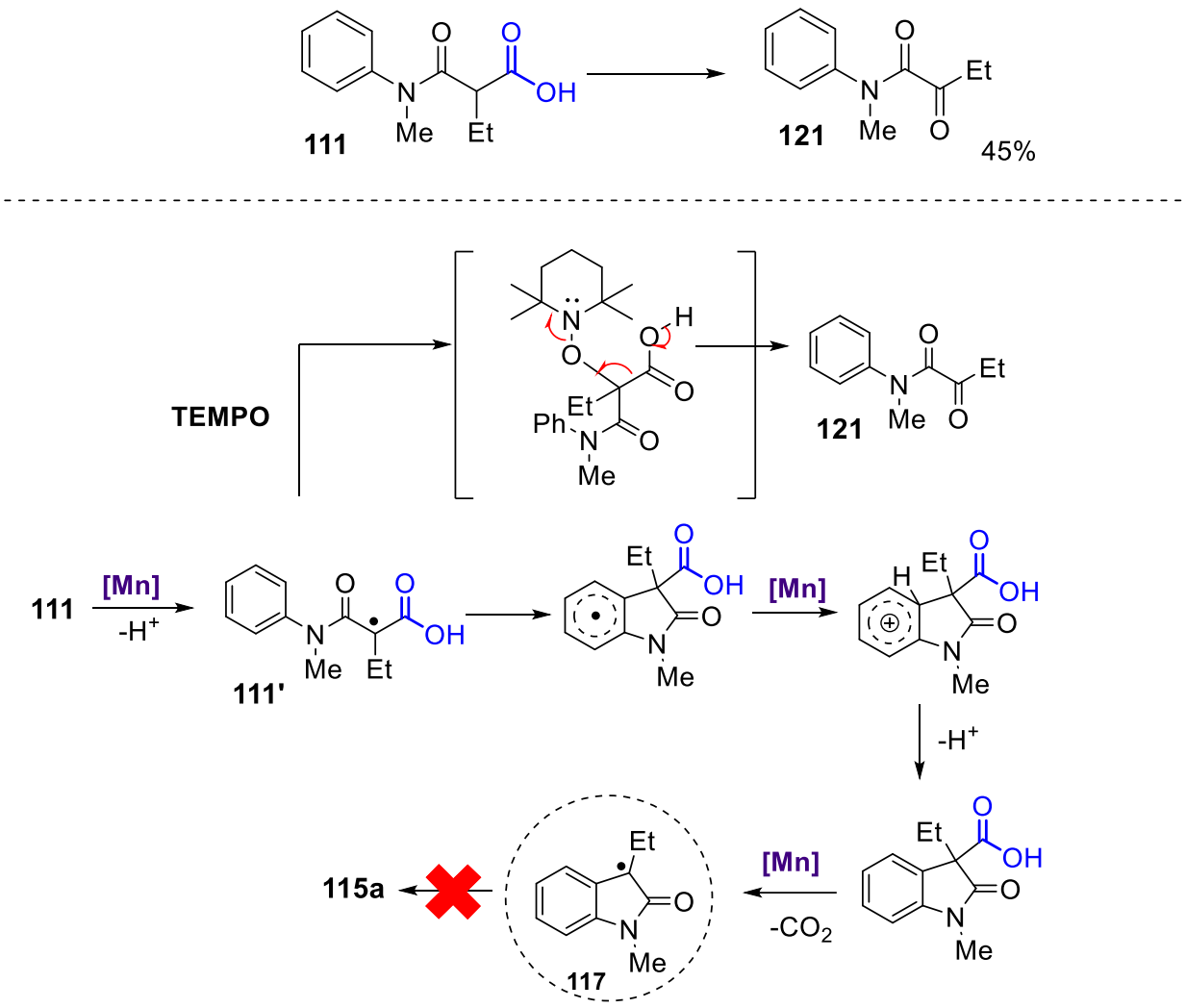

Figure 3.27. Products and proposed pathway to generate them of the TEMPO trapping experiment with acid **111**.

Photoredox method

Preliminary photocatalyst screen

For our initial photocatalyst screen, we looked to oxidising photocatalysts with similar reduction potentials to those of Mn^{3+} and Cu^{2+}. Additionally, while we had observed the competitive effect of molecular oxygen on the generated radicals under transition metal catalysis, it was of note that this effect seemed potent primarily at high temperatures (**Table 3.4**, entries 1 – 6). Indeed, refluxing at lower temperatures (**Table 3.4**, entries 7 – 8 & 11 – 12) yielded only desired dimer **115a**, albeit at low yields for the former entries. This however suggested that exclusion of high temperature conditions could inhibit this competitive effect.

Given that photoredox catalysis often proceeds under relatively benign conditions, typically in the absence of heat, we hoped to design a catalytic cycle with either oxygen as the terminal oxidant or proceed in the absence of a terminal oxidant (**Table 3.5**).

Table 3.5: Preliminary photocatalyst screen using both **105** and **111**. [a]Open to air. [b]Inert atmosphere and de-gassed solvent.

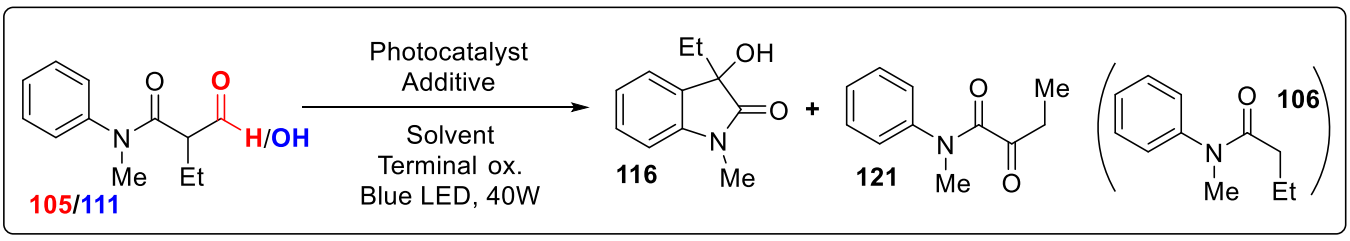

Entry	Substrate	Photocatalyst (X mol%)	Additive (equiv.)	Solvent	Terminal Oxidant	Yield (%)		
						106	116	121
1[a]	105	$[Ru[bpy)_3]Cl_2$ (**2 mol%**)	KOAc (**2.0**)	ACN	Oxygen	22	-	26
2[a]	111	$[Ru[bpy)_3]Cl_2$ (**2 mol%**)	KOAc (**2.0**)	ACN	Oxygen	30	-	-
3[a]	105	$Ir(d(CF_3)(ppy)_2)$ (dtbbpy) (**1 mol%**)	KOAc (**2.0**)	ACN	Oxygen	11	-	21

4[a]	111	Ir(d(CF_3)(ppy)$_2$) (dtbbpy) (**1 mol%**)	KOAc (**2.0**)	ACN	Oxygen	-	-	Trace
5[a]	105	Ir[(bpy)(ppy)$_2$] (**1 mol%**)	KOAc (**2.0**)	DMF	Oxygen	17	-	14
6[a]	111	Ir[(bpy)(ppy)$_2$] (**1 mol%**)	KOAc (**2.0**)	DMF	Oxygen	24	-	-
7[a]	105	4-CzIPN (**2 mol%**)	K^{t}OBu (**10 mol%**)	ACN	Oxygen	-	8	-
8[a]	111	4-CzIPN (**2 mol%**)	K^{t}OBu (**10 mol%**)	ACN	Oxygen	56	trace	-
9[b]	105	2-CTX (**20 mol%**)	K^{t}OBu (**2.0**)	TFE	-	19	-	trace
10[b]	111	2-CTX (**20 mol%**)	K^{t}OBu (**2.0**)	TFE	-	29	-	12
11[b]	105	Mes-Acr (**7.5 mol%**)	K^{t}OBu (**2.0**)	TFE	(4-Cl-PhS)$_2$ (**15 mol%**)	18	-	6
12[b]	111	Mes-Acr (**7.5 mol%**)	K^{t}OBu (**2.0**)	TFE	(4-Cl-PhS)$_2$ (**15 mol%**)	74	-	

Each screen was equipped with a base to facilitate the deprotonation as postulated in **Figure 2.21.** In all entries, we did not observed bisoxindole **115a**; any mass not included in the cumulative total of **106**, **116** and **121** was returned as starting material **105** or **111**.

Photocatalysis, particular those involving Ru, Ir and 4-CzIPN, have been shown to be effective oxidants on dicarbonyl systems; particularly for modifications at the tertiary hydrogen.[109–111] Given this, we began our catalytic screen with some of these photocatalysts (entries 1 – 6).

Under these conditions, with [Ru[bpy)$_3$]Cl$_2$ (entries 1 & 2), we primarily observed formation of the anilide starting material (**106**) (22% and 30% yield), and, in the case of **105** (entry 1), the ketoamide **121** in 26% yield. Although this was not present for the acid **111** (entry 2), there was notably higher % of anilide compared to entry 1.

Switching to Iridium photocatalysts, neither the strongly oxidising Ir(d(CF_3)(ppy)$_2$(dtbbpy)) nor Ir[(bpy)(ppy)$_2$] were able to furnish dimer **115a** (entries 3 – 6). Here, a similar trend to entries 1 & 2 was observed with primary formation of anilide **106** (11%) and ketoamide **121** (21%) for **105** with Ir(d(CF_3)(ppy)$_2$(dtbbpy)) (entry 3) while **111** was almost entirely unreactive (entry 4). Ir[(bpy)(ppy)$_2$] as the catalyst did not fare any better with similar conversion for **105** (entry 5) (31% total). Though in this case, there was marked improvement in the conversion of **111**, with 24% formation of anilide **106**.

Using 4-CzIPN had interesting results (entries 7 & 8); there was a notable difference in distribution of products, and, most interestingly it was the only catalyst that produced hydroxyoxindole **116**; in 8% yield with **105** (entry 7) and trace amounts with **111** (entry 8). Moreover, the majority of mass was converted in the case of **111**, with a 56% yield of anilide (entry 8).

From these results thus far, we can infer that there are two competing effects on the catalytic cycle (**Figure 3.19**). It is first, suggestive of premature decarboxylatation/decarbonylation *before* H-abstraction and cyclisation (**Figure 3.28**) and secondly, competition with molecular oxygen if H-abstraction and SET does occur to form the ketoamide as shown in **Figures 3.26** & **3.27**.

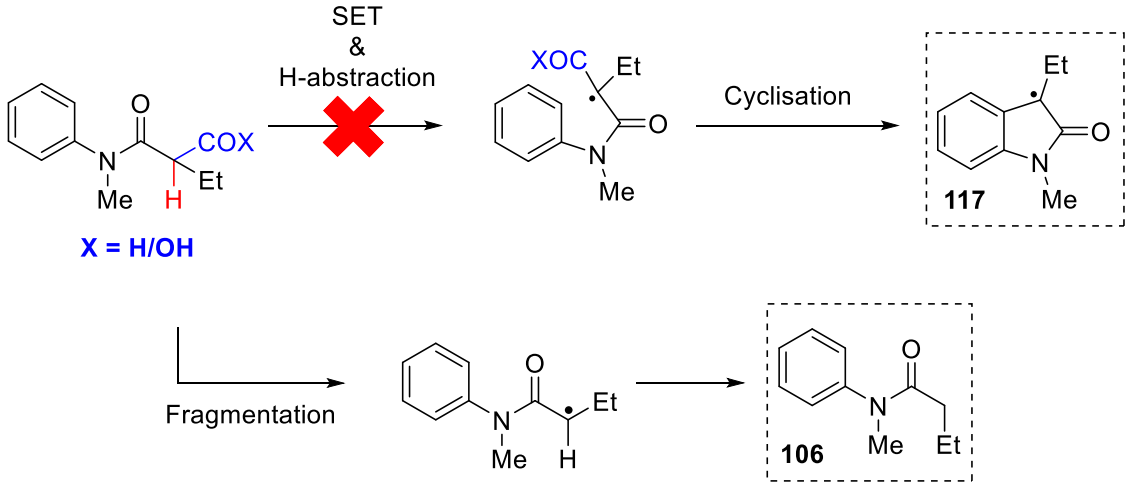

Figure 3.28. Proposed mechanistic explanation for degradation of **105** and **111** to **106**.

Although in the case of 4-CzIPN, there seemingly was some potential competing cyclisation then interception by O_2 but the abysmal yield of **116**, especially relative to **106** for **111** was not encouraging.

In light of this, we were inspired by work within our group that successfully used 2-chlorothioxanthone (2-CTX) to catalyse the photocyclization of *N*-acrylamides via direct energy transfer and we wondered whether this might be applicable to this system to overcome the competitive effect in **Figure 3.28**. A repetition of these conditions however, proved unfruitful (entries 9 & 10), with major product **106** (19% and 29% respectively) and minor product **121** (trace and 12% respectively).

Lastly in this screen, we looked to an air-excluded system, utilising 9-Mesityl-10-methylacridinium tetrafluoroborate (Mes-Acr), in the presence of catalytic disulfide $(4\text{-Cl-PhS})_2$ which can fragment to turnover the catalytic cycle and be regenerated through substrate oxidation as shown by MacMillan (entries 11 & 12).[5]

While this disappointingly yielded no new insights with regards to formation of the desired **115a**, we were surprised at the high conversion of starting material in the case of **111** with over 70% conversion to anilide **106**.

It was clear at this point, that generation of **115a** via a single photocatalytic system was disfavoured in favour of immediate fragmentation and protonation of the tertiary radical rather than the necessary cyclisation-dimerisation cascade.

Dual catalytic strategies

Consolidating the results of the optimisation screens in **Table 3.4** and **3.5**, we noted:

1) Catalytic metal ions (namely Cu^{2+} and Mn^{3+} at RT produced little to no reaction
2) Catalytic oxidants at mild temperature (50 – 60 °C) produces primarily hydroxy oxindole (**116**)
3) Catalytic oxidants at high temperatures produces mainly bisoxindoles (**115a**)
4) Different oxidants have different affinity for producing the bisoxindoles or hydroxy (e.g. CAN for **36** and Mn^{3+} for **115a**)
5) Photocatalysts primarily return either aniline **106** or ketoamide **121**.
6) Low conversion of starting material is observed at lower temperatures ($T \leq 66$ °C)

From these we can ascertain that, with transition metal catalysis, higher temperatures are often needed for significant bisoxindole formation ($T \geq 66$ °C) to outcompete

hydroxindole and ketoamide formation. This is possibly due to two non-exclusive events that are facilitated by the elevated temperature:

1) High temperature needed to turnover the active catalyst species as suggested by Taylor with respect to the regeneration of Cu^{2+} from Cu^{+} in the cyclisation of β-ketoesters.
2) The reaction proceeds through an inner-sphere complex; whereby preorganisation of the catalyst and/or coordination of a metal ion to the substrate via intermolecular bonds is required for orbital alignment and/or efficient electron transfer.

Given that most photoredox reactions proceed via an **outer-sphere complex**, electron transfer without coordination/preorganisation, it would plausibly explain why we observe relatively lower conversion of starting material and absence of dimer **115a**.

As a potential work around to this, we postulated a co-operative catalytic system, one containing a transition metal that can act either as a Lewis acid to co-ordinate with our substrate, or can oxidise the substrate directly, then be turnover via photoredox catalysis.

These types of systems are well documented and an example of each type of system is presented in **Figure 3.29 & 3.30**.

Here, we can see a co-operative system between the transition metal and photocatalytic cycles, developed by Rueping *et al*[112] where excitation by light gives the excited state photocatalyst $[Ir^{3+}]^*$ that activates the Palladium catalyst from Pd^{0} to Pd^{2+}. Thereafter, co-ordination of the aromatic enamine (**122**) by Pd^{2+} and sequential loss of acetic acid, oxidation and reductive elimination of the Palladium furnishes the desired indole (**123**), producing Pd^{0} that can begin the cycle anew.

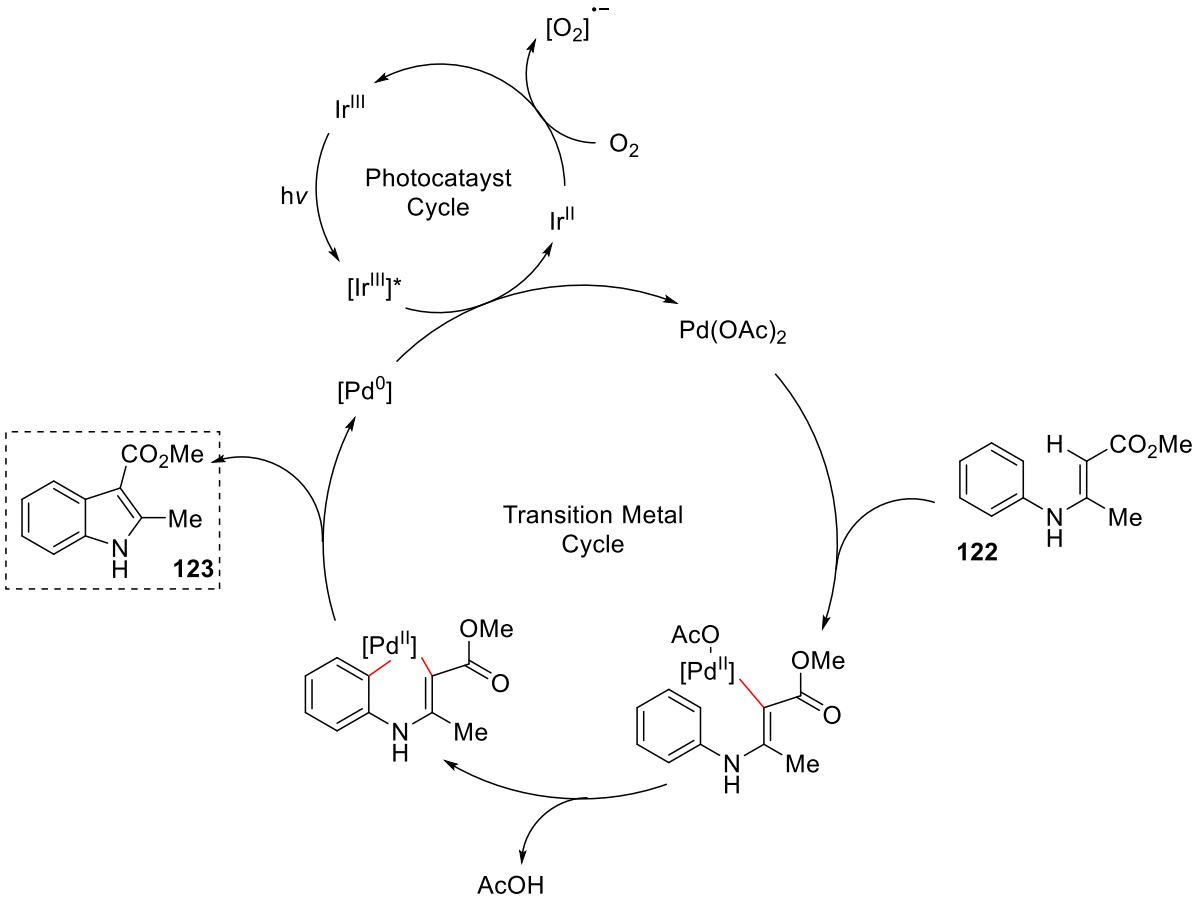

Figure 3.29. Photoredox-mediated C-H activation for Palladium catalysed C-H activation by Rueping *et al*.

In a similar fashion we can see a co-operative Lewis Acid/photoredox cycle by Scheidt *et al*[110] in **Figure 3.30.** Coordination of the scandium (III) ion to the arylidene malonate (**124**) forms the resulting ion-bound complex that is primed for SET by oxidised Ir^{2+}, forming the resulting radical **125**. This Ir^{2+} species is formed via a photoredox cycle that, post-excitation is oxidatively quenched by a modified Hantzch ester, **126**, which fragments to give the pyridinium cation and tertiary radical **127,** which circles back to intercept radical **125**, forming malonate **128**. Proton transfer by the pyridinium cation can then regenerate the active $Sc(OTf)_3$ to be used again.

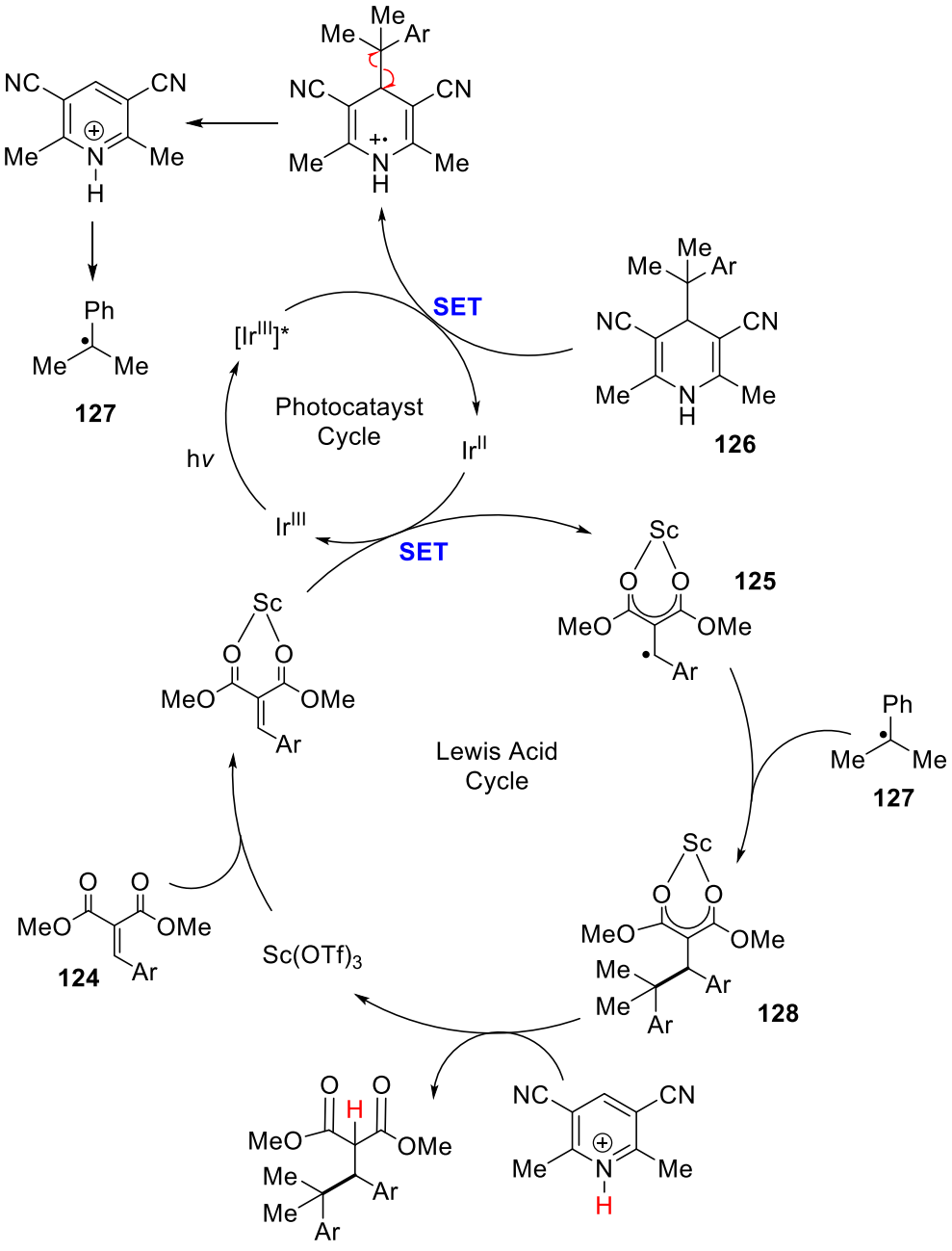

Figure 3.30. Dual Photoredox-Lewis acid cycle for the coupling of Arylidene malonates by Scheidt *et al*.

Photoredox screen: Reductive quenching cycle

With these dual catalytic cycles in mind, we first looked to a photoredox system under reductive quenching control, recalling from Chapter 2, **Figure 2.21**, this proceeds via quenching of the excited state catalyst by either substrate **105**/**111** or a second catalytic cycle to produce the reduced photocatalyst, which can be oxidised back to the active

catalytic species. Here the regeneration would proceed by a second catalytic cycle and turnover of that cycle by a terminal oxidant.

Table 3.6: Condition screen for dual photocatalytic/TM/Lewis acid cycle under reductive quenching control of **105** and **111**. [a]Under 120°C heat.

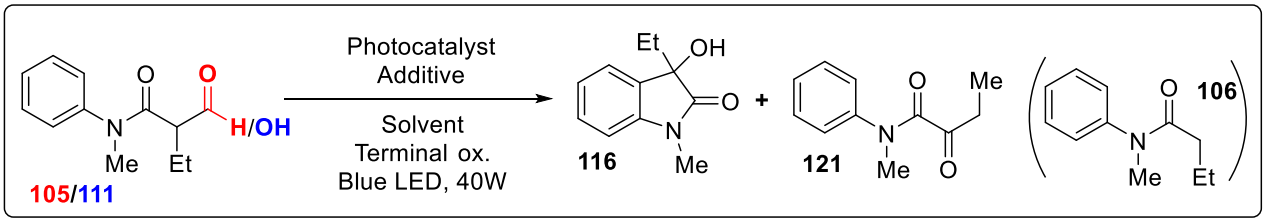

Entry	Substrate	Photocatalyst (X mol%)	Additive (equiv.)	Solvent	Atmosphere	Yield (%)		
						106	116	121
1	105	4-CzIPN (**2 mol%**)	$AgNO_3$ (**0.5**), $K_2S_2O_8$ (**3.0**)	ACN:H2O (1:1)	Inert	39	-	-
2	111	4-CzIPN (**2 mol%**)	$AgNO_3$ (**0.5**), $K_2S_2O_8$ (**3.0**)	ACN:H2O (1:1)	Inert	54	-	-
3[a]	105	$Ir[(bpy)(ppy)_2]$ (**1 mol%**)	$Pd(OAc)_2$ (**2 mol%**), K_2CO_3 (**3.0**)	DMF	Air	50	26	9
4[a]	111	$Ir[(bpy)(ppy)_2]$ (**1 mol%**)	$Pd(OAc)_2$ (**2 mol%**), K_2CO_3 (**3.0**)	DMF	Air	43	15	-
5[a]	105	$Ir[(bpy)(ppy)_2]$ (**1 mol%**)	$Cu(OAc)_2$ (**0.5**), K_2CO_3 (**3.0**)	ACN	Air	23	10	-
6[a]	111	$Ir[(bpy)(ppy)_2]$ (**1 mol%**)	$Cu(OAc)_2$ (**0.5**), K_2CO_3 (**3.0**)	ACN	Air	35	-	-

7	105	Ir(d(CF_3)(ppy)$_2$) (dtbbpy) (**1 mol%**)	$NiCl_2$ (**10 mol%**), K^tOBu (**2.0**)	THF	Air	-	-	-
8	111	Ir(d(CF_3)(ppy)$_2$) (dtbbpy) (**1 mol%**)	$NiCl_2$ (**10 mol%**), K^tOBu (**2.0**)	THF	Air	38	-	-

We began this screen by looking at 4-CzIPN as the active photocatalyst; having previously noted that it was the only trialled photocatalyst (**Table 3.5**) to successfully generate hydroxy oxindole (**116**). Additionally, another member of our group, Munashe Mazodze, published a dual 4-CzIPN/$AgNO_3$ system which could co-operatively be used in the formation of quinoline-2-ones,[113] which also proceeds via an oxidative pathway. As such it seemed the ideal starting point.

Disappointingly, under the reported conditions with inert atmosphere and catalytic 4-CzIPN/$AgNO_3$ and terminal persulfate (entries 1 & 2), we saw exclusive formation of the anilide precursor **106**, this time without any side formation of **116**. There was notably significantly more conversion of **105** (entry 1) compared to the previous 4-CzIPN screen (39% vs 8%), however this was not mirrored for **111** (entry 2, 54%).

Switching to the Pd-catalysed system previous shown (**Figure 3.29**) and reported by Mullins *et al*[114] with $Pd(OAc)_2$ and K_2CO_3 as a base under heat (120 °C) (entries 3 & 4) was far more fruitful. Here, we observed a significantly higher conversion of starting material (85% for **105** and 58% for **111**) which was some of the highest conversion under photocatalytic conditions thus far, possibly due to the elevated temperature which was shown in the CDC screen to be effective. Despite this however, formation of **115a** proved elusive, though in both cases **116** was formed (106% and 15% yield for entries 3 and 4 respectively), along with the major product **106** (50% and 43% respectively).

This result was however interesting from the standpoint of conversion of **105**/**111** since we had previously struggled to obtain >50% conversion in most photocatalytic conditions, thus we sought alternative transition metals for this cooperative process. Copper salts have recently generated interest in photoredox reactions,[115–117] many of

which have been implicated as terminal oxidants.[118] They possess many attractive features suitable for this role, namely they do not affect the photoactivity of photocatalysts in addition to them being easy to handle, inexpensive and easy to separate from the reaction mixture. For these reasons, we were hopefully that $Cu(OAc)_2$, which had already shown utility in our CDC screen, would be a good fit in this reaction (entries 5 & 6).

Under similar conditions to those in entries 3 & 4, oxoanilide **105** (entry 5) was converted to the anilide **106** as the major product (23%) and hydroxyoxindole **116** as the minor (10%) in overall 33% yield, a significant reduction when compared to entry 3 with $Pd(OAc)_2$. Oxoacid **111** (entry 6) likewise had a diminished conversion compared to entry 4 with $Pd(OAc)_2$: 35% conversion vs 58%, entirely towards **106**, no **116** was observed.

In addition to Copper, Nickel has also gained traction as an effective co-catalyst for various photoredox-mediated transformations. It also demonstrated ability to act as a second SET catalyst to speed up the rate of reactions when both photocatalyst and nickel oxidants were utilised.[119–121]

Similar to copper however, nickel was unable to compete with $Pd(OAc)_2$ in either conversion or yield of products (entries 7 & 8). In the case of the **105**, no reaction was observed at all (entry 7), while **111** as the substrate could only furnish anilide **106** in 38% yield (entry 8).

In conclusion, though we were able to increase the conversion of reacting starting material for these photocatalysed reactions compared to preliminary screen (**Table 3.5**), the increased conversion was not reflected in formation of the cyclised products **116** nor the desired **115a**, rather the competitive pathway to rapid decarbonylation/decarboxylation was still highly favoured, even in cases with increased temperature (entries 3 & 4, **Table 3.6**).

Photoredox screen: Oxidative quenching

As most trialled conditions (**Tables 3.5** and **3.6**) presumably proceeded via direct substrate activation in the photocatalytic cycle, it led us to wonder if the reaction would best be served if a photocatalytic cycle was utilised to turn over a catalytic transition metal cycle instead.

Thus, we switched to an oxidative quenching cycle, generating the oxidised photocatalyst that could be turnedover by reduction; typically for dual catalytic cycles involving these cycles, the partnering transition metal cycle was typically a Lewis acid, which had shown to be effective at activating and functionalising dicarbonyl substrates, similar to **105** and **111**, such as malonates (**Table 3.7**).

Table 3.7: Condition screen for dual photocatalytic/Lewis acid cycle under reductive quenching control of **105** and **111**. [a]Under 120 °C heat.

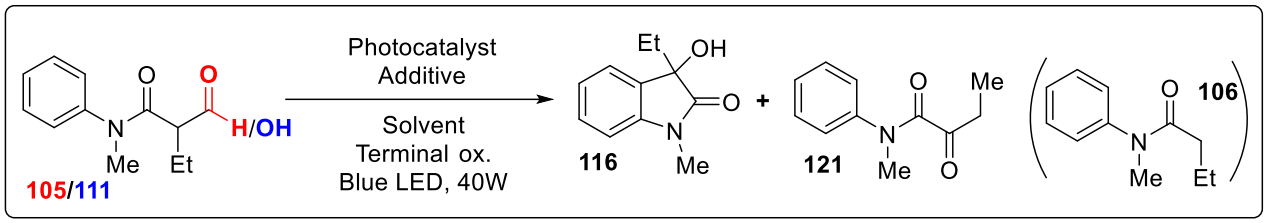

Entry	Substrate	Photocatalyst (X mol%)	Additive (equiv.)	Solvent	Atmosphere	Yield (%)		
						106	116	106
1	105	$Ir(d(CF_3)(ppy)_2)(dtbbpy)$ (**1 mol%**)	$Sc(OTf)_3$ (**0.2**)	ACN	Air	21	trace	-
2	111	$Ir(d(CF_3)(ppy)_2)(dtbbpy)$ (**1 mol%**)	$Sc(OTf)_3$ (**0.2**)	ACN	Air	-	-	-
3	105	$Ir(d(CF_3)(ppy)_2)(dtbbpy)$ (**1 mol%**)	BF_3.diethyl etherate (**0.2**)	ACN	Air	-	-	-
4	111	$Ir(d(CF_3)(ppy)_2)(dtbbpy)$ (**1 mol%**)	BF_3.diethyl etherate (**0.2**)	ACN	Air	-	-	-
5	105	$Ir[d(CF_3)]$ (**1 mol%**)	$Na_2S_2O_8$ (**3.0**)	ACN	Inert	trace (~5)	-	-
6	111	$Ir[d(CF_3)]$ (**1 mol%**)	$Na_2S_2O_8$ (**3.0**)	ACN	Inert	63	-	-
7	105	$[Ru[bpy)_3]Cl_2$ (**1 mol%**)	$Na_2S_2O_8$ (**3.0**)	ACN	Inert	36	-	-
8	111	$[Ru[bpy)_3]Cl_2$ (**1 mol%**)	$Na_2S_2O_8$ (**3.0**)	ACN	Inert	52	-	-

Figure 3.38 had shown an effective dual scandium/iridium system for the functionalisation of arylidines which proceeds via Lewis acid activation of the malonate by coordination, in tandem with photocatalysed oxidation of the substrate. Inspired by this, we sought to utilise this method to our system; the hope was that each catalytic system would handle a separate component of the reaction: $Sc(OTf)_3$ could coordinate and facilitate electron transfer via inner-sphere process while Ir-cycle would facilitate oxidation of the substrate and intermediates (**Figure 3.30**).

Despite this, a trial of these conditions (entries 1 & 2) was ineffective at promoting cyclisation over fragmentation, returning 21% yield of **106** with **105** and only trace amounts of **116** (entry 1), while **111** was completely inert to these conditions entirely (entry 2).

Thinking a stronger Lewis acid might be needed to help coordinate and facilitate this, we switched over to BF_3, which has also been implicated in these transformation (entries 3 & 4).[122] This was entirely unsuccessful at conversion for both substrates.

Switching away from Lewis acid mediation, we looked at the effect of a dual system with persulfates which have demonstrated in their ability to turnover ruthenium and iridium photocatalysts via homolytic fragmentation.[123] (Entries 5 – 8)

The oxoanilide **105** proved resilient to these systems with marginal conversion using both Ru and Ir under persulfate (entries 5 & 7, 5% and 116%, respectively), that went wholly towards formation of **106**. Oxoacid **111** was more amicable, with 52% and 63% for Ru and Ir respectively (entries 6 & 8) though, as previously, anilide **106** was shown as the only product.

Photoredox: Conclusion

Having looked at a wide array of photocatalysts, additives, as well as both oxidative and reductive quenching cycles, we are confident in our conclusion that the dimerization-cyclisation cascade sequence developed with $Mn(OAc)_3$ is transferable photocatalytically. As noted previously, this could be a consequence of ineffective inner-sphere coordination under photocatalysis even in the presence of Lewis acids. Alternatively, the near universal presence of anilide **106** in almost all screened conditions could be indicative of increased lability of the C-COX bond under visible light which

would accelerate fragmentation relative to cyclisation. As a result, it was concluded that catalytic development of this transformation would best be served under transition metal catalysis as was successfully demonstrated previously with stoichiometric $Mn(OAc)_3$.

Catalytic CDC screening

Initially we thought to begin optimisation of the catalytic CDC method with the conditions reported in **Table 3.3**, entry 9 as a baseline, as it previously delivered the highest yield of **115a** under aerobic conditions and sub-stoichiometric quantities of $Mn(OAc)_3.2H_2O$ with **105** as the substrate (**Figure 3.31**, **A**). However, it was later discovered within our research group by Munashe Mazodze, that an addition of 10 mol% $Co(OAc)_2.4H_2O$ to this condition under refluxing dioxane instead of toluene, could furnish dimer **115a** in 64% yield (**Figure 3.31**, **B**). While the total conversion of substrate in condition **A** was marginally higher (85%) compared to **B** (77% conversion of starting material), the favouritism towards formation of **115a** in the case of **B** compared to **A,** outweighed this difference, particularly since the bulk of the difference came from the formation of the hydroxyoxindole **116** (32% for **A** conditions vs 13% for **B**). Moreover, **B** could be achieved in lower temperature using dioxane. Thus, this was a promising point to further develop our catalytic CDC methodology.

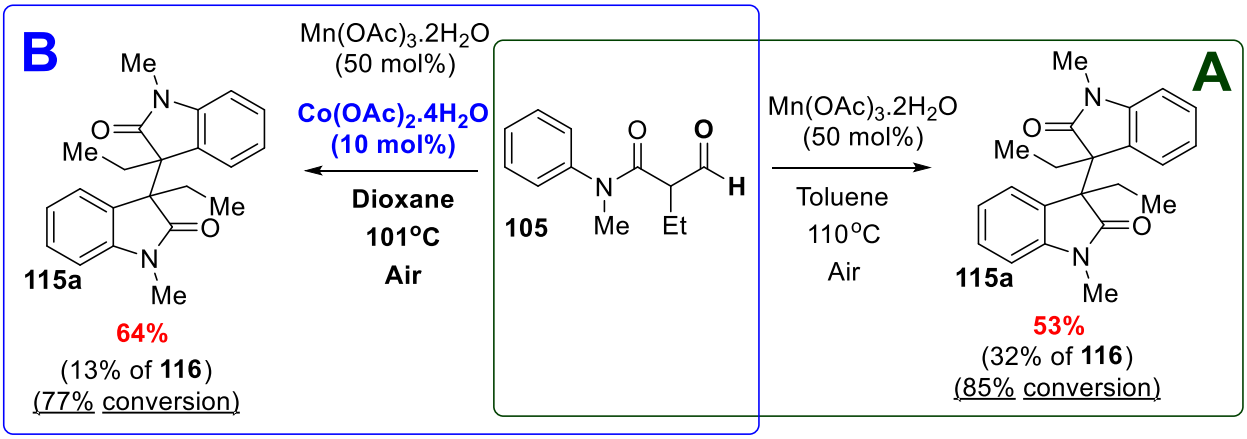

Figure 3.31. Comparison of best conditions with sub-stoichiometric amount of $Mn(OAc)_3.2H_2O$ (right) vs conditions discovered by Munashe Mazodze with addition of 10 mol% $Co(OAc)_2.4H_2O$.

A plausible explanation for this higher yield when 10 mol% $Co(OAc)_2$ was added, is the formation of a co-operative catalytic system, where the $Co(OAc)_2$ is able to turnover the Mn-cycle more effectively than molecular oxygen by itself. Indeed, if it this was the case, there would be a proportionately lower percentage of radical species post-oxidation to be trapped by molecular oxygen. Alternatively, the $Co(OAc)_2$ could be acting as a secondary oxidant for this transformation, speeding up the rate of oxidation, which would again, result in a lower amounts of radical to be scavenged by molecular oxygen.

Given this, the reaction was repeated and stopped at T = 24 hours, which yielded the same result as that at T = 48 hours, further reinforcing the idea of a more robust and effective dual catalytic system, though at this stage the exact mechanism is unknown.

To gain further insight into the mechanism and optimise this promising result we started with those conditions as a baseline (**Table 3.8**, entry 1). For our first screen we looked at the loading and identity of the co-catalyst and expanded the conditions to include **111** as the substrate.

Table 3.8: Co-catalyst loading and variation screen from conditions specified in **Figure 3.31**, on both **105** and **111**. [a]Reaction ran for 48 hours.

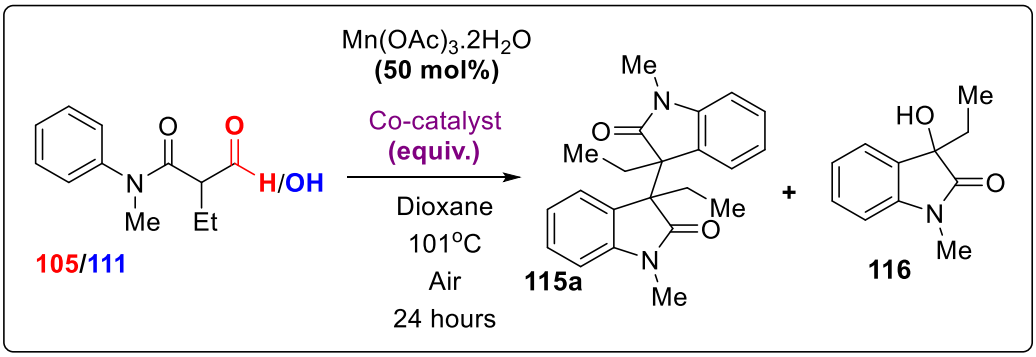

Entry	Substrate	Co-catalyst (equiv.)	Yield (%)	
			115a	116
1	105	$Co(OAc)_2$ (**0.1**)	64	13
2	111	$Co(OAc)_2$ (**0.1**)	36	15

3	105	$Co(OAc)_2$ (**0.5**)	66	27
4	111	$Co(OAc)_2$ (**0.5**)	45	47
5	105	$Cu(OAc)_2$ (**0.5**)	31	25
6	111	$Cu(OAc)_2$ (**0.5**)	70	17
7	105	$KMnO_4$ (**0.3**)	9	10
8	111	$KMnO_4$ (**0.3**)	41	10
9	105	$FeCl_3$ (**0.5**)	12	7
10	111	$FeCl_3$ (**0.5**)	8	Trace
11[a]	105	$Na_2S_2O_8$ (**3.0**)	25	-
12[a]	111	$Na_2S_2O_8$ (**3.0**)	15	-

We first subjected **111** to these conditions to set up a comparative baseline (entry 2), which we were gratified to observe, formed **115a** (entry 2), though in much lower yield compared to entry 1 (36%), with lower conversion of substrate as well (51%) compared to entry 1 (77%).

Results for both substrates in hand, we increased the loading of the $Co(OAc)_2$ to 50 mol% (entries 3 & 4); the idea was to keep the reaction catalytic, thus we wanted to avoid exceeding a combined 1.0 equivalent of both oxidants where possible. Doing so here, we were rewarded with an increase yield in both cases; **105** saw an increase in conversion of starting material from 77% (entry 1) to 93% (entry 3), with an increase in yield of **115a** to 66%, though this was only fractional compared to the yield increase of **116** (27% from 13%). Still, this represented the highest yield of **115a** produced under catalytic conditions. A similar trend was seen for **111** (entry 4) with almost complete conversion of starting material (92%), though this was notably due to a surge in **116** (47% from 15% in entry 2). However, there was a notable increase in dimer **115a** (45% vs 36% in entries 4 & 2, respectively), which at this point was our highest result for this substrate.

With this 1:1 ratio of oxidants established for high conversion of substrate (92% and 93% for **111** and **105**, respectively), we next looked to the effects of different oxidants.

First was $Cu(OAc)_2$, which has already demonstrated efficiency for this reaction when used as the sole oxidant. When employed as a co-catalyst (entries 5 & 6) there was a significant decrease in the yield **115a** with **105** (entry 5), compared to entries 1 and 3 (31% entry 5 vs 64% and 66% for entries 1 & 3). This was not mirrored with oxoacid **111** however, which furnished dimer **115a** in 70% yield and 87% overall conversion (17% of **116**). This represents the highest catalytic conversion towards the formation of **115a** with oxoacid **111** as the substrate.

Other oxidants were less efficient; $KMnO_4$ which is typically associated with efficient turnover of Mn^{2+} species,[80,124,125] performed poorly for **105** (9%, entry 7) and moderately (41%**,** entry 8) in generating dimer **115a**. $FeCl_3$ which has a similar reduction potential to Mn^{3+} was equally unimpressive for both substrates (12% and 8% of **115a**, entries 9 & 10 respectively). Lastly, we wondered whether a terminal oxidant, persulfate, could be an efficient reagent to turnover the Mn-cycle (entries 11 & 12). While **115a** was isolated as the only product, excluding **116**, the yields were significantly lower than previous entries (25% and 12% respectively) and the remainder returned as unreacted starting material, even after an additional 24 hours, the reaction did not go to completion.

From these, we were able to pinpoint **$Co(OAc)_2$** at **50 mol%** as the most effective co-catalyst, in conjunction with 50 mol% $Mn(OAc)_3$ for the cyclisation-dimerisation cascade using oxoanilide **105** (entry 3). While oxoacid **111**, was most successful with **$Cu(OAc)_2$** at **50 mol%** (entry 6).

With these in hand, we next moved to determining the effect of Mn(III) loading on the yield (**Table 3.9**).

Table 3.9: Effect of Mn(III) loading on yield of **115a** and **116** for both substrates **105** and **111**. [a]No co-catalyst ($Co(OAc)_2$ or $Cu(OAc)_2$). [b]No $Mn(OAc)_3$ or $Co(OAc)_2/Cu(OAc)_2$.

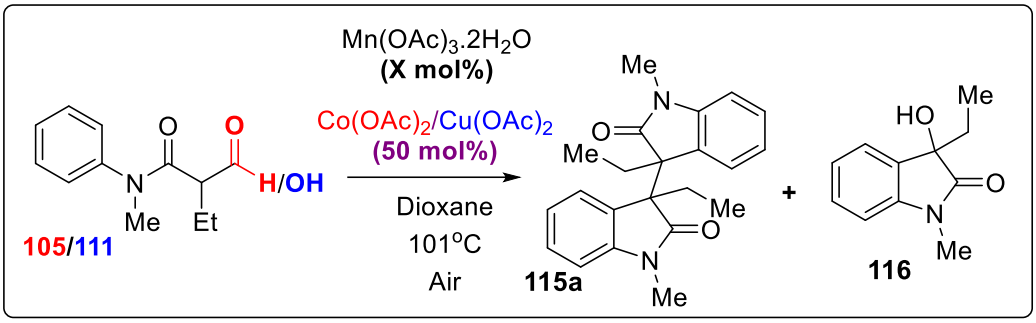

Entry	Substrate	Mn loading (equiv.)	Yield (%)	
			115a	116
1	105	0	Trace	12
2	111	0	-	Trace
3	105	0.1	20	19
4	111	0.1	22	16
5	105	0.25	35	Trace
6	111	0.25	27	14
7	105	0.40	56	9
8	111	0.40	32	14
9[a]	105	0.5	44	29
10[a]	111	0.5	30	Trace
11[b]	105	0	-	-
12[b]	111	0	-	-

As expected increasing the trend of increasing loading of $Mn(OAc)_3$ led to an increase in yield of both substrates from 0 – 0.5 equivalents (entries 1 – 8). Most notably in the absence of Mn^{3+} (entries 1 & 2) and only co-catalyst ($Co(OAc)_2$ for entry 1 and $Cu(OAc)_2$ for entry 2), neither substrate furnished any significant amount of **115a** and only marginal (12%) yield of **116** in entry 1.

This result is more suggestive of dual catalytic cycles with the secondary catalyst acting to turnover the Mn, rather than co-operative catalysts that both oxidise the substrate. Further supportive of this, are the results of entries 9 & 10, which show effective dimerization of both substrates under solely Mn, in the absence of co-catalyst; 44% of **115a** with 73% conversion for **105** (entry 9) and 30% of **115a** with **111** (entry 10).

No reaction was observed in the absence of both catalysts (entries 11 & 12), reinforcing that they are indeed the active reagents for this transformation.

Table 3.10: Solvent screen for the catalytic oxidation of **105** and **111** under Mn(III) with $Co(OAc)_2$ or $Cu(OAc)_2$ respectively.

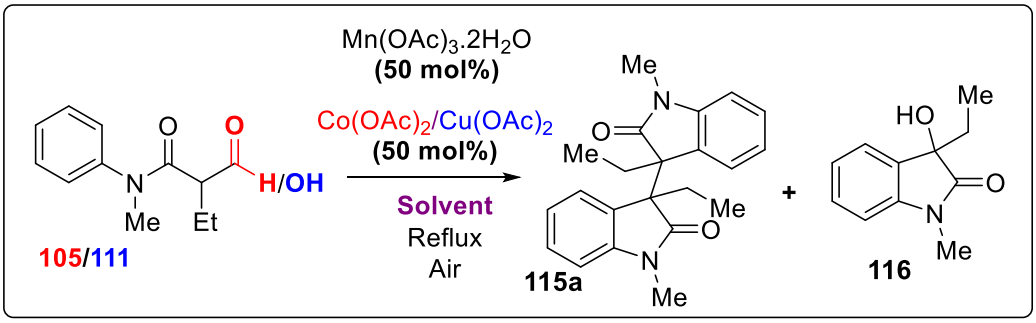

Entry	Substrate	Solvent	Yield (%)	
			115a	116
1	105	ACN	52	10
2	111	ACN	36	20
3	105	THF	21	27
4	111	THF	45	23
5	105	DMF	28	23
6	111	DMF	15	21
7	105	Toluene	58	23
8	111	Toluene	66	24

Lastly, we wanted to determine the optimal solvent; of those trialled (**Table 3.10**), none had yielded **115a** higher than dioxane, including, ACN or THF (entries 1 – 2 & 3 & 4), which was surprising given their use in the stoichiometric variation of this reaction for the respective oxoanilide **105** and oxoacid **111**.

Substrate scope

Using this complementary catalytic approach for oxoanilide and oxoacid this method, a variety of substrates were synthesised, **Figure 3.32**. The substrate scope included several of the previously synthesised substrates (**Figure 3.21** & **3.24**), including R-group variants, **115b** and **115d**, aromatic variant, **115h**, as well as new substrates bearing combinatory variations on the aromatic and R-group: **115v**, **115w**. The yields however, did not translate as well compared to model substrates **105** and **111** with the respective dimers being produced in mild yields: 49% for **115b**, 41% for **115d**, 35% for **115h**, 39% for **115v** and 43% for **115w**. Given this, the substrate scope was not explored further.

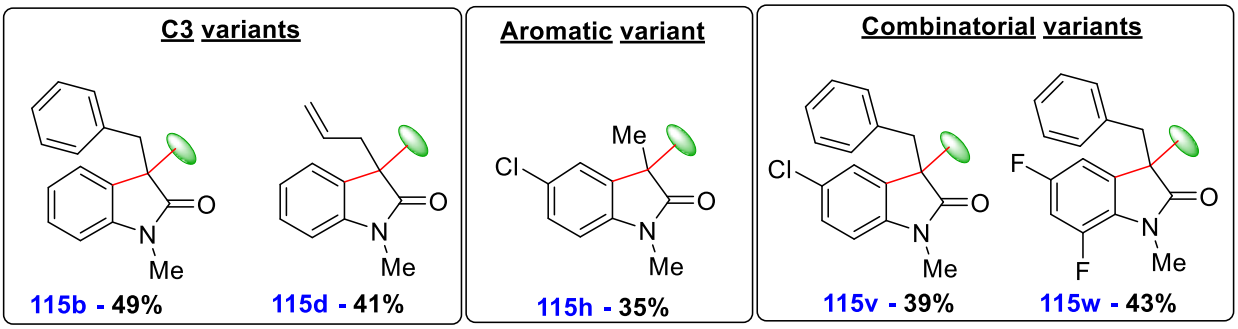

Figure 3.32. Substrates synthesised under specified conditions with either **105** or **111**.

Biological testing

The synthesised substrates **115c**, **115d**, **115i** and **115m** in **Figure 3.33** were subjected to *in vitro* biological evaluation. In all cases both *meso* and *dl* diastereomers were tested separately where possible. The choice was based on literature support for either steric or electronic effects. Fluorine-substituted molecules have extensive documentation supporting their incorporation into biological molecules, from increased their stability to degradation to increases basicity and lipophilicity among many other beneficial effects.[126–128] Similarly molecules containing nitro- and allyl groups have been implicated in triggering redox-mediated cytotoxicity in a variety of bacteria and parasites, in addition to increasing polarity and imparting strong interactions with amino acid residues owing

to the electronic properties of these groups by resonance and, in the case of -NO_2, the electronegative heteroatoms.[129,130] On the note of sterics, aliphatic rings such as cyclopentane have been incorporated across molecular scaffolds intended for pharmaceutical design as their three-dimensional structure and flexibility allow for effective protein-ligand binding, increased lipophilicity, scaffold replacement among others.[131–133]

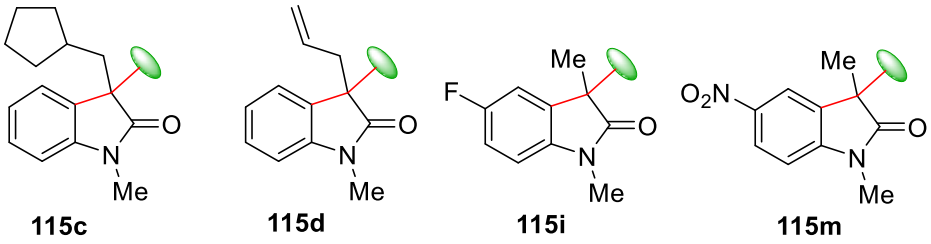

115c **115d** **115i** **115m**

Figure 3.33. Compounds chosen for *in vitro* biological evaluation *meso* and *dl* diastereomers were evaluated separately when possible.

Anti-bacterial activity

Evaluation was performed against two opportunistic bacterial species commonly found on human skin and mucosal membranes that are implicated in infection in immunocompromised individuals and in contamination of medical devices: *Staphylococcus epidermidis, Staphylococcus aureus, Escherichia Coli* and *Pseudomonas aeruginosa*.[134,135]

Testing was done by Siobhan Brigg through collaboration with the Dube lab in UCT's department of Cell and Molecular Biology. Compounds *meso*-**115d** and *dl*-**115i** were diluted to 10 mM in DMSO; (*dl*-**115d** and *meso*-**115i** were insoluble in DMSO and could not be evaluated) and tested performed using the cation-adjusted Mueller–Hinton broth. All compounds were tested to determine their minimum inhibitory concentration (MIC) values; this is the concentration where compounds are considered effective at inhibiting 50% growth. Smaller values of MIC are therefore ideal. To begin the compounds were tested at 500 µM, to determine inhibitory effects on the growth of the mentioned bacteria, which is the upper limit of the MIC where compounds are considered effective while not being non-specfically cytotoxic towards human cells. If effective, lower concentrations are evaluated until growth inhibition is no longer significant. A positive and negative

control were included for comparison: the negative (also known as 100%) control was untreated broth to which the % growth values are made relative to. The positive control was broth with an antibiotic, Kanamycin, added to make up a concentration of 50 µg/mL. All experiments were performed in triplicate with the mean ± SD shown (**Figure 3.34**).

The results show that at 500 µM neither *meso*-**115d** or *dl*-**115i** had any significant inhibitory effect on the % growth of any trailed organism compared to the negative control (kanamycin) which showed near 0% growth across all evaluated organisms.

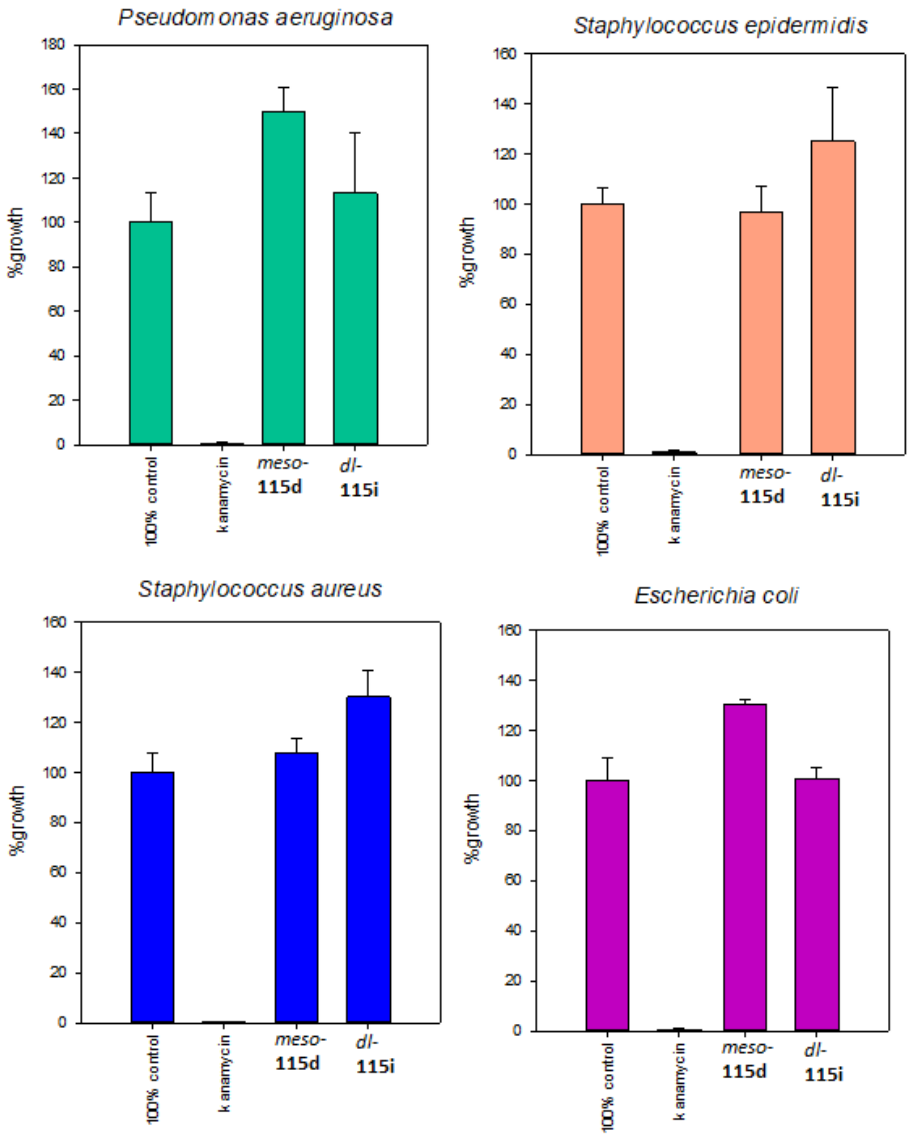

Figure 3.34. *In vitro* evaluation of 500 µM *meso*-**115d** and *dl*-**115i** referenced against positive 100% control (untreated) and 50 µg/mL Kanamycin negative control. Evaluation was performed for *Staphylococcus epidermidis, Staphylococcus aureus, Escherichia coli* and *Pseudomonas aeruginosa*.

Anti-tuberculosis activity

Anti-tuberculosis assays were performed by the H3D foundation on UCT's faculty of health sciences using a sensitivity assay on the H37Rv strain of *Mycobacterium tuberculosis*, which is a drug-sensitive strain of the bacteria used for determining initial hit compounds; protocols performed and materials used were according to the standardised MIC_{90} TB screening assays.[136,137]

Table 3.11: Drug-sensitivity assay of *meso* and *dl*-**115c**, **115i** and **115m**. Against sensitive H37Rv strain of *Mycobacterium tuberculosis* in three different, complementary growth media: Middlebrook 7H9 broth with albumin dextrose complex (ADC), 0.05% Tween 80 (TW) and either 0.2% glycerol (GLY), D-glucose (GLU) or Glutathione (GLU_N).

Compound	MIC_{90}(μM)	Strain	Media
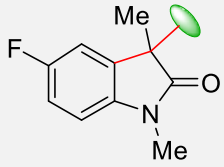 *dl*-**115i**	>62.5 >62.5 >62.5	H37Rv H37Rv H37Rv	7H9_ADC_GLY_TW 7H9_ADC_GLU_N_TW 7H9_ADC_GLU_TW
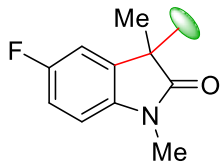 *meso*-**115i**	>62.5 >62.5 >62.5	H37Rv H37Rv H37Rv	7H9_ADC_GLY_TW 7H9_ADC_GLU_N_TW 7H9_ADC_GLU_TW
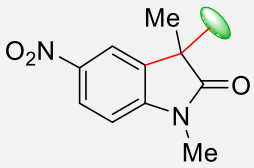 *dl*-**115m**	>62.5 >62.5 >62.5	H37Rv H37Rv H37Rv	7H9_ADC_GLY_TW 7H9_ADC_GLU_N_TW 7H9_ADC_GLU_TW
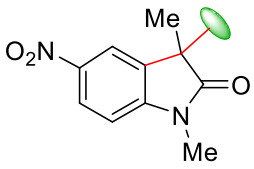 *meso*-**115m**	>62.5 >62.5 >62.5	H37Rv H37Rv H37Rv	7H9_ADC_GLY_TW 7H9_ADC_GLU_N_TW 7H9_ADC_GLU_TW

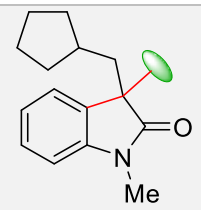 *dl*-**115c**	>62.5 >62.5 >62.5	H37Rv H37Rv H37Rv	7H9_ADC_GLY_TW 7H9_ADC_GLU_N_TW 7H9_ADC_GLU_TW
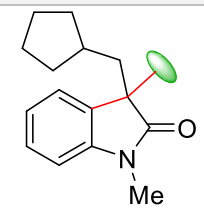 *meso*-**115c**	>62.5 >62.5 >62.5	H37Rv H37Rv H37Rv	7H9_ADC_GLY_TW 7H9_ADC_GLU_N_TW 7H9_ADC_GLU_TW

Respective compounds were added to each media at increasing concentrations until 90% of cell death was recorded, the minimum inhibitory concentration (MIC_{90}). Typically, an MIC_{90} above 62.5 µM is disregarded as above this threshold, there is cytotoxicity to human cells and potential inhibitory effects are non-specific. As per **Table 3.11**, we noted that all tested compounds had MIC_{90} >62.5 µM and were hence not considered viable pharmaceutical candidates.

Anti-plasmodium activity

Anti-malarial activity was similarly done by the H3D foundation on UCT upper campus. Sensitivity was determined by the standard parasite lactate dehydrogenase (pLDH) assay to determine the inhibition profile and IC_{50} (concentration required to achieve 50% cell death) against the sensitive NF54 strain of *Plasmodium falciparum*, for each both *meso* and *dl* of each **115c**, **115i** and **115m** (**Table 12**).

Table 3.12: pLDH sensitivity assay against *P.falciparum* of each *meso* and *dl*-**115c**, **115i** and **115m** with 5µM cut-off in IC_{50}.

Entry	Compound	IC_{50} (µM)
1	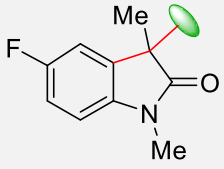 *dl*-**115i**	6

2	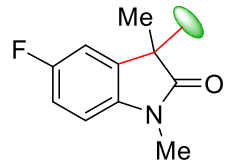 *meso*-**115i**	1.6875
3	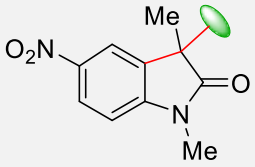 *dl*-**115m**	6
4	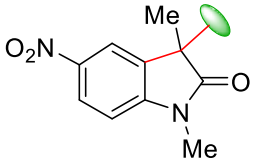 *meso*-**115m**	0.0117
5	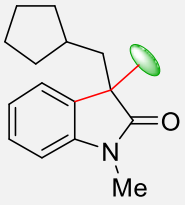 *dl*-**115c**	1.6579
6	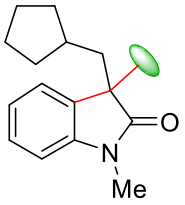 *meso*-**115c**	3.5868

The concentration required to achieve 50% cell death was noted, with lower values being ideal as this would hint at cell-specific targeting effects. Concentrations above 5 μM were disregarded to remove the effects of human cell cytotoxicity and inhibitory effects are considered non-specific, making those unviable drug candidates. Here we note entries 1 & 3, the *dl* of **115i** and **115m** respectively are >6 μM and hence not considered *Plasmodium falciparum*-specific inhibitors. Beyond these two, all others showed anti-plasmodial activity against NF54, with *meso*-**115c** having weak inhibitory effect (entry 6) at 3.5868 μM, while *meso*-**115i** and *dl*-**115c** displayed competent inhibition at 1.6875 and 1.6975 μM respectively. Most noteworthy, *meso*-**115m** displayed potent anti-plasmodial activity with an IC_{50} value of 0.0117 μM, a promising IC_{50} for future testing towards further strains and SAR-relationship studies.

Conclusion and future work

In conclusion we have successfully developed an efficient methodology to synthesise 3,3'-bisoxindoles from two different cyclic substrates, utilising simple, ubiquitous starting materials in moderate to excellent yields under both catalytic and stoichiometric methodologies, featuring a one-step, cascade radical cyclisation and dimerization. This is in line with our aims and at the time of writing and marks the first known complete bisoxindole synthesis from acyclic precursors. These methods have shown to be amenable to a variety of different substrates and tolerates to changes to the functional group at the *N*-1 position, C3 group and on the aromatic ring including both donating and withdrawing substituents. It should also be noted that other another member of the Petersen group, has successfully completed the formal synthesis of the natural product folicanthine using the stoichiometric method, in 7 steps, which marks the most step-count efficient procedure of this molecule to date, showcasing the versatility of the method.

Many potential avenues are available for further exploration with this method. additional substrate scope testing with aromatic substitutions at the ortho and meta position would be an interesting experiment to determine (if any) selectivity which would enable a deeper mechanistic understanding. On the topic of mechanism, cyclic voltammetry studies on the oxidation of the oxoanilides and oxoacids would be particularly useful to gain a better mechanistic understanding; particular in determining electron transfer kinetics which would help flesh out whether electron transfer proceeds via an inner-shell or outer-shell pathway amongst others. Furthermore, with the ability to quickly access the bisoxindole scaffold, the synthesis of many other C3 dimeric hexahydropyrrolidone molecules can done, many of which we hope would be possible quicker and more efficiently than the current literature routes. Finally, this could enable the synthesis of functionalised and potentially even new hexahydropyrrolidone molecules, which could be useful for biological testing, in addition to that discovered, the *meso*-**115m** which had a high potency towards NF54 strain of *Plasmodium falciparum*, that should be examined further against resistant strains, specificity studies and SAR-relationship studies.

Chapter 4: Methodology for synthesis of Isoxazoline indoles

3,3-Spiroindoles

3,3-disubstituted spiroindoles are a relatively small group of molecules characterised by a disubstituted, cyclic tether at the C3 of the indole (**Figure 4.1**).

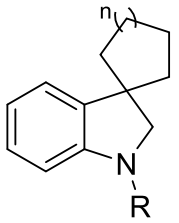

Figure 4.1. General structure of spiroindoles.

A variety of molecules of this type have been extracted as natural products, many from plants of *Apocynaceae* and *Rubiaceae* families where they are almost always produced as secondary metabolites.[138] Thus, they represent a highly privileged motif in nature.[139] Like the bisindoles described in Part 1, the structural complexity of these molecules was a major barrier for structure elucidation by early chemists. However, the advent of modern spectroscopic methods primarily, ^{13}C and 2D NMR, has allowed this barrier to be overcome and since then, many more spiroindole structures have been reported (**Figure 4.2**).[53] Despite the relatively small chemical space occupied, they exhibit remarkable structural diversity, even for spiroindoles isolated from the same species of plant. While five-membered ring tethers seem to be the most common, looking at **Figure 4.2**, it is far from the only motif that has been adopted, with a variety of different ring sizes **129** (potent antimalarial, inhibitor of P-type ATPase PfATP4),[140] different heteroatoms both within and out of rings **130** (antiproliferative inhibition of leukemic T-cells)[141] and **131** (mammalian cell cycle inhibitor),[142] fused rings **132** and **133** (antioxidant and antidiabetic effect via *in vitro* protection of cells through reactive oxygen and nitrogen scavenging)[143] and more. Considering this massive structural and biolactive diversity, and driven by the continuous need for novel pharmaceuticals, several of these molecules have been tested as potential pharmaceuticals and indeed have shown interesting biological properties beyond those mentioned, across a broad range of different diseases such as various cancers,[144] malaria,[145] parasites[146] and many more. As such, the past three decades has

seen a massive interest in their total syntheses and development of novel methodologies.[147]

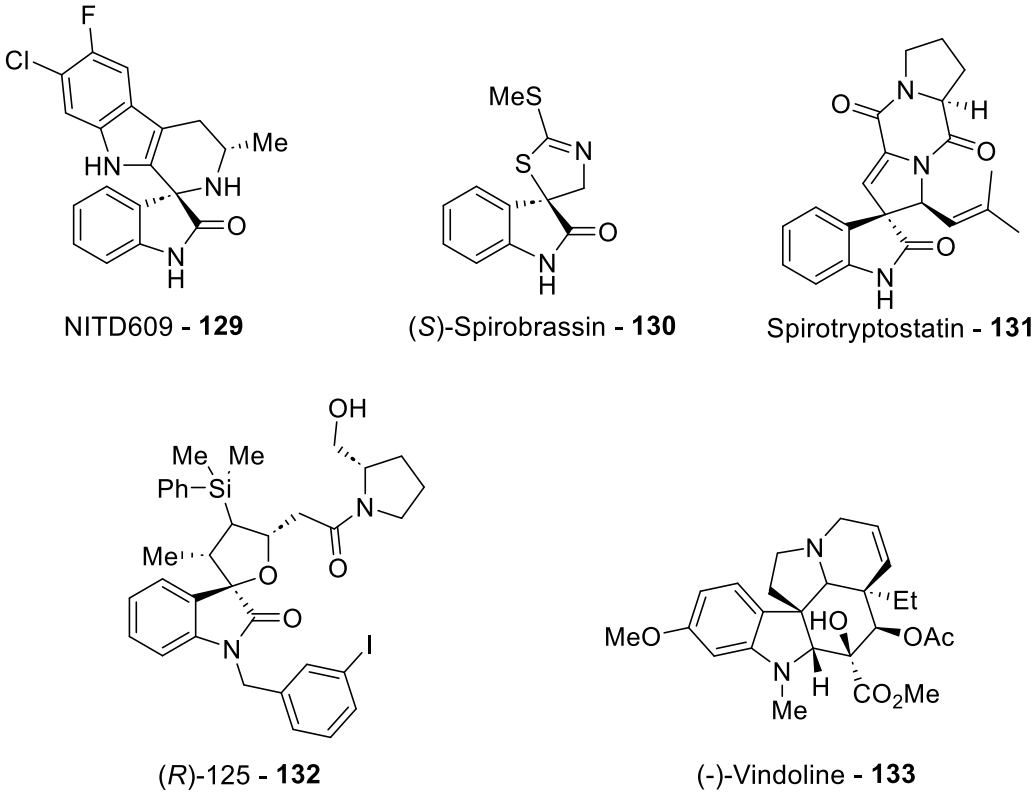

Figure 4.2. Examples of spiroindole natural products.

Diazospiroindole

Within the spiroindole sub-class, the diazospiroindole motif **134** is one of the rarest reported.

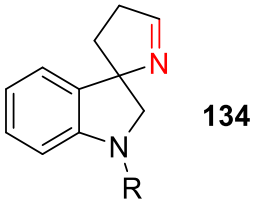

Figure 4.3. General structure of diazospiroindole motif.

Sor far, only two publications, to the best of our knowledge, have dealt with its synthesis. The first method was reported in 2004 by Tanaka, Mori and Narasaka,[148] which formed the

diazosprioindole scaffold using an intramolecular S_N2 reaction. They utilised the *anti*-isomer of 4-(3-indolyl)butan-2-one oxime **135** in the presence of MsCl and NEt_3 to form the corresponding mesylate *in situ*, which can readily undergo nucleophilic attack, **136** (**Figure 4.4**). However, using only these reagents, they were unable to isolate the desired compound **137**, presumably due to hydrolysis, thus C_6F_5COCl was added for N1 protection which gave the desired diazospiroindole **138** in 79% yield.

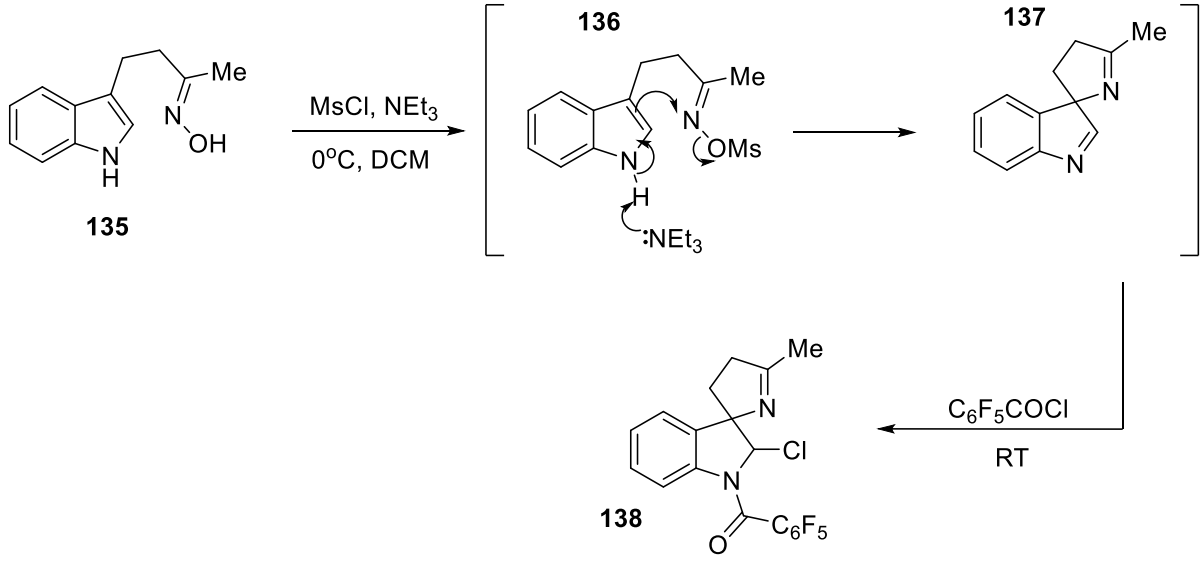

Figure 4.4. S_N2 method developed by Narasaka *et al*.

The second report was published more recently in 2017 by Wen and Xu *et al*.[149] Here they described a catalytic method to access the diazospiroindole motif (**140**) using indole oxime acetate **139** in the presence of a copper catalyst, base and heating to 120 °C (**Figure 4.5**). Critically, the desired scaffold could be formed without N1-protection as was the case for the previous method. Mechanistically, the Cu^+ species is proposed to cleave the N-O bond under the thermal conditions to generate iminyl radical **141**, which subsequently undergoes a 5-*exo*-trig cyclisation at the 3-position to form radical **142**. Thereafter **142** can get oxidised by Cu^{2+} to form **140** and regenerate the active Cu^+ catalyst. Importantly, the authors noted that in the absence of a group at the C2 position, the diazospiroindole **143** would re-arrange to the azacarbazole **144** via a 1,2-rearrangement.

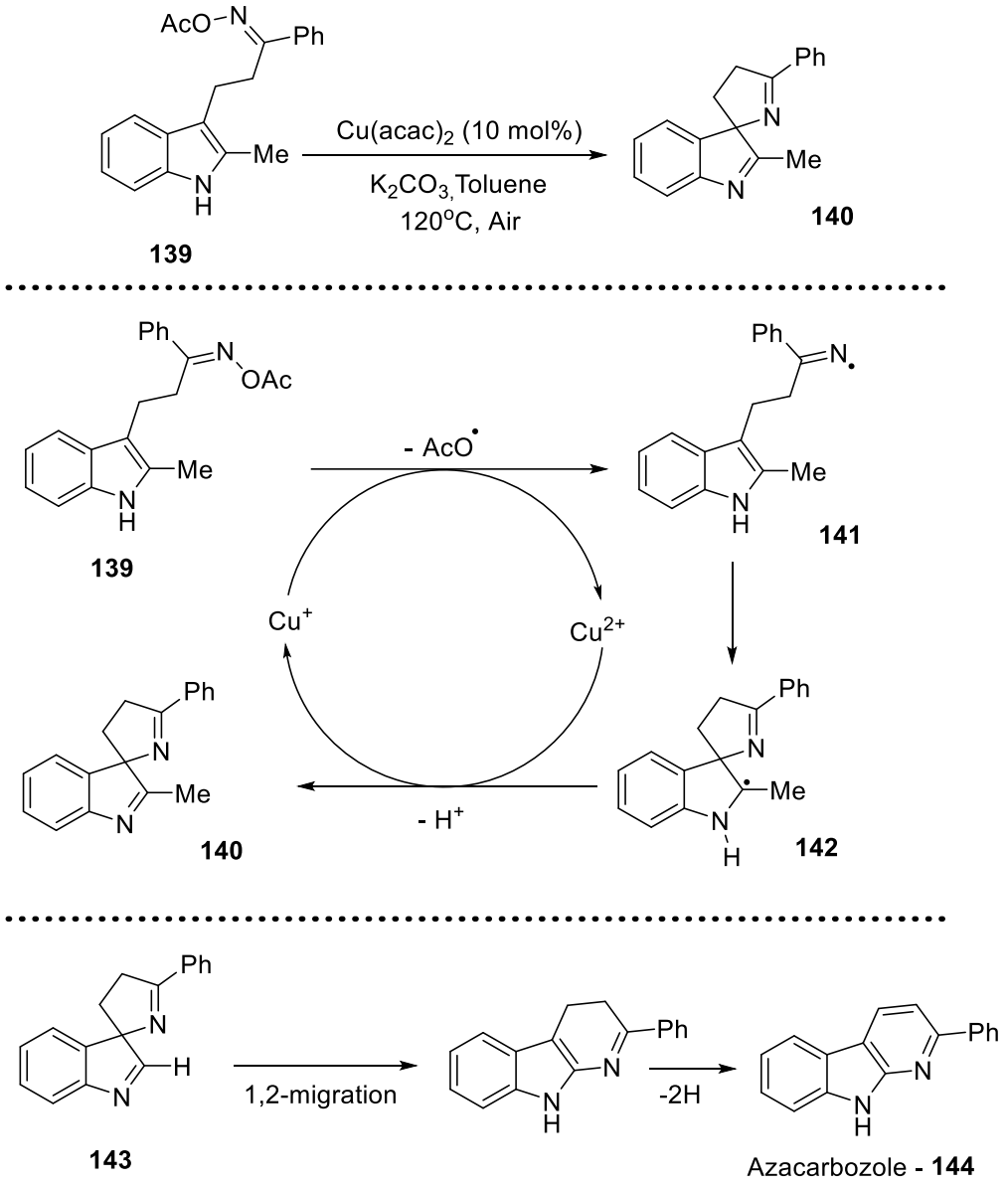

Figure 4.5. Cu-radical method developed by Wen and Xu *et al*.

Aim

In 2018 the Doyle group published a method to directly access O-centred and C-centred radicals **145** from inactivated hydroxyl and carboxylic acid groups **146**, respectively, via photoredox catalysis.[150] This was an important milestone as previously no methods existed which could photocatalytically generate these radicals from their inactivated substrates. Indeed, the generation of O-centred and C-centred radicals from -OH and -COOH groups respectively, first required modification of said groups. For example, to the trifluoroborates in the case of hydroxyl groups and to acid chlorides or anhydrides in the case of carboxylic acids. In addition to adding another step to the methodology, this

previous method was highly substrate specific and excluded certain classes of molecules such as tertiary alcohols and aliphatic carboxylic acids. The Doyle group circumvented this issue by exploiting the reactivity of phosphines **147** which in this case, act as a redox mediator in the photocatalytic cycle (**Figure 4.6**). Here reductive quenching of the photocatalyst by the phosphine forms the phosphoranyl radical **148** which can react with acids or alcohols to form the radical **149**. Critically, radical **149** can undergo β-scission to form a strong P-O double bond and in turn generate the desired radicals **145** in one step.

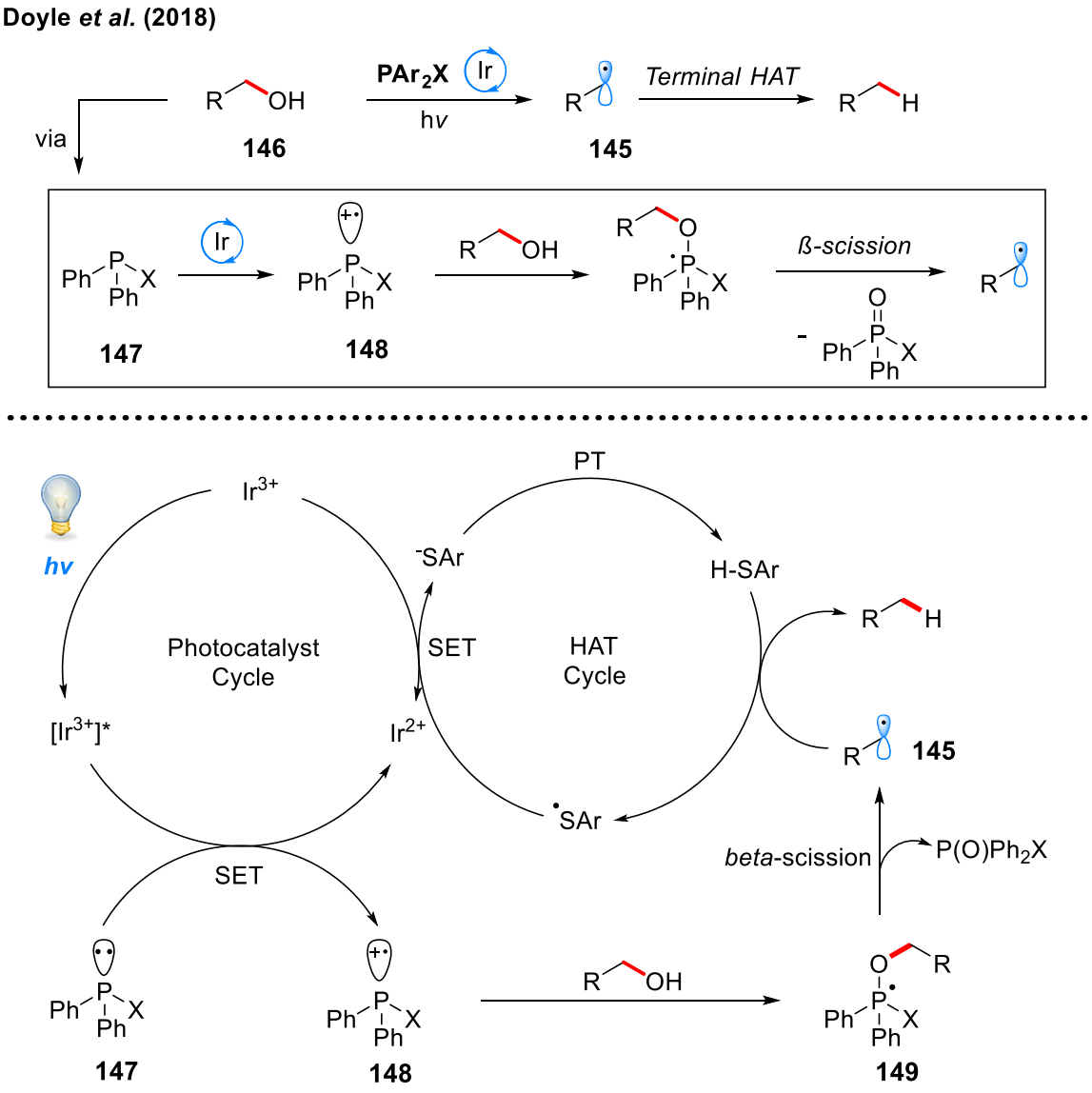

Figure 4.6. Phosphine mediated generation of radicals from inactivated alcohols and carboxylic acids.

As stated in Part 1, generation of amidyl radicals possesses the same issues as those described above, for O-centred and C-centred from -OH and -COOH respectively. However, this problem similarly extends when attempting to generate iminyl radicals as well, hence the use of oxime acetate by Wen and Xu in **Figure 4.5**, **139**.

Motivated by Doyle's work, we saw an opportunity to merge it with that done by Narasaka and Wen and Xu in the context of diazospiroindole synthesis (**Figure 4.7**). We envisioned that in place of an alcohol or acid, a 4-(3-indolyl)butan-2-one oxime **150** could be utilised as a substrate, in tandem with a phosphine mediator and photocatalyst to generate an iminyl radical **151** via the photocatalytic cycle postulated by Doyle. Following this, the radical would then presumably cyclise to furnish the diazospiroindole **152** as was suggested Wen and Xu.

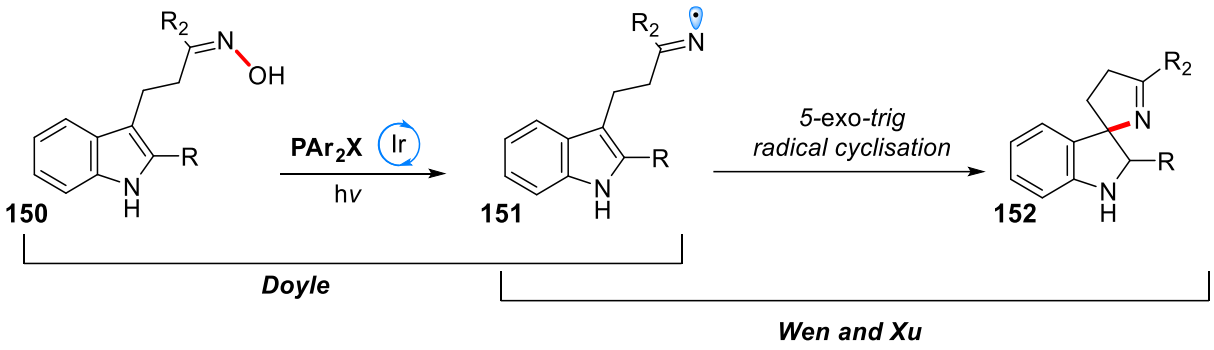

Figure 4.7. Illustration of how Doyle's method could generate iminyl radicals from inactivated oximes as per Wen and Xu.

This has several advantages over Wen and Xu's method, namely the *same* radical could be accessed via a substrate whose synthesis was similar to theirs, but one step shorter. Furthermore, the method of radical generation via photoredox catalysis, is much more benign environmentally as was described in Chapter 1.

Results and discussion

Studies began by synthesising oxime **153** in three-steps via the route shown in **Figure 4.8.**

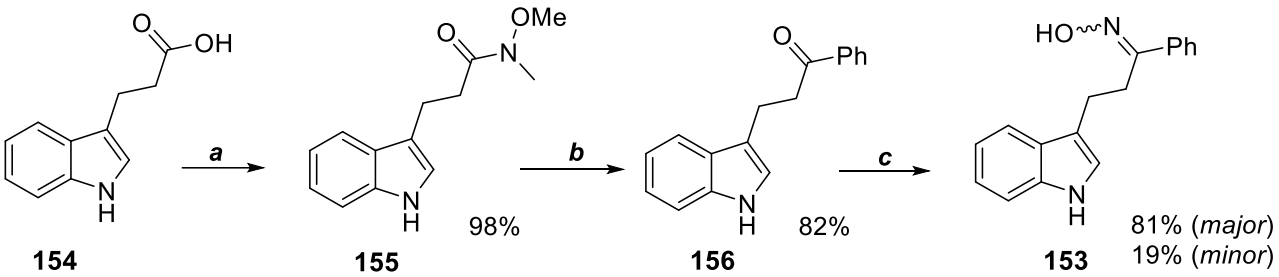

Figure 4.8. Synthesis of oxime **153**. Reagents and conditions: ***a***) T3P (1.5 eq.), MeNHOMe.HCl (1.1 eq.), DIPEA (3 eq.), DCM, RT, 1 hr. ***b***) PhMgBr (3 eq.), THF, 0°C →RT, 2 hrs. ***c***) $NH_2OH.HCl$ (2 eq.), NaOAc (2eq.), Ethanol, reflux, 4 hrs.

This route enabled rapid (total reaction time 6 hours), large scale synthesis of the oxime (>2g) in 66% overall yield. The product was a mixture two separable isomers of the oxime with one being produced in large excess (81% yield). We presumed this to be the *E*-isomer as it should in theory be more stable due to less steric clashing, however, without more concrete evidence we simply labelled them as *major* and *minor*.

Major of **153** (hereby referred to as **153a**) was taken forward and subject to a variety of conditions with Doyle's methodology as the template. Unfortunately, none of the desired diazospiroindole (**157**) was observed. A summary of the conditions can be seen in **Table 4.1.**

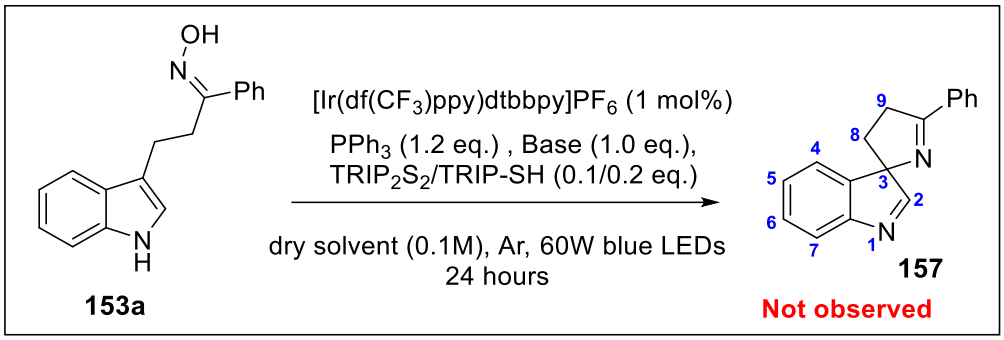

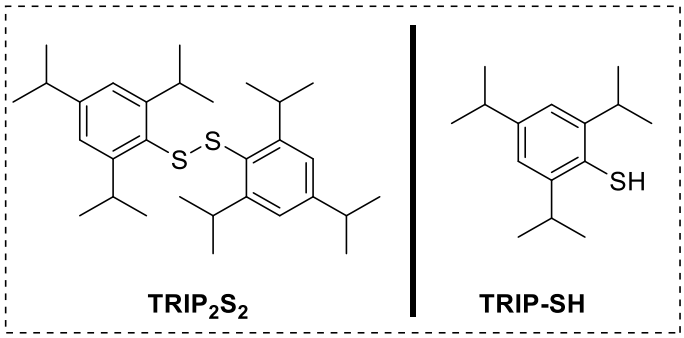

Table 4.1: Screen of Doyle's method and base screen effects on **153a**. *Conversion of **153a** was measured via NMR analysis of the crude sample, with addition of known amount of internal standard (0.03331 mmol of 1,3,5-trimethoxybenzene) and comparison of peak values to determine the mmols in reaction mixture at T = 24 hrs vs T = 0.

Entry	Base	$TRIP_2S_2$ or TRIP-SH	Solvent	Conversion of 153a (%)*
1	2,4,6-Collidine	$TRIP_2S_2$	Toluene	25
2	2,4,6-Collidine	TRIP-SH	Toluene	44
3	2,4,6-Collidine	TRIP-SH	DCM	60
4	Na_2CO_3	TRIP-SH	DCM	50
5	Cs_2CO_3	TRIP-SH	DCM	21
6	K_3PO_4	TRIP-SH	DCM	16
7	NaOAc	TRIP-SH	DCM	24
8	DBU	TRIP-SH	DCM	-
9	Na_2CO_3	-	DCM	66

While **157** had yet to be synthesised at the time of writing, a notable observation from the analysis of every diazospiroindole reported by both Wen/Xu and Narasaka *et al.*, was the presence of "roofing" signals in the ^{1}H-NMR spectrum, caused by the splitting of the diastereotopic protons 8 and 9 (**Figure 4.9**). Across all synthesised indolyisoxazolines, the splitting as per **Figure 4.9** is consistent. Consequently, observation of this pattern at ~2.5 – 3.5 ppm in ^{1}H-NMR spectrum of the crude samples, was to be the key landmark in determining the success of the reactions.

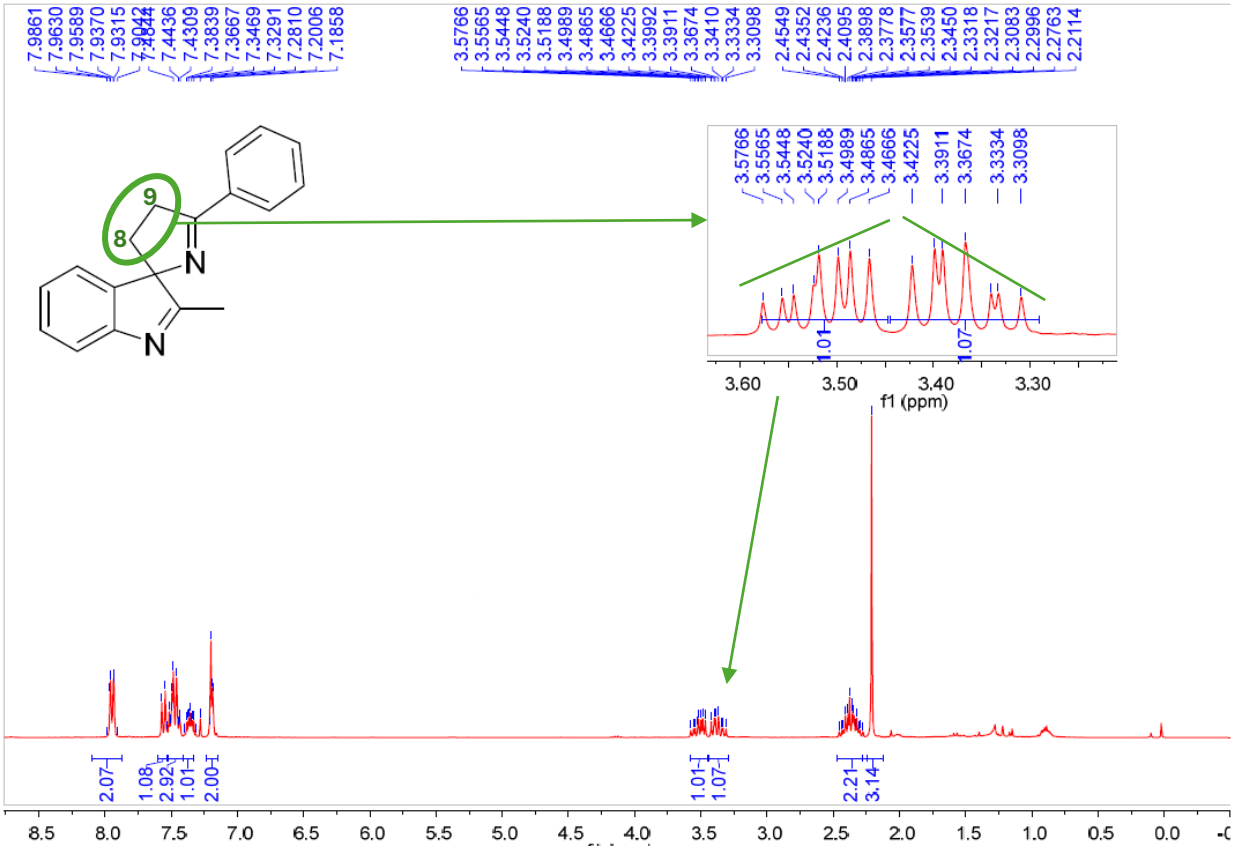

Figure 4.9. Example of diazospiroindole showing the diagnostic "roofing" protons (green). ^{1}H-NMR adapted from the supporting information provided by Wen and Xu *et al.* of the compound labelled 2a.[149]

We began by repeating Doyle's conditions (entries 1–3) using both $TRIP_2S_2$ and TRIP-SH. While their best results were obtained with toluene, we observed poor solubility of **153a**, thus we set up a parallel reaction in DCM (entry 3). Under these conditions, analysis of the crude and TLC (**Figure 4.10**, **A** and **B**). showed a complex mixture of products, notably absent however, were the characteristic roofing signals, leading us to conclude that **157** was not being formed.

While the complexity and number of products made complete isolation and analysis difficult, particularly on this scale (0.2 mmol), we were able to garner some insights: first, all entries 1 – 3, the reaction did not go to completion after 24 hours, **153a** was the major component though the amounts varied between each (~75%, 56% and 40% unreacted starting material for entries 1 – 3, respectively by NMR, **Figure 4.10**, **C**). Moreover, we observed >50% conversion of the PPh_3 to the respective triphenylphosphine oxide (TPPO) for entry 3 and spots relating to TPPO were observed for entries 1 and 2 in the TLC.

A – Reaction TLC of entries 1,2 and 3 (left to right)

B – Crude NMR of entry 1

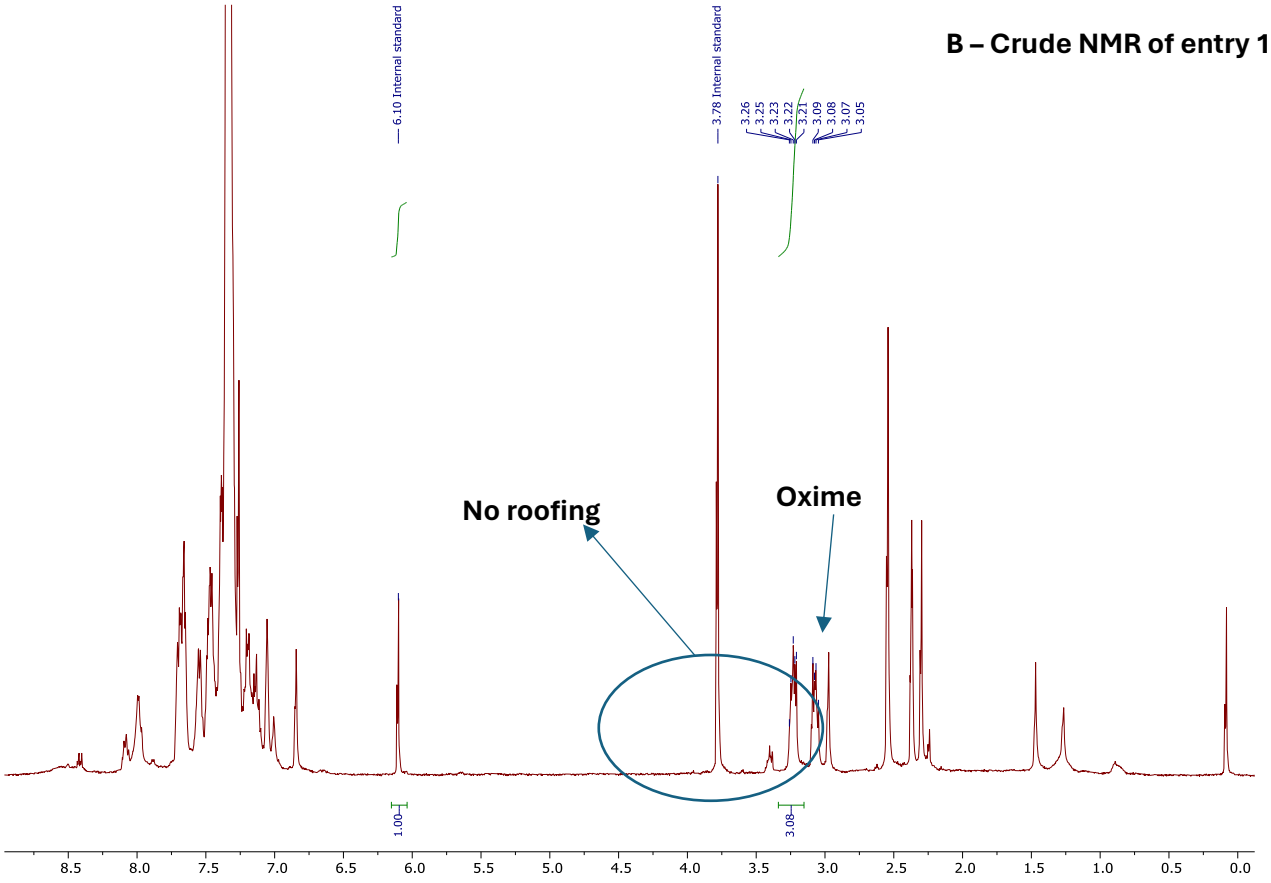

C – Determination of % conversion using internal standard peaks and oxime peaks in crude ^{1}H spectrum:

$$Ratio\ of\ compound\ protons\ vs\ standard\ protons = \frac{2H}{3H} = 0.6667$$

$$Ratio\ of\ compound\ vs\ standard = \frac{Compound\ peak}{Internal\ standard} = \frac{2.63}{1.00} = 2.63 \times 0.6667 = 4.545$$

$$mmols\ of\ oxime\ in\ crude\ (post-reaction) = 4.545 \times 0.33331\ (mmols\ of\ standard\ added)$$

$$= \mathbf{0.154\ mmols\ of\ oxime}$$

$$\%\ conversion = \left(1 - \frac{mmols\ of\ oxime\ in\ crude}{mmoles\ of\ oxime\ at\ reaction\ start}\right) \times 100 = \left(1 - \frac{0.154}{0.206}\right) \times 100$$

$$= \mathbf{25\%\ conversion}$$

Figure 4.10. A) TLC of the reaction mixture of entries 1 – 3 showing the number of UV-active products. B) Crude NMR of entry 1, highlighting the distinct lack of roofing protons, oxime **153a** peaks and integrations of internal standard and oxime -CH_2. C) Formulae for determination of **153a** conversion by NMR analysis of crude with internal standard peak at 6.10 ppm (3H) and oxime -CH_2 peak.

These two observations, given the significant conversion rate for entry 3 in particular, was tentatively suggestive of an active photocatalytic process with the source for majority of the oxygen in the formation of TPPO likely from **153a** rather than trace water, and thus warranted further investigation.

To begin, we noted that entry 3 in DCM had the highest consumption of starting material (55%) thus, we chose to continue to use it as the solvent for the grounds of further testing. Additionally, TRIP-SH had higher conversion of **153a** compared to $TRIP_2S_2$ (entries 2 vs 1; 44 and 25% respectively), thus we opted to use it going forward.

Following this, a base screen was done with a variety of inorganic bases (entries 4 – 8). We noted that Doyle's methodology had seen success with several of bases although the yields were diminished compared to collidine. Despite this, we hoped omitting an aromatic, organic base, would simplify the purification as well as provide more clarity in the crude NMR analysis. Though the conversion was indeed diminished compared to

collidine (16 – 50% conversion), we were successfully able to observe ketone **156** (**Figure 4.8**, page 119) in varying amounts across all entries 4 – 7, with entry 4 showing the highest conversion to the ketone in ~31% yield. was competing with intramolecular cyclisation. In addition to this, was, *minor* isomer **153b** isolated in all entries 4 – 7, in 12, 20, 22 and 8% yield respectively. While *E/Z* isomerisation via photoredox catalysis has been observed,[151] to our knowledge, it has not been seen in the case of oximes.

Piecing these observations together suggested a reductive pathway (**Figure 4.11**); the consumption of **153a** in the presence of the photocatalyst, marked with concurrent formation of the ketone precursor, **156**, in tandem with oxidation of >50% PPh_3 to the resultant oxide, implies a potential β-scission of **153a**, after formation of a phosphorenyl radical as seen in **Figure 4.6** (**149** to **145**). Given, the conversion of PPh_3 (>50% in entries 3 & 4), the oxime oxygen is a probable source for the majority of the observed TPPO which implies an active photocatalytic cycle. While this yields the desired iminyl radical (**158**), H-abstraction via TRIP-SH can occur instead of cyclisation to yield the imine, **159** which upon work-up /purification can be hydrolysed to the ketone **156**. Thus, under these conditions, the oxime is likely showing a preference for reduction of substrate over the desired 1,5-cyclisation.

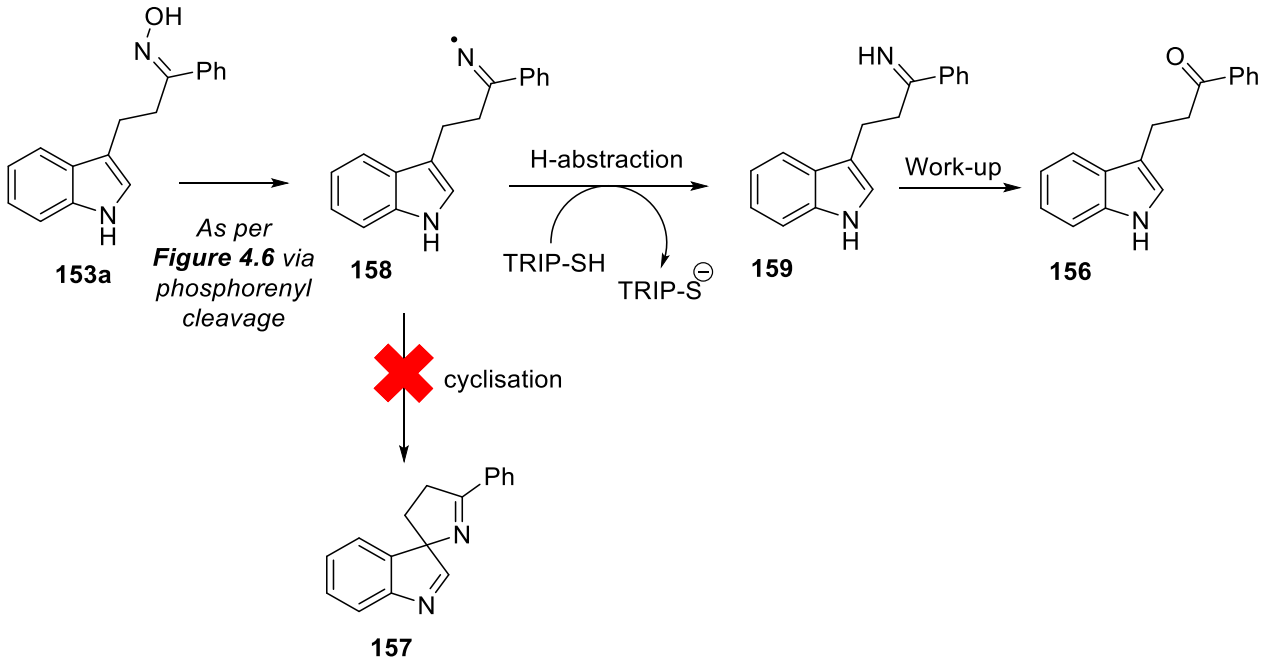

Figure 4.11. Probable mechanism for the formation of **156** from **153a** under Doyle conditions.

Based on these results, we then opted to exclude TRIP-SH (entry 9) to verify if this would inhibit H-abstraction and promote 1,5-cyclisation.

Our hypothesise proved useful, running the reaction in the absence of TRIP (entry 9), showed complete absence of **156**, though the spiroindole **157** could not be seen in either the crude or isolated fractions. With 66% conversion, the reaction was scaled up and repeated with products being isolated which showed that the azacarbazole **144** (**Figure 4.12**) was isolated in 20% yield as well as *minor* isomer, **153b** in 15% yield.

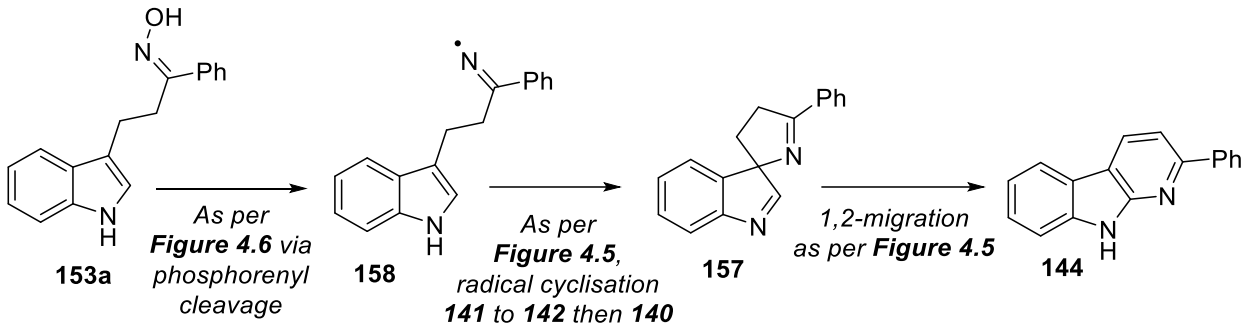

Figure 4.12: Mechanism for the formation of azacarbazole **144** from oxime **153a**.

The spectrum obtained (**Figure 4.13**) matches the reported spectrum for **144**, obtain by Wen and Xu; all signals integrate for 12 total protons, at resonance above 7 ppm, typically observed for aromatic signals, in line with what would be expected of an aromatic compound such as **144**. Additionally, we observe a singlet at 11.8 ppm that integrates for one proton which indicates a strongly deshielding environment, matching that of an N-H proton bonded to a withdrawing pyridyl ring.

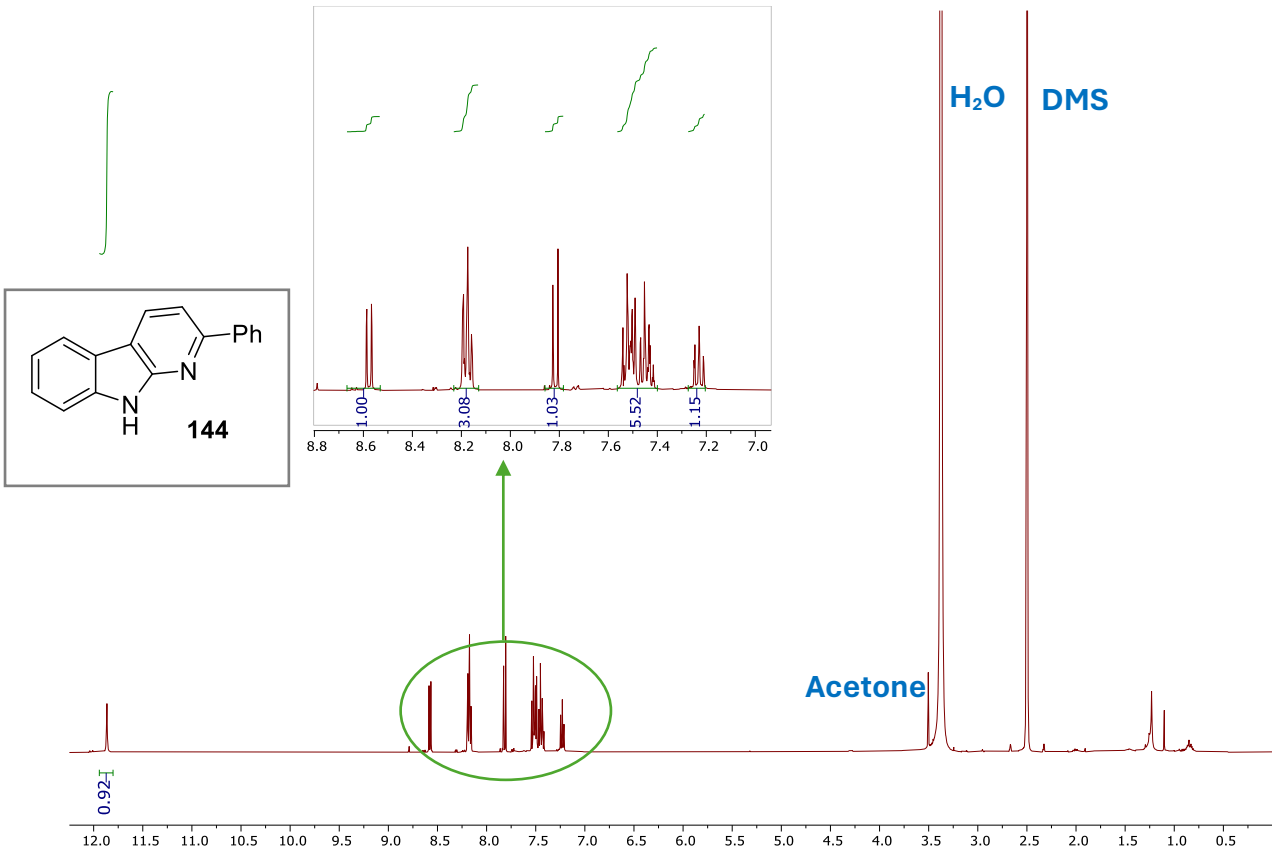

Figure 4.13. ^{1}H-NMR of the isolated azacarbazole **144** from reaction entry 9, **Table 4.1.**

When designing this process, we hoped that the milder photoredox conditions employed would disfavour 1,2-rearrangement seen under Wen and Xu's harsher method. Thus, while we succeeded in shutting down H-abstraction, going forward, it was clear that in order to form the spiroindole scaffold we would need to block the 2-position of the indole: as per Wen and Xu's work, carbazole formation was prevented by this substitution.

C2-blocked oxime

C2-blocked oxime indole **160** was synthesised via Wen and Xu's method as shown in **Figure 14.**

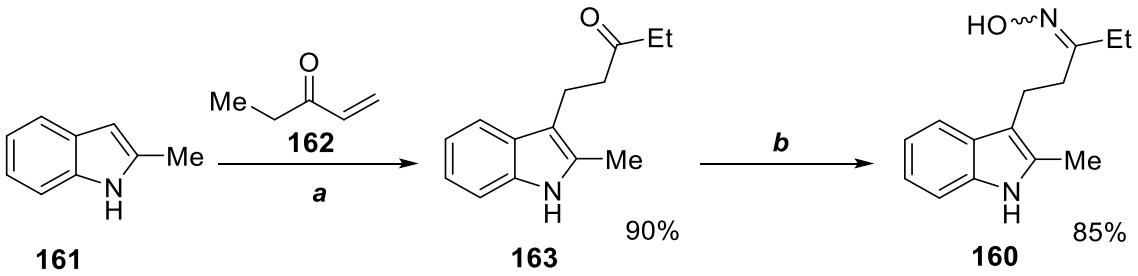

Figure 4.14. Synthesis of C2-blocked oxime **160**. Reagents and conditions: *a*) $InCl_3$ (3 mol%), **162** (1.0 eq.), DCM, RT, 20 hours. *b*) $NH_2OH.HCl$ (2 eq.), NaOAc (2eq.), Ethanol, reflux, 4 hrs.

Under these conditions **160** was produced in good overall yield (77%). Like **153**, a *major* and *minor* isomer was produced which distinct chemical shifts in the aliphatic region. Unlike **153** however, these isomers had the same R_f values and could not be separated via column chromatography. Moreover, the ratio of the isomers to each other was more equally distributed relative to **153** in ~1.5:1 ratio. Thus, further reactions on this substrate included both isomers. Nevertheless, the desired fragmentation to produce the iminyl radical was not expected to have any impact on the overall transformation.

Following this, **160** was subjected to the conditions shown in **Table 4.2**.

Table 4.2: Screen of Doyle's method and base screen effects on **160**. Conversion of **160** and yield of **163** determined by NMR.

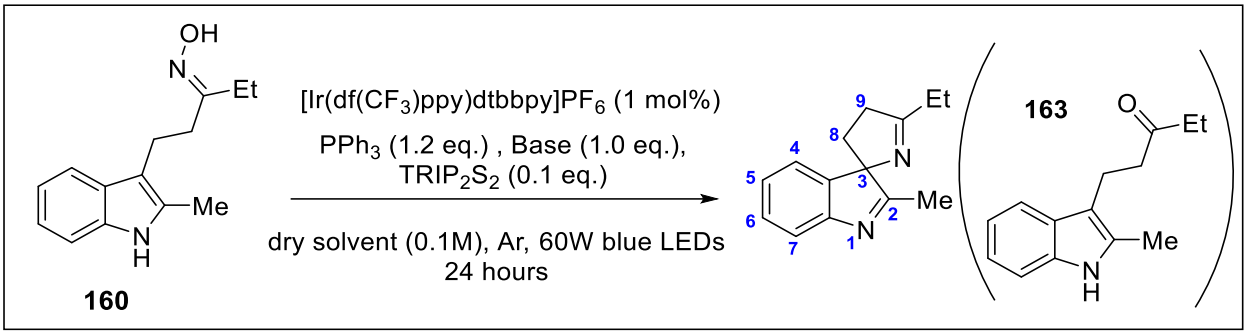

Entry	Base	$TRIP_2S_2$	Solvent	Conversion (%)	Yield of 163 (%)	Yield of 164 (%)
1	2,4,6-Collidine	✓	Toluene	51	30	-
2	Na_2CO_3	✓	Toluene	34	22	-
3	Na_2CO_3	✗	DCM	-	-	-
4	2,4,6-Collidine	✗	DCM	55	5	47

As a benchmark, Doyle's conditions were first repeated on **160** with DCM as the solvent using the two best bases, Na_2CO_3 and Collidine (**Table 4.2**, entry 1 and 2). The ketone **163** was once again the major product in both reactions, with higher yield seen with collidine as the base (entry 2), (34 and 51% respectively for entries 1 and 2) and no trace of the diazospiroindole in either crude or isolated fractions. Next, the reaction was repeated in the absence of the TRIP-SH (entry 3 and 4); here we observed no reaction with Na_2CO_3 (entry 3) as the base, with almost full recovery of starting material. However, with collidine as the base (entry 4), we observed 55% conversion of **160**; ~5% of the converted mass was determined to be ketone, **163**, while the bulk of the remaining mass, 47%, was isolated as seen as a single spot on TLC and isolated as a single fraction that could not immediately be identified. ^{1}H-NMR of the oxime **160** is compared against the isolated, unknown product in **Figure 4.15.**

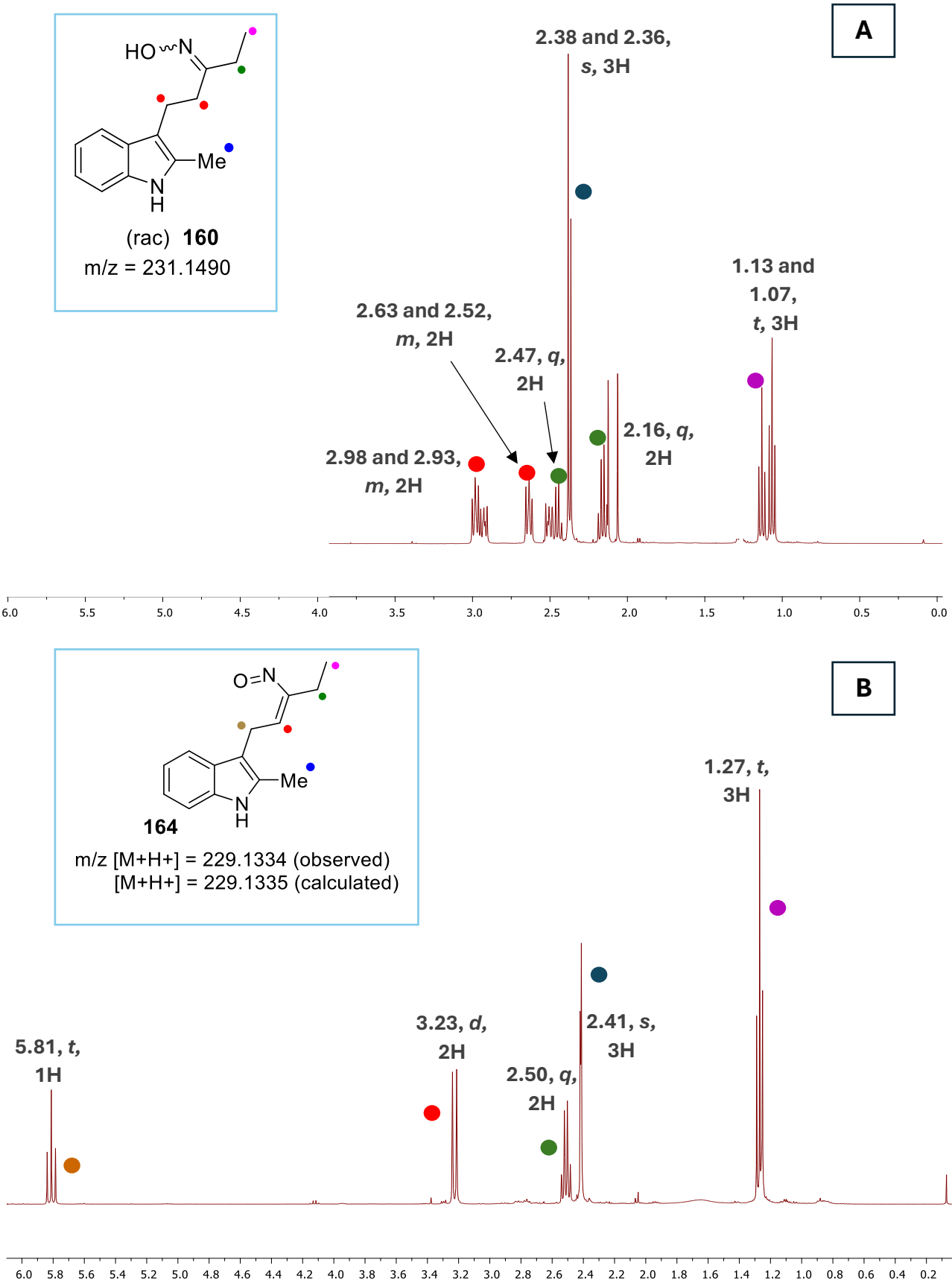

Figure 4.15. Comparison of ^{1}H-NMR of **160** (**A**) against the unknown product (**B**) obtained from entry 4, **Table 4.2**.

This product proved challenging to decipher though it was clear by the lack of "roofing" protons (ref. **Figure 4.9**) that it was not the desired diazospiroindole. The aromatic regions were very similar between **160** and that of the unknown compound, each containing four protons at similar chemical shifts, thus it seemed unlikely that an intramolecular CDC onto the aromatic ring had occurred. The biggest change in the non-aromatic region was seen in the signal labelled in red that integrates for two protons (**Figure 4.15B**); here it can be seen that in comparison to the starting material (**Figure 4.15A**), whose signals appear as complex multiplets between 2.50–3.00 ppm, the corresponding product protons are much neater with the first showing up as a clean doublet at 3.23 ppm, but more interesting, is the very large shift in the second pair (brown labelled) which now reveals a signal at 5.81 ppm, accompanied by a change in integration to 1H (from 2H). From this alone, we had suspected two things: a) based on the multiplicity, the 3-position of the indole had likely not undergone intramolecular cyclisation and remained as a linear, aliphatic chain, else we would observe diasterotopic splitting for the protons labelled red (**Figure 4.15B**); b) based on the chemical shift value of 5.81 ppm in tandem with the integration, there was likely a new double bond, as this region is highly emblematic of alkenes. Supporting this structure was the mass spec data of the compound which fit closely to that calculated (229.1334 [observed] vs 229.1335 [calculated]). Based on this, we initially assigned this as the nitroso compound **164**.

While the proton NMR and mass may have supported the unusual nitroso formation, the ^{13}C NMR and HMBC raised doubts about the structure's validity (**Figure 4.16**). More specifically, the chemical shifts of the carbon atoms labelled **a** and **b** were in unusual ranges for their proposed functional groups. In the case of the former, **a**, the observed chemical shift (160.4 ppm) was higher than what was expected for enamines (130 – 150 pppm) and was more suggestive of an (O-N=C) oxime-type bond. In the case of **b**, the discrepancy was even higher, the signal is seen at 76 ppm, which is extremely low for an expected alkene (110 – 160 ppm) and was more in line with a tertiary carbon (HC-R_3). The HMBC was even more telling; if the structure was correct for nitroso **37**, we expected to see a cross-peak between carbon **b** and proton **x**. Instead, a cross-peak was observed between **x** and the neighbouring carbon labelled in brown, **y**. In summary, this data

suggested that the order of the carbons labelled brown and red, needed to be switch around.

As a result, we revised our structure to isoxazoline **165**, which fit more in line with the observed ^{13}C and HMBC data and retained a good fit to the observed mass spec data.

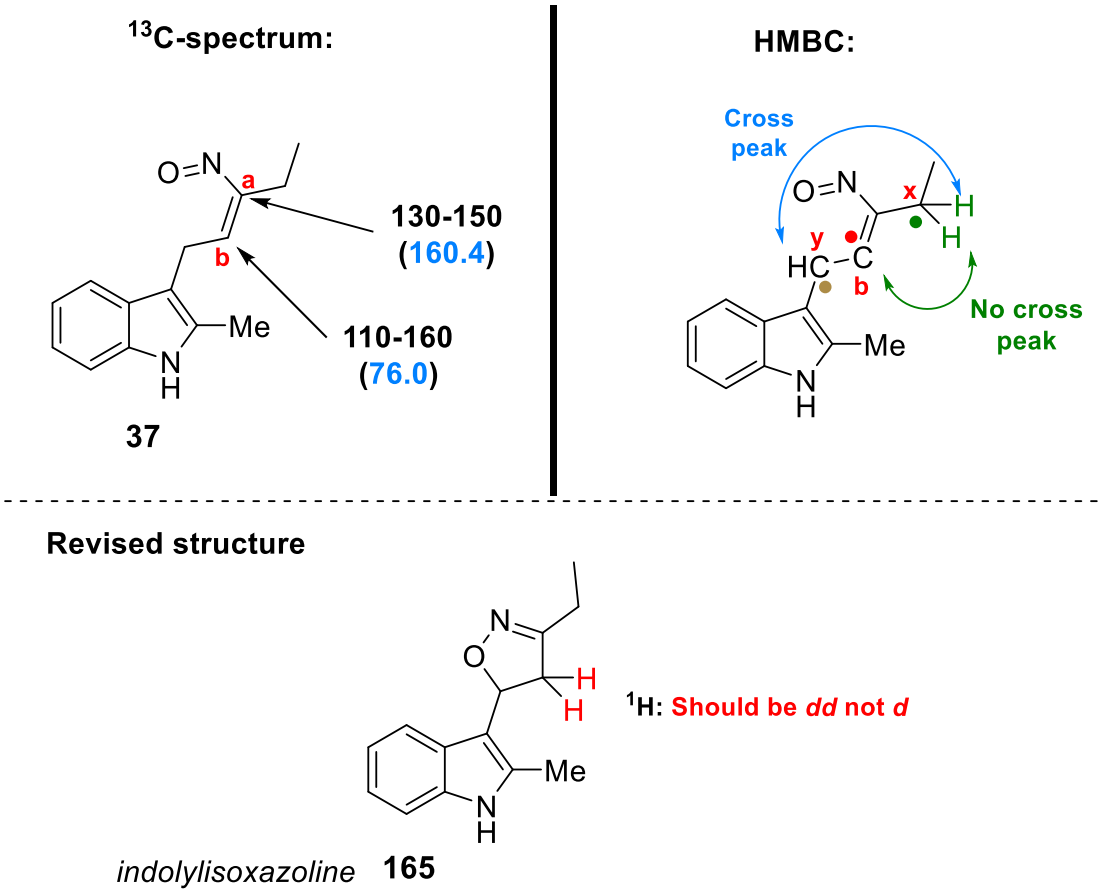

Figure 4.16. Problems associated with structure **164** and the new revised structure **165**.

It could not be ignored however, that the methylene protons of **165** are diastereotopic and should show separate signals. A possible explanation was that they had the same chemical shift in which case, they would appear as one signal. Alternatively, the ring geometry could have been such that the dihedral angle between the methine proton and the methylene protons were identical, with the rest of the molecule oriented in such a way that the environments are identical which would again, give a neat doublet.

Unfortunately, the compound was purified as an oil and as such, a crystal structure could not be obtained directly, thus we sought other ways to validate the structure. While

isoxazolines with indoles are not well known, literature reported isoxazolines with general aryls on one end (rather than indole)[152] showed distinct signals for the methylene protons contrasting to what we had. Thus, we reasoned that if we could repeat the conditions of **Table 4.2**, entry 4 on an oxime containing a general aryl group to form known isooxazalines, it would help validate structure **165**.

Starting from **166**, we formed **167** via the previous route with $NH_2OH.HCl$ and subjected it to the same conditions (**Figure 4.17**). Under these conditions however, no reaction occurred to form the known compound **168**, with almost complete recovery of **167** (95%).

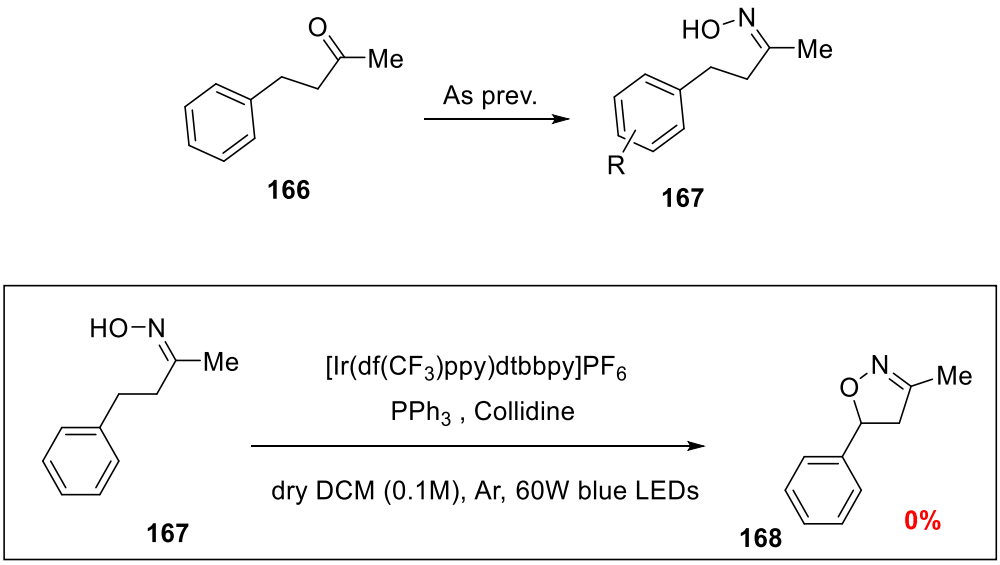

Figure 4.17. Attempted synthesis of known isoxazolines via Doyle-type methodology.

Next, we attempted tosylation (**Figure 4.18**) of **165**, the hope being that the *N*-tosylated derivative (**169**) could be purified as a crystalline solid and thus enable crystallographic analysis. Again however, the reaction was unsuccessful with 92% of **165** recovered.

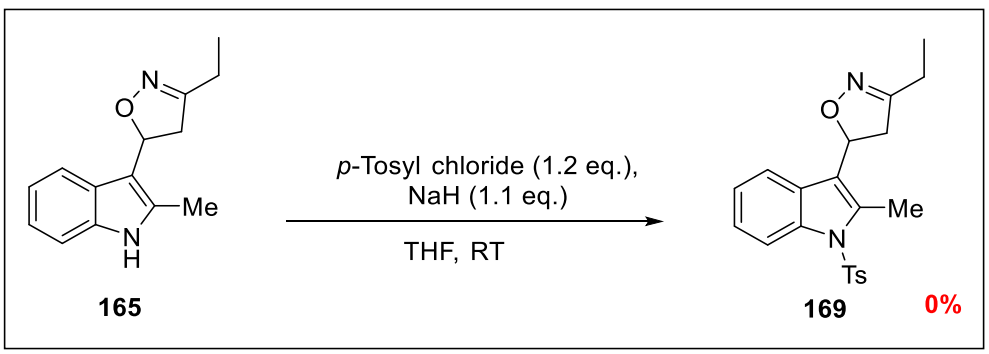

Figure 4.18. Tosylation procedure for **165**.

In light of the above, we reasoned the next best course of action would be to repeat the conditions on different slightly modified substrates with hope that they might either showing two distinct diastereotopic protons in the ^{1}H-spectrum or be purified as a solid for crystal structure analysis. Accordingly, substrates **170** and **171** (**Figure 4.19**) were chosen on the basis of adding steric bulk; it stood to reason that if ring geometry was causing the seen splitting patterns for the diastereotopic protons, sterically bulky groups could cause a conformational change, which would presumably change the dihedral angle and hence be able to distinguish between the methylene protons.

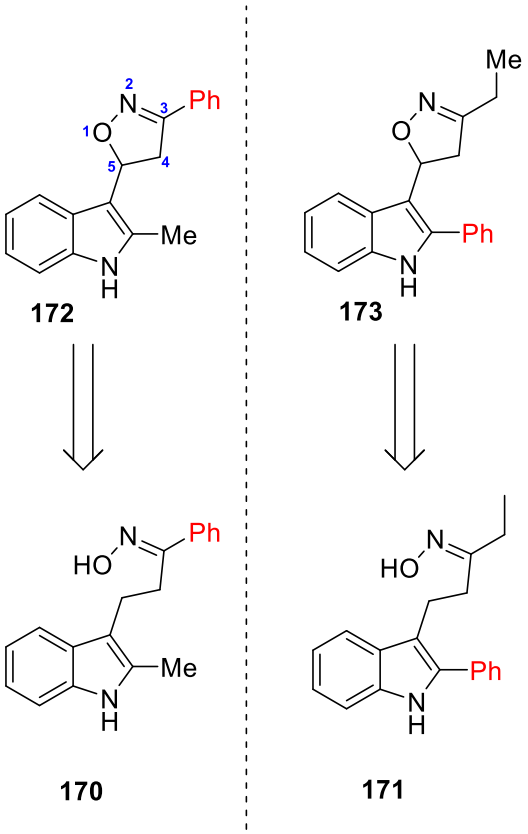

Figure 4.19. Intended substrate analogues of **165**, with phenyl groups either at the 3-position of the isoxazoline ring (**172**) or at the 2-position of the indole (**173**).

With **170**, the presumed isoxazoline **172** was formed in 18% yield. While this was encouraging, ^{1}H-NMR spectral analysis revealed the same observation as **165**; a neat doublet (red labelled) integrating for two protons in place of the expected two diastereotopic signals (**Figure 4.20**).

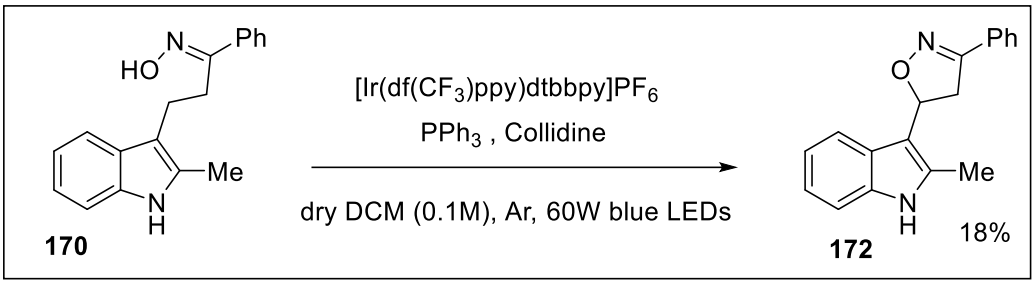

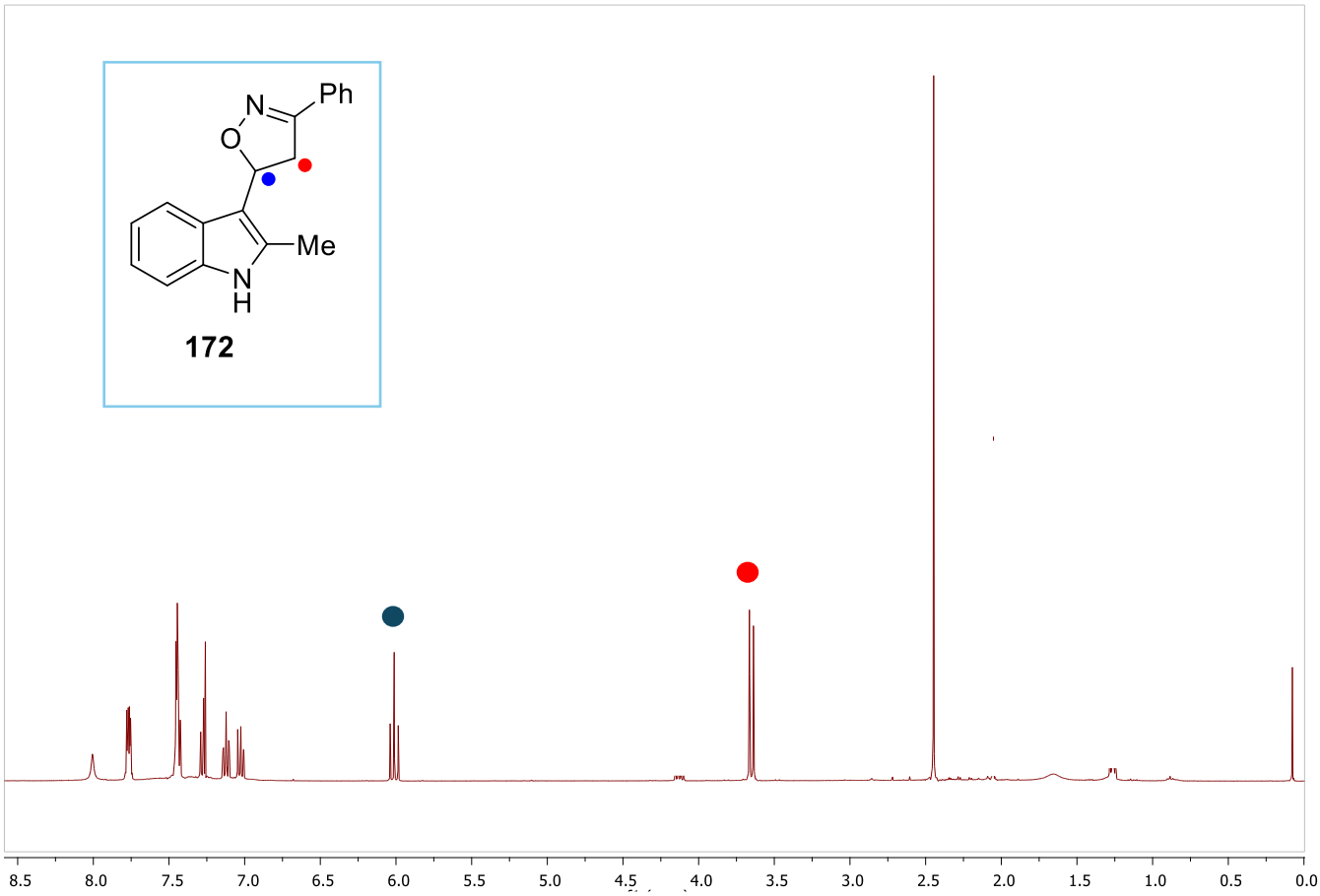

Figure 4.20. Conditions and spectra for the formation of presumed **172**.

A breakthrough was finally achieved using **171** as the substrate; under the same conditions, the presumed isoxazoline **173** was formed in 44% yield. ^{1}H-NMR analysis of this compound revealed two separate signals for the methylene protons, in line with what was expected of the isoxazoline structure. (**Figure 4.21**) With this result, our previous theory of the ring geometry in the case of **165** seemed more plausible. Additionally, it could then be reasoned why changing the identity of the group at the 3-position of the isoxazoline still gave the doublet in the case of **172**, as this group is presumably orientated away from the isoxazoline ring, with arguably minimal influence over ring

conformation, despite the added steric bulk. Conversely, the phenyl ring in **173** at the 3-position of the indole is much closer to the diastereotopic ring protons at the 2-position of the isoxazoline and can thus have a greater influence.

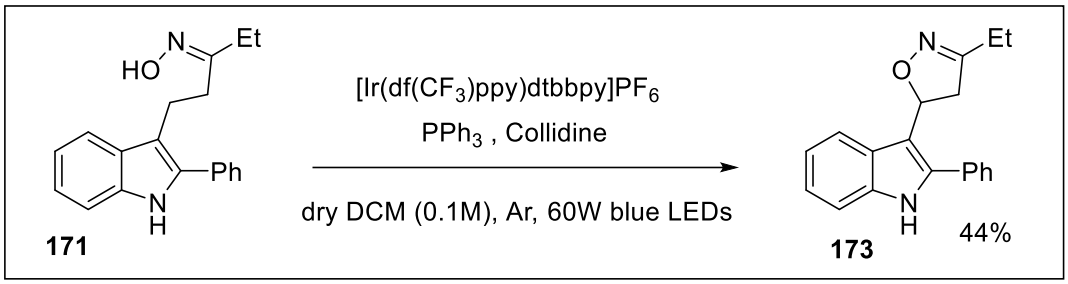

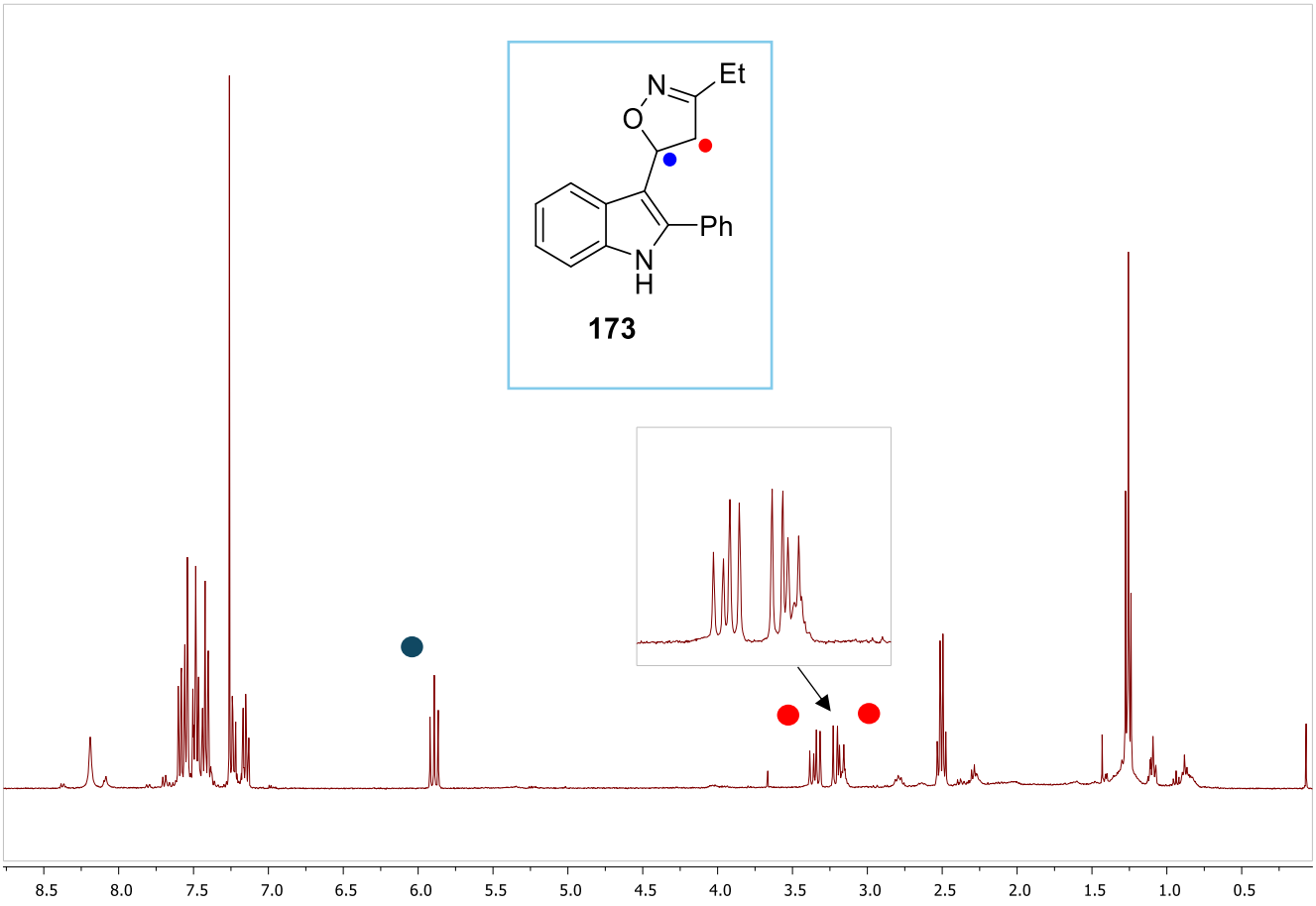

Figure 4.21. Conditions and spectra for the formation of presumed isoxazoline **173**.

With this result supporting the structure of the isoxazoline, it showed that even with the 2-postion of the indole blocked, intramolecular cyclisation to form spiroindole was still disfavoured. While this was not the expected result it was a serendipitous one; despite being known for decades isoxazolines have recently made a resurgence as potential pharmaceuticals for a broad range of different disorders.[153] Historically, the isoxazoline

ring was often formed through 1,3-dipolar cycloadditions of nitrile oxide or nitronates to alkenes (**Figure 4.22**, **A**). Though this had stereochemical implications, in terms of diastereoselectivity as two new stereogenic centres are often formed post cycloaddition, later reports included the addition of chiral Lewis-acids[154–156] or chiral auxilaries.[157–159] An example of this can be seen in **Figure 4.22**, **B** by Jiao *et al*, using Copper (II) triflate and chiral bisoxazoline ligands to form an *in situ* chiral Lewis acid for the catalysis of the cycloadditon of silyl nitronates to *N*-acryloyl-2-oxazolidinone.[160]

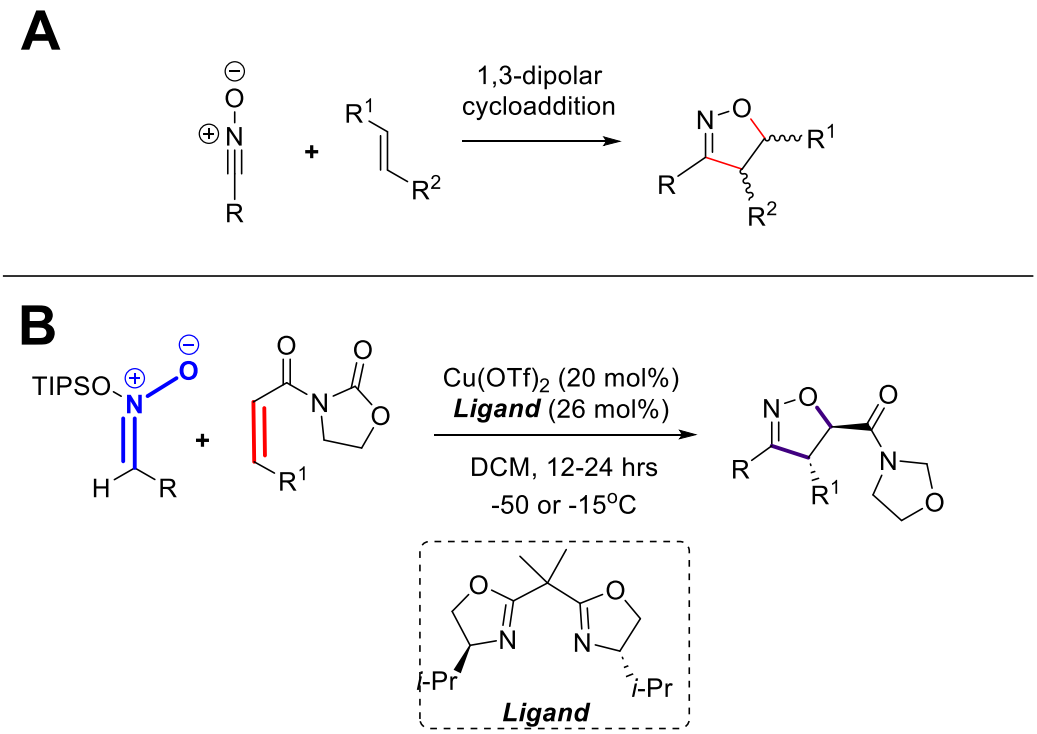

Figure 4.22. A) Summarised visual of the classical 1,3-dipolar cycloaddition of nitrile oxides to alkenes to form isoxazolines. B) 2015 report by Jiao *et al* on the Cu(II)-bisoxazoline mediated, diastereoselective synthesis of isoxazolines.

Though this did raise question regarding the exact mechanism of isoxazoline formation as, beyond cycloaddition, there are few methodologies to synthesis isoxazolines via radical methodologies, with those reported usually involving hypoiodine-mediated oxidations (**Figure 4.23 A**, **B** and **C**), such as those by Yoshimaru *et al*,[161] Minakata *et al*[152] and Zhu and Liu *et al*.[162] Notably, Reid *et al*[163] recently reported the synthesis of isoxazolines via an electrochemical, radical-mediated methodology involving an aldoxime and electron deficient alkenes with high diastereo- and regioselectivity under relatively benign conditions **Figure 4.23**, **D**.

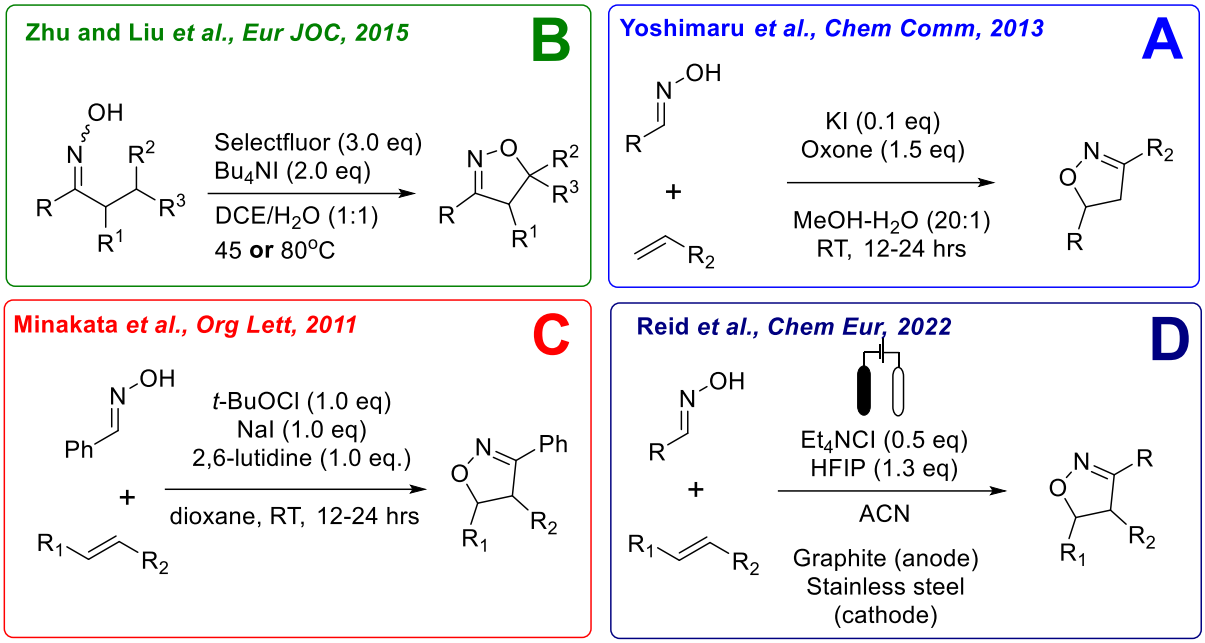

Figure 4.23. Some established routes to access the isoxazoline core via hypoiodated-species mediated oxidations.

Of note, the combination of isoxazoline with indole core is rarely reported. However, those that have showcased interesting and often potent biological activities. As part 1 noted, indoles are an extremely privileged motif in nature, and have high bioactivity owing to the vast chemical space they occupy, thus, in conjunction with the properties of isoxazolines, this combination presents interesting lead molecules such as those reported by Amir *et al* in 2010 (potent anti-inflammatory and low ulcerogenic activity),[164] Kumar and Shah *et al* in 2018 (tumour migratory inhibitors and apoptosis promoters in C4-2 cancer cells)[165] and Hawas and Baytas *et al* in 2021 (anti-cancer activity in various liver cell lines)[166] (**Figure 4.24**). As this junction, we opted to follow this lead and pursue reaction optimisation in favour of these indolyl-isoxazoline structures.

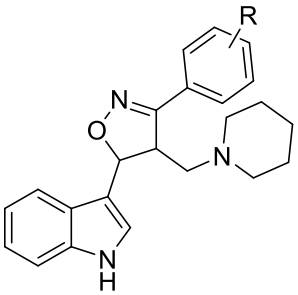

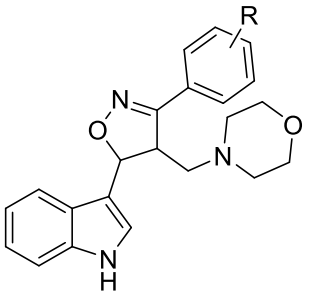

Potent anti-inflammatory agents;
low ulcerogenic activity
>50% anit-inflammatory activity vs indomethacin

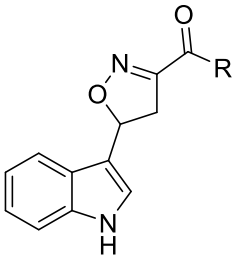

Anti-tumour activity vs Huh7 MCF7
and HCT116 Liver cancer cell lines;
Cell cycle arrest promoters and apoptosis inducers;
IC_{50} as low as 0.7 uM

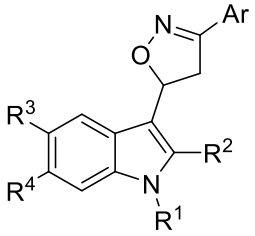

Potent cytoxicity vs C4-2 cancer cell line;
Apoptosis promoter and migratory inhibitor
IC_{50} 2.5 - 5.0 uM

Figure 4.24. Examples of bioactive indolyisoxazolines in reported literature.

Following the change in direction, control reactions were first set-up as described in (**Table 4.3**), to determine the role/necessity of each reagent in the reaction.

Table 4.3: Control conditions for the conversion of **160** to **165**.

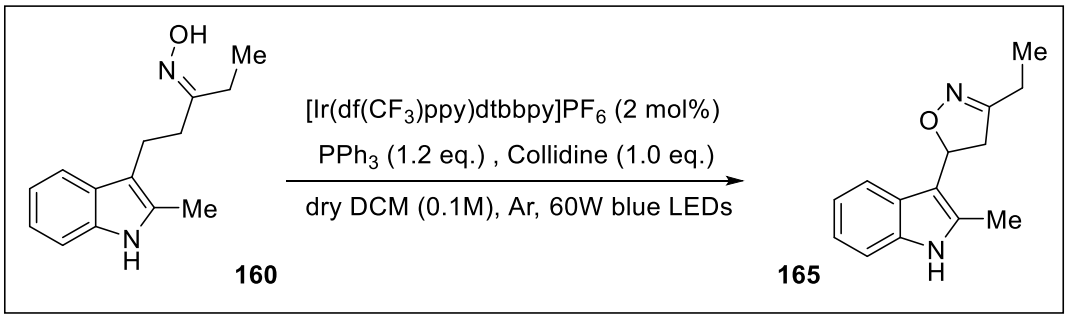

Entry	Photocatalyst	PPh_3	Collidine	Dry solvent	Atmosphere	Yield of 165 (%)
1	✓	✓	✓	✓	Argon	47
2	✗	✓	✓	✓	Argon	N/A
3	✓	✗	✓	✓	Argon	46
4	✓	✓	✗	✓	Argon	13
5	✓	✗	✗	✓	Argon	7
6	✓	✓	✓	✓	**Oxygen**	12
7	✓	✓	✓	✗	Argon	11
8	✓	✓	✓	✓	Air	49

First, each reagent was removed sequentially (entries 2–4 and 7). As expected, in the absence of photocatalyst no reaction occurs (entry 2). The role of TPP is less important, which produces the same yield in its absence (entry 3). This was expected, as our initial thoughts for role of TPP was to fragment the N-O bond and form the iminyl radical. In this case however, the N-O bond remains intact to form the isoxazoline scaffold. Base (collidine here), it seems, plays in important role as its absence (entry 4) substantially lowers the yield. It should be noted however that some amount of **165** is still produced, suggesting a potential alternate pathway involving two molecules of the substate or TPP, as removal of both TPP and base (entry 5), yields a further diminished amount of **165**. It cannot be confirmed however, without further experiments varying the amounts of base/TPP and which was not given priority given the larger scope of this study was towards optimisation of this method, for which the presence of base for effective yield (entry 4) was the more relevant result. Charging the reaction vessel with molecular oxygen proved detrimental to the yield (entry 6), although this was not unexpected as triplet oxygen has been known to quench excited states and as shown in Part 1, and trap radicals. However, in lower concentrations, under air (entry 8) the yield was roughly the same. The biggest takeaway from these studies was the seemingly spectator role played by TPP in the reaction, thus it could effectively be removed in further optimisations, as well as the importance of the base to the reaction.

While mechanistically, it was unclear the role it was playing, it was evident that its effect on the yield was substantial, thus we next opted to do a base screen (**Table 4.4**).

Table 4.4: Base screen for the conversion of **160** to **165**.

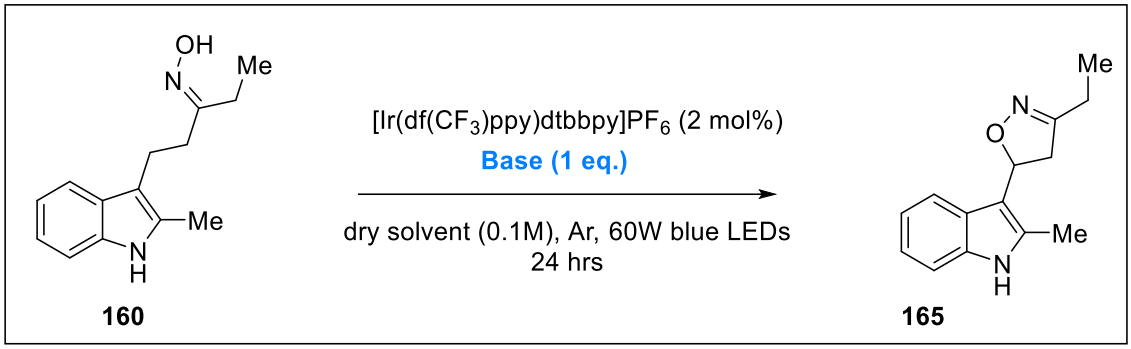

Entry	Base	Yield (%)
1	DBU	13
2	Triethylamine	15
3	NaOAc	35
4	$CsCO_3$	7
5	$NaCO_3$	17
6	K_3PO_4	2

While less illuminating than the control reactions, it did continue to highlight the importance of collidine, as none of the bases, apart from NaOAc (entry 3), were comparable in yield. Surprisingly even other nitrogenous bases, NEt_3 and DBU (entry 1 and 2) could not reproduce a similar result.

Next, we examined solvent effects (**Table 4.5**) As a pure solvent DCM was superior to all the screened solvents by themselves, with only DCE (entry 1) coming close to the same yield. Interestingly however we noted that a mixture of DCM:H_2O was most effective when used together, giving the highest yield so far at 53% (entry 6). While DCM and water are immiscible, a select report by Liu and Zhu in 2015[162] noted observations in a similar system, DCE/H_2O, had a beneficial effect in forming isoxazolines using Selectfluor®; seemingly this effect translates well in our system as well. Similar to what Liu and Zhang

observed, increases beyond this 20:1 ratio in entry 6 proved detrimental, as a 1:1 ratio of DCM and water (entry 7) severely attenuated the yield. No reaction occurred in pure water (entry 8).

Table 4.5: Solvent screen for the conversion of **160** to **165**.

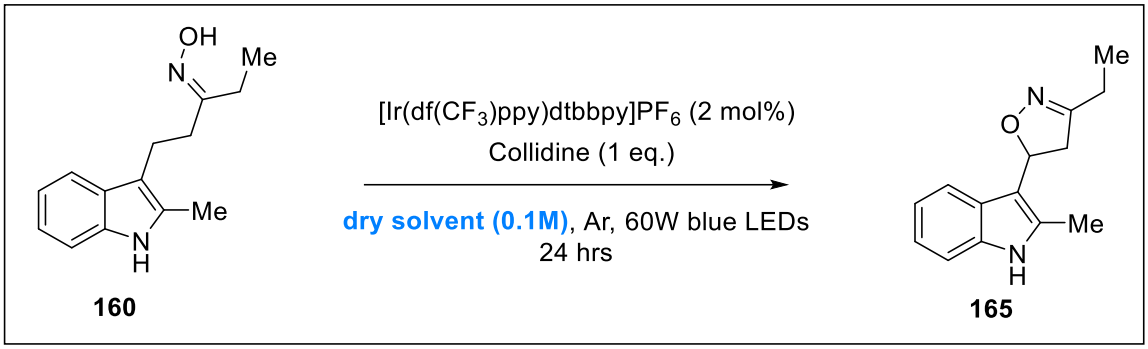

Entry	Solvent	Yield (%)
1	DCE	36
2	THF	18
3	ACN	23
4	Toluene	23
5	DMF	3
6	DCM:H_2O (20:1)	53
7	DCM:H_2O (1:1)	2
8	H_2O	0

The effect of varying the photocatalyst was also investigated (**Table 4.6**). Of the catalysts screened, the organic photocatalysts (entries 1–8) in general fared worse compared to the transition metal ones (entries 9–11). All however, had lower yield relative to the Ir[d(CF_3)$_2$ppy(dtbpy)] used originally, the closest being 4CzIPn at 33% (entry 12).

Table 4.6: Catalyst screen for the conversion of **160** to **165**.

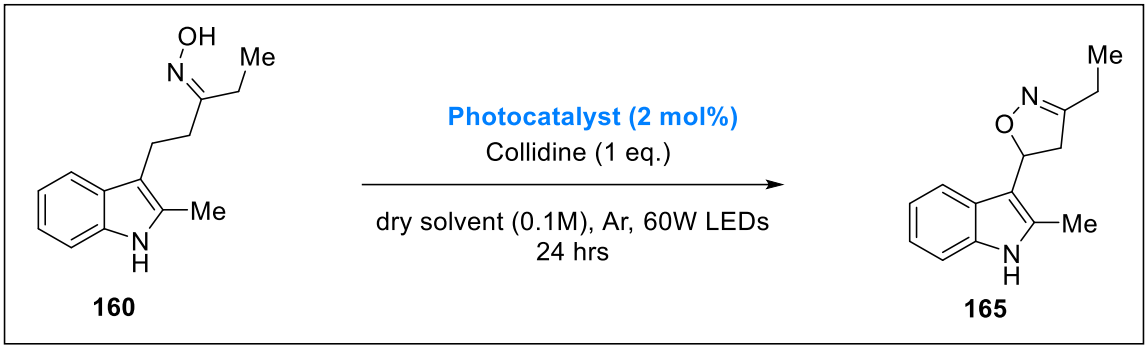

Entry	Photocatalyst	Yield (%)
1	Riboflavin	9
2	Rhodamine B	9
3	Fluoresin	19
4	9-mesityl-10-methyl-acridinium tetrafluoroborate	11
5	2,4,6-triphenylpyrylium tetrafluoroborate	7
6	9,10-dicyanoanthracene	11
7	Eosin Y	0
8	Methylene blue	7
9	$Ru(bpz)_3$	26
10	$Ru(dtbbpy)_3$	4
11	$Ir[(3,4'\text{-}dtbppy)_2(dtbbpy)]$	18
12	4-CzIPN	33

We next turned to investigate the effects of additives (**Table 4.7**). At this junction, the mechanism of the reaction was unclear; based on the control reactions in **Table 4.3**, particularly entry 3 which showed a 46% yield with only photocatalyst and base under

Argon, we were led to question how the catalytic cycle was being turned over. As we struggled to obtain yields over 50% in all but one trialled condition up to this point, we began to suspect the reaction required sacrificial amounts of stating material, **160** for effective catalytic turnover, which could be a cause for the diminished yields. Though the mechanism was unclear, based on the use of a strong oxidising photocatalyst, Ir(df(CF$_3$)ppy)dtbbpy that has a strong affinity for an oxidative cycle via $Ir^{3+} \rightarrow (Ir^{3+})^{*+} \rightarrow Ir^{2+}$, we postulated the need for a terminal oxidant to regenerate the active Ir^{3+} species, thus to test this hypothesis we turned to additives which had demonstrated terminal oxidative properties in photocatalytic cycles:[167] persulfates,[168] peroxides,[169] halocarbons[170] and some copper (II) salts.[118] In all cases the yield was lowered from its original 49%; in the case of entries 1–2, the drop was less substantial at 33% and 27%, however with $BrCCl_3$ and $Cu(OTf)_2$ was isolated and degradation of starting material was observed.\

Table 4.7: Additive screen for the conversion of **160** to **165**.

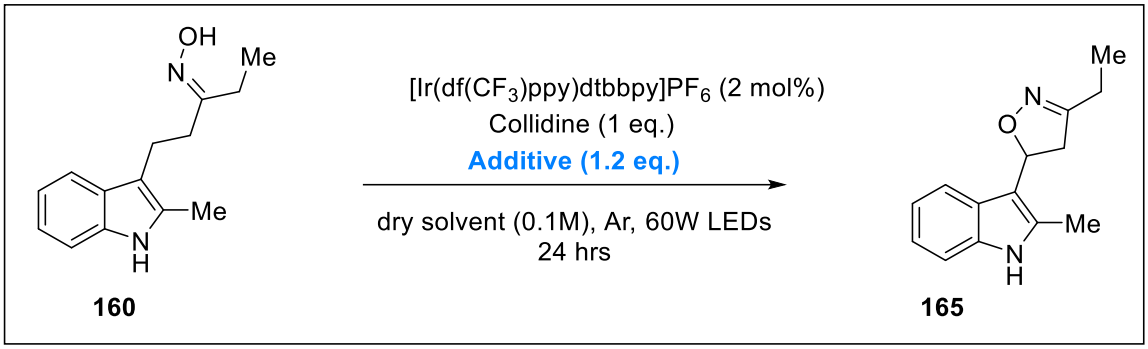

Entry	Additive	Yield (%)
1	Ammonium persulfate	33
2	*t*-Butyl hydroperoxide	27
3	$BrCCl_3$	0
4	$Cu(OTf)_2$	0

Optimised conditions: Jonathan Da Luz

Based on these finding, the project was handed over to another member of our research group, Jonathan da Luz, who optimised the reaction as part of his MSc research work and training. As such, the full set of additional optimisation studies will fall as part of his thesis, however, the final set of optimised conditions are shown in **Figure 4.25**.

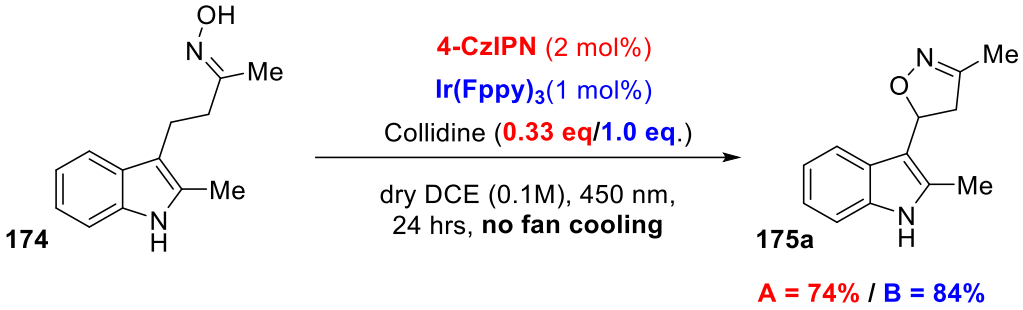

Figure 4.25. Optimal set of conditions A and B, discovered by Jonathan da Luz using oxime **174**.

It was discovered that using either 4-CzIPn or $Ir(ppy)_3$ as the photocatalyst in the absence of fan cooling, with only catalytic amounts of collidine, isoxazoline **175a** could be furnished in good to excellent yields, 74% and 84%, respectively. This was an exciting result as, it allows for a more robust methodology in the event specific substrates prove difficult with one specific photocatalyst. While method B is more effective at furnish the oxime in higher yields, it should be noted that, when taking into consideration sustainability elements, method A proved the most appealing; rare-earth metal such as iridium were absent, and the reaction ran efficiently with catalytic amounts of collidine. In both cases, the set up proved very simple; the absence of fan cooling meant that direct irradiation by 450 nm LEDs was effective at carrying out this transformation. We suspect that improvements with the effect of 'no fan-cooling' was by virtue of an increase in the reaction temperature, which was measured during the reaction to be approximately 55 °C.

Substrate scope

Utilising this result, we were able to begin development to expand the repertoire of isoxazolines (**176**) amenable to this methodology. This involved revisiting our plan to

access the oxime precursors (**177**); previously we had planned to do so via a Michael addition of the indole to a alkenyl ketone as per **Figure 4.14**. However, to access novel indoles we obtained commercially available phenyl hydrazines (**178**) that could be converted to the requisite indole via a plethora of literature methods including the popular Fischer Indole synthesis (**Figure 4.26**).

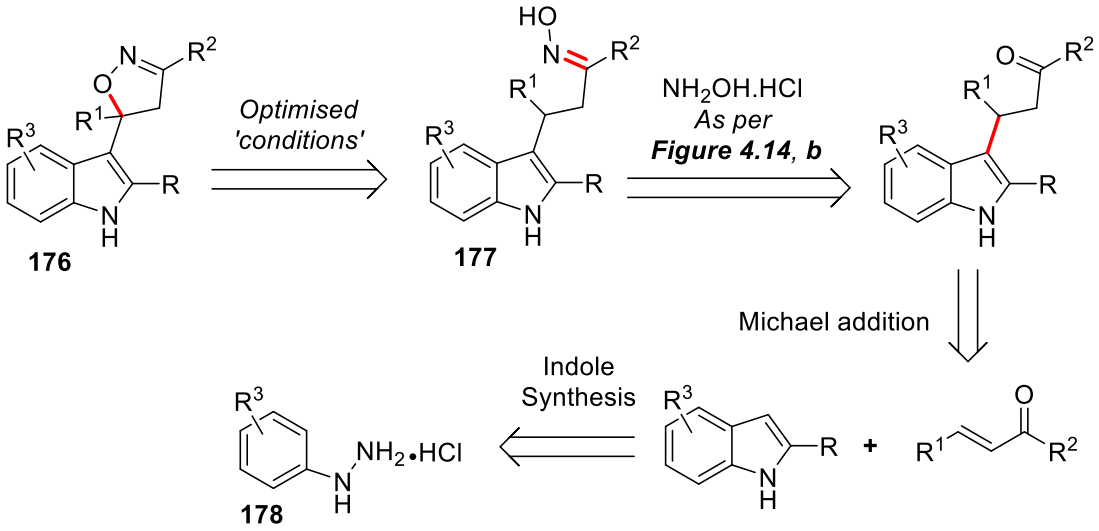

Figure 4.26. Retrosynthetic method to access desired isoxazolines **176** from commercially available phenyl hydrazines. **178**.

The Fischer Indole synthesis, discovered by Emil Fischer in 1883,[171] is the quintessential methodology and one of the most influential, not just towards indole synthesis but perhaps of all time. As such a ubiquitous method, it has been modified and adapted countless times, to accommodate for new technologies, reagents, and to greatly expand the repertoire of amendable substrates.[172] Consequently, it seemed the obvious choice to allow us to synthesise a library of indoles bearing a variety of functional groups at R^3.

Mechanistically (**Figure 4.27**), the Fischer indole synthesis proceeds via a key 3,3-sigmatropic rearrangement. Typically, this arises from a tautomerisation of a phenylhydrazone (**179**), to the resultant enamine (**180**), which then undergoes the 3,3-rearrangement to form **181**, which rapidly forms an aniline intermediate (**182**) by intra- or intermolecular proton transfer. It is here where an intramolecular S_N2 reaction can occur

to furnish the indoline ring system (**183**), after which, loss of ammonia via protonation and subsequent proton transfer, gives the desired indole, **184**.

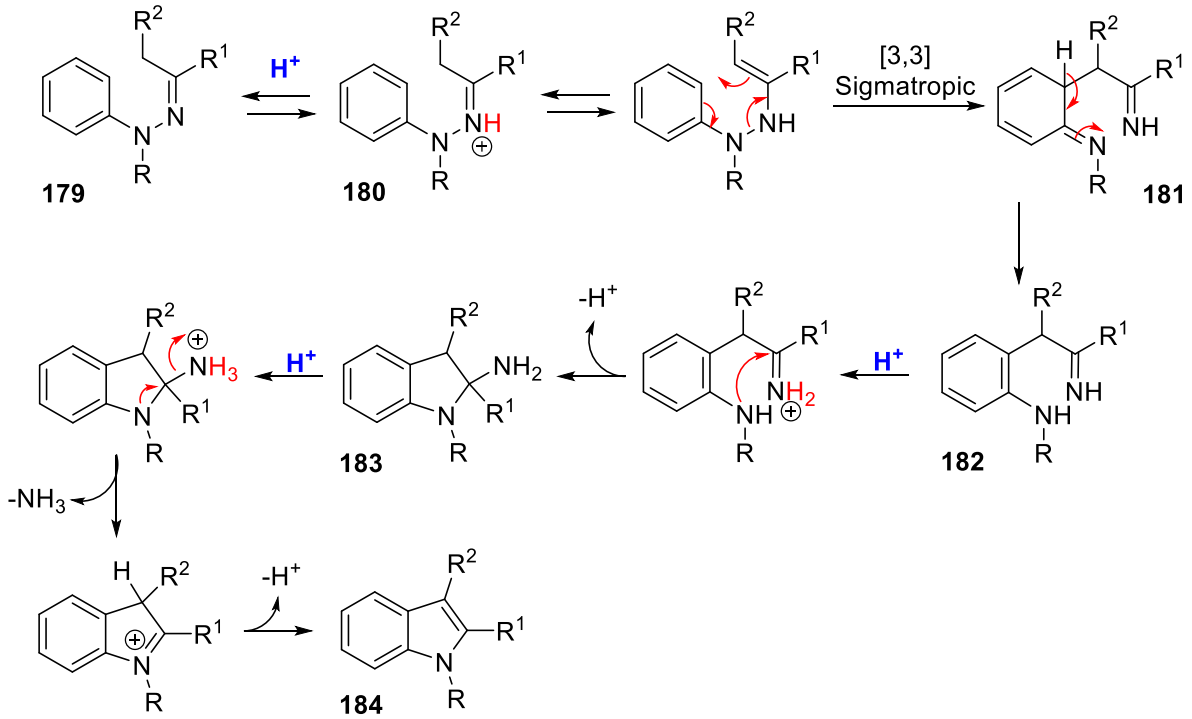

Figure 4.27. Mechanism of the classic Fischer indole synthesis.[32]

Using this method, we hoped to synthesise a variety of molecules bearing biologically relevant functional groups on the aromatic ring of the indole that had previously not been reported in literature such as -NO_2 group and disubstituted halogens.

Indole synthesis optimisation

Typically, the Fischer method utilises a hydrazone such as **179** as the starting material under the catalysis of $ZnCl_2$ in high heat (140°C). We were hesitant to replicate these conditions exactly, as Fischer's method was shown to be less efficient (>5% yield) or entirely not possible for synthesising indoles bearing a hydrogen at the 3-position, as we required for the Michael addition (**Figure 4.26**). Moreover, the harsh reaction conditions can exclude many functional groups. However, there have been a plethora of recent developments that have adapted this method to phenylhydrazines **178**, that can react

with a ketone to form the hydrazone then indole in one step.[173,174] Fortunately, many of these modifications have adapted to address this gap in synthesising indoles unfunctionalized at C3, as such we were confident that we could form the desired 3-indoles under one of these conditions starting from commercially available phenylhydrazines, **178**.

We began using substrate **185** as the model substrate (**Table 4.8**). Noting the acidic conditions required for the effective outcome of this method as per **Figure 4.27**, our first experiments involved the use of strong acids, HCl under reflux in ethanol (78 °C) (entry 1) and at 120 °C with polyphosphoric acid (entry 2), both of which had precedent with 3-indoles.[175–177] In the case of the former, the reaction returned primarily hydrazine **185** with a low amount of the resultant hydrazone **186** as the product, whereas in the latter we observed only trace amounts of hydrazone **186** and mass degradation of the starting material, analysis of which was made difficult by the volume of products that appeared by TLC and their similar R_f, however, NMR analysis of the crude sample showed no presence of signals of the desired indole.

Table 4.8: Trialled conditions for the modified Fischer conditions on substrate **185**. [a]Heated at 120 °C.

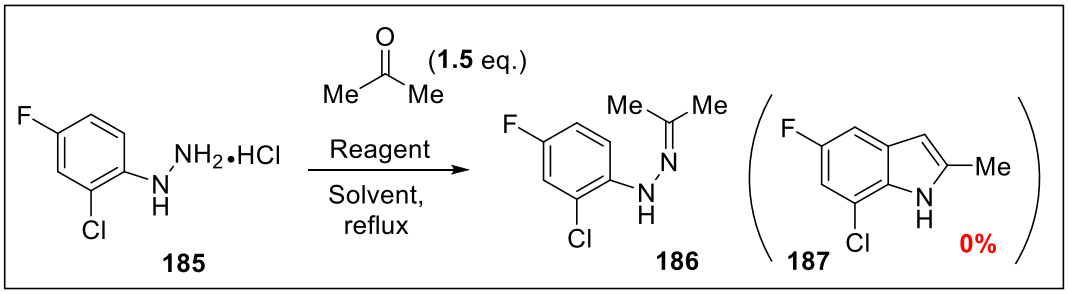

Entry	Reagent (eq.)	Solvent	Yield of *186* (%)
1	HCl (1.5)	EtOH	20
2[a]	-	Polyphosphoric acid	Trace
3	-	Acetic acid	70
4	CAN (20 mol%)	MeOH	11
5	-	Pyridine	100

Next, we mimicked the conditions described by Lin *et al.*,[178] which involved refluxing glacial acetic acid; this instead proved highly effective at producing the hydrazone (70% yield) but was still unable to undergo the 3,3-rearrangement as required for indole formation (entry 3). Given this, we looked to literature which revealed the works of Mahadevan and coworkers, who reported a modification of the classic Fischer indole synthesis using catalytic amounts of CAN.[179] Of particular interest, this had shown efficient at catalysing the synthesis of electron-poor aromatic indoles, such as **185**, presumably via a Lewis acid-type mediation. Unfortunately, however, repeating these conditions, even with increased loadings of CAN above their reported could not produce the desired indole (entry 4), yielding the hydrazone in 11% yield with remaining mass recovered indole **185**.

Similarly, pyridine hydrochloride-mediated Fischer indole modification has been known for quite some time.[180] While this might initially be puzzling given the need for an acidic medium as per the mechanism in **Figure 4.27**, the authors noted that a base, sufficiently weaker than the Fischer intermediates, would be more than sufficient at supplying a proton at the intermediate steps. Though, in this case the pyridine hydrochloride is a mildly acidic salt that can act dually as both a complexing agent and solvent, meaning that the strength of the acid reagent can be reduced to compensate relative to the initial Fischer reports which required a strong acid; they demonstrated that the single equivalent of hydrochloride from the phenylhydrazine was sufficient to carry out the transformation to the complete indoles, even with strongly withdrawing groups, to produce indoles bearing only a hydrogen at the 3-position.

Encouraged by this, we emulated their conditions (entry 5). While the efficiency of this reaction did indeed far surpass those previously trialled (entries 1 – 4), fully converting the phenylhydrazine to the hydrazone **186**, the indole product was still not produced, even with increased time and heat.

From these results, we can see that based on the mechanism (**Figure 4.27**), all conditions have only succeeded in formation of the first intermediate, the hydrazone, **179**, while the required 3,3-sigmatropic rearrangement seems to be the significant barrier to furnishing the indoles. With this in mind, we took the isolated hydrazone **186** and subjected it to the harsh Fischer conditions shown in **Figure 4.28**:

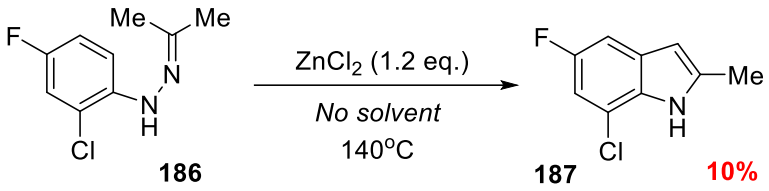

Figure 4.28. Fischer conditions for the formation of indoles from hydrozones.

While this was able to furnish the requisite indole, **187**, the yield (10%) was far below the efficiency we were hoping to achieve. Given that this method was primarily developed for analogues with substitutions on the aromatic ring and that the substrate scope included many other analogues with substitutions elsewhere (not on the indole ring) that were not dependent on this, we conceded to use this method, inefficient as it was. However, for future work, we would need to re-think this route as well as the starting material, as it is likely that the nature of the substitutions (withdrawing groups) was highly detrimental to the 3,3-rearrangement needed to furnish the indole from phenyldrazines.

Following this development, we adapted the conditions by McKew *et al.*[181] (**Figure 4.29**) that would allow for the rapid synthesis and purification of hydrazones for the $ZnCl_2$-mediated Fischer indole synthesis. This method used saturated $NaHCO_3$ in a biphasic mixture with DCM, followed by extraction and removal of solvent *in vacuo*, which allowed for the preparation of the indole without need for purification of the hydrazone first compared to that of entry 5, **Table 4.8**.

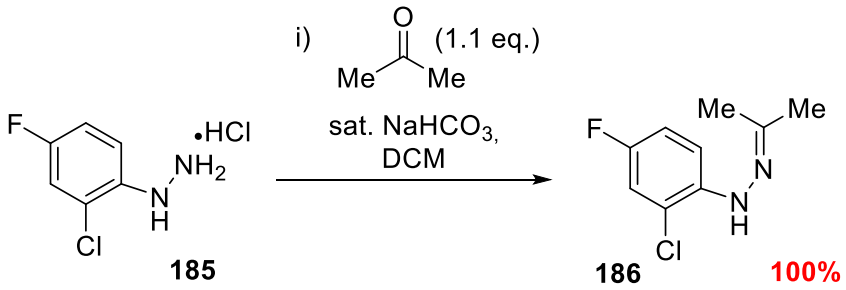

Figure 4.29. Optimised method to synthesise Phenylhydrazones from Phenylhydrazines with minimal work-up.

Substrate scope

With a method to synthesise novel indoles in place, in conjunction with our established route to synthesis the oxime precursor from the prerequisite indole as per **Figure 4.13**, we were able to synthesize a variety of isoxazolines bearing a variety of functional modifications throughout the molecule, including on the phenyl ring, at the 2-indole, on the isoxazoline ring as well as at the R^2 position. These, along with substrates that were unsuccessful can be seen in **Figure 4.30**.

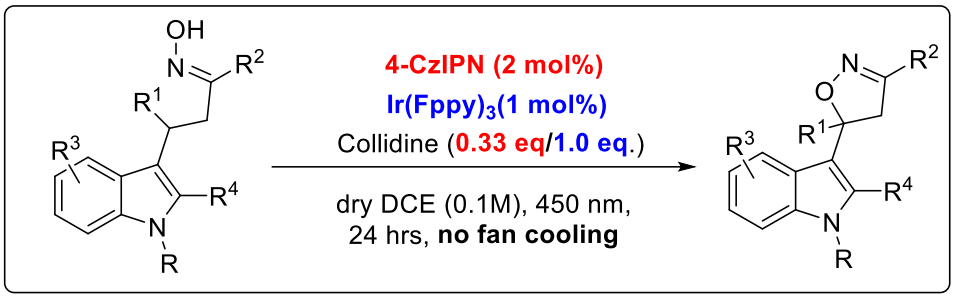

R-variant

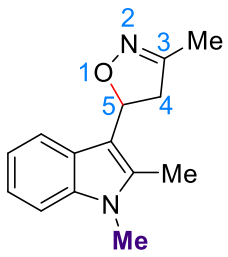

175b - 8%, Trace

R1-variants

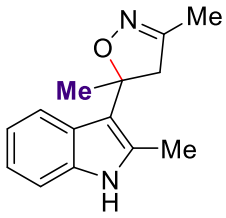

175c - 61%, 29%

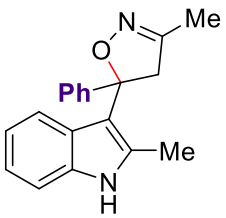

175d - 57%

R4-variants

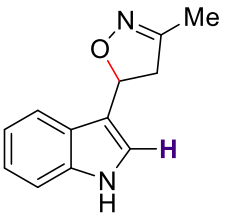

175q - 58%

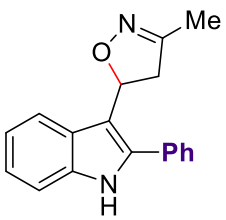

175r - 68%, 53%

R2-variants

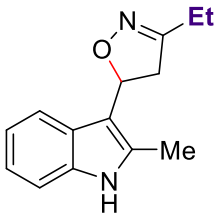

165 - 70%, 59%

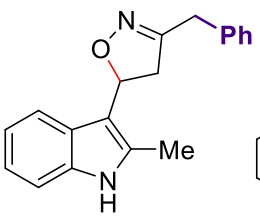

175e - 47%

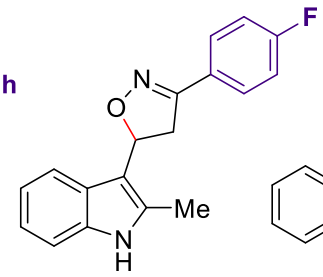

175f - 60%, 9%

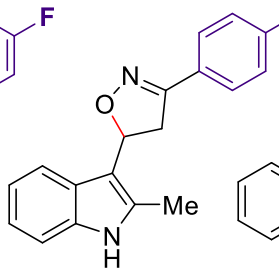

175g - 46%, Trace

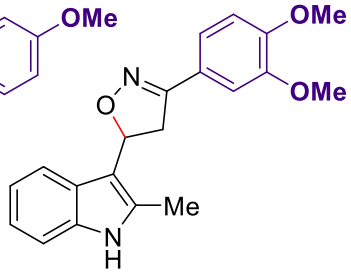

175h - 59%, Trace

R3-variants

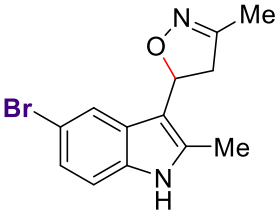

175i - 60%, 67%

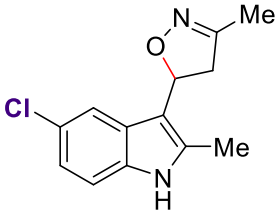

175j - 61%, 73%

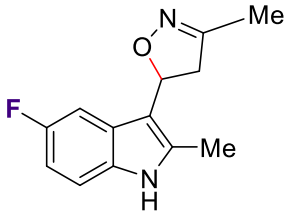

175k - 60%, 83%

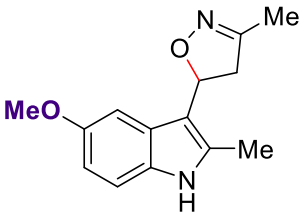

175l - 65%, 61%

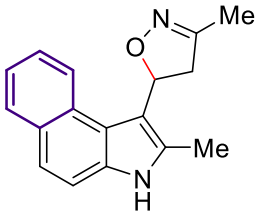

175m - 19%

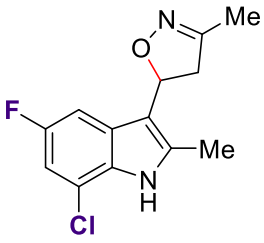

175n - 60%

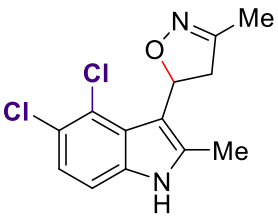

175o - 48%

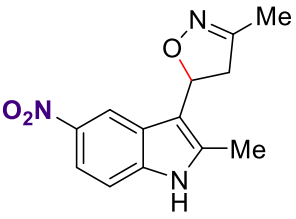

175p - 19%, 12%

Unsuccessful substrates

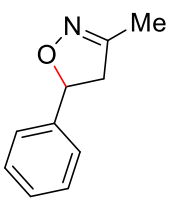

168 - 0%

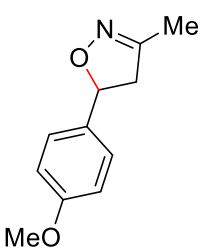

175s - 0%

Figure 4.30. The full isoxazoline substrate scope, including unsuccessful substrates.

As shown in **Figure 4.30**, the methodology was amenable to large variety of substrate with functional changes at various positions throughout the molecule being tolerated.

Of these, tweaking the R-group, **175b**, to the *N*-protected version was the least tolerated, though the product was successfully isolated, the yield was heavily diminished for both methods: 8% yield using the 4-CzIPN and trace amounts with iridium, respectively.

Substrates with variation at the R^1-group were remarkably well tolerated in comparison (**175c** and **175d**) with moderate yields for both when 4-CzIPN was utilised as the photocatalyst (61 and 57% yields, respectively). Given the steric strain expected for the formation of quaternary carbon centres, this was a surprising but welcome result.

We were able to validate the structure of these compounds with NMR analysis; typically, rapid validation for formation of the isoxalozine was seen via a doublet of doublets (such as **46**, **Figure 4.21**) or some cases, a doublet as noted with **165** and **172** (**Figure 4.15B** and **4.20** respectively) at ~3 – 4 ppm in conjunction with a triplet at ~5 – 6 ppm. The latter peak typically corresponds to the methylene proton, while the former is indicative of the diastereotopic splitting of the two protons in the ring α to the methylene.

In the case of **175c** (NMR spectrum: **Figure 4.31**) and **175d**, the absence of the triplet at 5 – 6 ppm, in tandem with the spectrum having one less total proton compared to the oxime, is already suggestive of ring closure. As further evidence, the presence of two doublets at 3 – 4 ppm adds to this conclusion as an α-quaternary centre would result in this type of splitting pattern; unlike all other synthesised isoxazolines, the absence of a proton at the α-position means that there is no vicinal coupling and hence a single doublet is observed rather than a doublet of doublets as the protons are still diastereotopic. This pattern is present for **175d** as well.

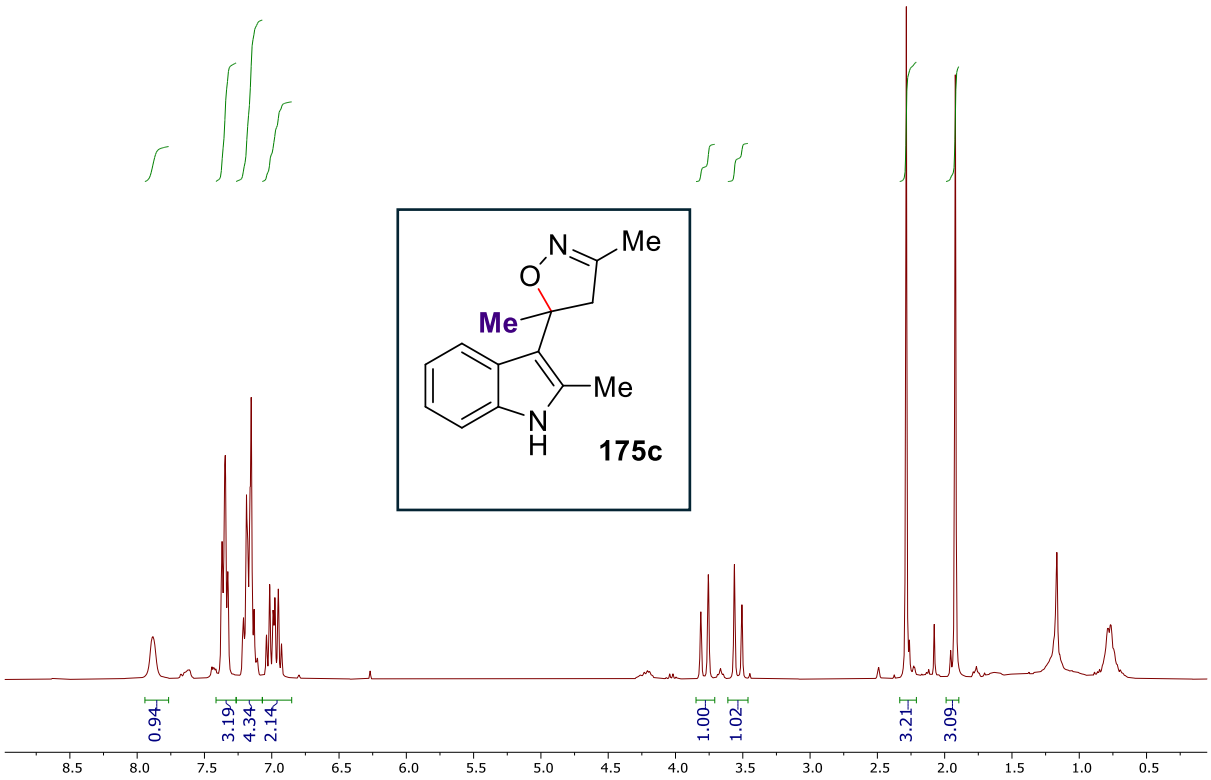

Figure 4.31., ^{1}H-spectrum of **175c** showing the lack of triplet at 5 – 6 ppm and observed two doublets at 3.5 – 4 ppm.

R^2-variants, at the 3-position of the isoxazoline ring were also very well tolerated for longer chain aliphatic groups with the ethyl chain (**165**) showing moderate yields for both 4-CzIPN (70%) and Iridium (59%). Aromatic groups were similarly tolerated showing decent yields for many electronic variants; benzyl group (**175e**) had 47% yield with 4-CzIPN, and similarly phenyl groups with both withdrawing (**175f**) and donating (**175g** and **175h**) groups showed 60, 46 and 59% yields respectively when 4-CzIPN was used. Though it must be noted that, the moderate to the good yields were primarily observed with 4-CzIPN, while Iridium performed poorly in comparison, showing only trace amounts for **175g** and **175h**, and a meagre 9% for **175f**.

Aromatic R^3-variants were the most extensively tested and, gratifyingly, well tolerated with monosubstitions (**175i** – **175l** and **175p**) that included halogens (**175i** – **175k**), which showed higher efficacy in Iridium: 60, 61 and 60% in 4-CzIPN vs 67, 73 and 83% with Iridium respectively, and donating groups (**175l**) (similar for both 4-CzIPn and Iridium, 65 and 61% respectively). An extended ring system (**175m**) was also successfully

synthesised though it must be noted, in poor yield (19% with 4-CzIPN). Di-substituted systems proved similarly possible and had moderate yields as well, **175n** and **175o**, 60 and 48% respectively with 4-CzIPN. The strongly withdrawing -NO_2 variant (**175p**) was also successfully synthesised, albeit in poor yield for both methods: 19% and 12% respectively.

In addition, we extended substitutions to the aromatic system of the indole to include the R^4-postion, which was adaptable to this methodology when a phenyl group was added (**175r**) (68% and 53% for 4-CzIPN and Iridium respectively) and far more surprisingly, a Hydrogen (**175q**), which formed the isoxazoline in a decent yield at that (58%) with 4-CzIPN, preferentially over the spiroindole that was initially sought after for this work (**Figure 4.7**, **152**) and azacarbozole that was previously formed via unoptimized conditions (**Figure 4.12**, **144**).

This concluded the substrate scope; we were gratified that all trialled oximes were able to form the desires isoxazoline in at least low yields though most far exceeded this, showing moderate to good yields (60 – 83%).

Of note, when we attempted to substitute the indole group with a phenyl group under these optimised conditions, as in **Figure 4.17**, we were similarly unsuccessful. Thinking that the electron donating effect of the indole-system via the lone pair on the nitrogen might be a contributing factor, we switched to a more donating ring system with a methoxy group. However, the proposed isoxazoline (**168**) still proved elusive, hinting the role of the indole system as a key factor in the mechanistic working of this reaction, discussed below.

Mechanism

Without a full, dedicated study, the exact mechanism of this reaction cannot be pinpointed. However, we can postulate theories about how the mechanism might proceed using the results generated.

Most notably, the key pieces of information available relevant for this are as follows:

1) As mentioned previously, the indole moiety is likely the central point for photocatalytic activation.

2) The presence of a base is necessary for efficacy of the reaction which is suggestive of PCET sequences for successful excited state and ground state quenching of the photocatalyst.
3) Collidine, an aromatic amine, being the best choice of those trialled both in this work and by Jonathan Da Luz. However, the reaction can proceed in low yields without one. Given the structure of substrate and collidine, hints at a potential open-shell association via H-bonding and/or π-π stacking.
4) The presence or absence of air is inconsequential to the reaction outcome.

Based on these observations, photocatalytic cycle (**Figure 4.32**) was proposed. Excitation by visible light is first necessary to promote the photocatalyst, PC to the excited PC*. Thereafter, it is highly likely an oxidation of the indolic nitrogen lone pair via PCET with a base (collidine, **189**) reductively quenches the PC* to the oxidised $PC^{\bullet-}$ (**188** to **188a**). Oxidation of indoles is extensively documented via several routes; direct photooxidation,[182,183] photocatalysts,[184,185] heat,[186] to name a few, while direct radical isoxazoline formation is typically not observed and rather radical transposition via fragmentation[162] (see **Figure 4.23**) or HAT-mediated oxidations[187] is needed to activate the oxime, thus this evidence, in conjunction the inability to form **168** and **175s** from the optimised conditions, suggests that oxime activation must proceed substrate activation via to indolic oxidation as the key step for photocatalytic initiation.

Further examination of this reductive quenching can reveal several nuances, which cannot be validated without a dedicated quenching study, however, we can infer based on the success of collidine, **189**, as a base compared to all trialled bases which were non-aromatic, as well as the track record of aromatic nitrogenous bases as effective charge transfer reagents,[188] that effective PCET is owed to an open-shell association by a combination of H-bonding and π-π stacking with the indole moiety, **188b**. Following this pre-organisation, the sequential two-step oxidation to the radical cation-collidine complex **188c** and rapid PT to yield anion **188a** and charge transfer to form **189a**.

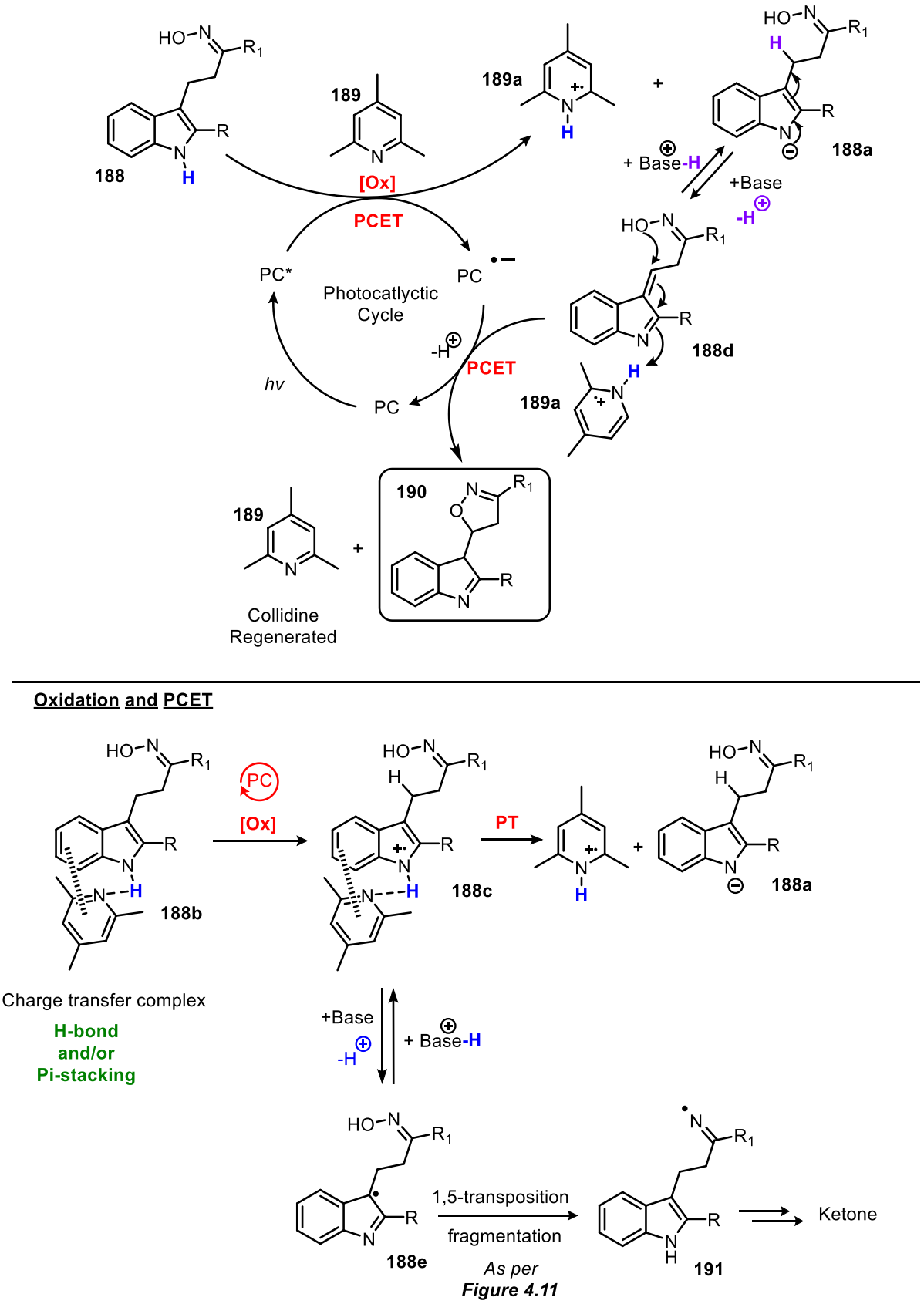

Figure 4.32. Proposed pathway for ring closure of oxime to isoxazoline.

Evidence for this over a concerted oxidation-PCET lies in the observed formation of ketone intermediates which potentially forms via PT of **188c** to yield **188e**, followed by 1,5-transposition, fragmentation, H-abstraction and work-up as per **Figure 4.11**. Whereas a concerted PCET-oxidation would selectively produce anion **188c**. This seeming chemoselectivity has been observed when the reaction pathway follows a multi-step PCET (MS-PCET).[188]

Regeneration of the active photocatalyst and collidine can be achieved after a second PCET of the oxidised collidine **189a** and de-protonated indole **188d**, driven by a SN_2 nucleophilic attack of the oxime oxygen onto the annulated C3-indole position which simultaneously furnishes the desired isoxazoline, **190**.

Conclusion and future work

In conclusion, while our original proof of concept to form the spirooxiandole via an adaptation of Doyle's method was unsuccessful, in the process we discovered a mild and catalytic route to access pharmacologically relevant indole isoxazoline scaffolds in moderate yield. This was then given to and optimised further with our group by Jonathan Da Luz to provide two parallel, effective and efficient methods which allowed us to expand the substrate scope significantly, showing good adaptability of the methodology across the molecule provided the indole moiety was kept intact.

For future work, it might do well to first perform mechanistic studies to validate the proposed mechanism as well as determine the role of the indole which would allow expansion to other similar electronic scaffolds. Moreover, this could then be extended to created other similar sized rings beyond the isoxazoline itself. Finally, if the above is found successful, we hope to utilise these compounds for biological testing.

References

(1) Hoffmann, N. Efficient Photochemical Electron Transfer Sensitization of Homogeneous Organic Reactions. *J. Photochem. Photobio. C: Photochem. Rev.* 2008, pp 43–60. https://doi.org/10.1016/j.jphotochemrev.2008.04.002.

(2) Tucker, J. W.; Stephenson, C. R. J. Shining Light on Photoredox Catalysis: Theory and Synthetic Applications. *J. Org. Chem.* **2012**, *77*, 1617–1622. https://doi.org/10.1021/jo202538x.

(3) Reckenthäler, M.; Griesbeck, A. G. Photoredox Catalysis for Organic Syntheses. *Adv. Synth. and Cat.* 2013, pp 2727–2744. https://doi.org/10.1002/adsc.201300751.

(4) Xi, Y.; Yi, H.; Lei, A. Synthetic Applications of Photoredox Catalysis with Visible Light. *Org. Biomol. Chem.* 2013, pp 2387–2403. https://doi.org/10.1039/c3ob40137e.

(5) Shaw, M. H.; Twilton, J.; MacMillan, D. W. C. Photoredox Catalysis in Organic Chemistry. *J. Org. Chem.* 2016, pp 6898–6926. https://doi.org/10.1021/acs.joc.6b01449.

(6) Lewis, N. S. Toward Cost-Effective Solar Energy Use. *Science (80-.).* **2007**, *315* (5813), 798–801. https://doi.org/10.1126/science.1137014.

(7) Wu, H. W.; Emadi, A.; De Graaf, G.; Leijtens, J.; Wolffenbuttel, R. F. Design and Fabrication of an Albedo Insensitive Analog Sun Sensor. *Procedia Eng.* **2011**, *25*, 527–530. https://doi.org/10.1016/j.proeng.2011.12.131.

(8) Blankenship, R. E. Early Evolution of Photosynthesis. *Plant Physiol.* **2010**, *154*, 434–438. https://doi.org/10.1104/pp.110.161687.

(9) Govindjee; Shevela, D.; Björn, L. O. Evolution of the Z-Scheme of Photosynthesis: A Perspective. *Photosyn. Res*. 2017, pp 5–15. https://doi.org/10.1007/s11120-016-0333-z.

(10) Narayanam, J. M. R.; Stephenson, C. R. J. Visible Light Photoredox Catalysis: Applications in Organic Synthesis. *Chem. Soc. Rev*. 2011, pp 102–113. https://doi.org/10.1039/b913880n.

(11) Ciamician, G. The Photochemistry of the Future. *Science (80-.).* **1912**, *36* (926), 385–394. https://doi.org/10.1109/TVT.2017.2766449.

(12) Ciamician, G.; Silber, P. Chemische Lichtwirkungen. *Berichte der Dtsch. Chem. Gesellschaft* **1910**, *43*, 1340. https://doi.org/10.1002/cber.190203503184.

(13) Fagnoni, M.; Dondi, D.; Ravelli, D.; Albini, A. Photocatalysis for the Formation of the C-C Bond. *Chem. Rev.* **2007**, *107*, 2725–2756. https://doi.org/10.1021/cr068352x.

(14) Schultz, D. M.; Yoon, T. P. Solar Synthesis: Prospects in Visible Light Photocatalysis. *Science (80-.).* **2014**, *343*, 1239176-1-1239176–1239178.

https://doi.org/10.1126/science.1239176.

(15) Skubi, K. L.; Blum, T. R.; Yoon, T. P. Dual Catalysis Strategies in Photochemical Synthesis. *Chem. Rev.* **2016**, *116*, 10035–10074. https://doi.org/10.1021/acs.chemrev.6b00018.

(16) Hedstrand, D. M.; Kruizinga, W. H.; Kellogg, R. M. Light Induced and Dye Accelerated Reductions of Phenacyl Onium Salts by 1,4-Dihydropyridines. *Tetrahedron Lett.* **1978**, *19* (14), 1255–1258. https://doi.org/10.1016/S0040-4039(01)94515-0.

(17) Cano-Yelo, H.; Deronzier, A. Photocatalysis of the Pschorr Reaction by Tris-(2,2'-Bipyridyl) Ruthenium(II) in the Phenanthrene Series. *J. Chem. Soc. Perkin Trans. 2* **1984**, *2*, 1093–1098. https://doi.org/10.1039/p29840001093.

(18) Koike, T.; Akita, M. Visible-Light Radical Reaction Designed by Ru- and Ir-Based Photoredox Catalysis. *Inorg. Chem. Front.* **2014**, *1*, 562–576. https://doi.org/10.1039/c4qi00053f.

(19) Nicewicz, D. A.; MacMillan, D. W. C. Merging Photoredox Catalysis with Organocatalysis: The Direct Asymmetric Alkylation of Aldehydes. *Science (80-.).* **2008**, *322*, 77–80. https://doi.org/10.1126/science.1161976.

(20) Ischay, M. A.; Anzovino, M. E.; Du, J.; Yoon, T. P. Efficient Visible Light Photocatalysis of [2+2] Enone Cycloadditions. *J. Am. Chem. Soc.* **2008**, *130* (39), 12886–12887. https://doi.org/10.1021/ja805387f.

(21) Narayanam, J. M. R.; Tucker, J. W.; Stephenson, C. R. J. Electron-Transfer Photoredox Catalysis: Development of a Tin-Free Reductive Dehalogenation Reaction. *J. Am. Chem. Soc.* **2009**, *131*, 8756–8757. https://doi.org/10.1021/ja9033582.

(22) Teplý, F. Photoredox Catalysis by [Ru(Bpy)3]2+ to Trigger Transformations of Organic Molecules. Organic Synthesis Using Visible-Light Photocatalysis and Its 20th Century Roots. *Collect. Czechoslov. Chem. Commun.* **2011**, *76* (7), 859–917. https://doi.org/10.1135/cccc2011078.

(23) Troy, T.; Jekic-McMullen, D.; Sambucetti, L.; Rice, B. Quantitative Comparison of the Sensitivity of Detection of Fluorescent and Bioluminescent Reporters in Animal Models. *Mol. Imaging* **2004**, *3* (1), 9–23. https://doi.org/10.1162/153535004773861688.

(24) Lower, S. K.; El-Sayed, M. A. The Triplet State and Molecular Electronic Processes in Organic Molecules. *Chem. Rev.* **1966**, *66* (2), 199–241. https://doi.org/10.1021/cr60240a004.

(25) Karunakaran, C. *Spin Resonance Spectroscopy 1st Edition*; 2018. https://doi.org/10.1002/cmr.a.20130.

(26) Neshvad, G.; Hoffman, M. Z. Reductive Quenching of the Luminescent Excited State of Tris(2,2'-Bipyrazine)Ruthenium(2+) Ion in Aqueous Solution. *J. Phys. Chem.* **1989**. https://doi.org/10.1021/j100343a044.

(27) Hoffman, M. Z. Cage Escape Yields from the Quenching of Excited Tris(Bipyridyl)Ruthenium(2+) by Methylviologen in Aqueous Solution. *J. Phys. Chem.* **1988**, *92* (12), 3458–3464. https://doi.org/10.1021/j100323a029.

(28) Darwent, J.R., K. K. Electron-Transf Er Reactions of Quinones , Hydroquinones and Methyl Viologen , Photosensitized By. *J. Chem. Soc. Faraday Trans. 2 Mol. Chem. Phys.* **1981**, *77*, 373–382.

(29) Ye, Y.; Sanford, M. S. Merging Visible-Light Photocatalysis and Transition-Metal Catalysis in the Copper-Catalyzed Trifluoromethylation of Boronic Acids with CF 3I. *J. Am. Chem. Soc.* **2012**, *134* (22), 9034–9037. https://doi.org/10.1021/ja301553c.

(30) Pindur, U.; Lemster, T. Advances in Marine Natural Products of the Indole and Annelated Indole Series: Chemical and Biological Aspects. *Curr. Med. Chem.* **2001**, *8*, 1681–1698.

(31) Gul, W.; Hamann, M. T. Indole Alkaloid Marine Natural Products: An Established Source of Cancer Drug Leads with Considerable Promise for the Control of Parasitic, Neurological and Other Diseases. *Life Sci.* **2005**, *78*, 442–453. https://doi.org/10.1016/j.lfs.2005.09.007.

(32) Gribble, G. W. *Indole Ring Synthesis: From Natural Products to Drug Discovery*; 2016.

(33) Russell Little, J.; Eisen, H. N. Evidence for Tryptophan in the Active Sites of Antibodies to Polynitrobenzenes. *Biochemistry* **1967**, *6* (10), 3119–3125. https://doi.org/10.1021/bi00862a020.

(34) Singhal, N.; Snow, C. D.; Pande, V. S. Using Path Sampling to Build Better Markovian State Models: Predicting the Folding Rate and Mechanism of a Tryptophan Zipper Beta Hairpin. *J. Chem. Phys.* **2004**, *121*, 415–425. https://doi.org/10.1063/1.1738647.

(35) Rosén, J.; Gottfries, J.; Muresan, S.; Backlund, A.; Oprea, T. I. Novel Chemical Space Exploration via Natural Products. *J. Med. Chem.* **2009**, *52*, 1953–1962. https://doi.org/10.1021/jm801514w.

(36) Cragg, G. M.; Grothaus, P. G.; Newman, D. J. Impact of Natural Products on Developing New Anti-Cancer Agents. *Chem. Rev.* **2009**, *109* (7), 3012–3043. https://doi.org/10.1021/cr900019j.

(37) Wu, Y. J. Heterocycles and Medicine. A Survey of the Heterocyclic Drugs Approved by the U.S. FDA from 2000 to Present. *Prog. Heterocycl. Chem.* **2012**, *24*, 1–53. https://doi.org/10.1016/B978-0-08-096807-0.00001-4.

(38) Larsen, L. K.; Moore, R. E.; Patterson, G. M. L. β-Carbolines from the Blue-Green Alga Dichothrix Baueriana. *J. Nat. Prod.* **1994**, *57* (3), 419–421. https://doi.org/10.1021/np50105a018.

(39) Hendrickson, J. B.; Göschke, R.; Rees, R. Total Synthesis of the Calycanthaceous Alkaloids. *Tetrahedron* **1964**, *20* (3), 565–579. https://doi.org/10.1016/S0040-4020(01)98619-3.

(40) Fang, C. L.; Horne, S.; Taylor, N.; Rodrigo, R. Dimerization of a 3-Substituted Oxindole at C-3 and Its Application to the Synthesis of (±)-Folicanthine. *J. Am. Chem. Soc.* **1994**, *116* (21), 9480–9486. https://doi.org/10.1021/ja00100a010.

(41) Johns, S. R.; Laimberton, J. A.; Smith, L. W.; Culvenor, C. C. J. The Isolation of Calycanthine and Pyrrolizidine Alkaloids from Bhesa Archboldiana (Celastraceae): An Unusual Co-Occurrence of Alkaloidal Types. **1970**, *23* (6), 1279–1282.

(42) Lebsack, A. D.; Link, J. T.; Overman, L. E.; Stearns, B. A. Enantioselective Total Synthesis of Quadrigemine C and Psycholeine. *J. Am. Chem. Soc.* **2002**, *124*, 9008–9009. https://doi.org/10.1021/ja0267425.

(43) Amador, T. A.; Verotta, L.; Nunes, D. S.; Elisabetsky, E. Antinociceptive Profile of Hodgkinsine. *Planta Med.* **2000**, *66*, 770–772. https://doi.org/10.1055/s-2000-9604.

(44) Nascimento, R. R. G.; Pimenta, A. T. A.; De Lima Neto, P.; Junior, J. R. C.; Costa-Lotufo, L. V.; Ferreira, E. G.; Tinoco, L. W.; Braz-Filho, R.; Silveira, E. R.; Lima, M. A. S. New Alkaloids from Margaritopsis Carrascoana (Rubiaceae). *J. Braz. Chem. Soc.* **2015**, *26*, 1152–1159. https://doi.org/10.5935/0103-5053.20150079.

(45) Jannic, V.; Guéritte, F.; Laprévote, O.; Serani, L.; Martin, M. T.; Sévenet, T.; Potier, P. Pyrrolidinoindoline Alkaloids from Psychotria Oleoides and Psychotria Lyciiflora. *J. Nat. Prod.* **1999**, *62*, 838–842. https://doi.org/10.1021/np9805387.

(46) Ghosh, S.; Bhunia, S.; Kakde, B. N.; De, S.; Bisai, A. Enantioselective Construction of Vicinal All-Carbon Quaternary Centers via Catalytic Double Asymmetric Decarboxylative Allylation. *Chem. Commun.* **2014**, *50*, 2434–2437. https://doi.org/10.1039/c3cc49064e.

(47) Link, J. T.; Overman, L. E. Stereocontrolled Total Syntheses of Meso-Chimonanthine and Meso-Calycanthine via a Novel Samarium Mediated Reductive Dialkylation. *J. Am. Chem. Soc.* **1996**, *118* (34), 8166–8167. https://doi.org/10.1021/ja961757m.

(48) Stephens, D. E.; Larionov, O. V. Straightforward Access to Hexahydropyrrolo[2,3-b]Indole Core by a Regioselective C3-Azo Coupling Reaction of Arenediazonium Compounds with Tryptamines. *European J. Org. Chem.* **2014**, *2014* (17), 3662–3670. https://doi.org/10.1002/ejoc.201402088.

(49) Overman, L. E.; Paone, D. V; Stearns, B. A.; Ir, V. Direct Stereo- and Enantiocontrolled Synthesis of Vicinal Stereogenic Quaternary Carbon Centers . Total Syntheses of Meso - and (-) -Chimonanthine and Uni V Ersity of California Recei V Ed May 24 , 1999 Among the Most Demanding Challenges Encountered In. **1999**, *121*, 7702–7703.

(50) Ghosh, S.; Chaudhuri, S.; Bisai, A. Oxidative Dimerization of 2-Oxindoles Promoted by KOtBu-I2: Total Synthesis of (±)-Folicanthine. *Org. Lett.* **2015**. https://doi.org/10.1021/acs.orglett.5b00032.

(51) Guo, C.; Song, J.; Huang, J. Z.; Chen, P. H.; Luo, S. W.; Gong, L. Z. Core-Structure-Oriented Asymmetric Organocatalytic Substitution of 3-Hydroxyoxindoles:

Application in the Enantioselective Total Synthesis of (+)-Folicanthine. *Angew. Chemie - Int. Ed.* **2012**, *51*, 1046–1050. https://doi.org/10.1002/anie.201107079.

(52) Mitsunuma, H.; Shibasaki, M.; Kanai, M.; Matsunaga, S. Catalytic Asymmetric Total Synthesis of Chimonanthine, Folicanthine, and Calycanthine through Double Michael Reaction of Bisoxindole. *Angew. Chemie - Int. Ed.* **2012**, *51*, 1–6. https://doi.org/10.1002/anie.201201132.

(53) Cordell, G. A.; Saxton, J. E. Chapter 1 Bisindole Alkaloids. *Alkaloids Chem. Physiol.* **1981**, *20*, 1–295. https://doi.org/10.1016/S1876-0813(08)60246-8.

(54) Wu, H.; He, Y. P.; Xu, L.; Zhang, D. Y.; Gong, L. Z. Asymmetric Organocatalytic Direct C(Sp2)-H/C(Sp3)-H Oxidative Cross-Coupling by Chiral Iodine Reagents. *Angew. Chemie - Int. Ed.* **2014**, *126*, 3534–3537. https://doi.org/10.1002/anie.201309967.

(55) Wang, J.; Yuan, Y.; Xiong, R.; Zhang-Negrerie, D.; Du, Y.; Zhao, K. Phenyliodine Bis(Trifluoroacetate)-Mediated Oxidative C-C Bond Formation: Synthesis of 3-Hydroxy-2-Oxindoles and Spirooxindoles from Anilides. *Org. Lett.* **2012**, *14* (9), 2210–2213. https://doi.org/10.1021/ol300418h.

(56) Moskowitz, M.; Balaraman, K.; Wolf, C. Organocatalytic Stereoselective Synthesis of Fluorinated 3,3'-Linked Bisoxindoles. *J. Org. Chem.* **2018**, *83*, 1661–1666. https://doi.org/10.1021/acs.joc.7b03084.

(57) Huang, Y. L.; Bao, W. H.; Ying, W. W.; Chen, W. T.; Gao, L. H.; Wang, X. Y.; Chen, G. P.; Ge, G. P.; Wei, W. T. Copper-Catalyzed Oxidative Dimerization of 2-Oxindoles under Base-Free Conditions. *Synlett* **2018**, *29* (11), 1485–1490. https://doi.org/10.1055/s-0037-1609757.

(58) Jia, W. L.; He, J.; Yang, J. J.; Gao, X. W.; Liu, Q.; Wu, L. Z. Homocoupling of 3-Halooxindole via Visible-Light Photocatalysis: A Mild Access to 3,3'-Bioxindoles. *J. Org. Chem.* **2016**. https://doi.org/10.1021/acs.joc.6b01045.

(59) Shen, X.; Zhou, Y.; Xi, Y.; Zhao, J.; Zhang, H. Copper Catalyzed Sequential Arylation-Oxidative Dimerization of o-Haloanilides: Synthesis of Dimeric HPI Alkaloids. *Chem. Commun.* **2015**, *51*, 14873–14876. https://doi.org/10.1039/c5cc05378a.

(60) Drouhin, P.; Hurst, T. E.; Whitwood, A. C.; Taylor, R. J. K. Substrate Scope in the Copper-Mediated Construction of Bis-Oxindoles via a Double C-H/Ar-H Coupling Process. *Tetrahedron* **2015**, *71* (39), 7124–7136. https://doi.org/10.1016/j.tet.2015.02.060.

(61) Min, B. K.; Lee, S.; Roh, H. J.; Ryu, J. Y.; Lee, J.; Kim, J. N. Synthesis of Dispirocyclohexadiene Bisoxindole from Morita-Baylis-Hillman Carbonate of Isatin. *Tetrahedron Lett.* **2017**, *58*, 3251–3255. https://doi.org/10.1016/j.tetlet.2017.07.013.

(62) Overman, L. E.; Paone, D. V.; Stearns, B. A. Direct Stereo- and Enantiocontrolled Synthesis of Vicinal Stereogenic Quaternary Carbon Centers. Total Syntheses of Meso- and (-)-Chimonanthine and (+)-Calycanthine [4]. *J. Am. Chem. Soc.* **1999**,

121, 7702–7703. https://doi.org/10.1021/ja991714g.

(63) De, S.; Das, M. K.; Roy, A.; Bisai, A. Synthesis of 2-Oxindoles Sharing Vicinal All-Carbon Quaternary Stereocenters via Organocatalytic Aldol Reaction. *J. Org. Chem.* **2016**, *81* (24), 12258–12274. https://doi.org/10.1021/acs.joc.6b02195.

(64) Hino, T.; Yamada, S. ichi. Total Synthesis of (±)-Folicanthine. *Tetrahedron Lett.* **1963**, *4* (25), 1757–1760. https://doi.org/10.1016/S0040-4039(01)90909-8.

(65) Chen, S. K.; Ma, W. Q.; Yan, Z. B.; Zhang, F. M.; Wang, S. H.; Tu, Y. Q.; Zhang, X. M.; Tian, J. M. Organo-Cation Catalyzed Asymmetric Homo/Heterodialkylation of Bisoxindoles: Construction of Vicinal All-Carbon Quaternary Stereocenters and Total Synthesis of (-)-Chimonanthidine. *J. Am. Chem. Soc.* **2018**, *140*, 10099–10103. https://doi.org/10.1021/jacs.8b05386.

(66) Tang, Z.; Shi, Y.; Mao, H.; Zhu, X.; Li, W.; Cheng, Y.; Zheng, W. H.; Zhu, C. Highly Enantioselective Synthesis of Bisoxindoles with Two Vicinal Quaternary Stereocenters via Lewis Base Mediated Addition of Oxindoles to Isatin-Derived Ketimines. *Org. Biomol. Chem.* **2014**, *12*, 6085–6088. https://doi.org/10.1039/c4ob01039f.

(67) Lee, H. J.; Lee, S.; Lim, J. W.; Kim, J. N. An Expedient Synthesis of Oxindole Dimers by Direct Oxidative Dimerization of Oxindoles. *Bull. Korean Chem. Soc.* **2013**, *34* (8), 2446–2450. https://doi.org/10.5012/bkcs.2013.34.8.2446.

(68) Nguyen, V. H.; Nishino, H. Novel Synthesis of Dihydropyrans and 2,8-Dioxabicylo[3.3.0]Oct-3-Enes Using Mn(III)-Based Oxidative Cyclization. *Tetrahedron Lett.* **2004**, *45* (17), 3373–3377. https://doi.org/10.1016/j.tetlet.2004.03.019.

(69) Snider, B. B.; Smith, R. B. Mn(III)-Based Oxidative Free-Radical Cyclizations of Alkenyl Meldrum's Acids. *Tetrahedron* **2002**, *58*, 25–34. https://doi.org/10.1016/S0040-4020(01)01054-7.

(70) Li, Y.; Wang, W. H.; Yang, S. D.; Li, B. J.; Feng, C.; Shi, Z. J. Oxidative Dimerization of N-Protected and Free Indole Derivatives toward 3,3'-Biindoles via Pd-Catalyzed Direct C-H Transformations. *Chem. Commun.* **2010**, *46*, 4553–4555. https://doi.org/10.1039/c0cc00486c.

(71) Wang, C. M.; Xia, P. J.; Xiao, J. A.; Li, J.; Xiang, H. Y.; Chen, X. Q.; Yang, H. Photoredox-Catalyzed Reductive Dimerization of Isatins and Isatin-Derived Ketimines: Diastereoselective Construction of 3,3'-Disubstituted Bisoxindoles. *J. Org. Chem.* **2017**, *82* (7), 3895–3900. https://doi.org/10.1021/acs.joc.6b03056.

(72) Zard, S. Z. Recent Progress in the Generation and Use of Nitrogen-Centred Radicals. *Chem. Soc. Rev.* **2008**, *31*, 1603–1618. https://doi.org/10.1039/b613443m.

(73) Horner, J. H.; Musa, O. M.; Bouvier, A.; Newcomb, M. Absolute Kinetics of Amidyl Radical Reactions. *J. Am. Chem. Soc.* **1998**, *120* (31), 7738–7748. https://doi.org/10.1021/ja981244a.

(74) Davies, J.; Svejstrup, T. D.; Fernandez Reina, D.; Sheikh, N. S.; Leonori, D. Visible-

Light-Mediated Synthesis of Amidyl Radicals: Transition-Metal-Free Hydroamination and N-Arylation Reactions. *J. Am. Chem. Soc.* **2016**, *138* (26), 8092–8095. https://doi.org/10.1021/jacs.6b04920.

(75) Perkins, M. J.; Ward, P.; Horsfield, A. A Probe for Homolytic Reactions in Solution. Part III.1Radicals by Hydrogen Abstraction. *J. Chem. Soc. B Phys. Org.* **1970**, No. 0, 395–400. https://doi.org/10.1039/J29700000395.

(76) Poelma, S. O.; Burnett, G. L.; Discekici, E. H.; Mattson, K. M.; Treat, N. J.; Luo, Y.; Hudson, Z. M.; Shankel, S. L.; Clark, P. G.; Kramer, J. W.; et al. Chemoselective Radical Dehalogenation and C-C Bond Formation on Aryl Halide Substrates Using Organic Photoredox Catalysts. *J. Org. Chem.* **2016**, *81* (16), 7155–7160. https://doi.org/10.1021/acs.joc.6b01034.

(77) Zhang, X. -M; Bordwell, F. G. Equilibrium Acidities and Homolytic Bond Dissociation Enthalpies of the Acidic C□H Bonds in Dialkyl Malonates and Related Compounds. *J. Phys. Org. Chem.* **1994**, *7* (12), 751–756. https://doi.org/10.1002/poc.610071214.

(78) Zhang, X. M.; Bordwell, F. G. Acidities and Homolytic Bond Dissociation Enthalpies (BDEs) of the Acidic H–A Bonds in Acyclic and Cyclic Alkoxycarbonyl Compounds (Esters and Carbamates). *J. Org. Chem.* **1994**, *59* (21), 6456–6458. https://doi.org/10.1021/jo00100a058.

(79) Zhang, X. M. Homolytic Bond Dissociation Energies of the Carbon-Halogen Bonds in the Benzyl Halide Radical Anion Intermediates Formed in Radical Nucleophilic Substitution Reactions. *J. Chem. Soc. Perkin Trans. 2* **1993**, 2275–2279. https://doi.org/10.1039/p29930002275.

(80) Melikyan, G. G. Manganese(III) Mediated Reactions of Unsaturated Systems. *Synthesis (Stuttg).* **1993**, 833–850.

(81) Klein, J. E. M. N.; Perry, A.; Pugh, D. S.; Taylor, R. J. K. First C-H Activation Route to Oxindoles Using Copper Catalysis. *Org. Lett.* **2010**, *12* (15), 3446–3449. https://doi.org/10.1021/ol1012668.

(82) Nicovich, J. M.; Shackelford, C. J.; Wine, P. H. Kinetics of the Br2-CH3CHO Photochemical Chain Reaction. *J. Photochem. Photobiol. A Chem.* **1990**, *51* (2), 141–153. https://doi.org/10.1016/1010-6030(90)87048-G.

(83) Chatgilialoglu, C.; Crich, D.; Komatsu, M.; Ryu, I. Chemistry of Acyl Radicals. *Chem. Rev.* **1999**, *99* (8), 1991–2069. https://doi.org/10.1021/cr9601425.

(84) Tanner, D. D.; Law, F. C. P. Free-Radical Acetoxy Group Migration. *J. Am. Chem. Soc.* **1969**, *91* (26), 7535–7537. https://doi.org/10.1021/ja01054a068.

(85) Grissom, J. W.; Klingberg, D.; Meyenburg, S.; Stallman, B. L. Enediyne- and Tributyltin Hydride-Mediated Aryl Radical Additions onto Various Radical Acceptors. *J. Org. Chem.* **1994**, *59* (25), 7876–7888. https://doi.org/10.1021/jo00104a053.

(86) Shepard, A. F.; Winslow, N. R.; John, R.; Johnson. The Simple Halogen Derivatives of Furan. *J. Am. Chem. Soc.* **1930**, *52*, 2083–2090.

https://doi.org/10.1021/ja01368a057.

(87) Shang, R.; Ji, D. S.; Chu, L.; Fu, Y.; Liu, L. Synthesis of α-Aryl Nitriles through Palladium-Catalyzed Decarboxylative Coupling of Cyanoacetate Salts with Aryl Halides and Triflates. *Angew. Chemie - Int. Ed.* **2011**, *50* (19), 4470–4474. https://doi.org/10.1002/anie.201006763.

(88) Shang, R.; Yang, Z. W.; Wang, Y.; Zhang, S. L.; Liu, L. Palladium-Catalyzed Decarboxylative Couplings of 2-(2-Azaaryl)Acetates with Aryl Halides and Triflates. *J. Am. Chem. Soc.* **2010**, *132*, 14391–14393. https://doi.org/10.1021/ja107103b.

(89) Shao, M.; Liang, H.; Liu, Y. L.; Qin, W.; Li, Z. Photo-Mediated Decarboxylative Cross Coupling of Quinoxalin-2(1H)-Ones with Aliphatic Carboxylic Acids in Aqueous Solution: Synthesis of Alkylated Quinoxalin-2(1H)-Ones and Preliminary Antifungal Evaluation Against Magnaporthe Grisea. *Asian J. Org. Chem.* **2020**, *9* (5), 782–787. https://doi.org/10.1002/ajoc.202000073.

(90) Huang, H.; Zhang, G.; Chen, Y. Dual Hypervalent Iodine(III) Reagents and Photoredox Catalysis Enable Decarboxylative Ynonylation under Mild Conditions. *Angew. Chemie - Int. Ed.* **2015**, *54* (27), 7872–7876. https://doi.org/10.1002/anie.201502369.

(91) Ventre, S.; Petronijevic, F. R.; MacMillan, D. W. C. Decarboxylative Fluorination of Aliphatic Carboxylic Acids via Photoredox Catalysis. *J. Am. Chem. Soc.* **2015**, *137*, 5654–5657. https://doi.org/10.1002/chin.201542087.

(92) Lu, S.; Gong, Y.; Zhou, D. Transition Metal-Free Oxidative Radical Decarboxylation/Cyclization for the Construction of 6-Alkyl/Aryl Phenanthridines. *J. Org. Chem.* **2015**, *80* (18), 9336–9341. https://doi.org/10.1021/acs.joc.5b01518.

(93) Ventre, S.; Petronijevic, F. R.; Macmillan, D. W. C. Decarboxylative Fluorination of Aliphatic Carboxylic Acids via Photoredox Catalysis. *J. Am. Chem. Soc.* **2015**, *137* (17), 5654–5657. https://doi.org/10.1021/jacs.5b02244.

(94) Rueda-Becerril, M.; Chatalova Sazepin, C.; Leung, J. C. T.; Okbinoglu, T.; Kennepohl, P.; Paquin, J. F.; Sammis, G. M. Fluorine Transfer to Alkyl Radicals. *J. Am. Chem. Soc.* **2012**, *134* (9), 4026–4029. https://doi.org/10.1021/ja211679v.

(95) Gooßen, L. J.; Rodríguez, N.; Gooßen, K. Carboxylic Acids as Substrates in Homogeneous Catalysis. *Angew. Chemie - Int. Ed.* **2008**, *47* (17), 3100–3120. https://doi.org/10.1002/anie.200704782.

(96) Jia, Y. X.; Kündig, E. P. Oxindole Synthesis by Direct Coupling of Csp2-H and C Sp3-H Centers. *Angew. Chemie - Int. Ed.* **2009**, *48* (9), 1636–1639. https://doi.org/10.1002/anie.200805652.

(97) Ding, S.; Jiao, N. N,N-Dimethylformamide: A Multipurpose Building Block. *Angew. Chemie - Int. Ed.* **2012**, *51* (37), 9226–9237. https://doi.org/10.1002/anie.201200859.

(98) Smith, L.; Nichols, J. The Synthesis of Aldehydes from Grignard Reagents. II. Polymethylbenzaldehydes. *J. Org. Chem.* **1941**, *6* (4), 489–506. https://doi.org/10.1021/jo01204a003.

(99) Jolit, A.; Vazquez-Rodriguez, S.; Yap, G. P. A.; Tius, M. A. Diastereospecific Nazarov Cyclization of Fully Substituted Dienones: Generation of Vicinal All-Carbon-Atom Quaternary Stereocenters. *Angew. Chemie - Int. Ed.* **2013**, *52*, 1–5. https://doi.org/10.1002/anie.201305218.

(100) Donald, J. R.; Taylor, R. J. K.; Petersen, W. F. Low-Temperature, Transition-Metal-Free Cross-Dehydrogenative Coupling Protocol for the Synthesis of 3,3-Disubstituted Oxindoles. *J. Org. Chem.* **2017**, *82* (20), 11288–11294. https://doi.org/10.1021/acs.joc.7b02085.

(101) Conrad, J. C.; Kong, J.; Laforteza, B. N.; MacMillan, D. W. C. Enantioselective α-Arylation of Aldehydes via Organo-SOMO Catalysis. An Ortho-Selective Arylation Reaction Based on an Open-Shell Pathway. *J. Am. Chem. Soc.* **2009**, *131*, 11640–11641. https://doi.org/10.1021/ja9026902.

(102) Bhunia, S.; Ghosh, S.; Dey, D.; Bisai, A. DDQ-Mediated Direct Intramolecular-Dehydrogenative-Coupling (IDC): Expeditious Approach to the Tetracyclic Core of Ergot Alkaloids. *Org. Lett.* **2013**, *15* (10), 2426–2429. https://doi.org/10.1021/ol400899e.

(103) Li, D.; Yu, W. Oxygen-Involved Oxidative Deacetylation of α-Substituted β-Acetyl Amides - Synthesis of α-Keto Amides. *Adv. Synth. Catal.* **2013**, *355* (18), 3708–3714. https://doi.org/10.1002/adsc.201300660.

(104) Gorokhovik, I.; Neuville, L.; Zhu, J. Trifluoroacetic Acid-Promoted Synthesis of 3-Hydroxy, 3-Amino and Spirooxindoles from α-Keto-N-Anilides. *Org. Lett.* **2011**, *13* (20), 5536–5539. https://doi.org/10.1021/ol202263a.

(105) Sai, K. K. S.; Esteves, P. M.; Da Penha, E. T.; Klumpp, D. A. Superacid-Promoted Reactions of α-Ketoamides and Related Systems. *J. Org. Chem.* **2008**, *73* (17), 6506–6512. https://doi.org/10.1021/jo801208m.

(106) Vogler, T.; Studer, A. Applications of TEMPO in Synthesis. *Synthesis (Stuttg).* **2008**, *13*, 1979–1993. https://doi.org/10.1055/s-2008-1078445.

(107) Jahn, U.; Hartmann, P.; Dix, I.; Jones, P. G. Lithium Malonate Enolates as Precursors for Radical Reactions - Convenient Induction of Radical Cyclizations with Either Radical or Cationic Termination. *European J. Org. Chem.* **2001**, *2001* (17), 3333–3355. https://doi.org/10.1002/1099-0690(200109)2001:17<3333::AID-EJOC3333>3.0.CO;2-A.

(108) Ward, R. M.; Schomaker, J. M. Allene TrifunctionalizationviaAmidyl Radical Cyclization and TEMPO Trapping. *J. Org. Chem.* **2021**, *86* (13), 8891–8899. https://doi.org/10.1021/acs.joc.1c00675.

(109) McDonald, B. R.; Scheidt, K. A. Intermolecular Reductive Couplings of Arylidene Malonates via Lewis Acid/Photoredox Cooperative Catalysis. *Org. Lett.* **2018**, *20* (21), 6877–6881. https://doi.org/10.1021/acs.orglett.8b02893.

(110) Betori, R. C.; McDonald, B. R.; Scheidt, K. A. Reductive Annulations of Arylidene Malonates with Unsaturated Electrophiles Using Photoredox/Lewis Acid Cooperative Catalysis. *Chem. Sci.* **2019**, *10*, 3353–3359.

https://doi.org/10.1039/C9SC00302A.

(111) Baś, S.; Yamashita, Y.; Kobayashi, S. Development of Brønsted Base-Photocatalyst Hybrid Systems for Highly Efficient C-C Bond Formation Reactions of Malonates with Styrenes. *ACS Catal.* **2020**, *10* (18), 10546–10550. https://doi.org/10.1021/acscatal.0c02716.

(112) Zoller, J.; Fabry, D. C.; Ronge, M. A.; Rueping, M. Synthesis of Indoles Using Visible Light: Photoredox Catalysis for Palladium-Catalyzed C-H Activation. *Angew. Chemie - Int. Ed.* **2014**, *53* (48), 13264–13268. https://doi.org/10.1002/anie.201405478.

(113) Mazodze, C. M.; Petersen, W. F. Silver-Catalysed Double Decarboxylative Addition-Cyclisation-Elimination Cascade Sequence for the Synthesis of Quinolin-2-Ones. *Org. Biomol. Chem.* **2022**, *20*, 3469–3474. https://doi.org/10.1039/d2ob00521b.

(114) Semmes, J. G.; Bevans, S. L.; Mullins, C. H.; Shaughnessy, K. H. Arylation of Diethyl Malonate and Ethyl Cyanoacetate Catalyzed by Palladium/Di-Tert-Butylneopentylphosphine. *Tetrahedron Lett.* **2015**, *56* (23), 3447–3450. https://doi.org/10.1016/j.tetlet.2015.01.072.

(115) Hossain, A.; Bhattacharyya, A.; Reiser, O. Copper's Rapid Ascent in Visible-Light Photoredox Catalysis. *Science (80-.).* **2019**, *364* (450), 1–11. https://doi.org/10.1126/science.aav9713.

(116) Kautzky, J. A.; Wang, T.; Evans, R. W.; Macmillan, D. W. C. Decarboxylative Trifluoromethylation of Aliphatic Carboxylic Acids. *J. Am. Chem. Soc.* **2018**, *140* (21), 6522–6526. https://doi.org/10.1021/jacs.8b02650.

(117) W. C. MacMillan, D.; Liang, Y.; Zhang, X. Decarboxylative Sp3 C–N Coupling via Dual Copper/Photoredox Catalysis. *Nature* **2018**, *559*, 83–88. https://doi.org/10.26434/chemrxiv.5877868.

(118) Reed, N. L.; Herman, M. I.; Miltchev, V. P.; Yoon, T. P. Photocatalytic Oxyamination of Alkenes: Copper(II) Salts as Terminal Oxidants in Photoredox Catalysis. *Org. Lett.* **2018**, *20* (22), 7345–7350. https://doi.org/10.1021/acs.orglett.8b03345.

(119) Shimazumi, R.; Tanimoto, R.; Tobisu, M. Nickel/Photoredox Dual-Catalyzed Conversion of Allyl Esters to Ketones via the Formal Deletion of Oxygen. *Org. Lett.* **2023**, *25* (34), 6440–6445. https://doi.org/10.1021/acs.orglett.3c02606.

(120) Badir, S. O.; Molander, G. A. Developments in Photoredox/Nickel Dual-Catalyzed 1,2-Difunctionalizations. *Chem* **2020**, *6* (6), 1327–1339. https://doi.org/10.1016/j.chempr.2020.05.013.

(121) Tellis, J. C.; Kelly, C. B.; Primer, D. N.; Jouffroy, M.; Patel, N. R.; Molander, G. A. Single-Electron Transmetalation via Photoredox/Nickel Dual Catalysis: Unlocking a New Paradigm for Sp3-Sp2 Cross-Coupling. *Acc. Chem. Res.* **2016**, *49* (7), 1429–1439. https://doi.org/10.1021/acs.accounts.6b00214.

(122) Koványi-Lax, G.; Hargitai, C.; Ábrányi-Balogh, P.; Nagy, T.; Tóth, G.; Garádi, Z.; Németh, G.; Pandur, A.; Horváth, S.; Dancsó, A.; et al. Experimental and

Computational Study of BF3-Catalyzed Transformations of Ortho-(Pivaloylaminomethyl)Benzaldehydes: An Unexpected Difference from TFA Catalysis. *Org. Biomol. Chem.* **2022**, *20*, 1933–1944. https://doi.org/10.1039/d1ob02308j.

(123) McLean, E. B.; Lee, A. L. Dual Copper- and Photoredox-Catalysed Reactions. *Tetrahedron* **2018**, *74* (38), 4881–4902. https://doi.org/10.1016/j.tet.2018.07.032.

(124) Snider, B. B. Manganese(III)-Based Oxidative Free-Radical Cyclizations. *Chem. Rev.* **1996**, *96*, 339–363. https://doi.org/10.1021/cr950026m.

(125) Ayhan S. Demir; Mustafa Emrullahoglu. Manganese(III) Acetate: A Versatile Reagent in Organic Chemistry. *Curr. Org. Synth.* **2007**, *4*, 321–350. https://doi.org/10.2174/157017907781369289.

(126) Böhm, H. J.; Banner, D.; Bendels, S.; Kansy, M.; Kuhn, B.; Müller, K.; Obst-Sander, U.; Stahl, M. Fluorine in Medicinal Chemistry. *ChemBioChem* **2004**, *5* (5), 637–643. https://doi.org/10.1002/cbic.200301023.

(127) Shimizu, M.; Hiyama, T. Modern Synthetic Methods for Fluorine-Substituted Target Molecules. *Angew. Chemie - Int. Ed.* **2004**, *44* (2), 214–231. https://doi.org/10.1002/anie.200460441.

(128) Mann, J. Modern Methods for the Introduction of Fluorine into Organic Molecules: An Approach to Compounds with Altered Chemical and Biological Activities. *Chem. Soc. Rev.* **1987**, *16*, 381–436. https://doi.org/10.1039/CS9871600381.

(129) Noriega, S.; Cardoso-Ortiz, J.; López-Luna, A.; Cuevas-Flores, M. D. R.; Flores De La Torre, J. A. The Diverse Biological Activity of Recently Synthesized Nitro Compounds. *Pharmaceuticals* **2022**, *15* (6), 717. https://doi.org/10.3390/ph15060717.

(130) Squella, J.; Bollo, S.; Nunez-Vergara, L. Recent Developments in the Electrochemistry of Some Nitro Compounds of Biological Significance. *Curr. Org. Chem.* **2005**, *9* (6), 565–581. https://doi.org/10.2174/1385272053544380.

(131) Taylor, R. D.; Maccoss, M.; Lawson, A. D. G. Rings in Drugs. *J. Med. Chem.* **2014**, *57* (14), 5845–5859. https://doi.org/10.1021/jm4017625.

(132) Bauer, M. R.; Di Fruscia, P.; Lucas, S. C. C.; Michaelides, I. N.; Nelson, J. E.; Storer, R. I.; Whitehurst, B. C. Put a Ring on It: Application of Small Aliphatic Rings in Medicinal Chemistry. *RSC Med. Chem.* **2021**, *12*, 448–471. https://doi.org/10.1039/d0md00370k.

(133) Lovering, F. Escape from Flatland 2: Complexity and Promiscuity. *Medchemcomm* **2013**, No. 4, 515–519. https://doi.org/10.1039/c2md20347b.

(134) O'Gara, J. P.; Humphreys, H. Staphylococcus Epidermidis Biofilms: Importance and Implications. *J. Med. Microbiol.* **2001**, *50* (7). https://doi.org/10.1099/0022-1317-50-7-582.

(135) Lau, G. W.; Hassett, D. J.; Ran, H.; Kong, F. The Role of Pyocyanin in Pseudomonas Aeruginosa Infection. *Trends Mol. Med.* **2004**, *10* (12), 599–606.

https://doi.org/10.1016/j.molmed.2004.10.002.

(136) Espinoza-Moraga, M.; Njuguna, N. M.; Mugumbate, G.; Caballero, J.; Chibale, K. In Silico Comparison of Antimycobacterial Natural Products with Known Antituberculosis Drugs. *J. Chem. Inf. Model.* **2013**, *53* (3), 649–660. https://doi.org/10.1021/ci300467b.

(137) Kumar, M.; Singh, K.; Naran, K.; Hamzabegovic, F.; Hoft, D. F.; Warner, D. F.; Ruminski, P.; Abate, G.; Chibale, K. Design, Synthesis, and Evaluation of Novel Hybrid Efflux Pump Inhibitors for Use against Mycobacterium Tuberculosis. *ACS Infect. Dis.* **2016**, *2* (10), 714–725. https://doi.org/10.1021/acsinfecdis.6b00111.

(138) Bindra, J. S.; Manske, R. H. *In The Alkaloids*; 1973.

(139) Saxton, J. E.; Cordell, G. A. Synthesis of the Aspidosperma Alkaloids. *In The Alkaloids* **1998**, *50*, 343.

(140) Turner, H. Spiroindolone NITD609 Is a Novel Antimalarial Drug That Targets the P-Type ATPase PfATP4. *Future Med. Chem.* **2016**, *8* (2). https://doi.org/10.4155/fmc.15.177.

(141) Pilátová, M.; Šarišský, M.; Kutschy, P.; Miroššay, A.; Mezencev, R.; Čurillová, Z.; Suchý, M.; Monde, K.; Mirossay, L.; Mojžiš, J. Cruciferous Phytoalexins: Antiproliferative Effects in T-Jurkat Leukemic Cells. *Leuk. Res.* **2005**, *29* (4), 415–421. https://doi.org/10.1016/j.leukres.2004.09.003.

(142) Frisvad, J. C.; Smedsgaard, J.; Larsen, T. O.; Samson, R. A. Mycotoxins, Drugs and Other Extrolites Produced by Species in Penicillium Subgenus Penicillium. *Stud. Mycol.* **2004**, *49*, 201–241.

(143) Goboza, M.; Meyer, M.; Aboua, Y. G.; Oguntibeju, O. O. In Vitro Antidiabetic and Antioxidant Effects of Different Extracts of Catharanthus Roseus and Its Indole Alkaloid, Vindoline. *Molecules* **2020**, *25* (23), 5546. https://doi.org/10.3390/molecules25235546.

(144) Shangary, S.; Qin, D.; McEachern, D.; Liu, M.; Miller, R. S.; Qiu, S.; Nikolovska-Coleska, Z.; Ding, K.; Wang, G.; Chen, J.; et al. Temporal Activation of P53 by a Specific MDM2 Inhibitor Is Selectively Toxic to Tumors and Leads to Complete Tumor Growth Inhibition. *Proc. Natl. Acad. Sci. U. S. A.* **2008**, *105*, 3933–3938. https://doi.org/10.1073/pnas.0708917105.

(145) Rottmann, M.; McNamara, C.; Yeung, B. K. S.; Lee, M. C. S.; Zou, B.; Russell, B.; Seitz, P.; Plouffe, D. M.; Dharia, N. V.; Tan, J.; et al. Spiroindolones, a Potent Compound Class for the Treatment of Malaria. *Science (80-.).* **2010**, *329*, 1175–1180. https://doi.org/10.1126/science.1193225.

(146) Očenášová, L.; Kutschy, P.; Gonda, J.; Pilátová, M.; Gönciová, G.; Mojžiš, J.; Pazdera, P. Synthesis of New 5-Bromo Derivatives of Indole and Spiroindole Phytoalexins. *Chem. Pap.* **2016**, *70*, 635–648. https://doi.org/10.1515/chempap-2015-0230.

(147) Lin, H.; Danishefsky, S. J. Gelsemine: A Thought-Provoking Target for Total Synthesis. *Angew. Chemie - Int. Ed.* **2003**, *42*, 36–51.

https://doi.org/10.1002/anie.200390048.

(148) Tanaka, K.; Mori, Y.; Narasaka, K. Synthesis of Spiro[Indoline-3,2'-Pyrrolidine] Derivatives from β-3-Indolyl Ketone Oximes. *Chem. Lett.* **2004**, *33* (1), 26–27. https://doi.org/10.1246/cl.2004.26.

(149) Wang, P. F.; Chen, C.; Chen, H.; Han, L. S.; Liu, L.; Sun, H.; Wen, X.; Xu, Q. L. Concise Synthesis of Spiro[Indoline-3,2'-Pyrrolidine] and 1-Azacarbazole Derivatives via Copper-Catalyzed Cyclization of Indoles. *Adv. Synth. Catal.* **2017**, *359* (14), 2339–2344. https://doi.org/10.1002/adsc.201700073.

(150) Stache, E. E.; Ertel, A. B.; Rovis, T.; Doyle, A. G. Generation of Phosphoranyl Radicals via Photoredox Catalysis Enables Voltage-Independent Activation of Strong C-O Bonds. *ACS Catal.* **2018**, *8* (12), 11134–11139. https://doi.org/10.1021/acscatal.8b03592.

(151) Fabry, D. C.; Ronge, M. A.; Rueping, M. Immobilization and Continuous Recycling of Photoredox Catalysts in Ionic Liquids for Applications in Batch Reactions and Flow Systems: Catalytic Alkene Isomerization by Using Visible Light. *Chem. - A Eur. J.* **2015**, *21* (14), 5350–5354. https://doi.org/10.1002/chem.201406653.

(152) Minakata, S.; Okumura, S.; Nagamachi, T.; Takeda, Y. Generation of Nitrile Oxides from Oximes Using t -BuOI and Their Cycloaddition. *Org. Lett.* **2011**, *13* (11), 2966–2969. https://doi.org/10.1021/ol2010616.

(153) Lopes, E. F.; Penteado, F.; Thurow, S.; Pinz, M.; Reis, A. S.; Wilhelm, E. A.; Luchese, C.; Barcellos, T.; Dalberto, B.; Alves, D.; et al. Synthesis of Isoxazolines by the Electrophilic Chalcogenation of β,γ-Unsaturated Oximes: Fishing Novel Anti-Inflammatory Agents. *J. Org. Chem.* **2019**, *84* (19), 12452–12462. https://doi.org/10.1021/acs.joc.9b01754.

(154) Young, D. G. J.; Gomez-Bengoa, E.; Hoveyda, A. H. Diastereoselective Intramolecular Cycloaddition of Vinylsilanes and Silyl Nitronates. Effective Control of Remote Acyclic Asymmetry. *J. Org. Chem.* **1999**, *64* (3), 692–693. https://doi.org/10.1021/jo982180p.

(155) Bonne, D.; Salat, L.; Dulcère, J. P.; Rodriguez, J. Sequential Organocatalyzed Michael Addition/[3 + 2]-Heterocyclization for the Stereoselective Synthesis of Fused-Isoxazoline Precursors of Enantiopure Cyclopentanoids. *Org. Lett.* **2008**, *10* (23), 5409–5412. https://doi.org/10.1021/ol8023133.

(156) Sibi, M. P.; Itoh, K.; Jasperse, C. P. Chiral Lewis Acid Catalysis in Nitrile Oxide Cycloadditions. *J. Am. Chem. Soc.* **2004**, *126* (17), 5366–5367. https://doi.org/10.1021/ja0318636.

(157) Jäger, V.; Buß, V.; Schwab, W. Syntheses via Isoxazolines III. Diastereoselective Synthesis of γ-Amino-Alcohols with 2 and 3 Chiral Centres. *Tetrahedron Lett.* **1978**, *34*, 3133–3136. https://doi.org/10.1016/S0040-4039(01)94963-9.

(158) Curran, D. P.; Kim, B. H.; Daugherty, J.; Heffner, T. A. The Preparation of Optically Active Δ2- Isoxazolines. A Model for Asymmetric Induction in the Non Lewis Acid Catalyzed Reactions of Oppolzer's Chiral Sultam. *Tetrahedron Lett.* **1988**, *29* (29),

3555–3558. https://doi.org/10.1016/0040-4039(88)85291-2.

(159) Oppolzer, W.; Kingma, A. J.; Pillai, S. K. Enantiomerically Pure Isoxazolines via Addition of Nitrile Oxides to Chiral N-Acryloyl Toluene-2,α-Sultams. *Tetrahedron Lett.* **1991**, *32* (37), 4893–4896. https://doi.org/10.1016/S0040-4039(00)93489-0.

(160) Dong, L.; Geng, C.; Jiao, P. Silyl Nitronate Cycloadditions Catalyzed by Cu(II)-Bisoxazoline. *J. Org. Chem.* **2015**, *80* (21), 10992–11002. https://doi.org/10.1021/acs.joc.5b02035.

(161) Yoshimura, A.; Zhu, C.; Middleton, K. R.; Todora, A. D.; Maskaev, A. V.; Zhdankin, V. V. Hypoiodite Mediated Synthesis of Isoxazolines from Aldoximes and Alkenes Using Catalytic KI and Oxone as the Terminal Oxidant. *Chem. Commun.* **2013**, *49* (42), 4800–4802. https://doi.org/10.1039/c3cc41164h.

(162) Shi, D.; Qin, H. T.; Zhu, C.; Liu, F. Selectfluor-Bu4NI-Mediated C(Sp3)-H Oxidation in Aqueous Media: Synthesis of Δ2-Isoxazolines from Oximes. *European J. Org. Chem.* **2015**, *2015* (23), 5084–5088. https://doi.org/10.1002/ejoc.201500780.

(163) Holman, S. D. L.; Wills, A. G.; Fazakerley, N. J.; Poole, D. L.; Coe, D. M.; Berlouis, L. A.; Reid, M. Electrochemical Synthesis of Isoxazolines: Method and Mechanism. *Chem. - A Eur. J.* **2022**, *28* (13), e202103728. https://doi.org/10.1002/chem.202103728.

(164) Amir, M.; Javed, S. A.; Kumar, H. Design and Synthesis of 3-[3-(Substituted Phenyl)-4-Piperidin-1-Ylmethyl/- 4-Morpholin-4-Ylmethyl-4,5-Dihydro-Isoxazol-5-Yl]-1H-Indoles as Potent Anti-Inflammatory Agents. *Med. Chem. Res.* **2010**, *19*, 299–310. https://doi.org/10.1007/s00044-009-9194-8.

(165) Chaitanya, M. V. S. K.; Reddy, P. O. V.; Nikhil, K.; Kumar, A.; Shah, K.; Kumar, D. Synthesis and Anticancer Activity Studies of Indolylisoxazoline Analogues. *Bioorganic Med. Chem. Lett.* **2018**, *28*, 2842–2845. https://doi.org/10.1016/j.bmcl.2018.07.035.

(166) Hawash, M.; Kahraman, D. C.; Ergun, S. G.; Cetin-Atalay, R.; Baytas, S. N. Synthesis of Novel Indole-Isoxazole Hybrids and Evaluation of Their Cytotoxic Activities on Hepatocellular Carcinoma Cell Lines. *BMC Chem.* **2021**, *15* (66). https://doi.org/10.1186/s13065-021-00793-8.

(167) Reed, N. L.; Yoon, T. P. Oxidase Reactions in Photoredox Catalysis. *Chem. Soc. Rev.* **2021**, *50*, 2954–2967. https://doi.org/10.1039/d0cs00797h.

(168) Jin, J.; MacMillan, D. W. C. Direct α-Arylation of Ethers through the Combination of Photoredox-Mediated C-H Functionalization and the Minisci Reaction. *Angew. Chemie - Int. Ed.* **2015**, *54* (5), 1565–1569. https://doi.org/10.1002/anie.201410432.

(169) Yayla, H. G.; Peng, F.; Mangion, I. K.; McLaughlin, M.; Campeau, L. C.; Davies, I. W.; Dirocco, D. A.; Knowles, R. R. Discovery and Mechanistic Study of a Photocatalytic Indoline Dehydrogenation for the Synthesis of Elbasvir. *Chem. Sci.* **2016**, *7* (3), 2066–2073. https://doi.org/10.1039/c5sc03350k.

(170) Freeman, D. B.; Furst, L.; Condie, A. G.; Stephenson, C. R. J. Functionally Diverse

Nucleophilic Trapping of Iminium Intermediates Generated Utilizing Visible Light. *Org. Lett.* **2012**, *14* (1), 94–97. https://doi.org/10.1021/ol202883v.

(171) Fischer, E.; Jourdan, F. Ueber Die Hydrazine Der Brenztraubensäure. *Berichte der Dtsch. Chem. Gesellschaft* **1883**, *16*, 2241–2245. https://doi.org/10.1002/cber.188301602141.

(172) Gribble, G. W. *Indole Ring Synthesis: From Natural Products to Drug Discovery*; 2016. https://doi.org/10.1002/9781118695692.

(173) Inman, M.; Moody, C. J. Indole Synthesis-Something Old, Something New. *Chem. Sci.* **2013**, *4*, 29–41. https://doi.org/10.1039/c2sc21185h.

(174) Humphrey, G. R.; Kuethe, J. T. Practical Methodologies for the Synthesis of Indoles. *Chem. Rev.* **2006**, *106* (7), 2875–2911. https://doi.org/10.1021/cr0505270.

(175) Rogers, C. U.; Corson, B. B. One-Step Synthesis of 1,2,3,4-Tetrahydrocarbazole and 1,2-Benzo-3,4-Dihydrocarbazole. *J. Am. Chem. Soc.* **1947**, *69*, 2910–2911. https://doi.org/10.1021/ja01203a506.

(176) Chen, S.; Cai, M.; Huang, J.; Yao, H.; Lin, A. Cobalt-Catalyzed Dearomatization of Indoles via Transfer Hydrogenation to Afford Polycyclic Indolines. *Org. Lett.* **2021**, *23* (6), 2212–2216. https://doi.org/10.1021/acs.orglett.1c00354.

(177) Bessard, Y. Process Development of 5-Methoxy-1H-Indole-2-Carboxylic Acid from Ethyl 2-Methylmalonate. *Org. Process Res. Dev.* **1998**, *2* (4), 214–220. https://doi.org/10.1021/op980006x.

(178) Fang, X.; Gao, S.; Wu, Z.; Yao, H.; Lin, A. Pd(II)-Catalyzed Oxidative Dearomatization of Indoles: Substrate-Controlled Synthesis of Indolines and Indolones. *Org. Chem. Front.* **2017**, *4*, 292–296. https://doi.org/10.1039/c6qo00698a.

(179) Varma, P. P.; Sherigara, B. S.; Mahadevan, K. M.; Hulikal, V. Efficient and Straightforward Synthesis of Tetrahydrocarbazoles and 2,3-Dimethyl Indoles Catalyzed by CAN. *Synth. Commun.* **2009**, *39* (1), 158–165. https://doi.org/10.1080/00397910802370719.

(180) Welch, W. M. Pyridine Hydrochloride-Catalyzed Fischer Indole Reactions. *Synth.* **1977**, *9*, 645–646. https://doi.org/10.1055/s-1977-24518.

(181) McKew, J. C.; Foley, M. A.; Thakker, P.; Behnke, M. L.; Lovering, F. E.; Sum, F. W.; Tam, S.; Wu, K.; Shen, M. W. H.; Zhang, W.; et al. Inhibition of Cytosolic Phospholipase A2α: Hit to Lead Optimization. *J. Med. Chem.* **2006**, *49* (1), 135–158. https://doi.org/10.1021/jm0507882.

(182) Lerch, S.; Unkel, L. N.; Brasholz, M. Tandem Organocatalysis and Photocatalysis: An Anthraquinone-Catalyzed Indole-C3-Alkylation/Photooxidation/1,2-Shift Sequence. *Angew. Chemie - Int. Ed.* **2014**, *53* (25), 6558–6562. https://doi.org/10.1002/anie.201402920.

(183) Frahm, M.; von Drathen, T.; Gronbach, L. M.; Voss, A.; Lorenz, F.; Bresien, J.; Villinger, A.; Hoffmann, F.; Brasholz, M. Visible-Light Cascade Photooxygenation

of Tetrahydrocarbazoles and Cyclohepta[b]Indoles: Access to C , N - Diacyliminium Ions. *Angew. Chemie* **2020**, *132* (30), 12550–12554. https://doi.org/10.1002/ange.202007549.

(184) Dinh, A. N.; Nguyen, A. D.; Aceves, E. M.; Albright, S. T.; Cedano, M. R.; Smith, D. K.; Gustafson, J. L. Photocatalytic Oxidative C-H Thiolation: Synthesis of Benzothiazoles and Sulfenylated Indoles. *Synlett* **2019**, *30* (14), 1648–1655. https://doi.org/10.1055/s-0039-1690107.

(185) Cheng, Y.; Zhao, Q.; Zhang, X.; You, S. Asymmetric Dearomatization of Indole Derivatives with N-Hydroxycarbamates Enabled by Photoredox Catalysis. *Angew. Chemie* **2019**, *131* (50), 18237–18242. https://doi.org/10.1002/ange.201911144.

(186) Oikawa, Y.; Yonemitsu, O. Selective Oxidation of the Side Chain at C-3 of Indoles. *J. Org. Chem.* **1977**, *42* (7), 1213–1216. https://doi.org/10.1021/jo00427a024.

(187) Yi, L.; Zhu, C.; Chen, X.; Yue, H.; Ji, T.; Ma, Y.; Cao, Y.; Kancherla, R.; Rueping, M. O-H Bond Activation of β,γ-Unsaturated Oximes via Hydrogen Atom Transfer (HAT) and Photoredox Dual Catalysis. *Chem. Sci.* **2023**, *14* (48), 14271–14279. https://doi.org/10.1039/d3sc04410f.

(188) Murray, P. R. D.; Cox, J. H.; Chiappini, N. D.; Roos, C. B.; McLoughlin, E. A.; Hejna, B. G.; Nguyen, S. T.; Ripberger, H. H.; Ganley, J. M.; Tsui, E.; et al. Photochemical and Electrochemical Applications of Proton-Coupled Electron Transfer in Organic Synthesis. *Chem. Rev.* **2022**, *122* (2), 2017–2291. https://doi.org/10.1021/acs.chemrev.1c00374.

Chapter 5: Experimental data

General remarks

Reactants and solvents were purchased from commercially available sources (Sigma-Aldrich/ScienceWorld/Kimix/Combi-Blocks) and used without further purification unless stated otherwise. THF was freshly distilled from sodium wire and benzophenone, and CH_2Cl_2 was distilled from phosphorus pentoxide. All reactions were carried out in oven-dried glassware at room temperature under an inert argon atmosphere, unless stated otherwise. Where necessary, increased temperatures were achieved via a Heidolph MR Hei standard hot plate and a silicone oil bath or heating mantle. In contrast, an ice bath with sodium chloride was used to achieve 0°C conditions. Reaction progress was monitored via TLC analysis was done using Merck silica gel 60F254 precoated aluminium plates and run in DCM:MeOH and/or Ethyl acetate:Hexane whenever possible and visualised under UV light using Lasec UV lamp at 254 nm and/or anisaldehyde, $KMnO_4$, Vanillin or Ninhydrin solution and heated using a heat gun. Solvents were reduced using a Buchi R-210 Rotavapor. All products were dried using a high-vacuum line pump before yields were determined and spectroscopic and analytical analyses were performed. ^{1}H, ^{13}C and ^{19}F Nuclear Magnetic Resonance (NMR) spectra were obtained on a Varian Mercury spectrophotometer for ^{1}H-NMR at 300 MHz (75.5 MHz for ^{13}C), a Bruker XR400 MHz spectrophotometer for ^{1}H-NMR at 400 MHz (101 for ^{13}C) 13C at 100.6 MHz) and a Bruker XR600 MHz for ^{1}H-NMR at 600 MHz (151 for ^{13}C). Spectral data was obtained at 295 K. All chemical shifts are reported in the customary δ notation of parts per million (ppm), using tetramethylsilane (TMS) as the internal standard where δ=0.0 ppm and referenced to residual solvent; $CDCl_3$ = 7.26 ppm for ^{1}H and 77.16 ppm for ^{13}C; DMSO = 2.50 ppm for ^{1}H and 39.52 for ^{13}C. Coupling constants are reported in Hertz (Hz) and spin multiplicities in abbreviated conventional format: s = singlet, d = doublet, dd = doublet of doublets, ddd = doublet of doublet of doublets and m = multiplet. Infrared (IR) spectra were obtained using a Perkin-Elmer 100 FT-IR spectrometer. High resolution mass spectrometry data was characterised by the University of Stellenbosch's mass spectrometry service via an electrospray positive mode with a time-of-flight analyser system on a Waters Synapt G2 machine.

Chapter 3 data

General schemes[1,2]

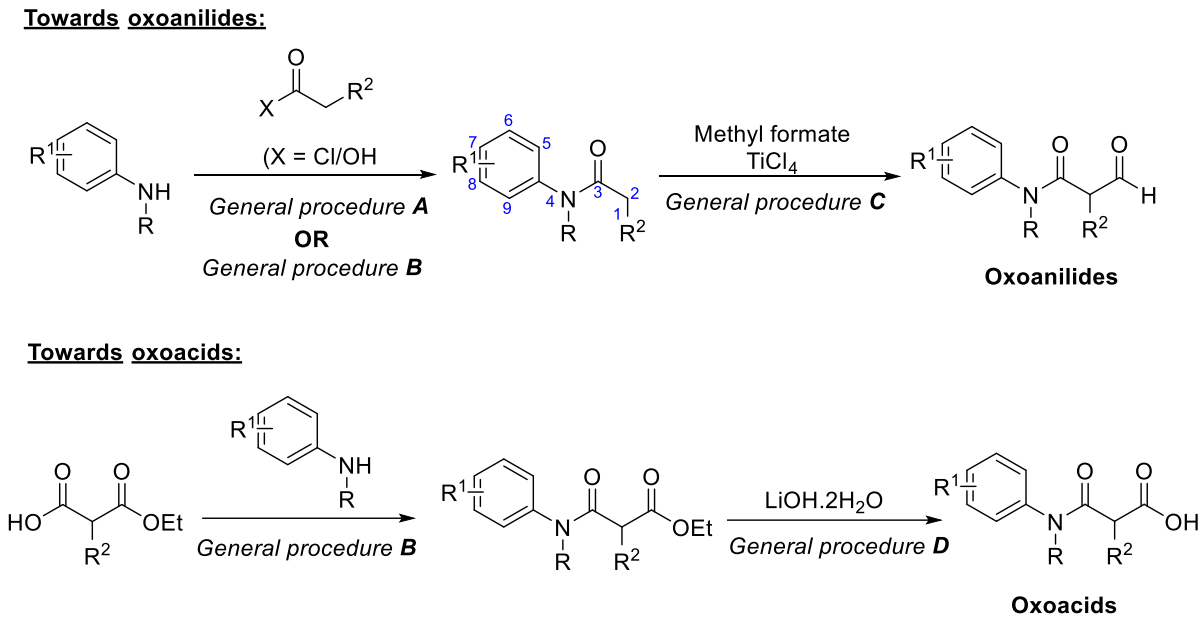

Figure 5.1. General scheme for the synthesis of oxoanilides and oxoacid precursors.

General procedure A: Synthesis of anilides from acid chlorides.

To aniline (1.0 eq.) and triethylamine (1.2 eq.) in dry CH_2Cl_2 (~3 mL/mmol of aniline) at 0 °C under Ar atomsphere, was added acid chloride (1.2 eq.) dropwise and the resultant solution allowed to warm up to room temperature. After TLC analysis indicated full conversion of the starting material (1.5–3 h) an equal amount of deionized water was added. The layers were separated, and the aqueous layer was reextracted with CH_2Cl_2 (x2). The combined organic extracts were washed with saturated aqueous $NaHCO_3$, dried over $MgSO_4$, filtered and concentrated in vacuo to give anilide which was sufficiently pure to be used without further purification.

General procedure B: Synthesis of anilides from carboxylic acids.

To a mixture of aniline (1 eq.), carboxylic acid (1.2 eq.) and 2-chloro-1-methylpyridinium iodide (1.2–1.4 eq.) in CH_2Cl_2 (5 mL/mmol of aniline) at 0 °C under argon, was added DIPEA (3 eq.) dropwise and the reaction mixture allowed to warm slowly to room

temperature. After 4 h an equal amount of deionized water was added, and the layers separated. The aqueous layer was reextracted with CH_2Cl_2 (x3), the combined organic extracts dried over $MgSO_4$ and concentrated in vacuo. The resulting crude product was purified by column chromatography on silica gel (Hexanes/EtOAc gradient) to give anilide.

General procedure C: Synthesis of β-oxoanilides.

To a solution of anilide (1 eq.) and methyl formate (6 eq.) in dry CH_2Cl_2 (4 mL/mmol of anilide) at 0 °C under Argon, was added neat $TiCl_4$ (3 eq.) dropwise. The reaction was left to stir at this temperature for 1 hr after which triethylamine (3.5 eq.) was added dropwise and the reaction allowed to warm up to room temperature over a period of 6 hours. The reaction was then quenched with an equal amount of deionized water, the organic layer separated and the aqueous layer reextracted with CH_2Cl_2 (x3). The combined organic extracts were washed with aq. $NaHCO_3$ (x2), dried over $MgSO_4$ and concentrated in vacuo. The resulting crude product was purified by column chromatography on silica gel (Hexanes/EtOAc gradient) to give the resultant oxoanilide.

General procedure D: Synthesis of β-oxoacids.

To a solution of oxoester (1 eq.) in THF, was added $LiOH.H_2O$, dissolved in deionized water (~4:1 THF/water) and the reaction allowed to stir at room temperature. The resultant mixture was stirred at room temperature until the starting ester was completely consumed by TLC analysis (18–24 h). The reaction mixture was then diluted with an equivalent amount of deionized water and EtOAc. The layers were separated, and the aqueous layer was washed with EtOAc (x2) before being acidified to pH ~2-3 by the dropwise addition of 6 M aqueous HCl. Thereafter, the aqueous layer was reextracted with EtOAc (x3), the combined organic extracts dried over $MgSO_4$ and concentrated in vacuo to give the appropriate β-oxoacids which could be purified by column chromatography on silica gel if needed.

General procedure E: $Mn(OAc)_3$ mediated one-step synthesis of bisoxindoles.

To a solution of oxoanilde (1.0 eq.) in acetonitrile (5 mL/mmol) OR oxo-acid (1 eq.) in tetrahydrofuran (5 mL/mmol), in a round bottom flask under argon atmosphere was added $Mn(OAc)_3.2H_2O$ (3 eq.) and the reaction left to stir at reflux until TLC analysis indicated consumption of the starting material (~48 hr). An equal amount of brine was then added, and the organic layer separated. The aqueous layer was reextracted with EtOAc (x3), the combined organic extracts dried over $MgSO_4$ and concentrated in vacuo. The resulting crude product was purified by column chromatography on silica gel (Hexanes/EtOAc gradient) to afford bisoxindoles as a separable mixture of diastereomers.

General procedure F: Dual catalytic $Mn(OAc)_3$ $Co(OAc)_2$ or $Cu(OAc)_2$-mediated one-step synthesis of bisoxindoles.

To a solution of oxoanilde in dioxane (5 mL/mmol) in a round bottom flask under argon atmosphere was added $Mn(OAc)_3.2H_2O$ (0.5 eq.) and $Co(OAc)_2.4H_2O$ OR oxoacid (1.0 eq.) in dioxane (5 mmL/mmol)) in a round bottom flask under argon atmosphere was added $Mn(OAc)_3.2H_2O$ (0.5 eq.) and $Cu(OAc)_2.H_2O$ and the reaction left to stir at refluxing temperature (~101 °C) for 24 hours. Thereafter, an equal amount of brine was added, and the organic layer separated. The aqueous layer was reextracted with EtOAc (x3), the combined organic extracts dried over $MgSO_4$ and concentrated in vacuo. The resulting crude product was purified by column chromatography on silica gel (Hexanes/EtOAc gradient) to afford bisoxindoles as a separable mixture of diastereomers.

Characterisation data for anilides

***N*-methyl-*N*-phenylpropionamide (82)**[1,3]

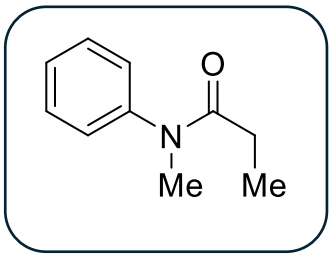

Prepared according to general procedure B using *N*-methylaniline (1.065 g, 9.94 mmol), propionic acid (0.89 mL, 11.9 mmol), 2-chloro-1-methylpyridinium iodide (3.55 g, 13.9 mmol) and DIPEA (5.20 mL, 29.8 mmol) in CH_2Cl_2 (30 mL). Chromatography on silica gel with EtOAc/hexanes (10–20%) afforded **82** as an orange oil (1.608 g, 99% yield). $\mathbf{R_f}$ = 0.23 (3:7 EtOAc:hexane); **IR** (film, vmax/cm^{-1}) 2988, 2948, 1490, 1434, 1382, 1282, 1122, 1040, 784, 704, 568; **^{1}H NMR** (400 MHz, $CDCl_3$) δ 7.44–7.38 (m, 2H), 7.35–7.30 (m, 1H), 7.20–7.15 (m, 2H), 3.26 (s, 3H), 2.13–2.05 (m, 2H), 1.05 (t, *J* = 7.5 Hz, 3H); **^{13}C NMR** (101 MHz, $CDCl_3$) δ 174.1, 144.5, 129.9, 127.8, 127.4, 37.5, 27.7, 9.8. All recorded data were in accordance with those previously reported.

***N*-methyl-*N*-phenylbutyramide (106)**[1–3]

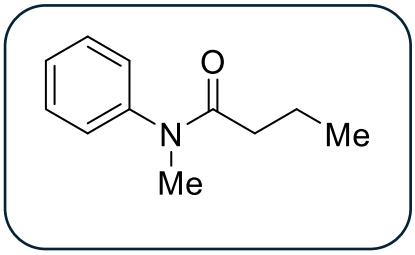

Prepared according to general procedure A using *N*-methylaniline (1.4835 g, 13.8 mmol), triethylamine (2.32 mL, 16.6 mmol) and butyryl chloride (1.73 mL, 16.6 mmol) in CH_2Cl_2 (50 mL). Chromatography on silica gel with EtOAc/hexanes (10–20%) afforded **106** as a pale brown-orange oil (2.422 g, 99% yield). $\mathbf{R_f}$ = 0.35 (3:7 EtOAc:hexane); **IR** (film, ν_{max}/cm^{-1}) 2988, 2948, 1490, 1434, 1382, 1282, 1122, 1040, 784, 704, 568; **^{1}H NMR** (400 MHz, $CDCl_3$) δ 7.44–7.38 (m, 2H), 7.35–7.31 (m, 1H), 7.19–7.17 (m, 2H), 3.26 (s, 3H), 2.07–2.03 (m, 2H), 1.60 (sext, *J* = 7.7 Hz, 2H), 0.83 (t, *J* = 7.2 Hz, 3H); **^{13}C NMR** (101 MHz, $CDCl_3$) δ 173.3, 144.6, 129.8, 127.8, 127.5, 37.5, 36.2, 19.1, 14.0. All recorded data were in accordance with those previously reported.

***N*-methyl-*N*-3-diphenylpropanamide (115ba)**[4]

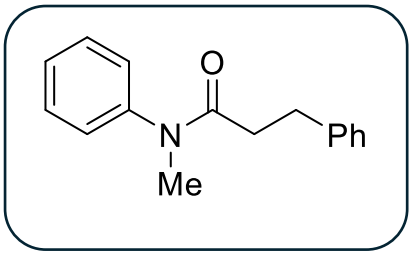

Prepared using general procedure B, using *N*-methylaniline (1.50 g, 14.0 mmol), 4-phenylbutanoic acid (2.52 g, 16.8 mmol), 2-chloro-1-methylpyridinium iodide (5.00 g, 19.6 mmol) and DIPEA (7.33 mL, 42.0 mmol). Chromatography on silica gel with EtOAc/hexanes (10–20%) afforded **115ba** (2.892 g, 86% yield) as a yellow oil; $\mathbf{R_f}$ = 0.31 (1:5 EtOAc:hexane); **^{1}H NMR** (300 MHz, $CDCl_3$) δ 7.41–7.28 (m, 3H), 7.26–7.11 (m, 3H), 7.10–6.99 (m, 4H), 3.25 (s, 3H), 2.91 (t, *J* = 7.8 Hz, 2H), 2.38 (t, *J* = 7.8 Hz, 2H); **^{13}C NMR** (101 MHz, $CDCl_3$) δ 172.3, 144.0, 141.3, 129.8, 128.5, 128.4, 127.9, 127.4, 126.1, 37.4, 36.1, 31.8. All data were in accordance with those previously reported.

***N*-methyl-*N*-phenylpent-4-enamide (115da)**[1]

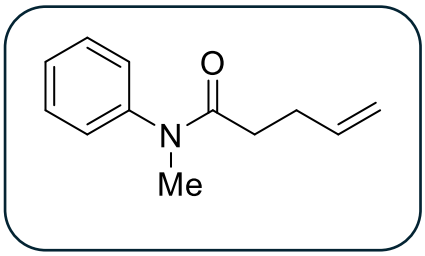

Prepared according to general procedure A using *N*-methylaniline (1.11 g, 10.2 mmol), pent-4-enoyl chloride (1.38 mL, 12.4 mmol), triethylamine (1.74 mL, 12.4 mmol) in CH_2Cl_2 (10 mL). Chromatography on silica gel with EtOAc/hexanes (10–15%) afforded **115da** as a yellow oil (1.916 g, 99% yield). $\mathbf{R_f}$ = 0.41 (3:7 EtOAc:hexane); **IR** (film, vmax/cm^{-1}) 2938, 1652, 1500, 1384, 1286, 1000, 774, 700, 564; **^{1}H NMR** (600 MHz, $CDCl_3$) δ 7.43–7.39 (m, 2H), 7.34 (m, 1H), 7.19–7.17 (m, 2H), 5.78–5.68 (m, 1H), 4.95–4.90 (m, 2H), 3.27 (s, 3H), 2.37–2.30 (m, *J* = 7.3 Hz, 2H), 2.19–2.12 (m, *J* = 7.6 Hz, 2H); **^{13}C NMR** (101 MHz, $CDCl_3$) δ (ppm) 172.5, 144.3, 137.7, 129.9, 127.9, 127.5, 115.1, 37.5, 33.6, 29.6; **HRMS** (ESI$^+$) *m/z*: [M + H] calcd for $C_{12}H_{16}NO^+$ 190.1226; found 190.1231.

***N*-(4-chlorophenyl)-*N*-methylpropionamide (115ha)**[1]

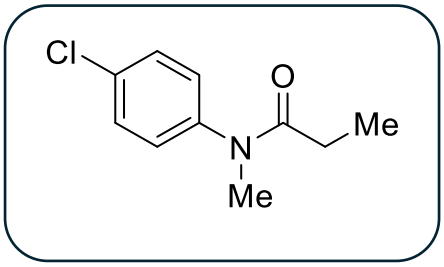

Prepared according to general procedure A using 4-Chloro-*N*-methylaniline (0.708 g, 5.00 mmol), propionyl chloride (0.53 mL, 6.00 mmol) and triethylamine (0.85 mL, 6.09 mmol) in CH_2Cl_2 (15 mL).

Chromatography on silica gel with EtOAc/hexanes (10–25%) afforded **115ha** as an orange-yellow oil (0.621 g, 63% yield). $\mathbf{R_f}$ = 0.32 (3:7 EtOAc:hexane); **IR** (film, vmax/cm^{-1}) 2940, 1656, 1488, 1380, 1282, 1098, 1024, 840, 736, 562; **^{1}H NMR** (400 MHz, $CDCl_3$) δ 7.41–7.35 (m, 2H), 7.15–7.09 (m, 2H), 3.24 (s, 3H), 2.08 (br s, 2H), 1.06 (t, *J* = 7.4 Hz, 3H); **^{13}C NMR** (101 MHz, $CDCl_3$) δ 173.9, 143.0, 133.6, 130.1, 128.8, 37.5, 27.7, 9.8; **HRMS** (ESI$^+$) *m/z*: [M + H] calcd for $C_{10}H_{13}ClNO^+$ 198.0680; found 198.0689.

***N*-(4-methoxyphenyl)-*N*-methylpropionamide (115ka)**[1,5]

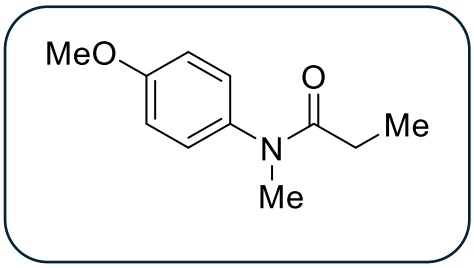

Prepared according to general procedure B using 4-methoxy-*N*-methylaniline (1.066 g, 7.77 mmol), propionic acid (0.70 mL, 9.33 mmol), 2-chloro-1-methylpyridinium iodide (2.781 g, 10.9 mmol) and DIPEA (4.05 mL, 23.3 mmol) in CH_2Cl_2 (15 mL). Chromatography on silica gel with EtOAc/hexanes (10–40%) afforded **115ka** as a pale orange oil (1.505 g, 77% yield). $\mathbf{R_f}$ = 0.21 (3:7 EtOAc:hexane); **IR** (film, vmax/cm^{-1}) 2960, 2846, 1640, 1442, 1390, 1244, 1116, 1034, 842, 568; **^{1}H NMR** (400 MHz, $CDCl_3$) δ 7.11–7.06 (m, 2H), 6.94–6.88 (m, 2H), 3.82 (s, 3H), 3.22 (s, 3H), 2.06 (q, *J* = 7.5 Hz, 2H), 1.04 (t, *J* = 7.5 Hz, 3H); **^{13}C NMR** (101 MHz, $CDCl_3$) δ 174.5, 159.0, 137.3, 128.5, 115.0, 55.7, 37.6, 27.6, 9.9; **HRMS** (ESI$^+$) *m/z*: [M + H] calcd for $C_{11}H_{16}NO_2^+$ 194.1176; found 194.1181. All recorded data were in accordance with those previously reported.

***N*-methyl-*N*-(4-nitrophenyl)-propionamide (115ma)**[1,2]

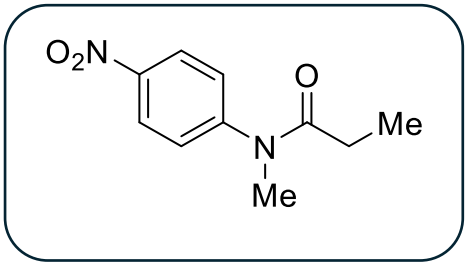

Prepared according to general procedure A using *N*-methyl-4-nitroaniline (1.03 g, 6.8 mmol), triethylamine (1.13 mL, 8.13 mmol) and propionyl chloride (0.71 mL, 8.13 mmol) in CH_2Cl_2 (20 mL). Chromatography on silica gel with EtOAc/hexanes (5–25%) afforded **115ma** as a yellow solid (1,317 g, 95% yield). $\mathbf{R_f}$ = 0.23 (3:7 EtOAc:hexane); **IR** (film, ν_{max}/cm^{-1}) 2979, 1649, 1591, 1521, 1342, 1106, 858; **^{1}H NMR** (400 MHz, CDCl3) δ 8.26 (d, *J* = 8.9, Hz, 2H), 7.38 (d, *J* = 8.9 Hz, 2H), 3.32 (s, Hz, 3H), 2.21 (q, *J* = 8.3 Hz, 2H), 1.10 (t, *J* = 8.3 Hz, 3H); **^{13}C NMR** (101 MHz, CDCl3) δ 173.5, 150.0, 146.4,

127.6, 125.1, 37.4, 28.0, 9.6; **HRMS** (ESI$^+$) *m/z*: [M + H] calcd for $C_{10}H_{13}N_2O_3^+$ 209.0921; found 209.0930. All recorded data were in accordance with those previously reported.

_N_-allyl-_N_-phenylpropionamide (115qa)

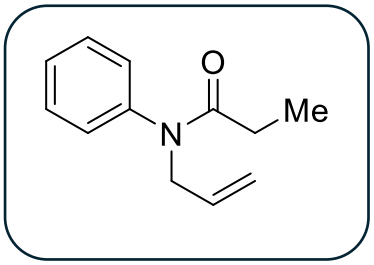

Prepared according to general procedure A using *N*-allylaniline (1.004 g, 7.54 mmol), propionyl chloride (0.80 mL, 9.15 mmol) and triethylamine (1.27 mL, 9.15 mmol) in CH_2Cl_2 (15 mL). Chromatography on silica gel with EtOAc/hexanes (10–15%) afforded **115qa** as a pale-yellow oil (0.731 g, 51% yield). $\mathbf{R_f}$ = 0.35 (3:7 EtOAc:hexane); **IR** (film, vmax/cm^{-1}) 2972, 1652, 1390, 1226, 936, 912, 698, 554; **^{1}H NMR** (400 MHz, $CDCl_3$) δ 7.42–7.35 (m, 2H), 7.35–7.28 (m, 1H), 7.17–7.10 (m, 2H), 5.85 (ddt, *J* = 16.7, 10.2, 6.3 Hz, 1H), 5.14–4.98 (m, 2H), 4.28 (dt, *J* = 6.3, 1.3 Hz, 2H), 2.05 (q, *J* = 7.3 Hz, 2H), 1.04 (t, *J* = 7.3 Hz, 3H); **^{13}C NMR** (101 MHz, $CDCl_3$) δ 173.6, 142.9, 133.5, 129.6, 128.4, 127.9, 117.8, 52.3, 27.9, 9.7; **HRMS** (ESI$^+$) *m/z*: [M + H] calcd for $C_{12}H_{16}NO^+$ 190.1226; found 190.1233.

2-cyclopentyl-_N_-methyl-_N_-phenylacetamide (115ra)

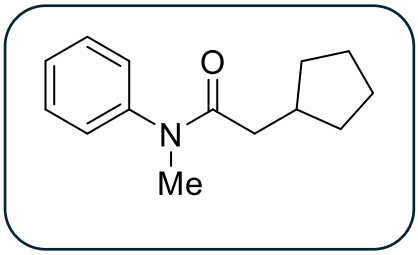

Prepared according to general procedure B using *N*-methylaniline (0.582 g, 5.45 mmol), 2-cyclopentylacetic acid (0.88 mL, 6.52 mmol) and triethylamine (0.91 mL, 6.52 mmol) in CH_2Cl_2 (10 mL). Chromatography on silica gel with EtOAc/hexanes (10–15%) afforded **115ra** as a brown oil (1.051 g, 89% yield). $\mathbf{R_f}$ = 0.47 (3:7 EtOAc:hexane); **IR** (film, vmax/cm^{-1}) 2948, 2872, 1654, 1384, 1290, 1118, 774, 702, 560; **^{1}H NMR** (600 Hz, $CDCl_3$) δ (ppm) 7.43–7.39 (m, 2H), 7.35–7.30 (app t, *J* = 7.4 Hz, 1H), 7.16 (app d, *J* = 7.1 Hz, 2H), 3.26 (s, 3H), 2.25 (hept, *J* = 7.3 Hz, 1H), 2.09 (d, *J* = 7.3 Hz, 2H), 1.81–1.72 (m, 2H), 1.54–1.43 (m, 4H), 1.00–0.96 (m, 2H); **^{13}C NMR** (101 MHz, $CDCl_3$) δ 173.1, 144.6, 129.8, 127.8, 127.6, 40.0, 37.5, 37.1, 32.7, 25.0; **HRMS** (ESI$^+$) *m/z*: [M + H] calcd for $C_{14}H_{20}NO^+$ 218.1539; found 218.1547.

***N*-(4-chlorophenyl)-*N*-methyl-3-phenylpropanamide (115va)**

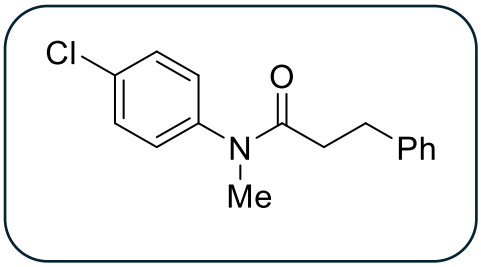

Prepared according to general procedure B using 4-Chloro-*N*-methylaniline (1.169 g, 8.25 mmol), 4-phenylbutanoic acid (1.4878 g, 9.90 mmol), 2-chloro-1-methylpyridinium iodide (2.9528 g, 11.6 mmol) and DIPEA (4.30 mL, 24.8 mmol) in CH_2Cl_2 (60 mL). Chromatography on silica gel with EtOAc/hexanes (10–15%) afforded **115va** as a pale-yellow oil (1.1458 g, 51% yield). $\mathbf{R_f}$ = 0.36 (3:7 EtOAc:hexane); **^{1}H NMR** (300 MHz, $CDCl_3$) δ 7.46 – 7.25 (m, 5H), 7.18 (d, J = 7.3 Hz, 2H), 7.01 (d, J = 8.1 Hz, 2H), 3.32 (s, 3H), 3.02 (t, J = 7.8 Hz, 2H), 2.46 (t, J = 7.7 Hz, 2H); **^{13}C NMR** (75 MHz, $CDCl_3$) δ 172.2, 142.5, 141.1, 133.6, 130.0, 128.7, 128.5, 128.5, 126.2, 37.4, 36.0, 31.8.

***N*-(3,5-difluorophenyl)-*N*-methyl-3-phenylpropanamide (115wa)**

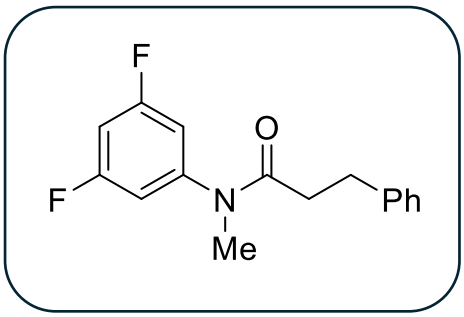

Prepared according to general procedure B using 3,5-difluoro-*N*-methylaniline (1.30 g, 9.08 mmol), 4-phenylbutanoic acid (1.6372 g, 10.9 mmol), 2-chloro-1-methylpyridinium iodide (3.2493 g, 12.7 mmol) and DIPEA (4.75 mL, 27.3 mmol) in CH_2Cl_2 (70 mL). Chromatography on silica gel with EtOAc/hexanes (10–15%) afforded **115wa** as a orange-brown oil (1.130 g, 45% yield). $\mathbf{R_f}$ = 0.17(3:7 EtOAc:hexane); **^{1}H NMR** (300 MHz, CDCl3) δ 7.33 – 7.05 (m, 5H), 6.76 (t, J = 8.6 Hz, 1H), 6.50 (d, J = 7.0 Hz, 2H), 3.21 (s, 3H), 2.93 (t, J = 7.7 Hz, 2H), 2.43 (t, J = 7.8 Hz, 2H);

Characterisation data for β-oxoesters

Ethyl 2-(methyl(phenyl)-carbamoyl)-butanoate (114)[1,2]

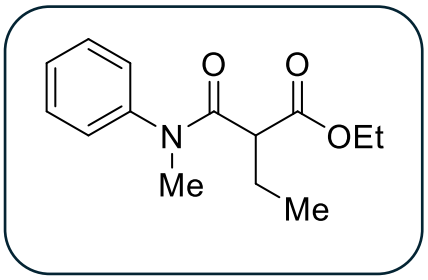

Prepared using general procedure B, using *N*-methylaniline (5.34 mL, 49.3 mmol), 2-(ethoxycarbonyl)butanoic acid (6.5816 g, 41.1 mmol), 2-chloro-1-*N*-methylpyridinium iodide (13.647 g, 53.4 mmol) and DIPEA (20.0 mL, 123 mmol). Chromatography on silica gel with EtOAc/hexanes (0–30%) afforded **114** (10.938 g, 89% yield) as an orange oil; $\mathbf{R_f}$ 0.37 (3:7 EtOAc:hexane); **IR** (film, vmax/cm^{-1}); 3397, 2971, 2936, 1734, 1655, 1595, 1498, 1461, 1389, 1114, 1024, 775, 702, 582; **^{1}H NMR** (400 MHz, $CDCl_3$) δ 7.53–7.16 (m, 3H), 7.22 (d, *J* = 8.2 Hz, 2H), 4.09 (m, 2H), 3.29 (s, 3H), 3.25–3.18 (m, 1H), 1.87 (m, 2H), 1.21 (t, *J* = 7.2 Hz, 3H), 0.81 (t, *J* = 7.4 Hz, 3H); **^{13}C NMR** (101 MHz, $CDCl_3$) δ 170.1, 169.2, 143.7, 129.9, 128.2, 127.8, 61.1, 50.7, 37.7, 22.9, 14.2, 12.0.

Characterization data for β-oxoanilides

***N*,2-dimethyl-3-oxo-*N*-phenylpropanamide (81)**[1]

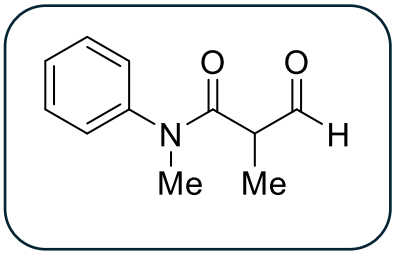

Prepared according to general procedure C using anilide **82** (1.072 g, 6.56 mmol), methyl formate (2.43 mL, 39.4 mmol), $TiCl_4$ (2.14 mL, 19.7 mmol) and triethylamine (3.20 mL, 23.0 mmol) in CH_2Cl_2 (20 mL). Chromatography on silica gel with EtOAc/hexanes (10–40%) afforded **81** as an orange-brown oil (1.188 g, 82% yield). $\mathbf{R_f}$ 0.17 (3:7 EtOAc:hexane); **IR** (film, vmax/cm^{-1}) 2954, 1728, 1644, 1490, 1388, 1112, 1044, 778, 700; **^{1}H NMR** (400 MHz, $CDCl_3$) δ 9.57 (d, *J* = 1.8 Hz, 1H), 7.46 – 7.34 (m, 3H), 7.21–7.17 (m, 2H), 3.32–3.24 (m, 1H), 3.30 (s, 3H), 1.28 (d, *J* = 7.2 Hz, 3H); **^{13}C NMR** (101 MHz, $CDCl_3$) δ 198.9, 170.1, 143.4, 130.2, 128.6, 127.5, 50.5, 37.7, 12.6; **HRMS** (ESI$^+$) *m/z*: [M + H] calcd for $C_{11}H_{14}NO_2^+$ 192.1019; found 192.1030.

2-formyl-*N*-methyl-*N*-phenylbutanamide (105)[1,2]

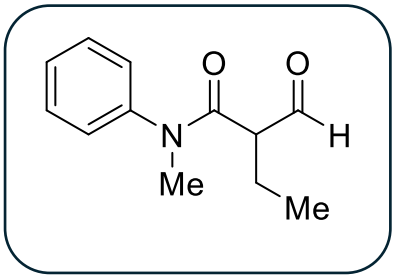

Prepared according to general procedure C using anilide **106** (2.9064 g, 16.4 mmol), methyl formate (6.1 mL, 98.4 mmol), $TiCl_4$ (5.36 mL, 49.2 mmol) and triethylamine (8.0 mL, 57.4 mmol) in CH_2Cl_2 (60 mL). Chromatography on silica gel with EtOAc/hexanes (10–40%) afforded **105** as a yellow oil (3.063 g, 91% yield); **R_f** 0.34 (3:7 EtOAc:hexane); **IR** (film, vmax/cm^{-1}); **^{1}H NMR** (600 MHz, $CDCl_3$) δ 9.56 (d, *J* = 2.7 Hz, 1H), 7.45–7.41 (m, 2H), 7.40–7.35 (m, 1H), 7.19–7.14 (m, 2H), 3.32 (s, 3H), 3.13 (ddd, *J* = 8.2, 6.2, 2.7 Hz, 1H), 1.98–1.90 (m, 1H), 1.83–1.75 (m, 1H), 0.85 (t, *J* = 7.4 Hz, 3H); **^{13}C NMR** (101 MHz, $CDCl_3$) δ 199.5, 169.1, 143.3, 130.20 (s), 128.5, 127.7, 58.1, 37.7, 21.9, 11.7; **HRMS** (ESI+) *m/z*: calcd for $C_{12}H_{16}NO_2^+$ 206.1176; found 206.1183.

2-benzyl-*N*-methyl-3-oxo-*N*-phenylpropanamide (115bb)[1,2]

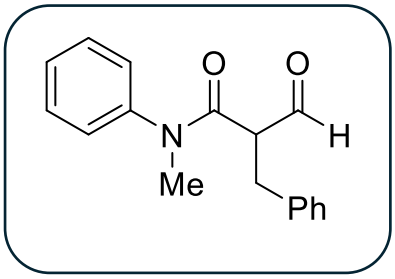

Prepared using general procedure C, anilide **115ba** (2.6463 g, 11.1 mmol), methyl formate (4.10 mL, 66.5 mmol), $TiCl_4$ (3.62 mL, 33.2 mmol) and triethylamine (5.40 mL, 38.7 mmol). Chromatography on silica gel with EtOAc/hexanes (5–30%) afforded **115bb** (2.817 g, 95% yield) as a yellow oil. **R_f** 0.21 (2:3 EtOAc:hexane); **IR** (film, v_{max}/cm^{-1}) 3390, 2833, 1730, 1646, 1496, 1378, 1115, 772, 697; **^{1}H NMR** (300 MHz, $CDCl_3$) δ 9.60 (d, *J* = 1.9 Hz, 1H), 7.31 – 7.13 (m, 7H), 7.03 – 6.90 (m, 2H), 6.56 (s, 1H), 3.47 – 3.40 (m, 1H), 3.25 – 3.09 (m, 4H), 3.00 – 2.92 (m, 1H); **^{13}C NMR** (101 MHz, $CDCl_3$) δ 198.3, 168.4, 142.9, 137.8, 130.0, 129.3, 128.7, 128.4, 127.6, 127.0, 58.7, 37.6, 34.4; **HRMS** (ESI+) *m/z*: [M + H] calcd for $C_{17}H_{18}NO_2^+$ 268.1332; found 268.1344.

2-formyl-*N*-methyl-*N*-phenylpent-4-enamide (115db)[1]

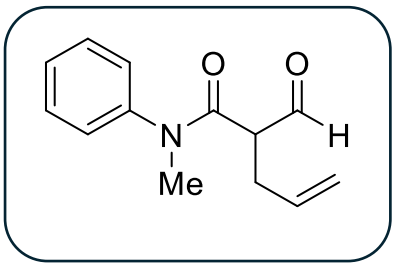

Prepared according to general procedure C using anilide **115da** (0.965 g, 5.12 mmol), methyl formate (1.80 mL, 30.7 mmol), $TiCl_4$ (1.68 mL, 15.4 mmol) and triethylamine (2.50 mL, 17.9 mmol) in CH_2Cl_2 (20 mL). Chromatography on silica gel with EtOAc/hexanes (10–35%) afforded **115db** as a pale-yellow oil (0.978 g, 88% yield). **R_f** 0.27 (3:7 EtOAc:hexane); **IR (**film, vmax/cm^{-1}) 1648, 1612, 1458, 1398, 1122, 1014, 914, 776, 704; **^{1}H NMR** (400 MHz, $CDCl_3$) δ 9.55 (d, *J* = 2.3 Hz, 1H), 7.45–7.36 (m, 3H), 7.19–7.15 (m, 2H), 5.63 (ddt, *J* = 17.1, 10.1, 7.0 Hz, 1H), 5.10–4.99 (m, 2H), 3.34–3.29 (m, 1H), 3.31 (s, 3H), 2.69–2.62 (m, 1H), 2.55–2.46 (quintet, *J* = 6.6 Hz, 1H); **^{13}C NMR** (101 MHz, $CDCl_3$) δ 198.4, 168.4, 143.2, 133.9, 130.2, 128.6, 127.8, 117.9, 56.1, 37.7, 32.3; **HRMS** (ESI$^+$) *m/z*: [M + H] calcd for $C_{13}H_{16}NO_2^+$ 218.1176; found 218.1180.

***N*-(4-chlorophenyl)-*N*,2-dimethyl-3-oxopropanamide (115hb)**[1]

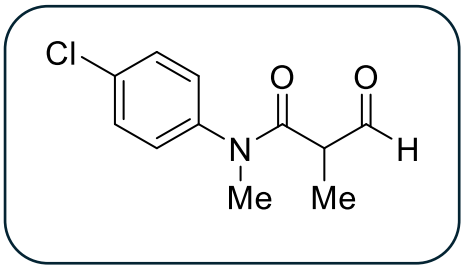

Prepared according to general procedure C, using anilide **115ha** (0.503 g, 2.54 mmol), methyl formate (0.94 mL, 15.3 mmol), $TiCl_4$ (0.83 mL, 7.63 mmol) and triethylamine (1.24 mL, 8.91 mmol) in CH_2Cl_2 (10 mL). Chromatography on silica gel with EtOAc/hexanes (10–40%) afforded **115hb** as a yellow oil (0.231 g, 40% yield). **R_f** 0.30 (3:7 EtOAc:hexane); **IR** (film, vmax/cm^{-1}) 1732, 1648, 1490, 1382, 1310, 1264, 1096, 1026, 926, 840, 730, 558; **^{1}H NMR** (400 MHz, $CDCl_3$) δ 9.53 (br s, 1H), 7.43–7.36 (m, 2H), 7.16–7.10 (m, 2H), 3.29–3.20 (m, 1H), 3.27 (s, 3H), 1.28 (d, *J* = 7.1 Hz, 3H); **^{13}C NMR** (101 MHz, $CDCl_3$) δ 198.7, 169.9, 141.8, 134.5, 130.4, 128.9, 50.5, 37.7, 12.6; **HRMS** (ESI$^+$) *m/z*: [M + H] calcd for $C_{11}H_{13}ClNO_2^+$ 226.0629; found 226.0634.

***N*-(4-methoxyphenyl)-*N*,2-dimethyl-3-oxopropanamide (115kb)**[1]

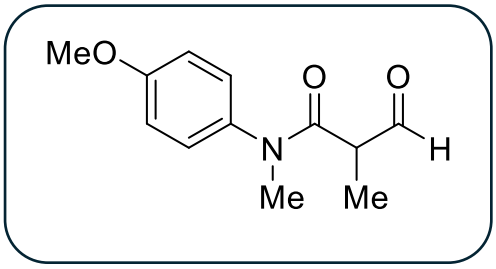

Prepared according to general procedure C using anilide **115ka** (0.8165 g, 4.23 mmol), methyl formate (1.56 mL, 25.4 mmol), $TiCl_4$ (1.38 mL, 12.7 mmol) and triethylamine (2.06 mL, 14.8 mmol) in CH_2Cl_2 (40 mL). Chromatography on silica gel with EtOAc/hexanes (10–50%) afforded **115kb** as a yellow-brown oil (0.7955 g, 84% yield). $\mathbf{R_f}$ 0.13 (3:7 EtOAc:hexane); **IR** (film, vmax/cm^{-1}) 2946, 2850, 1490, 1726, 1642, 1514, 1460, 1392, 1248, 1116, 1034, 842, 574; **^{1}H NMR** (400 MHz, $CDCl_3$) δ 9.56 (d, *J* = 1.8 Hz, 1H), 7.13–7.08 (m, 3H), 6.95–6.90 (m, 2H), 3.82 (s, 3H), 3.33–3.26 (m, 1H), 3.27 (s, 3H), 1.27 (d, *J* = 7.1 Hz, 3H); **^{13}C NMR** (101 MHz, $CDCl_3$) δ 199.0, 170.4, 159.5, 136.1, 128.7, 115.4, 55.7, 50.5, 37.8, 12.6; **HRMS** (ESI$^+$) *m/z*: [M + H] calcd for $C_{12}H_{16}NO_3^+$ 222.1125; found 222.1132.

***N*,2-dimethyl-*N*-(4-nitrophenyl)-3-oxopropanamide (115mb)**[1,2]

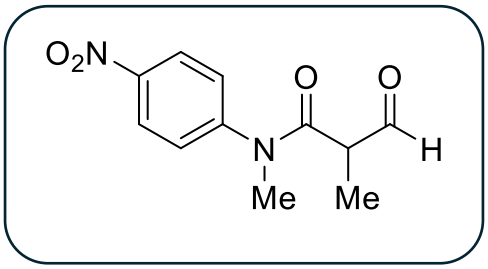

Prepared according to general procedure C using anilide **115ma** (0.5362 g, 2.57 mmol), methyl formate (0.95 mL, 15.5 mmol), $TiCl_4$ (0.84 mL, 7.73 mmol) and triethylamine (1.26 mL, 9.01 mmol) in CH_2Cl_2 (20 mL). Chromatography on silica gel with EtOAc/hexanes (15–35%) afforded **115mb** as a bright yellow oil (0.887 g 64% yield). $\mathbf{R_f}$ 0.38 (6:4 EtOAc:hexane); **IR** (film, vmax/cm^{-1}) 2979, 1732, 1649, 1591, 1521, 1342, 1309, 1106, 858; **^{1}H NMR** (400 MHz, $CDCl_3$) (rotamers) δ 9.55 (s, 1H), 8.30 (d, *J* = 8.7 Hz, 2H), 7.41 (d, *J* = 8.6 Hz, 2H), 3.36 (m, 4H), 1.36 (d, *J* = 7.1 Hz, 3H); **^{13}C NMR** (101 MHz, $CDCl_3$) δ 198.4, 169.5, 128.2, 126.5, 125.5, 50.7, 37.8, 12.6; **HRMS** (ESI$^+$) *m/z*: [M + H] calculated for $C_{11}H_{13}N_2O_4^+$ 237.0870; found 237.0881.

2-benzyl-*N*-(4-chlorophenyl)-*N*-methyl-3-oxopropanamide (115vb)

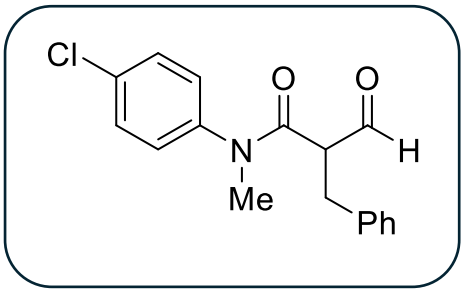

Prepared according to general procedure C, using anilide **115va** (0.7570 g, 2.75 mmol), methyl formate (1.02 mL, 16.5 mmol), $TiCl_4$ (0.90 mL, 8.24 mmol) and triethylamine (1.34 mL, 9.61 mmol) in CH_2Cl_2 (20 mL). Chromatography on silica gel with EtOAc/hexanes (10–40%) afforded **115vb** as a pale-yellow oil (0.3705 g, 45% yield). $\mathbf{R_f}$ 0.26 (3:7 EtOAc:hexane); **^{1}H NMR** (300 MHz, CDCl3) δ 9.72 (s, 1H), 7.44 – 7.27 (m, 5H), 7.21 – 7.04 (m, 2H), 6.57 (br s, 2H), 3.59 – 3.50 (m, 1H), 3.36 (t, J = 11.7 Hz, 1H), 3.28 – 3.02 (m, 4H); **^{13}C NMR** (75 MHz, CDCl3) δ 198.2, 168.1, 141.2, 137.6, 134.2, 130.1, 129.2, 128.9, 128.8, 127.0, 58.7, 37.5, 34.5.

2-benzyl-*N*-(3,5-difluorophenyl)-*N*-methyl-3-oxopropanamide (115wb)

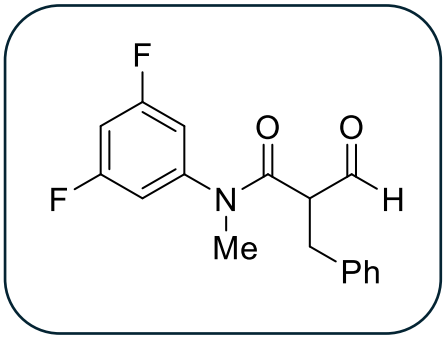

Prepared according to general procedure C, using anilide **115wa** (0.5650 g, 2.05 mmol), methyl formate (0.76 mL, 12.3 mmol), $TiCl_4$ (0.67 mL, 6.16 mmol) and triethylamine (1.00 mL, 7.18 mmol) in CH_2Cl_2 (15 mL). Chromatography on silica gel with EtOAc/hexanes (5–40%) afforded **115wb** as a bright yellow oil (0.3726 g, 60% yield). $\mathbf{R_f}$ 0.32 (3:7 EtOAc:hexane); **^{1}H NMR** (300 MHz, CDCl3) δ 9.65 (s, 1H), 7.31 – 7.25 (m, 3H), 7.16 – 6.92 (m, 2H), 6.75 (t, J = 9.2 Hz, 1H), 6.01 (br s, 2H), 3.52 – 3.37 (m, 1H), 3.27 (t, J = 11.9 Hz, 1H), 3.18 – 2.96 (m, 4H);

Characterization data for β-oxoacids

2-(methyl(phenyl)carbamoyl)butanoic acid (111)[1,2]

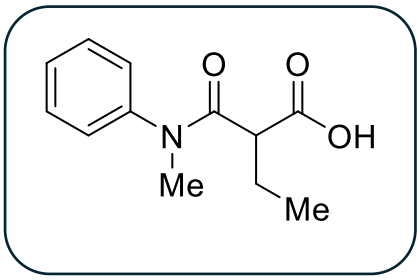

Prepared using general procedure D using oxoester **114** (0.8060 g, 3.24 mmol), LiOH.H_2O (0.5470 g, 12.9 mmol) afforded **111** as a yellow oil (0.5855 g, 91% yield), $\mathbf{R_f}$ 0.21 (1:9 MeOH:DCM); **IR** (film, vmax/cm^{-1}); 3381, 2968, 1732, 1627, 1591, 1498, 1391, 1192, 775, 771; **^{1}H NMR** (400 MHz, $CDCl_3$) δ 7.51–7.40 (m, 3H), 7.21 (d, *J* = 7.5 Hz, 2H), 3.34 (s, 3H), 3.27 (t, *J* = 6.8 Hz, 1H), 1.83 (ddq, *J* = 21.2, 14.0, 7.0 Hz, 2H), 0.87 (t, *J* = 7.4 Hz, 3H); **^{13}C NMR** (101 MHz, $CDCl_3$) δ 172.8, 171.4, 142.3, 130.4, 129.0, 127.2, 49.0, 38.1, 25.9, 11.6; **HRMS** (ESI$^+$) *m/z*: [M + H] calcd for $C_{12}H_{16}NO_3^+$ 222.1125; found 222.1132.

Characterization data for bisoxindoles

1,1',3,3'-tetramethyl-[3,3'-biindoline]-2,2'-dione (89)[1]

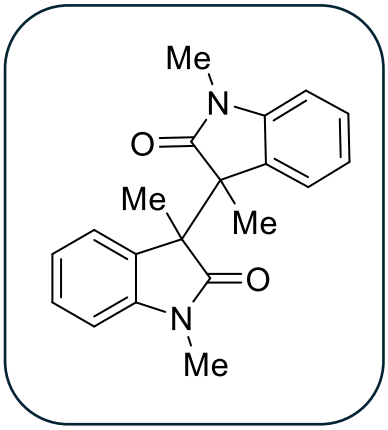

Prepared according to general procedure E using oxoanilide **81** (0.137 g, 0.72 mmol) and Mn(OAc)$_3$.H_2O (0.576 g, 2.15 mmol) in acetonitrile (5 mL). Chromatography on silica gel with EtOAc/hexanes (10–25%) afforded **89** as a 1:1.1 mixture of separable diastereomers (0.081 g, 70% combined yield).

(±)-*dl*: Obtained as a white solid (0.042 g). $\mathbf{R_f}$ 0.45 (3:7 EtOAc:hexane); **IR** (film, vmax/cm^{-1}) 2936, 1698, 1610, 1478, 1362, 1260, 1110, 1074, 916, 738, 730, 548, 488; **^{1}H NMR** (400 MHz, $CDCl_3$) δ 7.06–7.03 (m, 2H), 7.00 (m, 2H), 6.80 (m, 2H), 6.43 (d, *J* = 7.7 Hz, 2H), 3.07 (s, 6H), 1.74 (s, 6H); **^{13}C NMR** (101 MHz, $CDCl_3$) δ 178.3, 142.7, 131.3, 128.2, 122.9, 121.8, 107.4, 51.2, 25.7, 16.2. All recorded data were in accordance with those previously reported.

meso: Obtained as a brown solid (0.039 g); $\mathbf{R_f}$ 0.14 (3:7 EtOAc:hexane); **IR** (film, vmax/cm^{-1}) 2938, 1706, 1610, 1472, 1492, 1356, 1102, 1030, 914, 742, 482; **^{1}H NMR** (400 MHz, $CDCl_3$) δ 7.22 (m, 2H), 6.84 (m, 2H), 6.70 (d, *J* = 7.8 Hz, 2H), 6.60 (d, *J* = 7.6 Hz, 2H), 2.95 (s, 6H), 1.66 (s, 6H); **^{13}C NMR** (101 MHz, $CDCl_3$) δ 177.7, 143.9, 131.2, 128.6, 123.7, 121.6, 107.9, 51.7, 25.9, 17.4. All recorded data were in accordance with those previously reported.

3,3'-diethyl-1,1'-dimethyl-[3,3'-biindoline]-2,2'-dione (115a)[1,2]

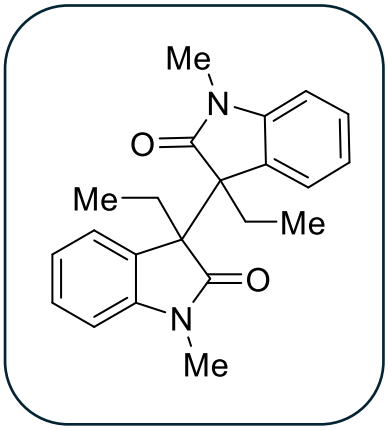

Prepared according to general procedure E using oxoanilide **105** (0.0949 g, 0.46 mmol) and $Mn(OAc)_3.2H_2O$ (0.371 g, 1.39 mmol) in acetonitrile (4 mL). Chromatography on silica gel with EtOAc/hexanes (5–20%) afforded **115a** as a 1:1.1 mixture of separable diastereomers (0.074 g, 92% combined yield).

Prepared according to general procedure E using oxoacid **111** (0.130 g, 0.63 mmol) and $Mn(OAc)_3.H_2O$ (0.509 g, 1.90 mmol) in THF (5 mL). Chromatography on silica gel with EtOAc/hexanes (5–20%) afforded **115a** as a mixture of 1:1.7 separable diastereomers (0.090 g, 81% combined yield).

(±)-*dl*: Obtained as a white solid (0.035 g); $\mathbf{R_f}$ = 0.59 (3:7 EtOAc:hexane); **^{1}H NMR** (300 MHz, $CDCl_3$) δ 7.05–6.96 (m, 4H), 6.81 (m, 2H), 6.40 (dd, *J* = 8.1, 1.0 Hz, 2H), 3.06 (s, 6H), 2.79 (dq, *J* = 13.4, 7.5 Hz, 2H), 2.34 (dq, *J* = 13.4, 7.3 Hz, 2H), 0.40 (t, *J* = 7.4 Hz, 6H); **^{13}C NMR** (101 MHz, $CDCl_3$) δ 177.7, 143.8, 128.9, 128.1, 123.3, 121.7, 107.2, 57.6, 25.7, 21.7, 9.0. All recorded data were in accordance with those previously reported.

meso: Obtained as an orange solid (0.039 g); $\mathbf{R_f}$ = 0.24 (3:7 EtOAc:hexane); **^{1}H NMR** (300 MHz, $CDCl_3$) δ 7.15 (m, 1H), 6.78 (m, 1H), 6.61 (d, *J* = 7.9, 0.8 Hz, 1H), 6.47 (d, *J* = 7.5 Hz, 1H), 2.87 (s, 3H), 2.68 (dq, *J* = 13.0, 7.3 Hz, 1H), 2.02 (dq, *J* = 13.8, 7.6 Hz, 1H), 0.36 (t, *J* = 7.3 Hz, 3H). All recorded data were in accordance with those recorded previously.

3,3'-dibenzyl-1,1'-dimethyl-[3,3'-biindoline]-2,2'-dione (115b)[1,2]

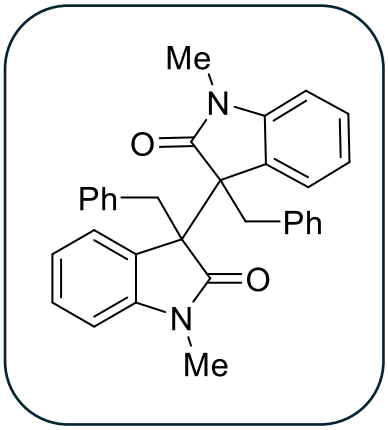

Prepared according to general procedure E, using oxoanilide **115bb** (0.236 g, 0.884 mmol), $Mn(OAc)_3.2H_2O$ (0.710 g, 2.65mmol) and acetonitrile (5 mL). Chromatography on silica gel with EtOAc/hexanes (5–30%) afforded **115b** as a 1:1 mixture of separable diastereomers (0.169 g, 81% combined yield).

(±)-*dl*: Obtained as a white solid (0.85 g); $\mathbf{R_f}$ = 0.51 (3:7 EtOAc: hexane); **M.P.** 214–217 °C; **IR** (film, ν_{max}/cm^{-1}) 3060, 2942, 1697, 1607, 1465, 1351, 1262,1088, 1026, 755, 700; **^{1}H NMR** (300 MHz, $CDCl_3$) δ 7.26–7.19 (m, 2H), 7.01–6.75 (m, 14H), 6.17 (d, *J* = 7.6 Hz, 2H), 4.35 (d, *J* = 12.8 Hz, 2H), 3.81 (d, *J* = 12.8 Hz, 2H), 2.92 (s, 6H); **^{13}C NMR** (101 MHz, $CDCl_3$) δ 177.1, 143.2, 136.1, 130.4, 128.4, 128.0, 127.3, 126.1, 124.0, 121.5, 107.2, 57.6, 35.5, 25.5. All data were in accordance with those previously reported.

meso: Obtained as an off-white solid (0.84 g); $\mathbf{R_f}$ = 0.23 (3:7 EtOAc:hexane); **M.P.** 218–221 °C; **IR** (film, ν_{max}/cm^{-1}); 3045, 2951, 1709, 1614, 1496, 1443, 1342, 1267, 1079, 777, 734; **^{1}H NMR** (300 MHz, $CDCl_3$) δ 7.24–7.11 (m, 2H), 7.07–6.76 (m, 16H), 6.47 (dd, *J* = 7.9, 3.0 Hz, 2H), 4.30 (dd, *J* = 12.5, 3.2 Hz, 2H), 3.55 (dd, *J* = 12.4, 3.2 Hz, 2H), 2.72 (s, 6H); **^{13}C NMR** (101 MHz, $CDCl_3$) δ 176.0, 144.6, 135.5, 130.4, 128.6, 128.6, 127.3, 126.3, 124.7, 121.3, 107.8, 58.2, 37.0, 25.6. All data were in accordance with those previously reported.

3,3'-diallyl-1,1'-dimethyl-[3,3'-biindoline]-2,2'-dione (115d)[1]

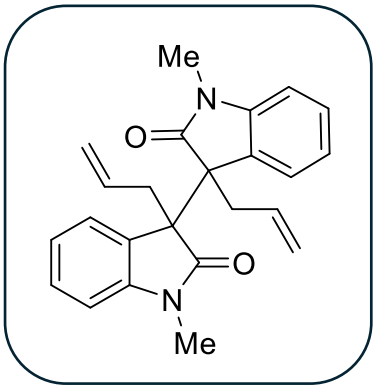

Prepared according to general procedure E using oxoanilide **115db** (0.235 g, 1.08 mmol) and $Mn(OAc)_3.2H_2O$ (0.870 g, 3.24 mmol) in toluene (6 mL). Chromatography on silica gel with EtOAc/hexanes (10–30%) afforded **115d** as a 1:1 mixture of separable diastereomers (0.112 g, 56% combined yield).

(±)-*dl*: Obtained as a yellow solid (0.054 g); $\mathbf{R_f}$ = 0.49 (3:7 EtOAc:hexane); **IR** (film, ν_{max}/cm^{-1}) 2934, 2890, 1694, 1600, 1490, 1480, 1366, 1258, 1096, 998, 920, 754, 640, 496; **^{1}H NMR** (600 MHz, $CDCl_3$) δ 7.04 (app dd, *J* = 7.5, 0.7, 2H), 6.99 (m, 2H), 6.81 (m, 2H), 6.40 (d, *J* = 7.7 Hz, 2H), 5.07–4.96 (m, 4H), 4.76–4.72 (m, 2H), 3.63 (dd, *J* = 13.7, 6.2 Hz, 2H), 3.05 (s, 6H), 3.05–3.01 (m, 2H); **^{13}C NMR** (101 MHz, $CDCl_3$) δ 177.0, 143.5, 132.6, 128.4, 128.3, 123.6, 121.8, 118.9, 107.3, 56.1, 33.4, 25.7; **HRMS** (ESI^+) *m/z*: [M + H] calcd for $C_{24}H_{25}N_2O_2^+$ 373.1911; found 373.1919. All recorded data were in accordance with those previously reported.

meso: Obtained as an orange solid (0.058 g); $\mathbf{R_f}$ = 0.23 (3:7 EtOAc:hexane); **IR** (film, ν_{max}/cm^{-1}) 2938, 1710, 1618, 1484, 1366, 1264, 1102, 998, 933, 756; **^{1}H NMR** (600 MHz, $CDCl_3$) δ 7.23 (m, 2H), 6.86 (m, 2H), 6.67 (d, *J* = 7.6 Hz, 2H), 6.62–6.56 (m, 2H), 5.09 (ddt, J = 17.1, 10.0, 7.1 Hz, 2H), 4.95–4.92 (m, 2H), 4.77–4.75 (m, 2H), 3.46 (dd, *J* = 13.0, 7.4 Hz, 2H), 2.93 (s, 6H), 2.86 (ddt, *J* = 13.2, 6.9, 1.0 Hz, 2H); **^{13}C NMR** (101 MHz, $CDCl_3$) δ 176.1, 144.7, 132.1, 128.7, 128.5, 124.3, 121.6, 119.3, 107.9, 56.7, 34.9, 25.9; **HRMS** (ESI^+) *m/z*: [M + H] calcd for $C_{24}H_{25}N_2O_2^+$ 373.1911; found 373.1914. All recorded data were in accordance with those previously reported.

5,5'-dichloro-1,1',3,3'-tetramethyl-[3,3'-biindoline]-2,2'-dione (115h)[1,2]

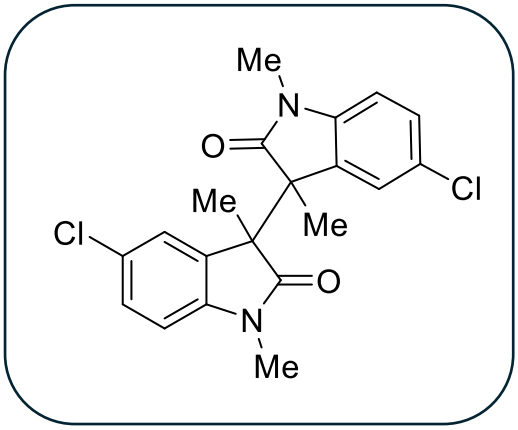

Prepared according to general procedure E using oxoanilide **115hb** (0.104 g, 0.46 mmol) and $Mn(OAc)_3.2H_2O$ (0.371 g, 13.8 mmol) in acetonitrile (4 mL). Chromatography on silica gel with EtOAc/hexanes (10–30%) afforded **115h** as a 1:1.2 mixture of separable diastereomers (0.086 g, 96% combined yield).

(±)-*dl*: Obtained as a yellow solid (0.044 g); $\mathbf{R_f}$ = 0.55 (3:7 EtOAc:hexane); **IR** (film, vmax/cm^{-1}) 2932, 1702, 1488, 1438, 1354, 1112, 828, 764; **^{1}H NMR** (400 MHz, $CDCl_3$) δ 7.04–7.00 (m, 4H), 6.41 (dd, *J* = 8.0 Hz, 2H), 3.11 (s, 6H), 1.72 (s, 6H); **^{13}C NMR** (101 MHz, $CDCl_3$) δ 177.5, 141.3, 132.5, 128.3, 127.6, 123.6, 108.6, 51.5, 26.0, 15.8. All recorded data were in accordance with those previously reported.

meso: Obtained as a red-orange solid (0.042 g); $\mathbf{R_f}$ = 0.14 (3:7 EtOAc:hexane); **IR** (film, vmax/cm^{-1}) 2955, 1716, 1490, 1420, 1354, 1102, 822, 762; **^{1}H NMR** (400 MHz, $CDCl_3$) δ 7.25(dd, *J* = 8.3, 2.1 Hz, 2H), 6.67 (d, *J* = 8.3 Hz, 2H), 6.60 (br s, 2H), 2.96 (s, 6H), 1.63 (s, 6H); **^{13}C NMR** (101 MHz, $CDCl_3$) δ 176.9, 142.5, 132.4, 128.8, 127.2, 124.2, 109.0, 51.9, 26.2, 17.2. All recorded data were in accordance with those previously reported.

5,5'-dimethoxy-1,1',3,3'-tetramethyl-[3,3'-biindoline]-2,2'-dione (115k)[1,2]

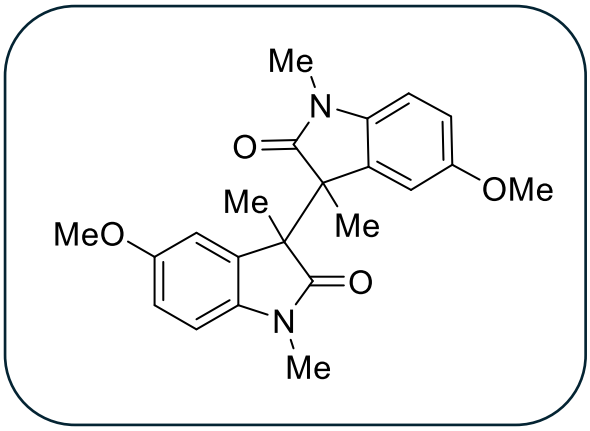

Prepared according to general procedure E using oxoanilide **115kb** (0.866 g, 3.91 mmol) and $Mn(OAc)_3.2H_2O$ (3.147 g, 11.7 mmol) in acetonitrile (12 mL). Chromatography on silica gel with EtOAc/hexanes (10–30%) afforded **115k** as a 1:1 mixture of separable diastereomers (0.449 g, 60% combined yield).

(±)-dl: Obtained as a white solid (0.226 g); $\mathbf{R_f}$ = 0.28 (3:7 EtOAc:hexane); **IR** (film, vmax/cm^{-1}) 2942, 2874, 1960, 1700, 1484, 1460, 1362, 1288, 1224, 1122, 1038, 902, 808, 734, 620, 566, 480; **^{1}H NMR** (400 MHz, $CDCl_3$) δ 6.72 (d, *J* = 2.6 Hz, 2H), 6.56 (dd, *J* = 8.4, 2.6 Hz, 2H), 6.37 (d, *J* = 8.4 Hz, 2H), 3.67 (s, 6H), 3.08 (s, 6H), 1.72 (s, 6H); **^{13}C NMR** (101 MHz, $CDCl_3$) δ 177.9, 155.8, 136.2, 132.6, 113.1, 110.3, 107.8, 55.9, 51.5, 25.9, 16.6; **HRMS** (ESI$^+$) *m/z*: [M + H] calcd for $C_{22}H_{25}N_2O_4^+$ 381.1809; found 381.1816. All recorded data were in accordance with those previously reported.

meso: Obtained as an orange solid (0.223 g); $\mathbf{R_f}$ = 0.11 (3:7 EtOAc:hexane); **IR** (film, vmax/cm^{-1}) 2942, 2838, 1988, 1706, 1444, 1366, 1286, 1238, 1160, 1036, 908, 812, 728, 478; **^{1}H NMR** (400 MHz, $CDCl_3$) δ 6.75 (dd, *J* = 8.5, 2.6 Hz, 2H), 6.60 (d, *J* = 8.5 Hz, 2H), 6.27 (br s, 2H), 3.62 (s, 6H), 2.92 (s, 6H), 1.63 (s, 6H); **^{13}C NMR** (101 MHz, $CDCl_3$) δ 177.3, 155.3, 137.5, 132.3, 113.2, 111.3, 108.1, 55.8, 51.9, 26.0, 17.5; **HRMS** (ESI$^+$) *m/z*: [M + H] calcd for $C_{22}H_{25}N_2O_4^+$ 381.1809; found 381.1812. All recorded data were in accordance with those previously reported.

1,1',3,3'-tetramethyl-5,5'-dinitro-[3,3'-biindoline]-2,2'-dione (115m)[1,2]

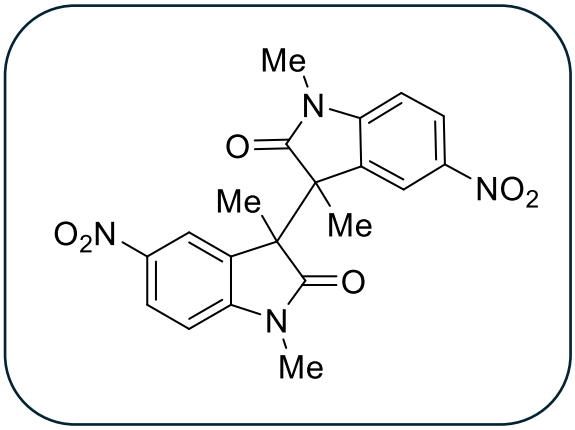

Prepared according to general procedure E using oxoanilide **115mb** (0.130 g, 0.55 mmol) and $Mn(OAc)_3.H_2O$ (0.444 g, 1.66 mmol) in acetonitrile (5 mL). Chromatography on silica gel with EtOAc/hexanes (10–35%) afforded **115m** as a 1:1 mixture of separable diastereomers (0.079 g, 70% combined yield).

(±)-*dl*: Obtained as a white solid (0.038 g); $\mathbf{R_f}$ = 0.79 (1:1 EtOAc/hexanes); **M.P.** 294–296 °C; **IR** (film, vmax/cm^{-1}) 2954, 2869, 1696, 1607, 1465, 1355, 755, 700, 496; **^{1}H NMR** (400 MHz, $CDCl_3$) δ 8.03 (d, *J* = 8.5 Hz, 2H), 7.90 (s, 2H), 6.59 (d, *J* = 8.6 Hz, 2H), 3.22 (s, 6H), 1.81 (s, 6H); **^{13}C NMR** (101 MHz, $CDCl_3$) δ 177.7, 148.3, 143.2, 131.2, 125.9, 118.6, 107.6, 51.0, 26.6, 15.8; **HRMS** (ESI^+) *m/z* calcd: [M + H] for $C_{20}H_{19}N_4O_6^+$ 411.1299; found 411.1307.

meso: Obtained as a yellow solid (0.041 g); $\mathbf{R_f}$ = 0.23 (1:1 EtOAc/hexanes); **M.P.** 204–206 °C**; IR** (film, vmax/cm^{-1}) 3088, 2943, 1705, z1613, 1513, 1495, 1328, 1294, 1091, 1044; **^{1}H NMR** (400 MHz, $CDCl_3$) (rotamers) δ 8.30 (m, 2H), 7.73 (m, 0.5H), 7.58 (br s, 1.5H) 6.94 (d, *J* = 8.4 Hz, 0.5H), 6.85 (d, *J* = 8.4 Hz, 1.5H), 3.28 (s, 2H) 3.06 (s, 4H), 1.74 (s, 4H), 1.66 (s, 2H); **^{13}C NMR** (101 MHz, $CDCl_3$) δ 177.30, 149.28, 142.95, 132.12, 130.93, 126.94, 126.48, 119.76, 119.47, 108.39, 108.05, 73.30, 51.62, 26.84, 26.66, 24.94, 17.39; **HRMS** (ESI^+) *m/z* calcd: [M + H] for $C_{20}H_{19}N_4O_6^+$ 411.1299; found 411.1313.

3,3'-dibenzyl-5,5'-dichloro-1,1'-dimethyl-[3,3'-biindoline]-2,2'-dione (115v)

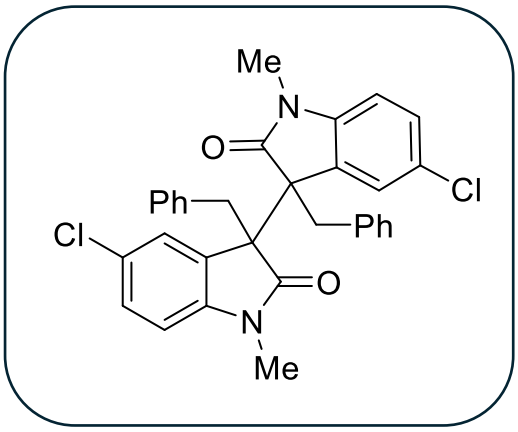

Prepared according to general procedure F using oxoanilide **115vb** (0.2824 g, 0.94 mmol), $Mn(OAc)_3.2H_2O$ (0.1254 g, 4.67 mmol) and $Co(OAc)_2.4H_2O$ (0.1165 g, 4.67 mmol) in dioxane (5 mL). Chromatography on silica gel with EtOAc/hexanes (5–25%) afforded **115v** as a 1:1 mixture of separable diastereomers (0.099 g, 39% combined yield).

(±)-*dl*: Obtained as a yellow solid (0.048 g); $\mathbf{R_f}$ = 0.68 (3:7 EtOAc/hexanes); **^{1}H NMR** (300 MHz, $CDCl_3$) δ 7.17 (br s, 2H), 7.02 – 6.82 (m, 12H), 6.11 (d, J = 8.0 Hz, 2H), 4.24 (d, J = 12.8 Hz, 2H), 3.74 (d, J = 12.8 Hz, 2H), 2.93 (s, 6H); **^{13}C NMR** (75 MHz, CDCl3) δ 176.4, 141.6, 135.4, 130.4, 129.7, 128.2, 127.7, 127.2, 126.5, 124.4, 108.4, 57.8, 35.0, 25.8.

meso: Obtained as an orange solid (0.051 g); $\mathbf{R_f}$ = 0.35 (3:7 EtOAc/hexanes); **^{1}H NMR** (300 MHz, $CDCl_3$) δ 7.17 (d, J = 8.3 Hz, 2H), 7.01 – 6.98 (m, 6H), 6.90 – 6.71 (m, 6H), 6.39 (d, J = 8.3 Hz, 2H), 4.21 (d, J = 12.5 Hz, 2H), 3.41 (d, J = 12.8 Hz, 2H), 2.68 (s, 6H); **^{13}C NMR** (75 MHz, CDCl3) δ 175.4, 143.1, 134.7, 130.4, 129.9, 128.9, 127.6, 126.9, 126.7, 124.9, 108.9, 58.4, 36.8, 25.9.

3,3'-dibenzyl-4,4',6,6'-tetrafluoro-1,1'-dimethyl-[3,3'-biindoline]-2,2'-dione (115w)

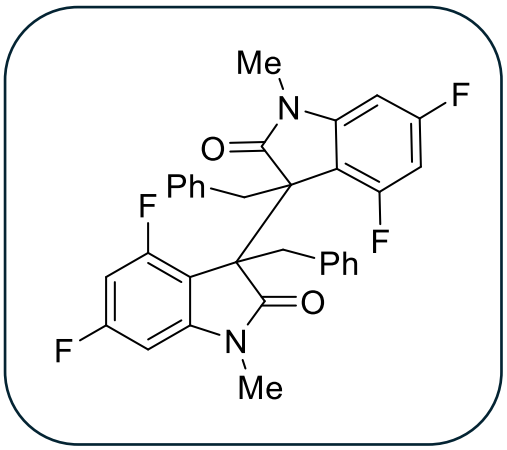

Prepared according to general procedure F using oxoanilide **115wb** (0.1589 g, 0.52 mmol), $Mn(OAc)_3.2H_2O$ (70.2 mg, 0.26 mmol) and $Co(OAc)_2.4H_2O$ (65.2 mg, 0.26 mmol) in dioxane (3.5 mL). Chromatography on silica gel with EtOAc/hexanes (0–10%) afforded **115w** as a 1:1.2 mixture of separable diastereomers (61.3 mg, 43% combined yield).

(±)-*dl*: Obtained as a yellow solid (27.9 mg); **R_f** = 0.71 (3:7 EtOAc/hexanes); **^{1}H NMR** (300 MHz, CDCl3) δ 7.00 (s, 10H), 6.19 (m, 2H), 5.88 (d, J = 8.3 Hz, 2H), 4.28 (d, J = 13.0 Hz, 2H), 3.70 (d, J = 13.2 Hz, 2H), 2.93 (s, 6H);

meso: Obtained as a yellow solid (33.4 mg); **R_f** = 0.69 (3:7 EtOAc/hexanes); **^{1}H NMR** (300 MHz, CDCl3) δ 6.91 (s, 6H), 6.85 (s, 4H), 6.25 (t, J = 9.9 Hz, 2H), 5.94 (d, J = 8.4 Hz, 2H), 4.02 (d, J = 12.9 Hz, 2H), 3.56 – 3.52 (d, J = 12.6 Hz) 2.67 (s, 6H);

Characterisation of side products

3,4-dimethyl-1-phenylpyrrolidin-2-one (51)[6]

Prepared according to general procedure D using oxoanilide **5n** (0.305 g, 1.40 mmol) and $Mn(OAc)_3.H_2O$ (1.129 g, 4.21 mmol) in toluene (10 mL). Chromatography on silica gel with EtOAc/hexanes (10–25%) afforded **11** as a brown oil (0.125 g, 47% yield). R_f 0.61 (3:7

3-cyclopentyl-1-methylindolin-2-one (115r')

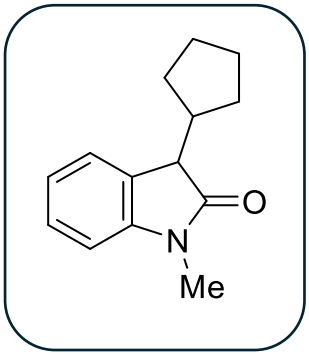

Prepared according to general procedure D using oxoanilide **115rb** (0.099 g, 0.46 mmol) and $Mn(OAc)_3.H_2O$ (0.327 g, 1.22 mmol) in toluene (4 mL). Chromatography on silica gel with EtOAc/hexanes (10–35%) afforded **115r'** as a white solid (0.054 g, 62% yield). **R_f** 0.35 (3:7 EtOAc/hexanes); **^{1}H NMR** (400 MHz, $CDCl_3$) δ 7.80 (dd, *J* = 7.7, 0.8 Hz, 1H), 7.30 (m, 1H), 7.04 (td, *J* = 7.7, 1.2 Hz, 1H), 6.78 (dd, *J* = 7.8, 0.8 Hz, 1H), 3.17 (s, 3H), 2.55–2.43 (m, 1H), 1.38–1.10 (m, 8H), 0.74–0.60 (m, 1H); **^{13}C NMR** (101 MHz, $CDCl_3$) δ 177.71, 144.5, 129.2, 128.7, 128.1, 121.7, 107.2, 58.5, 45.4, 27.9, 27.7, 26.1, 25.3, 24.7.

3-hydroxy-1,3-dimethylindolin-2-one (90)[7]

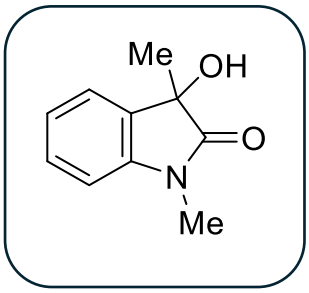

R_f 0.10 (3:7 EtOAc/hexanes); **^{1}H NMR** (300 MHz, $CDCl_3$) δ 7.47 – 7.30 (m, 2H), 7.11 (m, 1H), 6.85 (m, 1H), 3.20 (s, 3H), 1.60 (s, 3H). All recorded data were in accordance with those previously reported.

_N_-methyl-2-oxo-_N_-phenylpropanamide (91)[8]

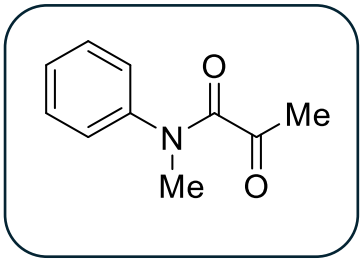

R_f 0.55 (3:7 EtOAc/hexanes); **^{1}H NMR** (300 MHz, $CDCl_3$) δ 7.40 – 7.28 (m, 3H), 7.17 (ddd, J = 7.9, 3.6, 1.4 Hz, 2H), 3.35 (s, 3H), 2.22 (s, 3H). All recorded data were in accordance with those previously reported.

3-ethyl-3-hydroxy-1-methylindolin-2-one (116)[7]

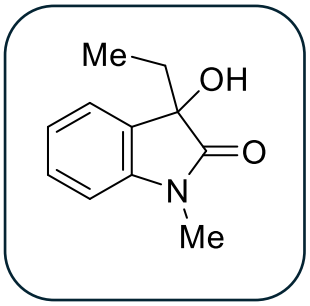

R_f 0.09 (3:7 EtOAc/hexanes); **^{1}H NMR** (600 MHz, $CDCl_3$) δ 7.39 – 7.30 (m, 2H), 7.14 – 7.07 (m, 1H), 6.84 (d, J = 7.7 Hz, 1H), 3.20 (d, J = 0.7 Hz, 3H), 2.04 – 1.93 (m, 2H), 0.76 (t, J = 7.5 Hz, 3H); **^{13}C NMR** (151 MHz, $CDCl_3$) δ 178.32, 143.78, 129.88, 129.79, 124.00, 123.25, 108.50, 31.80, 26.29, 7.69. All recorded data were in accordance with those previously reported.

Chapter 4 data

General procedure A: Synthesis of indoyl ketones

To a solution of 2-indole (1 eq.) and $InCl_3$ (5-10 mol%) in dry DCM (40 mL) was added vinyl ketone (1 eq.) dropwise, and the solution left to stir at room temperature. After 4–6 hours an equal amount of deionized water was added, and the layers separated. The aqueous layer was reextracted with DCM (20 mL x3), the combined organic extracts washed with brine (30 mL) before being dried over $MgSO_4$ and concentrated in vacuo. The crude product was purified by column chromatography with 0-15% EtOAc/Hex gradient to give ketone.

General procedure B: Synthesis of oximes

To EtOH was added indoyl ketone (1 eq.), $NH_2OH.HCl$ (2 eq.) and NaOAc (2 eq.) and the solution warmed up to 80°C and left to reflux for 2.5 hours. After cooling down, deionized water (50 mL) was added, and the solution extracted with DCM (50 mL x3). The combined organic extracts were dried over $MgSO_4$, and the crude product purified by column chromatography with 0-15% EtOAc/Hex gradient to give oxime as an inseparable mixture of *E*/*Z*-isomers.

General procedure C: Synthesis of isoxazolines

To a vial under Argon, containing oxime (1 eq.), PPh_3 (1.2 eq.) and Iridium photocatalyst (2 mol%) was added degassed DCM (1 mL/0.1 mmol of oxime) followed by Collidine (1 eq.). The solution was then degassed and irradiated with a 60W LED blue bulb. After 24 hours, 50 µL of internal standard (0.5606g of 1,3,5-trimethoxybenzene in 5 mL of $CDCl_3$) was added to the solution and crude NMR taken. The triplet peak of the methine ~5-5. ppm was referenced against the internal standard peak at 6.1 ppm and the ratios compared to determine the product yield.

General procedure D: Synthesis of Fischer indoles

To a biphasic mixture of DCM (0.6 M) and sat. $NaHCO_3$ (0.6 M) was added Phenylhydrazine hydrochloride (1.0 eq.) and acetone (1.1 eq.), which was left to stir for 3 hrs. Thereafter, the layers were separated and the aqueous layer extracted with 3x , dried over $MgSO_4$ and concentrated *in vacuo*. To the crude, ZnC_2 (1.2 eq.) was added and the

mixture heated at 140°C for 12 hrs. The resultant gummy residue was mixed with 1M HCl and DCM and the layers separated. The aqueous was then extracted with 3x EtOAc, and the combined organic extracts dried over $MgSO_4$ and concentrated *in vacuo*. The crude extract was purified by column chromatography with a 0-10% EtOAc/Hex gradient to afford the resultant indoles.

General Procedure E: Synthesis of Isoxazolines 5 via 4-CzIPN Photocatalysis by Jonathan Da Luz

To oxime (1 eq.) in 6 mL dry DCE, in a vial equipped with a magnetic stirrer bar was added 4-CzIPN (2 mol%) and collidine (0.3 eq.). The mixture was sealed with parafilm and a needle inserted through the lid to vent the system. Thereafter, the mixture was irradiated directly with an 18 W blue LED (@450 nm) without fan cooling (temperature recorded ranged from 55 to 60 °C) for 24 hours or until TLC analysis indicated consumption of the starting material. DCE was removed *in vacuo* and the residue loaded directly onto silica gel and purified by column chromatography using a EtOAc/Hex to furnish the resultant isoxazolines.

Characterisation data of acrylophenone[9]

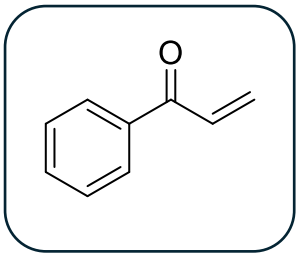

To a solution of N-methoxy-N-methylbenzamide (1.1 mL, 7.23 mmol, 1 eq.) in dry THF (30 mL) at 0°C was added 1M in THF of vinyl magnesium bromide (21.7 mL, 21.7 mmol, 3 eq.). After 2 hours, deionized water (20 mL) was added and the solution extracted with EtOAc (30 ml x3), washed with brine (20 mL) and dried over $MgSO_4$. The crude product was purified by column chromatography on silica gel with EtOAc/hexanes (0-10%) to afford **5** (15% yield). $\mathbf{R_f}$ = 0.82 (3:7 EtOAc:hexane);); **^{1}H NMR** (400 MHz, $CDCl_3$) δ 7.95 (d, *J* = 7.7 Hz, 2H), 7.60–7.56 (m, 1H), 7.49 (m, 2H), 7.17 (dd, *J* = 16.9, 10.7 Hz, 1H), 6.44 (d, *J* = 17.9 Hz, 1H), 5.94 (d, *J* = 10.6 Hz, 1H). All recorded data were in accordance with those previously reported.

Characterisation data of indolyl ketones

3-(1H-indol-3-yl)-1-phenylpropan-1-one (156)[10]

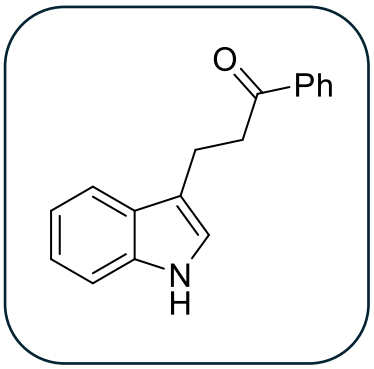

Prepared via **Figure 4.8**, using Weinreb amide **155** (2.016 g, 8.67 mmol) and PhMgBr (8.68 mL, 26.0 mmol) in THF (50 mL). Chromatography on silica gel with EtOAc/hexanes (5–25%) afforded **156** as a white, crystalline solid (1.783 g, 82% yield). $\mathbf{R_f}$ = 0.25 (3:7 EtOAc:hexane); **^{1}H NMR** (400 MHz, $CDCl_3$) δ 7.99 – 7.90 (m, 3H), 7.64 (d, *J* = 7.8 Hz, 1H), 7.58–7.53 (m, 1H), 7.48–7.43 (m, 2H), 7.38–7.36 (m, 1H), 7.23–7.19 (m, 1H), 7.16–7.12 (m, 1H), 7.06 (d, *J* = 2.3 Hz, 1H), 3.42–3.38 (m, 2H), 3.26–3.21 (m, 2H). All recorded data were in accordance with those previously reported.

1-(2-methyl-1H-indol-3-yl)pentan-3-one (163)[10]

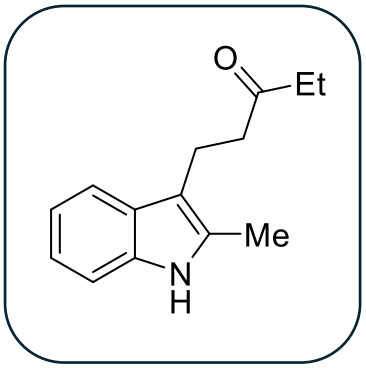

Prepared according to general procedure A, using 2-methyl-1H-indole (1.44 g, 11 mmol), $InCl_3$ (0.07 g, 0.03 mmol) and ethyl vinyl ketone **162** (1.09 mL, 11 mmol) in DCM (40 mL). Chromatography on silica gel with EtOAc/hexanes (0–15%) afforded **163** as a cream-coloured solid (1.993 g, 90% yield). $\mathbf{R_f}$ = 0.5 (3:7 EtOAc:hexane); **^{1}H NMR** (400 MHz, $CDCl_3$) δ 7.83 (d, *J* = 18.0 Hz, 1H), 7.52–7.46 (m, 1H), 7.29–7.20 (m, 1H), 7.16–7.03 (m, 2H), 3.04–2.94 (m, 2H), 2.79–2.68 (m, 2H), 2.36–2.29 (m, 5H), 1.02 (t, *J* = 7.3 Hz, 3H). All recorded data were in accordance with those previously reported.

3-(2-methyl-1H-indol-3-yl)-1-phenylpropan-1-one (170a)

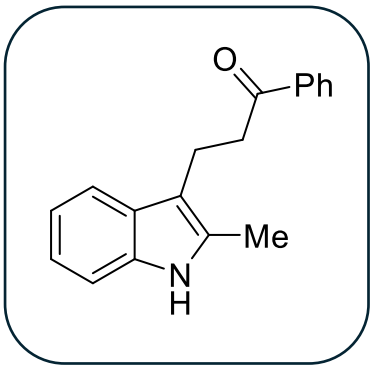

Prepared according to general procedure A, using 2-methyl-1H-indole (0.218 g, 1.66 mmol), $InCl_3$ (0.037 g, 0.17 mmol) and acrylophenone (0.22 g, 1.66 mmol) in DCM (20 mL). Chromatography on silica gel with EtOAc/hexanes (0–10%) afforded **170a** as a white solid (0.28 g, 64% yield). $\mathbf{R_f}$ = 0.74 (3:7 EtOAc:hexane); **^{1}H NMR** (400 MHz, $CDCl_3$) 7.96–7.89 (m, 2H), 7.74 (s, 1H), 7.57–7.50 (m, 2H), 7.44–7.40 (m, 2H),

7.29–7.26 (m, 1H), 7.16–7.06 (m, 2H), 3.32–3.28 (m, 2H), 3.18 – 3.12 (m, 2H), 2.40 (s, 3H); **HRMS** (ESI$^+$) *m/z*: [M + H] calcd for $C_{18}H_{18}NO^+$ 264.1383; found 264.1385.

1-(2-phenyl-1H-indol-3-yl)pentan-3-one (171a)[10]

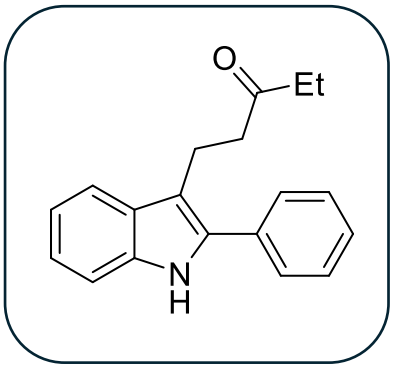

Prepared according to general procedure A, using 2-phenyl-1H-indole (1.071 g, 5.54 mmol), $InCl_3$ (0.061 g, 0.28 mmol) and ethyl vinyl ketone (0.55 mL, 5.54 mmol) in DCM (40 mL). Chromatography on silica gel with EtOAc/hexanes (0–10%) afforded **171a** as a pale-yellow solid (1.436 g, 93% yield). $\mathbf{R_f}$ = 0.66 (3:7 EtOAc:hexane); ^{1}**H NMR** (400 MHz, $CDCl_3$) 8.05 (br s, 1H), 7.60 (d, *J* = 7.9 Hz, 1H), 7.54 (d, *J* = 7.5 Hz, 2H), 7.48 (m, 2H), 7.39–7.36 (m, 2H), 7.22 (m, 1H), 7.15 (m, 1H), 3.25–3.16 (m, 2H), 2.81–2.77 (m, 2H), 2.39 (q, *J* = 7.1 Hz, 2H), 1.03 (t, *J* = 7.6 Hz, 3H). All recorded data were in accordance with those previously reported.

4-(7-chloro-5-fluoro-2-methyl-1H-indol-3-yl)butan-2-one (175na)

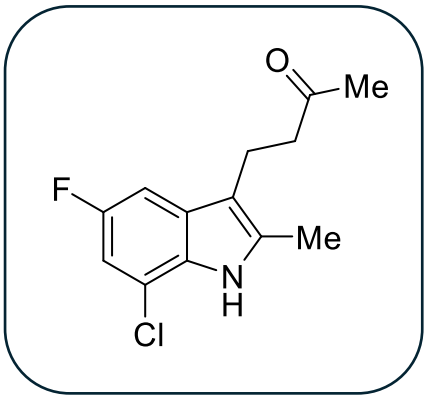

Prepared according to general procedure A, 2-methyl-1H-indole (0.1181 g, 0.64 mmol), $InCl_3$ (14.2 mg, 10 mol%) and methyl vinyl ketone (52.2 µL, 0.64 mmol) in DCM (10 mL). Chromatography on silica gel with EtOAc/hexanes (0–10%) afforded **17na** as a yellow oil (72.4 mg, 46% yield). $\mathbf{R_f}$ = 0.51 (3:7 EtOAc:hexane); ^{1}**H NMR** (300 MHz, $CDCl_3$) δ 7.97 (br s, 1H), 7.04 (dd, J = 9.2, 2.3 Hz, 1H), 6.90 (dd, J = 9.1, 2.3 Hz, 1H), 2.90 (t, J = 7.3 Hz, 2H), 2.72 (t, J = 7.3 Hz, 2H), 2.41 (s, 3H), 2.11 (s, 3H).

Characterisation data of oximes

3-(1H-indol-3-yl)-1-phenylpropan-1-one oxime (153a)[10]

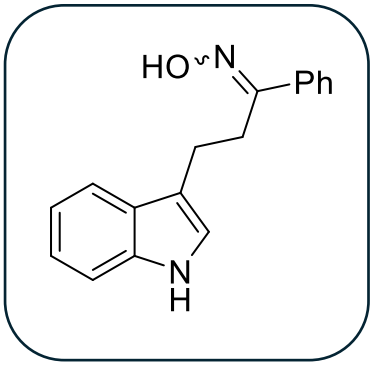

Prepared according to general procedure B, using ketone **156** (2.033 g, 8.16 mmol), $NH_2OH.HCl$ (1.134 g, 16.3 mmol) and sodium acetate (1.338 g, 16.3 mmol) in EtOH (50 mL). Chromatography on silica gel with EtOAc/hexanes (0–10%) afforded **153a** as a yellow solid (0.28 g, 64% yield). $\mathbf{R_f}$ = 0.74 (3:7 EtOAc:hexane); **IR** (film, vmax/cm^{-1}) 3416, 3240, 2911, 1455, 1334; **^{1}H NMR** (400 MHz, $CDCl_3$) δ 7.94 (br s, 1H), 7.71–7.60 (m, 3H), 7.41–7.34 (m, 4H), 7.22–7.18 (m, 1H), 7.13 (m, 1H), 7.05 (d, *J* = 2.2 Hz, 1H), 3.24–3.20 (m, 2H), 3.08–3.03 (m, 2H); **HRMS** (ESI^+) *m/z*: [M + H] calcd for $C_{17}H_{17}N_2O^+$ 265.1335; found 265.1333. All recorded data were in accordance with those previously reported.

1-(2-methyl-1H-indol-3-yl)- pentan-3-one oxime (160)[10]

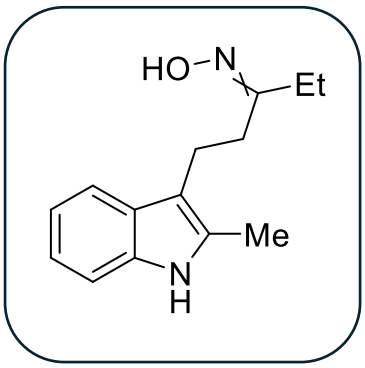

Prepared according to general procedure B, using ketone **163** (2.312 g, 11.5 mmol), $NH_2OH.HCl$ (1.597 g, 23.0 mmol) and sodium acetate (1.885 g, 23.0 mmol) in EtOH (50 mL). Chromatography on silica gel with EtOAc/hexanes (5–20%) afforded **160** as a yellow oil (1.891 g, 85% yield). $\mathbf{R_f}$ = 0.34 (3:7 EtOAc:hexane); **IR** (film, vmax/cm^{-1}) 3409, 2932, 1464, 1300; **^{1}H NMR** (400 MHz, $CDCl_3$) (stereoisomers: *E*/*Z*) δ 7.76 (br s, 2H), 7.54 (dd, *J* = 26.2, 7.1 Hz, 2H), 7.26 (d, *J* = 7.5 Hz, 2H), 7.11 (p, *J* = 7.2, 6.8 Hz, 4H), 3.00–2.96 (m, 2H), 2.95–2.89 (m, 1.33 H), 2.68–2.59 (m, 2H), 2.54–2.41 (m, 2.67H), 2.38 (s, 3H), 2.37 (s, 2H), 2.16 (q, *J* = 7.5 Hz, 2H), 1.13 (t, *J* = 7.6 Hz, 2H), 1.07 (t, *J* = 7.3 Hz, 3H); **HRMS** (ESI^+) *m/z*: [M + H] calcd for $C_{14}H_{19}N_2O^+$ 231.1492; found 231.1490. All recorded data were in accordance with those previously reported.

4-phenylbutan-2-one oxime (167)[11]

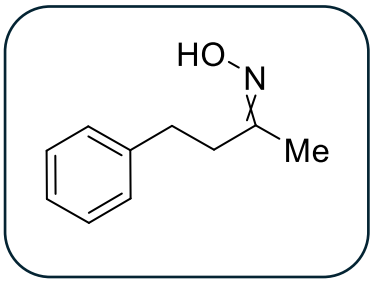

Prepared according to general procedure B, using 4-phenylbutan-2-one (1.2 mL, 8 mmol), $NH_2OH.HCl$ (0.668 g, 9.61 mmol) and sodium acetate (0.788 g, 9.61 mmol) in EtOH (30 mL). Chromatography on silica gel with EtOAc/hexanes (5–20%) afforded **167** as a colourless oil (0.752 g, 57% yield). $\mathbf{R_f}$ = 0.5 (3:7 EtOAc:hexane); **IR** (film, vmax/cm^{-1}) 3196, 2925, 1452, 1362; **^{1}H NMR** (400 MHz, $CDCl_3$) (stereoisomers: *E*/*Z*) δ 7.30 (m, 2H), 7.25–7.17 (m, 3H), 2.88–2.81 (m, 2H), 2.71–2.66 (m, 0.4H) 2.56 – 2.49 (m, 1.6H), 1.93 (s, 2.4H), 1.85 (s, 0.6H); **HRMS** (ESI^+) *m/z*: [M + H] calcd for $C_{10}H_{14}NO^+$ 164.1070; found 164.1069. All recorded data were in accordance with those previously reported.

3-(2-methyl-1H-indol-3-yl)-1-phenylpropan-1-one oxime (170)

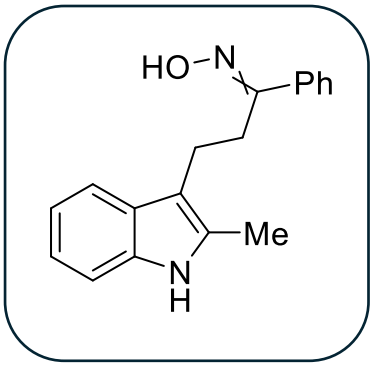

Prepared according to general procedure B, using ketone **170a** (0.279 g, 1.06 mmol), $NH_2OH.HCl$ (0.147 g, 2.12 mmol) and sodium acetate (0.174 g, 2.12 mmol) in EtOH (15 mL). Chromatography on silica gel with EtOAc/hexanes (5–15%) afforded **170** as a cream-coloured solid (0.293 g, 99% yield). $\mathbf{R_f}$ = 0.63 (3:7 EtOAc:hexane); **IR** (film, vmax/cm^{-1}) 3413, 3390, 1459, 1301; **^{1}H NMR** (400 MHz, $CDCl_3$) (stereoisomers: *E*/*Z*) δ 7.71 (br s, 1H), 7.63–7.54 (m, 3H), 7.40–7.34 (m, 3H), 7.27–7.24 (m, 2H), 7.14–7.06 (m, 2H), 3.14–3.06 (m, 2H), 3.04–2.96 (m, 2H), 2.34 (s, 3H); **HRMS** (ESI^+) *m/z*: [M + H] calcd for $C_{18}H_{19}N_2O^+$ 279.1492; found 279.1492. All recorded data were in accordance with those previously reported.

1-(2-phenyl-1H-indol-3-yl)pentan-3-one oxime (171)

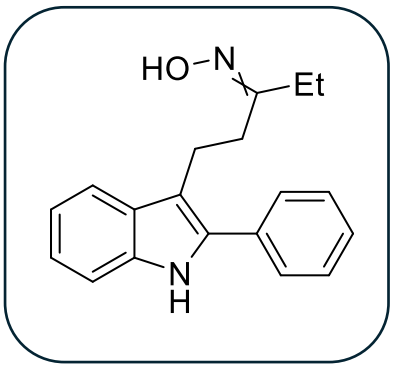

Prepared according to general procedure B, using ketone **171a** (1.675 g, 6.04 mmol), $NH_2OH.HCl$ (0.840 g, 12.1 mmol) and sodium acetate (0.991 g, 12.1 mmol) in EtOH (40 mL). Chromatography on silica gel with EtOAc/hexanes (5–15%) afforded **171** as a cream-coloured solid (0.293 g, 99% yield). $\mathbf{R_f}$ = 0.51 (3:7 EtOAc:hexane); **IR** (film, vmax/cm^{-1}) 3392,

3143, 2964, 1451, 1306; **^{1}H NMR** (400 MHz, $CDCl_3$) (stereoisomers: *E*/*Z*) δ 8.06 (s, 1H), 7.73 (d, *J* = 7.8 Hz, 1H), 7.66–7.54 (m, 2H), 7.49–7.45 (m, 2H), 7.40–7.35 (m, 2H), 7.24–7.12 (m, 2H), 3.17–3.11 (m, 2H), 2.78–2.74 (m, 1.6H), 2.63–2.58 (m, 0.4H), 2.40 (q, *J* = 7.7 Hz, 0.4H). 2.25 (q, *J* = 7.3 Hz, 1.6H), 1.10 (t, *J* = 7.3 Hz, 3H); **HRMS** (ESI^+) *m/z*: [M + H] calcd for $C_{19}H_{21}N_2O^+$ 293.1648; found 293.1649. All recorded data were in accordance with those previously reported.

4-(2-methyl-1H-indol-3-yl)-4-phenylbutan-2-one oxime (175da)

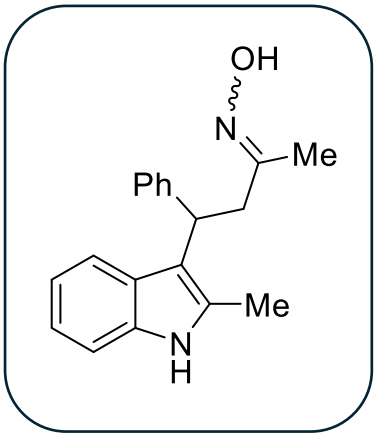

Prepared according to general procedure B, using 4-(2-methyl-1H-indol-3-yl)-4-phenylbutan-2-one (83.6 mg, 0.30 mmol), $NH_2OH.HCl$ (41.9 mg, 0.60 mmol) and sodium acetate (49.5 mg, 0.60 mmol) in EtOH (20 mL). Chromatography on silica gel with EtOAc/hexanes (0–15%) afforded **175da** as 2:1 ratio of separately isomers (78.5 mg combined, 87% yield).

Isomer 1: obtained as a colourless oil (54.5 mg); $\mathbf{R_f}$ = 0.15 (3:7 EtOAc:hexane); ^{1}**H NMR** (300 MHz, $CDCl_3$) δ 7.64 (s, 1H), 7.39 (d, J = 7.8 Hz, 1H), 7.27 (d, J = 7.7 Hz, 2H), 7.22 – 6.88 (m, 7H), 4.54 – 4.40 (m, 1H), 3.05 (qd, J = 13.9, 8.0 Hz, 2H), 2.20 (s, 3H), 1.65 (s, 3H).

Isomer 2: obtained as a colourless oil (24.0 mg); $\mathbf{R_f}$ = 0.12 (3:7 EtOAc:hexane); **^{1}H NMR** (300 MHz, $CDCl_3$) δ 7.77 (s, 1H), 7.40 (dd, J = 10.2, 7.8 Hz, 3H), 7.26 (dd, J = 8.4, 6.8 Hz, 3H), 7.20 – 6.93 (m, 3H), 4.83 (dd, J = 10.2, 6.2 Hz, 1H), 3.55 (dd, J = 12.8, 6.2 Hz, 1H), 3.00 (dd, J = 12.8, 10.2 Hz, 1H), 2.36 (s, 3H), 1.43 (s, 3H).

4-(7-chloro-5-fluoro-2-methyl-1H-indol-3-yl)butan-2-one oxime (175nb)

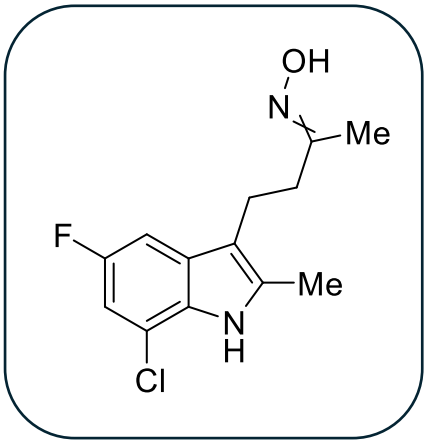

Prepared according to general procedure B, **175na** (72.4 mg, 0.28 mmol), $NH_2OH.HCl$ 39.7 mg, 0.57 mmol) and sodium acetate (46.8 mg, 0.57 mmol) in EtOH (3 mL). Chromatography on silica gel with EtOAc/hexanes (10–25%) (0–10%) afforded **175nb** as a brown oil (71.9 mg, 96% yield). $\mathbf{R_f}$ = 0.42 (3:7 EtOAc:hexane); **^{1}H NMR** (300 MHz, $CDCl_3$) δ 7.92 (s, 1H), 7.05 (dd, J = 9.2, 2.2 Hz, 1H), 6.91 (dd, J = 9.2, 2.2 Hz, 1H), 2.84 (dd, J = 9.5, 6.4 Hz, 2H), 2.52 – 2.32 (m, 5H), 1.91 (s, 3H).

Characterisation data of azacarbazole

2-phenyl-9H-pyrido[2,3-b]indole (144)

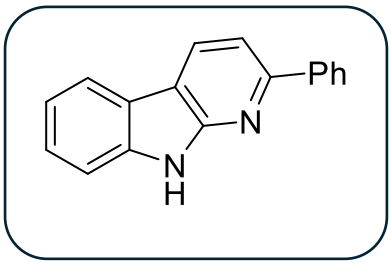

Prepared according to **Table 4.1**, entry 9, using oxime **153a** (28.1 mg, 0.1 mmol), PPh_3 (33.2 mg, 0.13 mmol), $[Ir(df(CF_3)ppy)dtbbpy]PF_6$ (2.3 mg, 2 mol%), Na_2CO_3 (5.6 mg, 0.05 mmol) in degassed DCM (1 mL). Preparative chromatography on silica-coated plate with 2:3 EtOAc:hexane afforded **144** as pale-yellow solid (5.3 mg, 20% yield). $\mathbf{R_f}$ = 0.38 (3:7 EtOAc:hexane); **^{1}H NMR** (400 MHz, DMSO-d6) δ 11.87 (s, 1H), 8.58 (d, *J* = 7.7 Hz, 1H), 8.21–8.15 (m, 3H), 7.82 (d, 8.0 Hz, 1H), 7.55–7.41 (m, 5H), 7.23 (t, *J* = 7.3 Hz, 1H); **HRMS** (ESI^+) *m/z*: [M + H] calcd for $C_{17}H_{13}N_2O^+$ 245.1073; found 245.1066. All recorded data were in accordance with those previously reported.

Characterisation data of isooxazolines

3-ethyl-5-(2-methyl-1H-indol-3-yl)-4,5-dihydroisoxazole (165)

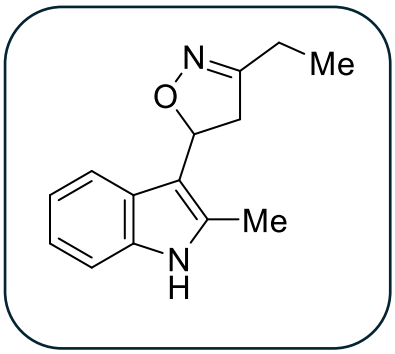

Prepared according to general procedure C, using oxime **160** (45.7 mg, 0.2 mmol), [Ir(df(CF_3)ppy)dtbbpy]PF_6 (4.5 mg, 2 mol%), PPh_3 (62.5 mg, 0.24 mmol) and collidine (26 µL, 0.2 mmol) in degassed DCM (2 mL). Preparative chromatography on silica-coated plate with 2:3 EtOAc:hexane afforded **165** as yellow oil (21.3 mg, 47% yield). $\mathbf{R_f}$ = 0.26 (3:7 EtOAc:hexane); **IR** (film, vmax/cm^{-1}) 3276, 2925, 2854, 1703, 1620, 1461; **^{1}H NMR** (400 MHz, $CDCl_3$) δ 7.94 (s, 1H), 7.44 (d, *J* = 7.8 Hz, 1H), 7.27 (d, *J* = 8.2 Hz, 1H), 7.13 (m, 1H), 7.07 (m, 1H), 5.81 (t, *J* = 10.7 Hz, 1H), 3.23 (d, *J* = 10.7 Hz, 2H), 2.51 (q, *J* = 7.5 Hz, 2H), 2.42 (d, *J* = 3.1 Hz, 3H), 1.27 (t, *J* = 7.6 Hz, 4H); **^{13}C NMR** (101 MHz, $CDCl_3$) δ 160.2, 135.7, 133.2, 126.3, 121.7, 120.0, 118.8, 110.7, 110.5, 76.0, 42.7, 21.7, 12.0, 11.3; **HRMS** (ESI^+) *m/z*: [M + H] calcd for $C_{14}H_{17}N_2O^+$ 229.1335; found 229.1334.

5-(2-methyl-1H-indol-3-yl)-3-phenyl-4,5-dihydroisoxazole (172)

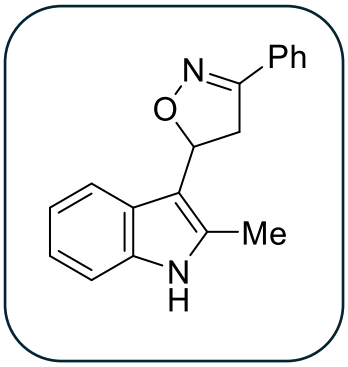

Prepared according to general procedure C, using oxime **170** (60 mg, 0.21 mmol), [Ir(df(CF_3)ppy)dtbbpy]PF_6 (4.8 mg, 2 mol%), PPh_3 (67.9 mg, 0.26 mmol) and collidine (29 µL, 0.21 mmol) in degassed DCM (1 mL). Preparative chromatography on silica-coated plate with 1:1 EtOAc:hexane afforded **172** as pale-yellow oil (11 mg, 18% yield). $\mathbf{R_f}$ = 0.28 (3:7 EtOAc:hexane); **IR** (film, vmax/cm^{-1}) 3393, 3059, 2923, 2251, 1461, 1446, 1355; **^{1}H NMR** (400 MHz, $CDCl_3$) δ 8.01 (br s, 1H), 7.79–7.74 (m, 2H), 7.46–7.42 (m, 4H), 7.28 (d, *J* = 7.7 Hz, 1H), 7.14–7.10 (m, 1H), 7.05–7.01 (m, 1H), 6.01 (t, *J* = 10.6 Hz, 1H), 3.65 (d, *J* = 10.7 Hz, 2H), 2.45 (s, 3H); **^{13}C NMR** (101 MHz, $CDCl_3$) δ 156.7, 135.7, 133.5, 130.1, 130.1, 128.9, 126.8, 126.2, 121.8, 120.1, 118.9, 110.7, 110.2, 77.4, 40.6, 12.0; **HRMS** (ESI^+) *m/z*: [M + H] calcd for $C_{18}H_{17}N_2O^+$ 277.1335; found 277.1336.

3-ethyl-5-(2-phenyl-1H-indol-3-yl)-4,5-dihydroisoxazole (173)

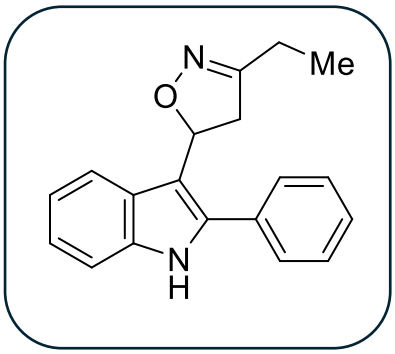

Prepared according to general procedure C, using oxime **171** (40.5 mg, 0.14 mmol), $[Ir(df(CF_3)ppy)dtbbpy]PF_6$ (3.1 mg, 2 mol%), PPh_3 (43.6 mg, 0.16 mmol) and collidine (18 µL, 0.14 mmol) in degassed DCM (1.5 mL). Preparative chromatography on silica-coated plate with 3:7 EtOAc:hexane afforded **173** as yellow oil (17.8 mg, 44% yield). $\mathbf{R_f}$ = 0.62 (3:7 EtOAc:hexane); **IR** (film, vmax/cm^{-1}) 3300, 3059, 2927, 1455; **^{1}H NMR** (400 MHz, $CDCl_3$) δ 8.19 (br s, 1H), 7.60–7.54 (m, 3H), 7.50–7.46 (m, 2H), 7.44–7.38 (m, 2H), 7.23 (d, *J* = 8.1 Hz, 1H), 7.15 (m, 1H), 5.89 (t, *J* = 11.0 Hz, 1H), 3.35 (dd, *J* = 17.2, 10.3 Hz, 1H), 3.19 (dd, *J* = 16.9, 11.4 Hz, 1H), 2.50 (q, *J* = 7.5 Hz, 2H), 1.26 (t, *J* = 7.3 Hz, 3H); **HRMS** (ESI^+) *m/z*: [M + H] calcd for $C_{19}H_{19}N_2O^+$ 291.1492; found 291.149

3-methyl-5-(2-methyl-1H-indol-3-yl)-5-phenyl-4,5-dihydroisoxazole (175d)

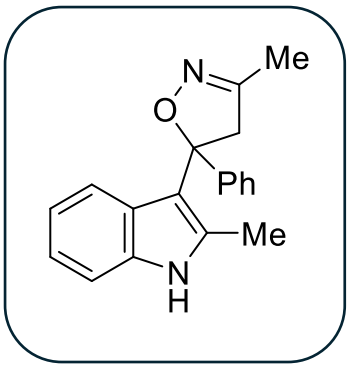

Prepared according to general procedure E using oxime **175da** (78.5 mg, 0.27 mmol), 4-CzIPN (4.2 mg, 2 mol%) and collidine (10.6 µL, 0.08 mmol) in degassed DCE (6 mL). Chromatography on silica gel with EtOAc/hexanes (5 –15%) afforded **175d** as a white solid (44.4 mg, 57% yield); $\mathbf{R_f}$ 0.39; **^{1}H NMR** (300 MHz, $CDCl_3$) δ 7.96 (s, 1H), 7.45 (t, J = 6.6 Hz, 3H), 7.32 – 7.21 (m, 4H), 7.09 (m, 2H), 3.89 (d, J = 16.7 Hz, 1H), 3.64 (d, J = 16.7 Hz, 1H), 2.40 (s, 3H), 2.03 (s, 3H); **^{13}C NMR** (75 MHz, $CDCl_3$) δ 155.5, 145.1, 135.2, 132.8, 128.4, 127.5, 127.1, 125.9, 121.1, 119.8, 119.4, 113.9, 110.6, 89.4, 52.5, 14.0, 13.6.

3-(3,4-dimethoxyphenyl)-5-(2-methyl-1H-indol-3-yl)-4,5-dihydroisoxazole (175h)

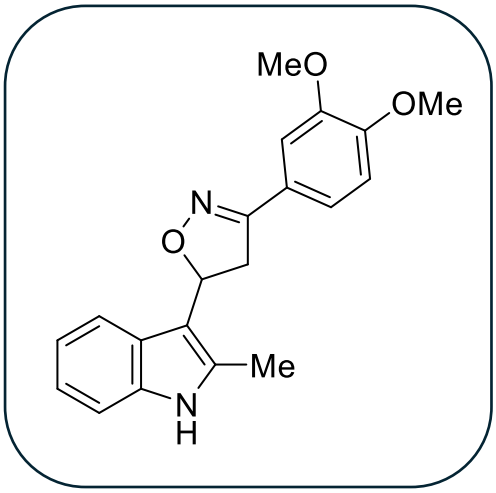

Prepared according to general procedure E using 1-(3,4-dimethoxyphenyl)-3-(2-methyl-1H-indol-3-yl)propan-1-one oxime (71.1 mg, 0.21 mmol), 4-CzIPN (3.3 mg, 2 mol%) and collidine (8.32 µL, 30 mol%) in DCE (6 mL). Chromatography on silica gel with EtOAc/hexanes (5 –15%) afforded **175h** as a yellow solid (41.7 mg, 59% yield); R_f 0.39; **^{1}H NMR** (300 MHz, $CDCl_3$) δ 8.07 (s, 1H), 7.53 (s, 1H), 7.45 (d, J = 7.8 Hz, 1H), 7.29 – 7.26 (m, 1H), 7.17 – 6.99 (m, 3H), 6.89 (d, J = 8.3 Hz, 1H), 5.99 (t, J = 10.6 Hz, 1H), 3.94 (s, 3H), 3.93 (s, 3H), 3.63 (d, J = 10.8 Hz, 2H), 2.42 (s, 3H); **^{13}C NMR** (75 MHz, $CDCl_3$) δ 156.6, 150.8, 149.3, 135.7, 133.6, 126.1, 122.8, 121.7, 120.4, 120.0, 118.8, 110.8, 110.6, 110.0, 108.7, 77.2, 56.1, 56.0, 40.7, 12.0.

5-(7-chloro-5-fluoro-2-methyl-1H-indol-3-yl)-3-methyl-4,5-dihydroisoxazole (175n)

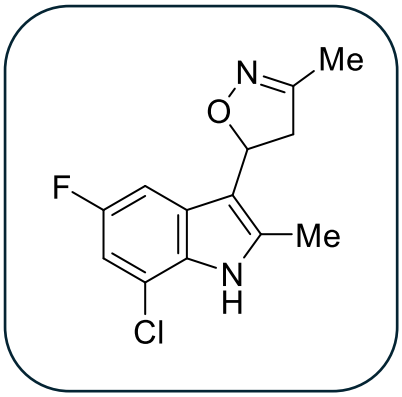

Prepared according to general procedure E using **175nb** (70.0 mg, 0.26 mmol), 4-CzIPN (4.1 mg, 2 mol%) and collidine (10.3 µL, 30 mol%) in DCE (6 mL). Chromatography on silica gel with EtOAc/hexanes (10 – 30%) afforded **175n** as a brown-orange solid (41.6 mg, 60% yield); **R_f** 0.13; **^{1}H NMR** (300 MHz, $CDCl_3$) δ 8.13 (s, 1H), 7.01 (d, J = 8.8 Hz, 1H), 6.94 (d, J = 9.0 Hz, 1H), 5.75 (t, J = 10.5 Hz, 1H), 3.24 (dd, J = 17.2, 11.2 Hz, 1H), 3.10 (dd, J = 17.2, 10.1 Hz, 1H), 2.45 (s, 3H), 2.13 (s, 3H); **^{13}C NMR** (75 MHz, $CDCl_3$) δ 155.4, 135.5, 129.6, 116.0, 111.8, 109.9, 109.5, 103.2, 102.9, 75.7, 44.4, 13.4, 12.0.

3-methyl-5-(2-phenyl-1H-indol-3-yl)-4,5-dihydroisoxazole (175r)

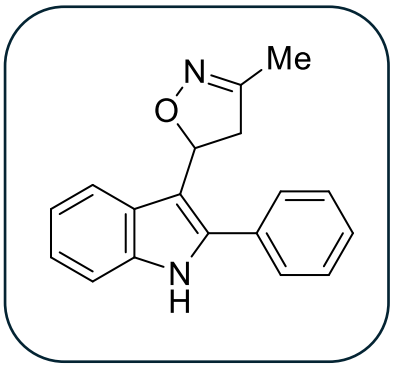

Prepared according to general procedure E using 4-(2-phenyl-1H-indol-3-yl)butan-2-one oxime (70 mg, 0.25 mmol), 4-CzIPN (3.9 mg, 2 mol%) and collidine (9.96 µL, 30 mol%) in DCE (6 mL). Chromatography on silica gel with EtOAc/hexanes (10–20%) afforded **175r** as a pale brown-orange solid (47.2 mg, 68% yield); $\mathbf{R_f}$ 0.27; **^{1}H-NMR** (300 MHz, $CDCl_3$) δ 8.16 (s, 1H), 7.59 – 7.40 (m, 6H), 7.25 – 7.13 (m, 3H), 5.90 (t, J = 10.7 Hz, 1H), 3.35 (dd, J = 17.4, 10.2 Hz, 1H), 3.19 (dd, J = 17.5, 11.3 Hz, 1H), 2.13 (s, 3H); **^{13}C NMR** (75 MHz, $CDCl_3$) δ 155.5, 137.5, 136.4, 132.1, 129.1, 129.0, 128.6, 128.1, 126.5, 122.9, 120.6, 120.0, 119.8, 119.1, 111.4, 111.1, 44.3, 13.5.

References

(1) Dobah, F.; Mazodze, C. M.; Petersen, W. F. Cross-Dehydrogenative Cyclization-Dimerization Cascade Sequence for the Synthesis of Symmetrical 3,3'-Bisoxindoles. *Org. Lett.* **2021**, *23* (14), 5466–5470. https://doi.org/10.1021/acs.orglett.1c01799.

(2) Mazodze, C. M.; Petersen, W. F. Radical Decarboxylation Strategies for Synthesis of Nitrogen- Containing Heterocycles, University of Cape Town, South Africa, 2023.

(3) Drouhin, P.; Hurst, T. E.; Whitwood, A. C.; Taylor, R. J. K. Copper-Mediated Construction of Spirocyclic Bis-Oxindoles via a Double C-H, Ar-H Coupling Process. *Org. Lett.* **2014**, *16* (18), 4900–4903. https://doi.org/10.1021/ol5024129.

(4) Yang, P.; Wang, X.; Ma, Y.; Sun, Y.; Zhang, L.; Yue, J.; Fu, K.; Zhou, J. S.; Tang, B. Nickel-Catalyzed: C-Alkylation of Thioamide, Amides and Esters by Primary Alcohols through a Hydrogen Autotransfer Strategy. *Chem. Commun.* **2020**, *56*, 14083–14086. https://doi.org/10.1039/d0cc06468h.

(5) Drouhin, P.; Hurst, T. E.; Whitwood, A. C.; Taylor, R. J. K. Substrate Scope in the Copper-Mediated Construction of Bis-Oxindoles via a Double C-H/Ar-H Coupling Process. *Tetrahedron* **2015**, *71* (39), 7124–7136. https://doi.org/10.1016/j.tet.2015.02.060.

(6) Naito, T.; Honda, Y.; Miyata, O.; Ninomiya, I. Radical Cyclisation in Heterocycle Synthesis. Part 1. Sulfanyl Radical Addition-Cyclisation of Dienylamides for Lactam Synthesis. *J. Chem. Soc. Perkin Trans. 1* **1995**, *1*, 19–26. https://doi.org/10.1039/p19950000019.

(7) Gorokhovik, I.; Neuville, L.; Zhu, J. Trifluoroacetic Acid-Promoted Synthesis of 3-Hydroxy, 3-Amino and Spirooxindoles from α-Keto-N-Anilides. *Org. Lett.* **2011**, *13* (20), 5536–5539. https://doi.org/10.1021/ol202263a.

(8) Ma, B.; Miao, T.; Sun, Y.; He, Y.; Liu, J.; Feng, Y.; Chen, H.; Fan, Q. H. A New Class of Tunable Dendritic Diphosphine Ligands: Synthesis and Applications in the Ru-Catalyzed Asymmetric Hydrogenation of Functionalized Ketones. *Chem. - A Eur. J.* **2014**, *20* (32), 9969–9978. https://doi.org/10.1002/chem.201402709.

(9) Sorbera, L. A.; Serradell, N.; Bolós, J.; Rosa, E. Enzastaurin Hydrochloride. *Drugs Future* **2007**, No. 32, 297–309. https://doi.org/10.1358/dof.2007.032.04.1095514.

(10) Wang, P. F.; Chen, C.; Chen, H.; Han, L. S.; Liu, L.; Sun, H.; Wen, X.; Xu, Q. L. Concise Synthesis of Spiro[Indoline-3,2'-Pyrrolidine] and 1-Azacarbazole Derivatives via Copper-Catalyzed Cyclization of Indoles. *Adv. Synth. Catal.* **2017**, *359* (14), 2339–2344. https://doi.org/10.1002/adsc.201700073.

(11) Holman, S. D. L.; Wills, A. G.; Fazakerley, N. J.; Poole, D. L.; Coe, D. M.; Berlouis, L. A.; Reid, M. Electrochemical Synthesis of Isoxazolines: Method and Mechanism. *Chem. - A Eur. J.* **2022**, *28* (13), e202103728. https://doi.org/10.1002/chem.202103728.

Appendix – NMR spectra

^{1}H NMR (400 MHz, $CDCl_3$)

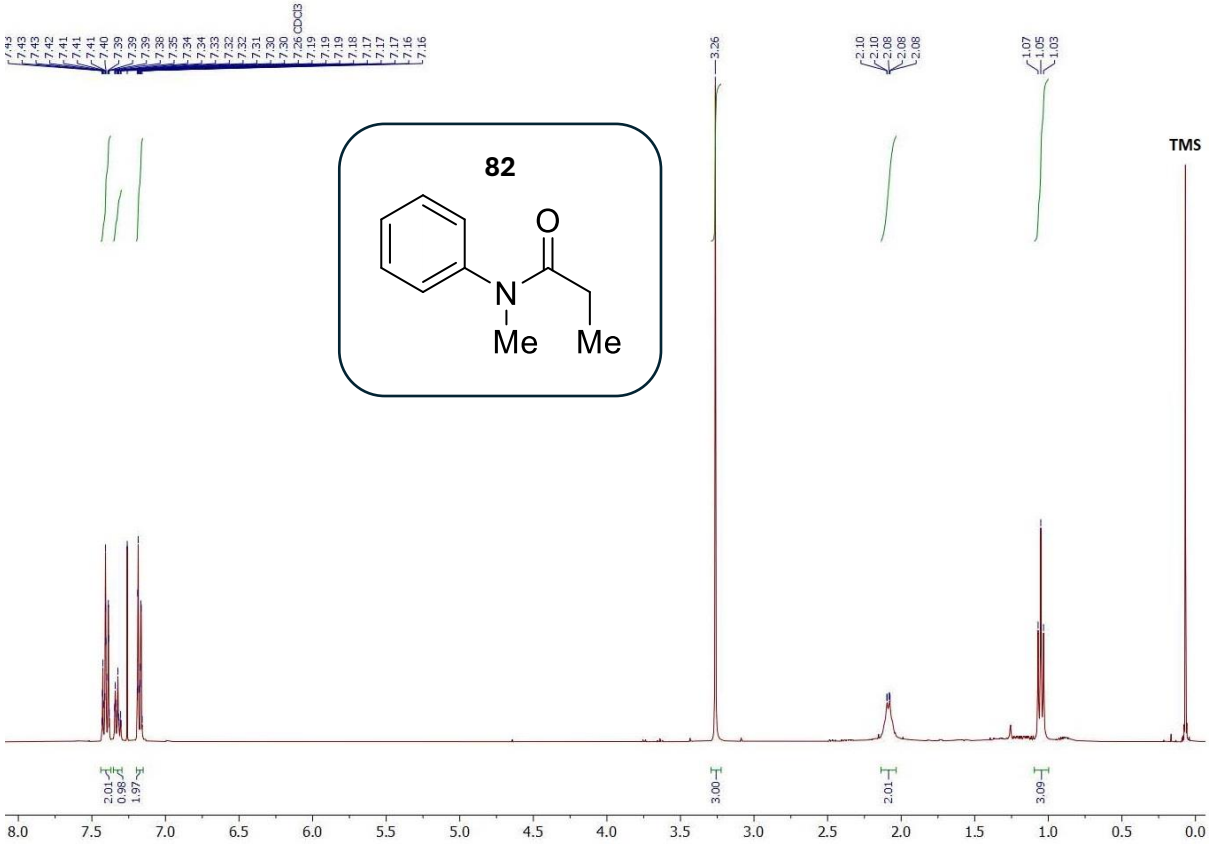

^{13}C NMR (101 MHz, $CDCl_3$)

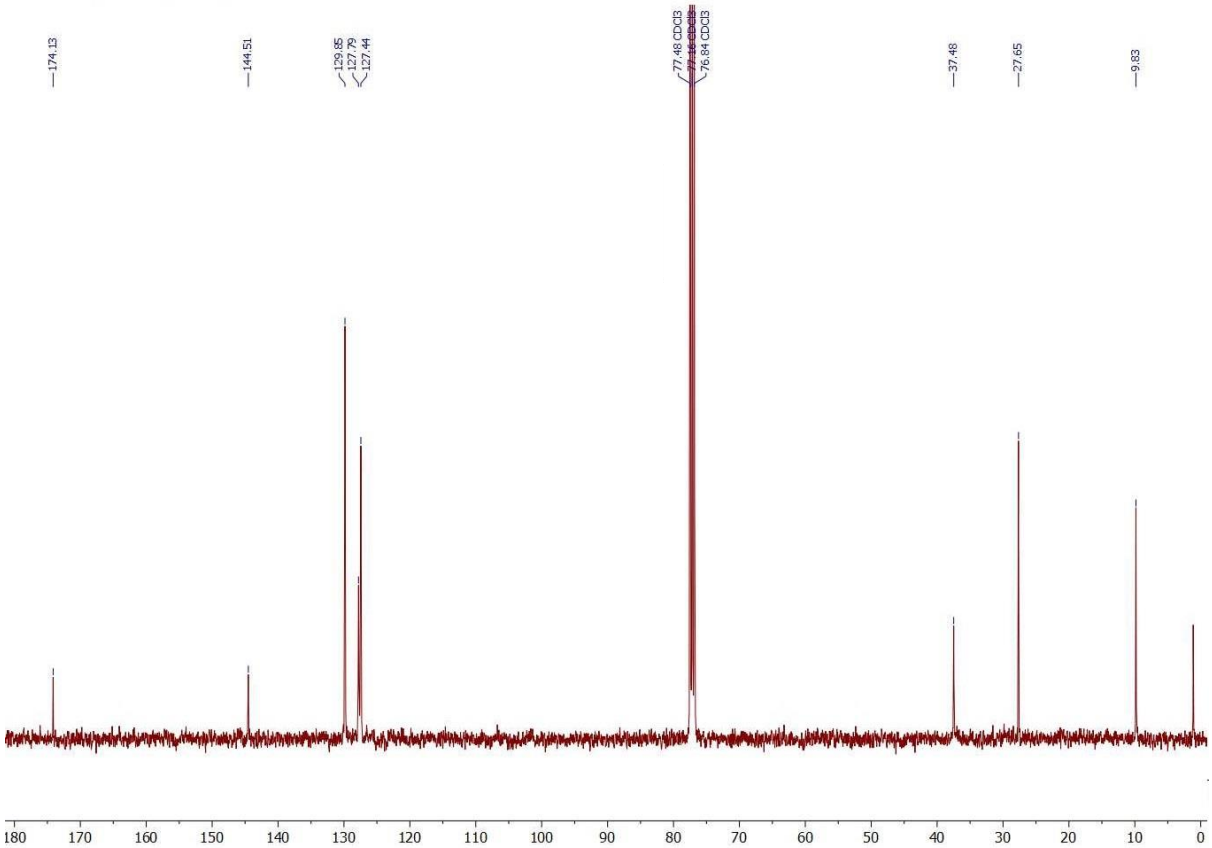

^{1}H NMR (400 MHz, $CDCl_3$)

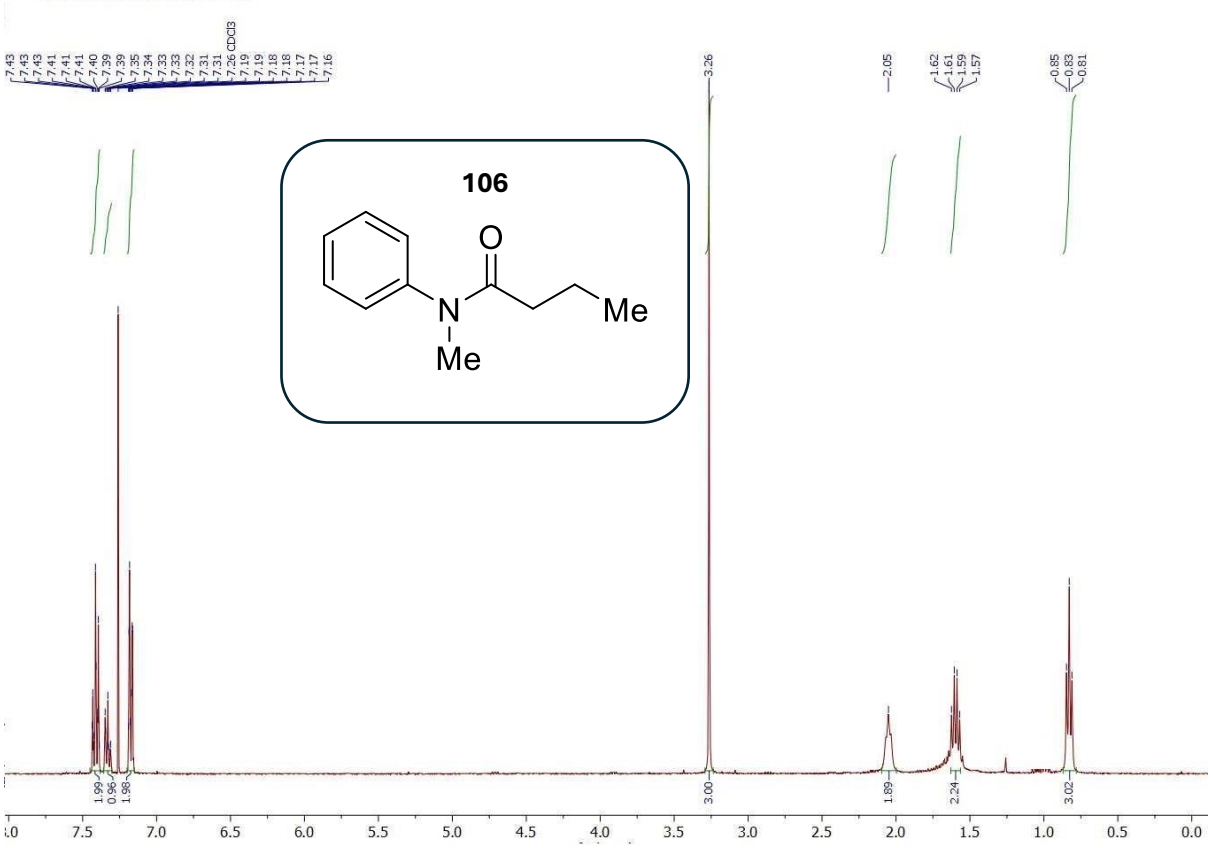

^{13}C NMR (101 MHz, $CDCl_3$)

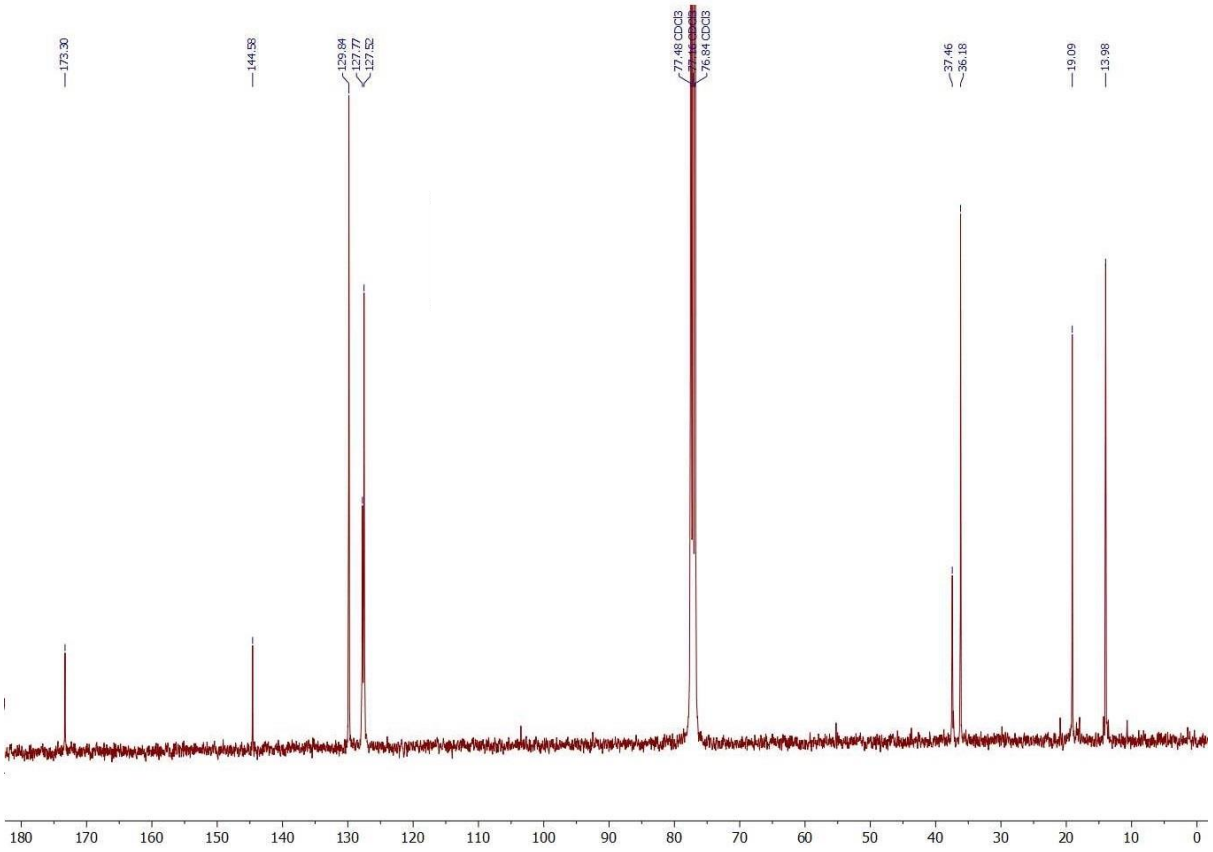

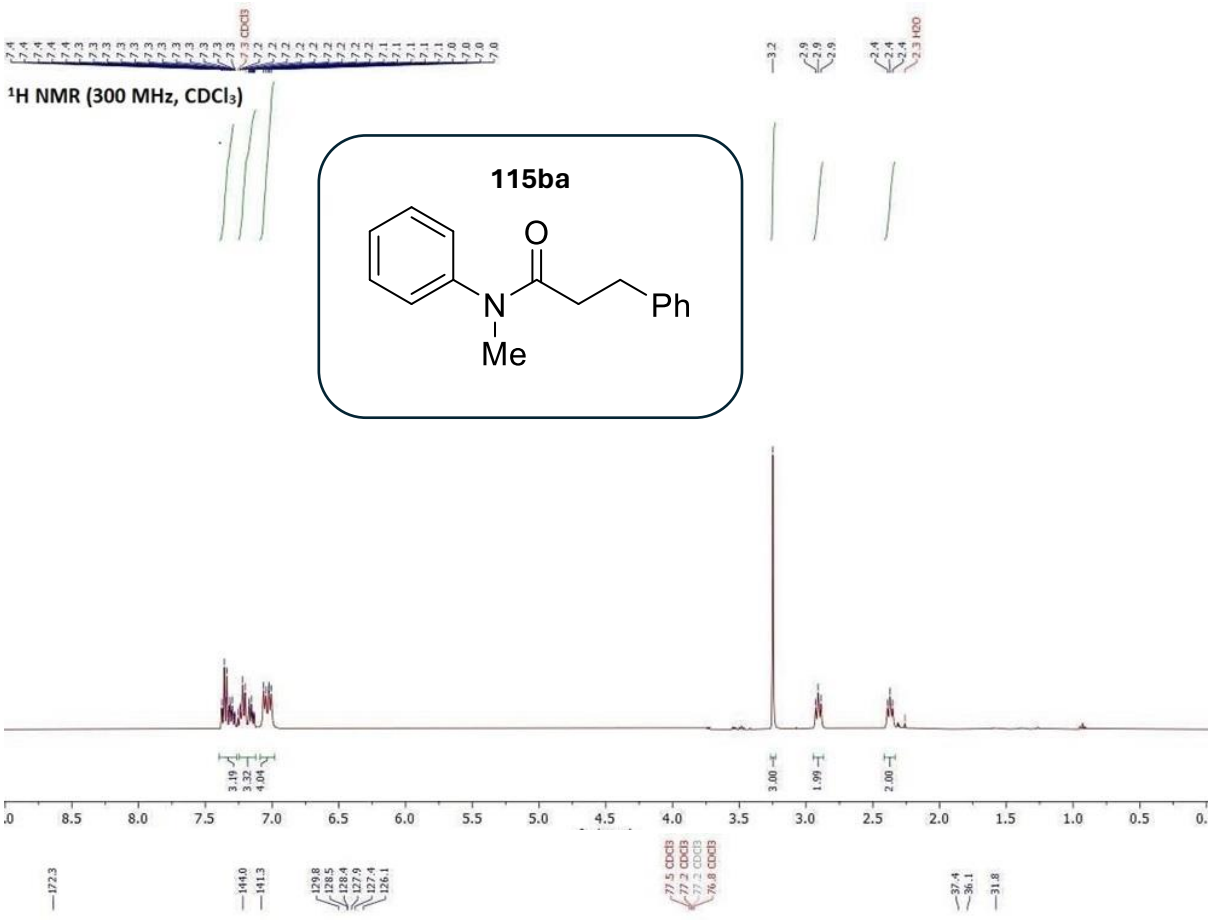
¹H NMR (300 MHz, CDCl₃)
115ba
O
N
Me
Ph
¹³C NMR (101 MHz, CDCl₃)
f1 (ppm)

^{1}H NMR (600 MHz, $CDCl_3$)

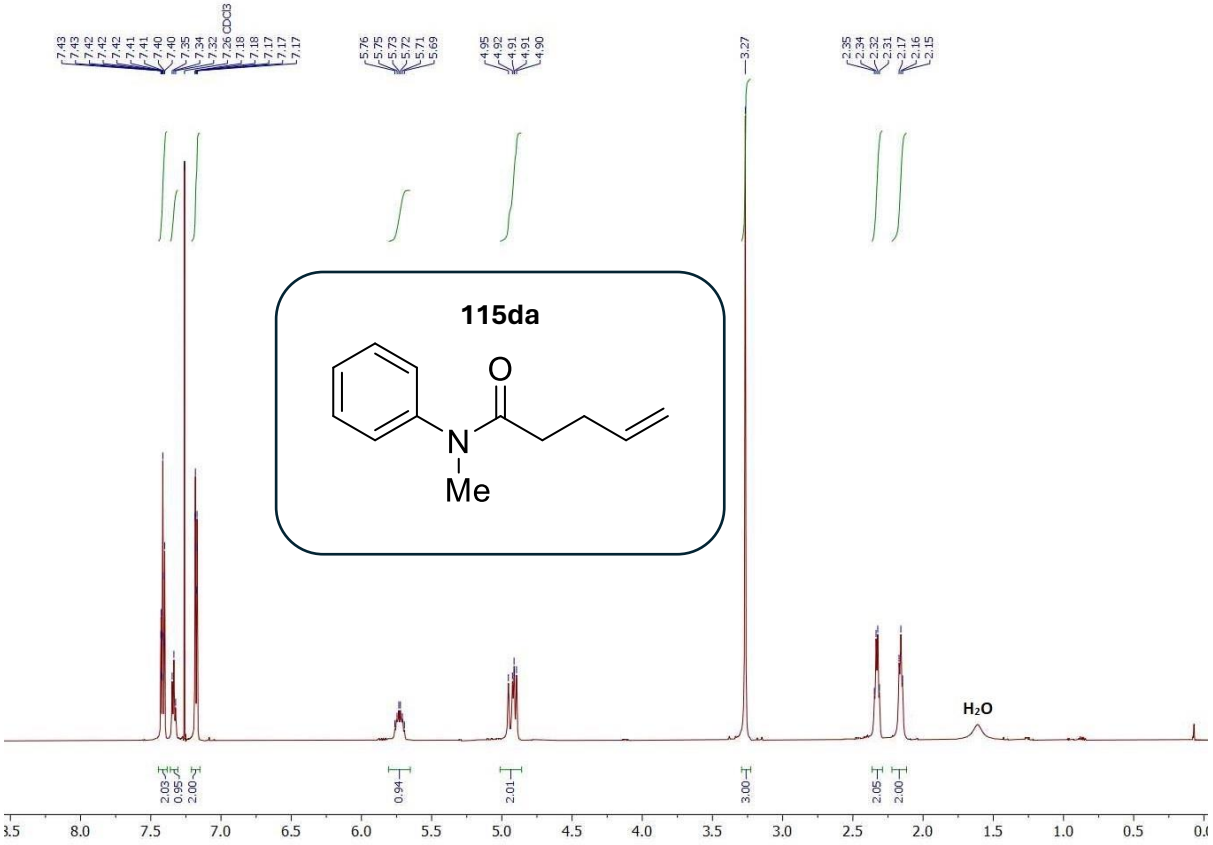

^{13}C NMR (151 MHz, $CDCl_3$)

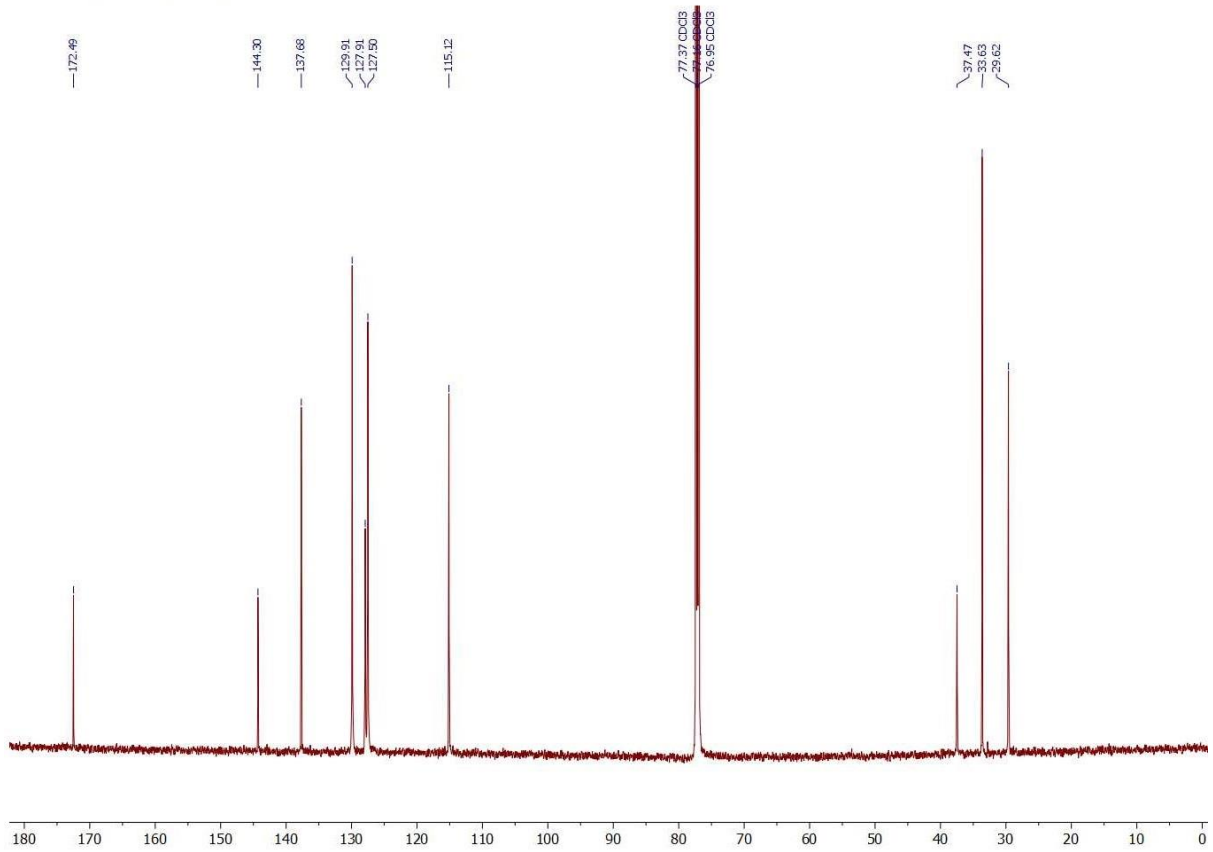

^{1}H NMR (400 MHz, $CDCl_3$)

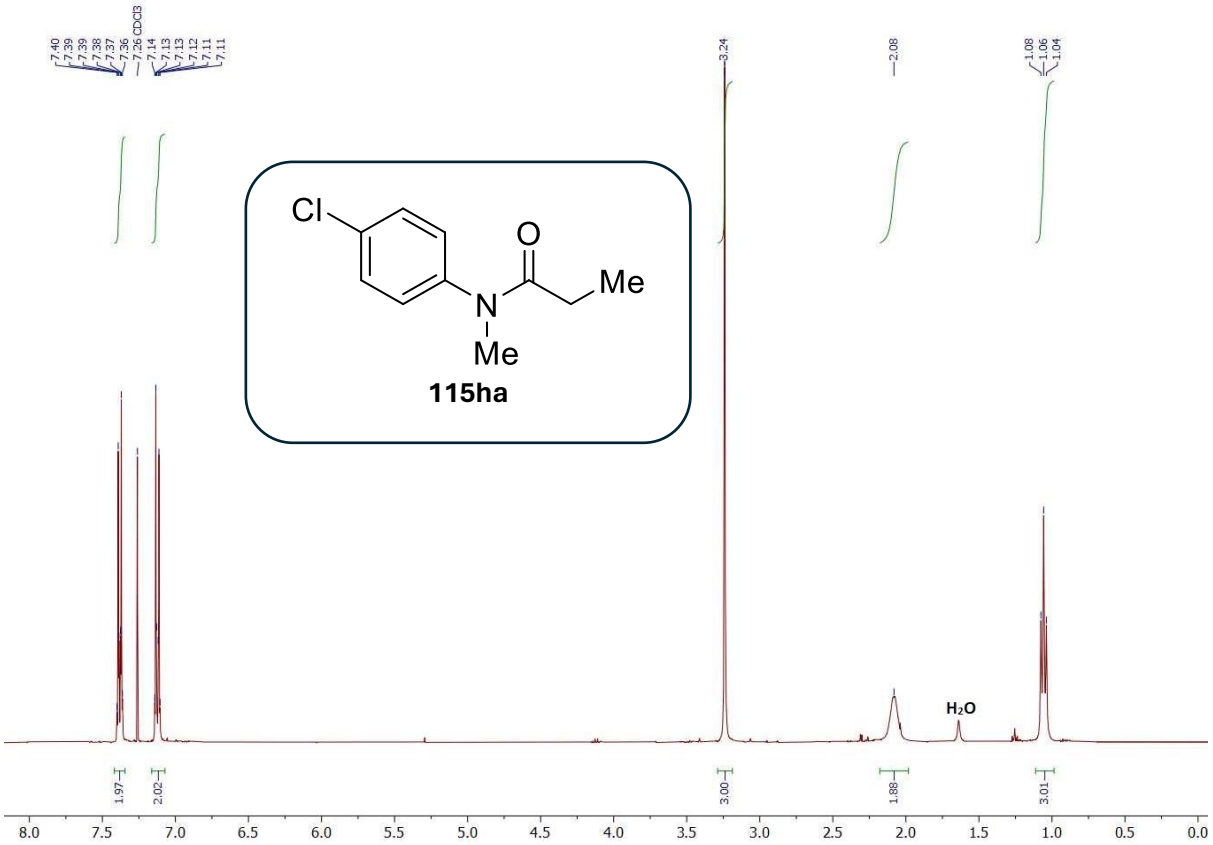

^{13}C NMR (101 MHz, $CDCl_3$)

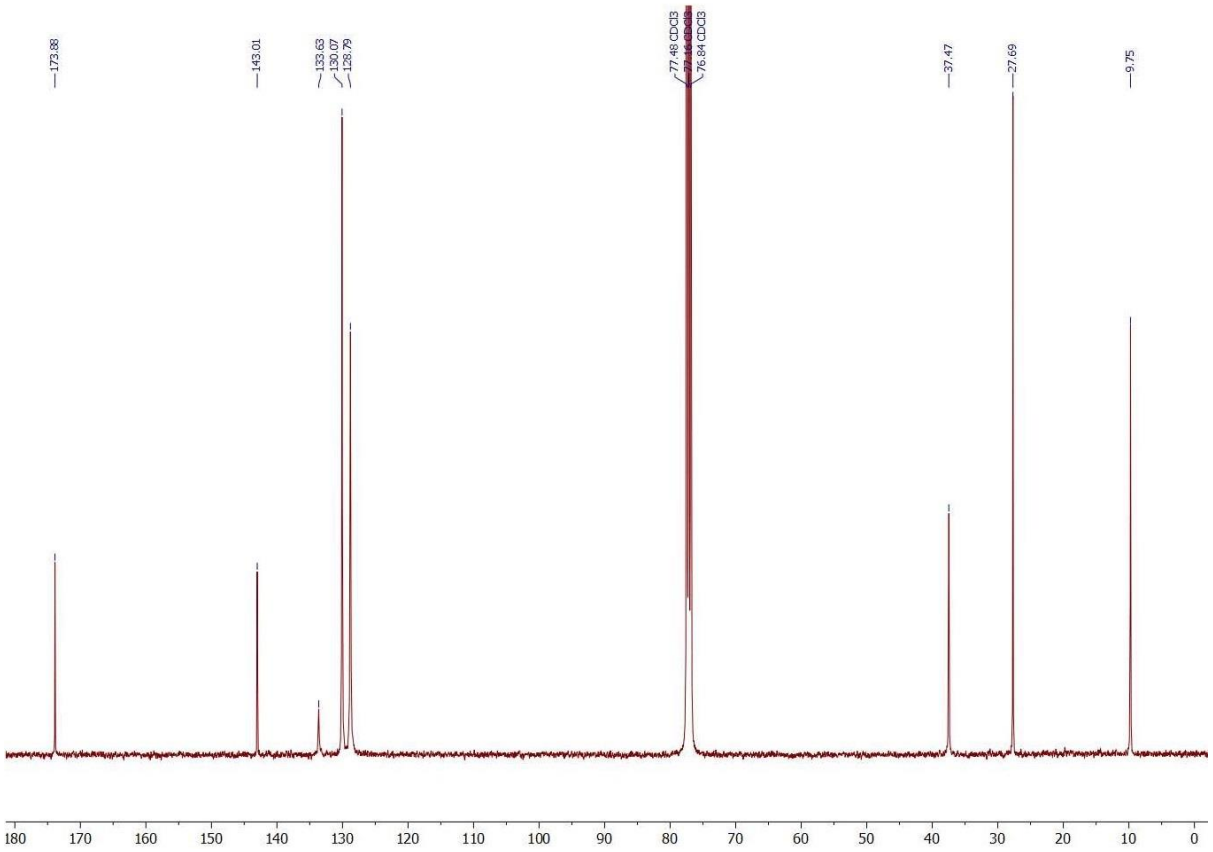

^{1}H NMR (400 MHz, $CDCl_3$)

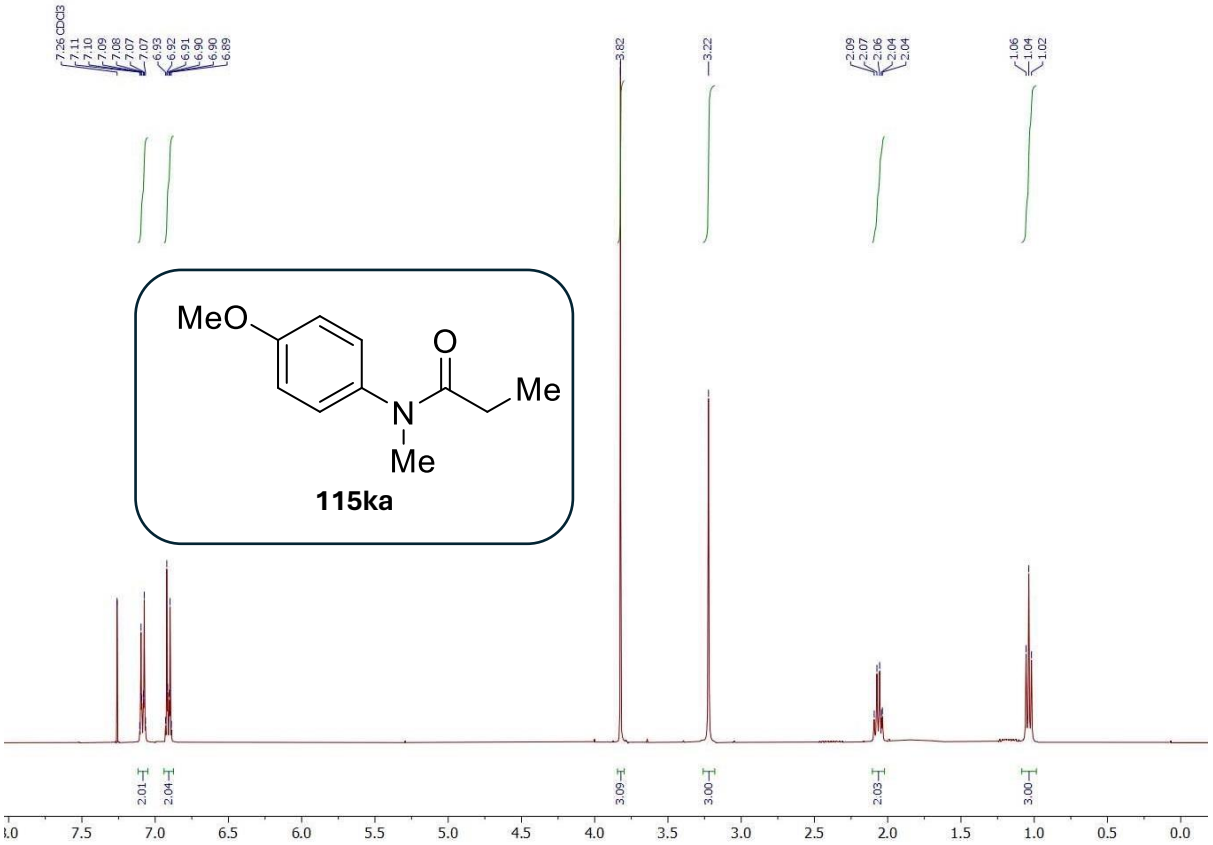

^{13}C NMR (101 MHz, $CDCl_3$)

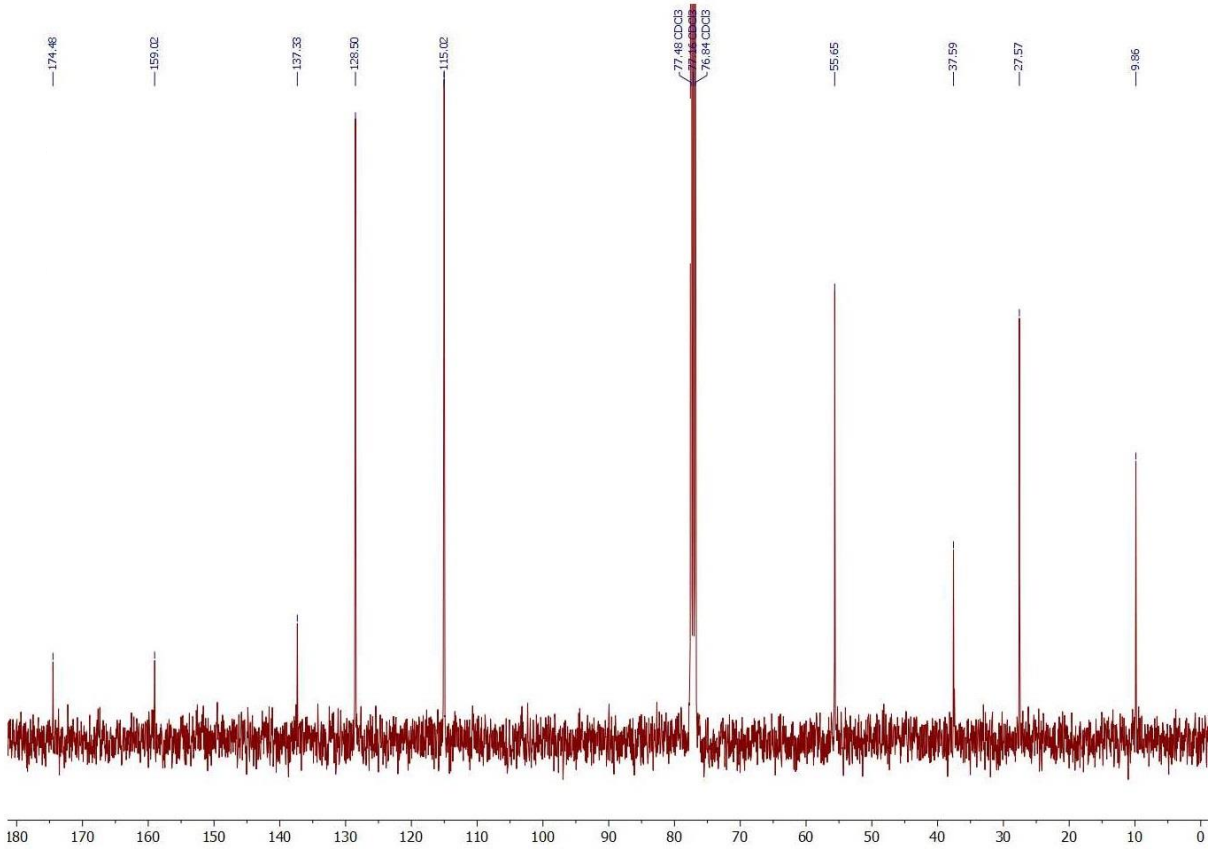

^{1}H NMR (400 MHz, $CDCl_3$)

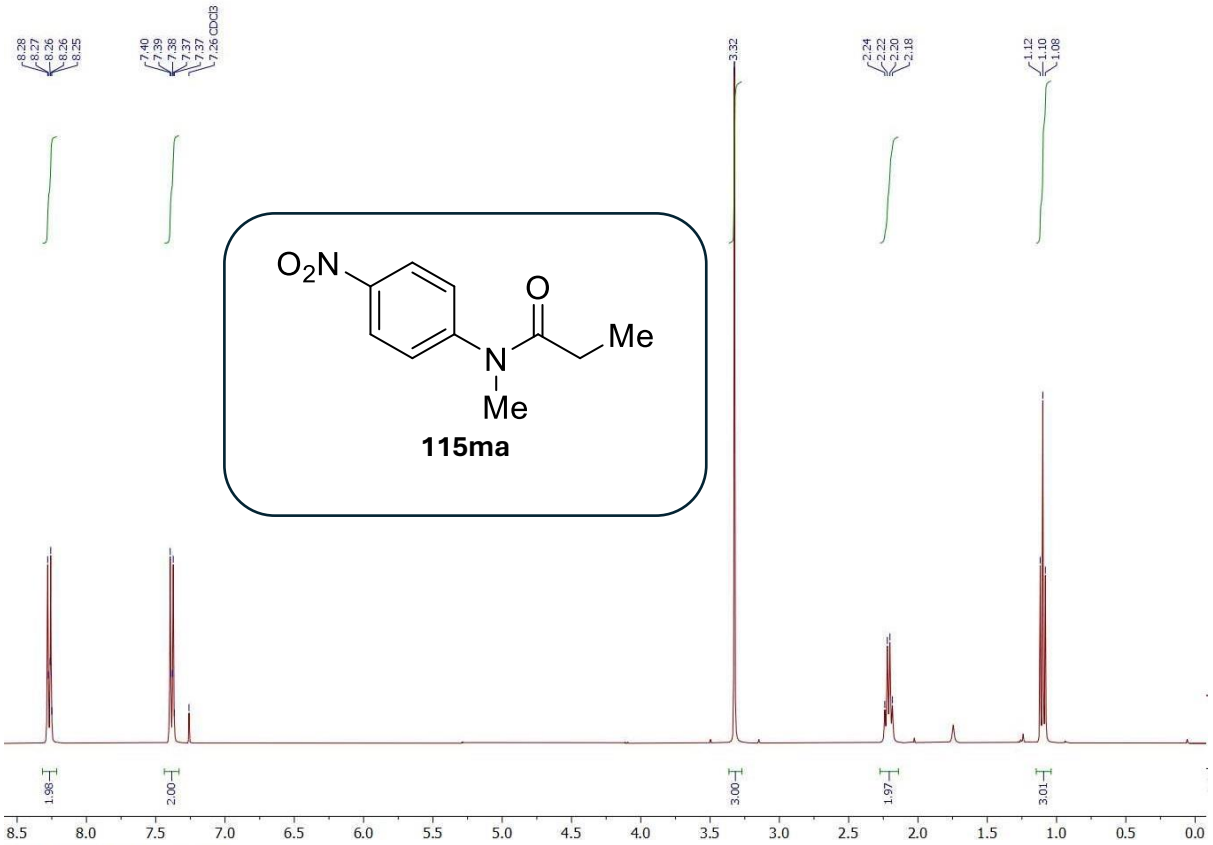

^{13}C NMR (101 MHz, $CDCl_3$)

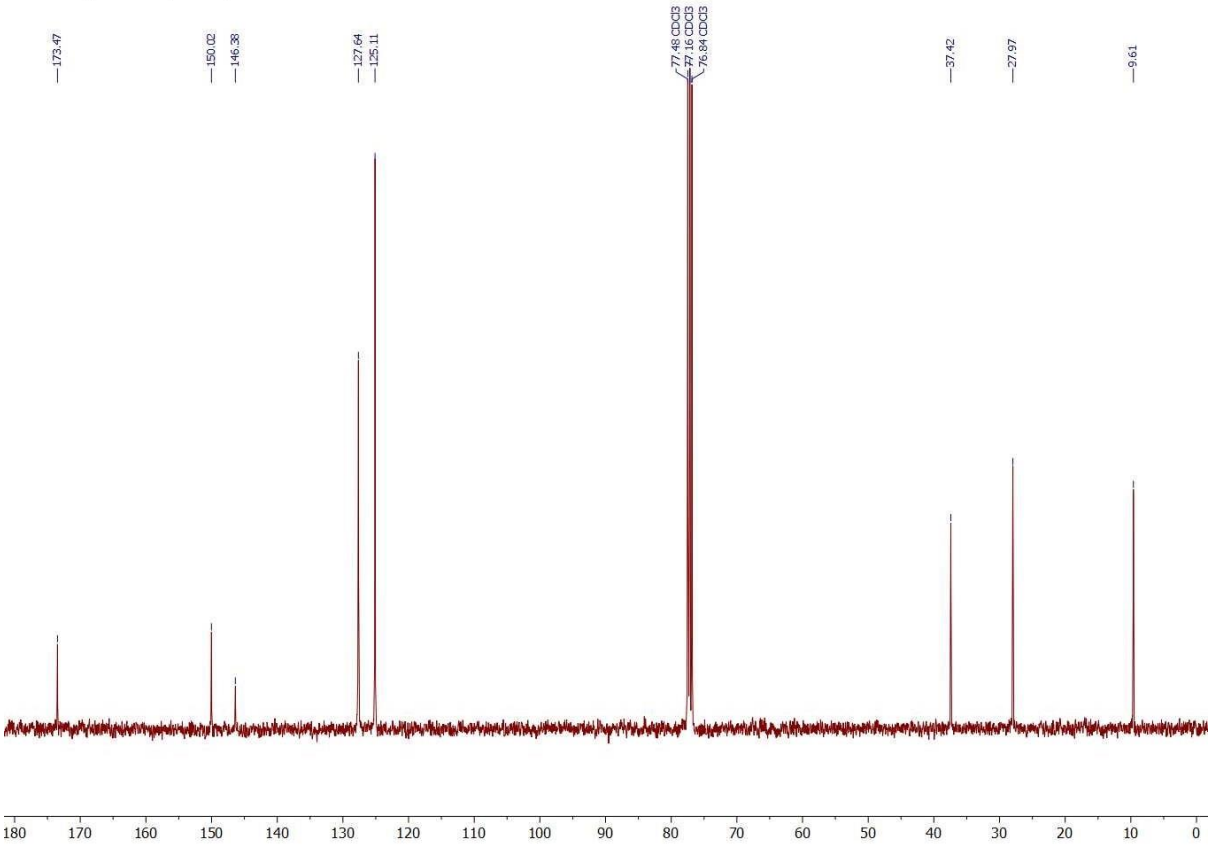

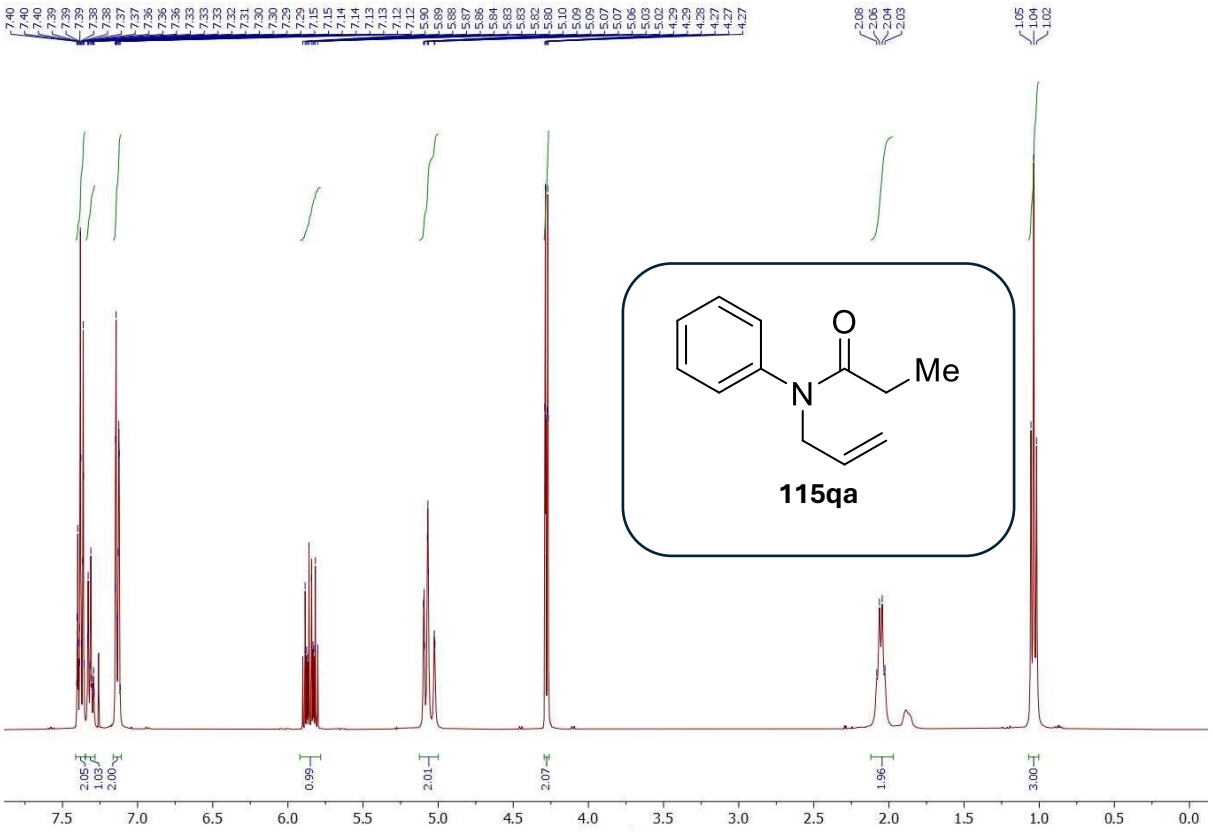
O
N
Me
115qa

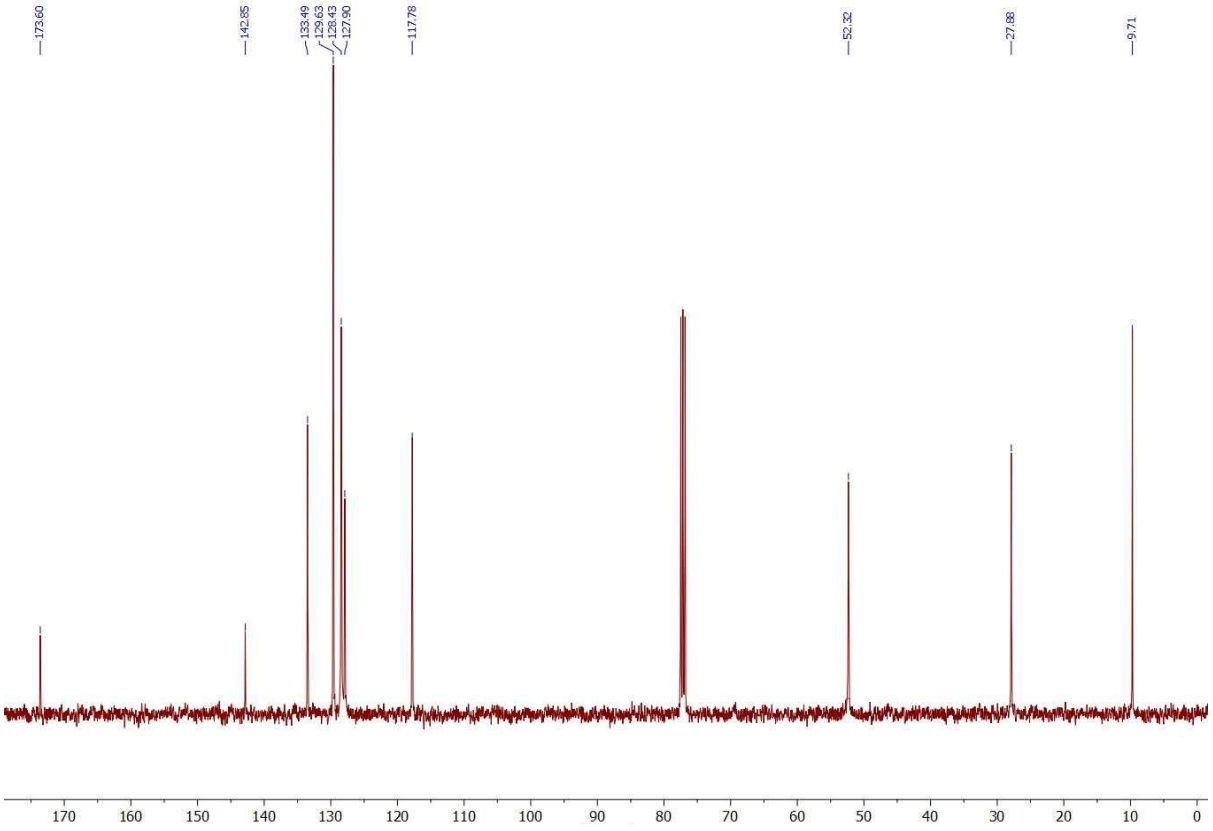

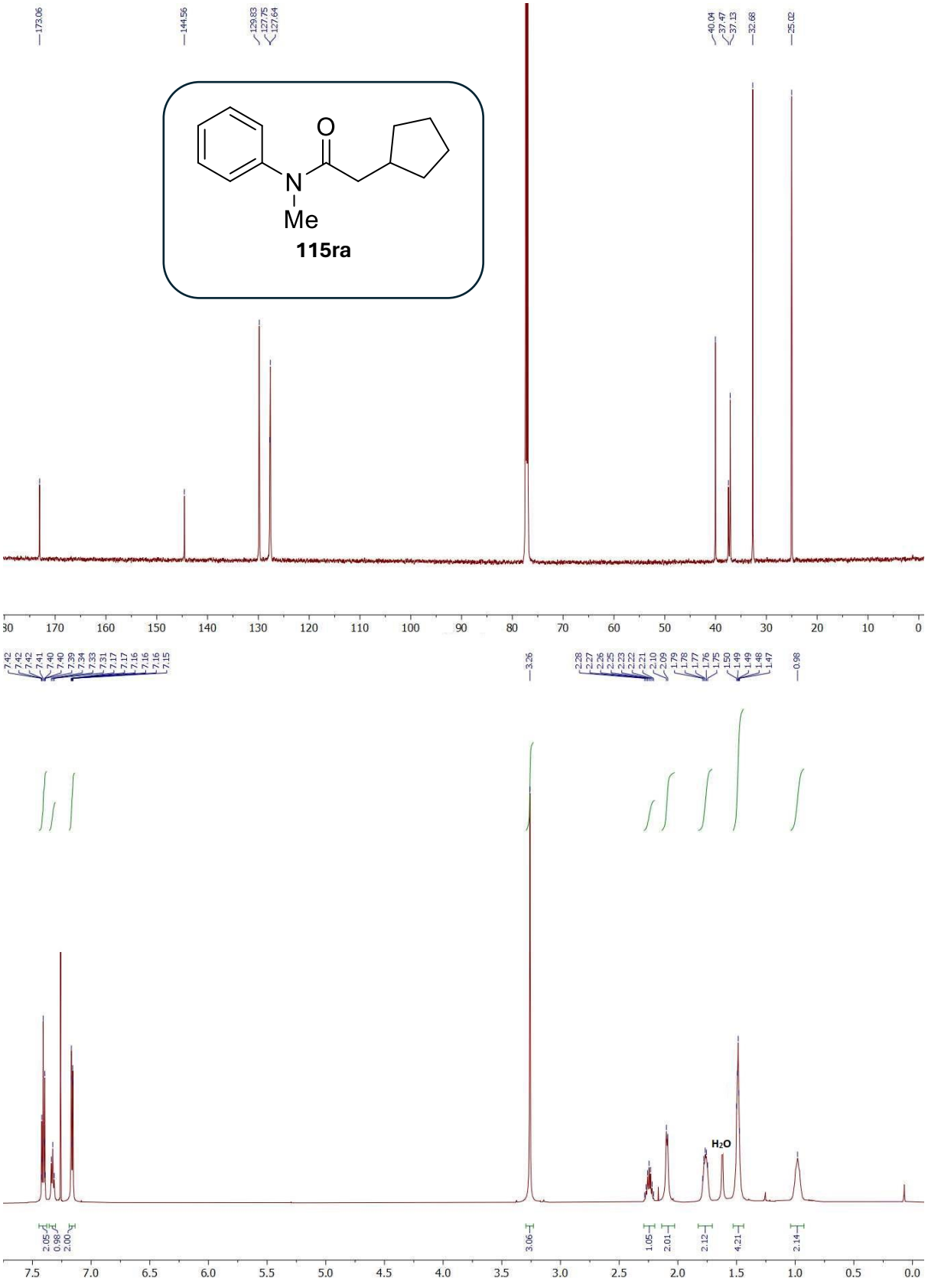
173.06
144.56
129.83
127.75
127.64
40.04
37.47
37.13
32.68
25.02
O
N
Me
115ra
7.42
7.42
7.42
7.41
7.40
7.40
7.39
7.34
7.33
7.31
7.17
7.17
7.16
7.16
7.16
7.15
3.26
2.28
2.27
2.26
2.25
2.23
2.22
2.21
2.10
2.09
1.79
1.78
1.77
1.76
1.75
1.50
1.49
1.49
1.48
1.47
0.98
H2O
2.05
0.98
2.00
3.06
1.05
2.01
2.12
4.21
2.14

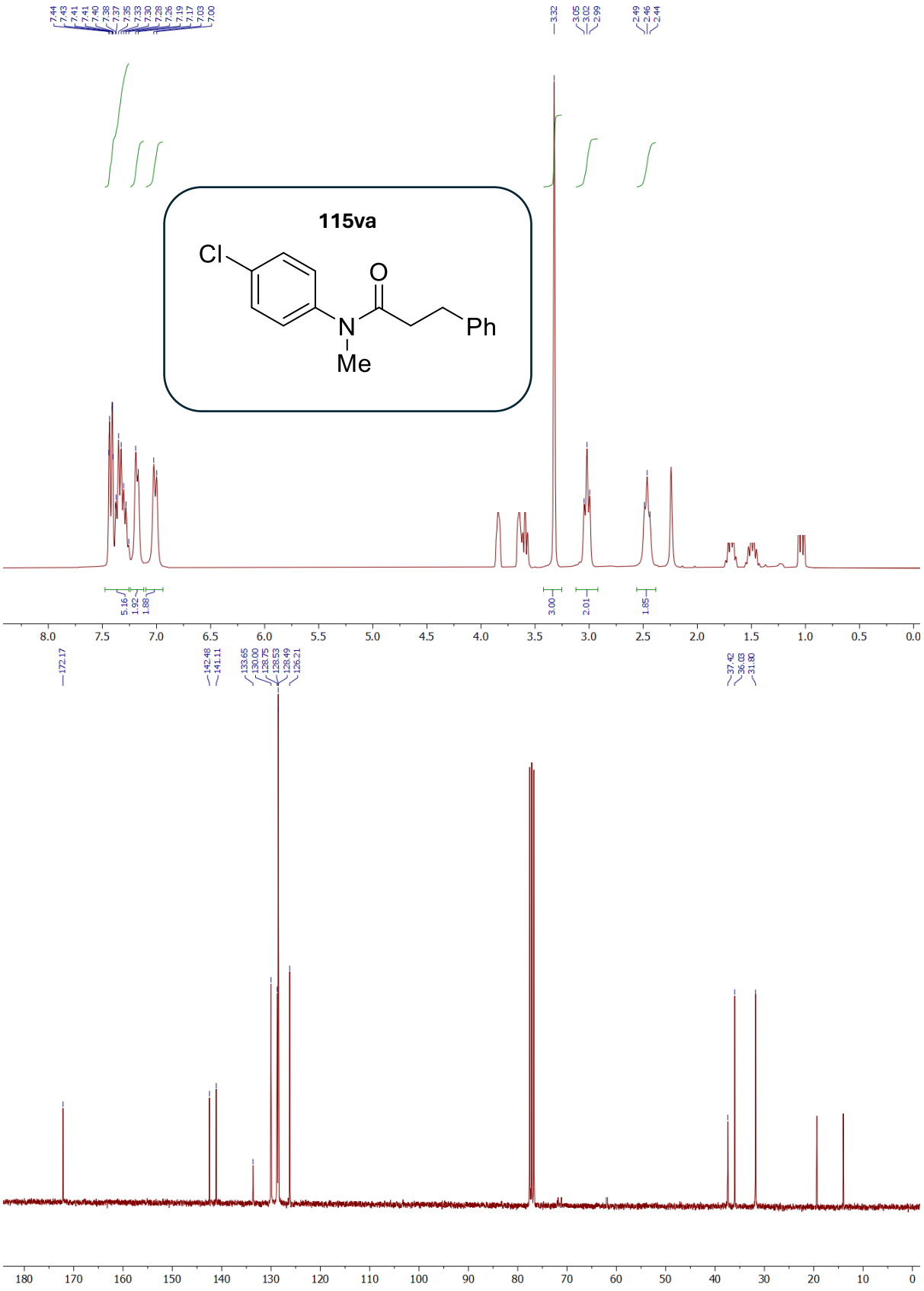
115va
Cl
O
N
Me
Ph

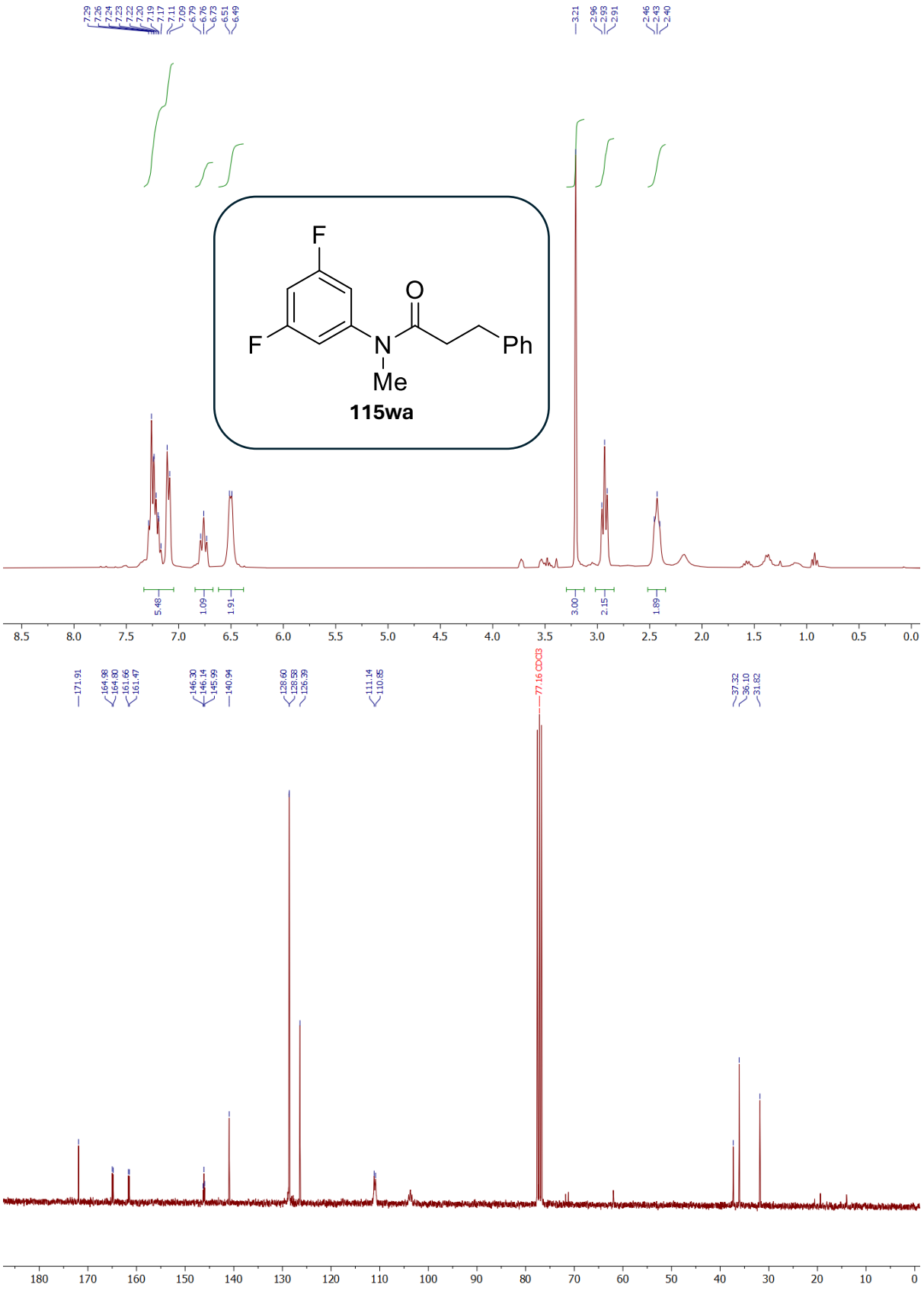
7.29
7.26
7.24
7.23
7.22
7.20
7.19
7.17
7.11
7.09
6.79
6.76
6.73
6.51
6.49
3.21
2.96
2.93
2.91
2.46
2.43
2.40
F
F
O
N
Me
Ph
115wa
5.48
1.09
1.91
3.00
2.15
1.89
8.5
8.0
7.5
7.0
6.5
6.0
5.5
5.0
4.5
4.0
3.5
3.0
2.5
2.0
1.5
1.0
0.5
0.0
171.91
164.98
164.80
161.66
161.47
146.30
146.14
145.99
140.94
128.60
128.38
126.39
111.14
110.85
77.16 CDCl3
37.32
36.10
31.82
180
170
160
150
140
130
120
110
100
90
80
70
60
50
40
30
20
10
0

^{1}H NMR (400 MHz, $CDCl_3$)

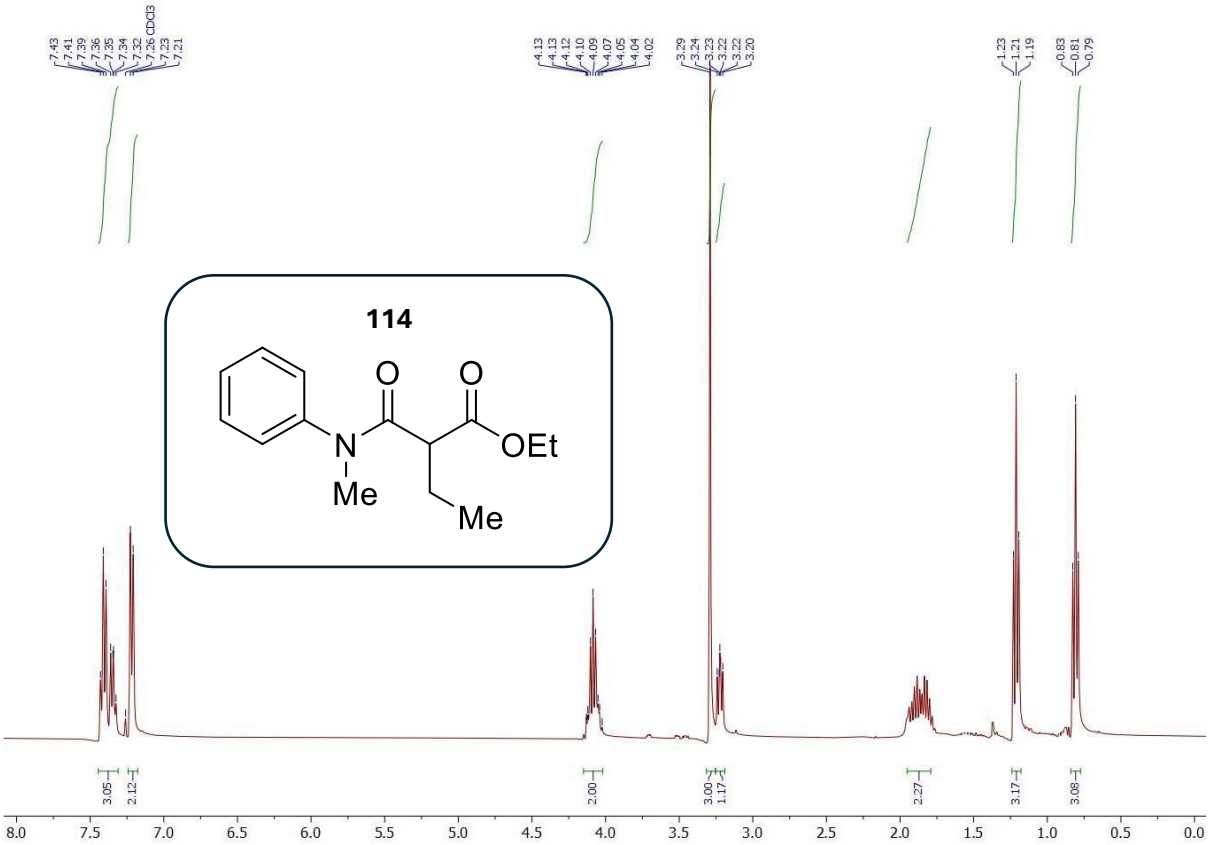

^{13}C NMR (101 MHz, $CDCl_3$)

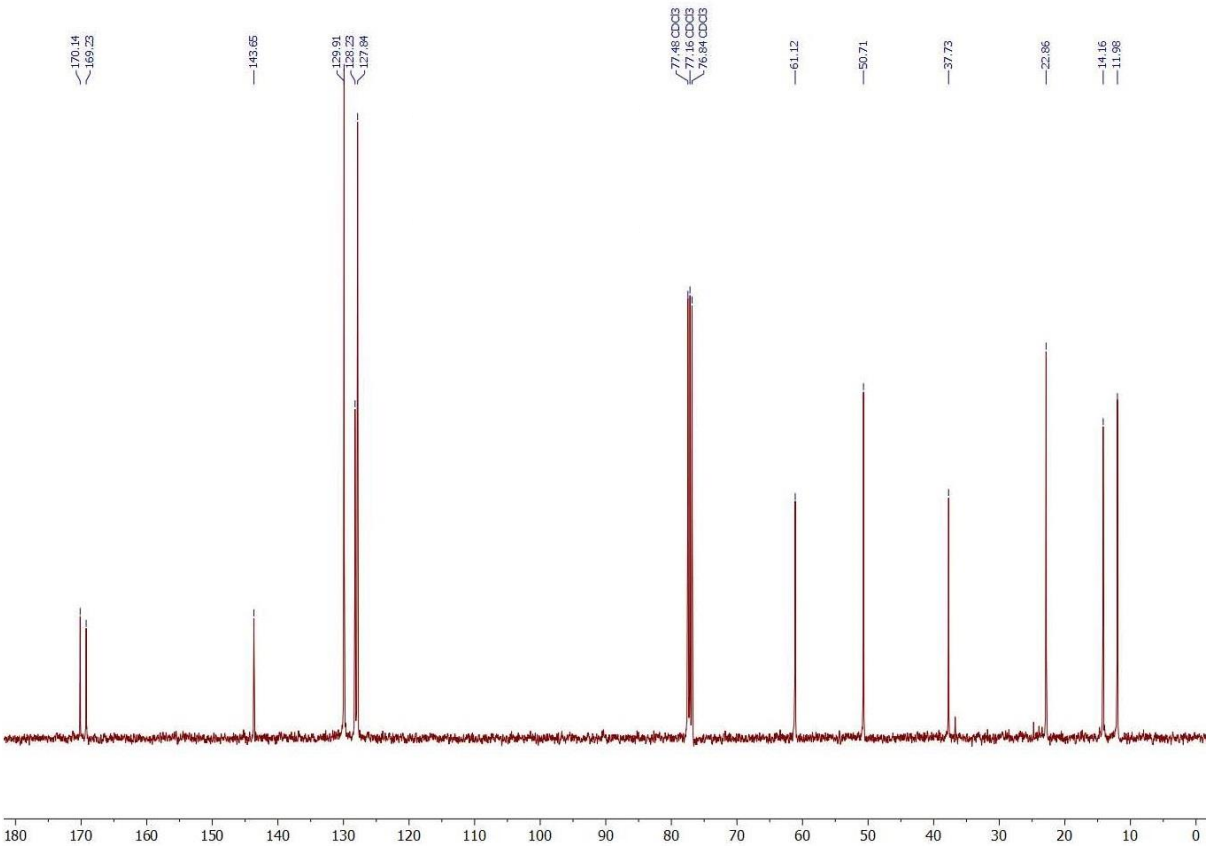

^{1}H NMR (400 MHz, $CDCl_3$)

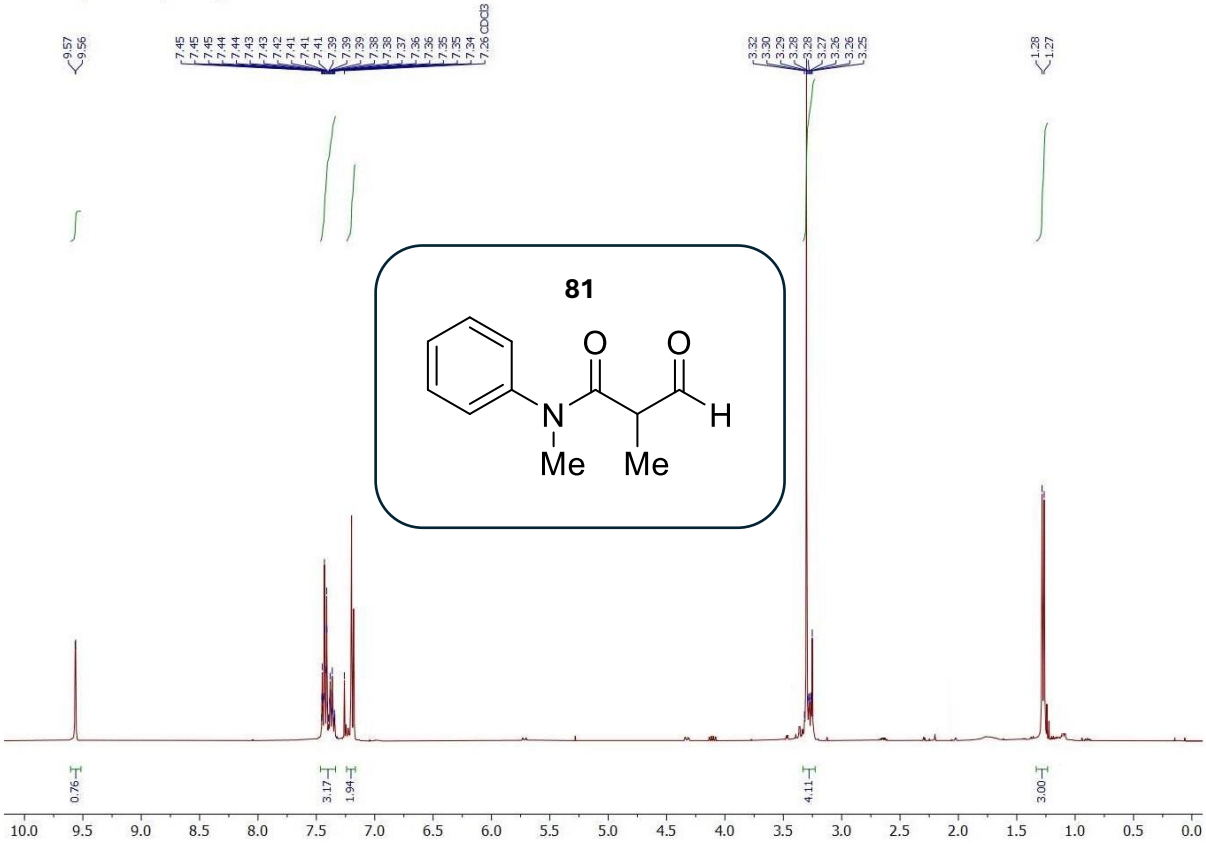

81

^{13}C NMR (101 MHz, $CDCl_3$)

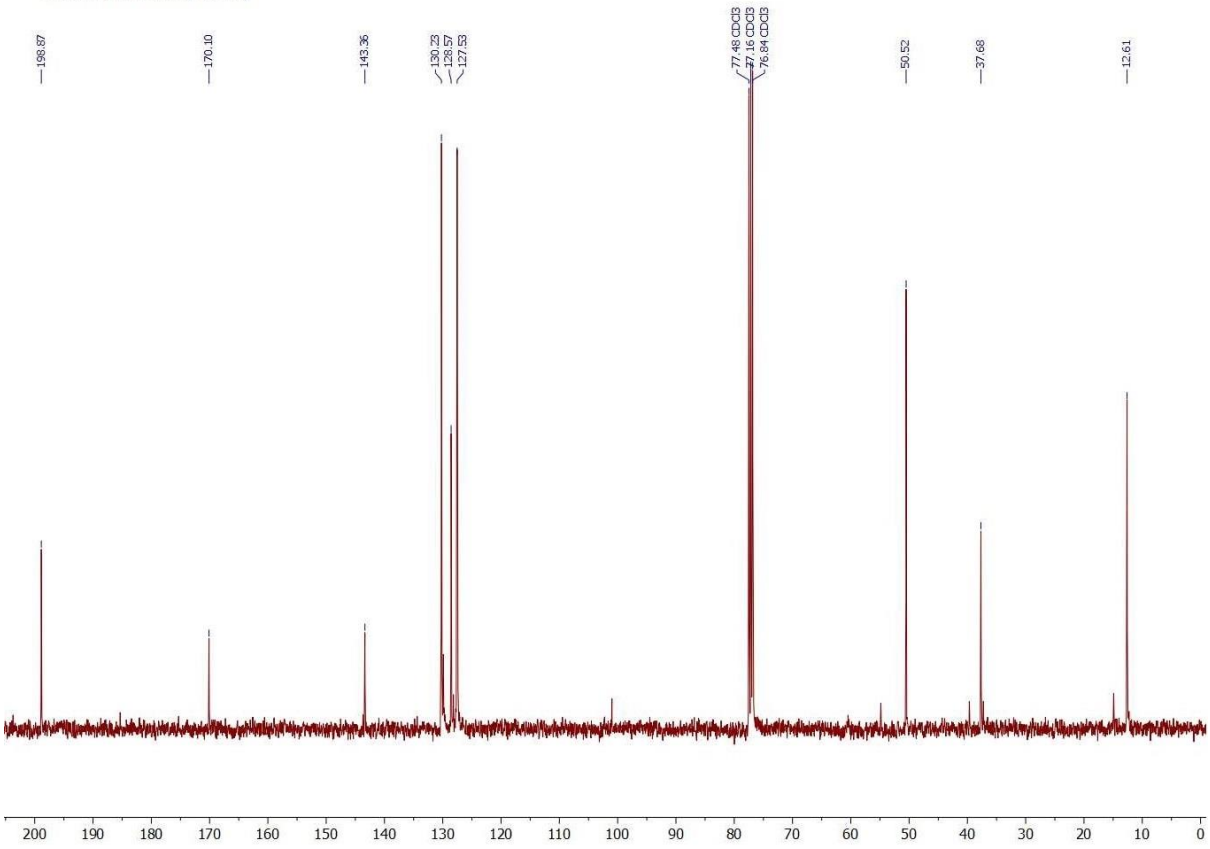

^{1}H NMR (600 MHz, $CDCl_3$)

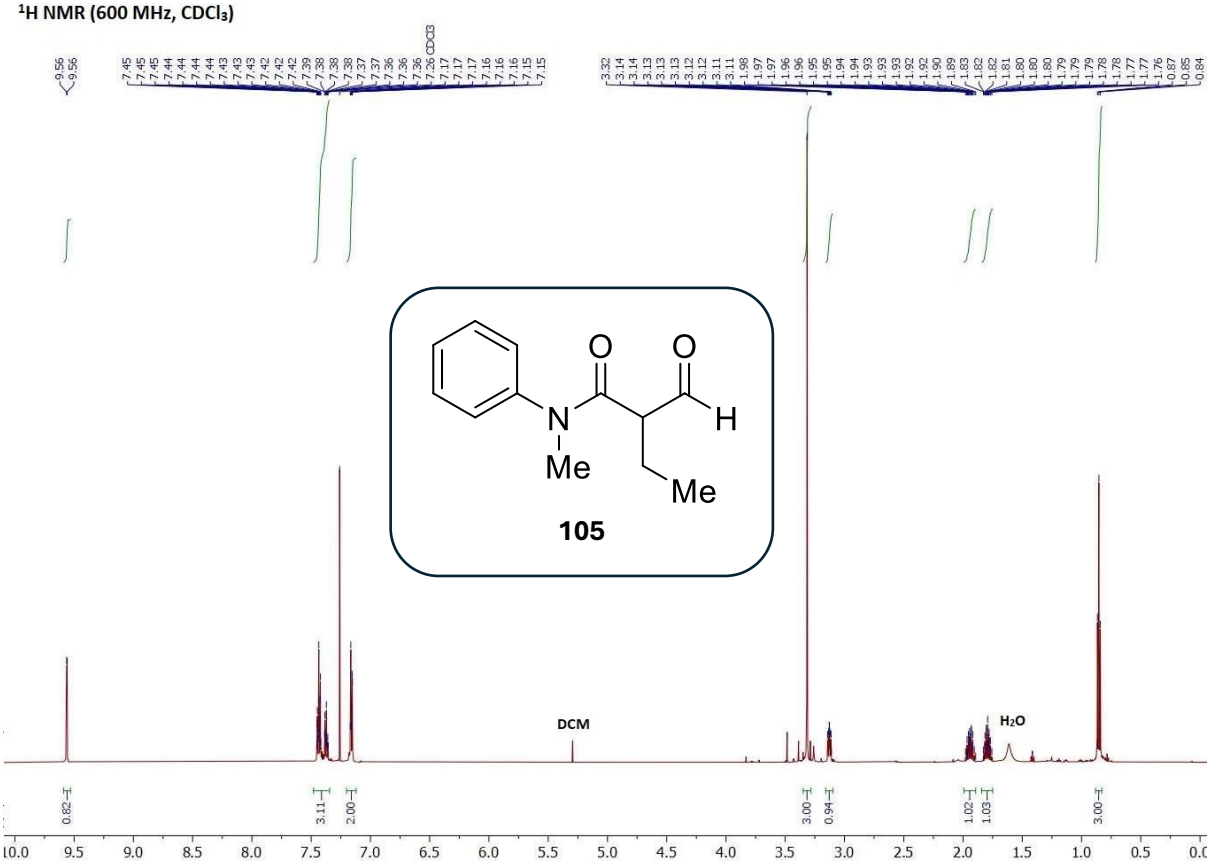

^{13}C NMR (151 MHz, $CDCl_3$)

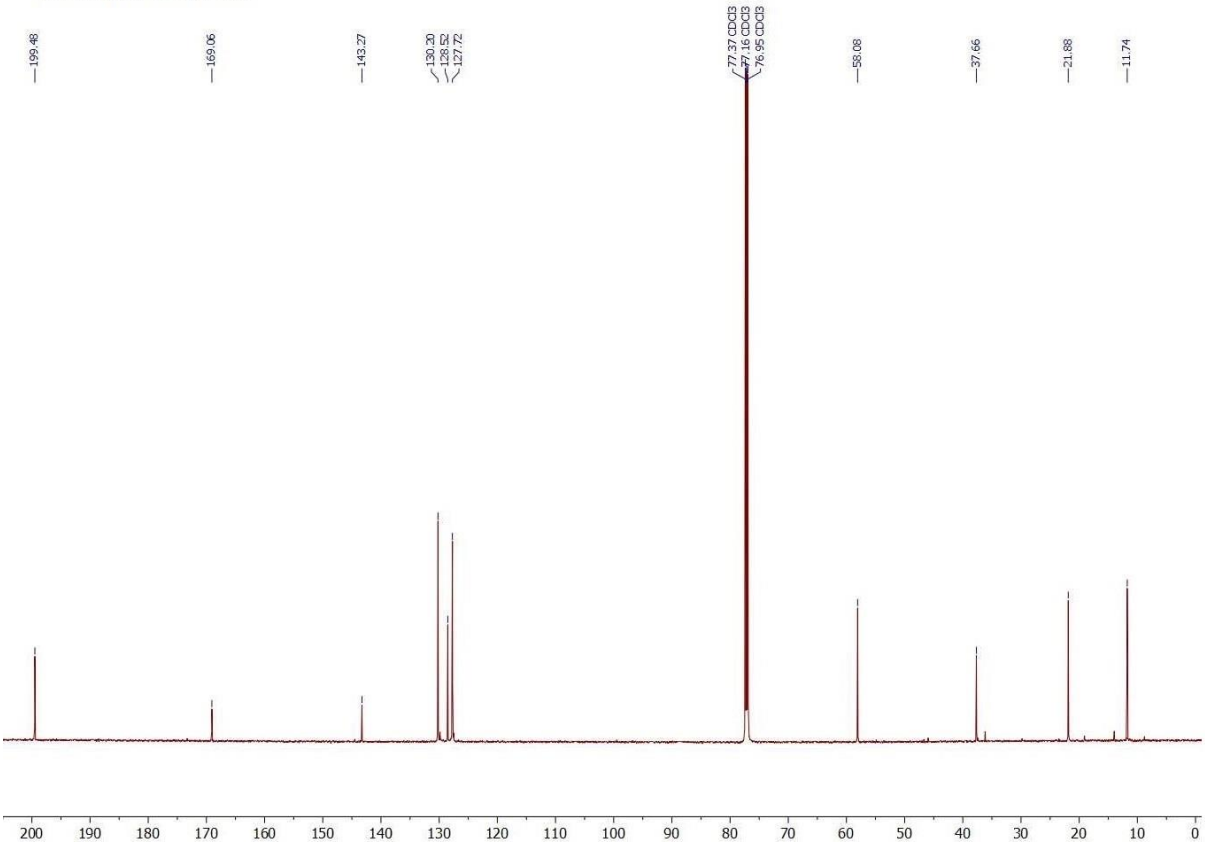

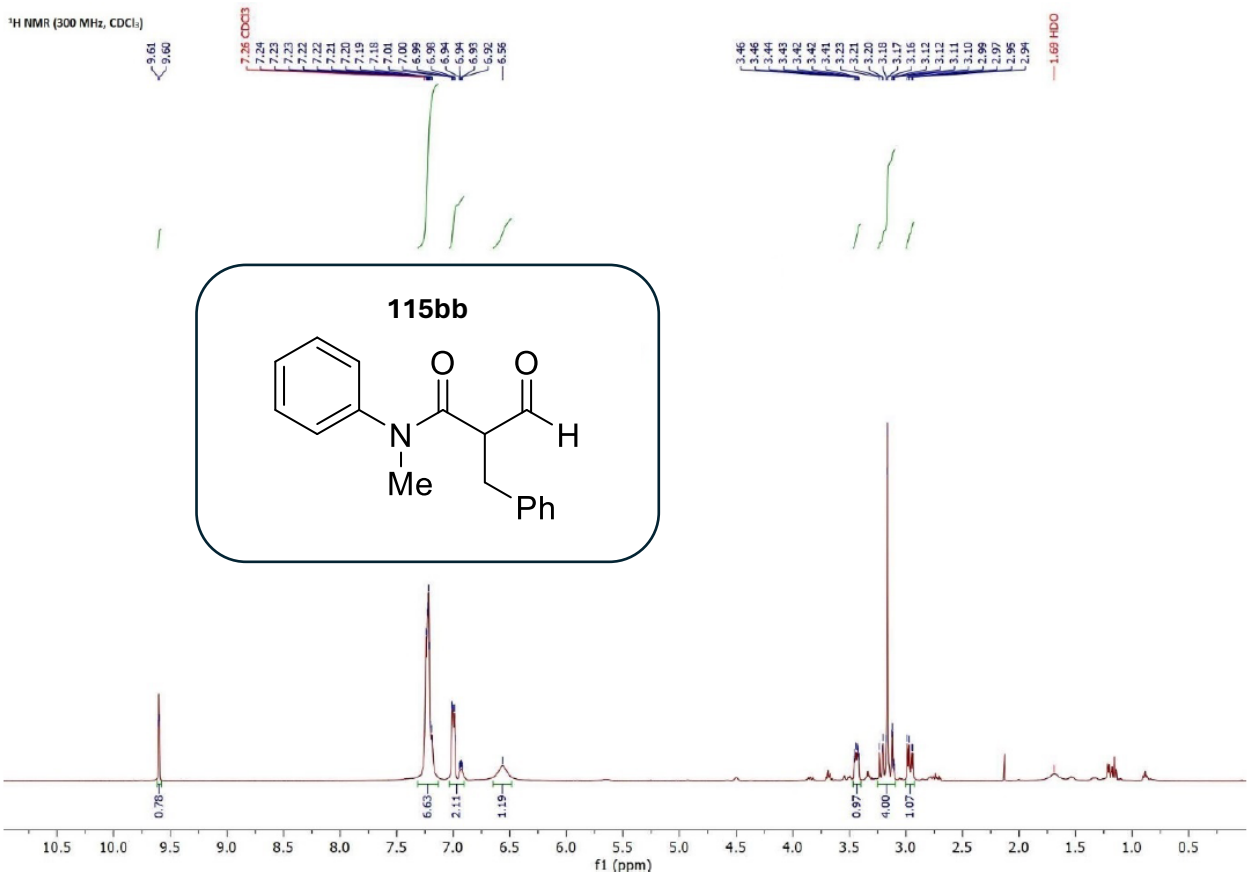
¹H NMR (300 MHz, CDCl₃)
115bb
f1 (ppm)

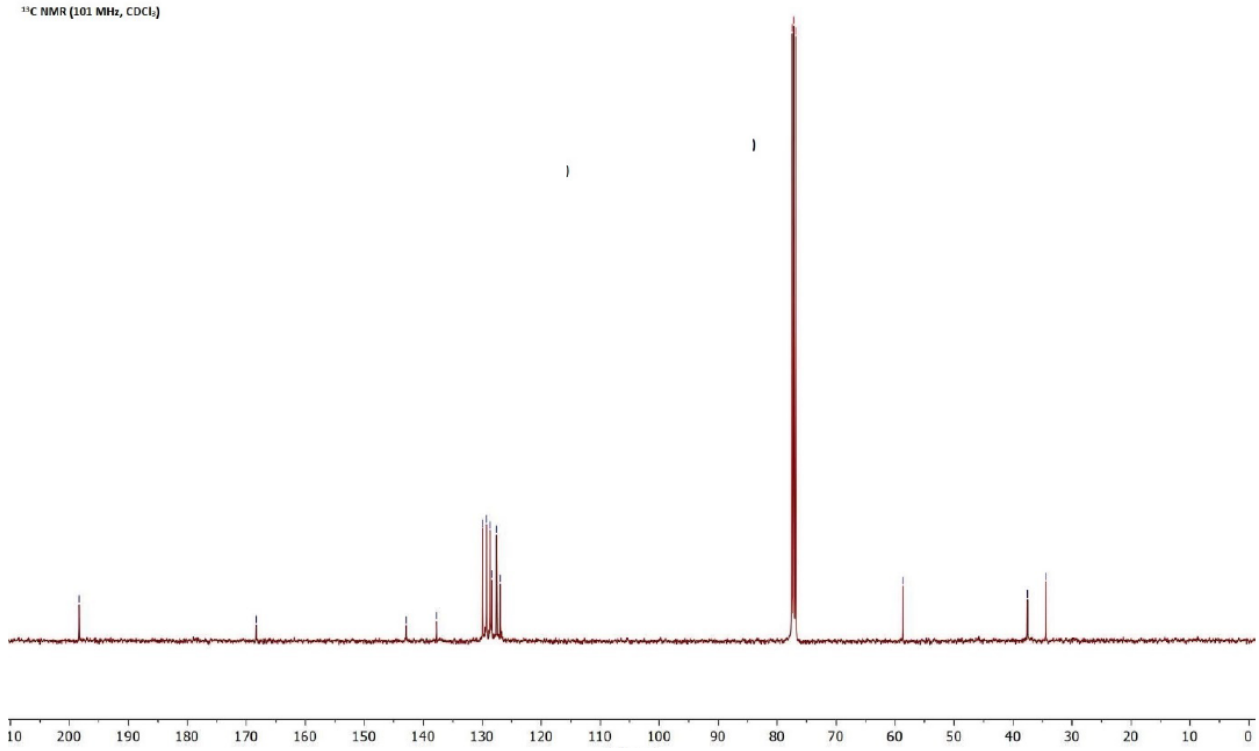
¹³C NMR (101 MHz, CDCl₃)

^{1}H NMR (400 MHz, $CDCl_3$)

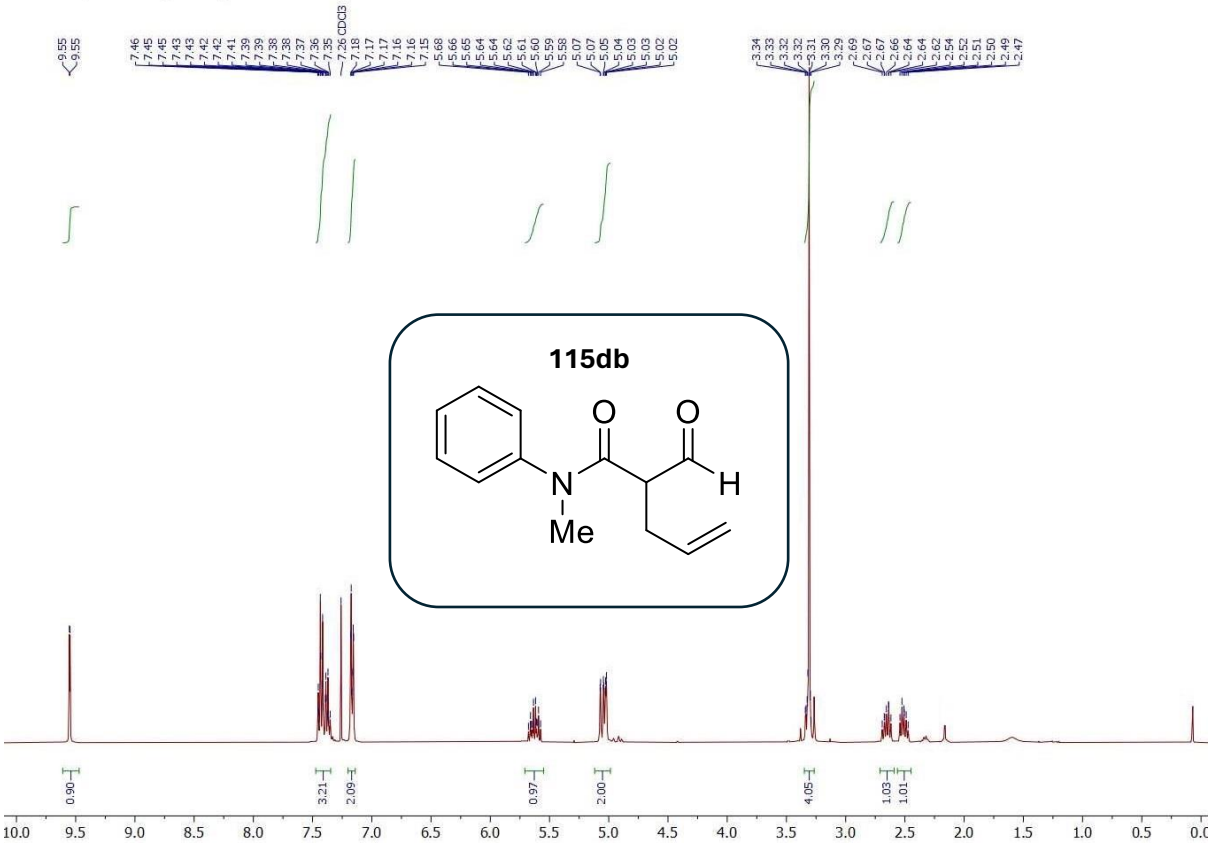

^{13}C NMR (101 MHz, $CDCl_3$)

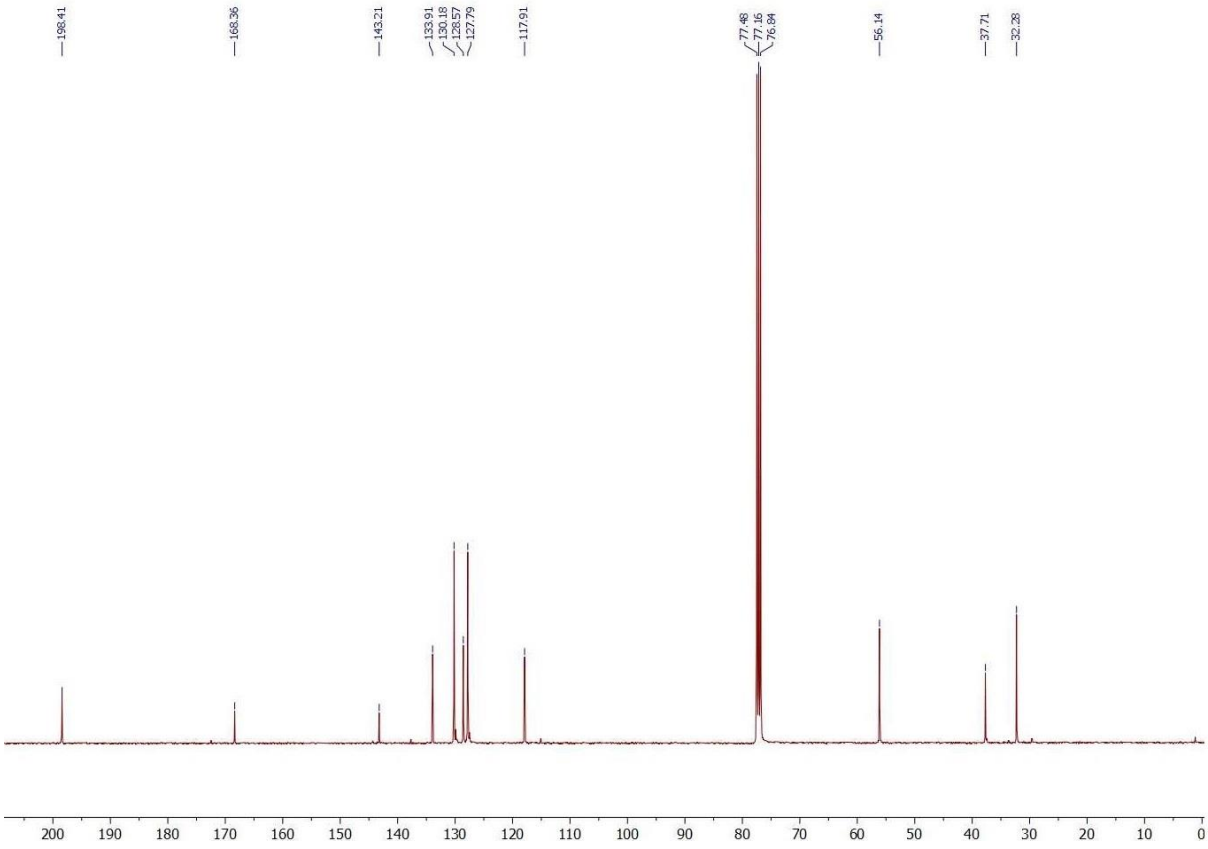

^{1}H NMR (400 MHz, $CDCl_3$)

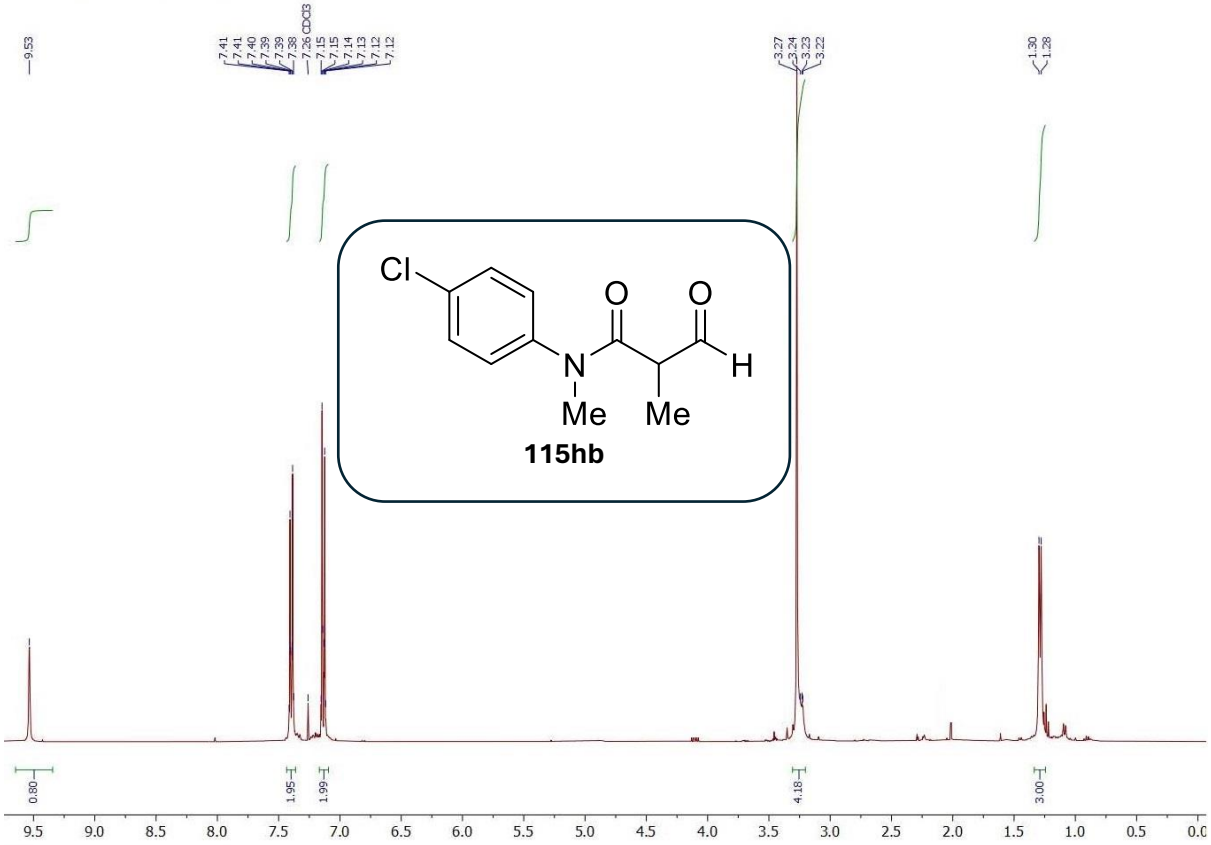

^{13}C NMR (101 MHz, $CDCl_3$)

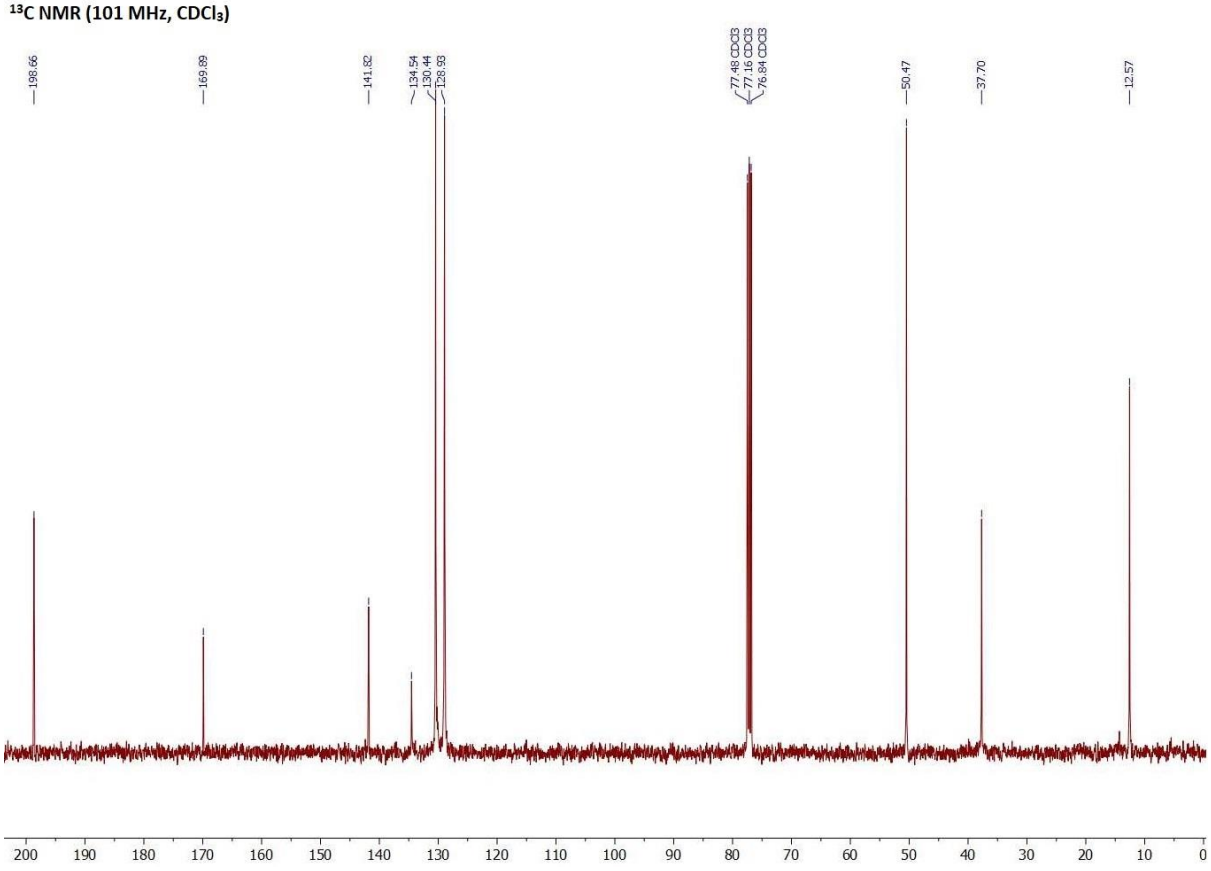

^{1}H NMR (400 MHz, $CDCl_3$)

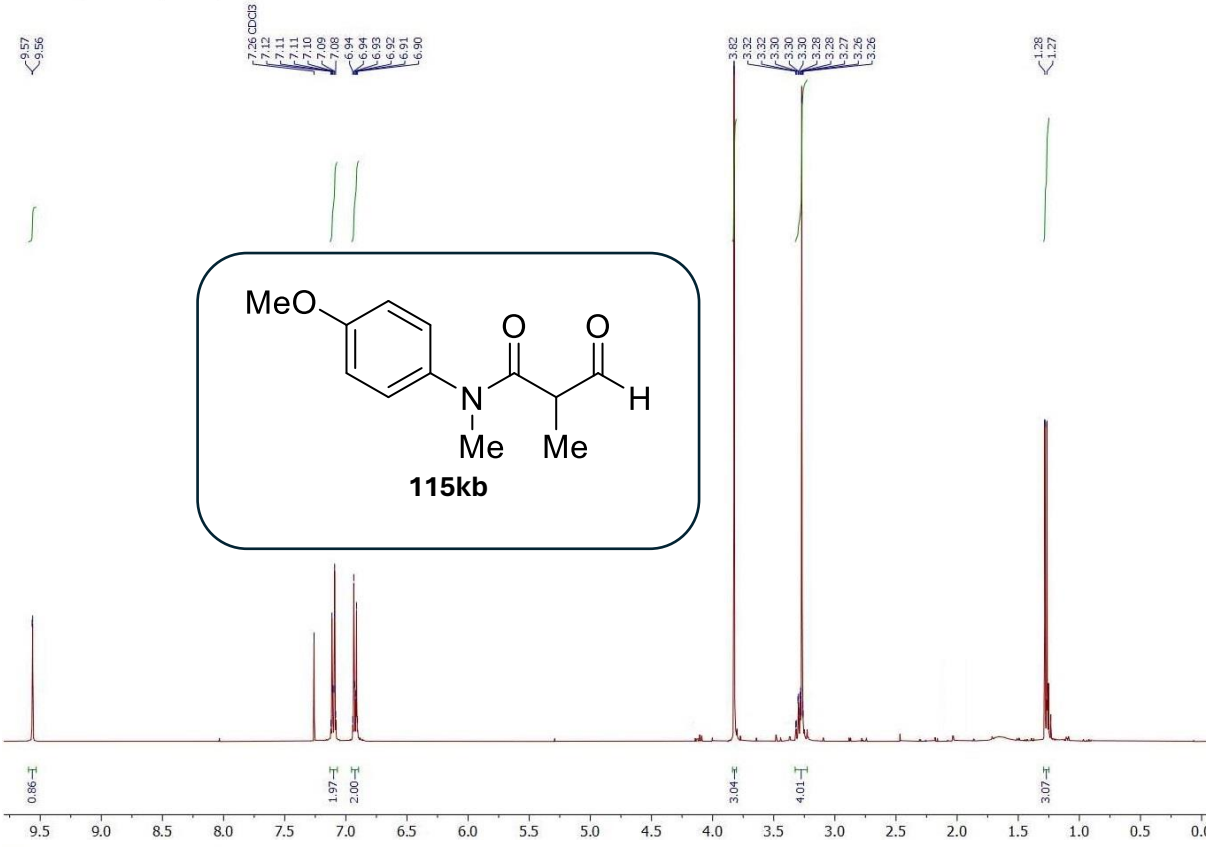

^{13}C NMR (101 MHz, $CDCl_3$)

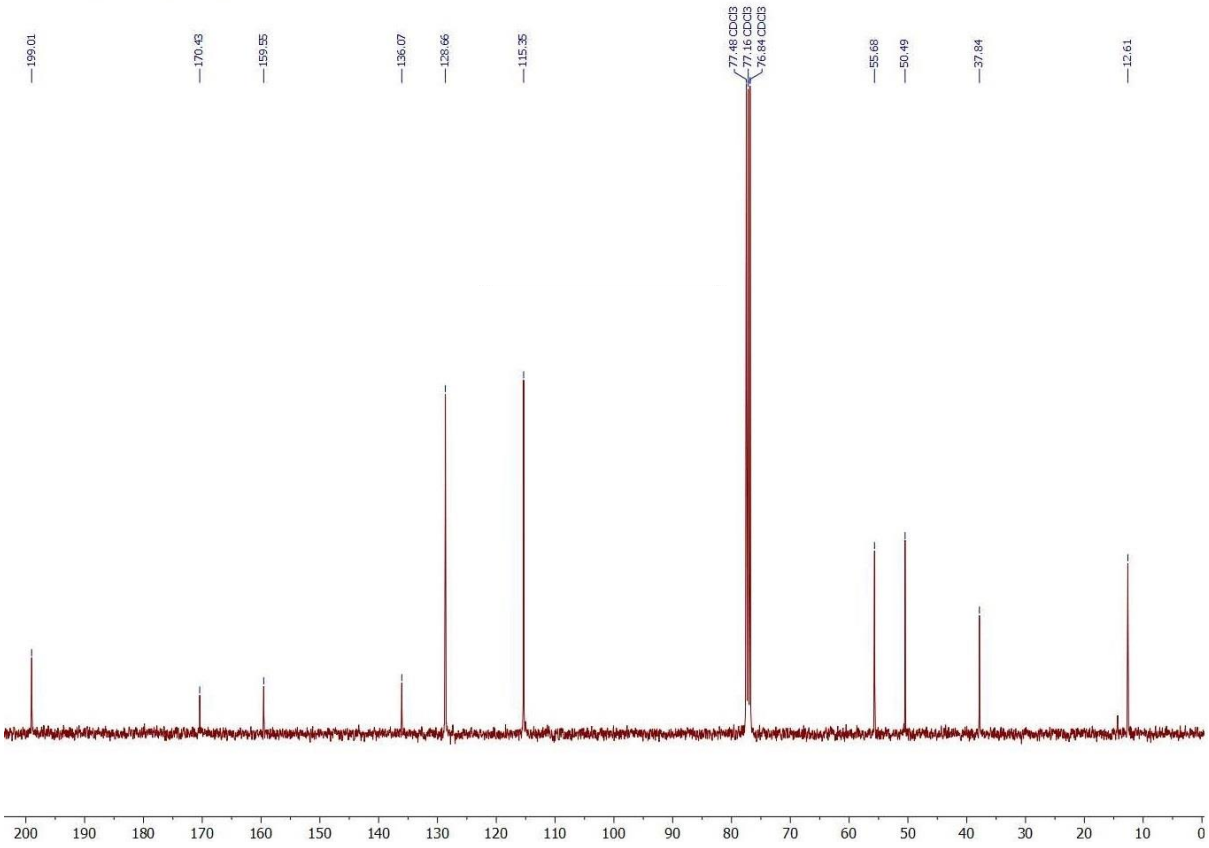

^{1}H NMR (400 MHz, $CDCl_3$)

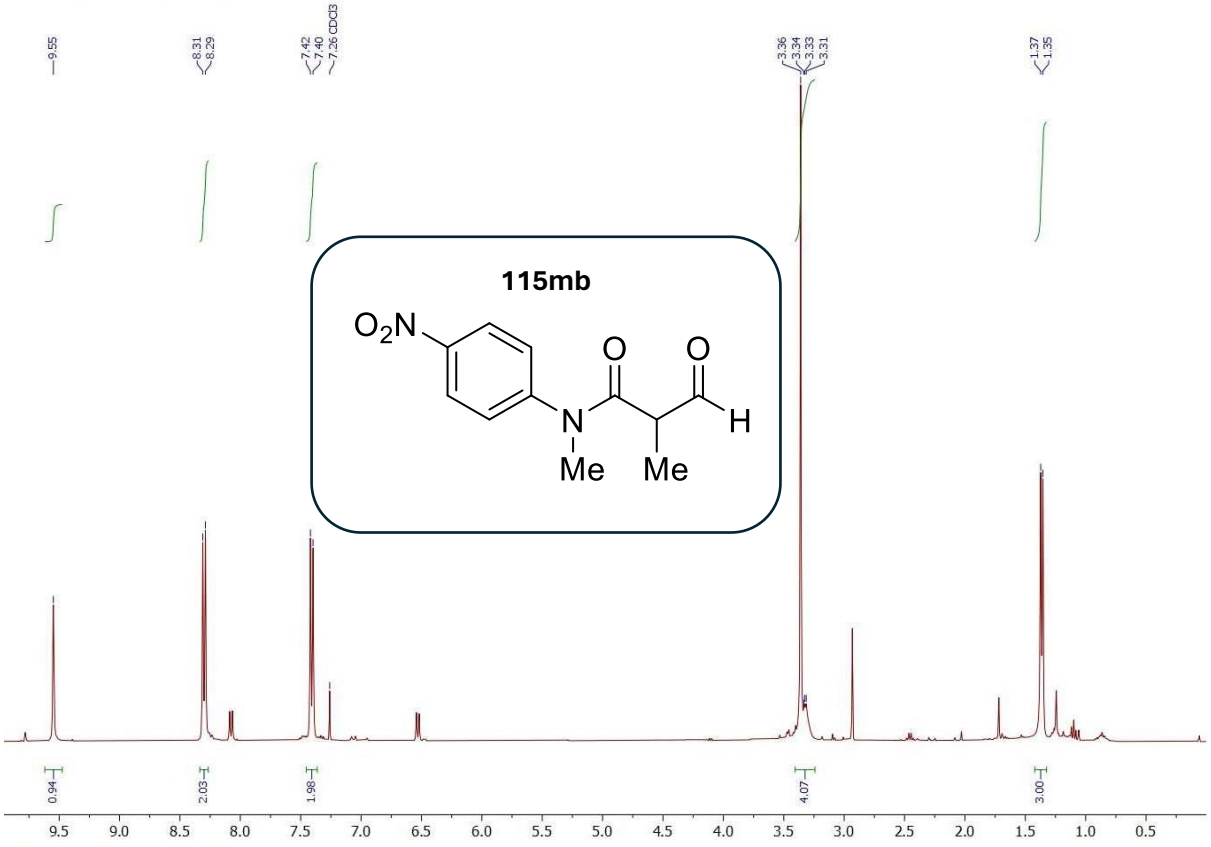

^{13}C NMR (101 MHz, $CDCl_3$)

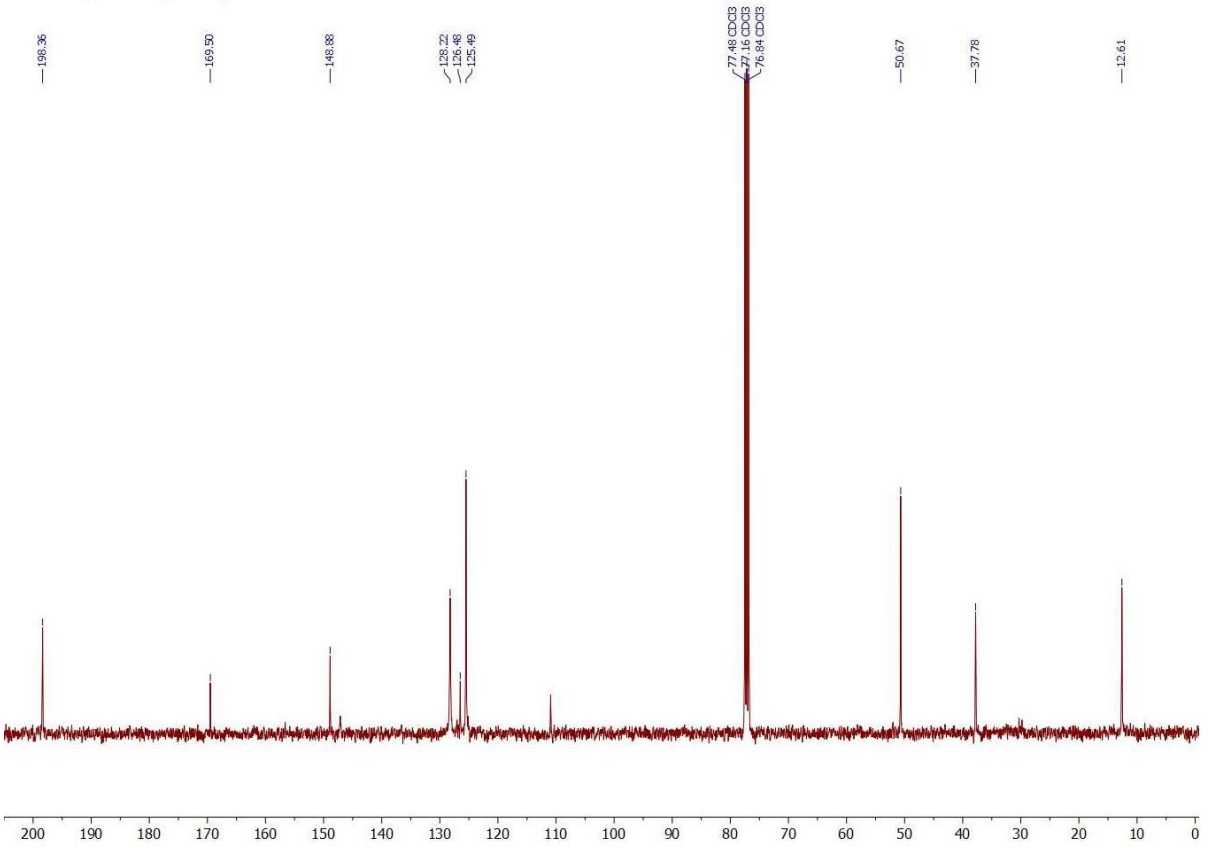

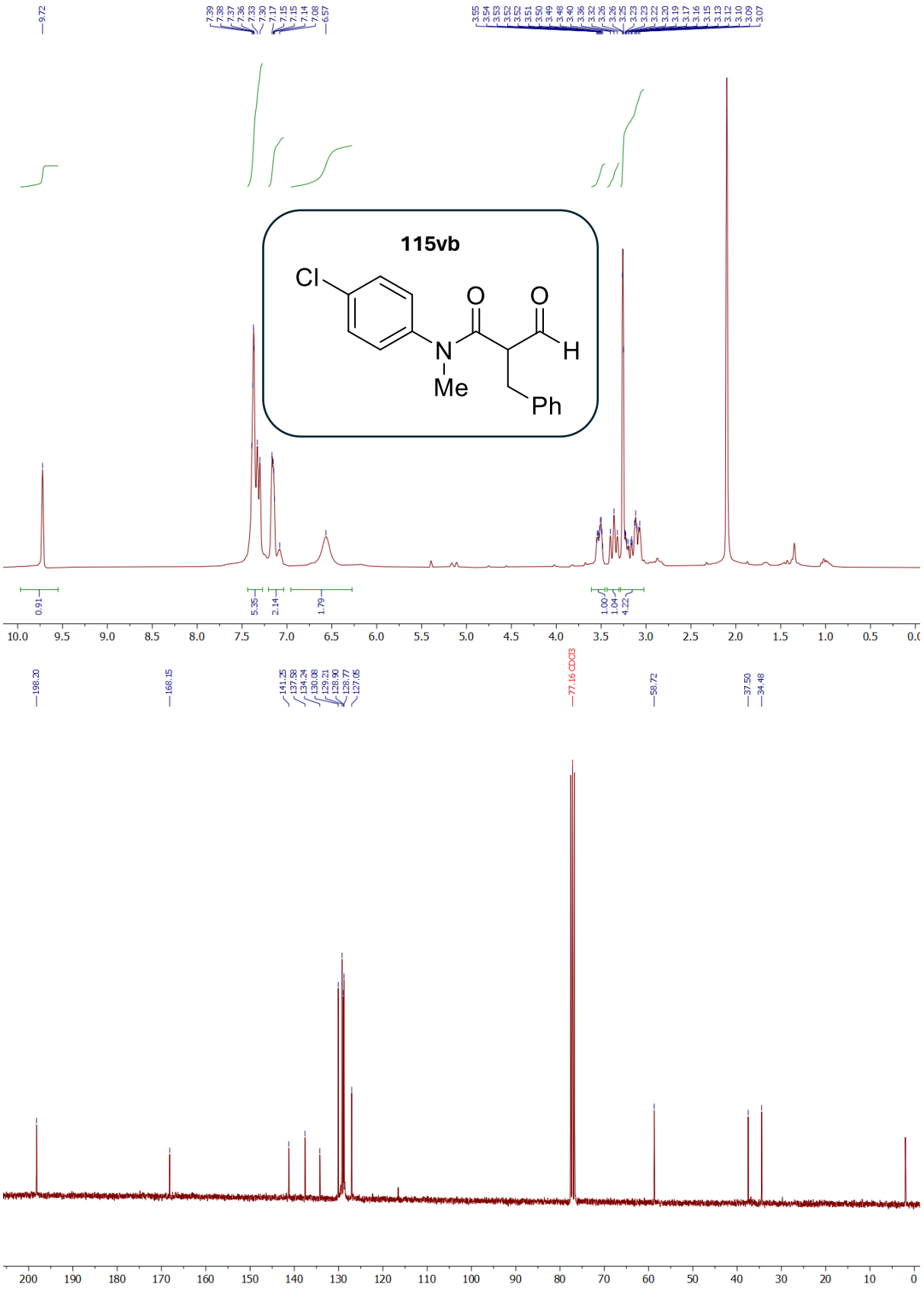
115vb
Cl
O
O
H
N
Me
Ph
9.72
7.39
7.38
7.37
7.36
7.33
7.30
7.17
7.15
7.15
7.14
7.08
6.57
3.55
3.54
3.53
3.52
3.52
3.51
3.50
3.49
3.48
3.40
3.36
3.32
3.26
3.26
3.25
3.23
3.23
3.22
3.20
3.19
3.17
3.16
3.15
3.13
3.12
3.10
3.09
3.07
0.91
5.35
2.14
1.79
1.00
1.04
4.22
198.20
168.15
141.25
137.59
134.24
130.08
129.21
128.90
128.77
127.65
77.16 CDCl3
58.72
37.50
34.48

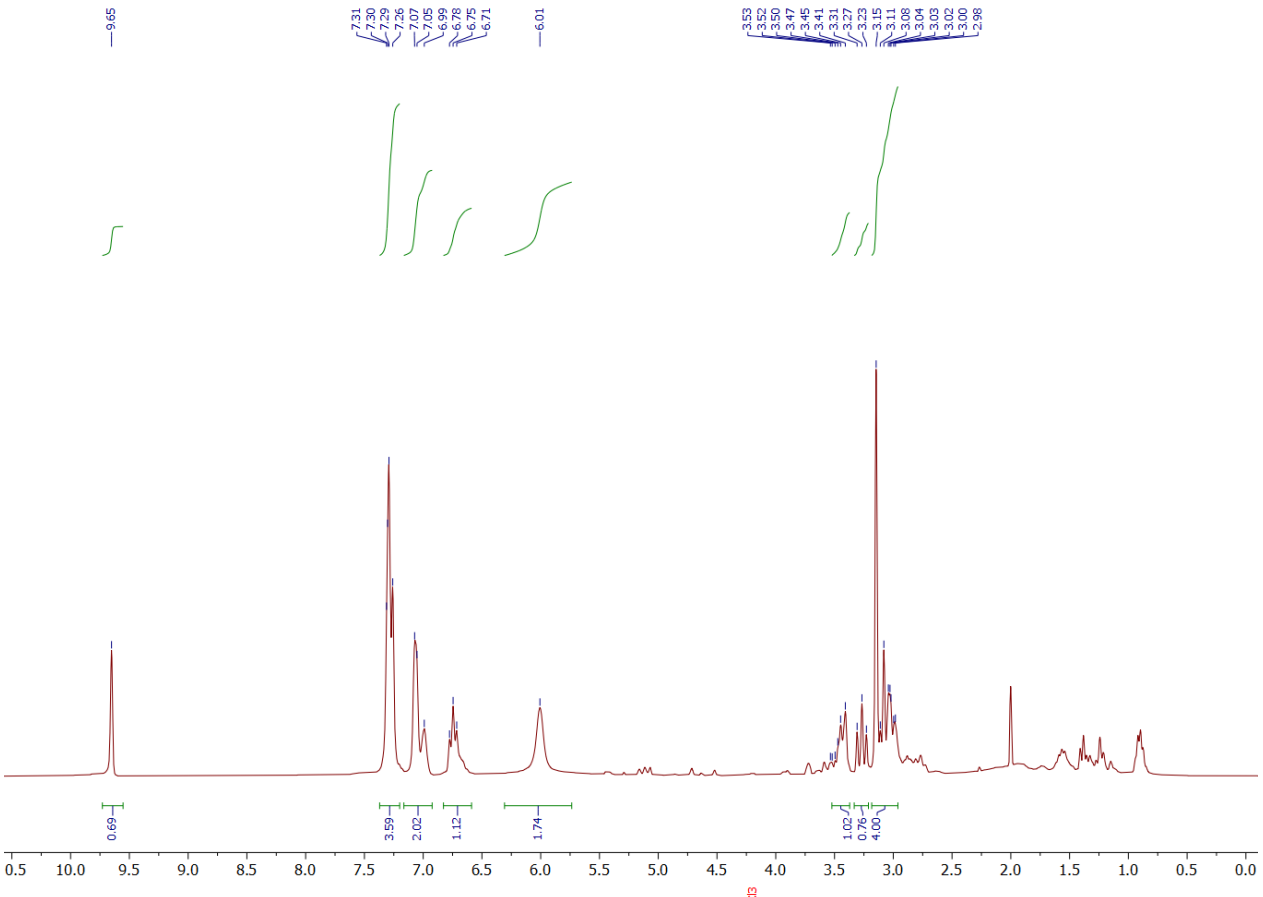
9.65
7.31
7.30
7.29
7.26
7.07
7.05
6.99
6.78
6.75
6.71
6.01
3.53
3.52
3.50
3.47
3.45
3.41
3.31
3.27
3.23
3.15
3.11
3.08
3.04
3.03
3.02
3.00
2.98
0.69
3.59
2.02
1.12
1.74
1.02
0.76
4.00

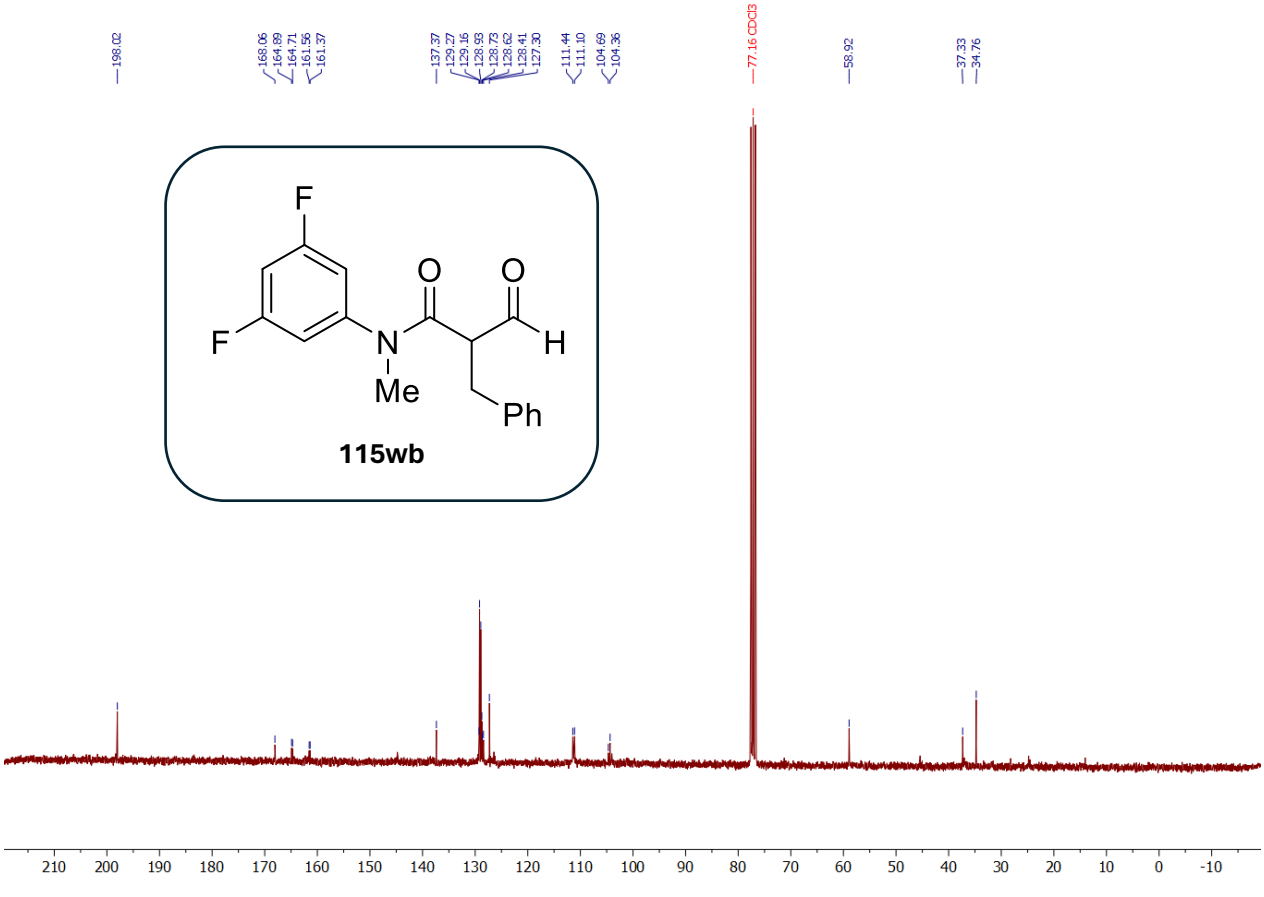
198.02
168.06
164.89
164.71
161.56
161.37
137.37
129.27
129.16
128.93
128.73
128.62
128.41
127.30
111.44
111.10
104.69
104.36
77.16 CDCl3
58.92
37.33
34.76

F
F
N
O
O
H
Me
Ph
115wb

^{1}H NMR (400 MHz, $CDCl_3$)

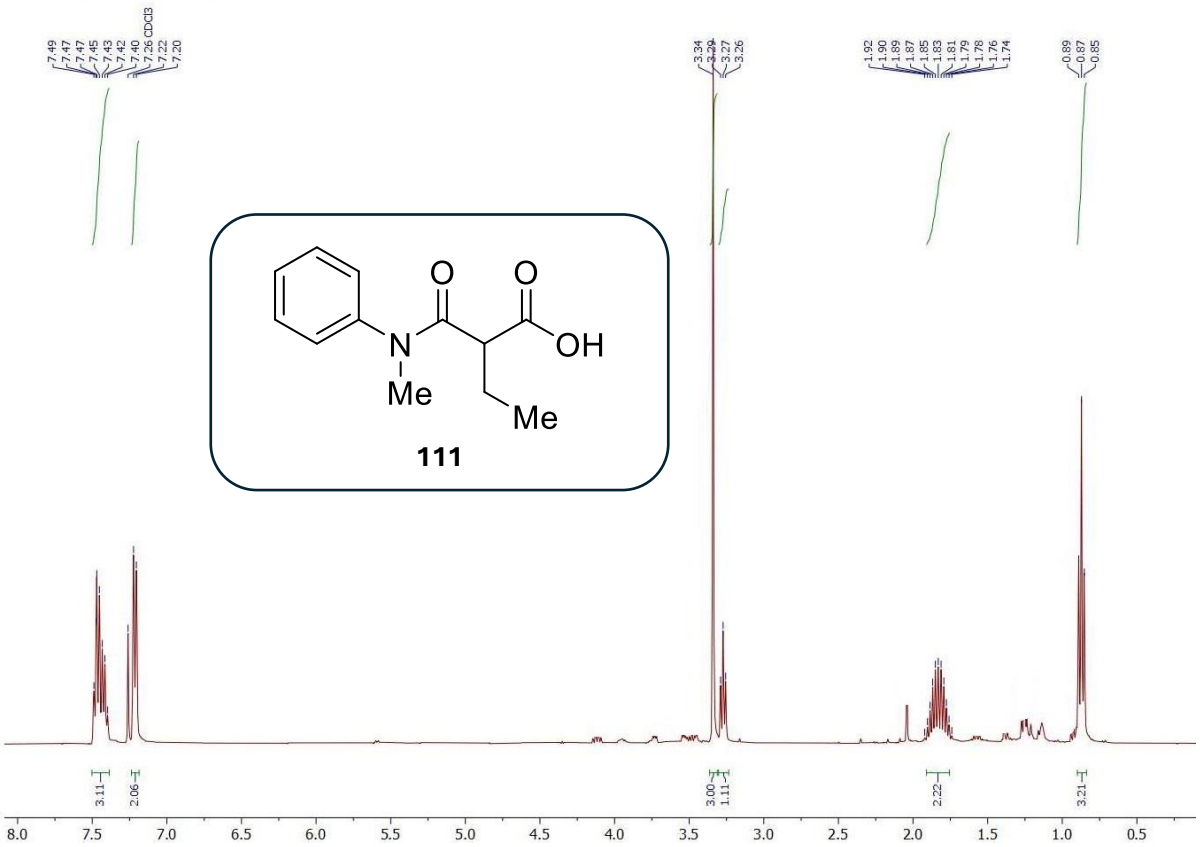

^{13}C NMR (101 MHz, $CDCl_3$)

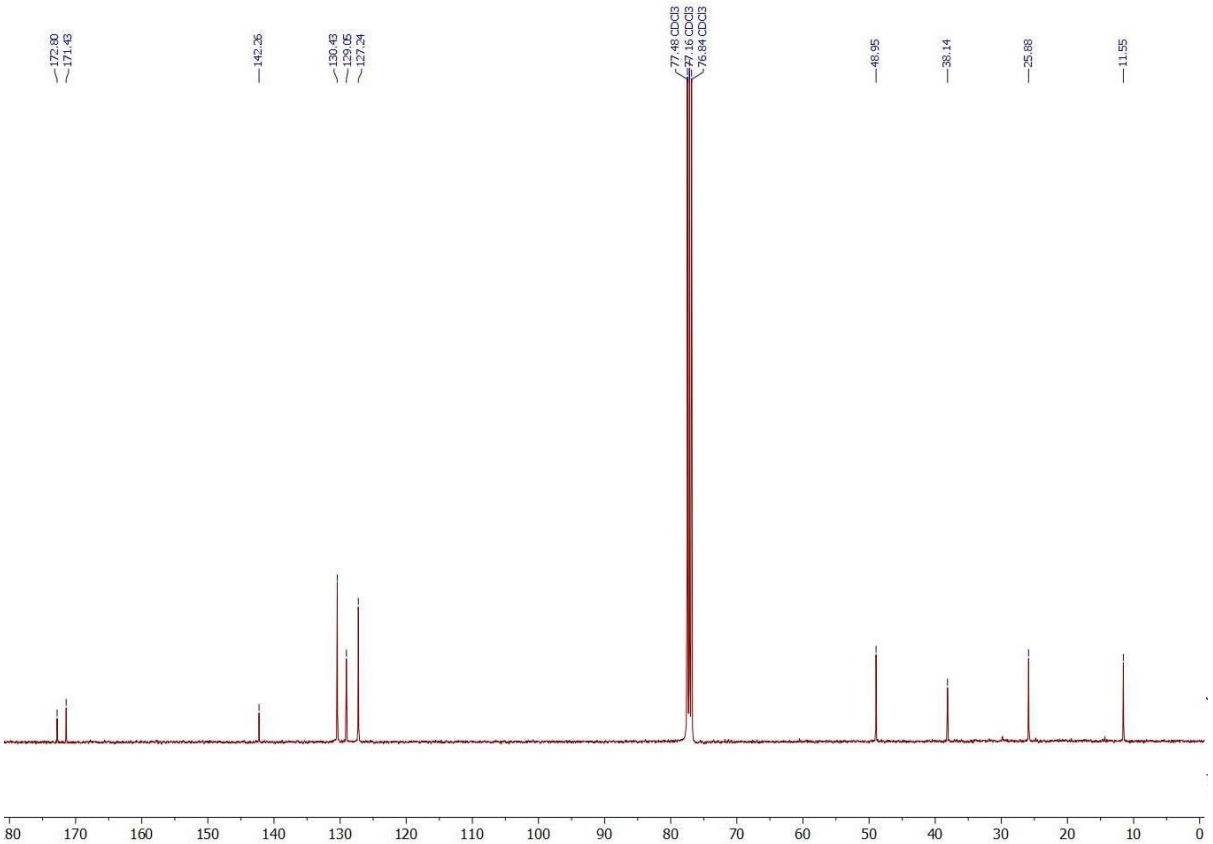

^{1}H NMR (400 MHz, $CDCl_3$)

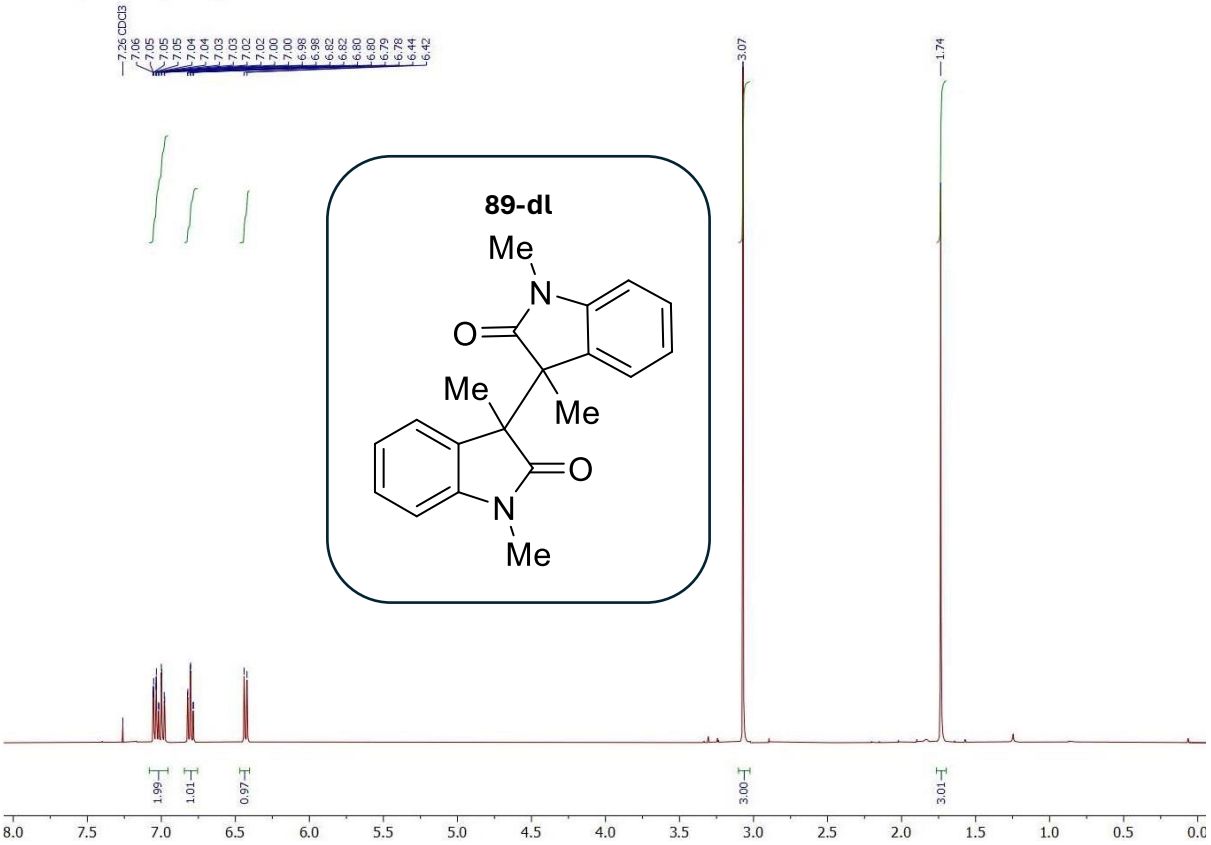

^{13}C NMR (101 MHz, $CDCl_3$)

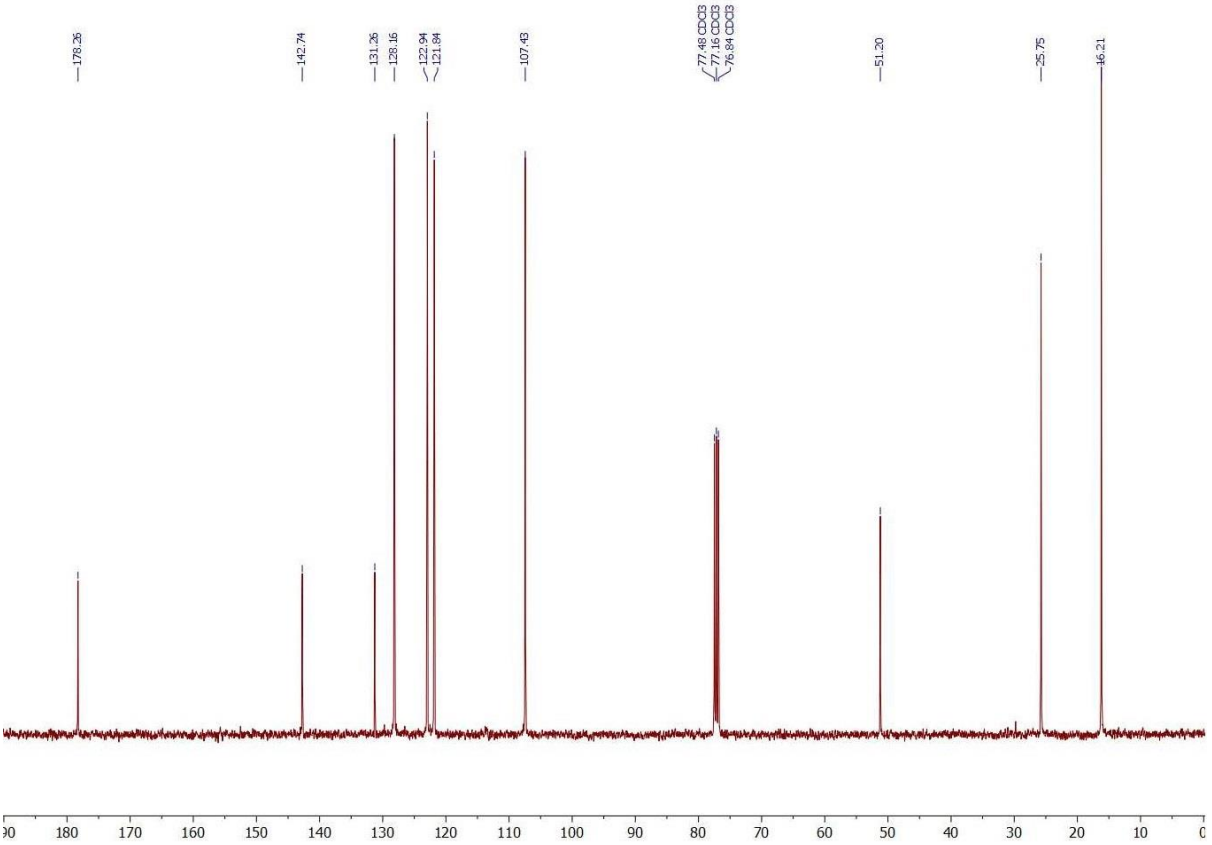

^{1}H NMR (400 MHz, $CDCl_3$)

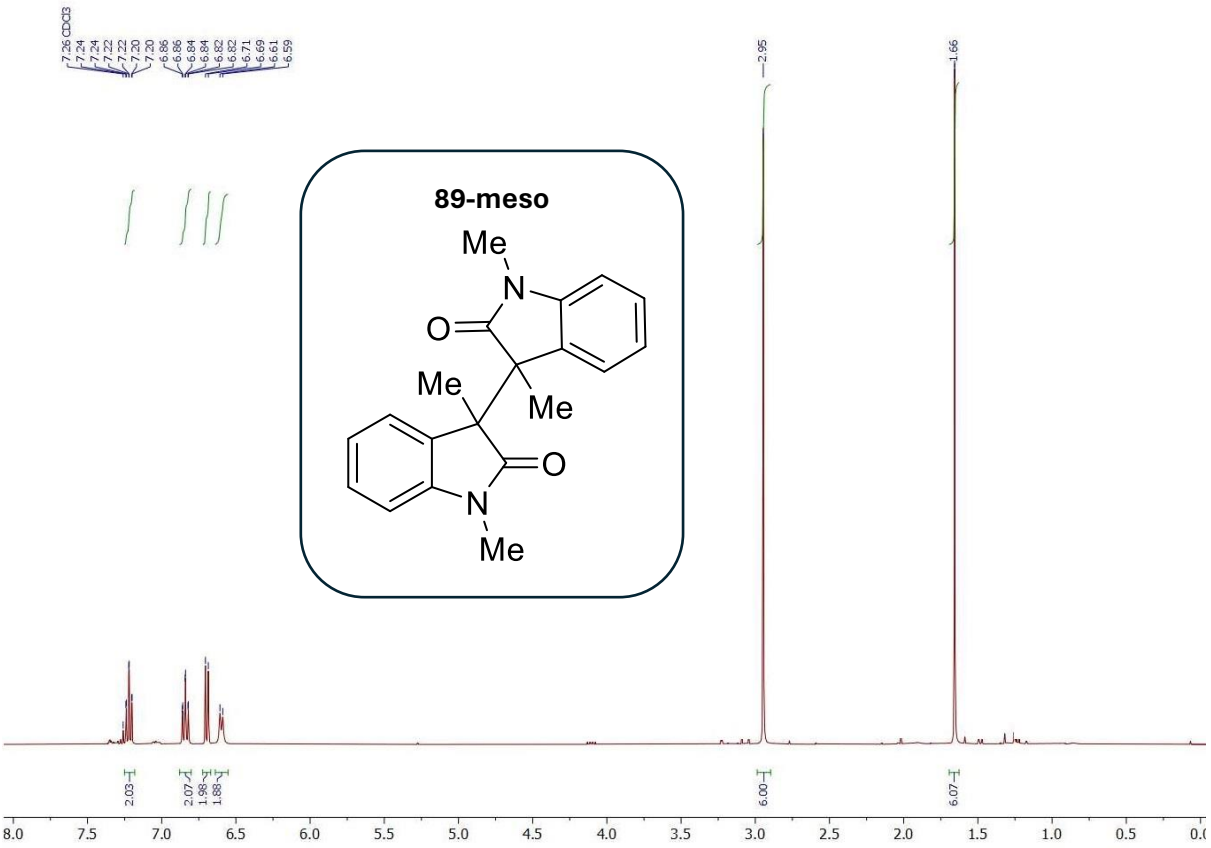

^{13}C NMR (101 MHz, $CDCl_3$)

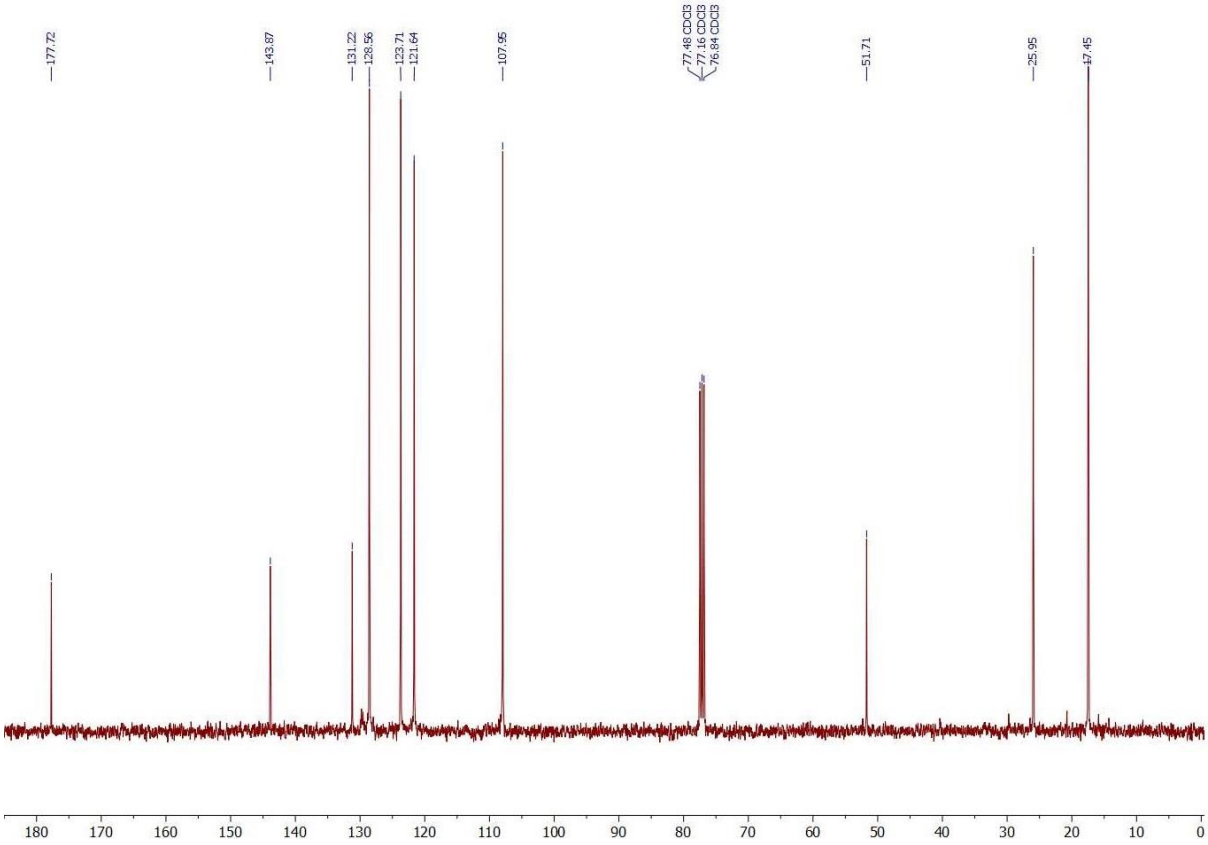

^{1}H NMR (300 MHz, $CDCl_3$)

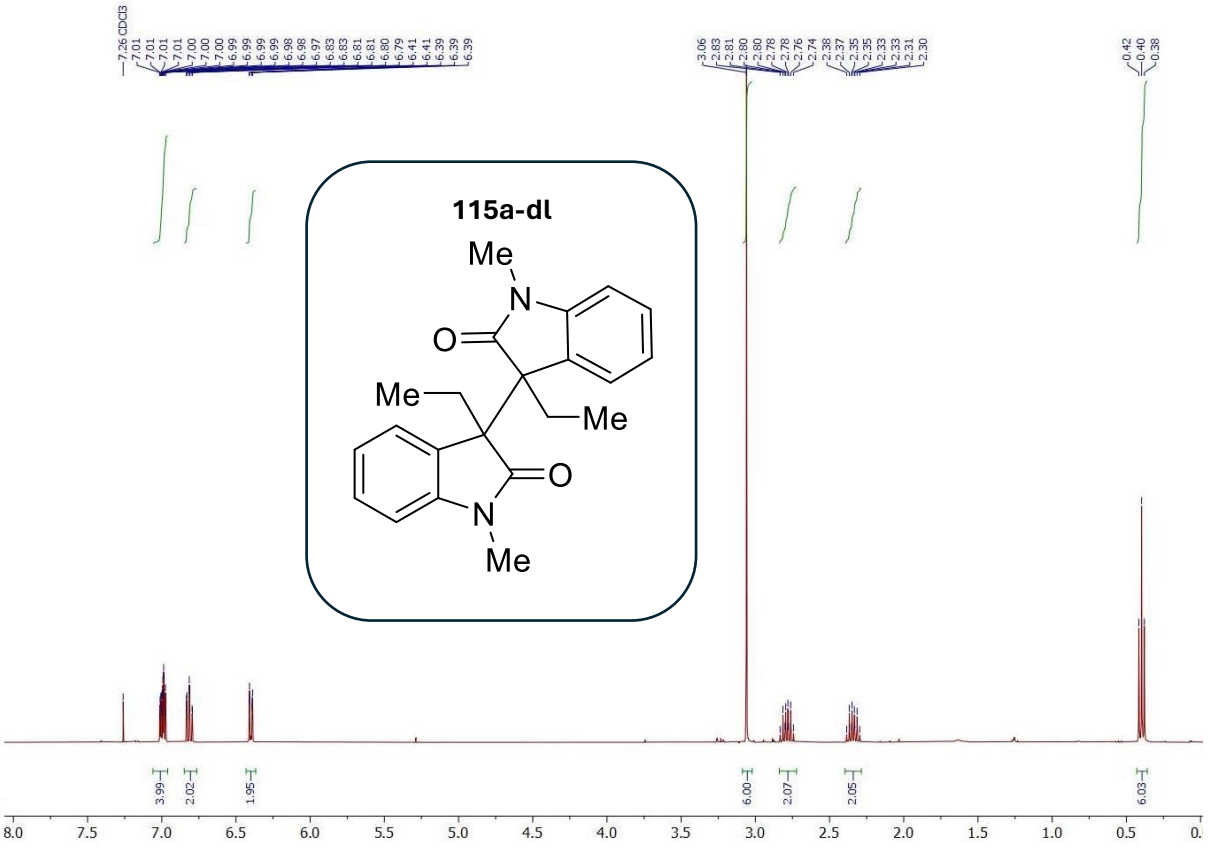

^{13}C NMR (101 MHz, $CDCl_3$)

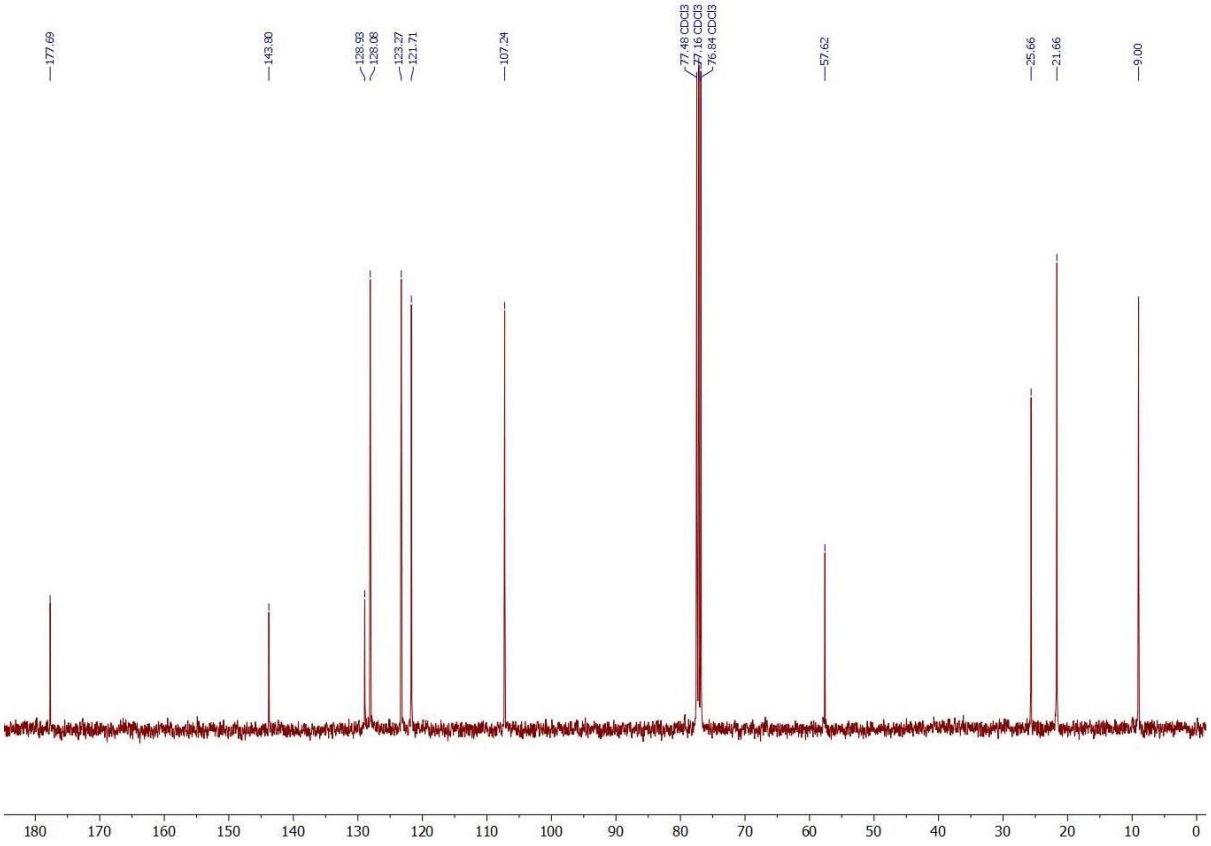

^{1}H NMR (300 MHz, $CDCl_3$)

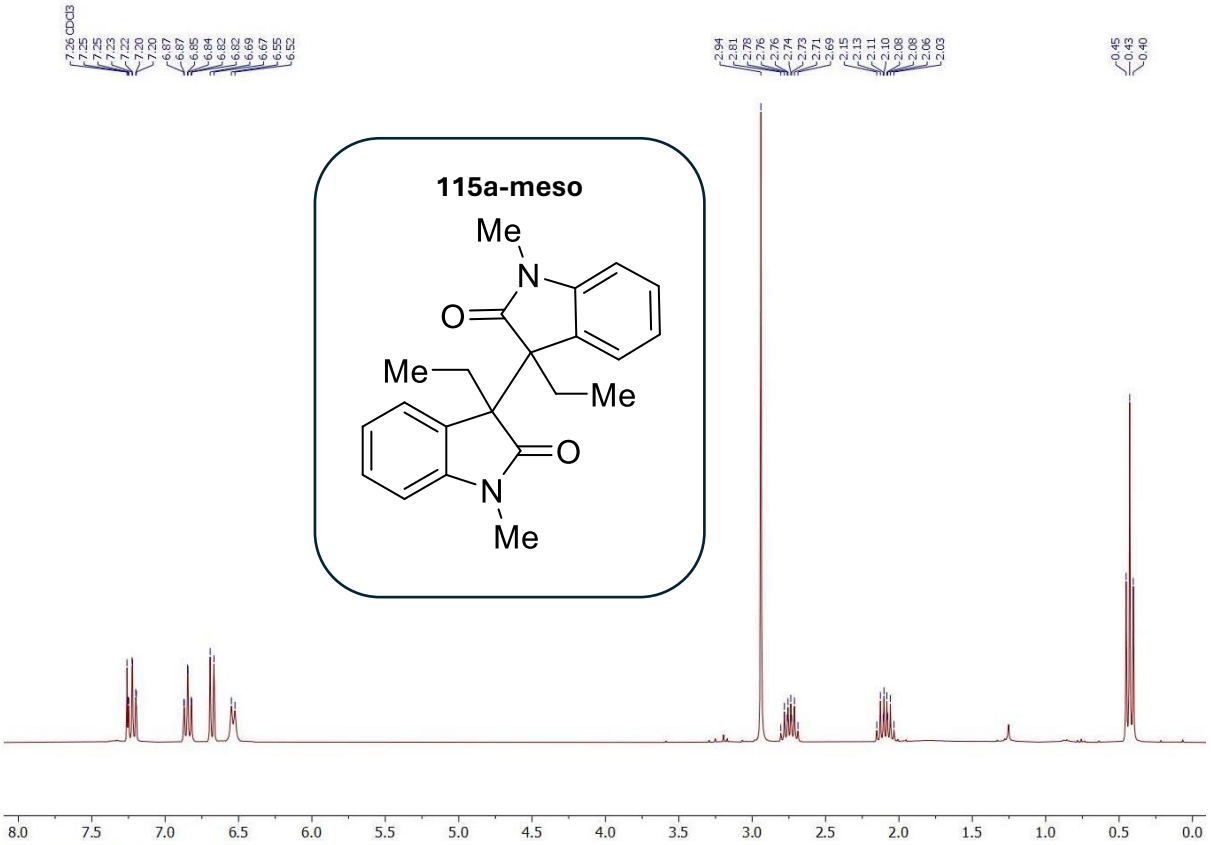

^{13}C NMR (101 MHz, $CDCl_3$)

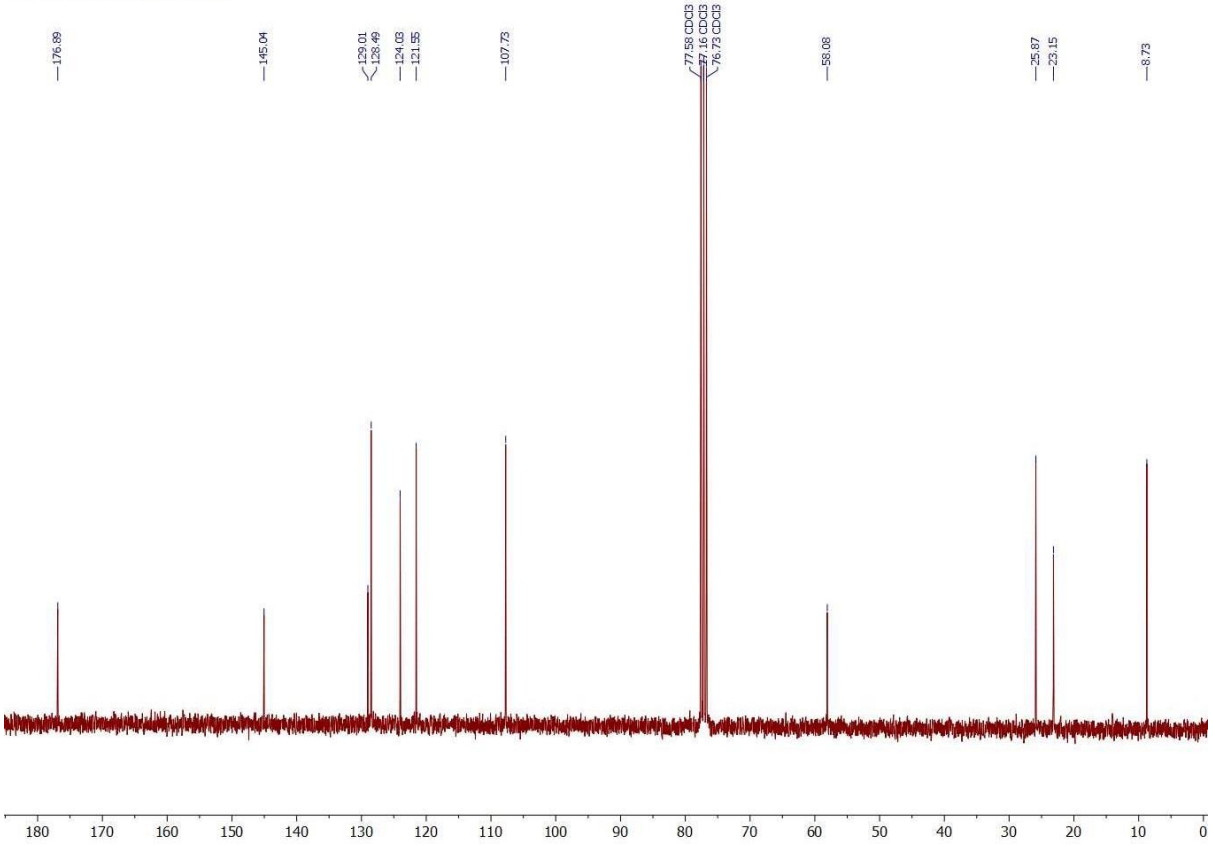

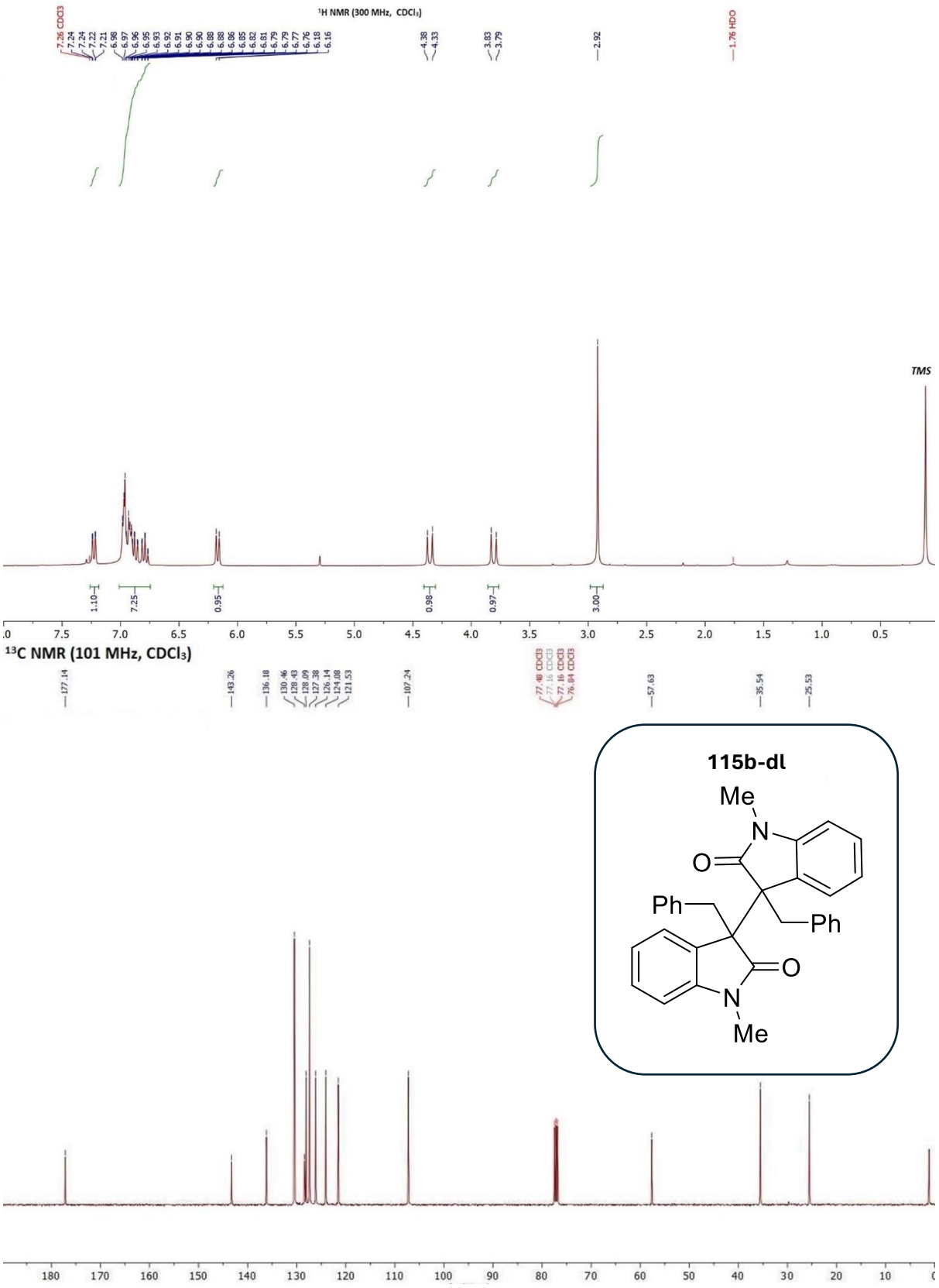
¹H NMR (300 MHz, CDCl₃)
TMS
¹³C NMR (101 MHz, CDCl₃)
115b-dl
Me
N
O
Ph
Ph
O
N
Me

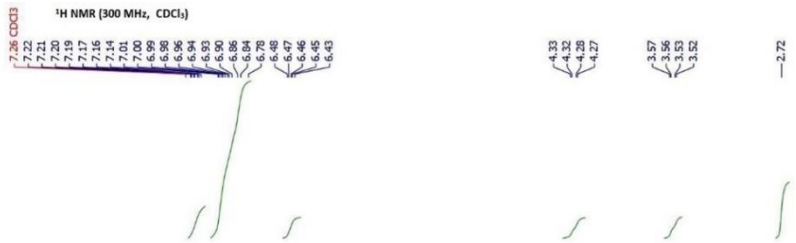
¹H NMR (300 MHz, CDCl₃)

115b-meso

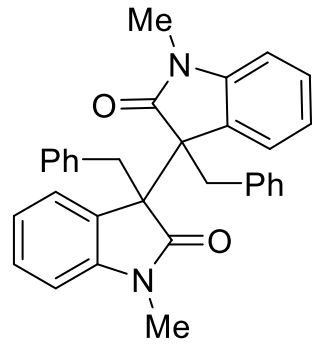
Me
N
O
Ph
Ph
O
N
Me

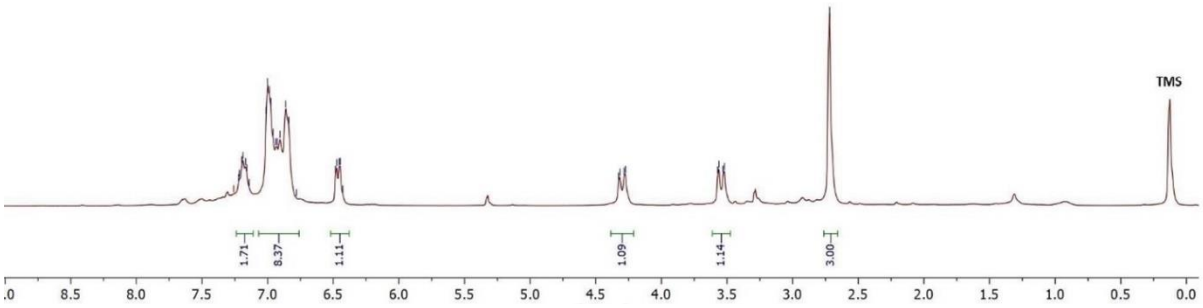
TMS
1.71
8.37
1.11
1.09
1.14
3.00


¹³C NMR (101 MHz, CDCl₃)

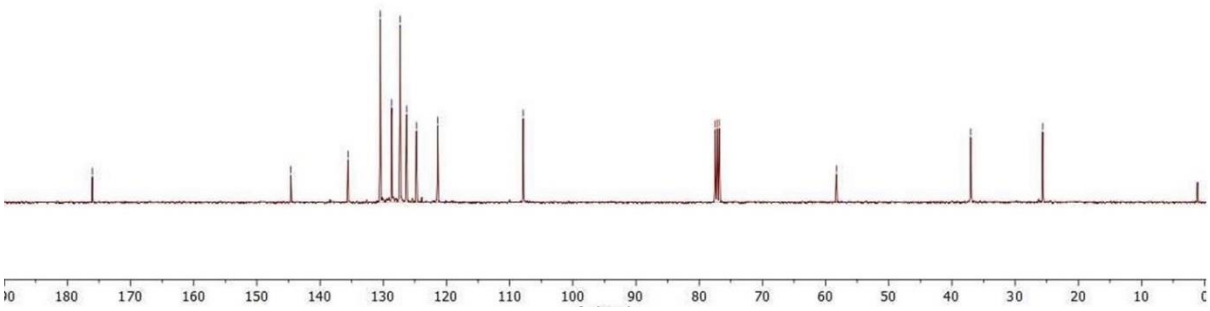

^{1}H NMR (600 MHz, $CDCl_3$)

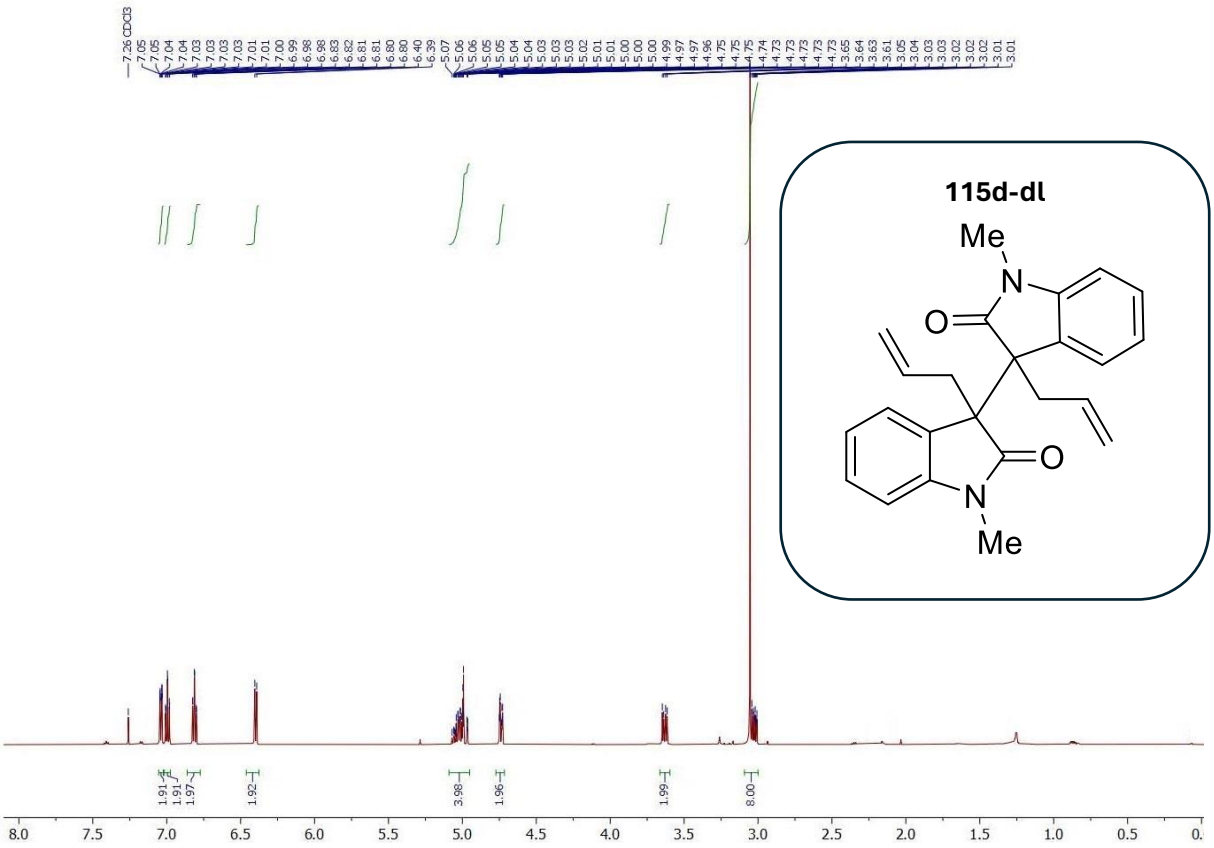

^{13}C NMR (151 MHz, $CDCl_3$)

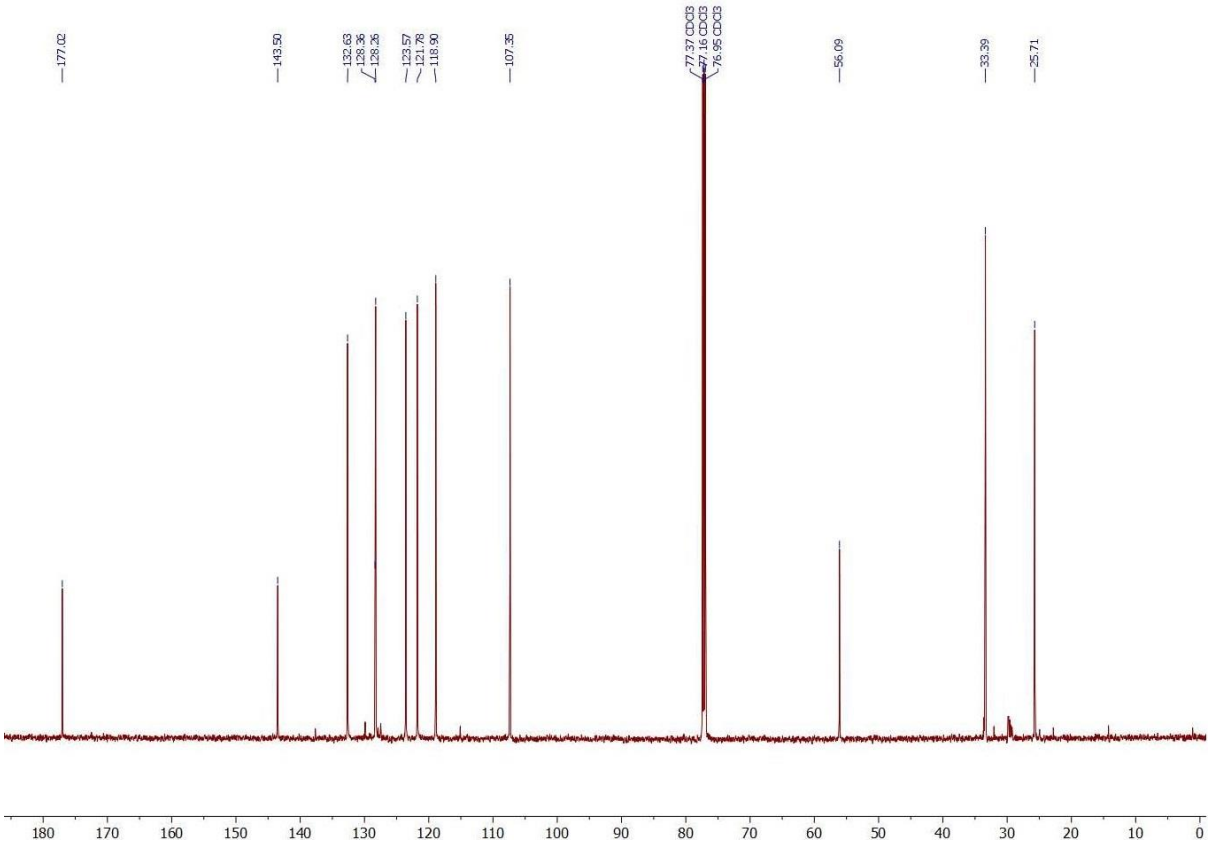

115d-meso

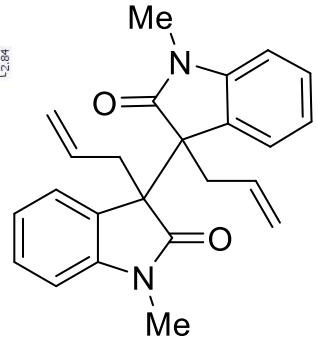

^{1}H NMR (600 MHz, $CDCl_3$)

^{13}C NMR (151 MHz, $CDCl_3$)

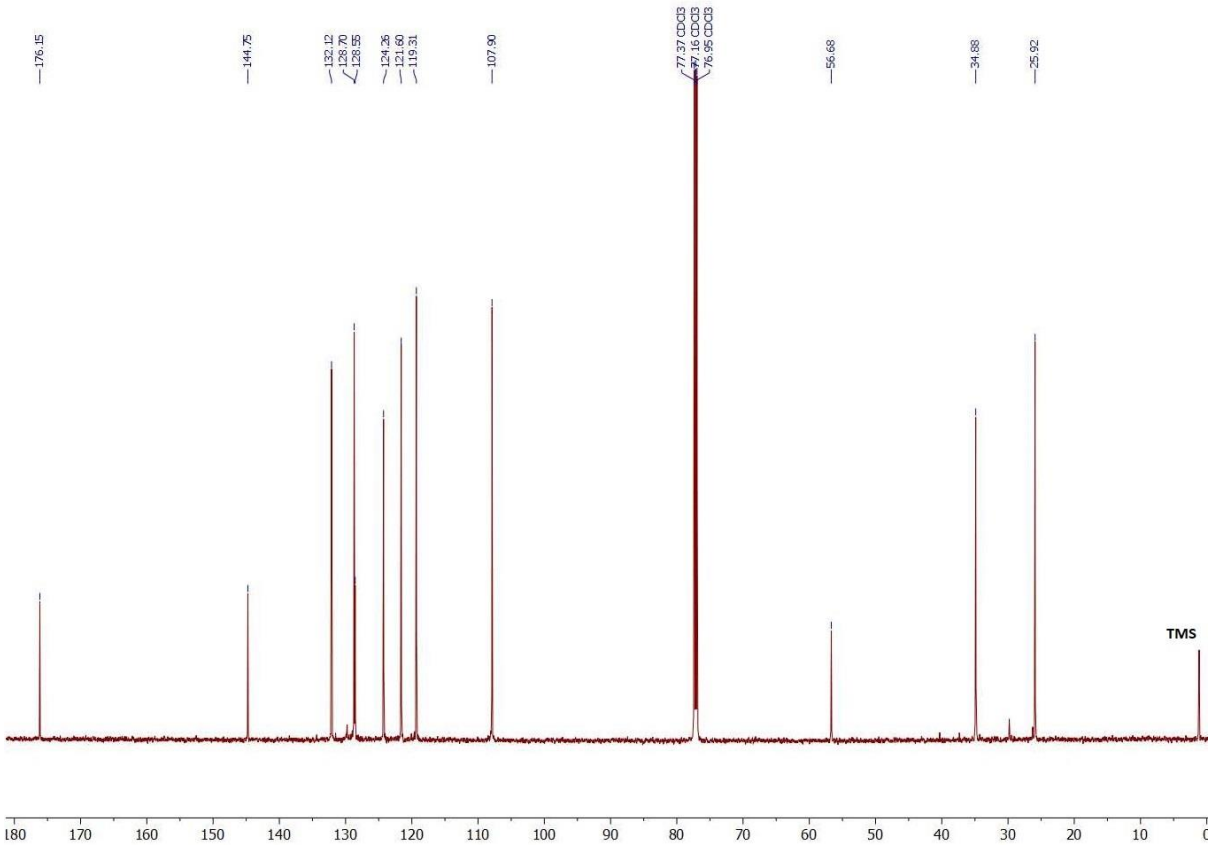

^{1}H NMR (400 MHz, $CDCl_3$)

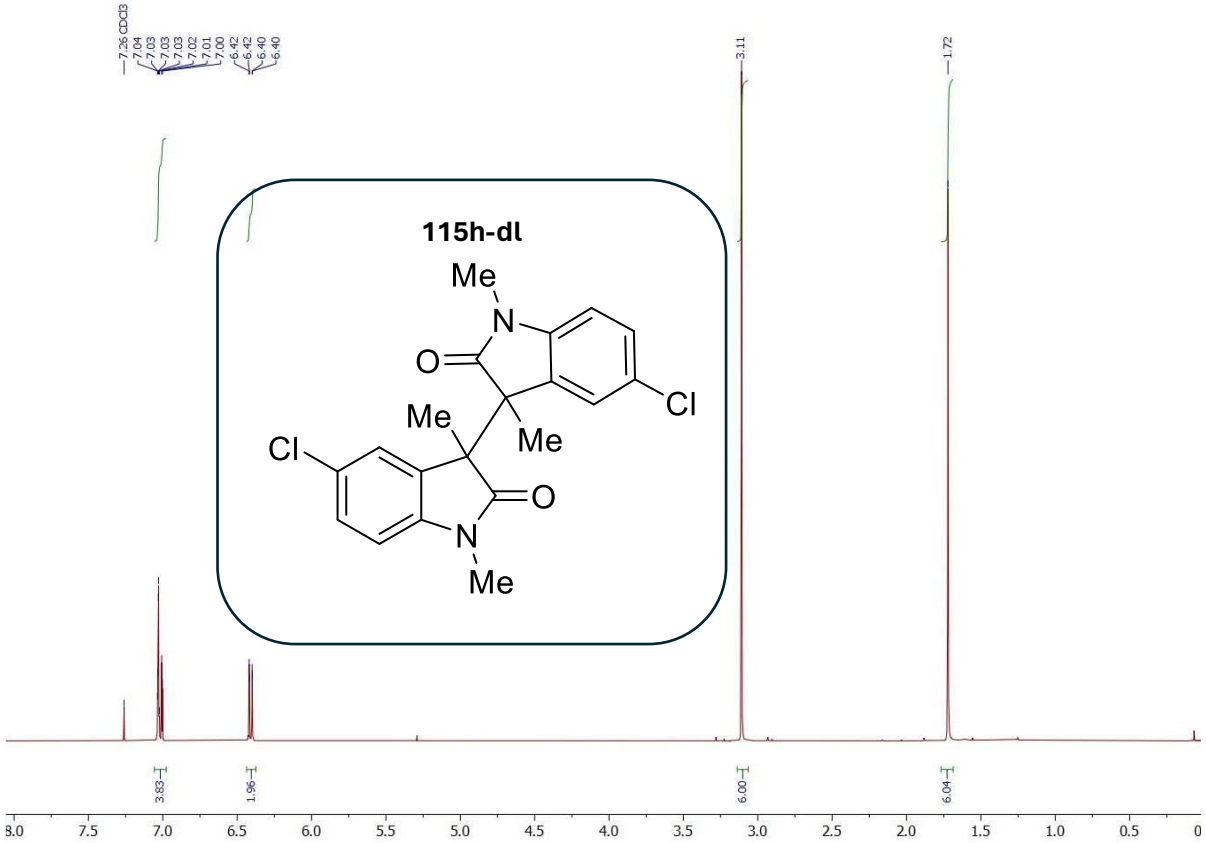

^{13}C NMR (101 MHz, $CDCl_3$)

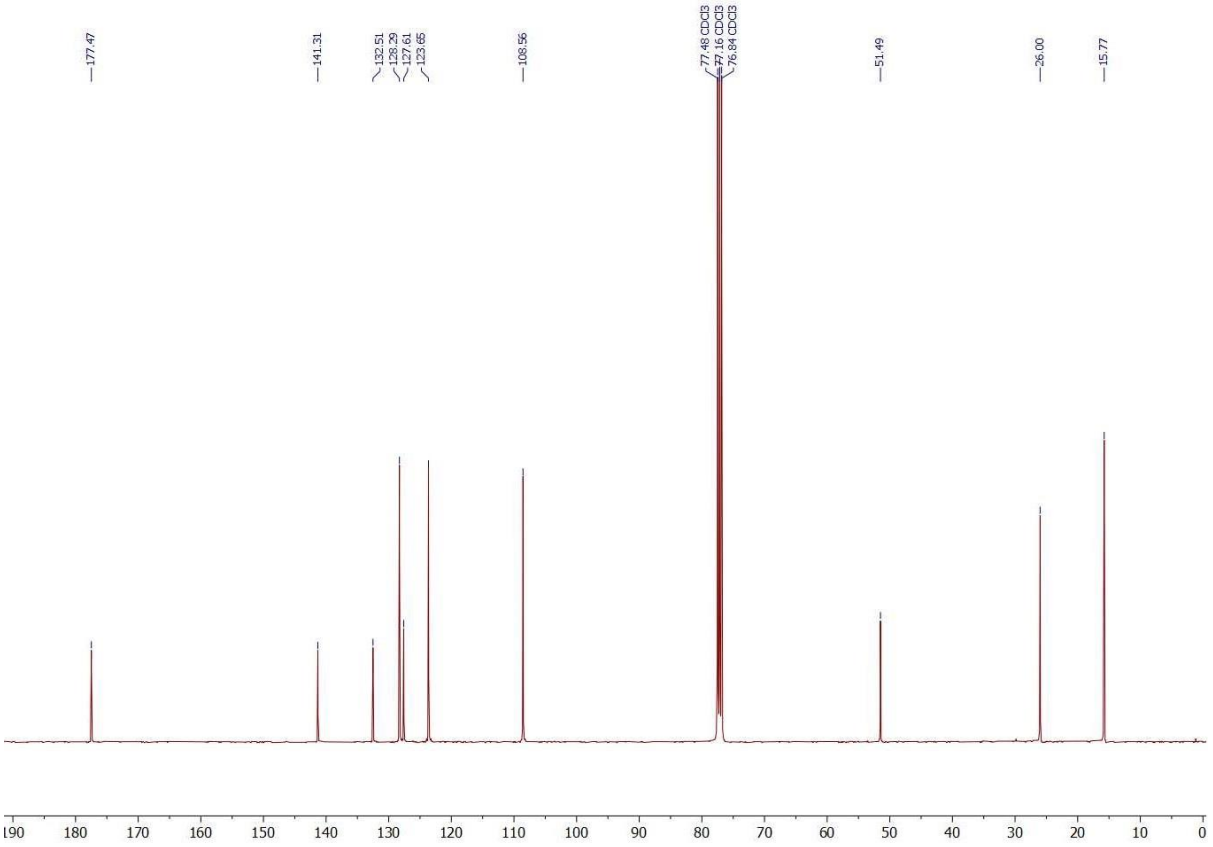

^{1}H NMR (400 MHz, $CDCl_3$)

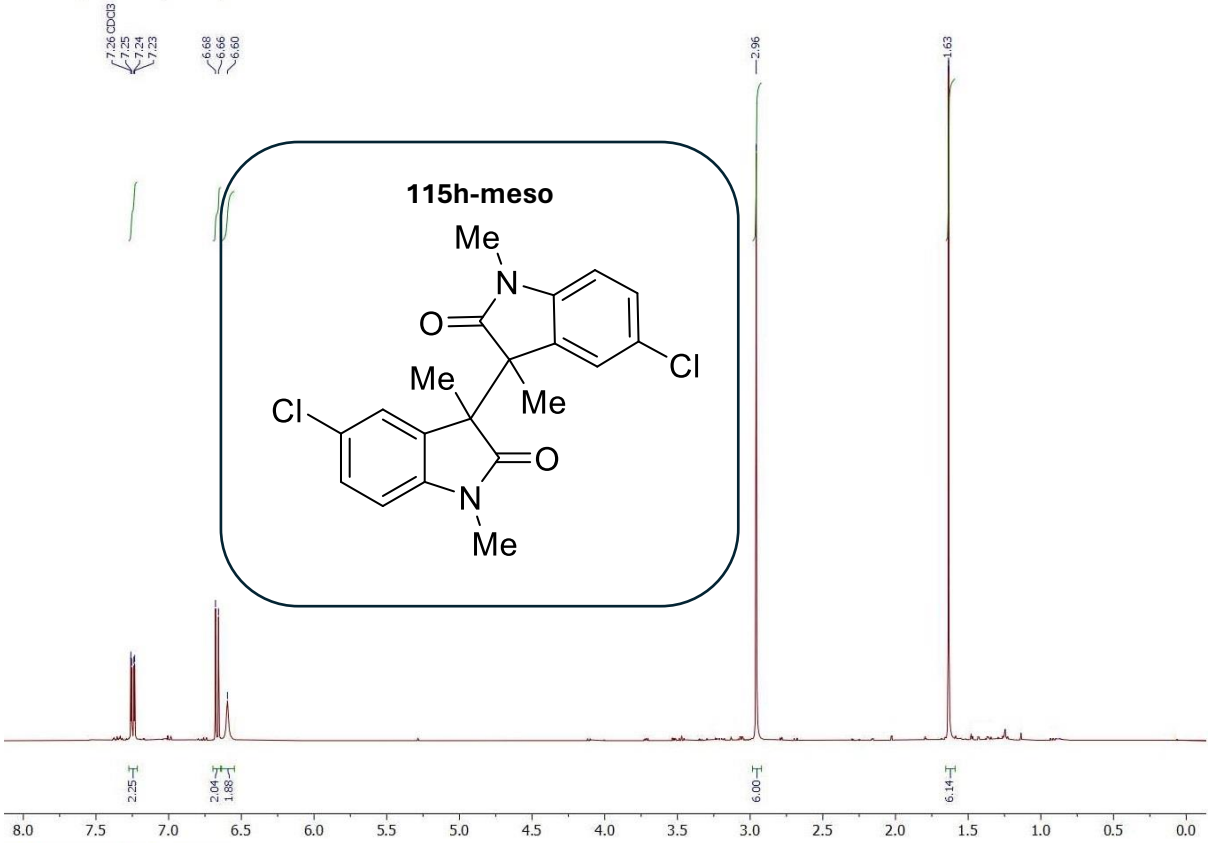

^{13}C NMR (101 MHz, $CDCl_3$)

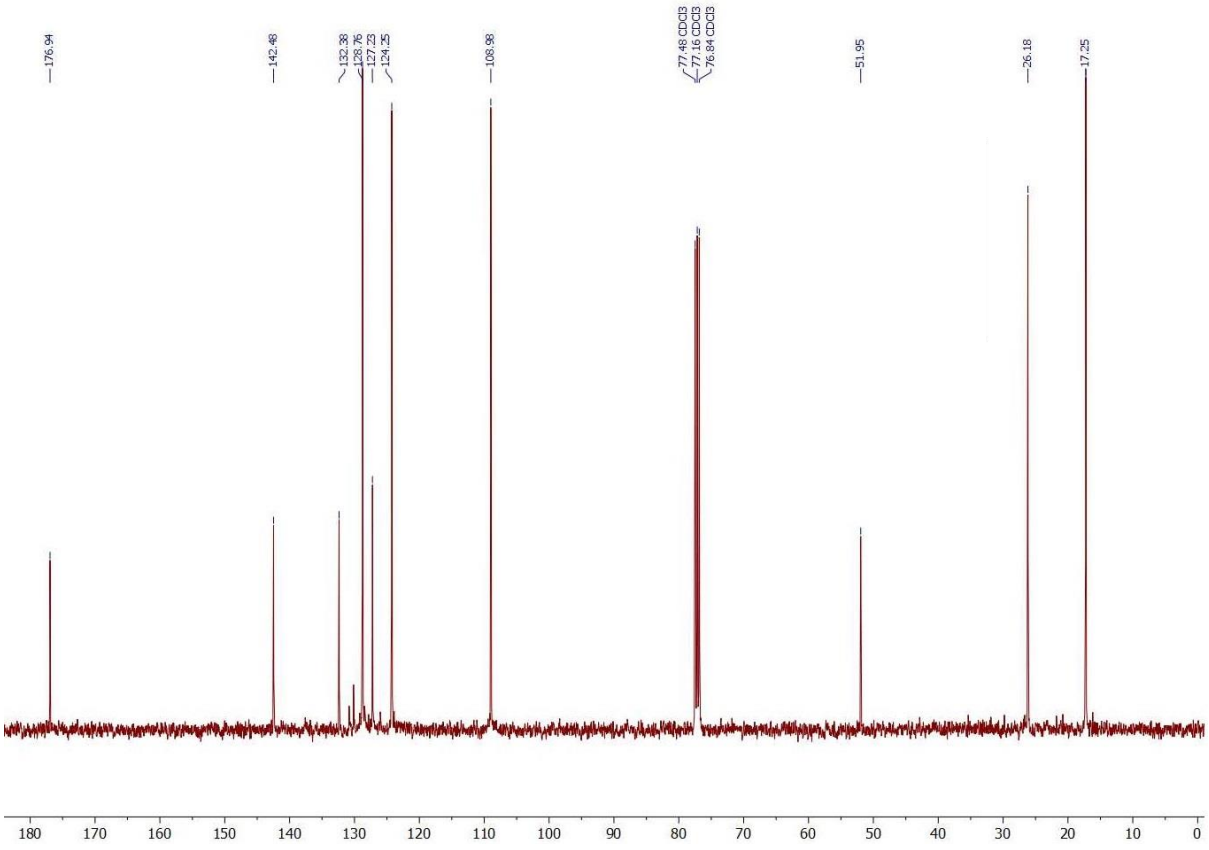

^{1}H NMR (400 MHz, $CDCl_3$)

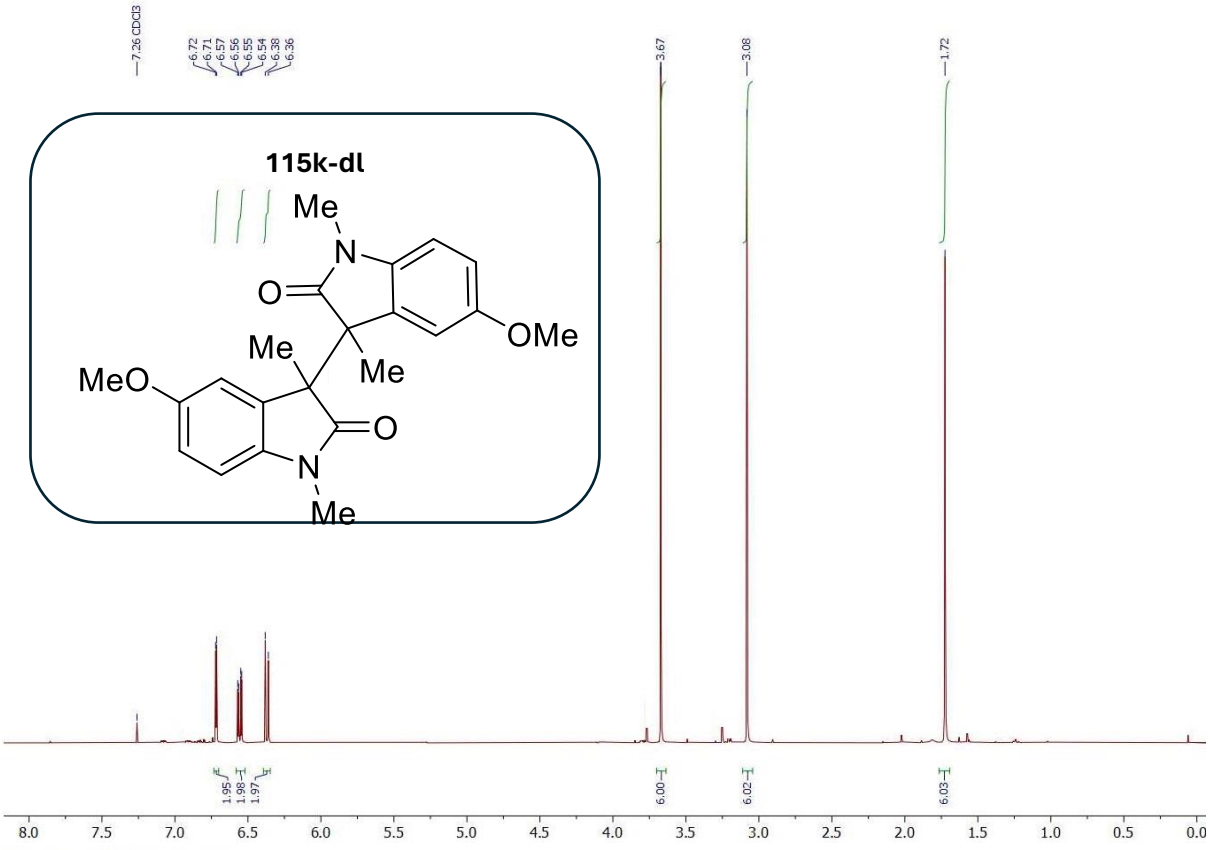

^{13}C NMR (101 MHz, $CDCl_3$)

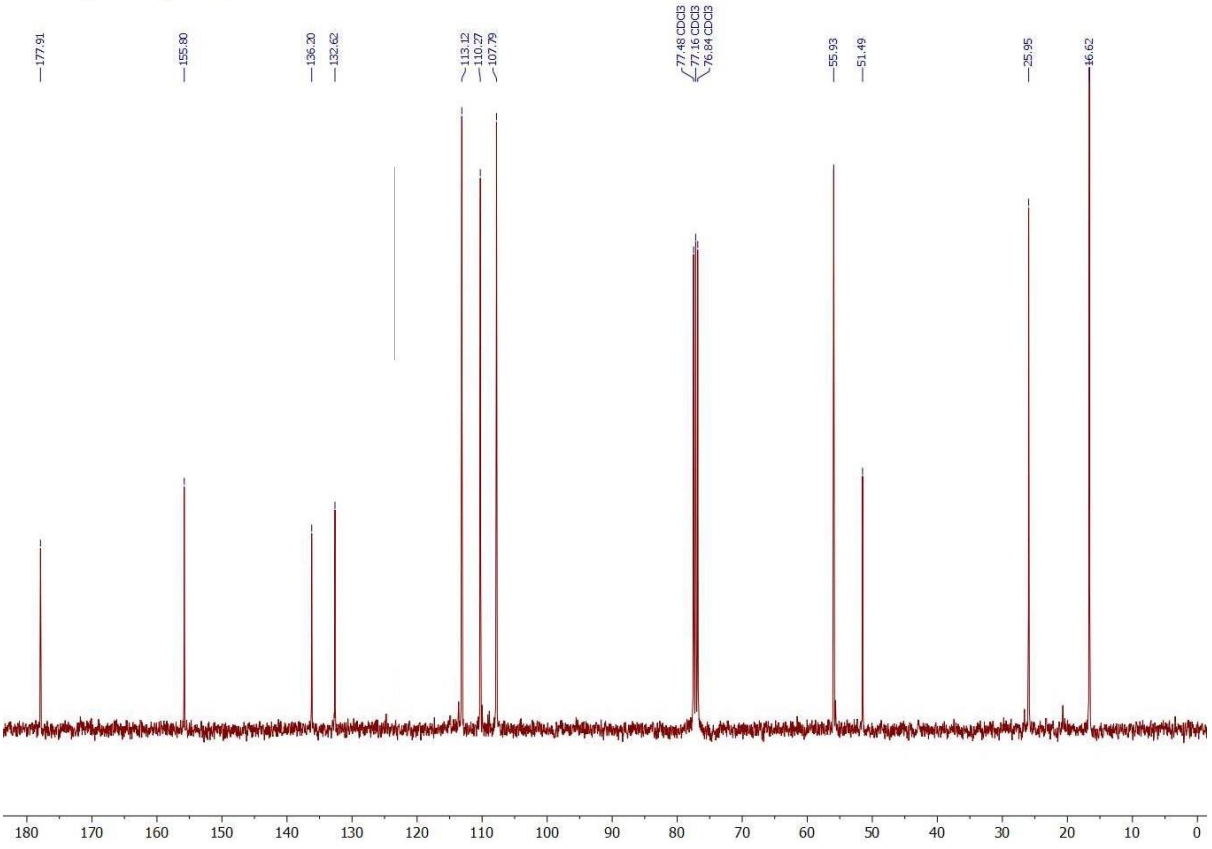

^{1}H NMR (400 MHz, $CDCl_3$)

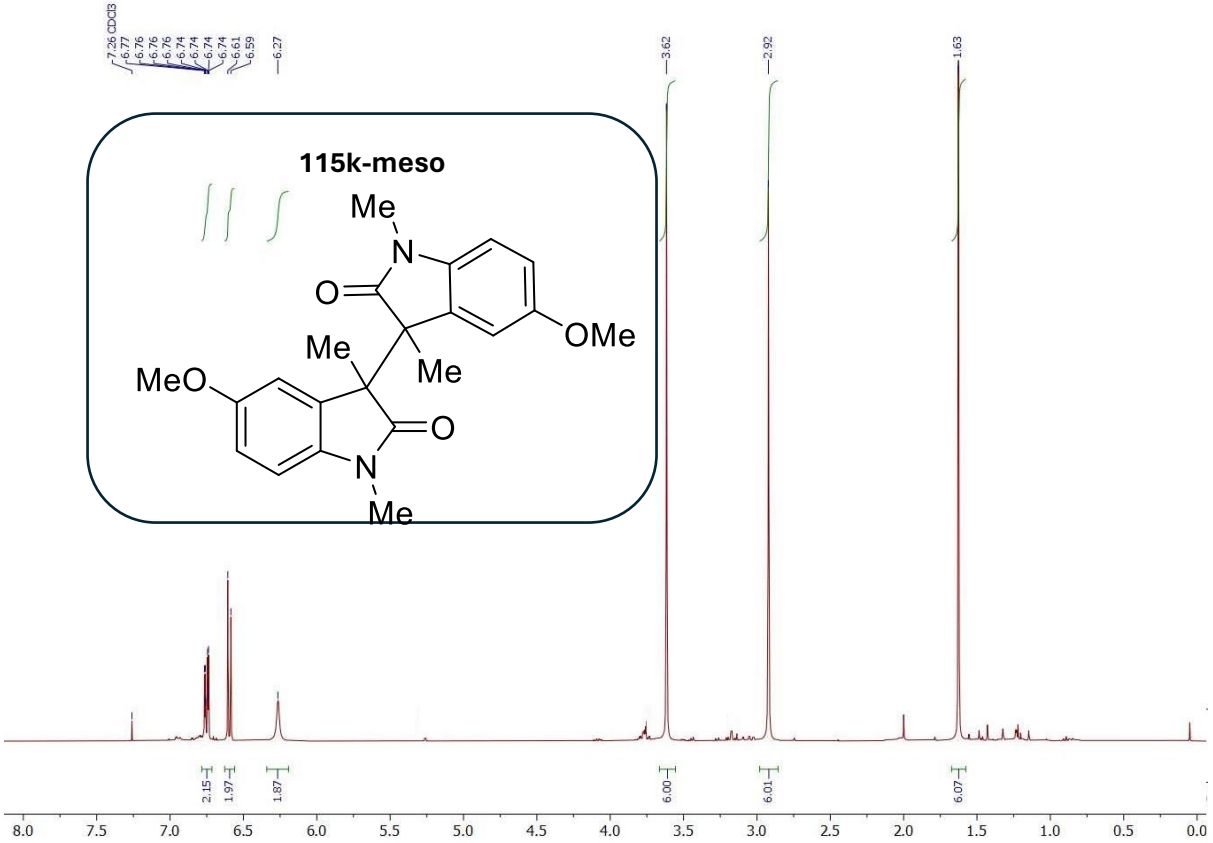

^{13}C NMR (101 MHz, $CDCl_3$)

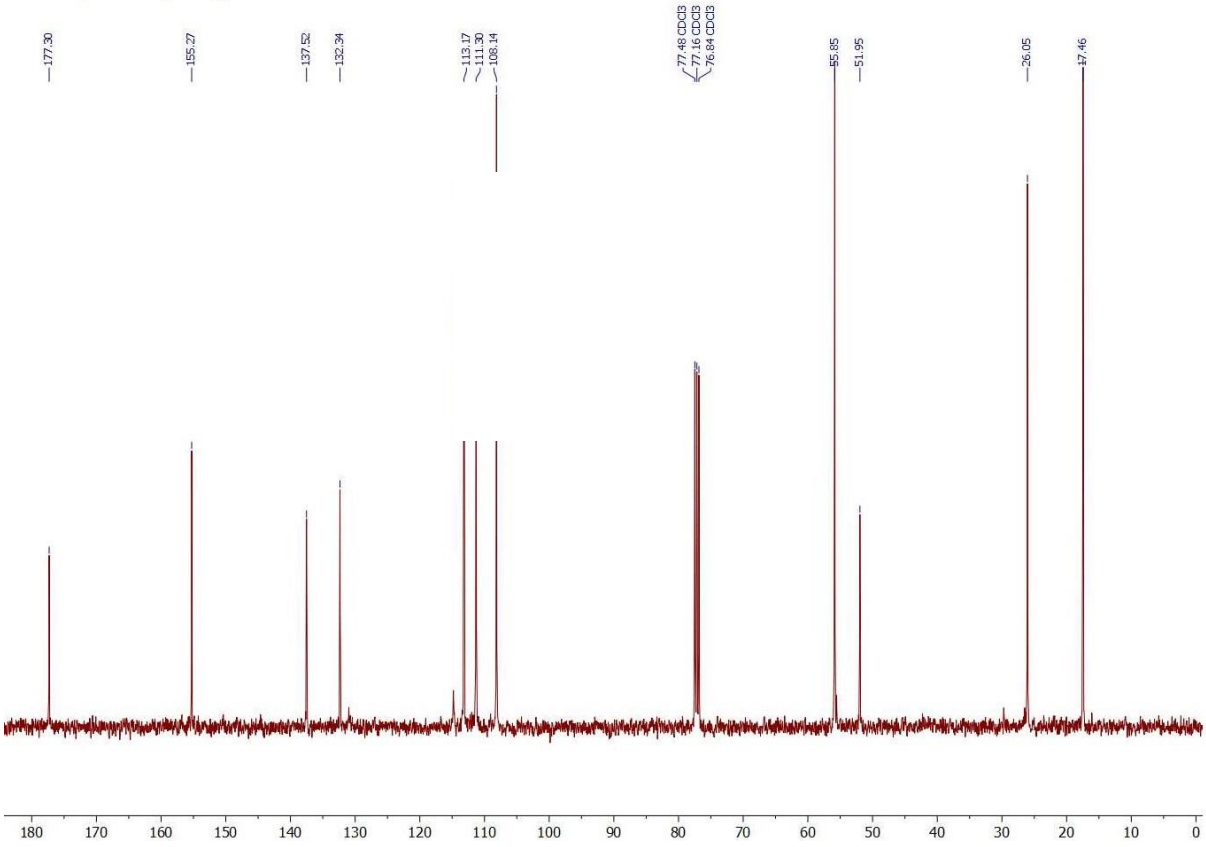

^{1}H NMR (400 MHz, $CDCl_3$)

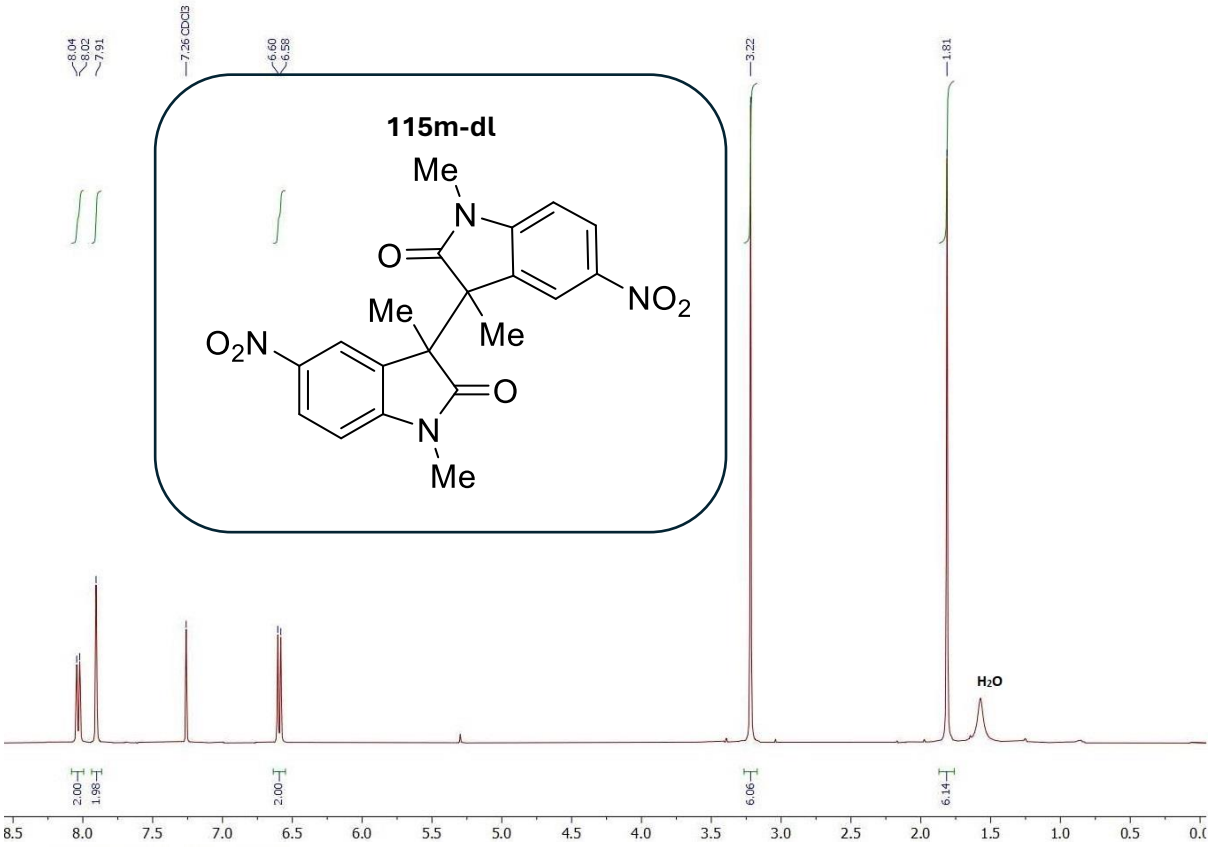

^{13}C NMR (101 MHz, $CDCl_3$)

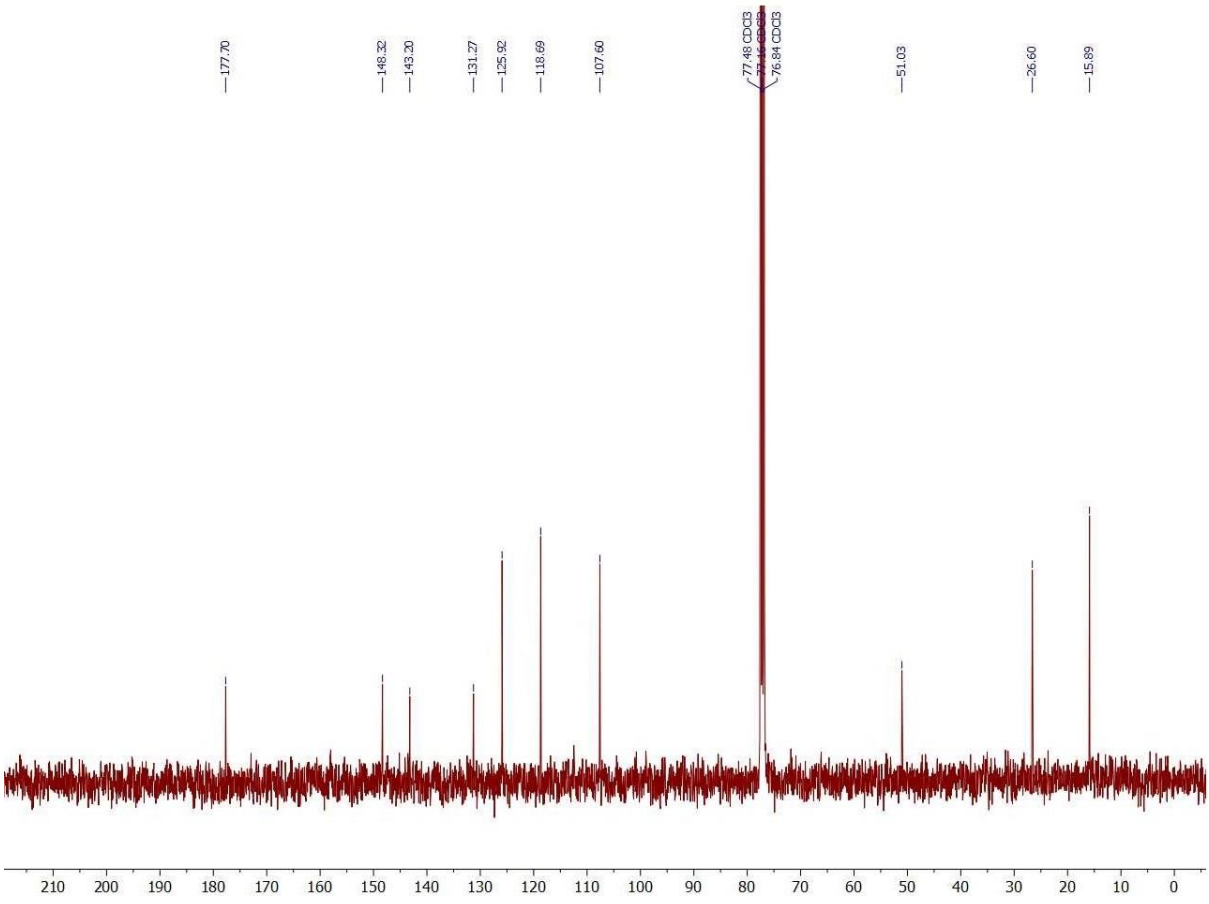

^{1}H NMR (400 MHz, $CDCl_3$)

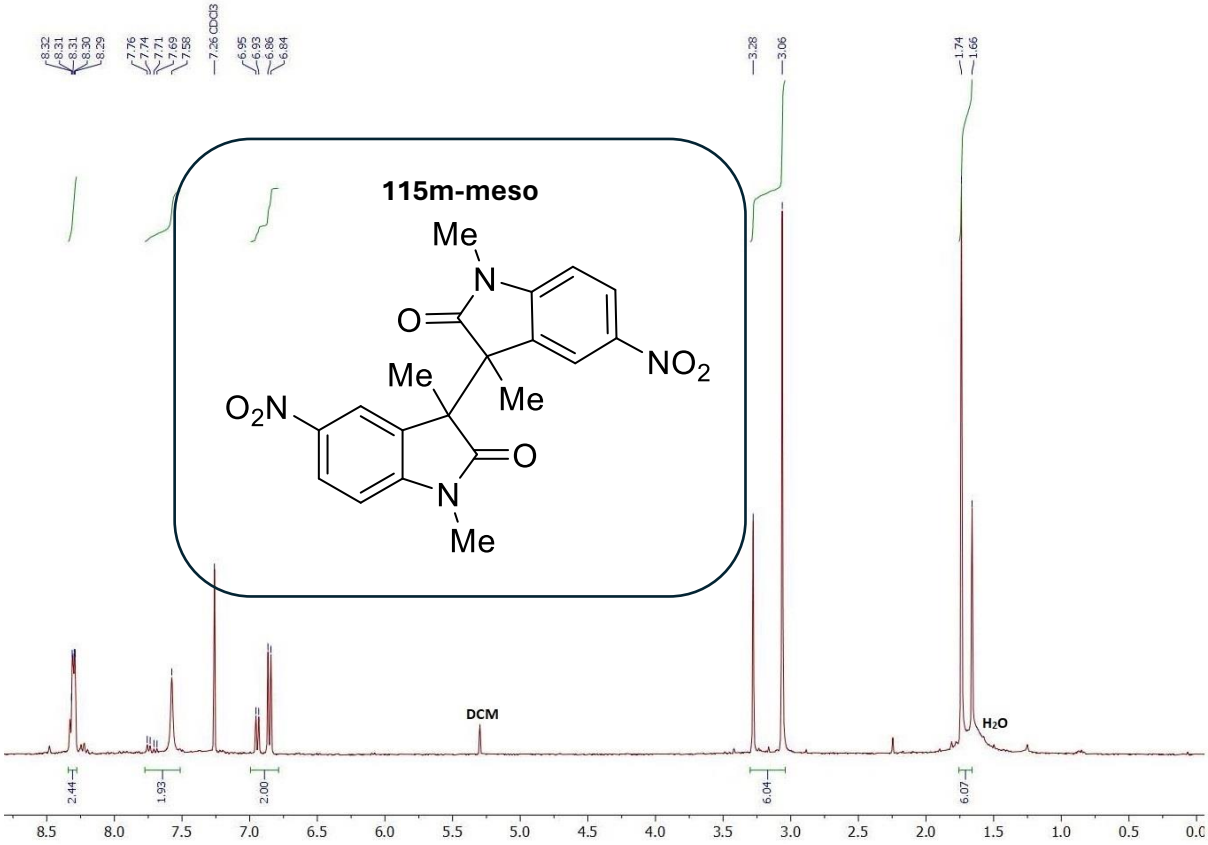

^{13}C NMR (101 MHz, $CDCl_3$)

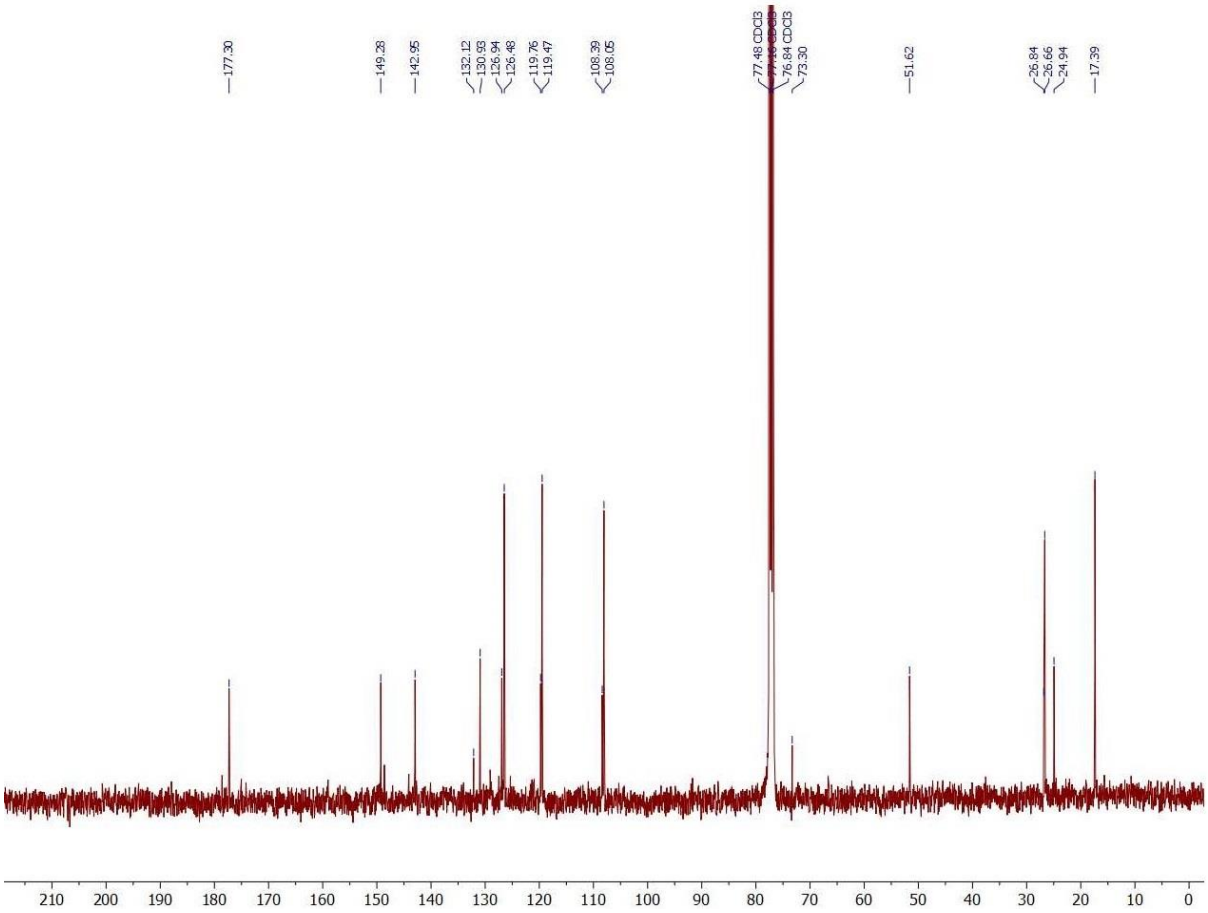

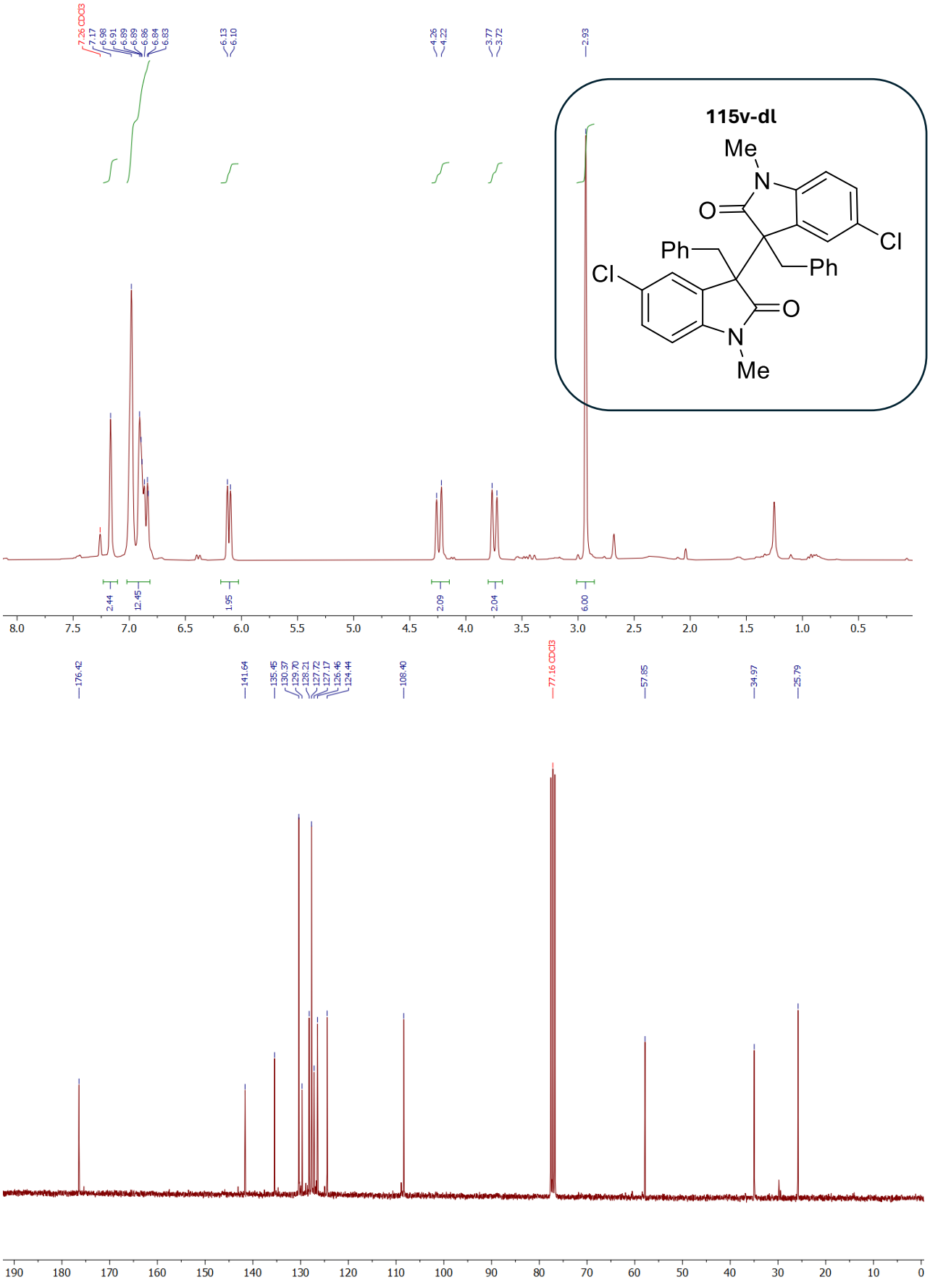
115v-dl
Me
N
O
Cl
Ph
Ph
Cl
O
N
Me
7.26 CDCl3
7.17
6.98
6.91
6.89
6.89
6.86
6.84
6.83
6.13
6.10
4.26
4.22
3.77
3.72
2.93
2.44
12.45
1.95
2.09
2.04
6.00
176.42
141.64
135.45
130.37
129.70
128.21
127.72
127.17
126.46
124.44
108.40
77.16 CDCl3
57.85
34.97
25.79

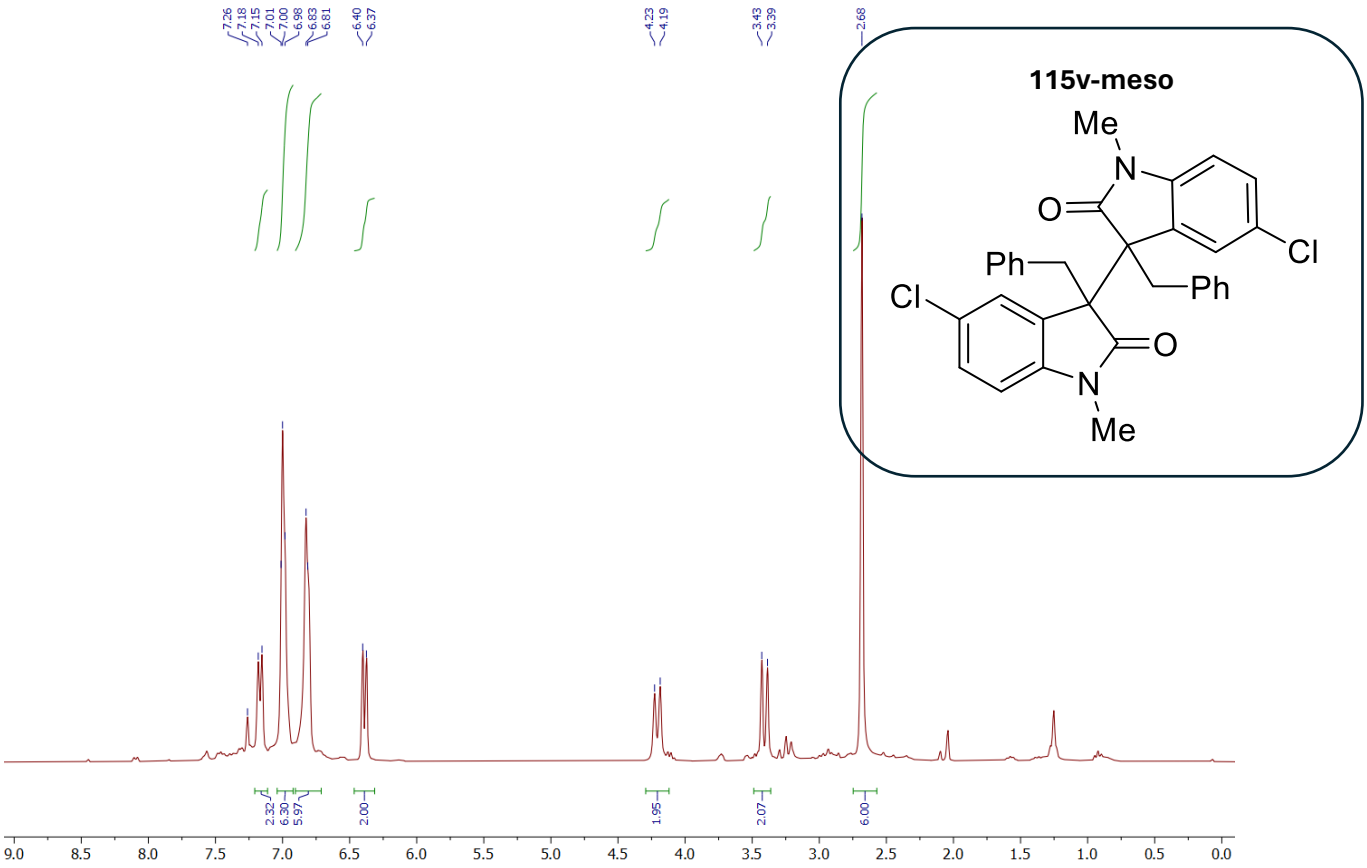
7.26
7.18
7.15
7.01
7.00
6.98
6.83
6.81
6.40
6.37
4.23
4.19
3.43
3.39
2.68
2.32
6.30
5.97
2.00
1.95
2.07
6.00
9.0
8.5
8.0
7.5
7.0
6.5
6.0
5.5
5.0
4.5
4.0
3.5
3.0
2.5
2.0
1.5
1.0
0.5
0.0

115v-meso
Me
N
O
Cl
Ph
Ph
Cl
O
N
Me

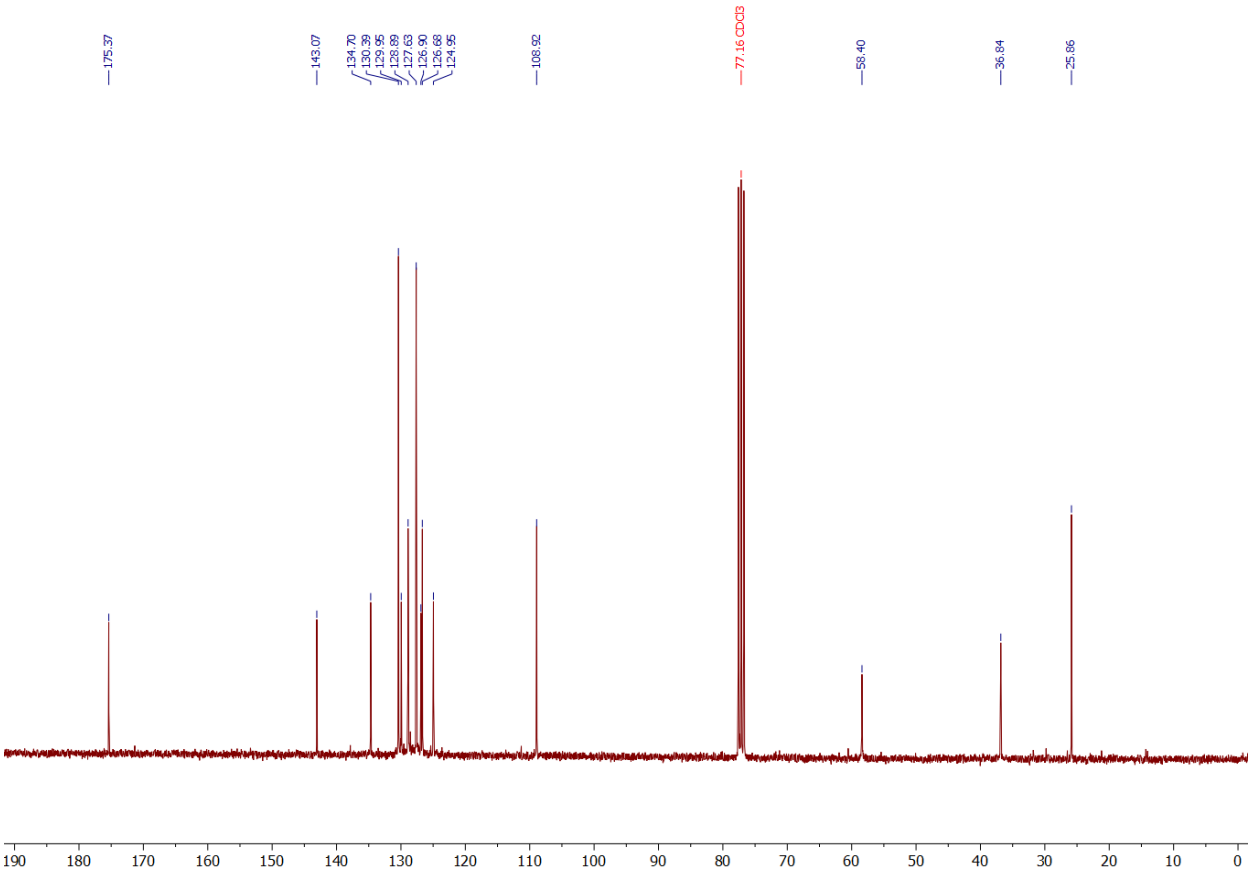
175.37
143.07
134.70
130.39
129.95
128.89
127.63
126.90
126.68
124.95
108.92
77.16 CDCl3
58.40
36.84
25.86
190
180
170
160
150
140
130
120
110
100
90
80
70
60
50
40
30
20
10
0

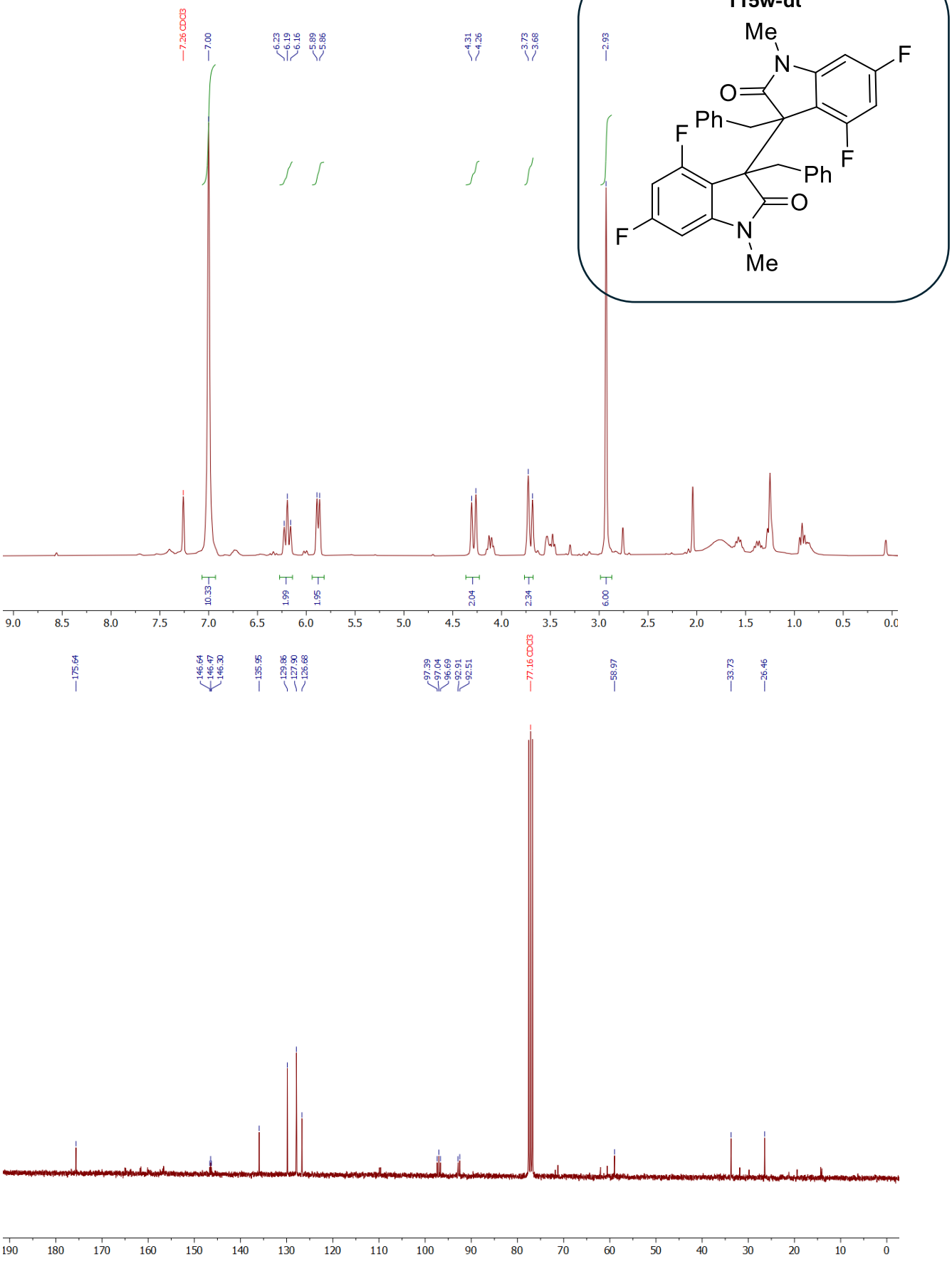
115w-dl
Me
N
O
F
Ph
F
F
Ph
O
F
N
Me
7.26 CDCl3
7.00
6.23
6.19
6.16
5.89
5.86
4.31
4.26
3.73
3.68
2.93
10.33
1.99
1.95
2.04
2.34
6.00
9.0
8.5
8.0
7.5
7.0
6.5
6.0
5.5
5.0
4.5
4.0
3.5
3.0
2.5
2.0
1.5
1.0
0.5
0.0
175.64
146.64
146.47
146.30
135.95
129.86
127.90
126.68
97.39
97.04
96.69
92.91
92.51
77.16 CDCl3
58.97
33.73
26.46
190
180
170
160
150
140
130
120
110
100
90
80
70
60
50
40
30
20
10
0

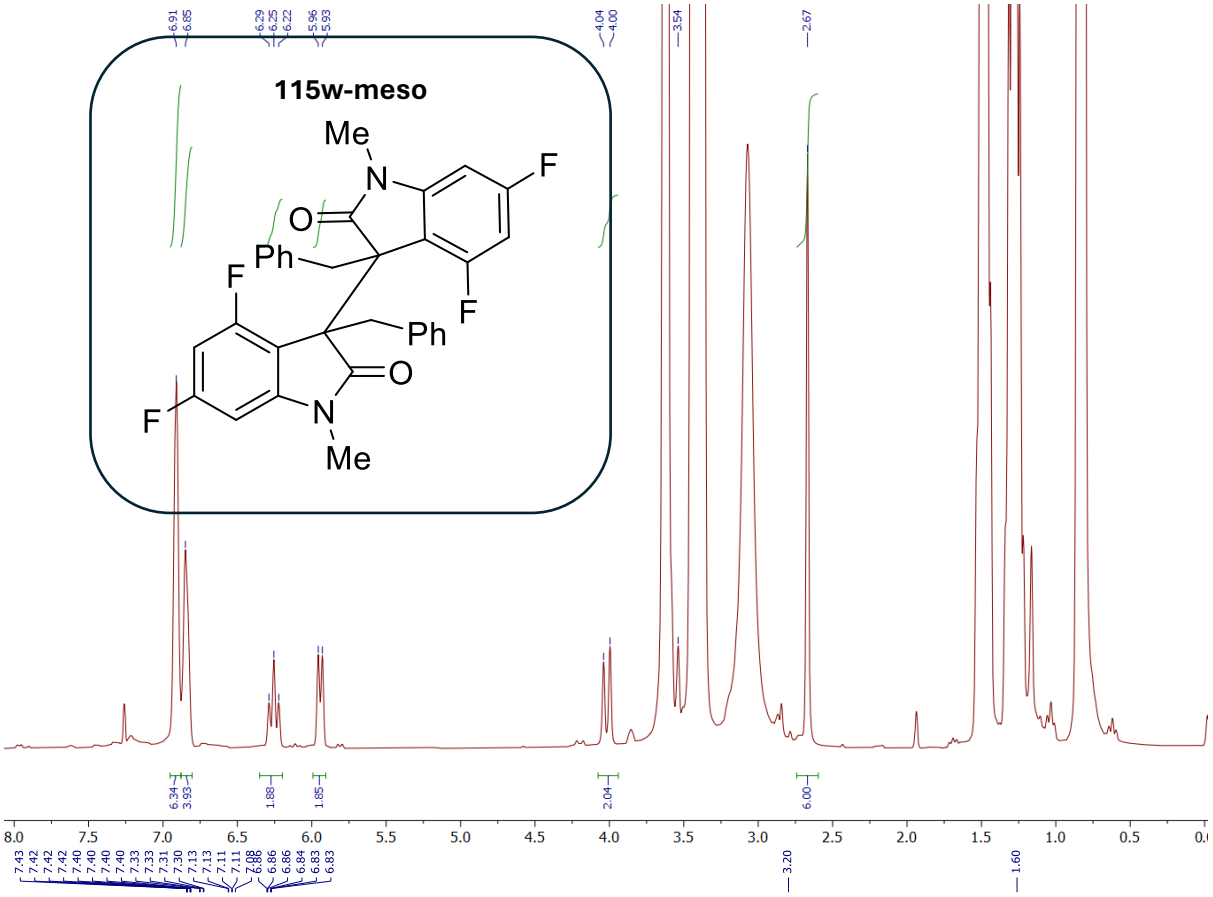
115w-meso
Me
N
O
Ph
F
F
F
Ph
O
N
F
Me

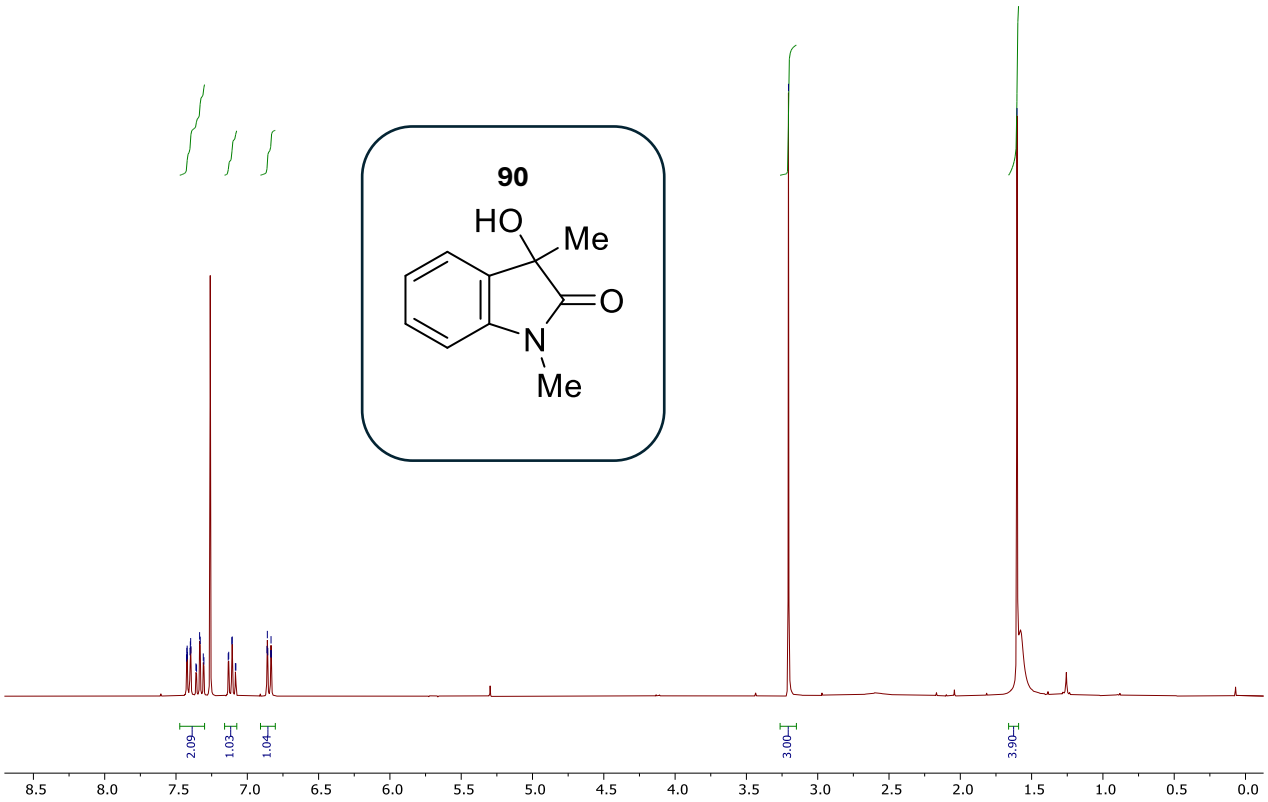
90
HO
Me
O
N
Me

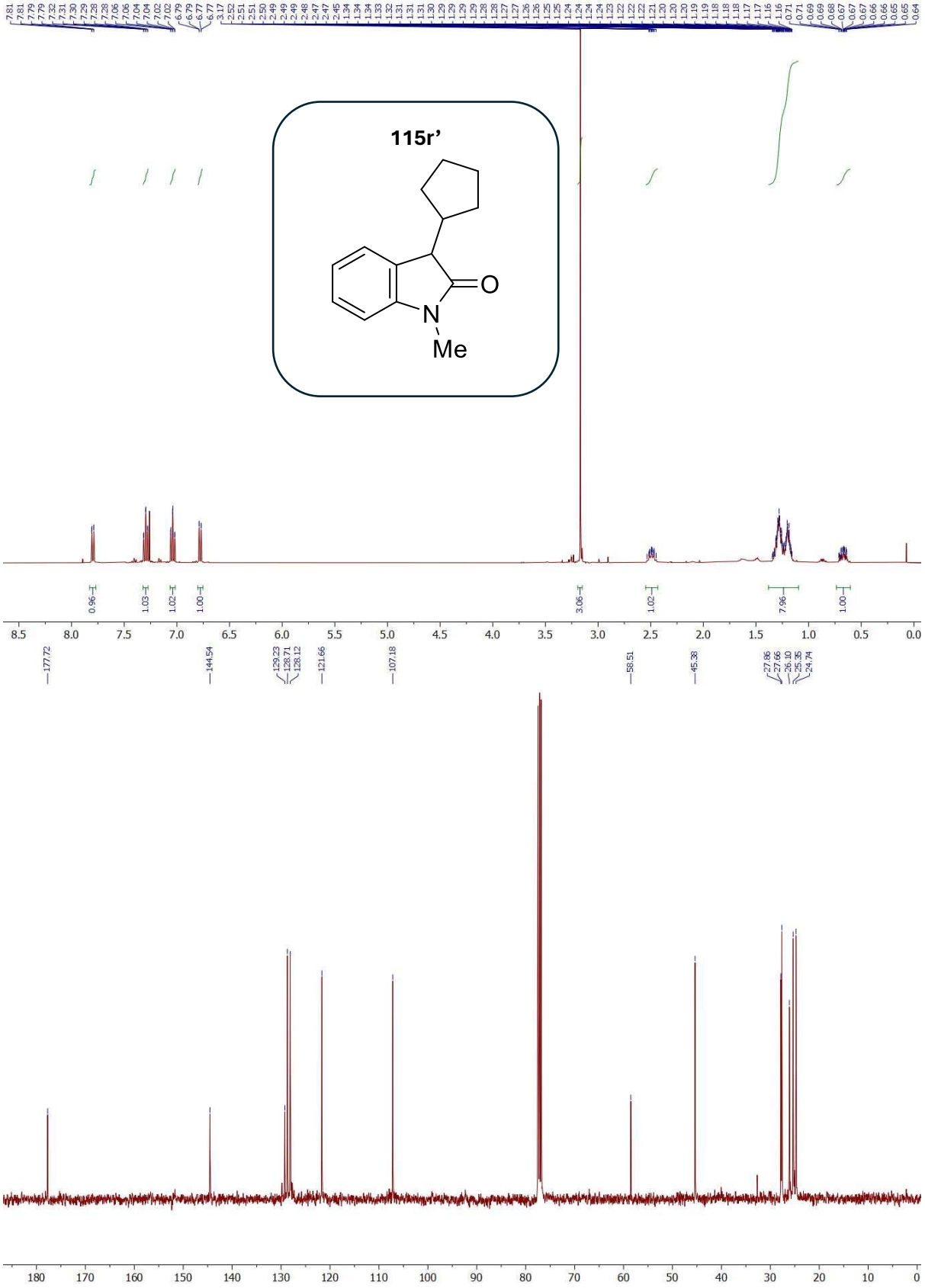
115r'
O
N
Me

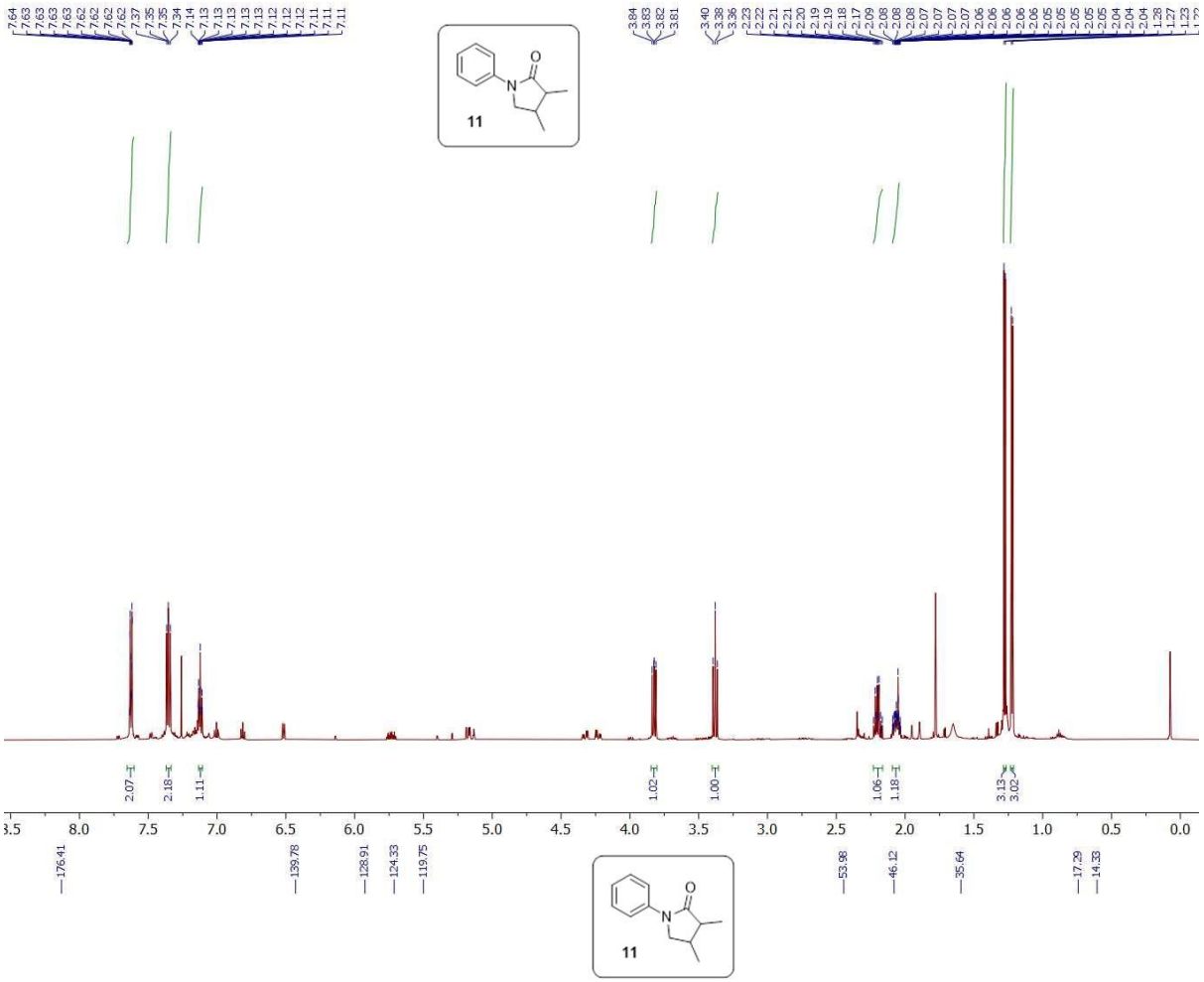
11

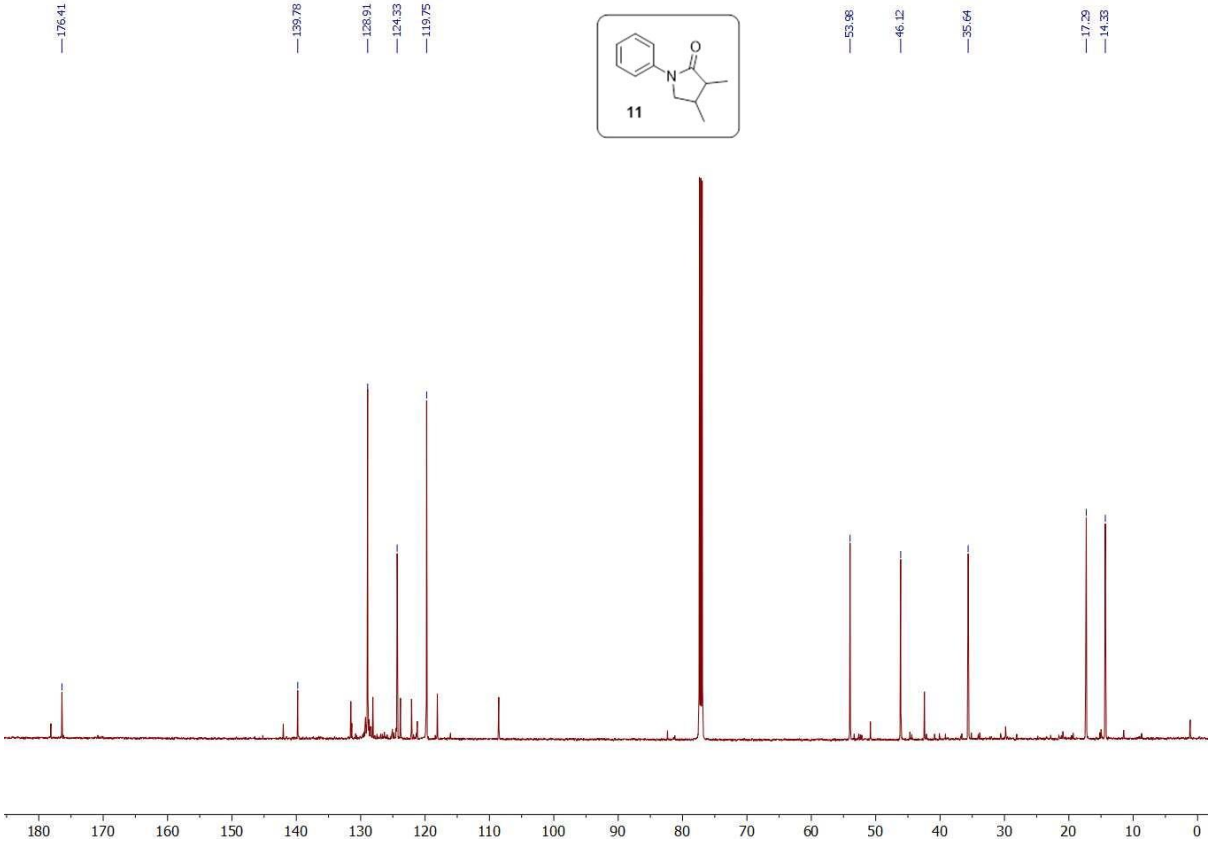
11

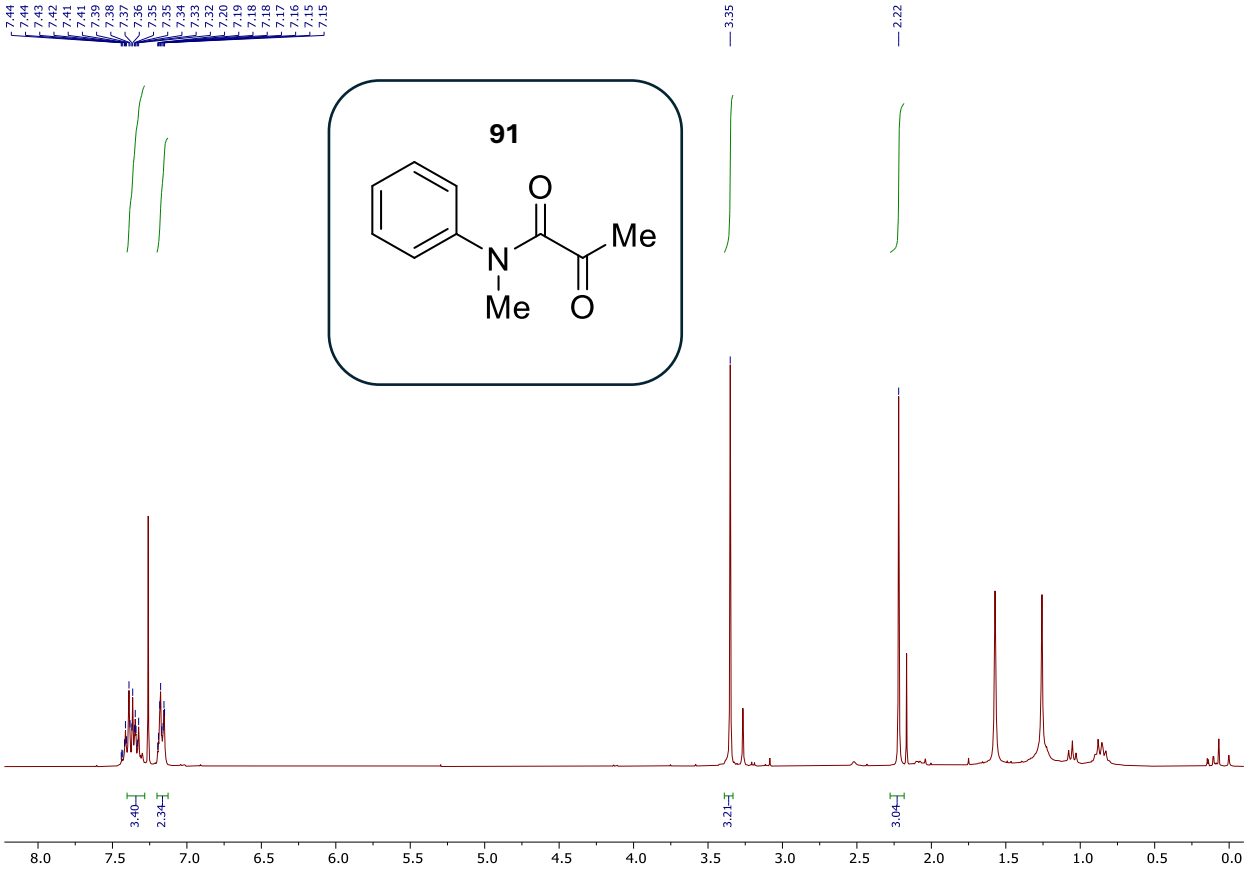
91
O
Me
N
Me
O
7.44
7.44
7.43
7.42
7.41
7.41
7.39
7.38
7.37
7.36
7.35
7.35
7.34
7.33
7.32
7.20
7.19
7.18
7.18
7.17
7.16
7.15
7.15
3.35
2.22
3.40
2.34
3.21
3.04
8.0
7.5
7.0
6.5
6.0
5.5
5.0
4.5
4.0
3.5
3.0
2.5
2.0
1.5
1.0
0.5
0.0

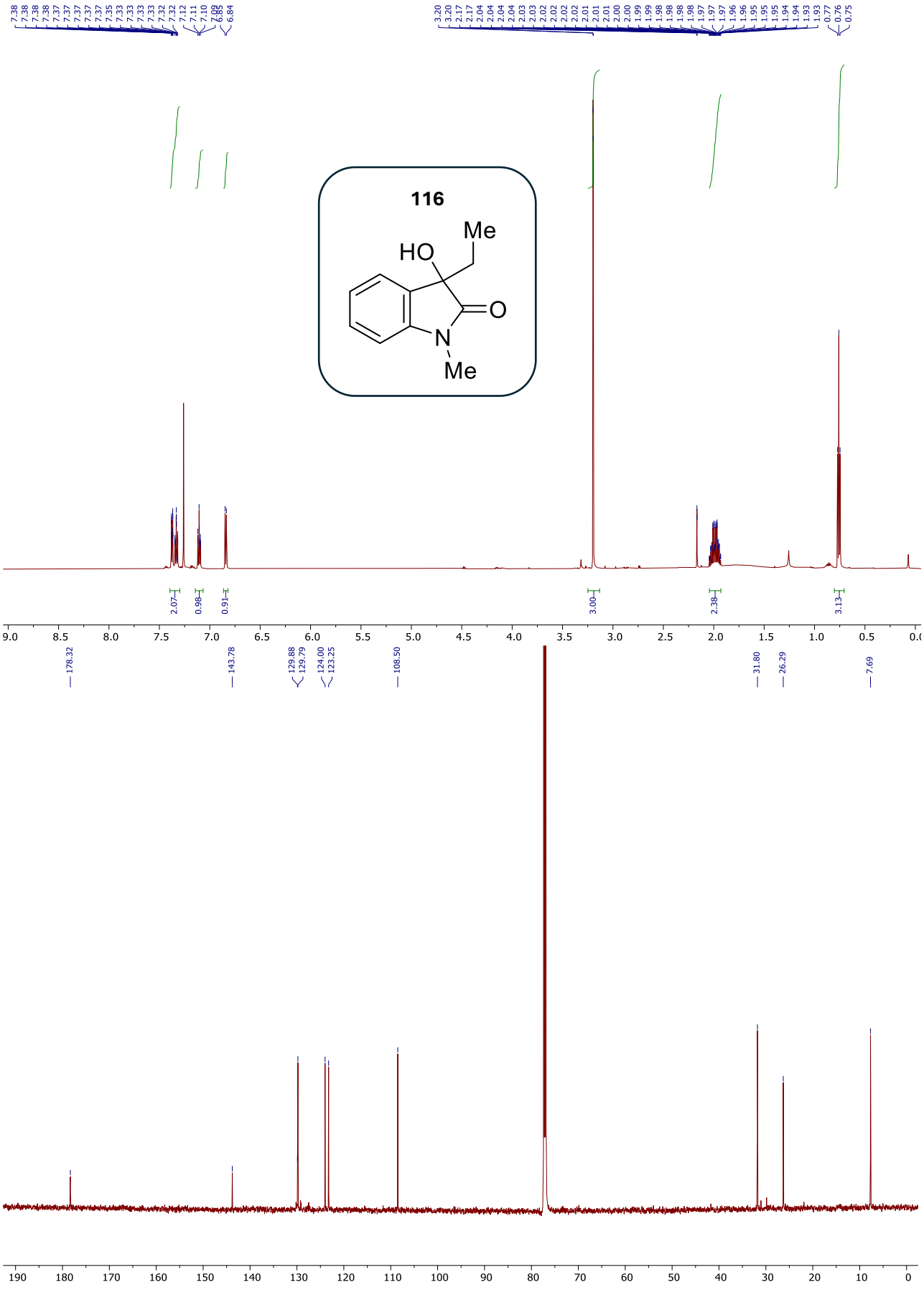
116
Me
HO
O
N
Me

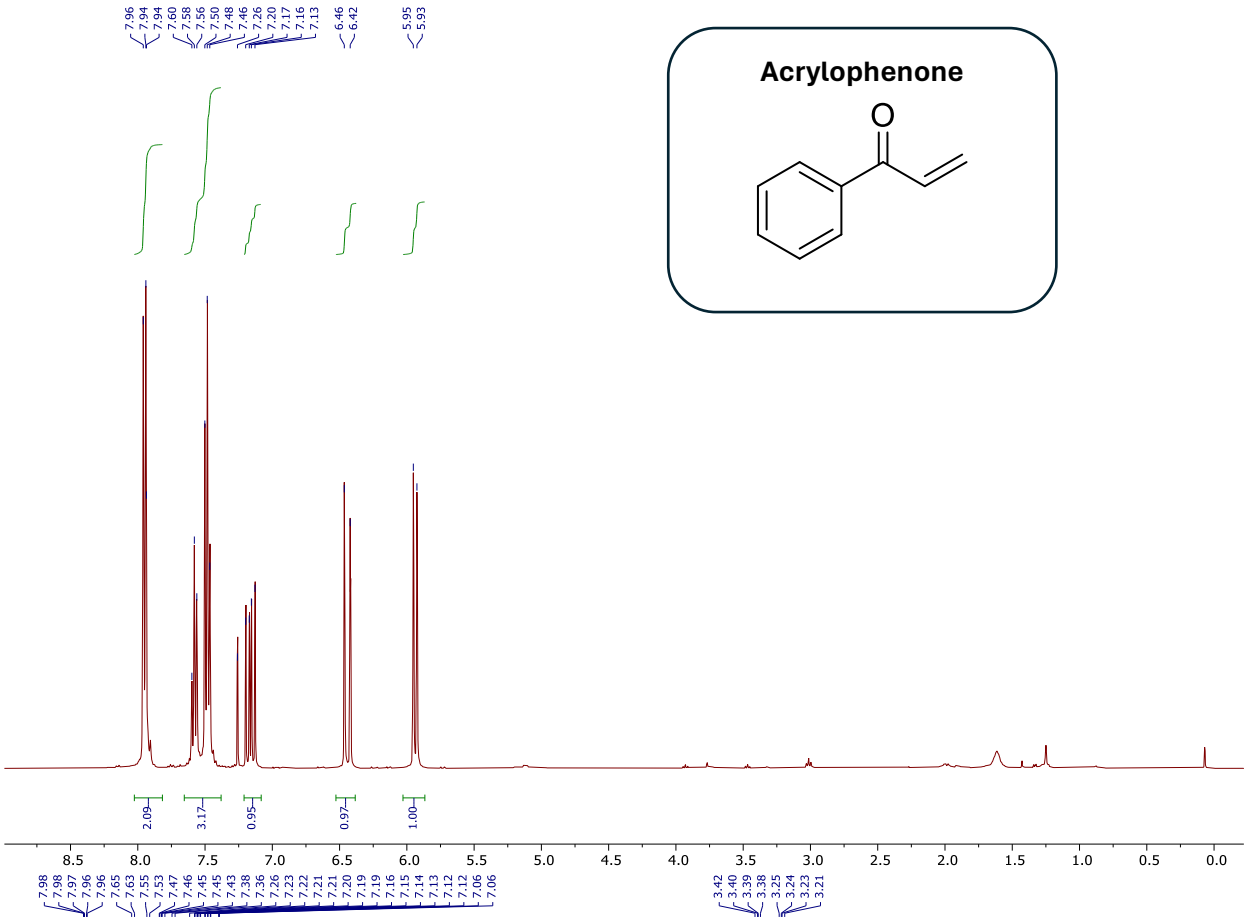
Acrylophenone
O

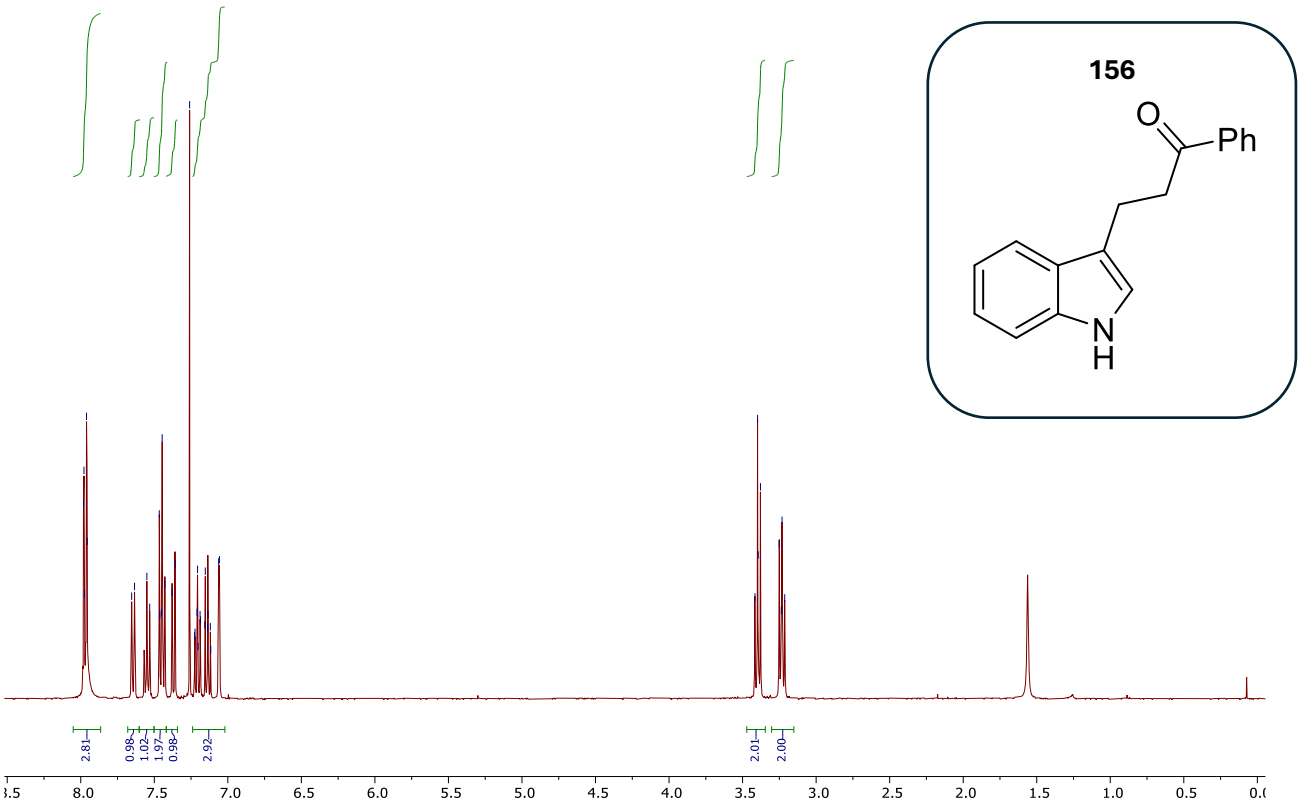
156
O
Ph
N
H

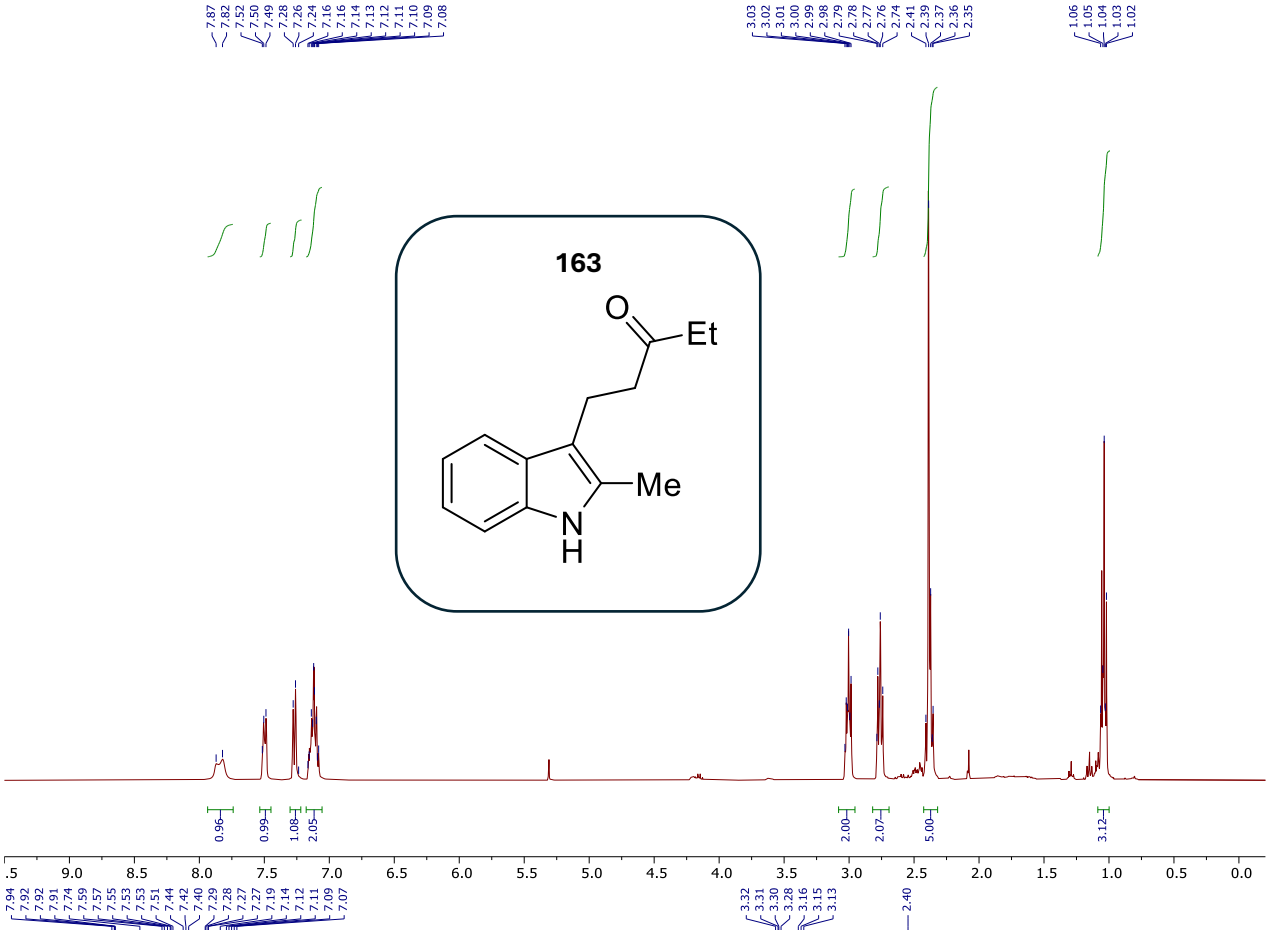
163
O
Et
Me
N
H

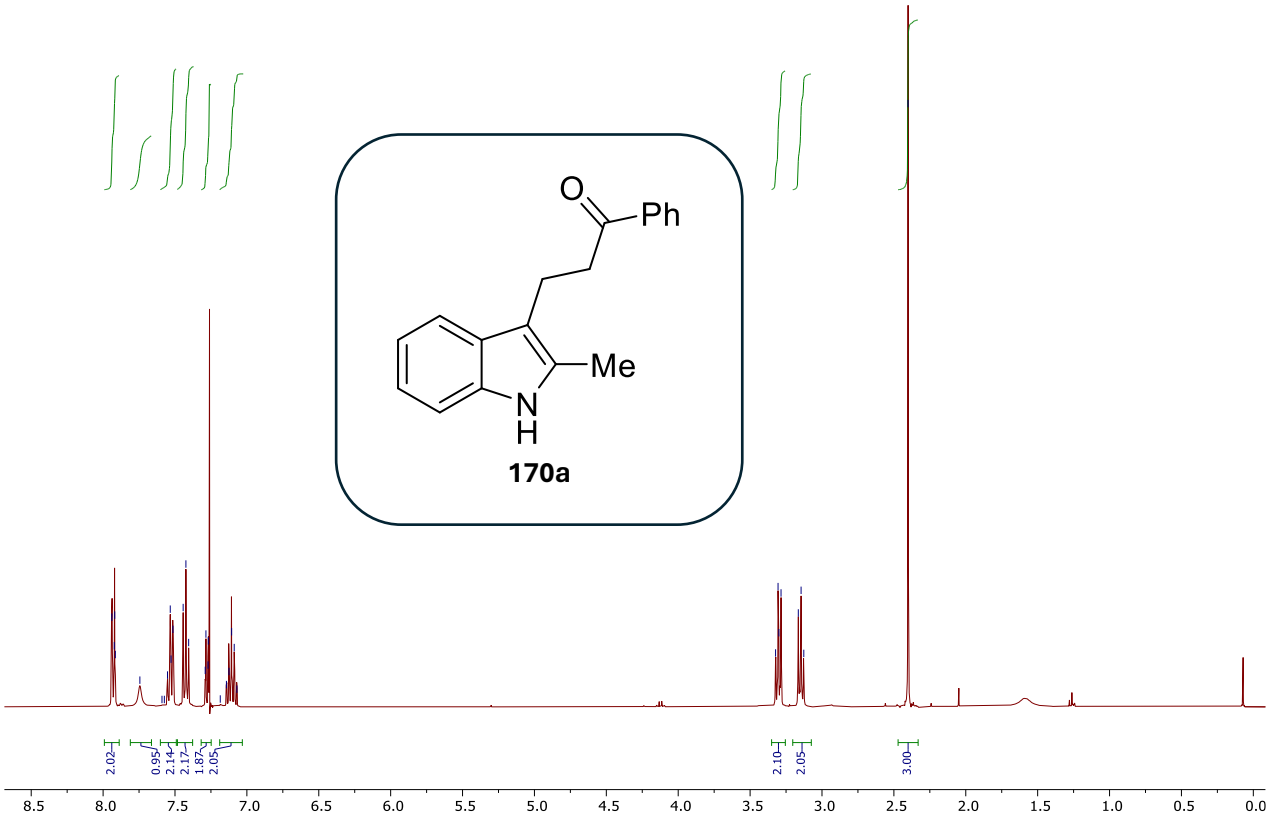
O
Ph
Me
N
H
170a

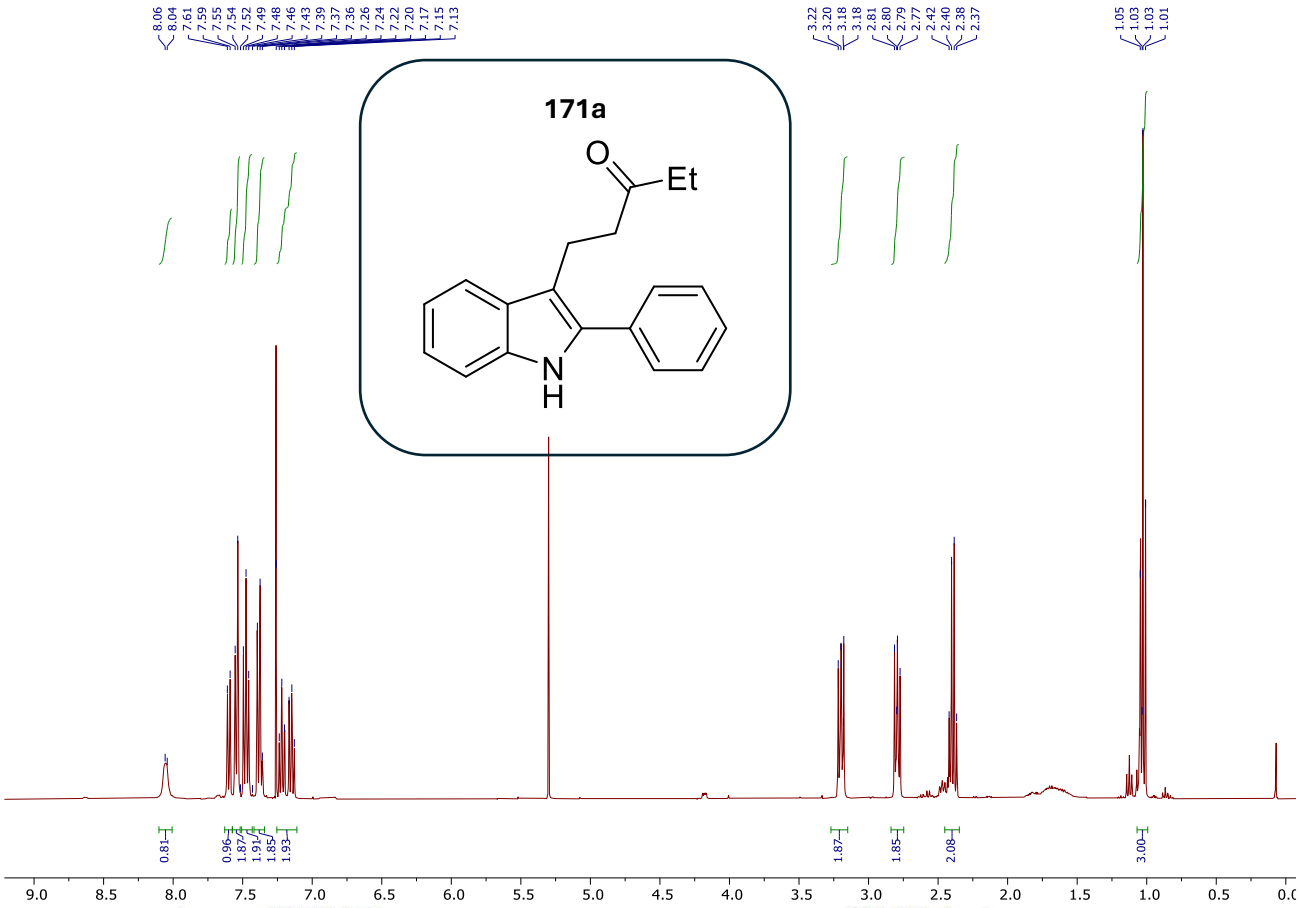
171a
O
Et
N
H

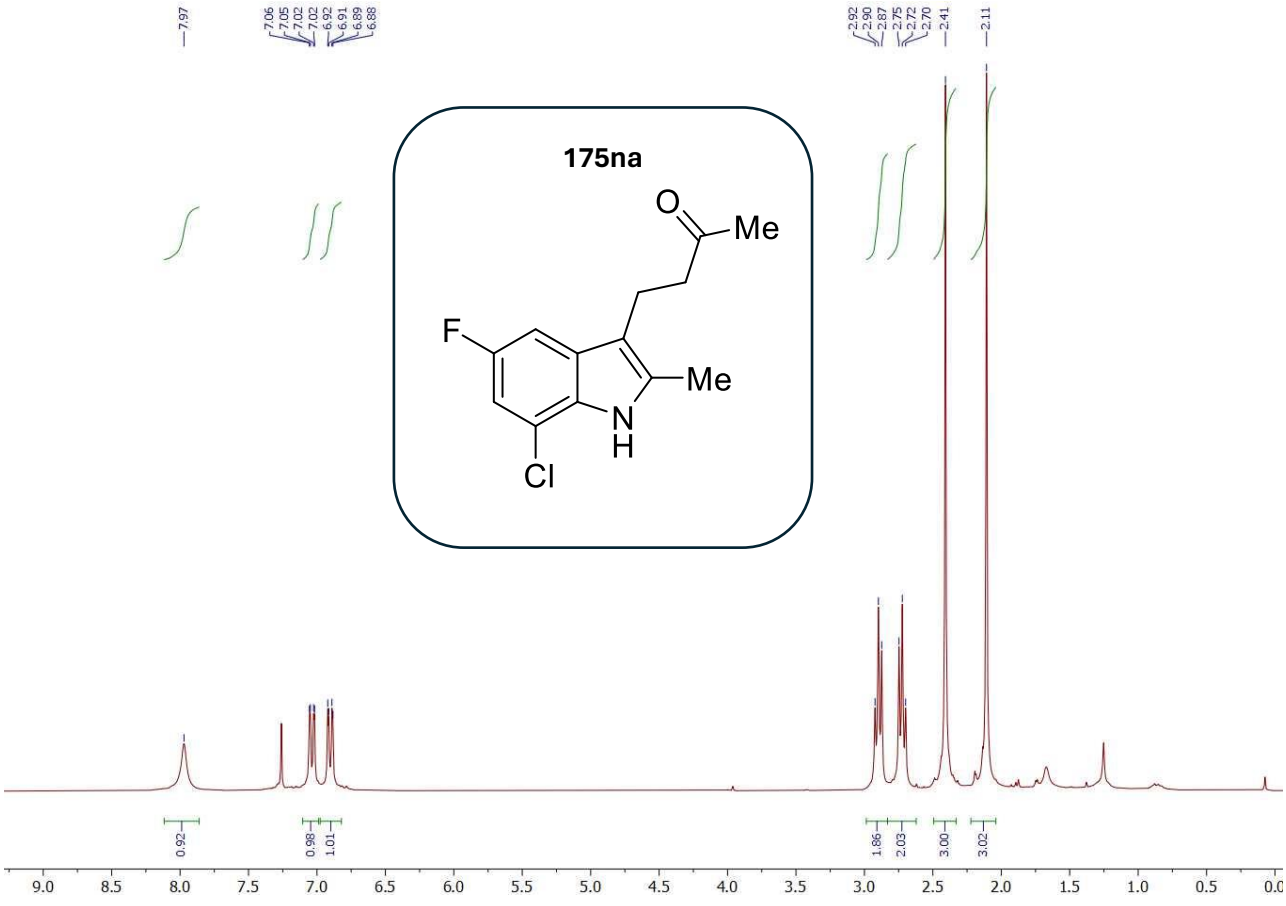
175na
O
Me
F
Me
N
H
Cl

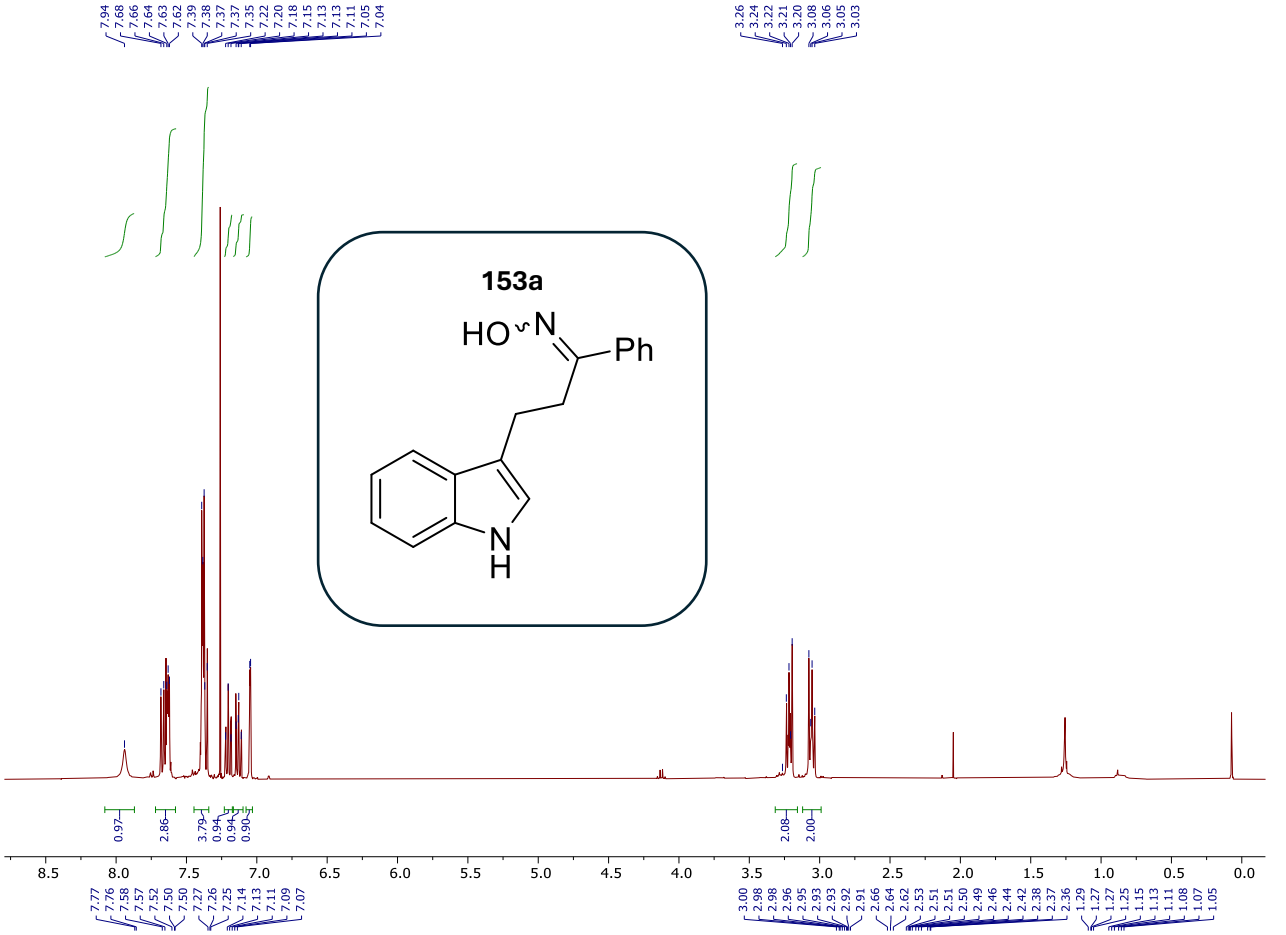
153a
HO
N
Ph
N
H

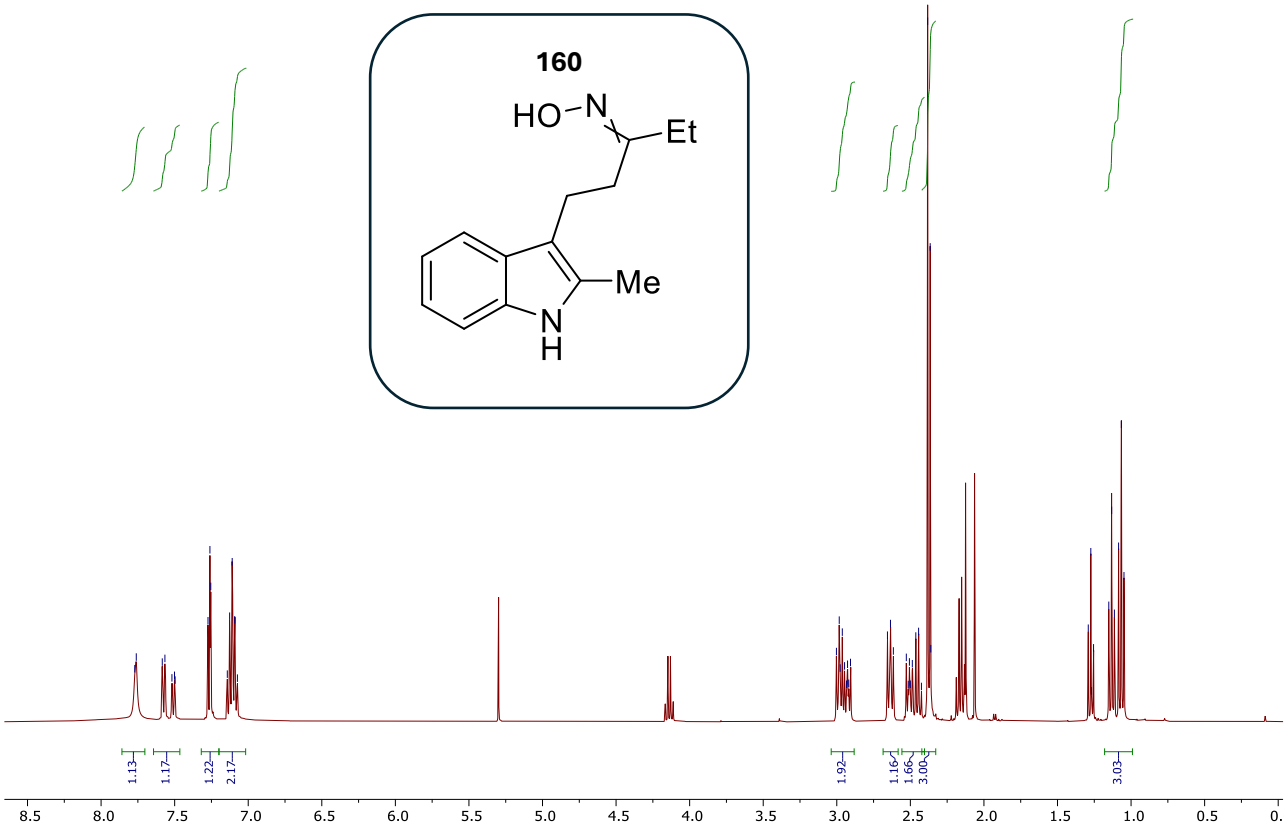
160
HO
N
Et
Me
N
H

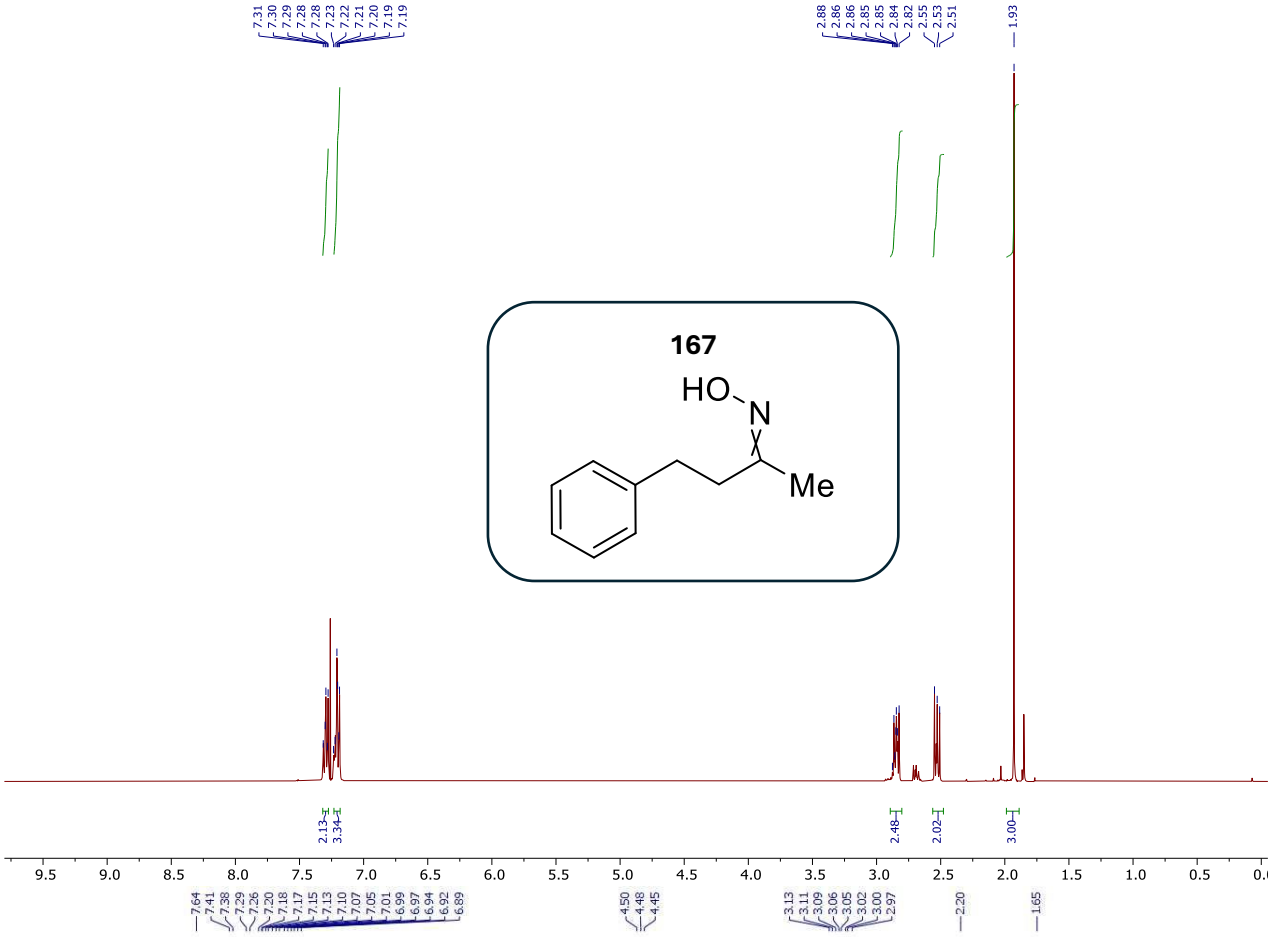
167
HO
N
Me

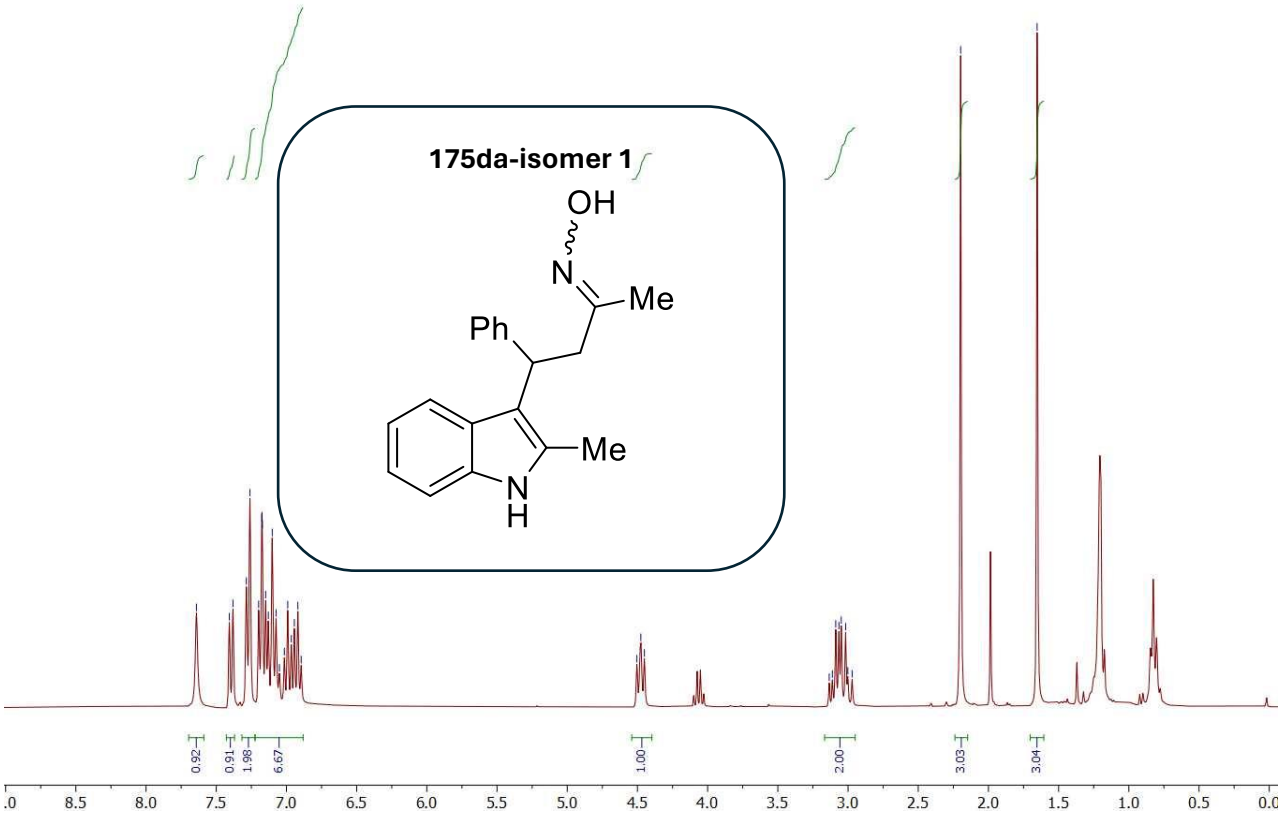
175da-isomer 1
OH
N
Me
Ph
Me
N
H

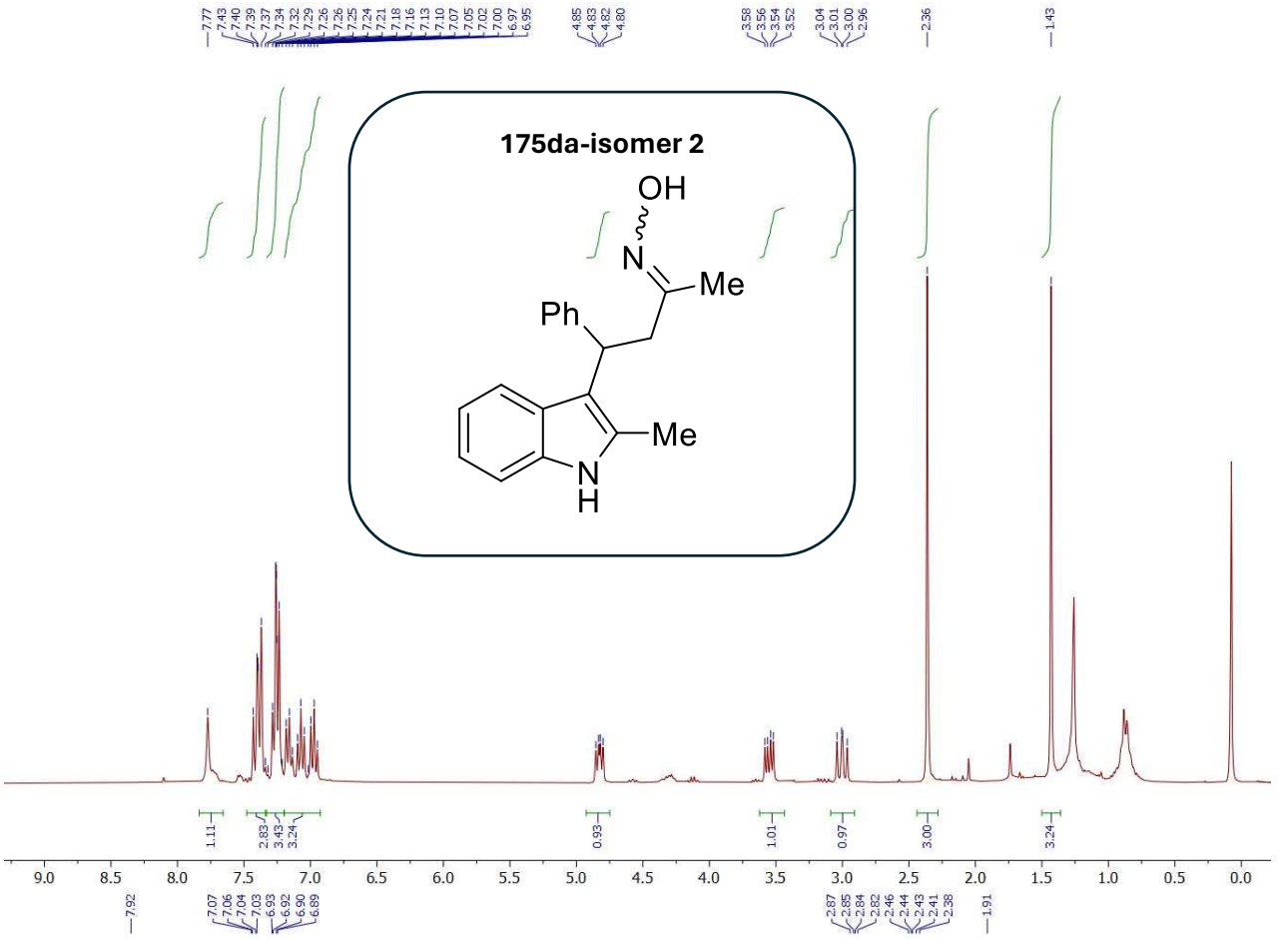
175da-isomer 2
OH
N
Me
Ph
Me
N
H

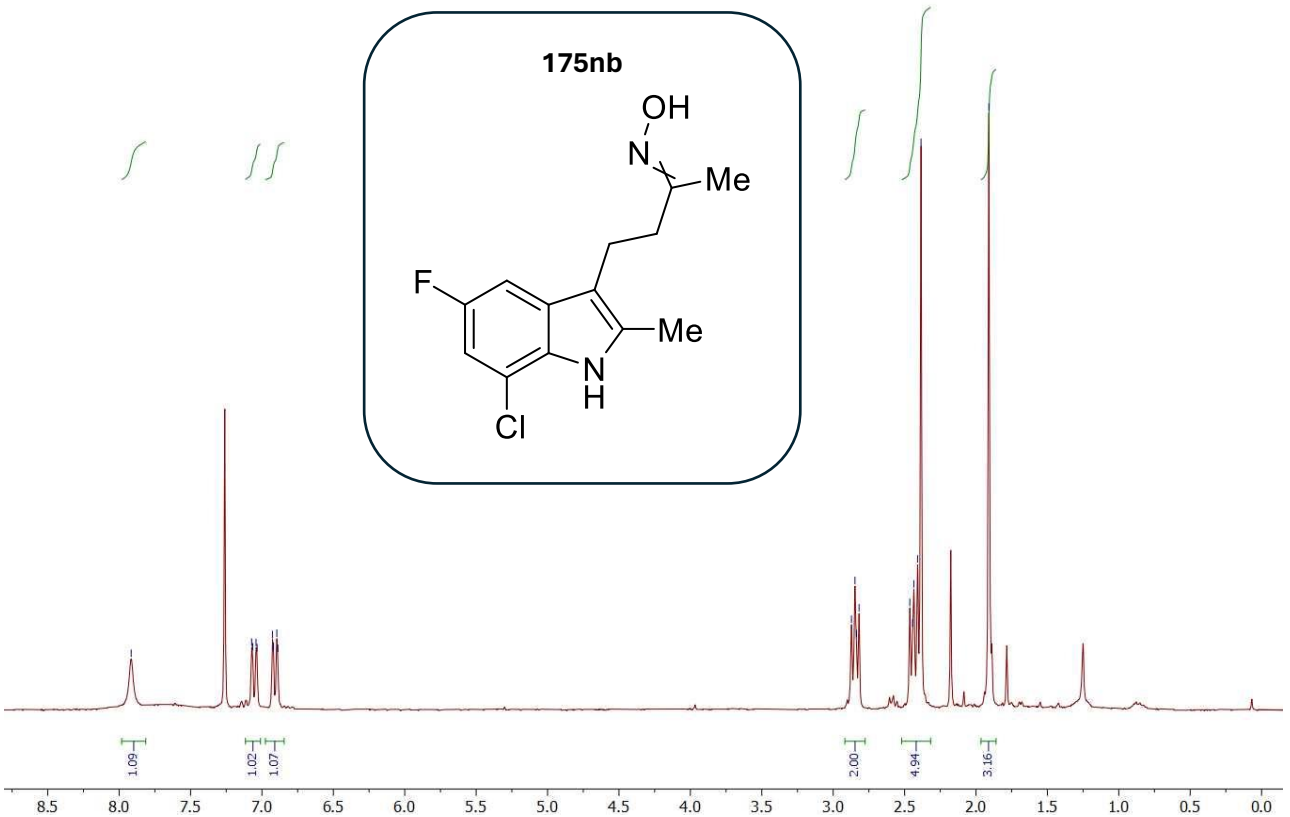
175nb
OH
N
Me
F
Me
N
H
Cl

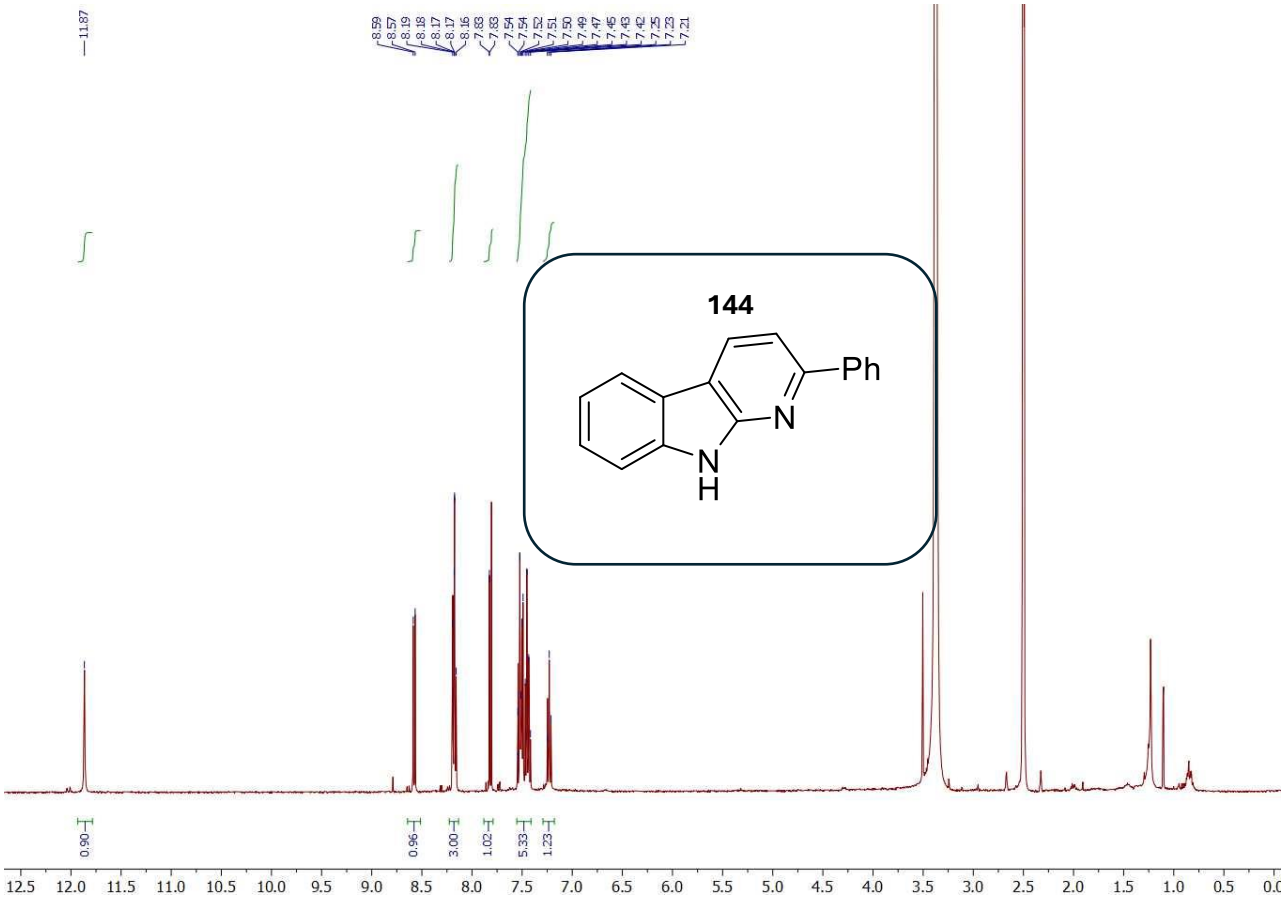
144
Ph
N
N
H

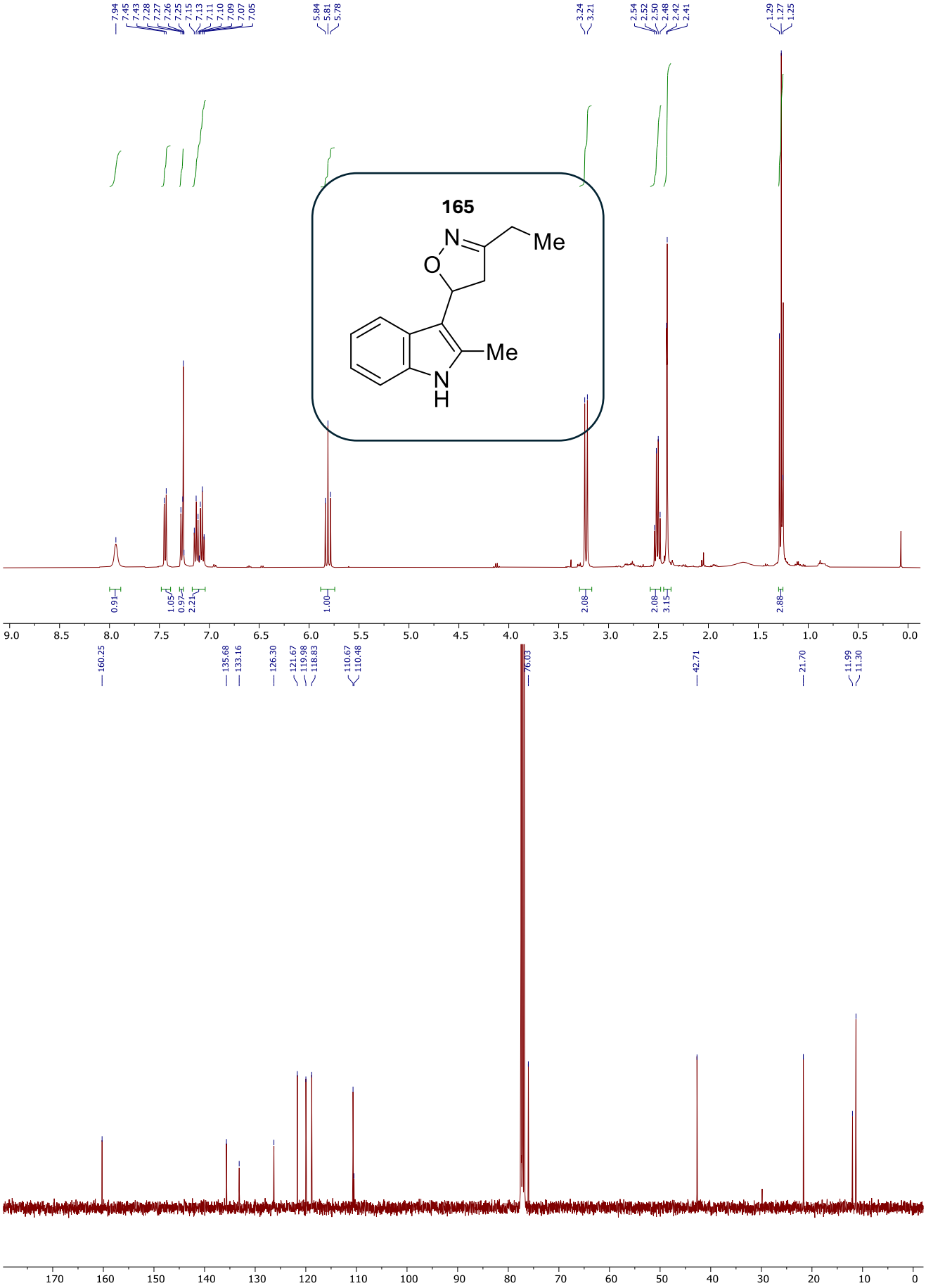
7.94
7.45
7.43
7.28
7.27
7.26
7.25
7.15
7.13
7.11
7.10
7.09
7.07
7.05
5.84
5.81
5.78
3.24
3.21
2.54
2.52
2.50
2.48
2.42
2.41
1.29
1.27
1.25
165
N
O
Me
Me
N
H
0.91
1.05
0.97
2.21
1.00
2.08
2.08
3.15
2.88
9.0
8.5
8.0
7.5
7.0
6.5
6.0
5.5
5.0
4.5
4.0
3.5
3.0
2.5
2.0
1.5
1.0
0.5
0.0
160.25
135.68
133.16
126.30
121.67
119.98
118.83
110.67
110.48
76.03
42.71
21.70
11.99
11.30
170
160
150
140
130
120
110
100
90
80
70
60
50
40
30
20
10
0

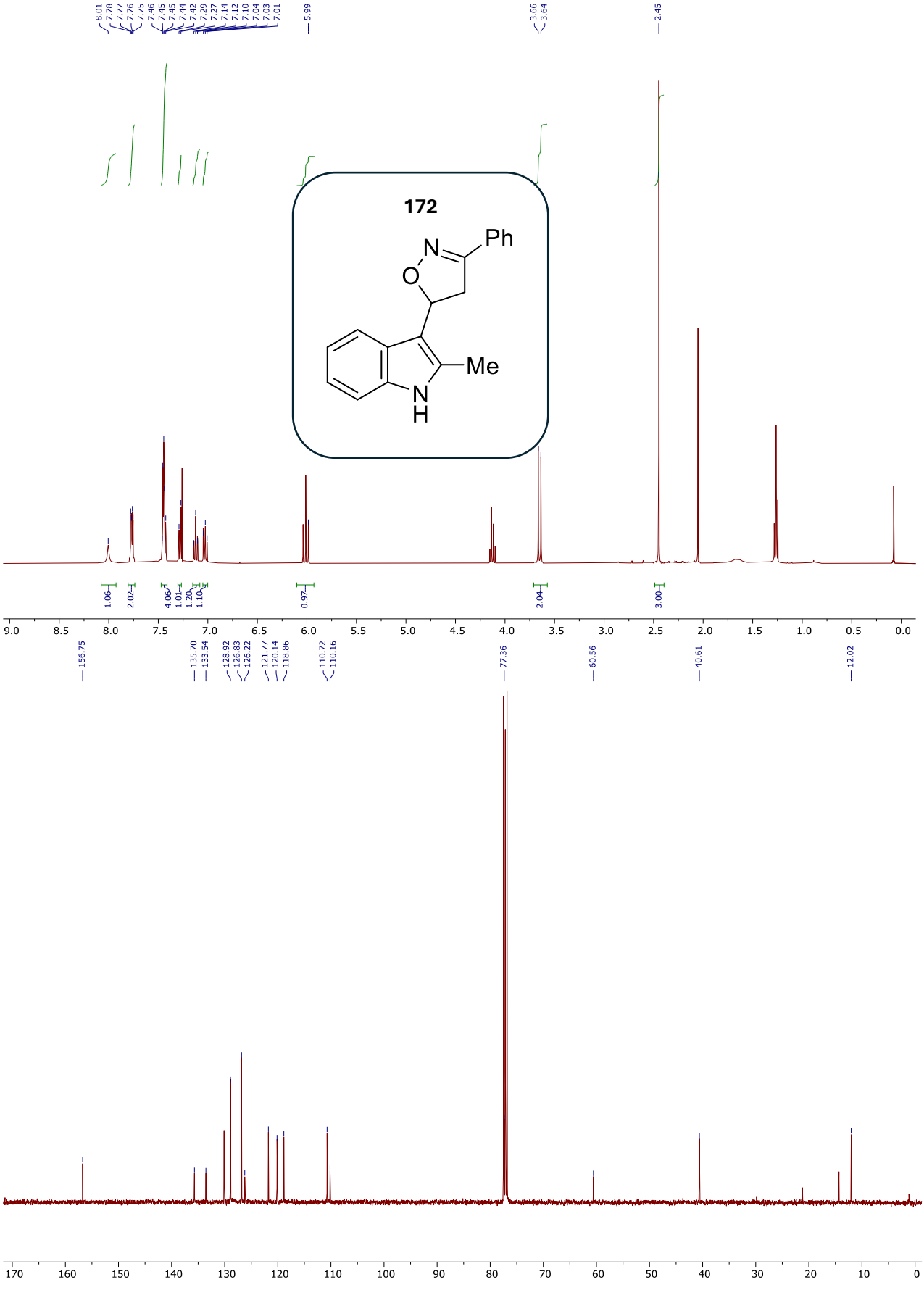
8.01
7.78
7.77
7.76
7.75
7.46
7.45
7.45
7.44
7.42
7.29
7.27
7.14
7.12
7.10
7.04
7.03
7.01
5.99
3.66
3.64
2.45
172
Ph
N
O
Me
N
H
1.06
2.02
4.06
1.01
1.20
1.10
0.97
2.04
3.00
9.0
8.5
8.0
7.5
7.0
6.5
6.0
5.5
5.0
4.5
4.0
3.5
3.0
2.5
2.0
1.5
1.0
0.5
0.0
156.75
135.70
133.54
128.92
126.83
126.22
121.77
120.14
118.86
110.72
110.16
77.36
60.56
40.61
12.02
170
160
150
140
130
120
110
100
90
80
70
60
50
40
30
20
10
0

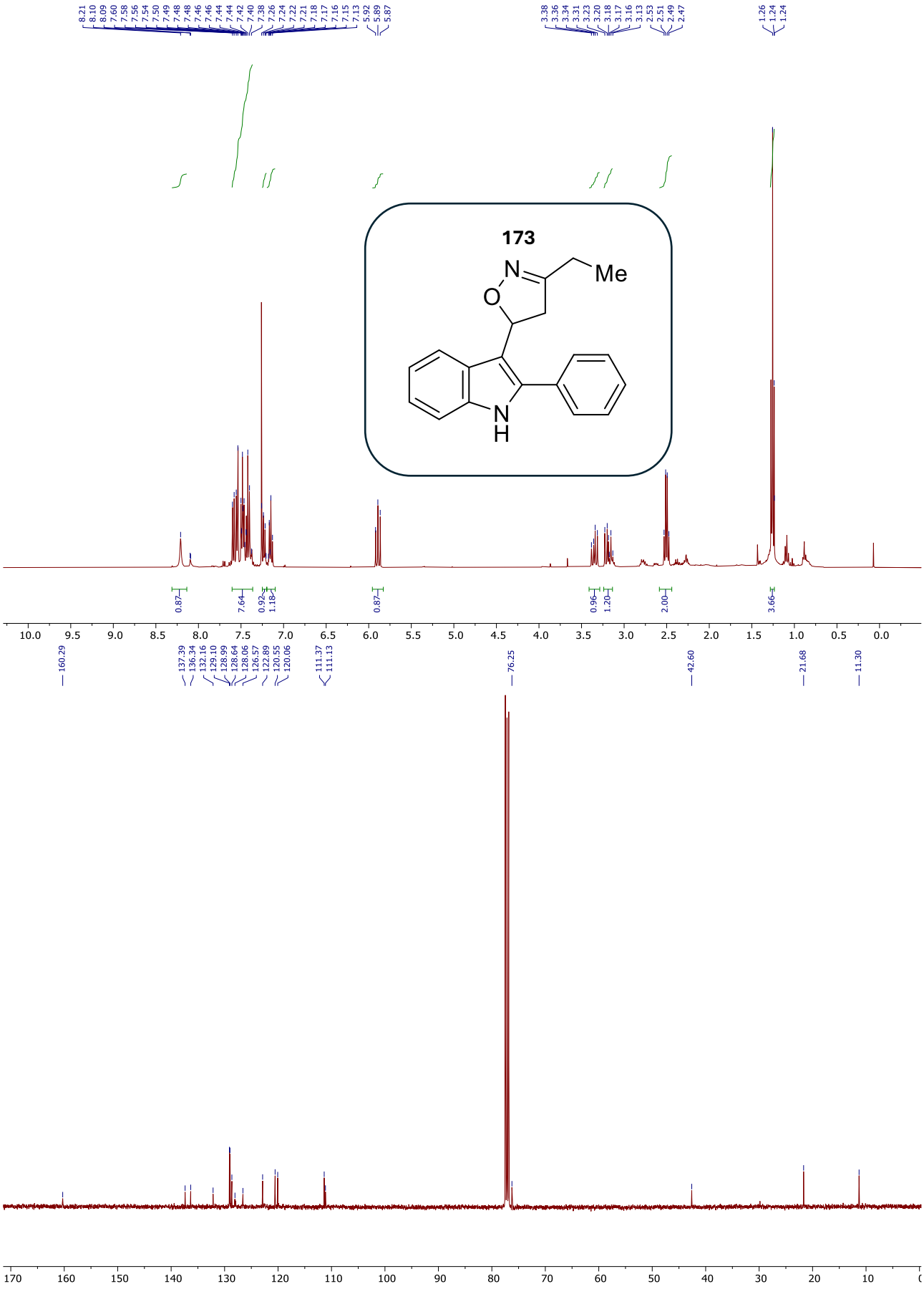
173
N
O
Me
N
H

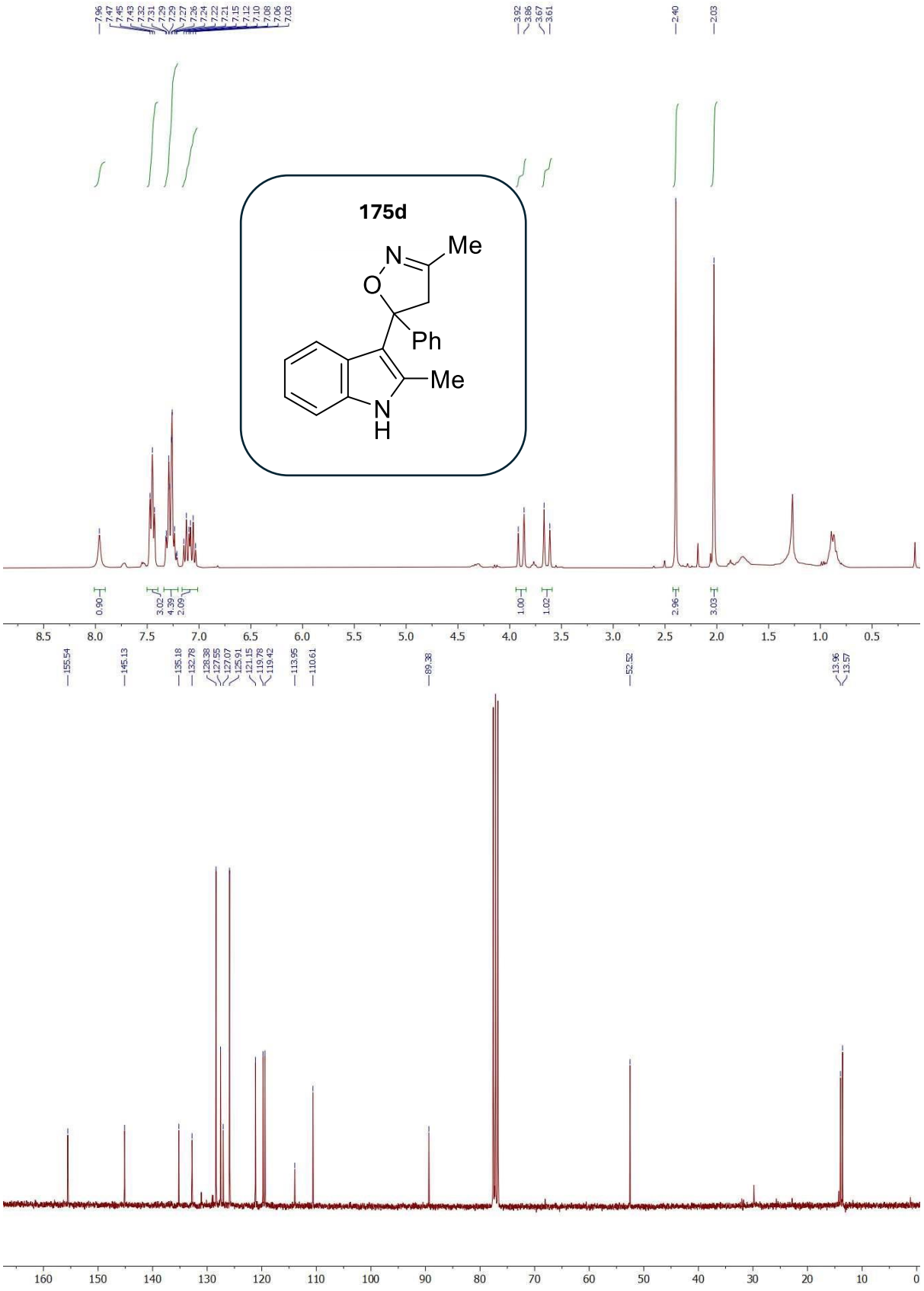
175d
Me
N
O
Ph
Me
N
H

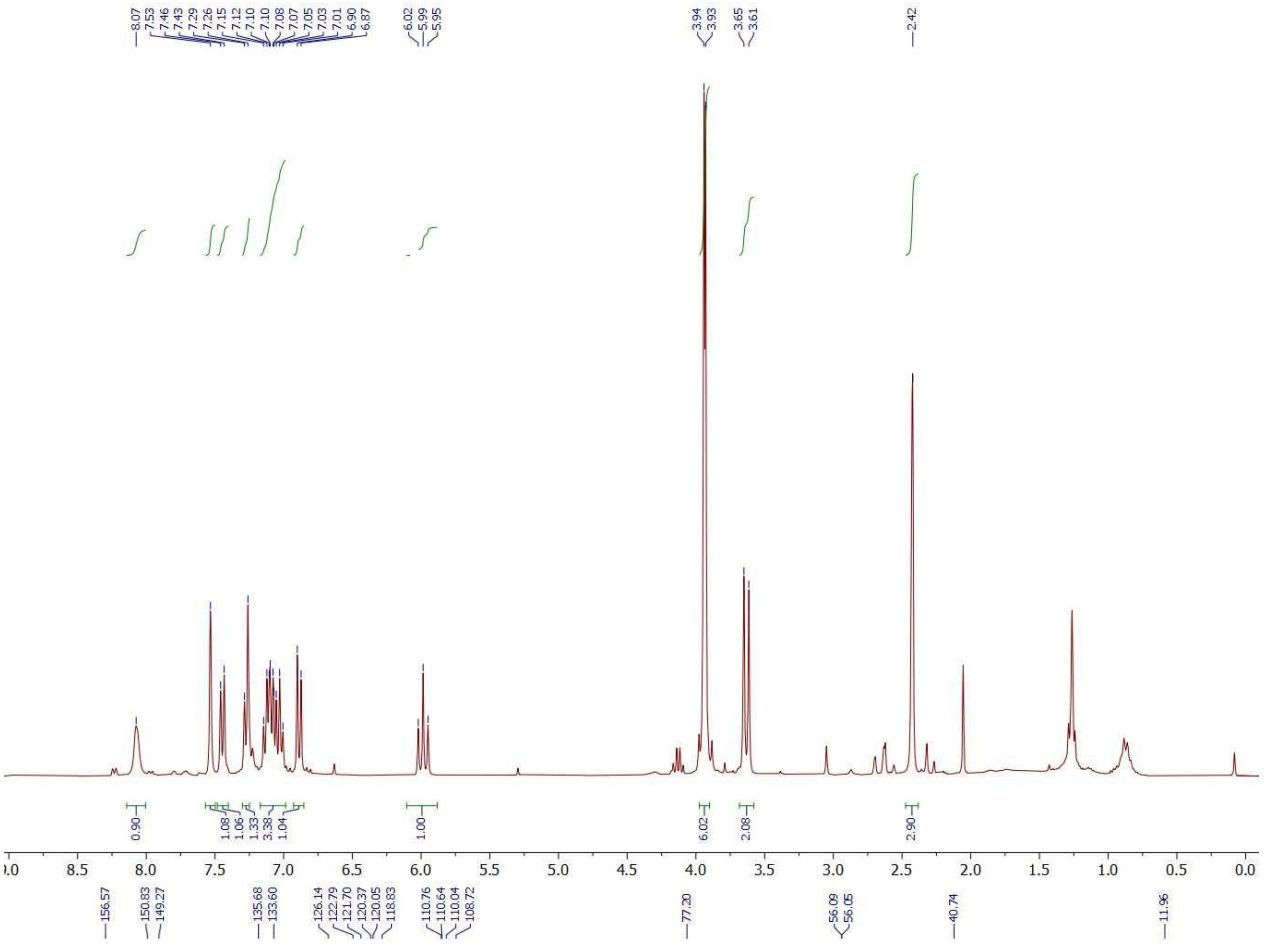
8.07
7.53
7.46
7.43
7.29
7.26
7.15
7.12
7.10
7.10
7.08
7.07
7.05
7.03
7.01
6.90
6.87
6.02
5.99
5.95
3.94
3.93
3.65
3.61
2.42
0.90
1.08
1.06
1.33
3.38
1.04
1.00
6.02
2.08
2.90
156.57
150.83
149.27
135.68
133.60
126.14
122.79
121.70
120.37
120.05
118.83
110.76
110.64
110.04
108.72
77.20
56.09
56.05
40.74
11.96

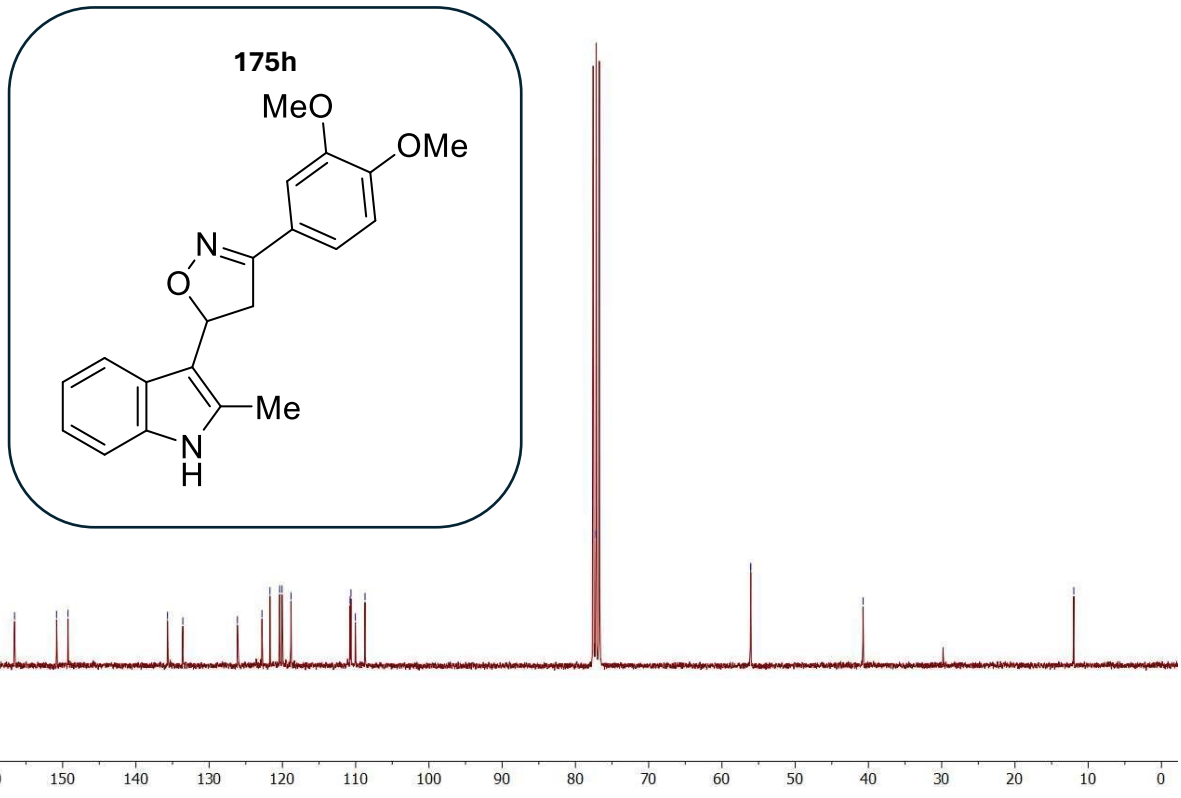
175h
MeO
OMe
N
O
Me
N
H

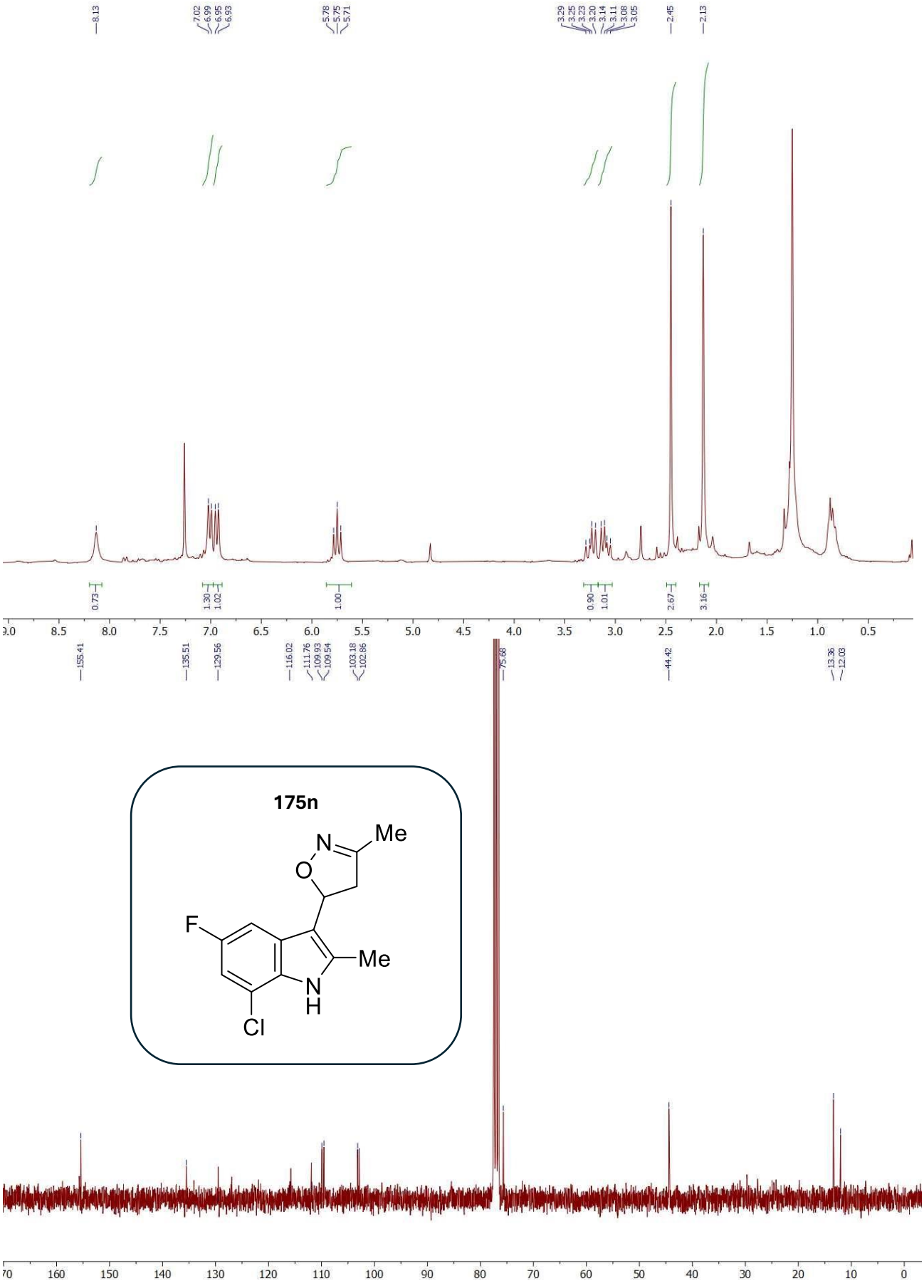
8.13
7.02
6.99
6.95
6.93
5.78
5.75
5.71
3.29
3.25
3.23
3.20
3.14
3.11
3.08
3.05
2.45
2.13
0.73
1.30
1.02
1.00
0.90
1.01
2.67
3.16
155.41
135.51
129.56
116.02
111.76
109.93
109.54
103.18
102.86
75.68
44.42
13.36
12.03
175n
N
Me
O
F
Me
N
H
Cl